UNIVERSITY OF TRENTO
Department of Industrial Engineering
XXXII cycle

Doctoral School in Materials, Mechatronics and Systems Engineering

Multifunctional polymer composites for thermal energy storage and thermal management

Giulia Fredi

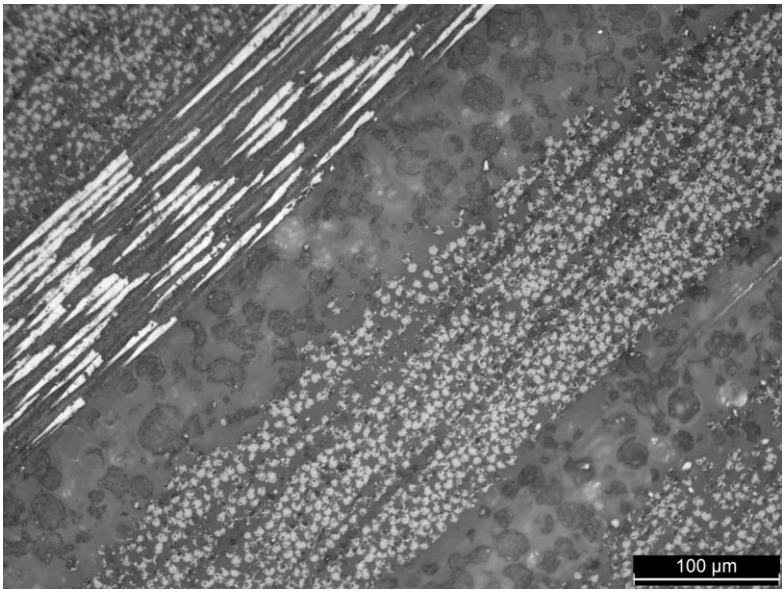

June 2020

MULTIFUNCTIONAL POLYMER COMPOSITES FOR THERMAL ENERGY STORAGE AND THERMAL MANAGEMENT

Giulia Fredi

E-mail: giulia.fredi@unitn.it/giuliafredi@hotmail.it

Approved by:

Prof. Alessandro Pegoretti, Advisor
Department of Industrial Engineering
University of Trento, Italy.

Prof. Luca Fambri, Advisor
Department of Industrial Engineering
University of Trento, Italy.

Ph.D. Commission:

Prof. Leif E. Asp ,
Department of Industrial and Materials Science
Chalmers University of Technology, Sweden.

Prof. Miroslav Šlouf ,
Department of Polymer Morphology
Institute of Macromolecular Chemistry, Czech Academy of Sciences (IMC), Czech Republic.

Prof. Andrea Dorigato
Department of Industrial Engineering
University of Trento, Italy.

University of Trento,

Department of Industrial Engineering

June 5, 2020

University of Trento - Department of Industrial Engineering

Doctoral Thesis

Giulia Fredi - 2020
Published in Trento (Italy) by University of Trento

Cover image: optical microscope micrograph of the polished cross-section of a carbon fiber laminate containing paraffin microcapsules and a reactive acrylic thermoplastic matrix.

To my family

Abstract

Thermal energy storage (TES) consists in storing heat for a later use, thereby reducing the gap between energy availability and demand. The most diffused materials for TES are the organic solid-liquid phase change materials (PCMs), such as paraffin waxes, which accumulate and release a high amount of latent heat through a solid-liquid phase change, at a nearly constant temperature. To avoid leakage and loss of material, PCMs are either encapsulated in inert shells or shape-stabilized with porous materials or a nanofiller network. Generally, TES systems are only a supplementary component added to the main structure of a device, but this could unacceptably rise weight and volume of the device itself. In the applications where weight saving and thermal management are both important (e.g. automotive, portable electronics), it would be beneficial to embed the heat storage/management in the structural components.

The aim of this thesis is to develop polymer composites that combine a polymer matrix, a PCM and a reinforcing agent, to reach a good balance of mechanical and TES properties. Since this research topic lacks a systematic investigation in the scientific literature, a wide range of polymer/PCM/reinforcement combinations were studied in this thesis, to highlight the effect of PCM introduction in a broad range of matrix/reinforcement combinations and to identify the best candidates and the key properties and parameters, in order to set guidelines for the design of these materials.

The thesis in divided in eight Chapters. Chapter I and II provide the introduction and the theoretical background, while Chapter III details the experimental techniques applied on the prepared composites. The results and discussion are then described in Chapters IV-VII. Chapter IV presents the results of PCM-containing composites having a thermoplastic matrix. First, polyamide 12 (PA12) was melt-compounded with either a microencapsulated paraffin (MC) or a paraffin powder shape-stabilized with carbon nanotubes (ParCNT), and these mixtures were used as matrices to produce thermoplastic laminates with a glass fiber fabric via hot-pressing. MC was proven more suitable to be combined with PA12 than ParCNT, due to the higher thermal resistance. However, also the MC were considerably damaged by melt compounding and the two hot-pressing steps, which caused paraffin leakage and degradation, as demonstrated by the relative enthalpy lower than 100 %. Additionally, the PCM introduction decreased the mechanical properties of PA12 and the tensile strength of the laminates, but for the laminates containing MC the elastic modulus and the strain at break were not negatively affected by the PCM. Higher TES properties were achieved with the production of a semi-structural composite that combined PA12, MC and discontinuous carbon fibers. For example, the composite with 50 wt% of MC and 20 wt% of milled carbon fibers exhibited a total melting enthalpy of 60.4 J/g and an

increase in elastic modulus of 42 % compared to the neat PA. However, the high melt viscosity and shear stresses developed during processing were still responsible for a not negligible PCM degradation, as also evidenced by dynamic rheological tests. Further increases in the mechanical and TES properties were achieved by using a reactive thermoplastic matrix, which could be processed as a thermosetting polymer and required considerably milder processing conditions that did not cause PCM degradation. MC was combined with an acrylic thermoplastic resin and the mixtures were used as matrices to produce laminates with a bidirectional carbon fabric, and for these laminates the melting enthalpy increased with the PCM weight fraction and reached 66.8 J/g. On the other hand, the increased PCM fraction caused a rise in the matrix viscosity and so a decrease in the fiber volume fraction in the final composite, thereby reducing the elastic modulus and flexural strength. Dynamic-mechanical investigation evidenced the PCM melting as a decreasing step in E'; its amplitude showed a linear trend with the melting enthalpy, and it was almost completely recovered during cooling, as evidenced by cyclic DMA tests.

Chapter V presents the results of PCM-containing thermosetting composites. A further comparison between MC and ParCNT was performed in a thermosetting epoxy matrix. First, ParCNT was mixed with epoxy and the mixtures were used as matrices to produce laminates with a bidirectional carbon fiber fabric. ParCNT kept its thermal properties also in the laminates, and the melting enthalpy was 80-90 % of the expected enthalpy. Therefore, ParCNT performed better in thermosetting than in thermoplastic matrices due to the milder processing conditions, but the surrounding matrix still partially hindered the melting-crystallization process. Therefore, epoxy was combined with MC, but the not optimal adhesion between the matrix and the MC shell caused a considerable decrease in mechanical strength, as also demonstrated by the fitting with the Nicolais-Narkis and Pukanszky models, both of which evidenced scarce adhesion and considerable interphase weakness. However, the Halpin-Tsai and Lewis-Nielsen models of the elastic modulus evidenced that at low deformations the interfacial interaction is good, and this also agrees with the data of thermal conductivity, which resulted in excellent agreement with the Pal model calculated considering no gaps at the interface. These epoxy/MC mixtures were then reinforced with either continuous or discontinuous carbon fibers, and their characterization confirmed that the processing conditions of an epoxy composite are mild enough to preserve the integrity of the microcapsules and their TES capability. For continuous fiber composites, the increase in the MC fraction impaired the mechanical properties mostly because of the decrease in the final fiber volume fraction and because the MC phase tends to concentrate in the interlaminar region, thereby lowering the interlaminar shear strength. On the other hand, a small amount of MC enhanced the mode I interlaminar fracture toughness (G_{ic} increases of up to 48 % compared to the neat epoxy/carbon laminate), as the MC introduced other energy dissipation mechanisms such as the debonding, crack deflection, crack pinning and micro-cracking, which added up to the fiber bridging.

Chapter VI introduces a fully biodegradable TES composite with a thermoplastic starch matrix, reinforced with thin wood laminae and containing poly(ethylene glycol) as the PCM. The wood laminae successfully acted as a multifunctional reinforcement as they also stabilized PEG in their inner pores (up to 11 wt% of the whole laminate) and prevent its leakage. Moreover PEG was proven to increase the stiffness and strength of the laminate, thereby making the mechanical and TES properties synergistic and not parasitic.

Finally, Chapter VII focused on PCM microcapsules. The synthesis of micro- and nano-capsules with an organosilica shell via a sol-gel approach clarified that the confinement in small domains and the interaction with the shell wall modified the crystallization behavior of the encapsulated PCM, as also evidenced by NMR and XRD studies and confirmed by DSC results. In the second part of Chapter VII, a coating of polydpamine (PDA) deposited onto the commercial microcapsules MC. The resulting PDA coating was proven effective to enhance the interfacial adhesion with an epoxy matrix, as evidenced by SEM micrographs. XPS demonstrated that the PDA layer was able to react with oxirane groups, thereby evidencing the possibility of forming covalent bond with the epoxy matrix during the curing step.

Table of contents

List of acronyms and symbols ..... **xiii**

Chapter I
Introduction and aim of the work **1**
1.1 Motivations and objectives **1**
1.2 Methodological approaches **3**
1.3 Thesis outline **4**

Chapter II
Background **7**
2.1 Introduction to thermal energy storage (TES) **7**
2.1.1 Importance of energy conservation and management 7
2.1.2 Energy storage technologies 8
2.1.3 Concept of thermal energy storage 8
2.1.4 Classification of TES technologies 10
2.1.4.1 Sensible heat storage (SH-TES) 11
2.1.4.2 Latent heat storage (LH-TES) 12
2.1.4.3 Thermochemical energy storage (TH-TES) 14
2.2 Latent heat TES and phase change materials (PCMs) **15**
2.2.1 Principle and advantages of latent heat TES 15
2.2.2 Selection and properties of a phase change material 16
2.2.3 Classification of PCMs 17
2.2.3.1 Organic PCMs 18
2.2.3.2 Inorganic PCMs 19
2.2.3.3 Eutectic PCMs 20
2.2.4 Confinement techniques for organic PCMs 20
2.2.4.1 Encapsulation 21
2.2.4.2 Shape-stabilization 24
2.2.5 Cost and sustainability of PCMs 26
2.2.6 Thermal conductivity enhancement of organic PCMs 27
2.3 Applications of PCMs for heat management **28**
2.3.1 Thermal management in buildings 28
2.3.1.1 Passive storage systems 29
2.3.1.2 Active storage systems 30

2.3.2 Smart textiles 30
2.3.3 Thermal management of electronics 31
2.3.4 Biomedical applications 34
2.3.5 Thermoregulating packaging 35
2.3.6 Flame resistance of organic PCMs 35
2.4 Structural and semi-structural polymer composites 36
2.4.1 Introduction to polymer composites 36
2.4.1.1 Definition and classification 36
2.4.1.2 Significance and applications 38
2.4.2 Reinforcements 38
2.4.2.1 Continuous and discontinuous fibers 38
2.4.2.2 Particles and other reinforcements 40
2.4.3 Matrices 42
2.4.3.1 Thermosetting matrices 43
2.4.3.2 Thermoplastic matrices 44
2.4.4 Fabrication of fiber-reinforced composites 45
2.4.4.1 Continuous fibers and thermosetting matrices 46
2.4.4.2 Continuous fibers and thermoplastic matrices 47
2.4.4.3 Discontinuous-fiber composites 49
2.5 Multifunctional composites and structural TES materials 49
2.5.1 Multifunctional materials 49
2.5.1.1 Multifunctionality of polymer composites 50
2.5.1.2 Applications and examples 51
2.5.2 Structural TES polymer composites 53
2.6 PCMs in polymers and polymer composites 56
2.6.1 PCMs in polymer matrices 56
2.6.2 PCMs in structural polymer composites 59

Chapter III
Experimental 61
3.1 Introduction 61
3.2 Materials 61
3.2.1 Phase change materials 62
3.2.1.1 Paraffin shape-stabilized with carbon nanotubes 62
3.2.1.2 Paraffin microcapsules 64
3.2.1.3 Docosane 65
3.2.1.4 Poly(ethylene glycol) 66
3.2.2 Matrices 66
3.2.2.1 Polyamide 12 66
3.2.2.2 Liquid thermoplastic resin 67
3.2.2.3 Polypropylene 67

3.2.2.4 Thermoplastic starch 67
3.2.2.5 Epoxy resin 68
3.2.3 Reinforcements 68
3.2.3.1 Bidirectional glass fiber fabric 68
3.2.3.2 Bidirectional carbon fiber fabric 69
3.2.3.3 Unidirectional carbon fiber fabric 69
3.2.3.4 Discontinuous carbon fibers 70
3.2.3.5 Ultra-thin wood laminae 70
3.2.4 Summary and labels of the investigated materials 72
3.3 Characterization techniques 73
3.3.1 Microstructural properties 73
3.3.1.1 Optical microscopy (OM) 73
3.3.1.2 Scanning electron microscopy (SEM) 73
3.3.2 Physical properties 73
3.3.2.1 Density 73
3.3.2.2 Melt flow index (MFI) 74
3.3.2.3 Dynamic rheological properties 74
3.3.2.4 Brookfield viscosimetry 75
3.3.3 Thermal and thermo-mechanical properties 75
3.3.3.1 Differential scanning calorimetry (DSC) 75
3.3.3.2 Thermogravimetric analysis (TGA) 76
3.3.3.3 Thermal camera imaging 76
3.3.3.4 Thermal conductivity 77
3.3.3.5 Dynamic-mechanical analysis (DMA) 78
3.3.3.6 Vicat tests 79
3.3.4 Weight and volume fraction of the constituents 79
3.3.5 Mechanical properties 80
3.3.5.1 Tensile tests 80
3.3.5.2 Flexural tests 81
3.3.5.3 Charpy impact tests 82
3.3.5.4 Mode I fracture toughness 82
3.3.5.5 Short-beam shear tests 84

Chapter IV
Thermoplastic TES composites 87
4.1 Introduction 88
4.2 PCM-enhanced glass/polyamide12 laminates 88
4.2.1 Materials and methods 88
4.2.1.1 Materials 88
4.2.1.2 Sample preparation 89
4.2.1.3 Characterization 90

4.2.2 Results and discussion 91
4.2.2.1 Characterization of the PA/PCM samples 91
4.2.2.2 Characterization of the PA/PCM/GF laminates 99
4.2.2.3 Conclusions 104
4.3 Discontinuous carbon fiber/polyamide composites containing paraffin microcapsules 105
4.3.1 Materials and methods 105
4.3.1.1 Materials 105
4.3.1.2 Sample preparation 106
4.3.1.3 Characterization 107
4.3.2 Results and discussion 107
4.3.3 Conclusions 126
4.4 Reactive thermoplastic resin as a matrix for carbon fiber laminates containing paraffin microcapsules 127
4.4.1 Materials and methods 128
4.4.1.1 Materials 128
4.4.1.2 Sample preparation 128
4.4.1.3 Characterization 129
4.4.2 Results and discussion 130
4.4.2.1 Characterization of the samples EL-MCx 130
4.4.2.2 Characterization of the samples EL-MCx-CF 132
4.4.3 Conclusions 157
4.5 Melt-spun polypropylene filaments containing a microencapsulated PCM 158
4.5.1 Materials and methods 159
4.5.1.1 Materials 159
4.5.1.2 Sample preparation 159
4.5.1.3 Characterization 160
4.5.2 Results and discussion 162
4.5.2.1 Microstructure 162
4.5.2.2 Physical properties 166
4.5.2.3 Thermal properties 171
4.5.2.4 Mechanical properties 177
4.5.3 Conclusions 179
4.6 General conclusions of Chapter IV 179
4.7 Acknowledgements 180

Chapter V
Thermosetting TES composites 181
5.1 Introduction 182

5.2 Carbon fiber/epoxy laminates containing paraffin shape-stabilized with carbon nanotubes 182
5.2.1 Materials and methods 183
5.2.1.1 Materials 183
5.2.1.2 Sample preparation 183
5.2.1.3 Characterization 185
5.2.2 Results and discussion 185
5.2.2.1 Results of the EP/ParCNT samples 186
5.2.2.2 Results of the EP/ParCNT/CF laminates 190
5.2.3 Conclusions 206
5.3 Effect of paraffin microcapsules on the thermo-mechanical properties of an epoxy resin 207
5.3.1 Materials and methods 208
5.3.1.1 Materials 208
5.3.1.2 Sample preparation 209
5.3.1.3 Characterization 209
5.3.2 Results and discussion 210
5.3.2.1 Viscosity 210
5.3.2.2 Microstructural characterization 211
5.3.2.3 Density and porosity 212
5.3.2.4 Thermal characterization 213
5.3.2.5 Mechanical characterization 224
5.3.3 Conclusions 233
5.4 Unidirectional carbon fiber/epoxy laminates containing PCM microcapsules 234
5.4.1 Materials and methods 234
5.4.1.1 Materials 235
5.4.1.2 Sample preparation 235
5.4.1.3 Characterization 236
5.4.2 Results and discussion 237
5.4.3 Conclusions 259
5.5 Epoxy/milled carbon fibers composites containing paraffin microcapsules 259
5.5.1 Materials and methods 260
5.5.1.1 Materials 260
5.5.1.2 Sample preparation 261
5.5.1.3 Characterization 261
5.5.2 Results and discussion 261
5.5.3 Conclusions 270
5.6 General conclusions of Chapter V 270
5.7 Acknowledgements 271

Chapter VI
Biodegradable TES laminates: thermoplastic starch/wood laminate containing poly(ethylene glycol) 273
6.1 Introduction 274
6.2 Materials and methods 274
6.2.1 Materials 274
6.2.2 Sample preparation 275
6.2.3 Characterization 277
6.3 Results and discussion 277
6.4 General conclusions of Chapter VI 288
6.5 Acknowledgements 288

Chapter VII
Tailoring the properties of PCM microcapsules 289
7.1 Introduction 290
7.2 Encapsulation of docosane in organosilica microcapsules via a sol-gel approach 290
7.2.1 Materials and methods 291
7.2.1.1 Materials 291
7.2.1.2 Sample preparation 291
7.2.1.3 Characterization 293
7.2.2 Results and discussion 295
7.2.2.1 Sample preparation and quality of the docosane o/w emulsion 295
7.2.2.2 SEM microscopy 295
7.2.2.3 FTIR spectroscopy 297
7.2.2.4 XRD analysis 298
7.2.2.5 Solid state NMR analysis 299
7.2.2.6 DSC analysis 304
7.2.2.7 TGA tests 307
7.2.3 Conclusions 309
7.3 Bioinspired polydopamine coating as an adhesion enhancer between paraffin microcapsules and an epoxy matrix 310
7.3.1 Materials and methods 311
7.3.1.1 Materials 311
7.3.1.2 Sample preparation 311
7.3.1.3 Reaction of neat and PDA-coated microcapsules with oxirane-carrying molecules 312
7.3.1.4 Preparation of the MC-filled epoxy composites 312
7.3.1.5 Characterization 312
7.3.2 Results and discussion 314
7.3.2.1 Surface morphology of neat and PDA-coated microcapsules 315

7.3.2.2 FTIR spectroscopy 315
7.3.2.3 XPS characterization 320
7.3.2.4 Hot-stage optical microscopy 325
7.3.2.5 Thermal analysis 326
7.3.2.6 Interfacial adhesion and characterization of the epoxy/MC composites 329
7.3.3 Conclusions 331
7.4 General conclusions of Chapter VII 332
7.5 Acknowledgements 333

Chapter VIII
Conclusions 335
8.1 Summary and comparison of the investigated systems 335
8.2 Recommendations and future perspectives 344

References 349

Scientific production 367
Participation to Congresses, Schools and Workshops 369
Side research activities 371
Scientific production from side research activities 371

Acknowledgements 373

List of acronyms and symbols

ATR	Attenuated total reflectance
BE	Binding energy
BET	Brunauer, Emmett and Teller
BMC	Bulk molding compound
BPO	Benzoyl peroxide
CMC	Ceramic matrix composite
CNTs	Carbon nanotubes
CP-MAS	Cross-polarization magic angle spinning
CTAB	Cetyltrimethylammonium bromide
DGEBA	Diglycidyl ether of Bisphenol A
DMA	Dynamic-mechanical analysis
DSC	Differential scanning calorimetry
E/P	ethylene-propylene copolymer
EG	Expanded graphite
EPDM	ethylene-propylene diene monomer
EV	Electric vehicle
FE-SEM	Field-emission scanning electron microscope
FTIR	Fourier-transformed infrared spectroscopy
GO	Graphene oxide
HDT	Heat deflection temperature
HLB	Hydrophile-lipophile balance
ILSS	Interlaminar shear strength
LCA	Life Cycle Assessment
LFA	Laser flash analysis
LH-TES	Latent heat thermal energy storage
LLDPE	Linear low-density polyethylene
LOI	Limiting oxygen index
MA	Myristyl alcohol
MF	melamine-formaldehyde
MFI	Melt flow index
MMC	Metal matrix composite
MTES	Methyltriethoxysilane
MUF	melamine-urea-formaldehyde
MW	Molecular weight
NMR	Nuclear Magnetic Resonance
O/W	Oil-in-water
OBC	Olefin block copolymer
OM	Optical microscopy
PA	Polyamide
PA12	Polyamide 12
PBO	poly(*p*-phenylene-2,6-benzobisoxazole)
PCM	Phase change material
PDA	Polydopamine

PE	Polyethylene
PEEK	Polyetheretherketone
PEG	Poly(ethylene glycol)
PEI	Polyetherimide
PEKK	Polyetherketoneketone
PET	Poly(ethylene terephthalate)
PMC	Polymer matrix composite
PMMA	Polymethylmethacrylate
PP	Polypropylene
PPS	Polyphenylene sulfide
PVC	Poly(vinyl chloride)
rpm	Rounds per minute
SBS	Short-beam shear
SDS	Sodium dodecyl sulphate
SEM	Scanning electron microscopy
SFRC	short fiber reinforced composites
SH-TES	Sensible heat thermal energy storage
SMC	Sheet molding compound
SSA	Specific surface area
TEOS	Tetraethyl orthosilicate
TES	Thermal energy storage
TGA	Thermogravimetric analysis
TGMDA	Tetraglycidyl methylene dianiline
TH-TES	Thermochemical heat storage
TM	Thermal management
TPS	Thermoplastic starch
UHMWPE	ultra-high molecular weight polyethylene
VST	Vicat softening temperature
xGnPs	Expanded graphite nanoplatelets
XPS	X-ray photoelectron spectroscopy
XRD	X-Ray Diffraction

ν	Applied frequency
δ	Ratio between outer and inner particle radius
λ	Thermal conductivity
$\dot{\gamma}$	Shear rate
ε_{MAX}	Tensile strain at maximum stress
ε_b	Tensile strain at break
ε_{fb}	Flexural strain at break
ε_y	Tensile strain at yield
η^*	Complex viscosity
$\eta_{\dot{\gamma}}$	Viscosity at a specific shear rate
η_0	Viscosity at zero shear rate
η_∞	Viscosity at infinite shear rate
η_L	Coefficient L (Halpin-Tsai model)
η_T	Coefficient T (Halpin-Tsai model)

ρ_{MC}	Density of the PCM microcapsules
ρ_{exp}	Experimental density of the composite
ρ_f	Density of the reinforcement
ρ_m	Density of the matrix
ρ_{th}	Theoretical density of the composite
σ_M	Tenacity of the filament
σ_{MAX}	Tensile strength (maximum stress)
σ_b	Tensile stress at break
σ_{fM}	Flexural strength
σ_y	Tensile stress at yield
τ_0	Yield stress in viscosity measurements
ω_D	Weight fraction of docosane
ω_{MC}	weight fraction of PCM microcapsules
ω_{PCM}	PCM weight fraction
ω_{ParCNT}	weight fraction of ParCNT
ω_f	Fiber weight fraction
ϑ_{MC}	Volume fraction of PCM microcapsules
ϑ_{ParCNT}	Volume fraction of ParCNT
ϑ_f	Fiber volume fraction
ϑ_{fi}	Filler (generic) volume fraction
ϑ_m	Matrix volume fraction
ϑ_{max}	Maximum filler volume fraction
ϑ_v	Volume fraction of voids
α	Thermal diffusivity
ζ	Shape factor of the filler (Halpin-Tsai model)
η	Viscosity - or Encapsulation efficiency
ρ	Density
φ	Heating/cooling rate
ΔE	Total amount of energy
ΔH_c^{rel}	Relative crystallization enthalpy
ΔH_m^{rel}	Relative melting enthalpy
ΔH_{pc}	Latent heat of phase change
ΔH_c	Crystallization enthalpy
ΔH_m	Melting enthalpy
E'	Storage modulus
E''	Loss modulus
E_L	Longitudinal elastic modulus (fiber direction)
E_R'	Residual storage modulus (after T_g)
E_T	Transversal elastic modulus
E_a	Activation energy
E_f	Elastic modulus of the fibers (Halpin-Tsai model) or flexural modulus
E_i	Initiation energy
E_m	Elastic modulus of the matrix (Halpin-Tsai model)
E_p	Propagation energy
$E_{sp,max}$	Specific energy absorbed at maximum load (Charpy)

$E_{sp,tot}$	Specific energy absorbed at break (Charpy)
F_{max}	Maximum load (Charpy)
G_{IC}	Critical strain energy release rate for steady-state propagation
G_{Ii}	Critical strain energy release rates for crack initiation
H_1	Initial enthalpy
H_2	Final enthalpy
K_{IC}	Critical stress intensity factor
K_Q	Conditional value of critical stress intensity factor
R_f	Residual mass of the fibers (in TGA)
R_m	Residual mass of the matrix (in TGA)
S_1	Storage medium (in TH-TES)
S_2	First reaction product (in TH-TES)
S_3	Second reaction product (in TH-TES)
$T_{1\%}$	Temperature at a mass loss of 1 wt% (in TGA)
T_1	Initial temperature
T_2	Final temperature
$T_{3\%}$	Temperature at a mass loss of 3 wt% (in TGA)
$T_{5\%}$	Temperature at a mass loss of 5 wt% (in TGA)
T_c	Crystallization temperature
T_d	Peak temperature of mass loss derivative (TGA)
T_g	Glass transition temperature
T_m	Melting temperature
T_{onset}	Onset degradation temperature (in TGA)
T_{pc}	Phase change temperature
c_L	Specific heat capacity of the liquid phase
c_P	Specific heat capacity
c_S	Specific heat capacity of the solid phase
k_E	Generalized Einstein coefficient
m_r	Residual mass (after TGA tests)
a	Crack length
R-II	Rotator phase
S_a	Mean surface roughness
$T1_C$	spin-lattice relaxation time
B	load-transfer capability parameter (Pukanszky model)
E	Elastic modulus
G'	Shear storage modulus
G''	Shear loss modulus
K	Interfacial adhesion parameter (Nicolais-Narkis model)
R	Universal gas constant
l	Fiber length (Halpin-Tsai model)
m	Mass
r	Fiber radius (Halpin-Tsai model)
$tan\delta$	Loss factor

Chapter I

Introduction and aim of the work

1.1 Motivations and objectives

Thermal energy storage (TES) is one of the key technologies for a more efficient and rational use of energy resources, as it allows the temporary conservation of excess heat that can be released when the demand for thermal energy overcomes its availability. Among the most promising materials for TES in the low-medium temperature range (0-100 °C) are the organic solid-liquid phase change materials (PCMs), such as paraffin waxes, which accumulate heat when they melt and release it upon crystallization. PCMs can store a high amount of latent heat at a nearly constant temperature, and therefore they are often used to maintain the temperature in a specific range; this makes them suitable for thermal management applications, such as to regulate the indoor environment in buildings, or to avoid overheating of batteries and other electronic devices. To prevent leakage and loss of material above the melting temperature, PCMs can be either encapsulated in macro-, micro- or nano-shells, or "shape-stabilized" in porous materials or nanofiller networks.

Generally, TES systems represent a supplementary component to be added to the main structure of a device. In applications where weight and volume savings are critical design parameters, it would be beneficial to embed heat storage/management functionalities directly into structural or semi-structural materials. In this context, polymer-matrix composites have the potentialities to be designed as multifunctional

materials with both structural and non-structural functions. Lightweight polymer composites combining good mechanical properties and TES capability could find applications in different fields, such as the automotive industry, where the diffusion of lightweight structures could complicate the thermal management of the environment in the cockpit, or the portable electronics field, where the reduction in volumes and masses also limits the space available for the cooling system. Although the scientific literature reports some examples of polymers containing a PCM, little has been done to investigate their mechanical properties and enhance these properties with a reinforcing agent.

The aim of this thesis is to develop polymer-matrix composites containing an organic PCM and a reinforcing agent, and to characterize their properties as a function of their composition, in order to design systems that combine structural/semi-structural function and heat storage/management capability. Since this research topic has not been addressed systematically in the scientific literature, the work of this thesis considers and compares several polymer/PCM/reinforcement systems, to highlight advantages and drawbacks and select combinations with the highest potential from the point of view of the synergism between mechanical and TES properties.

More precisely, the specific objectives of this work can be listed as follows:

- **Investigate the effects of the introduction of a PCM on the properties of a polymer composite.** Considering the intrinsic brittleness and low stiffness and strength of paraffin waxes and other organic PCMs, it is crucial to evaluate how PCM addition impacts the microstructural, thermal, mechanical, and viscoelastic properties of a polymer composite, below and above the melting temperature of the PCM.

- **Compare microencapsulated and shape-stabilized PCMs as TES materials in a polymer composite,** by considering differences in thermal and mechanical stability, assessing the impact on viscosity and other physical properties of the matrix during processing, and foreseeing potential sources of defects in the final composite, always taking into account the differences in processing a thermoplastic or a thermosetting composite.

- **Perform benchmark experiments and proofs of concept.** Since the scientific literature reports a very limited number of examples of polymer composites containing a PCM, this work aims at investigating a broad range of matrices, reinforcements and PCMs, to highlight which parameters are the most important and suggest guidelines for designing with structural or semi-structural TES composites. The selected matrices encompass thermoplastic, thermosetting and reactive thermoplastic polymers, while the reinforcements comprise

continuous and discontinuous carbon and glass fibers and less traditional reinforcements such as wood laminae.

- **Evaluate potential multifunctional reinforcements.** All the considered composites were produced combining a polymer matrix, a reinforcement and a PCM. However, ultra-thin wood laminae were considered as both the reinforcement and the shape-stabilizing agent for the PCM. In this way, multifunctionality was shifted from the composite level to the element level

- **Study the properties of PCM microcapsules,** to evidence which parameters make them suitable to be incorporated in a polymer matrix, such as size, melting enthalpy, surface reactivity, and mechanical strength of the shell.

1.2 Methodological approaches

The first activity of the thesis work was a detailed literature review aimed at selecting the most promising PCMs to be incorporated into a polymer composite, at choosing the matrix/reinforcement systems that could host a PCM, at evaluating the lab-scale production processes to fabricate thermoplastic and thermosetting composite samples. For each of the selected matrix/reinforcement/PCM combination, samples were prepared containing various fractions of PCMs, and the processing parameters were tuned to obtain samples of the best possible quality. From these samples, specimens were extracted for a detailed and all-round characterization, encompassing (i) microstructural evaluation via optical and scanning electron microscopy, (ii) the assessment of density and porosity of the prepared composites, correlated with the measurements of the viscosity variation of the matrix upon PCM addition, (iii) the determination of the TES capability on two size scales, via differential scanning calorimetry (DSC) and thermal camera imaging, (iv) the measurement of other important thermal properties via thermogravimetric analysis (TGA), laser flash analysis (LFA) and dynamic-mechanical analysis (DMA), (v) the evaluation of the mechanical performance via quasi-static, dynamic and fracture mechanics tests. The measured properties were evaluated as a function of the composition and PCM content, and theoretical models were applied to highlight interesting relationships between the measured parameters. The property evaluation was followed by a comparison of the produced composites via the construction of property charts.

The study of the properties of PCM microcapsules was performed via the synthesis of core-shell microcapsules via a sol-gel approach and the characterization of their morphology, microstructure and thermal properties via spectroscopy and nuclear magnetic resonance (NMR) techniques. Moreover, the study and improvement of the surface reactivity of the microcapsules was performed by modifying commercial PCM microcapsules via polydopamine (PDA) deposition

through a wet-chemical approach and by analyzing the surface reactivity with infrared spectroscopy and X-ray photoelectron spectroscopy (XPS).

1.3 Thesis outline

This thesis is divided into eight Chapters.

Chapter II presents a detailed literature review on the TES techniques, with a special focus on the various classes of PCMs and their applications for thermal management. This Chapter then provides a concise overview on structural and semi-structural polymer composites and describes the concept of multifunctional material, especially focusing on the combination between mechanical and TES properties. Chapter III describes all the materials used in this thesis, which are classified as polymer matrices, reinforcements and PCMs. It also illustrates all the characterization techniques applied on the prepared composites, divided into physical, microstructural, thermal, thermo-mechanical and mechanical methods.

The following three Chapters describe the sample preparation and the results of the characterization for all the prepared composites, divided according to the type of matrix. Chapter IV illustrates the composites with a thermoplastic matrix. Four case studies were investigated, namely (i) glass/polyamide laminates containing either a microencapsulated or a shape-stabilized PCM; (ii) polyamide composites containing paraffin microcapsules and reinforced with discontinuous carbon fibers; (iii) carbon fiber laminates containing paraffin microcapsules and a reactive thermoplastic matrix; (iv) polypropylene filaments containing PCM microcapsules, produced with the aim of fabricating multifunctional commingled yarns.

The results of the composites with a thermosetting matrix are described in Chapter V. The only considered thermosetting matrix was an epoxy resin, combined with (i) a bidirectional carbon fabric and shape-stabilized paraffin powder, (ii) a microencapsulated PCM and unidirectional carbon fibers, and (iii) the same microencapsulated PCM and discontinuous carbon fibers.

Chapter VI illustrates the methods and the results of the characterization of a thermoplastic starch/wood laminate containing poly(ethylene glycol) (PEG) as a PCM. Even though it has a thermoplastic matrix, this system has been described in a standalone Chapter due to its peculiarities, i.e. the full biodegradability, the use of a non-paraffinic PCM, the non-fibrous nature of the reinforcement (constituted by thin wood laminae) and the fact that the reinforcement is also the shape-stabilizing agent for the PCM, thus being a multifunctional element itself.

Chapter VII focuses on tailoring the thermo-mechanical or interfacial properties of paraffin microcapsules and deals with (i) the synthesis of docosane microcapsules via a sol-gel route and (ii) the modification of commercial paraffin microcapsules with a polydopamine coating to enhance the interfacial adhesion with an epoxy matrix.

Lastly, Chapter VIII contains concluding remarks, a comparison among all investigated systems, and recommendations for future research.

The results of this thesis would not have been possible without the help of several researchers and collaborators. Therefore, at the end of each Chapter, a paragraph acknowledges the contribution of other researchers by detailing clearly the input of each of them (where applicable).

Chapter II

Background

2.1 Introduction to thermal energy storage (TES)

The storage and management of thermal energy have become object of increasing interest in the last decades, due to their importance for the conservation and efficient use of energy and energy sources. The present Subchapter starts explaining the reasons at the basis of energy conservation and management, and then it illustrates the concept of thermal energy storage and the classification of TES technologies (Kalaiselvam and Parameshwaran, 2014).

2.1.1 Importance of energy conservation and management

The growing concerns about fossil fuels depletion, climate change, and greenhouse gases emissions have recently increased the interest of researchers, industries, and governments for developing technologies aimed at a more efficient use of energy. As the strategies for energy production based on fossil fuels have been lately undoubtedly related to environmental pollution and global warming, the research attention has shifted towards sustainable and renewable energy sources, such solar, wind and geothermal energy (Dincer and Ezan, 2018).

The two main obstacles against the wide diffusion of such sources are the high initial plant cost and the intermittent nature of these sources. If the first issue will be

attenuated by technological development, an effective answer to source intermittency can be provided by boosting energy storage technologies. The amount of solar energy varies on a daily and seasonal basis, and the wind and geothermal power can be unpredictable; therefore, the energy production plants must be supplemented with energy storage systems, to provide a significant and constant output also in the off-peak periods (Dincer and Ezan, 2018).

Energy storage systems can bring benefits also in the exploitation of conventional energy sources, when they are implemented in buildings, vehicles and industrial applications (Dincer and Rosen, 2011; Dincer and Ezan, 2018). For instance, in the transportation sector, an increased performance of batteries could encourage the usage of electric vehicles, thereby reducing the demand for traditional fuels. Energy storage systems can help to decrease equipment sizes and initial and maintenance prices, to boost plant flexibility and efficiency, and to reduce the necessity of emergency power generators that would consume primary energy sources, all of which would lower the overall energy consumption and cost (Dincer and Rosen, 2011; Kalaiselvam and Parameshwaran, 2014).

2.1.2 Energy storage technologies

Energy storage systems can be classified according to the form of intermediate energy, which can be (Dincer and Ezan, 2018):

- chemical (e.g. hydrogen storage);
- electrical (e.g. capacitors);
- electrochemical (e.g. batteries, fuel cells);
- mechanical (e.g. compressed air);
- thermal (e.g. sensible heat storage in water tanks).

Other classifications consider the form of input energy (e.g. electrical, thermal), the form of output energy (e.g. thermal energy, liquid fuels), or the involved conversion process (e.g. power-to-power, power-to-gas, power-to-liquid). Even though the mentioned forms of energy storage are characterized by different power rates, discharge rates, efficiency, and technological maturity, they all have considerable positive impact in their own applications, as they can maintain a continuous power supply and increase the system performance and reliability (Dincer and Ezan, 2018).

The following Sections focus on thermal energy storage and illustrate the technologies and the applications of such concept.

2.1.3 Concept of thermal energy storage

Thermal energy storage (TES) can be defined as the temporary storage of heat, which can be used later and/or in a different place. The TES systems are meant to

reduce the mismatch between thermal energy availability and demand, thereby contributing to the recovery of waste heat and a more efficient exploitation of intermittent energy sources (Cabeza, 2014). Compared to the other aforementioned energy storage systems, the storage of energy in the form of heat (or cold) exhibits longer storage times and higher efficiency (Dincer and Ezan, 2018). The cycle of a typical TES system, reported in Figure II - 1, comprises charging, storage and discharging steps.

Figure II - 1. Typical working cycle of a TES system (adapted from (Dincer and Ezan, 2018)).

TES materials and technologies have been object of a growing interest, as demonstrated by the noteworthy increase in the number of scientific publications on the topic. Figure II - 2 shows the yearly number of publications found with the search phrase “thermal energy storage” on the database Web of Science. The number of scientific studies has increased of approximately 11 times in the last 10 years (from 2009 to 2019), which proves the considerable effort of the scientific community to expand the knowledge and the technologies in the field.

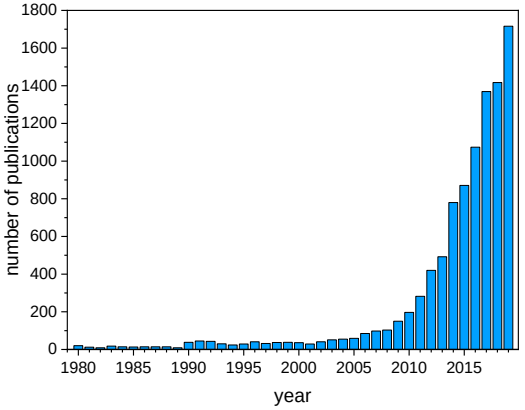

Figure II - 2. Number of scientific papers published yearly about thermal energy storage from 1980 to 2019 (ISI Web of Science database, consulted on March 6, 2020).

TES technologies are currently employed for three main purposes:

(1) to store waste/excess heat that will be released during off-peaks periods, e.g. to recover waste industrial heat (Zhang et al., 2016), or in solar thermal power plants (Sheng et al., 2019);
(2) to contribute to temperature regulation, e.g. in buildings to store excess energy during the day and release it during the night or in off-peak times (Ostry and Charvat, 2013), or for body temperature regulation through smart thermoregulating garments (Cherif et al., 2018);
(3) to temporarily store heat and prevent a temperature rise that would otherwise damage a component, as in the thermal management of electronic devices (Kandasamy et al., 2007).

From the classification presented above, it is clear that sometimes the desired product is the stored and released thermal energy, as in the cases (1) and (2): the excess energy is stored for later uses, which can involve temperature regulation (as in the case of buildings) or an increase in efficiency (as in the case of power plants). These examples are generally referred to as cases of "thermal energy storage or TES *properly said*", and they normally need energy storage systems with high thermal capacity, to store as much energy as possible. In other situations, the excess heat is not stored for a later use, but only to avoid a dangerous rise in temperature, as in the aforementioned case (3): these are examples of "thermal management" (TM), and their main requirement is usually a well-defined energy storage rate. However, it is not always easy to distinguish between TES properly said and TM. Some other classifications categorize as TES properly said only the case (1), while the other cases are examples of TM as the main goal is to keep the temperature in an optimal range.

This thesis will discuss about TES or TM without a strict distinction, although the materials investigated in this work would be more suitably employed for thermal management applications.

2.1.4 Classification of TES technologies

TES technologies can be classified according to the way the internal energy of the storage medium is varied. The thermal energy can be stored and released by changing the temperature of a material (*sensible heat TES*, SH-TES), through an endo/exothermic phase change (*latent heat TES*, LH-TES), or through a thermochemical reaction (*thermochemical heat TES*, TH-TES). The selection of a TES system over another depends on several parameters, such as the required heat storage period (hours, months, days), economic considerations, working temperature, available volume. A list of the main parameters of the different TES systems is reported in Table II - 1 (Safari et al., 2017). Even though the TH-TES system allow a higher

energy density per unit mass and volume and a greater efficiency, the technological maturity of TH-TES is lower than that of the other two classes, and according to some recent reviews on the topic, considerable effort should be put to study advanced materials and produce efficient prototypes (Jarimi et al., 2019). On the other hand, LH-TES systems such as underground thermal energy storage and the domestic hot water storage are characterized by low risk and high commercialization potential (Dincer and Ezan, 2018).

Table II - 1. Main performance parameters of sensible, latent and thermochemical heat TES technologies (adapted from (Safari et al., 2017)).

TES system	Capacity (kWh/t)	Efficiency (%)	Storage period (h, d, m)	Cost (€/kWh)
Sensible heat	10-50	50-90	d/m	0.1-10
Latent heat	50-150	75-90	h/m	10-50
Thermochemical heat	120-250	75-100	h/d	8-100

The following Sections summarize the characteristics and the governing equations of each of the three TES classes, while Subchapter 2.2 focuses on the description of latent heat TES materials and technologies, as they are the focus of this thesis.

2.1.4.1 Sensible heat storage (SH-TES)

SH-TES is performed by increasing or decreasing the temperature of the storage medium, since the enthalpy variation is proportional to the temperature difference, as depicted in Figure II - 3.

More specifically, the total amount of energy ΔE (J) stored in the system can be defined by Equation (II - 1), as

$$\Delta E = \int_{H_1}^{H_2} mdH = m(H_2 - H_1) = \int_{T_1}^{T_2} mcdT = mc(T_2 - T_1), \qquad \textbf{(II - 1)}$$

where m is the mass of the storage medium, H_1 and H_2 the initial and final enthalpy values (J/g), c the specific heat capacity (J/(g·K)) and T_1 and T_2 the initial and final temperature (°C). An analogous equation can be written for the energy release, which results in the cooling of the storage medium.

From Equation (II - 1) it is evident that the effectiveness of a storage medium and the total amount of exchanged energy depends on the available mass and volume, while the energy stored per unit mass increases with the specific heat capacity. It is also desirable that the medium is non-toxic, not expensive, and maintains long-term stability over many thermal cycles. Moreover, the medium should be well insulated, as any fluctuations of the surrounding temperature results in a variation of the stored

energy, and it should have a high thermal diffusivity, which enhances heat transfer rate within the medium itself and thus the total thermal exchange rate.

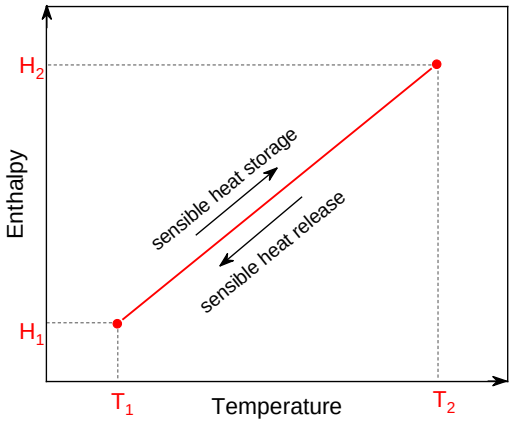

Figure II - 3. Variation of enthalpy of the storage medium as a function of its temperature in an SH-TES unit cycle (adapted from (Dincer and Ezan, 2018)).

Typical materials used as sensible heat storage media are liquids such as water, oils or molten salts, or solids such as metals or rocks (Hasnain, 1998). One of the most widespread sensible heat storage media is water, as it has a considerably high specific heat, is cheap and widely available. As it can be used over a wide temperature range and is employable both as a storage and transport medium, it is the most widely used storage medium for solar-based hot water and in radiation systems for indoor heating (Hasnain, 1998).

2.1.4.2 Latent heat storage (LH-TES)

LH-TES involves the storage and release of heat through a phase transition. The vast majority of LH-TES systems are based on the melting-solidification phase transition, with the storage medium absorbing heat during melting and releasing it upon solidification. On the other hand, evaporation-condensation phase changes are generally avoided, as the considerable volume variation increases the requirements and the complexity of the confinement units.

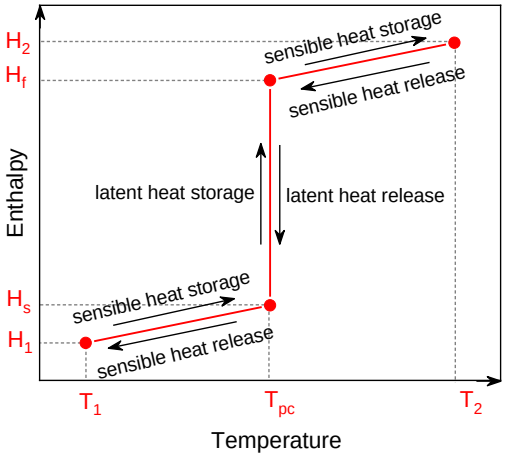

Figure II - 4. Variation of enthalpy of the storage medium as a function of its temperature in an LH-TES unit cycle (adapted from (Dincer and Ezan, 2018)).

The enthalpy variation as a function of temperature for a solid-to-liquid phase transition is illustrated in Figure II - 4. During an energy storage process, the storage medium initially behaves like an SH-TES unit and absorbs sensible heat, with a consequent increase in temperature. This behaviour continues until the phase change temperature (T_{pc}), at which the phase transition takes place, is reached. The system remains at T_{pc} until the completion of the phase transition, during which the absorbed energy is equal to the latent heat of phase change ($\Delta H_{pc} = H_f - H_s$). Further increases in enthalpy rise the temperature of the storage medium, and the slope of the enthalpy-temperature relationship depends on the specific heat capacity of the substance after phase change and can be different from the slope between T_1 and T_{pc}.

The total enthalpy variation ΔE (J) of such process is described by Equation (II - 2), as

$$\Delta E = \int_{H_1}^{H_2} m dH = m(H_2 - H_1) = \int_{T_1}^{T_{pc}} m c_S dT + m\Delta H_{pc} + \int_{T_{pc}}^{T_2} m c_L dT \ , \qquad \textbf{(II - 2)}$$

where ΔH_{pc} (J/g) is the latent heat of phase change, T_{pc} is the phase change temperature and c_S and c_L are the specific heat capacity of the solid and liquid phase, respectively. Generally, the latent heat is considerably higher than the sensible heat

absorbed, which means that LH-TES systems normally require less material usage, as they can store a high amount of energy in a smaller volume.

2.1.4.3 Thermochemical energy storage (TH-TES)

The third type of TES systems consists in storing and releasing heat in a reversible endo/exothermic thermochemical reaction. During an endothermic reaction (charging), the storage medium absorbs heat from the surrounding environment as the reaction enthalpy and it typically splits into two or more chemical substances, as illustrated in Equation (II - 3), as

$$S_1 + heat \rightarrow S_2 + S_3, \qquad \textbf{(II - 3)}$$

S_1 representing the storage medium and S_2 and S_3 the reaction products, which can be stored individually for a long time. The reverse reaction represents the discharging process, and the reaction between S_2 and S_3 releases the same amount of heat stored during the endothermic reaction. The total heat released depends on the reaction enthalpy (J/mol) and the quantity of material (mol).

The potential of thermochemical heat storage is noteworthy, as the TH-TES materials have up to 10 times higher energy storage density then SH-TES media, and approximately two times higher than the most common LH-TES materials (Figure II - 5) (Aydin et al., 2015). This aspect and the remarkably low heat losses are the two main advantages of TH-TES systems. However, the full exploitation of the potential of these materials is possible only with an efficient heat and mass transfer to and from the storage volume, which can put limitations over the maximum size of the storage volume itself. Achieving an efficient heat and mass transfer and coping with slow reaction kinetics are the key targets of the research on TH-TES systems, as they are the main issues to be overcome for the scale-up and commercialization of these systems (Aydin et al., 2015; Vasta et al., 2018).

TH-TES materials can be further classified as chemical or sorption systems. Chemical systems are those in which a considerable amount of heat is generated from an exothermic synthesis reaction and their working principle is properly described by the model reaction reported in Equation (II - 3). In the sorption systems, a gas, the sorbate, reacts with a sorbent, which can be solid (absorption reactions) or liquid (adsorption reactions) (Aydin et al., 2015). Sorption systems are characterized by faster kinetics and lower working temperatures than chemical systems, but the energy storage density is also lower (Vasta et al., 2018).

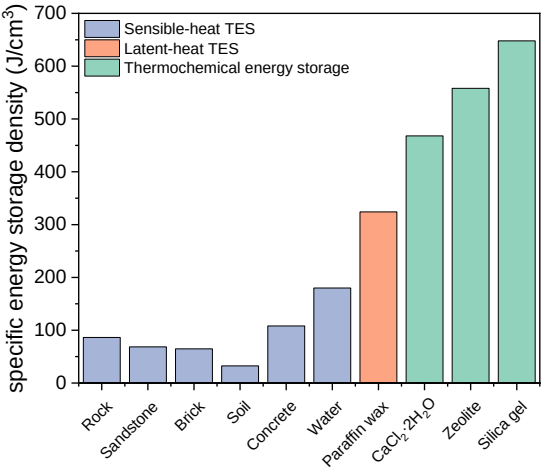

Figure II - 5. Comparison of specific energy storage density values of different sensible, latent and thermochemical TES media (adapted from (Aydin et al., 2015)).

2.2 Latent heat TES and phase change materials (PCMs)

The present Subchapter focuses on latent heat TES, as this is the TES technology selected for this thesis work. It explains the working principles and the advantages of latent heat storage systems more in detail and describes the classes of LH-TES materials, the confinement techniques, and the cost and environmental impact issues that derive from their application. As the melting-crystallization phase change is undoubtedly the most widely employed transition in LH-TES technologies, the discussion from now on will refer to this specific transition also with the more generical terms “phase change” or “phase transition”, unless specified differently.

2.2.1 Principle and advantages of latent heat TES

Latent heat TES has become attractive over the other TES technologies for a wide number of applications, and this stems from three main reasons.

The first advantage of LH-TES is the possibility to store and release a considerable amount of heat per unit mass or volume, which derives from the high energy density of the phase change materials (PCMs). This results in requiring much less material compared to the traditional sensible heat storage systems, thereby increasing the system flexibility and the design possibilities and reducing the initial and maintenance costs.

The second advantage is associated to the heat storage and release at a nearly constant temperature, the phase change temperature (T_{pc}). During the energy storage step (charging), the PCM reaches the melting temperature and maintains the temperature constant over the whole melting process, regardless of the applied heat flux or small variations of the surrounding temperature. An analogous situation happens during heat release (discharging): when the PCM approaches the crystallization phase change, the temperature is kept constant until the transition is completed. This feature is attractive in all the thermal management applications, where the temperature should be stably maintained in a certain range (e.g. indoor thermal regulation of buildings) or under a critical value (e.g. cooling of electronic devices).

The third advantage is represented by the technological maturity of LH-TES systems, which often makes LH-TES a preferred choice over thermochemical heat storage techniques. Even though TH-TES systems exceed LH-TES in energy storage density, solid-liquid phase change materials are generally easier to handle and exhibit a little volume variation as they do not involve gas phase, thereby requiring smaller systems and less support equipment.

2.2.2 Selection and properties of a phase change material

There are many types of PCMs available on the market, and constant effort is being put in studying new materials that can be used as latent heat storage media. It is therefore important to identify the key material properties that make a PCM the most suitable for a specific application.

One of the most significant properties, and the primary criterion for selecting a PCM, is the phase change temperature. This temperature should be below that of the heat source but above that of the working environment, because a PCM already melted before absorbing heat from the designated source would be purposeless. For LH-TES systems designed to avoid overheating, the most suitable PCM is the one that has the melting point just slightly below the maximum allowed temperature, as this reduces the melting rate and increases the thermal management window.

Another striking property is the phase change enthalpy, which represents the amount of energy that a PCM can store and release per unit mass or volume. High phase change enthalpy values result in smaller system sizes, as less material is required to store a certain energy amount. The PCMs with high melting enthalpy generally exhibit high specific heat capacity, which is also desirable as it increases the sensible heat stored before and after the melting temperature range, thereby enhancing the overall energy exchange.

A good PCM also shows a high thermal conductivity both in the solid and in the liquid phase, as this enhances heat transfer from the source into the whole PCM mass. The density and density variation between the molten and the solid state are also factors to be considered in the processes of materials selection and system design.

Additionally, the ideal PCM should be physically and chemically stable over many thermal cycles, chemically compatible with the container, non-corrosive and non-toxic, and it should exhibit congruent melting, low supercooling degree and completely reversible melting/crystallization cycles.

The currently available PCMs do not match all these criteria at once, but the recent progresses in materials research and design are opening new possibilities for selecting the most suitable PCM with enhanced performance.

2.2.3 Classification of PCMs

The number of materials currently used as PCMs is noteworthy and constantly growing. Therefore, it is difficult – and out of the scope of this thesis – to develop a fully comprehensive list. The present Section aims at describing a commonly accepted way to classify the PCMs, illustrating the working principle, advantages, and disadvantages. The solid-liquid PCMs can be divided into organic PCMs, inorganic PCMs, and eutectic mixtures of organic and inorganic PCMs (Pielichowska and Pielichowski, 2014). The main classes of solid-liquid PCMs are reported in Figure II - 6.

The following Sections describe the characteristics and the advantages of each PCM class. Organic PCMs will be covered more in detail, as they are the PCMs selected for this thesis work.

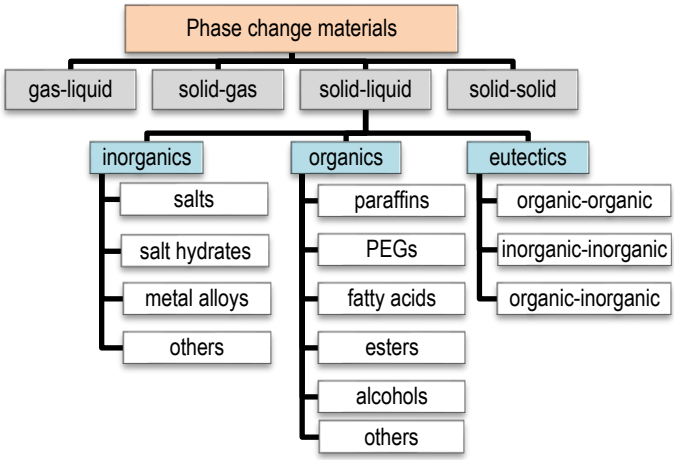

Figure II - 6. Classification of solid-liquid phase change materials (adapted from (Kapsalis and Karamanis, 2016)).

2.2.3.1 Organic PCMs

Organic PCMs are the most widely used PCMs in the low-medium temperature range (0-100 °C) and are diffused in thermal management of buildings and electronic devices. They are generally inexpensive and easy to handle, exhibit a relatively high energy density and comprise classes of oligomers or polymers with a broad range of molecular weights, thus allowing a wide choice of the working temperature. They are non-toxic, do not release volatile substances and are characterized by congruent melting and negligible supercooling. On the other hand, their thermal conductivity is generally low; this issue is addressed by increasing the heat transfer area, by using highly thermally conductive containers or by adding metallic or carbon-based micro/nano-fillers (Pielichowska and Pielichowski, 2014). The second disadvantage of organic PCMs is related to their flammability, which derives from their hydrocarbon nature; however, their flash point is approx. 200 °C, well above the operating temperature range.

Organic PCMs comprise paraffin waxes, poly(ethylene glycol)s, and fatty acids, but also other compounds such as ketones, esters, ethers, halogen derivatives, sulphur compounds and oleochemical carbonates.

Paraffin waxes. The most widely used organic PCMs are the paraffin waxes, saturated hydrocarbons with chemical formula C_nH_{2n+2}. Paraffins embody all the aforementioned advantages of organic PCMs, and they are generally cheaper and exhibit higher heat of fusion (200-240 J/g) and specific heat capacity (2.1-2.4 kJ/(kg·K)) than the other organic compounds (Sharma et al., 2015). They present a superior thermal stability over repeated thermal cycles (also after 1000-2000), are largely commercially available, have a relatively low vapor pressure and a small melting volume change (Kahwaji et al., 2018). Paraffins are available with a broad range of chain lengths; those between C5 (pentane) and C15 (pentadecane) are liquid at room temperature, while those containing a higher number of carbon atoms are solid with a waxy appearance. Commercial paraffins are mixtures of different hydrocarbons that do not exhibit phase segregation even after many thermal cycles, and the formulation is designed to select the desired melting temperature and the highest possible melting enthalpy. Paraffins are generally resistant to chemical and environmental degradation, but it has been shown (Lane, 1983) that they can manifest slow oxidation when exposed to oxygen, which encourages the use of sealed containers.

Fatty acids. Fatty acids, represented by the chemical formula $CH_3(CH_2)_{2n}COOH$, are the second most popular organic solid-liquid PCM. They are divided into six classes: lauric, myristyl, caprylic, capric, palmitic and stearic. Fatty acids show high melting enthalpy values (45-210 J/g) and a wide range of melting temperatures (-5 to 70 °C) but are three times more expensive than paraffins. As they can be produced from vegetal or animal bio-sources and are biodegradable, they have been the subject of extensive studies to replace paraffins for low/medium temperature

applications, such as the solar energy storage and thermal management of indoor environment (Sharma et al., 2015).

Poly(ethylene glycol)s (PEGs). Known also as poly(ethylene oxide)s (PEOs), they are composed of dimethyl ether chains HO-CH_2-(CH_2-O-CH_2-)$_n$-CH_2-OH. Due to the amphiphilic nature of their chain, which presents hydrocarbon sequences and polar groups such as -OH, PEGs are soluble in water and in some organic solvents (Sarier and Onder, 2012). Also for PEGs, the melting temperature and enthalpy increase with the molecular weight; for example, PEG600 melts at 18.5 °C absorbing 121.1 J/g, while PEG2000 has a melting temperature of 61.2 °C and a melting enthalpy of 176.2 J/g. As for the other organic PCMs, the low thermal conductivity is an issue that must be considered in the applications (Sundararajan et al., 2017). PEGs are biodegradable and biocompatible and are also used in drug delivery systems. This feature has expanded the use of PEG as a PCM in applications inside the human body, e.g. to subtract heat during the in-situ polymerization of acrylic bone cements and avoid overheating and damage to the surrounding biological tissues (Król et al., 2016).

2.2.3.2 Inorganic PCMs

Inorganic PCMs generally show higher density than organic PCMs, and therefore, even though they exhibit similar enthalpy per unit mass, they can have a remarkably higher enthalpy per volume, thereby allowing the production of more compact TES systems. Moreover, the thermal conductivity of inorganic PCMs can be several times higher than that of their organic counterpart. For these reasons, they are the preferred choice in the medium/high temperature range (100-1000 °C) and when there are no strict requirements on non-corrosiveness. Inorganic PCMs comprise several classes of materials, such as salts, salt hydrates and metal alloys (Fleischer, 2015).

Salts and salt hydrates. Salts and salt hydrates have similar molecular structure, but in the case of salt hydrates the crystalline lattice is not so closely packed and can easily host water molecules. Common salts and salt hydrates used as PCMs are $NaNO_3$, KNO_3, KOH, $MgCl_2$, NaCl, $MgCl_2 \cdot 6H_2O$, $CaCl_2 \cdot 6H_2O$, and $Na_2SO_4 \cdot 10H_2O$, also called Glauber's Salt (Fleischer, 2015).

While salts undergo a proper melting/crystallization behavior at the transition temperature, for salt hydrates the solid-liquid phase change is a dehydration/hydration process of the compound, which decomposes into an anhydrous salt (or a lower hydrate) and water molecules. Their higher vapor pressure, which increases with the hydration degree, can cause loss of water and change in thermal behaviour of the compound. Salt hydrates often suffer from supercooling problems: above the dehydration temperature, the anhydrous salt may experience segregation and settle at the bottom of the container due to its higher density, thereby hindering the rehydration process. This issue is usually overcome by stirring, by adding excess

water to favor solubilization of the whole mass of anhydrous salt and prevent precipitation, or by adding a thickening agent (e.g. borax, graphite, etc.) that reduces the extent of phase separation and often acts as a nucleating agent (Zalba et al., 2003; Dincer et al., 2017).

The phase change temperature of these compounds ranges from 10 °C to 900 °C. However, for applications where a melting point up to 70-80 °C is required, organic PCMs are often preferred due to the lower cost, easier handling, lower vapor pressure, superior long term stability, lower supercooling and lower tendency to incongruent melting (Zalba et al., 2003).

Metal alloys. Metals have not been extensively investigated as PCMs so far, but they are starting to attract considerable attention thanks to their high thermal conductivity and their stability at high temperature. The most promising metallic PCMs are cesium, gallium, indium, tin and bismuth for low-temperature applications, and zinc, magnesium, and aluminum for applications at higher temperatures. Metallic PCMs cover a broad range of melting temperatures, from 28 °C of neat gallium to 661 °C of aluminum, but they are not widely used for low temperature applications due to their low phase change enthalpy. Despite of their high density, which partially offsets the limited enthalpy and determines a high enthalpy per unit volume, their physical and TES properties do not match those of the most common organic PCMs. On the other hand, high-melting metals such as Al and Mg alloys also exhibit a considerable phase change enthalpy (350-500 J/g), which makes them attractive for high-temperature solar heating applications, in replacement of inorganic salts that are thermally unstable and prone to phase segregation (Fleischer, 2015).

2.2.3.3 Eutectic PCMs

Eutectic PCMs are mixtures of organic or inorganic compounds that melt and solidify congruently. They present a sharp melting point and a high phase change enthalpy, and their properties can be tailored to meet the requirements of a specific application. They are completely miscible in the molten state and freeze forming an intimate mixture of crystals (Dincer et al., 2017), which accounts for a phase transition without segregation. As they are generally designed for a target application, they are usually more expensive than the other classes of PCMs.

2.2.4 Confinement techniques for organic PCMs

One of the major drawbacks for PCMs is the need for being confined to avoid leakage and loss of material above the melting temperature. The confinement techniques can be divided into two main groups: (1) encapsulation methods and (2) shape-stabilization methods. The present Section will focus on the confinement techniques for organic PCMs, with particular attention to the micro/nano-encapsulation techniques and the shape-stabilization with nanofillers, because they are the most

suitable and widely used techniques to embed a PCM in a polymer matrix, thus being the selected techniques for this thesis work.

2.2.4.1 Encapsulation

Encapsulation methods involve a container that physically separates the PCM from the surrounding environment, is stable in the whole working temperature range and accommodates the phase transition and the associated volume change. The containers can be of various sizes, shapes, and materials; one can talk about macro-, micro- or nano-encapsulation.

Macro-encapsulation is the simplest method of confining a PCM, as it involves the use of a box or a tank, made of a thermally conductive material (e.g. aluminum, stainless steel) that is chemically compatible with the PCM. The container should be properly sealed to avoid the leakage also of the least viscous PCMs, and the design should always consider the volume expansion and contraction during the phase change. When there are no strict requirements on the strength, also thin flexible plastic (e.g. polyethylene) bags can be used, as they accommodate the volume change and do not require an ullage space.

Micro- and nano-encapsulation are interesting as they allow avoiding bulky containers and feature microbeads with a polymeric or inorganic shell and a PCM core. This confinement technique, with capsules in the micron- or sub-micron-scale range, offers two main advantages. The first is that a microencapsulated PCM is easy to handle and to embed in other materials such as gypsum and concrete by simple mixing, and it can be also added to liquids to produce PCM-enhanced heat transfer fluids. The second advantage is represented by the augmented specific surface area (SSA), which increases the heat transfer surface and enhances the overall thermal exchange. The capsule shells must be stable over many melting/solidification cycles and must not have any chemical interaction with the PCM.

There are several physical, physical-chemical, and chemical techniques available to produce PCM microcapsules (Table II - 2). Among all techniques, the most diffused, researched, and developed on industrial scale is the in-situ polymerization, which includes interfacial, suspension and emulsion polymerization (Jamekhorshid et al., 2014; Konuklu et al., 2015). These techniques differ from each other mainly in terms of polarity and solubility of the monomers and the initiator. A schematic representation of these techniques is depicted in Figure II - 7. In the interfacial polymerization (Figure II - 7a), the polymeric shell wall is the result of the polymerization of polar and non-polar monomers dissolved in the water and oil phase of an oil-in-water emulsion, respectively. The shell growing at the interface of the two phases becomes a barrier to diffusion and limits the reaction kinetics, thereby influencing the shell thickness and morphology. Common shell materials are polyurea, urea-formaldehyde and melamine-formaldehyde. In the suspension polymerization (Figure II - 7b), all the reactants are liposoluble and are dispersed in the water-based

medium due to continuous agitation and the help of surfactants. Therefore, with this technique it is difficult to encapsulate hydrophilic PCMs such as PEGs or salt hydrates. The shape and size of the resulting particles is strongly influenced by the stirring speed, amount of stabilizer, fraction of the monomer phases and relative viscosity of the droplets and the water medium. This technique is similar to the emulsion polymerization (Figure II - 7c); the main difference is the hydrophilic nature of the initiator, which is dissolved in the water phase. Common shell materials for both these techniques are acrylic and styrenic polymers such as poly(methyl methacrylate) (PMMA), polystyrene, and styrene-divinylbenzene copolymers (Tyagi et al., 2011; Zhao and Zhang, 2011).

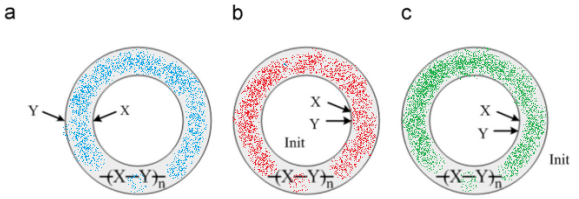

Figure II - 7. Schematic representation of the chemical microencapsulation methods. (a) interfacial polymerization; (b) suspension polymerization; (c) emulsion polymerization (X and Y: monomers; Init: initiator). Adapted from (Jamekhorshid et al., 2014).

Another interesting technique to prepare microcapsules is the sol-gel method, in which a solid shell forms through the gelation of a colloidal suspension (the "sol"). This colloidal suspension, which is often more accurately a solution, is prepared starting from a molecular precursor, such as a metal alkoxide $[M^{n}\text{-}(OR)_n]$ (Wang et al., 2006; Ciriminna et al., 2011).

Figure II - 8 illustrates the general sol-gel encapsulation route to obtain a silica (SiO_2) shell starting from tetraethyl orthosilicate (TEOS) as the molecular precursor. The PCM is first dispersed in an aqueous medium with the help of surfactants to form a stable oil-in-water (O/W) emulsion. The amount of PCM, the polarity of the aqueous medium and the type and concentration of surfactant are important parameters determining the final micelle size and thus the capsule dimension. Separately, TEOS is dissolved in a water medium, e.g. a water-ethanol solution, and the pH of the solution is generally lowered to favor the hydrolysis reaction. Once the hydrolysis is complete, the precursor solution is added to the PCM emulsion; here, a controlled condensation reaction of the precursor happens around the PCM droplets, under basic conditions. The result of the condensation reaction is the formation of an extended silica network around the PCM droplet. The main advantage of sol-gel techniques is the possibility to form a ceramic (e.g. SiO_2, TiO_2, $CaCO_3$) shell, which is generally

stronger and stiffer and exhibits a higher thermal conductivity than the polymeric shells (Lin et al., 2019). On the other hand, pure metal oxides are usually brittle and subjected to cracks. To mitigate their fragile behavior, the molecular precursor can be chosen that contains a hydrocarbon side group, which will be present also in the final network, resulting in a hybrid organo-ceramic material. For example, organosilica shells produced from methyltriethoxysilane $CH_3Si(OCH_3)_3$ (MTES) are less brittle and more flexible than those produced from TEOS, thanks to the side methyl group that remains in the resulting network (Chen et al., 2013a; Tang et al., 2017).

Table II - 2. Advantages and disadvantages of the main microencapsulation methods (adapted from (Jamekhorshid et al., 2014), with data from (Freitas et al., 2005))

Technique	Advantages	Disadvantages	Particle size (μm)	Encap. ratio (%)
Physical methods				
Spray drying	- Low cost - Easy to scale-up - Versatility	- Particle agglomeration - High temperature - Uncoated particles - Difficult control of the particle size	0.1-5000	38-63
Solvent evaporation	- Low cost	- Difficult to scale-up	5-1500	
Physic-chemical methods				
Coacervation	- Versatility - Precise control of the particle size	- Difficult to scale-up - Agglomeration	2–1200	6–68
Sol-gel	- Inorganic shell with high thermal conductivity	- Difficult to bring to industrial level - Complex reactions involved	0.2–20	30–87
Chemical methods				
Interfacial polymerization	- Wide range of shell materials - Already at industrial level - Versatility	- Moderate cost - Solvent handling	0.5–1000	15–88
Suspension polymerization			2–4000	7–75
Emulsion polymerization			0.05–5	14–67

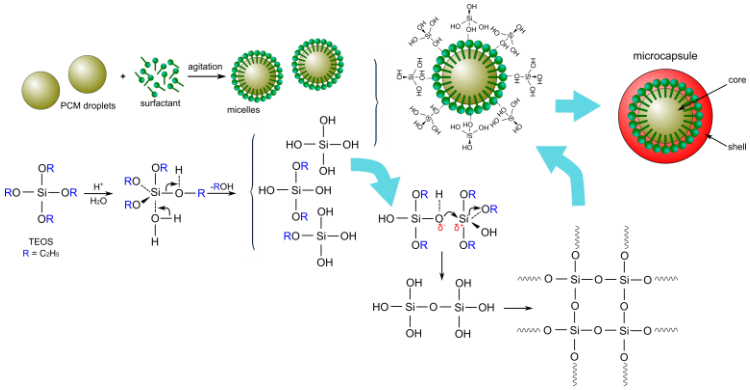

Figure II - 8. Encapsulation of an organic PCM via a sol-gel process starting from TEOS (adapted from (Zhang et al., 2010a)).

2.2.4.2 Shape-stabilization

In the field of phase change materials, the term “shape-stabilization” is sometimes used as a synonym of “confinement”, also including the microencapsulation techniques (Umair et al., 2019). However, the vast majority of the dedicated literature refers to “shape-stabilization” to indicate all methods to prevent PCM leakage *besides* encapsulation, and this is the meaning that this term assumes also in this thesis work. Shape-stabilization techniques involve the creation of a composite PCM via the addition of layered or porous materials, inorganic nanofillers, or polymer matrices, to produce a compound without any manifest leakage or exudation even when the PCM is in the molten state. Such techniques are generally less expensive than the microencapsulation and yield a higher thermal conductivity, but the PCM is not completely isolated from the external environment and some leakage may happen after several thermal cycles.

One of the simplest techniques to obtain a composite PCM is the dispersion of nanoparticles, such as carbon nanotubes (CNTs) (Zhang and Liu, 2019), graphene oxide (GO) (Xia et al., 2019), expanded graphite (EG) (Sarı and Karaipekli, 2007; Zhang et al., 2010b), expanded graphite nanoplatelets (xGnPs) (Biswas et al., 2014), nanoclays (Xie et al., 2019), metallic and metal oxide/nitride nanofillers (Fang et al., 2014), which increase the mixture viscosity and prevent the leakage thanks to their high specific surface area (Umair et al., 2019). The shape-stabilization effect can be achieved by simple melt blending, vacuum impregnation or grafting of the PCM chains onto the nanofillers. Moreover, the inclusion of carbon- or metal-based fillers can enhance the thermal conductivity, thereby improving the energy storage rate and efficiency especially of the organic PCMs (Yuan et al., 2018).

An analogous effect of enhanced thermal conductivity can be achieved by shape-stabilizing the PCM through a highly conductive foam, where the PCM can be accommodated within the interconnected porosity. Such foams are generally metallic, ceramic, or carbon-based and are characterized by a high porosity, interesting mechanical properties, and thermochemical stability. For example, Huang et al. (Huang et al., 2017) explored the possibility to infiltrate nickel and copper foams with myristyl alcohol (MA), an organic PCM with chemical formula $C_{14}H_{30}O$, melting point of 40.4 °C and latent heat of fusion of 218.4 J/g, for solar thermal energy storage (Figure II - 9). The infiltration of molten PCM, performed under vacuum conditions, resulted in a total PCM content of 60-80 wt%, and it increased with the pore size. The thermal conductivity of the impregnated foams was up to 7.5 times higher than that of the neat MA and increased with decreasing pore size.

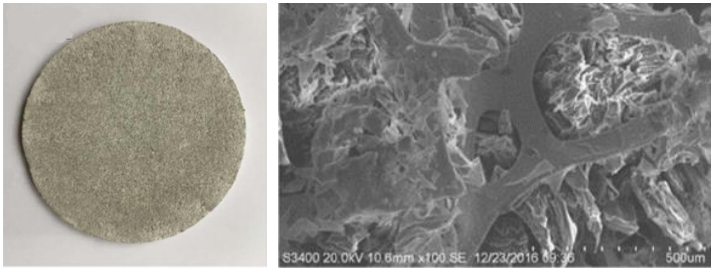

(a) (b)

Figure II - 9. MA-impregnated nickel foam. (a) full image; (b) SEM micrograph (adapted from (Huang et al., 2017)).

Blending organic PCMs with polymer matrices is another diffused technique to prevent leakage in the temperature interval between the transition temperature of the PCM and the melting point (for semicrystalline polymers) or the glass transition temperature (for amorphous polymers) of the surrounding matrix (Pielichowska and Pielichowski, 2014). One of the most widely used strategies consists in combining paraffinic PCMs with polyolefins like polyethylene (PE) and polypropylene (PP), due to their physical-mechanical properties and the chemical compatibility with paraffins, but other commonly used polymers are acrylics, poly(vinyl chloride), polyurethanes and elastomers as ethylene-propylene diene monomer (EPDM) rubbers (Pielichowska and Pielichowski, 2014). For example, Resch-Fauster and Feuchter (Resch-Fauster and Feuchter, 2018) compared the properties of PE, PP and an ethylene-propylene copolymer (E/P) as shape-stabilizing matrices for high-molecular weight paraffin waxes. Samples were prepared via melt blending and compression molding; the total amount of PCM in the blends varied between 25 and 38 wt%, which resulted in a phase change enthalpy of 53-71 J/g. A co-crystallization was evident in the PE-PCM

composites, while for PP and E/P the crystallization of the PCM was not affected by compounding, but the PCM acted as a plasticizer and a nucleating agent for the surrounding matrix, thereby increasing the crystallinity of the matrix. Nevertheless, the satisfactory heat storage properties were accompanied by a decreasing in the mechanical performance after PCM addition. This was noticed especially above the PCM melting transition, associated to a decrease up to 85 % in the elastic modulus and 54 % in the tensile strength, which led the authors to conclude that such PCM-polymer blends are not suitable as load bearing materials. This aspect is described more in detail in Section 2.6.1.

2.2.5 Cost and sustainability of PCMs

TES systems based on PCMs are generally more expensive than sensible heat storage materials. Although the PCMs are widely studied in many different fields, and new materials with a high latent heat of phase change are constantly being discovered and synthesized, PCMs are currently being massively employed only in building and construction applications (Dincer et al., 2017), but even in this sector the time required to recover the initial investment cost can be of up to several decades. Besides the buildings field, PCMs do not have a fully developed market or high demands, which determines a considerable cost increase. The majority of the total cost of a PCM system is represented by the cost of the material (some tens of dollars per kWh) and its confinement (encapsulation or shape-stabilization), as the cost of macroencapsulation can reach approx. 20 % of the total, while the price of microencapsulation can also represent the 50 % (Dincer et al., 2017).

For the PCM classes, commercial paraffins are by-products of oil refining and their cost is limited, but it strongly depends on the purity of the material. The price per kilogram ranges from units of dollars for technical grade alkanes (purity $\approx$ 90%) to tens of dollars for the analytical grade variations with ultra-low concentrations of impurities (Fleischer, 2015).

The environmental impact of materials and systems must be evaluated throughout the whole life of the component. One of the most complete and valuable approaches to comprehensively assess the environmental footprint of any products or systems is Life Cycle Assessment (LCA) (Kylili and Fokaides, 2016), which considers all the inputs and outputs of a system from the extraction of the raw materials to the manufacture, service time, maintenance and end of life. The inputs are evaluated as the raw materials and the required energy for each step, while the outputs are regarded as all the solid, liquid, and gaseous waste materials released into the environment during the whole life cycle. The PCMs, and in general the TES systems, have a positive environmental impact during their operating period, as they reduce the gap between energy demand and availability, help saving primary energy resources, and reduce CO_2 emissions. On the other hand, the other life cycle stages, such as production, fabrication, and disposal, can have a negative impact on the environment.

To estimate the balance between these contributions and calculate the net environmental impact, the LCA has been proven an effective approach, as it considers all the single contributions and evaluates the performance even of complex systems. In this way, the LCA helps industries and organizations to select specific indicators to describe the effect of a system on the environment and to identify opportunities for improving the environmental impact of the evaluated product.

LCA has been performed on PCM systems especially for building applications, following the general guidelines described in the international standards ISO 14040 and ISO 14044, and the results of this investigation has been illustrated in some broad-ranging review papers (Kylili and Fokaides, 2016). Several PCM-containing systems (e.g. polyurethane foams containing microencapsulated paraffins or hydrated salts, PCM-enhanced alveolar bricks, concrete structures incorporating PCMs) were investigated and compared with more traditional counterparts. In all the cases, the solutions including a PCM resulted more environmentally friendly than the conventional thermally insulating systems (Kylili and Fokaides, 2016). However, as the implementation of this technology is at its infancy, a deeper investigation is required to fully understand the environmental implications of PCMs and to assess their impact compared to their alternatives (Dincer et al., 2017).

2.2.6 Thermal conductivity enhancement of organic PCMs

One of the main disadvantages of organic PCMs is their inherent low thermal conductivity, which reduces the charging/discharging rate and may inhibit the completion of the phase change process in applications with fast heating or cooling, thereby limiting a full exploitation of the TES capability of the storage medium (Qureshi et al., 2018). To overcome this problem and enhance heat transfer rate, several solutions have been proposed and implemented, which involve the increase in the heat exchange surface and/or the use of highly conductive fillers, containers, and stabilizing agents (Liu et al., 2016a; Lin et al., 2018).

Among these techniques, the addition of highly conductive fillers is the most common technique to specifically tackle the thermal conductivity issue. Several types of fillers are currently employed, which can be classified as carbon-based, metallic, and ceramic (Fan and Khodadadi, 2011; Lin et al., 2018).

Carbon-based fillers are among the most popular additives, because, besides a high thermal conductivity, they feature considerable thermal stability and low density. They are available in several morphologies, such as carbon fibers and nanofibers, carbon nanotubes and nanospheres, graphene oxide, expanded graphite, and expanded graphite nanoplatelets. Sari et al. (Sarı and Karaipekli, 2007) impregnated the porous lamellar structure of EG with *n*-docosane, and the produced PCM composite could be considered as shape-stabilized for an EG content of 10 wt%. Moreover, the thermal conductivity increased linearly with the EG content, from 0.22

W/(m·K) of the pure docosane to 0.82 W/(m·K) of the composite containing 10 wt% of EG.

Besides the thermal conductivity, also the shape, size, aspect ratio, orientation and dispersion of nanofillers have great impact on the final thermal properties of the PCM (Qureshi et al., 2018). Recently, Zhang et al. (Zhang and Liu, 2019) evaluated the performance of an anisotropic ordered CNT array as shape-stabilizer and thermal conductivity enhancer for a paraffinic PCM. Embedding the CNT array resulted in a decrease in the phase change enthalpy by 15 %, but the thermal conductivity increased from 0.235 W/(m·K) of the neat paraffin up to 12.3 W/(m·K) for the composite PCM in the direction of the CNT axis (for the transversal direction, the thermal conductivity was 4.17 W/(m·K)).

The combination of microencapsulation and the use of conductive materials can further enhance the thermal conductivity. For example, Lin et al. (Lin et al., 2019) encapsulated stearic acid in silica shells, and the microcapsules had a higher thermal conductivity than the neat PCM, due to the synergistic effect between the increase in the heat transfer area and the high intrinsic thermal conductivity of the ceramic shell. The authors also modified the prepared microcapsules by grafting GO on the shell surface and noticed a further increase in thermal conductivity.

2.3 Applications of PCMs for heat management

The present Subchapter introduces some examples and case studies about the use of PCMs in several applications of thermal energy storage and thermal management, to highlight the variety of potentialities of such materials and provide the instruments for a deeper understanding of their working principle. This Subchapter will focus especially on the thermal management applications, as these are the intended applications for the materials developed in this thesis work.

2.3.1 Thermal management in buildings

The energy consumption in buildings has dramatically increased in the last decades due to population growth, climate change, and raised demand for thermal comfort and indoor environmental quality (Cao et al., 2016). Housing and tertiary buildings account for the consumption more than 40 % of the total primary energy and approximatively 19 % of the overall CO_2 emissions (Cabeza, 2014; Cao et al., 2016). Considering the residential buildings, among the energy end-uses, space heating and water heating are responsible for the largest portion of total energy consumption, which is 57 % in the U.S., 71 % in China and 80 % in the E.U. (Cao et al., 2016). Hence, it is of primary importance to address and constantly improve the energy efficiency of buildings; one of the solutions implemented in the last decades involves the use of PCMs in passive or active energy storage systems.

2.3.1.1 Passive storage systems

Passive storage systems include the heating/cooling technologies without an active mechanical device and with little or no external energy inputs. An example of passive storage system is represented by the inclusion of PCMs in wallboards, ceilings or flooring materials, which can store excess energy during the day (peak hours) to release it during the night (off-peak hours), helping to regulate the temperature also in extreme weather conditions (Pielichowska and Pielichowski, 2014). As the indoor thermal comfort is generally considered achieved in a temperature interval between 18 °C and 25 °C, this is also the range of phase change temperatures of the selected PCMs (Kenisarin and Mahkamov, 2016).

Even though the concept of using LH-TES in buildings has been known for decades, one of the first systematic studies was performed by Feldman and Banu (Feldman and Banu, 1996), who fabricate PCM-enhanced lab-scale gypsum wallboard samples. The PCM phase, represented by a mixture of fatty acids, was introduced by impregnation (without further encapsulation or shape-stabilization), and it accounted for approx. 25 % of the total wallboard weight. The thermal storage capacity of the produced wallboards was studied on different scales. First, differential scanning calorimetry (DSC) was employed to measure the specific melting enthalpy of small specimens and allowed the evaluation of the uniformity of PCM distribution. The authors then upscaled the experiments and evaluated the total TES performance of a room lined with such wallboards. They concluded that, after the shooting off of the heating/cooling system, the room temperature could be maintained in the thermal comfort range for several hours longer compared to a room with traditional wallboards, without impairing the air quality (Scalat et al., 1996).

Particularly attractive are the technologies that allow the storage of excessive solar thermal energy, in order to release heat during the night or to reduce overheating due to solar radiation in the peak hours. An example of this second case is provided by Wang and Zhao (Wang and Zhao, 2015), who proposed a PCM-enhanced curtain to reduce the solar heat gain through the windows and thus the energy required for cooling, especially useful for modern glass-wall buildings. Numerical investigation demonstrated that the selection of the PCM with the most appropriate melting temperature plays a key role in determining the curtain performance, and that the heat gain of the indoor space can be reduced of up to 16.2 % with a PCM layer of 5 mm.

When talking about structural or rigid building elements, there are several ways of integrating PCMs. Besides the aforementioned direct impregnation, which can involve exudation of PCM and loss of performance over time, other techniques follow two approaches, namely the use of microencapsulated PCMs to be mixed with construction materials, and the addition of a macroencapsulated or variously stabilized PCM as a supplementary layer (Akeiber et al., 2016). One of the most recent studies implementing the first approach is that of Bao et al. (Bao et al., 2019), who developed a high performance PCM-enhanced cement composite for passive solar buildings. The

PCM phase is represented by a paraffin wax (T_m = 28 °C) microencapsulated in polymeric shells containing graphite flakes, added during microcapsule synthesis to enhance the thermal conductivity. Such microencapsulated PCM was mixed with the cement matrix together with nanosilica and short carbon fibers, in order to preserve the mechanical properties and further enhance the thermal conductivity.

2.3.1.2 Active storage systems

Active storage systems are used to store heat produced when the primary energy source is more abundant or less expensive. In buildings, active storage systems based on PCMs are used to store heat produced by the heating systems during the night, so that the energy peak is effectively reduced and shifted to nighttime when the cost of electricity is lower. Lin et al. (Lin et al., 2005) developed a floor heating technology integrated with shape-stabilized PCM panels. Such panels, made of paraffin with a melting temperature of 52 °C (75 wt%) and polyethylene as supporting material, were placed under a wood floor onto electric heaters. Large-scale experiments proved that the system was effective in increasing the indoor temperature and in keeping the temperature in an acceptable range long after the heaters were switched off.

2.3.2 Smart textiles

The embedment of PCMs in textile fabrics leads to the production of smart textiles that help regulating the body temperature and are particularly useful in situations of extreme weather conditions. One of the first examples of PCM-enhanced textiles was produced by NASA; nonadecane was added to garment fabrics (e.g. in the space suits) to limit the impact of the extreme temperature changes to which the astronauts are subjected during space missions (Mondal, 2008). Later, such smart thermoregulating textiles were employed to enhance the thermal comfort of mountain outdoor clothing and apparel, but also of blankets, mattresses and pillow cases (Pielichowska and Pielichowski, 2014).

There are five main ways to embed a PCM in a synthetic textile: (a) the mixing of the PCM with the melt/wet spun polymer in the form of core filament; (b) the production of core-sheath fibers, in which the core is composed by the PCM and the shell is the supporting polymer; (c) the introduction of PCM microcapsules in the melt/wet spun polymer; (d) the application of microencapsulated PCMs on fabrics using suitable binders or coating materials; (e) the introduction of a PCM-enriched inner layer (e.g. polyurethane foam containing PCM microcapsules) (Iqbal et al., 2019). Among these techniques, the first three methods are often preferred as they result in versatile multifunctional polymer fibers with the PCM phase stably confined into the surrounding polymer, which reduces the risk of removal during washing (Iqbal and Sun, 2015). However, the shear stresses, high temperature and/or aggressive

solvents present during the fiber spinning process could damage the PCM microcapsules, thereby causing PCM leakage and low final phase change enthalpy.

Among the most famous examples of PCM-containing polymer fibers are those marketed by Outlast Technologies. This company produces viscose/rayon and acrylic fibers containing a microencapsulated PCM, and the final fiber has a phase change enthalpy of 1-20 J/g (Hartmann et al., 2007) (Figure II - 10a). The same company also produces PCM-enriched coatings for outwear, footwear, bedding and seating, and it patented a technology to print PCM microcapsules onto flat fabrics, which can be directly introduced in the fabric production line (Figure II - 10b,c) (Outlast®, 2018).

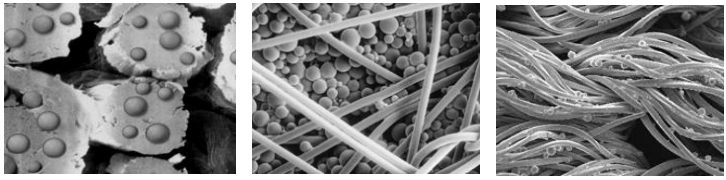

(a) (b) (c)

Figure II - 10. PCM-enriched textiles marketed by Outlast. (a) Acrylic fibers embedded with microencapsulated PCMs; (b) Coated materials; (c) Matrix infusion coating (adapted from (Outlast®, 2018)).

The embedment of PCMs in fibers is interesting not only for the production of smart textiles, but also to fabricate multifunctional polymer filaments that can be co-woven with continuous reinforcing glass or carbon fibers, to produce a multifunctional yarn containing the matrix, the reinforcement and the PCM. This is an interesting route that can be explored to fabricate thermoplastic composites with TES properties. This topic has also been developed in this thesis and is described in Subchapter 4.5.

2.3.3 Thermal management of electronics

Electronic devices are well known to be sensitive to temperature, since their performance and lifetime span depend strictly on their maintenance in a precise temperature range, with a particular attention to avoid overheating. As the electronic components are being equipped with increasingly sophisticated electronics while their dimensions have decreased, the risk of overheating has also grown. Without a proper thermal management system, the heat generation and associated temperature rise may deteriorate the performance, bring critical components to failure and decrease the user-device interaction comfort (Fok et al., 2010). Overheating is among the most common causes of failure of electronic components, as approximately 55 % of failures can be related to high temperature problems or poor thermal management (Sahoo et

al., 2016). It has been shown that a decrease of 1 °C can decrease the failure rate of up to 4%, and an increase of 10-20 °C can double the failure probability (Sahoo et al., 2016).

An effective thermal management system must also comply with the weight and size limitations, as these design parameters are increasingly important for electronic components that must be carried around, such as portable and wearable electronic devices, but also batteries and circuitry for electric vehicles (EVs). In this perspective, PCMs are becoming an attractive alternative to more bulky solutions as the natural or forced convection (active cooling), also because electronic devices do not normally need to operate continuously for long periods (Kandasamy et al., 2007). When the device is in a heat peak and its temperature starts rising, the PCM melts and absorbs excess heat, thereby preventing an excessive temperature burst (passive cooling). When the temperature starts decreasing again, the PCM crystallizes and releases the heat back to the environment. The ideal PCM for this application has a high energy density per unit mass and volume, a phase change temperature slightly below the maximum operating temperature of the component, and a high thermal conductivity.

Pioneering experimental work of investigation on using PCMs on mobile electronic devices was carried out by Tan and Tso (Tan and Tso, 2004), who assessed the efficacy of a passive cooling unit based on *n*-eicosane for the thermal management small hand-held personal computers (personal digital assistants). The PCM was contained in an aluminum case and placed under the heaters simulating the heat generation units of such a device, i.e. the processor and other integrated circuit packaging. The authors concluded that the PCM units were indispensable to keep the working temperature of the device under an acceptable threshold of 50 °C and that the efficacy of the heat storage unit depended not only on the amount of PCM but also on its orientation, which determined the heat flux distribution in the whole device. The same concept was developed by Tomizawa et al. (Tomizawa et al., 2016), who investigated numerically and experimentally a passive cooling unit for mobile phones, containing a commercial microencapsulated paraffin with a melting temperature of 32 °C. The PCM was mixed with polyethylene and molded as a sheet to be included in the mobile phone (Figure II - 11). The authors concluded that the PCM sheet actively contributed to slow down the temperature increase, and this effect was more evident with thick sheets.

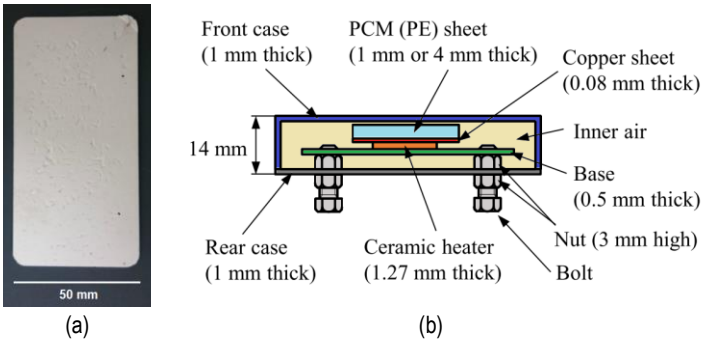

Figure II - 11. (a) PCM sheet; (b) cross-sectional view of the mobile phone heating simulator (adapted from (Tomizawa et al., 2016)).

PCMs can be also employed for the thermal management of EV batteries, to support or replace the traditional cooling systems based on liquid/air circulation (Dincer et al., 2017; Ianniciello et al., 2018). The first attempts to integrate PCMs in automotive field date back to the early 2000s, when Al Hallaj and Selman (Al Hallaj and Selman, 2000) proposed a battery pack in which each cylindrical Li-ion cell was wrapped with a PCM layer with a melting temperature in the range 30-60 °C. The authors demonstrated experimentally and numerically that the total temperature fluctuation was considerably lower with the PCM.

Successive approaches tried to address the low thermal conductivity of PCMs and the need for improving the thermal uniformity inside the battery pack. The most promising solutions involve metal or graphite foams as shape-stabilizers and thermal conductivity enhancers. Goli et al. (Goli et al., 2014) prepared a composite PCM combining paraffin wax and exfoliated graphene, which exhibited a thermal conductivity two order of magnitude greater than that of the neat paraffin. Experimental and numerical simulations proved that this composite PCM led to a considerable decrease in the heating rate and maximum temperature inside the battery pack, outperforming not only the design without a PCM, but also that with unfilled paraffin. More recently, Zou et al. (Zou et al., 2019) studied the introduction of various carbon based nanofillers (e.g. EG, CNTs, graphene) in a paraffin wax, to produce a shape-stabilized PCM to be employed in a 38120-type $LiFeO_4$ battery pack. They found that this composite PCM was able to reduce not only the maximum operating temperature, but also the temperature oscillations.

Other approaches tackle the problem of thermal management using hybrid systems that combine PCMs with forced convection systems, thereby exploiting active and passive cooling. Qin et al. (Qin et al., 2019) included a paraffin wax (T_m = 56 °C) in the design of a forced air circulation system (Figure II - 12), showing that the

combination of the two contributions helps in maintaining the temperature within the acceptable range.

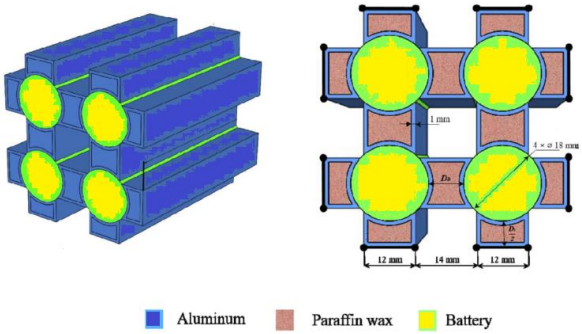

Figure II - 12. Hybrid thermal management system for EV batteries combining a PCM and forced air circulation (adapted from (Qin et al., 2019)).

2.3.4 Biomedical applications

Due to their ability to store excess heat at a nearly constant temperature, PCMs are becoming appealing for biomedical applications that require thermal protection. Smart thermoregulating biocompatible fabrics can be used to keep the skin in a certain temperature range, which can be useful for heat/cool therapy and burn wound dressing.

Controlled heat absorption and release can also be employed to protect living tissues from excessive heat or cold. For example, Król et al. (Król et al., 2016) added shape-stabilized PEG to a PMMA-based bone cement formulation, in order to decrease the peak polymerization temperature and prevent overheating and damage to the surrounding tissues. The results showed that this biodegradable and biocompatible PCM, added in a weight fraction of 15 %, led to a significant decrease in the peak temperature, from 70.2 °C to 58.3 °C. Moreover, the PEG addition determined the formation of micrometric pores on the bone cement surface, which caused a decrease in the compression strength but also favored cell proliferation during bone formation and improved the final osteointegration.

PCMs can be also used during cryosurgery of tumors, as in the concept proposed by Lv et al. (Lv et al., 2011); if PCMs are injected in the tissues surrounding the tumor, the heat released during PCM crystallization prevents an excessive temperature drop of the healthy tissue, thereby protecting it from damages and necrosis. Theoretical studies showed that PCM addition could maximize the necrosis of tumoral cells and minimize the injury to the surrounding tissues.

2.3.5 Thermoregulating packaging

Food, medical supply, or other perishable products must be marketed and distributed while kept in a specific temperature range, usually under refrigerating conditions, in order to avoid spoilage and preserve product quality and safety. This may be an issue during product transportation and temporary storage in provisional warehouses that may lack temperature control (Cabeza, 2014; Singh et al., 2018; Alehosseini and Jafari, 2019). The traditional way to address this problem is to provide an effective insulation, but this might not be sufficient, and the tendency to produce low-cost and lightweight packages often leads to packaging materials with limited thermal buffering capacity (Singh et al., 2018).

A recent conceptual advancement was obtained by imbuing packaging with heat management properties, and organic PCMs with a melting temperature between -5 °C and 10 °C are a suitable choice for producing smart thermoregulating packages that protect the contents from perishing while reducing the need for active refrigeration and energy consumption (Alehosseini and Jafari, 2019).

An example of PCM-enhanced packaging was proposed by Johnston et al. (Johnston et al., 2008), who employed a highly porous nanostructured calcium silicate powder to shape-stabilize a paraffin wax with a melting point of 8 °C. The authors used such PCM composite to line a paperboard container, which was proven able to maintain the inner temperature below 10 °C for 5 hours after the outside temperature was increased from 2 °C to 23 °C. Recently, for food applications, there has been a strong tendency towards choosing the PCM in the fatty acid family, as they are biodegradable and can be produced from renewable resources. For example, Ünal et al. (Ünal et al., 2019) designed a three-layer cardboard box where the middle layer was filled with bulk or microencapsulated octanoic acid, and the experimental results showed that the PCM-enhanced box was able to provide up to 8.8 hours of thermal buffering.

2.3.6 Flame resistance of organic PCMs

Due to their chemical composition, organic PCMs, and paraffin waxes in particular, are highly flammable, which is an issue especially when PCMs are employed as thermal management media in buildings, textiles, and electronic devices.

To address this problem, the most common solution is to incorporate conventional flame retardants (e.g. clays (Cai et al., 2007), metal oxides (Song et al., 2010), intumescent agents (Li et al., 2016), halogenated compounds (Zhang et al., 2010c)) in the microcapsule shell or directly in the PCM mass, where they can also contribute to improve the shape-stabilization and the thermal conductivity. Zhang et al. (Zhang et al., 2010b) incorporated expanded graphite and an intumescent fire retardant in a shape-stabilized polyethylene/paraffin PCM, and noticed that the fire resistance increased with the content of fire retardant, as the values of peak

heat-release rate measured in cone calorimetry tests were halved with a total filler content of 25 wt%. Similar results were also found by Li et al. (Li et al., 2016), who used the same strategy to improve the flame resistance of a polypropylene/paraffin PCM. The authors concluded that a total flame retardant content of 30 wt% considerably increased the PCM performance in the limiting oxygen index (LOI) and cone calorimetry tests.

2.4 Structural and semi-structural polymer composites

The present Subchapter gives a concise overview of polymer-matrix composite materials, with a special focus on the materials and methods employed in this thesis. After a brief introduction illustrating the definition and classification of polymer composites, the Subchapter presents the most diffused matrices and reinforcements and describes some of the state-of-the-art fabrication techniques.

2.4.1 Introduction to polymer composites

This Section describes the general definition and classification of polymer composites and then focuses on their applications.

2.4.1.1 Definition and classification

Composite materials are generally regarded as those consisting of two or more distinct materials or phases, which exhibit remarkably different mechanical and/or physical properties. Therefore, the properties of the resulting material are noticeably different from those of each constituent, and the composition is tailored to obtain the combination of properties that best suits the constraints given by the production process and the application (Agarwal et al., 2018).

Composite materials pervade our world. Besides being the most widespread material type among natural and biological materials, composites have been produced and used by mankind for thousands of years; one of the first examples of man-made structural composites is represented by the straw-reinforced mud bricks, found in Mesopotamia and dating back to 4900 BC. However, it is only in the last century, with the advent of high-strength synthetic fibers and the enormous advances in polymer chemistry and technology, that composite materials can be made that offer performance comparable or even superior to those of well-established structural materials such as metals (Campbell, 2010).

Composites are generally constituted by a continuous phase, the *matrix*, and one or more discontinuous phases, the *fillers*, which are generally stronger and stiffer than the matrix and therefore can be also called *reinforcements* or *reinforcing agents* (Petrucci and Torre, 2017). Composite materials can be classified according to the matrix material as polymer matrix composites (PMCs), ceramic matrix composites

(CMCs) and metal matrix composites (MMCs). Each of these classes has a particular set of properties and specific application fields, as the matrix has a strong influence on several mechanical properties of the composite, such as transverse modulus and strength and the properties in shear and in compression, as well as on the maximum service temperature (Agarwal et al., 2018). For the purpose of this thesis, only polymer composites were taken into account, as they are the most widely used in structural and semi-structural applications at low-medium temperatures (0-250 °C), due to their lightness and high specific stiffness and strength. Therefore, the discussion will focus on this type of composites.

Polymer composites combine a polymer matrix with one or more fillers, commonly added to improve stiffness, strength, toughness, and high-temperature performance. As the mechanism of improving a property strongly depends on the filler geometry, it is convenient to classify polymer composites according to the reinforcement type, shape, and size. The reinforcement can be made of fibers or particles, as observable from the commonly accepted classification reported in Figure II - 13. The most common types of reinforcements and matrices used to produce polymer composites are described in Sections 2.4.2 and 2.4.3, respectively.

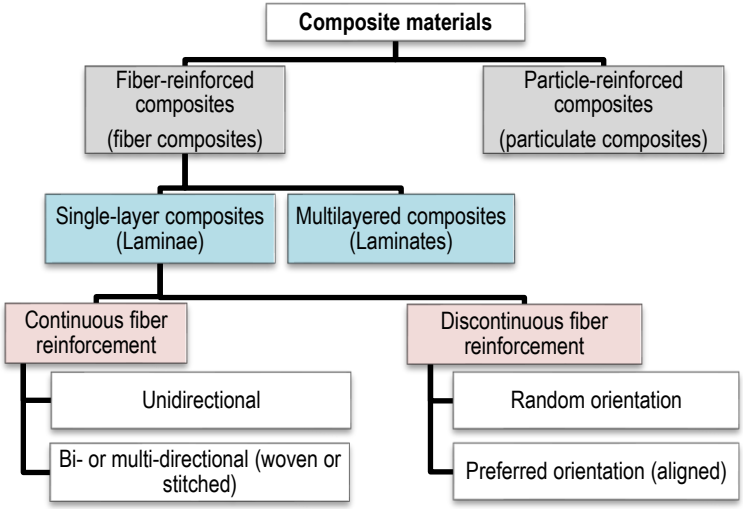

Figure II - 13. Classification of composite materials according to the geometry of the reinforcement (adapted from (Agarwal et al., 2018)).

2.4.1.2 Significance and applications

The main advantages of structural polymer-matrix composites are (i) the possibility to be tailored for optimum strength and stiffness in the different loading directions, and (ii) the combination of low density and high strength and modulus. This latter aspect results in higher specific (i.e. normalized by density) mechanical properties than those of comparable aerospace metal alloys, which in turn allows designing lightweight structures, thereby leading to improved performance and fuel savings, especially in the automotive and aerospace industries. Other advantages of structural composites compared lo lightweight metal alloys are the high fatigue life and the corrosion resistance (Campbell, 2010). Due to these features, composite materials are mainly applied in construction and transportation fields, but their application is expanding also in marine goods, sports equipment, and infrastructures.

On the other hand, among the main disadvantages of composite materials are the expensiveness of raw materials, fabrication, and assembly, as well as the higher sensitivity to temperature and moisture, which generally lead to a decrease in performance. Moreover, composites exhibit poor strength in the out-of-plane direction where the matrix carries the primary load, but this aspect can be mitigated by orienting the reinforcement properly. Composites are also more susceptible than metals to impact damage, are prone to suffer from delamination, and can be challenging to repair.

2.4.2 Reinforcements

Reinforcements in polymer composites are mainly divided into fibers and particles (Petrucci and Torre, 2017). For the samples prepared in this thesis work, the reinforcing agent was almost exclusively constituted by fibers, because their stiffness and strength combined with the high aspect ratio make them the most suitable reinforcement for structural and semi-structural components. The following Sections will focus on the main fiber classes and give some hints on the other reinforcement types.

2.4.2.1 Continuous and discontinuous fibers

Fibers are the primary load bearing components in fiber-reinforced composites. Several types of fibers are available for the reinforcement of different matrix materials in different applications, and the most widely used are glass, carbon, and aramid fibers.

Glass fibers dominate the market for large structures such as wind turbine blades, ships, and civil engineering structures, due to their low cost, high tensile strength, high impact strength and good thermal and chemical resistance. Although there are many kinds of glass fibers, the three most diffused in composites are E-glass,

S-2 glass, and quartz. E-glass is the least expensive and the most common, exhibiting a good combination of tensile strength (3.5 GPa) and modulus (70 GPa). S-2 glass is more expensive but stronger than E-glass, featuring a tensile strength of 4.5 GPa and a modulus of 87 GPa, and it has better mechanical performance at elevated temperature. Quartz fibers are made of a rather expensive, highly pure silica glass, used primarily in demanding electrical applications (Agarwal et al., 2018).

Carbon and graphite fibers are the most prevalent fiber types used in highly demanding applications such as aerospace, but their use is increasing also in the general automotive field. They outperform glass fibers in tensile stiffness and fatigue resistance. Graphite fibers are subjected to heat treatments of graphitization above 1650 °C, which determines a carbon content higher than 99 % and the growth of bigger and more aligned crystallites. This is the reason for their superior elastic modulus, greater than 345 GPa. On the other hand, carbon fibers do not undergo graphitization and have lower carbon contents (93-95 %) and lower stiffness (Wang et al., 2011a; Agarwal et al., 2018).

Aramid fibers (e.g. Kevlar) are the preferred choice when good impact energy-absorbing properties are required, such as in the military field.

An overview of the properties of these fiber types is reported in Table II - 3.

Table II - 3. Typical fiber properties (adapted from (Talreja and Varna, 2015)).

Fiber	Density (g/cm^3)	Young's modulus (GPa)	Tensile strength (MPa)	Strain at break (%)	Coefficient of thermal expansion ($10^{-6}/K$)	Filament diameter (μm)
E-glass	2.6	76	2000	2.6	4.9	5-20
Kevlar	1.45	130 (axial); 10 (radial).	3000	2.3	-6	12
HM carbon	1.95	380 (axial); 12 (radial).	2400	0.6	-0.7	5-10
HS carbon	1.75	230 (axial); 20 (radial).	3400	1.4	-0.4	5-10

HM = high modulus carbon fibers; HS = high strength carbon fibers.

Fibers are available on the market in several forms to suits different fabrication processes. Single filaments are produced with diameters of units to tens of micrometers, and they are collected in single bundles called strands or tows. Such bundles can be gathered in rovings, which generally contain 20 to 60 bundles, to produce the desired linear density. The strands can be also twisted together to form yarns. The most effective way to tailor the architecture of a composite so that the directional dependence of strength and stiffness matches that of the loading environment is to weave tows, rovings and yarns into fabrics, which can be unidirectional or bidirectional and have a different weave, classified by the pattern of

interlacing (e.g. plain, twill, satin weave, see Figure II - 14) (Mallick, 2007; Campbell, 2010).

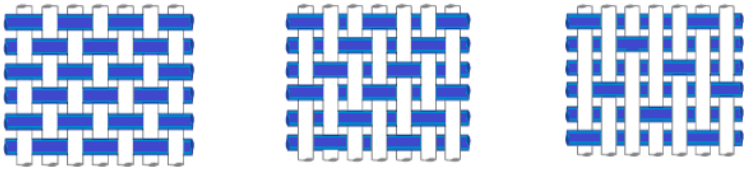

Figure II - 14. Common two-dimensional weave styles: (a) plain; (b) twill; (c) satin (adapted from (Campbell, 2010)).

Unidirectional fibers or woven textiles can also be impregnated with a controlled amount of resin to form a prepreg, an important product form largely used for advanced composite manufacturing. Prepregs usually consist single textile layers impregnated in B-staged (advanced to a tacky semisolid) resin, which are kept refrigerated to prevent further advancement and change in the resin state (Long, 2006).

Discontinuous fibers are obtained by chopping rovings into small fiber length, which can vary between 1 and 50 mm, while even shorter fibers can be produced by hammer-milling. Long chopped fibers are usually integrated in thermosetting resins for compression and transfer moldings, while shorter chopped reinforcements are suitable to be blended with thermoplastic systems for injection molding. Milled fibers provide a good combination of reinforcing properties with processing ease and are used to reinforce thermoplastics when the strength requirements are low to moderate.

2.4.2.2 Particles and other reinforcements

Particle-reinforced composites, or particulate composites, are not generally employed for structural applications. Due to the much lower aspect ratio, particles are less effective than fibers in enhancing mechanical properties such as stiffness and strength of the host polymer. On the other hand, particulate composites are widely employed where the demands on mechanical properties must be subordinated to cost and/or processing requirements. In this sense, particulate composites fill the properties and applications gap between fiber-reinforced composites and unreinforced plastics (Rothon, 2003; Campbell, 2010).

Particulate reinforcements include a wide variety of materials, which can be classified as natural or synthetic. Natural reinforcing fillers are of mineral origin and are mainly represented by carbonates (e.g. calcite and dolomite), clays (aluminum silicates) and talcs (magnesium silicates). Such fillers are used for cost reduction, but they also increase the stiffness and strength of the host polymer; some mineral fillers

are used for their good electrical insulation properties, chemical inertness, low water absorption, low coefficient of thermal expansion (Rothon, 2003).

Synthetic reinforcing fillers include carbon black, synthetic silicas, hydroxides, basic carbonates, and precipitated calcium carbonate. Carbon black is produced on large scale for being incorporated in polymer matrices, and it is especially used as a reinforcing agent for elastomers in tire applications, as it improves tensile strength, tear strength, stiffness, abrasion resistance and dynamic-mechanical properties of the resulting composite (Shenoy, 1999). It is also used in some thermoplastics to improve the resistance to outdoor conditions (uv protection) and in the production of antistatic compounds (Biron, 2013).

Among the most important properties of reinforcing particles are geometrical factors like shape and size. Particle shape is fundamental in determining the final composite stiffness and strength, but also the melt rheology and the surface smoothness (Shenoy, 1999). The shape is determined not only by the chemistry and crystal structure of the filler, but also by the production conditions. The particles can be isodimensional (roughly spherical or irregular, 0D) or can assume a preferred orientation if they are acicular (1D) or platy (2D). In the latter case, they can be oriented during processing and the composite may result anisotropic or orthotropic. Some common particle shapes can be observed in Figure II - 15. Despite being such an important parameter, defining a particle shape is not always easy, as the literature abounds with vague terms and it can be difficult to distinguish between primary particles, aggregates and agglomerates (Sperling, 2006).

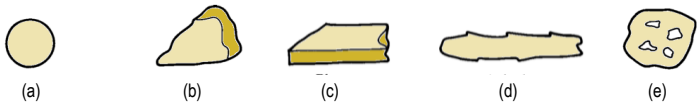

Figure II - 15. Common particle shapes. (a) spherical; (b) irregular; (c) platy; (d) acicular; (e) porous aggregate (adapted from (Rothon, 2003)).

Another fundamental parameter is the particle size. Size is determined by the processing conditions, affects a wide variety of properties and is fundamental for determining the specific surface area (SSA) of the filler, which influences the extent of the filler-matrix interface and all the related factors. The size of the particulate fillers in polymer composites is micrometric and ranges from units to hundreds of micrometers. Since size is such an important property, a variety of techniques have been developed to measure it, such as sieving, sedimentation, laser diffraction, or microscopic techniques. The SSA is usually measured by the permeability of a packed particle bed to a fluid or by the quantitative absorption of nitrogen according to the Brunauer, Emmett and Teller (BET) method. The value of particle size can be strongly influenced by the measurement technique and complicated if the particle shape is irregular. Moreover, beside the average particle size, it is also important to consider the particle

size distribution, which can be broadened also by the presence of particle fragments, aggregates and agglomerates (Petrucci and Torre, 2017).

A filler class that is gaining increasing attention is that of nanofillers, which include particles having at least one dimension in the nanoscale. To make this definition less vague, some authors (Rothon, 2003) have proposed to include in this class only the fillers that, when dispersed in a polymer matrix, are made of effective particles with at least one dimension below 20 nm. In this way, the SSA is at least of 150 m^2/g, being one or two orders or magnitude higher than that of microfillers. This definition excludes fillers such as carbon black: even though the primary particles meet the conditions, they are strongly aggregated into larger structures that can be considered as the effective particles.

Due to their considerable SSA, the surface is remarkably important for nanofillers. Even though they are used in lower volume fractions than microfillers, the total filler-matrix interface is still significantly higher. This determines an increase in the polymer fraction that is modified by the interaction with the filler surface and may have microstructure and properties remarkably different from the bulk polymer. The most common nanofillers include intercalated nanoclays, carbon nanotubes and nanofibers, colloidal or fumed silica. Although some nanofillers are added to increase the mechanical properties of the host polymer, such as stiffness and heat deflection temperature (HDT), nanofillers are mostly employed to enhance functional properties, e.g. to reduce the gas and fluid permeability or to increase the flame resistance or the thermal conductivity (Burger et al., 2016; Shen et al., 2017).

2.4.3 Matrices

In a composite, the matrix binds the reinforcement together, transfers load to the fibers or particles, and protects the fillers against the surrounding environment and the possible damage due to handling. The matrix is also critical in compression loading, to prevent premature failure due to fiber buckling, and it supplies the composite with toughness and damage tolerance. Polymer matrices are the most widely used for fiber composites due to their low cost, easy processability, good chemical resistance, and low density. On the other hand, their low thermal resistance limits their employment to applications below 300 °C (Sperling, 2006).

Polymer matrices for advanced composites are generally classified as thermoplastics or thermosets. Thermoplastics are high-molecular-weight polymers with no intermolecular covalent bonds; this requires them to be processed in the molten state, some degrees above the melting temperature or tens of degrees above the glass transition temperature, according to their semi-crystalline or amorphous nature. After being molded, their shape is consolidated upon cooling. Conversely, thermosetting polymers are supplied as monomers or oligomers having low molecular weight and low viscosity, and they are converted in a three-dimensional crosslinked structure upon heating. This allows them to be processed at mild temperature and

pressure conditions, but the crosslinking (curing) step, which traditionally happens in autoclave or in an oven, can be time consuming and limits a high output production. The result of the crosslinking is a hard, non-crystalline and often transparent resin with high modulus and strength, which is used for high-end applications in combination with high performance fibers. Unlike thermoplastics, thermosetting-based composites cannot be post-thermoformed, reshaped or welded, which limits their mendability and recyclability (Campbell, 2010).

The following two Sections report examples, advantages and applications of each of these two polymer classes, with a special focus on the matrices used in this thesis.

2.4.3.1 Thermosetting matrices

Thermosetting matrices encompass epoxies, polyesters, vinyl esters, bismaleimides, cyanate esters, polyimides, and phenolic resins. In the low-medium temperature range (up to 135 °C), polyesters and vinyl esters are extensively used for commercial applications, while epoxies are the preferred choice for high-performance composites and adhesives, due to the better mechanical properties and the higher environmental resistance. Bismaleimides and phenolics are most suitable resins in the medium-high temperature range (up to 175 °C), while polyimides are the matrix of choice for applications at very high temperatures, up to 315 °C (Wang et al., 2011a).

Epoxy matrices are extensively used for high-end applications due to their strength and excellent adhesion. They also exhibit low shrinkage during curing and high processing versatility. Epoxy resins are supplied as a bi-component system, as they are obtained through the chemical reaction between a prepolymer, carrying at least two oxirane rings, and the curing agent, usually containing amine groups. The reaction of oxirane ring opening and crosslinking with the curing agent is reported in Figure II - 16.

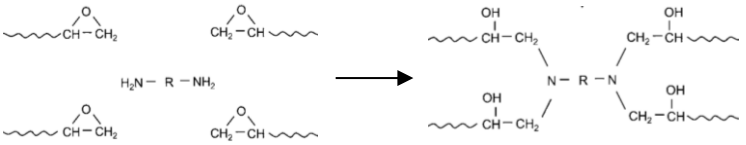

Figure II - 16. Example of oxirane ring opening and crosslinking reaction with an amine curing agent (adapted from (Campbell, 2010)).

Commercial epoxy matrices generally comprise one major and two minor epoxy prepolymers and one or two curing agents. The minor epoxies are added to tune the viscosity and/or to improve temperature resistance, toughness, and moisture absorption. The most widely used major epoxies, especially in the aerospace sector, are diglycidyl ether of Bisphenol A (DGEBA) and tetraglycidyl methylene dianiline

(TGMDA). The epoxy formulation also contains diluents in small amounts (3-5 %), to reduce the curing shrinkage, increase the shelf and pot life and control the exothermicity of the curing reaction. Typical diluents include butyl glycidyl ether, cresyl glycidyl ether, phenyl glycidyl ether, and aliphatic alcohol glycidyl ethers (Campbell, 2010).

During the curing of an epoxy resin, higher temperatures and longer times determine a higher crosslink density and therefore a higher glass transition temperature, especially if the precursors have high functionality (e.g. four reactive end groups per molecule). To avoid excessive brittleness, the resin can contain toughening agents, but this may result in lower thermal resistance (Campbell, 2010).

2.4.3.2 Thermoplastic matrices

Thermoplastic composites received considerable attention during 1980s-1990s, when massive investments were made to try to substitute thermosets with thermoplastics in the fabrication of aerospace composites. However, although thermoplastics have some undeniable advantages, their drawbacks limit their diffusion in some high-end fields, and therefore the vast majority of applications involving high-performance continuous fiber composites still prefer thermosetting matrices (Campbell, 2010).

As thermoplastics are not crosslinked, they are generally tougher than thermosets, and therefore they attracted the attention of the aerospace industry as they are more damage tolerant and have a greater low-velocity impact resistance. However, the toughening mechanisms available today for thermosets allow reaching a toughness comparable with that of thermoplastic systems. Moreover, thermoplastics exhibit a lower moisture absorption than thermosets, but some thermoplastics, especially those having an amorphous structure, also show a low solvent resistance (Biron, 2013).

Another potential advantage of thermoplastics is that they are fully reacted, and therefore they present a low risk of chemical hazard for the worker, who is not exposed to low-molecular-weight components. Additionally, they do not require refrigeration and have an infinite shelf life. Their state of fully reacted polymers also makes their processing in principle easier and faster. The shaping and consolidation time for thermoplastics is shorter than that of the thermosets, as it takes minutes instead of hours. Nevertheless, thermoplastic require high temperatures, in the range of 250-450 °C, considerably higher than the curing temperatures for thermosets (120-175 °C), which demands for presses and tooling materials that can withstand this temperature regime (Biron, 2013).

Due to the possibility of being remelted, thermoplastics can be joined via techniques as resistance welding or ultrasonic welding. They can also be post-thermoformed, which is very attractive as it suggests the possibility of producing continuous-fiber-reinforced flat boards to be subsequently cut and thermoformed into

the desired shape. However, since traditional continuous fibers have very little extensibility, this can be achieved only with very simple geometries, and also the defect healing via remelting can hardly be practiced without fiber distortion (Agarwal et al., 2018).

Due to these difficulties, the market of continuous fiber thermoplastics is limited to some specific polymers and applications. The most important matrices in this field are high-performance thermoplastics like polyetheretherketone (PEEK), polyetherketoneketone (PEKK), polyphenylene sulfide (PPS) and polyetherimide (PEI). They are highly aromatic thermoplastics with high glass transition temperature, good mechanical properties and good flame resistance (Biron, 2013).

Since the scarce diffusion of continuous fiber thermoplastic composites is mainly linked to the difficult processability of high-performance thermoplastics, new formulations are being developed that are supplied as liquid low-molecular-weight compounds and can be processed at room temperatures with the fabrication techniques typical of thermosets. The most recent example of such materials is the Elium resin (Arkema, France), an acrylic methyl-methacrylate-based formulation supplied as a low-viscosity liquid and processed at room temperature. The final material has a glass transition of approx. 100 °C and thermomechanical properties close to those of an epoxy resin, but it preserves the advantages of a thermoplastic composite related to the post-thermoformability and weldability (Bhudolia et al., 2017; 2018).

On the other hand, traditional thermoplastics like polypropylenes and polyamides are largely employed as matrices for discontinuous fiber composites in semi-structural applications in the automotive, sporting goods and electronic industries, due to their relatively low cost, easy processing and superior mechanical properties over unreinforced polymers (Kulshreshtha and Vasile, 2002).

2.4.4 Fabrication of fiber-reinforced composites

Unlike the majority of metals and unreinforced plastics, for which the material is first produced and then processed in the final product, fiber composite parts are generally produced together with the creation of the material. This is more evident for thermosetting composites, in which the final shape and material properties are produced during the matrix crosslinking. In thermoplastic composites, it is more common to fabricate the material first and subsequently shape it, but some material properties, like the fiber length and orientation, can be still influenced in this latter step. The following Sections will summarize the processing ways for continuous and discontinuous fiber composites.

2.4.4.1 Continuous fibers and thermosetting matrices

For this class of composites, the fabrication processes can be classified as (i) wet-forming processes and (ii) processes using premixes or prepregs (Agarwal et al., 2018). In the wet-forming processes, the resin is still fluid when the final component is formed and hardens during curing under heating. Such processes encompass hand lay-up, resin-transfer molding, bag molding, filament winding, and pultrusion. In the processes using premixes, the material is supplied as an intermediate product, which can be a bulk molding compound (BMC) or a sheet molding compound (SMC) containing fibers and partially cured matrix. The use of premixes and prepregs simplifies the manufacturing, increases the possibility of automation, and helps in obtaining a uniform filler distribution and a higher fiber weight fraction (Agarwal et al., 2018). On the other hand, it limits the *a posteriori* modification of the material composition with additional fillers, fiber coatings, or resin additives. Even though this is not normally an issue for composite manufacturers, who agree with their suppliers on the specific composition for large volume productions, it can be a limitation towards a systematic study of the effect of the composition on the thermomechanical properties of the produced laminates.

In this thesis work, all the composites containing a continuous fiber reinforcement and a thermosetting resin were prepared via hand lay-up and vacuum bagging operations. Hand lay-up is the oldest, simplest, and still the most diffused technique for the manufacture of small and large fiber reinforced products, especially in the applications where a low production volume does not justify the high plant size and cost of other fabrication techniques.

The typical layup for a bag molding process is illustrated in Figure II - 17.

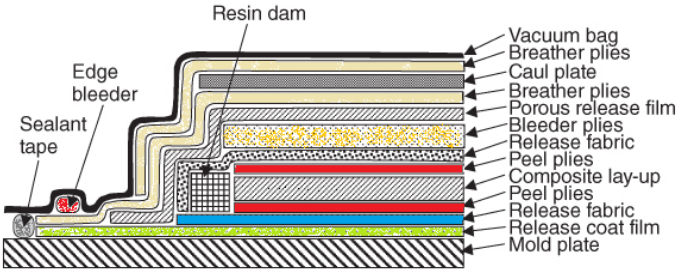

Figure II - 17. Typical layup for a bag molding process (adapted from (Agarwal et al., 2018))

The composite laminate is only one of the many layers composing the bag layup. These layers include release agents and films, peel plies, bleeder/breather plies, bagging film and sealant tape. Release films and agents are used to separate the composite from the mold or the breather/bleeder materials; the release film cam

be porous to allow excess resin flow through the film. Peel plies protect the surface of the molded part from contamination. Bleeder/breather plies are porous fabrics or nonwovens used to absorb excess resin during processing and to allow air and volatiles out of the composite during curing. Finally, bagging films form a barrier between the composite laminate and the external environment (e.g. oven or autoclave environment) (Wang et al., 2011a).

2.4.4.2 Continuous fibers and thermoplastic matrices

The high viscosity of polymer melts complicates the incorporation of continuous fibers into thermoplastic matrices, but several techniques have been developed to produce "thermoplastic prepregs" or semi-manufactured thermoplastic composites containing continuous fibers (Biron, 2013). Unlike the thermosetting prepregs, these have the advantage of having a virtually infinite shelf life and, when required, they can be stacked and consolidated in a laminate by applying heat and pressure.

Among the techniques developed to produce thermoplastic prepregs, hot-melt impregnation is one of the most diffused for semicrystalline polymers (Figure II - 18). Collimated fiber tows are pulled through a die attached to the end of an extruder, and a thin sheet of polymer melt is deposited on the fibers, previously separated by an air jet. The prepreg then is cooled and wound on a take up roll. For the polymers that can be easily dissolved in a solvent, this process can be substituted by a solution impregnation. It produces tacky and drapable prepregs, but an accurate solvent removal is a critical issue, fundamental for obtaining high quality laminates with low porosity (Mallick, 2007).

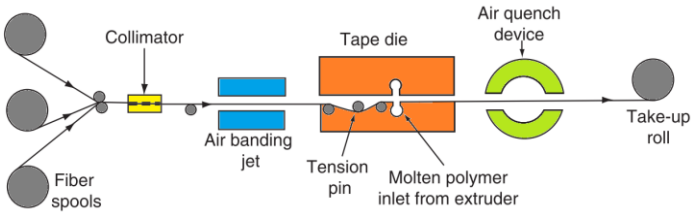

Figure II - 18. Hot-melt impregnation process (adapted from (Mallick, 2007)).

A different technique is the film stacking, in which polymer sheets are interleaved between woven fabrics or random fiber mats, and then the layup is heated and pressed to melt the polymer and wet the fibers.

Fiber mixing is an interesting process in which the matrix is inserted in fiber form. Polymer fibers are intimately mixed with reinforcement fibers via commingling, wrapping, or co-weaving. The hybrid yarns are then used to form a 2D or 3D hybrid fabric, and the subsequent application of heat and compression melts and spreads the matrix fibers during the consolidation stage. The main advantage of this technique is

that, unlike most thermoplastic prepregs, the hybrid yarns and fabrics are highly flexible and drapable, which allows them to perfectly fit a contoured mold with a complex shape. Figure II - 19 illustrates the production of a glass fiber reinforced polypropylene part starting from a commingled hybrid yarn (Long, 2006).

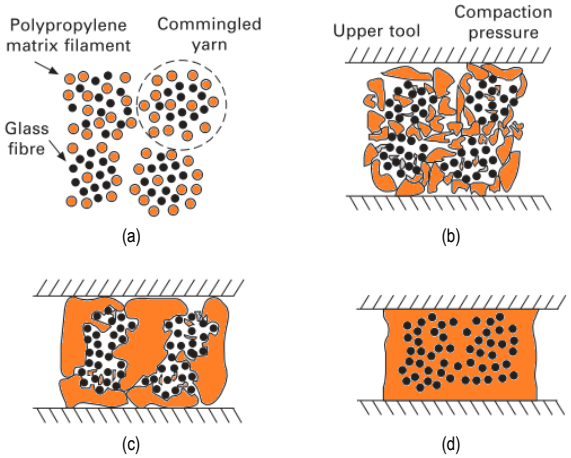

Figure II - 19. Consolidation of commingled hybrid yarns. (a) dry commingled yarns; (b) heat and pressure favor matrix melting and yarn aggregation and bridging; (c) matrix pools coalesce at the edge of the bundles; (d) the matrix flows to impregnate bundles and the subsequent flow on micro-scale dissolve trapped porosity (adapted from (Long, 2006)).

The use of hybrid yarns also allows the homogeneous dispersion of other functional fillers in a thermoplastic composite. Conductive particles, sensors, or dyes can be integrated in the matrix filaments or inserted as an additional filament type. This is interesting especially for the development of multifunctional composites, in which the combination of different fillers results in a unique set of properties, designed to perform several tasks simultaneously (Risicato et al., 2014; Hsiao et al., 2019).

Finally, liquid impregnation is a technique in which the matrix is supplied as a low-viscosity liquid made of monomers or prepolymers. Due to the low viscosity, it is processable as a thermosetting resin with all the techniques mentioned in Section 2.4.4.1. Up to some years ago, this process was commonly used only for some thermoplastic polyimides, but the inherent advantages of processing a low-viscosity precursor have paved the way for the development of new formulations (e.g. Elium®, see Section 2.4.3.2).

2.4.4.3 Discontinuous-fiber composites

The majority of discontinuous-fiber-reinforced composites has a thermoplastic matrix. The process of making such composites is generally divided in two steps. In the first step, the matrix is compounded with the fibers, generally by means of an extruder, to obtain a uniform dispersion while trying to minimize the fiber breakage. In the second step, the compounded material is remelted or softened and molded to obtain the final product. Injection molding is the most common way to obtain short-fiber-reinforced thermoplastic products.

Even though the machines, molds, plungers, and screws can be the same as those used for unreinforced plastics, the processing parameters must be adjusted to deal with the modification of rheological properties and thermal conductivity introduced by the fibers (Agarwal et al., 2018). This is important also because the properties of discontinuous-fiber composites are strongly influenced by the fiber length and orientation, which can both change according to the processing conditions (Shokrieh and Moshrefzadeh-Sani, 2016).

2.5 Multifunctional composites and structural TES materials

The previous Subchapters have introduced the concept of thermal energy storage and the principal materials and technologies through which it is translated into real applications. An introduction on polymer-matrix composites was also presented, illustrating the main polymer matrices, reinforcement phases and production processes, as well as their potentialities for lightweight design.

As the general aim of this thesis is to study the possibility of integrating the TES technology into a structural material to produce a multifunctional component, the present Subchapter introduces the concept of multifunctional material and explains the role of polymer composites in the development of multifunctionality.

2.5.1 Multifunctional materials

A material can be classified as multifunctional if it features a set of properties that make it suitable to simultaneously sustain stimuli of different nature and to be ready to perform different functions when required. Multifunctional materials can combine a set of properties chosen among the structural mechanical properties, like stiffness, strength and toughness, and the non-structural properties, like sensoring functions, optical and magnetic properties, self-healing, thermal/electrical conductivity or insulation, corrosion resistance, tribological properties, and energy harvesting and storage (Asp and Greenhalgh, 2014; Friedrich, 2015).

Such materials have enormous potential to impact future structural performance by reducing weight, volume, cost, and energy consumption while enhancing efficiency, versatility, and safety. Since they expand design possibilities and increase the material added value, they are attracting increasing interest from the industrial and academic point of view. New combinations of properties are being embedded in the next-generation of multifunctional materials, which can find applications in the automotive and aerospace industries, but also in civil engineering and in medicine (Friedrich, 2015).

The combination of properties of a multifunctional material should act synergistically and not parasitically. If the addition of self-sensing and self-healing capabilities to a structural material impairs its stiffness and strength excessively, the combination of properties in this material will not bring benefits at the system level.

When designing a multifunctional material, multifunctionality should be considered from the very early stages of the design process. Unlike natural materials, whose properties are the result of a locally random evolution process, in the synthetic engineering materials the design must start from the functions and proceed in a specific direction. This is important because multifunctionality could be expressed at different length scales (at the phase, material or structure level), which must be taken into account during the design of the material and the prediction of final properties (Gibson, 2010).

2.5.1.1 Multifunctionality of polymer composites

Composite materials are particularly suitable to be designed as multifunctional, as they achieve multifunctionality by gathering in one material the properties of multiple phases. Many natural and synthetic materials that have to perform more than one function are polymer-matrix composites. In fact, they combine outstanding polymer-related properties, like toughness and low density, with the specific properties of the discontinuous phase(s), which can provide stiffness and strength, but also several non-structural functions.

Multifunctional composites can perform (i) multiple structural functions, (ii) structural and non-structural functions, or (iii) both. Most of the recent developments in multifunctional materials tend to be polymer-matrix structural composites featuring one or more additional non-structural functions. This strategy allows large weight savings at the system level, through the elimination or reduction in the number of multiple monofunctional constituents (Asp and Greenhalgh, 2014), and it gives better results than the conventional approach of optimizing weight and geometry of the single subsystems individually.

Composite materials can also reach a high level of multifunctionality by combining reinforcements on different scales, which range from continuous fibers to particles on the micro- and nanoscale (Friedrich, 2015).

2.5.1.2 Applications and examples

As described in Subchapter 2.4, polymer composites have become the materials of election for lightweight structures. As the employment of multifunctional composites can lead to considerable weight savings, these materials have become attractive because, besides their remarkable specific stiffness and strength, they open the possibility of adding other functionalities with a negligible weight and volume increase.

One of the most interesting examples of combination of structural and non-structural functions is provided by structural batteries, devices that can carry mechanical load and store electrical energy at the same time (Asp and Greenhalgh, 2014). This is a powerful design concept, as it allows storing energy directly in the structure of a component, or, in other words, using a battery to build the structural parts. In this way, the total mass of the device is lower than the sum of the masses of the monofunctional components, namely the structure and the battery. This concept is particularly attractive in all those applications that must be carried around and need a power supply, like electric vehicles and portable electronics. The advantage is greater the more the multifunctional composite has structural and energy storage properties close to those of a conventional structural material and a conventional battery, respectively. However, in real cases, a structural battery exhibits neither the mechanical performance of the purely structural component nor the electrochemical characteristics of a monofunctional traditional battery, but the advantages of multifunctionality, and the effective mass and volume saving, must be evaluated at the level of the whole system.

Several approaches have been taken to develop structural batteries. One of the most recent concepts is that pursued at the research center Swerea-SICOMP (Piteå, Sweden) (Asp and Greenhalgh, 2014). This structural battery (Figure II - 20) employs single carbon fibers as negative electrodes, coated by a thin layer of solid polymer electrolyte, and immersed in a common cathode-doped matrix. This concept offers the advantage of being multifunctional at the phase level; the fibers are both the reinforcement and the negative electrode, the interphase is also a conductor for Li-ions, and the surrounding polymer matrix also plays the role of positive electrode. When designing a structural battery like this, challenges arise as the optimization of the mechanical properties of each phase often cause a decrease in the electrochemical performance. For example, a solid polymer electrolyte exhibiting high ion conductivity often shows poor stiffness and strength, and highly graphitized carbon fibers featuring excellent stiffness are not the optimal choice from the point of view of the Li-ion intercalation efficiency (Fredi et al., 2018). It is therefore important to fully understand how the microstructure of each phase correlates with the mechanical and electrochemical properties, as each component should be tailored to reach the best property set, and this must be taken into account already during the fabrication of each phase.

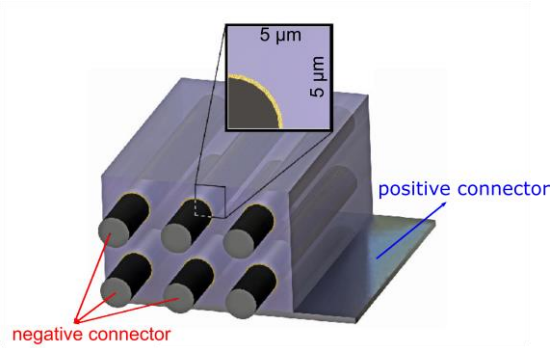

Figure II - 20. Scheme of the Swerea-SICOMP structural battery (adapted from (Asp and Greenhalgh, 2014)).

Another class of materials generally classified as multifunctional is that of the "smart" materials, able to adapt and respond to external stimuli by performing both as sensors and as actuators (Salonitis et al., 2010). The state-of-the-art smart materials are able to change their properties (e.g. mechanical, electrical, magnetic, rheological), color or shape depending on external stimuli such as heat, electricity, light, solvent, and pH value. Several applications of such materials can be found in buildings and automotive/aerospace fields, to actively control vibrations, noise and deformations (Salonitis et al., 2010).

A powerful example of this concept is represented by the self-sensing concrete, increasingly attractive for civil engineering applications as it exhibits a sensible change in electrical resistivity with applied stress or strain, which makes it useful for structural health monitoring (Tian et al., 2019). One of the most frequently pursued strategies to produce self-sensing concrete is to embed conductive fillers (e.g. CNTs and xGnPs) at or near the percolation threshold. In this way, the formation of damages and cracks interrupt the conductive paths, thereby causing a remarkable increase in electrical resistivity (Papanikolaou et al., 2019). Moreover, some conductive additives such as the xGnPs have proven to enhance the durability and the compression and flexural strength of the host concrete, thus being a multifunctional filler themselves (Papanikolaou et al., 2019).

The same concept can be applied to polymer composites. Several examples have been proposed of continuous-fiber composites containing CNTs, either dispersed in the matrix or deposited onto the fiber surface. In such composites, the electrical conductivity is dominated by the formation of a percolative path of CNTs, and this is the case also when the reinforcement is made of carbon fibers, due to the remarkably higher electrical conductivity of CNT compared to CF.

2.5.2 Structural TES polymer composites

The previous Sections showed that polymer composites exhibit great potential to be designed as multifunctional, as their properties are the result of the combination of two or more phases. This can further expand the weight saving possibilities pursued when composites are selected as structural materials. The scientific literature reports multiple examples of multifunctional composites combining structural properties and a wide range of non-structural functions, which respond to a wide variety of needs in the most diverse applications.

An interesting field in which multifunctionality of polymer composites can be exploited, although not yet thoroughly investigated, is that of structural composites with thermal energy storage capability. As explained in the previous Sections, among the applications of TES materials are (i) the heat storage for temperature control, for example in the buildings industry, or to produce smart textiles for body temperature regulation, and (ii) the temporary storage of heat to prevent overheating, as in the cooling systems for electronic devices.

When a TES material is used for thermal management, it is usually only an extra component added to the main structure of a device. However, the resulting increase in weight and volume may be unacceptable for some applications where weight and volume reduction are crucial design parameters. In this case, it would be useful to have a multifunctional material combining good mechanical properties and the heat storage/management function. With an approach similar to that developed with structural batteries, with such materials it would be possible to build part of the structure with the "thermal battery" material, or, in other words, to design a structure that is part of the thermal management system.

According to the author's opinion, these structural TES lightweight composites would be attractive in four main applications:

1. In the transportations field, polymer composites are becoming increasingly employed to build structural or semi-structural components, thanks to their high specific mechanical properties. However, the considerable application of polymer composites in replacement of traditional materials could complicate the thermal management in the indoor vehicle environment, due to the different (generally lower) thermal conductivity and heat capacity. This could result in an increasing difficulty in maintaining the indoor temperature in the human thermal comfort range. This issue could be addressed by introducing a TES system able to store and release thermal energy in that temperature range, and the overall performance-to-weight ratio would be maximized if this TES material is part of structural components themselves. This concept could be extended

to other temperature ranges, which may be interesting for the transportation of food, biomedical items, or other perishable goods.

2. In the field of portable electronics, there is an increasing tendency of enhancing the performance, power and functionalities of the devices while reducing weight and volume. This trend brings issues in the thermal regulation of the device, especially in the peak power operations. As already described in Section 2.3.3, passive cooling systems based on PCMs are attracting attention due to their capacity of maintaining the temperature in the desired range – more specifically, under a certain threshold value – and of coping with the momentaneous but rapid heat generation during peak power operations. However, in all the solutions implemented so far, the PCM is contained in an additional module, while it would be advantageous to embed it directly inside the structural components such as the phone or laptop cases. Another interesting application in the electronics field would be the production of PCM-enhanced circuit boards, traditionally made of glass fiber reinforced epoxy resin.

3. Among the main drawbacks of polymer-matrix composites, compared to metals or ceramics, are the lower thermal resistance and the loss of mechanical properties with increasing temperature. This can be detrimental for some applications where the composite material is subjected to external heating in service, as in the case of luxury car chassis entirely made in carbon fiber composite. However, local overheating and loss of properties could be also determined by dynamic loading and lack of heat dissipation, which can bring to premature failure by fatigue. This effect, critical especially for thermoplastic composites, could be limited by adding a PCM, which absorbs excess heat and avoids temperature rise. This concept has been proven effective by Casado et al. (Casado et al., 2016), who inserted a hydrated salt with a transition temperature of 50 °C in a polyamide-based composite reinforced with glass fibers. In this case, however, the PCM was not employed as an additional filler, but it was added in the gaps of the flanged plate made of the glass-reinforced polyamide. Much more capillary would be the action of the PCM if it was dispersed in the whole composite mass, or at least in those parts more subjected to the fatigue damage.

4. One of the main problems of outdoor infrastructures operating in cold environments is related to the formation and accretion of ice. Critical structures such as transmission lines, wind-driven power generators, off-shore oil rigs, and means of transportation like aircrafts and ships can be damaged by excessive weight of the ice layer and the stress induced by the freeze-thaw cycles (Kreder et al., 2016). The solutions implemented so far rely on heating methods, mechanical methods, or the circulation of de-icing fluids underneath the surface, which are effective but extremely energy-consuming (Zhu et al., 2018). More recently, slippery or superhydrophobic coatings have been developed that prevent ice adhesion or reduce ice shear strength, but they generally have low resistance to mechanical abrasion and poor durability to the outdoor weather agents. For the structures built in polymer composites, e.g. the wind turbine blades, an effective alternative could be the introduction of a PCM with phase transition at approx. 0 °C in the whole composite thickness or only in the outermost layers (Goitandia et al., 2018). The heat released during crystallization of the PCM would help in decreasing the ice accretion rate, while reducing the need for heating through an external energy supply.

In all these applications, PCMs are the ideal TES materials, as they work at a nearly constant temperature and exhibit a high enthalpy per unit mass, thus being suitable for applications where weight saving is a key factor. It is therefore fundamental to understand how the PCM addition influences the mechanical properties of the host composite and how this effect varies below and above the PCM phase change.

So far, this investigation has been carried out to some extent only on construction materials like concrete and gypsum, in which a PCM phase is added to enhance the thermal management of indoor environments while reducing the energy consumption for indoor heating/cooling. As described in Section 2.3.1, the majority of TES systems integrated in walls or flooring materials are represented by organic PCMs with a phase transition temperature in the range 18-25 °C, microencapsulated in polymeric shells. The characterization of such PCM-enhanced construction materials generally evidences that an increase in the PCM fraction brings an increase in the thermal management properties and a decrease in the heating/cooling power consumption. On the other hand, PCM addition determines a decrease in compressive and flexural properties, due to the introduction of a less mechanically strong phase. Therefore, the authors of the revised papers generally conclude that it is important to select the PCM that determines the smallest decrease in mechanical properties while providing the highest TES capability, and that it is fundamental to identify the optimal PCM content to obtain a material with the most suitable property set for a specific application (Cao et al., 2018).

The open scientific literature provides some examples of polymers containing a PCM, but very few cases of PCM-enhanced polymers employable as structural materials. Subchapter 2.6 reports some examples of PCM-containing polymers and polymer composites, with the main investigation techniques and the principal conclusions.

2.6 PCMs in polymers and polymer composites

The present Subchapter reports examples of variously stabilized PCMs contained in polymer matrices and polymer composites. The research was narrowed to the PCMs with a phase change temperature in the low-medium temperature range (15-80 °C), as this is the interval of interest for the aforementioned applications of structural TES composites (Section 2.5.2). In this temperature range, the organic PCM dominate the market and the academic research, and thus the present review focuses on this PCM class and specifically describes how the added PCM affects the host polymer.

2.6.1 PCMs in polymer matrices

The scientific literature reports many examples of polymer matrices containing organic PCMs (mostly paraffins) without further stabilization. In this way, a sort of polymer/PCM blend is obtained. This is commonly referred to as the simplest and cheapest way to avoid leakage of the PCM while defining the shape of the PCM-containing component. A large number of polymers have been used as supporting materials, such as traditional thermoplastics (PE, PP, polyamide (PA), polymethylmethacrylate (PMMA)), thermosets (epoxy) and elastomers (styrene block copolymers, ethylene-propylene-diene-monomer (EPDM)).

Chen and Wolcott (Chen and Wolcott, 2014; Chen and Wolcott, 2015) blended a paraffinic PCM with HDPE, LDPE and LLDPE via melt mixing, and the total paraffin content was fixed at 70 wt% in all the three cases. Morphological investigations showed the formation of a co-continuous structure between the two phases; this was considered as the main cause for the paraffin leakage from the prepared blends, which was up to the 10 wt% of the total initial paraffin fraction. The phase change enthalpy and temperature of the paraffin varied only slightly after blending, while the PE crystallinity decreased sensibly, especially for low-density PE (LDPE) and linear low-density PE (LLDPE). The authors focused on the miscibility of the PCM with the polymer matrices and the blend morphology, but they did not investigate the mechanical properties nor the long-term stability of the prepared samples. This is a crucial aspect even if the materials are not meant to be applied under heavy load-bearing conditions, as clearly underlined by other authors (Resch-Fauster and Feuchter, 2018; Resch-Fauster et al., 2018) who investigated the thermo-physical and mechanical properties of polyolefins/paraffin blends. The blends contained a paraffin

weight fraction of up to 38 wt% and a melting enthalpy of up to 71 J/g. A slight alteration in the matrix crystallinity upon blending with paraffin was detected also by these authors, who attributed the decreased melting temperature of the host polymer to a plasticizing effect of the PCM, especially for the samples without co-crystallization (PCM/PP). The authors highlighted that the mechanical performance of the host matrices, measured under quasi-static and dynamic conditions, decreased with an increase in the paraffin content, and this was even more evident above the PCM melting temperature. The authors concluded that such blends cannot be applied as load-bring components but only as functional materials.

To increase the mechanical properties of the polymer/PCM blends, some authors proposed the addition of fillers such as EG, xGnP or nanoclays, which are also helpful to enhance the thermal conductivity. This was proved by Sobolciak et al. (Sobolciak et al., 2015; Sobolciak et al., 2016), who investigated the thermo-mechanical performance of paraffin/LLDPE blends containing EG microparticles and exhibiting a phase change enthalpy of up to 31 J/g. For the blends containing 15 wt% of EG, the storage modulus of was doubled compared to that of the neat LLDPE/paraffin blends, and the thermal conductivity increased from 0.25 to 1.32 W/(m·K). The same concept was applied by Wu et al. (Wu et al., 2019), who designed an EG/paraffin/olefin-block-copolymer (OBC) composite with thermally induced flexibility. The authors conclude that the addition of EG not only contributes to the mechanical stability of the composite, but it also helps in preventing leakage due to the capillary force and surface tension.

PCMs can also be added to polymer matrices in the form of microcapsules, and in this case they are added as any other fillers in the production process. The capsule shells provide unmatched PCM containment and are more effective in avoiding leakage compared to any other shape-stabilization techniques. However, this is the case only if the processing conditions of the host polymer matrix are mild enough to preserve the shell integrity, as the high temperatures, pressures and shear stresses can cause cracks and damages in the thin capsule shell. Zhang et al. (Zhang et al., 2005) produced core-sheath polyethylene fibers containing microencapsulated *n*-octadecane via a melt-spinning process, for textile applications. The capsules, having a diameter in the range 0.4-4.5 μm, were confined in the fiber core, while the sheath was entirely made of PE and accounted for the 60 % of the total fiber mass. The produced filaments had a melting enthalpy of up to 13 J/g and mechanical properties suitable for fabricating textile products. The authors highlighted that the processing parameters during melt blending and melt spinning were fundamental for determining the capsule integrity and thus the final total phase change enthalpy.

More recently, Krupa et al. (Krupa et al., 2014) inserted paraffin microcapsules in an HDPE matrix. The authors synthesized paraffin microcapsules with a 1.5-μm-thick melamine-formaldehyde shell and a total melting enthalpy of approx. 60 J/g. The capsule introduction caused a considerable decrease in all the mechanical

properties of the HDPE matrix (elastic modulus, stress and strain at yield and at break). Although the shell material is stiffer than the PE matrix, its small thickness caused the capsules to deform when the composite is strained, which, together with the insufficient interfacial adhesion to HDPE, prevented the capsules to act as a reinforcement. Also in this case, the authors concluded that the produced blends retained sufficient mechanical properties to be safely manipulated and be applied in real service conditions, but they were not suitable to be employed as load-bearing components.

Thermosetting materials such as epoxies have been also enriched with microencapsulated or variously stabilized PCMs. The advantage of these materials compared to thermoplastics is that the processing starts from low-viscosity liquids and is generally performed at room temperature, and this helps to preserve the capsule integrity and to avoid PCM degradation, thereby enhancing the phase change enthalpy at the end of the process. Su et al. (Su et al., 2011a; Su et al., 2012) provided an important contribution to the study of the thermo-mechanical behavior of epoxies containing paraffin microcapsules, focusing in particular on the capsule/epoxy adhesion and interfacial stability. The authors observed that, during repeated thermal cycles, the expansion and shrinkage of the microcapsules and the surrounding matrix occurred with different thermal expansion coefficients. This happens in all the materials composed of several different phases, but with PCMs the situation is complicated by the additional volume variation caused by the phase change. Even though the volume variation is not as enormous as in the case of a phase change involving vapor phases, it must be considered since it can undermine the interfacial stability of the composite and thus its overall mechanical performance. As represented in Figure II - 21, these phenomena may cause microcracks and fractures in the matrix, which can not only lead to PCM leakage, but also to a decrease in the mechanical properties of the surrounding matrix.

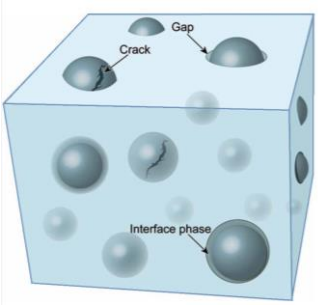

Figure II - 21. PCM microcapsules in a polymer matrix (adapted from (Su et al., 2011a)).

The same authors synthesized melamine-formaldehyde-based microcapsules and observed that the addition of methanol during the synthesis led to a higher interface bonding and an enhanced ductility of the interphase region. They also concluded that the stability behavior was greatly influenced by the thermal cycling conditions, as higher heating rates caused a higher interfacial damage. The authors formulated a theoretical approach to model the mechanical strength of the composite as a function of the thickness and integrity of the capsule-matrix interphase region, but they recognize that it is generally difficult to model the mechanical properties of such composites in normal service conditions, especially when the thickness of the interphase region is not clearly measurable (Wang et al., 2011b).

2.6.2 PCMs in structural polymer composites

Excluding the construction materials field, there is a surprisingly limited number of publications about materials designed to combine structural and TES functions. One of the first reported examples is that presented by Wirtz et al. (Wirtz et al., 2003), who developed a sandwich structure made of a graphitic foam impregnated with paraffin (T_m = 56 °C) as the core and carbon/epoxy laminates as the skin, intended for the thermal management of electronic devices. The graphitic foam had the twofold function of immobilizing the molten paraffin and enhancing the thermal conductivity, while the carbon/epoxy skins increased the flexural stiffness. The higher the foam porosity, the higher the paraffin amount that could be accommodated into the foam pores, the lower its mechanical properties. Therefore, the foam porosity was the main parameter dominating the balance between the core's mechanical properties and the overall TES performance, which acted competitively also in this system, even though the carbon-fiber-based skins were the main enhancers of the mechanical performance of the whole sandwich structure. The literature reports several other studies on carbon foams as shape-stabilizers for organic PCMs, but they are generally employed only to enhance the thermal conductivity, and little attention is given to the mechanical performance (Mesalhy et al., 2006; Zhong et al., 2010; Jana et al., 2015).

More recently, a research group at RMIT University (Melbourne, Australia) developed a woven glass fiber/epoxy laminate containing paraffin microcapsules and investigated the impact of the PCM on the mechanical and thermal properties of the host laminate (Yoo et al., 2016; Yoo et al., 2017a; Yoo et al., 2017b). An increase in the PCM weight fraction determined a decrease in the tensile, flexural and compressive properties, due to the intervention of additional damaging mechanisms as delamination, matrix cracking, and fiber/matrix debonding, and the authors indicated the weak interfacial adhesion between the capsules and the matrix as one of the causes for the mechanical performance decrease. On the other hand, the mild processing conditions allowed retaining most of the initial PCM enthalpy, but thermogravimetric analysis (TGA) showed that a fraction of the capsules was damaged during processing. Nevertheless, these results were promising for the

development of such structural TES polymer-matrix composites, which exhibited a phase change enthalpy of up to 40 J/g.

Chapter III

Experimental

3.1 Introduction

The present Chapter introduces all the polymer matrices, reinforcements and PCMs employed in this thesis and subsequently describes the main characterization techniques used to investigate the prepared composites. On the other hand, the techniques of sample preparation and the description of the specimens for each test are not reported here, as they are specific of each matrix-reinforcement-PCM combination and will be described in each particular Chapter.

3.2 Materials

The present section lists the materials employed in this thesis. They are divided into three groups, namely the PCMs, the matrices, and the reinforcing agents, as each multifunctional composite presented in this thesis work is the combination of these three main elements. Section 3.2.4 summarizes the presented materials and defines labels and abbreviations through which the materials will be recalled in the following Chapters. This can be a useful reference as this thesis work investigates several combinations of matrices, reinforcements and PCMs.

3.2.1 Phase change materials

Four organic PCMs were used in this thesis work. They were selected with a melting point in the range 40-55 °C, which can be interesting for applications in the thermal management of electronic devices. This melting temperature range was also selected because these PCMs are completely solid at room temperature but do not require a too high temperature to be melted, thereby easing the characterization techniques in the temperature interval around the phase change temperature.

The two most extensively used PCMs in this thesis work are two paraffinic PCMs; the first is a paraffin wax (alkane mixture) shape-stabilized with carbon nanotubes (CNTs) (Section 3.2.1.1), and the second is a commercially available microencapsulated paraffin (Section 3.2.1.2). They have comparable melting temperatures and enthalpies, and the comparison between them provides an interest insight on the advantages and disadvantages of the two different confinement techniques. Two additional PCMs were employed; the first is docosane, an *n*-alkane with a known and precise chemical structure and molecular weight distribution (Section 3.2.1.3), while the second is a fully biodegradable poly(ethylene glycol) (Section 3.2.1.4).

3.2.1.1 Paraffin shape-stabilized with carbon nanotubes

The shape-stabilized PCM was produced starting from a commercial paraffin wax, the Rubitherm RT44HC® supplied by Rubitherm Technologies GmbH (Berlin, Germany) and presented in Figure III - 1a. This paraffin wax has a melting temperature range of 41-44 °C, a density at 25 °C of 0.8 g/cm^3 and a total heat storage capacity (between 35 °C and 50 °C) of 250 J/g, as declared by the producer. The shape-stabilizing agent consisted in multi-walled CNTs NC7000® (average diameter 9.5 nm, average length 1.5 µm, BET surface area 250-300 m^2/g), provided by Nanocyl SA (Sambreville, Belgium).

In a first preliminary activity, the paraffin was mixed with various kinds of carbon-based nanofillers, such as carbon black, CNTs, exfoliated graphite nanoplatelets, and expanded graphite, at different concentrations (from 5 to 20 wt %) to assess their capability to avoid PCM leakage above its melting temperature.

Carbon nanofillers were added to melted paraffin at 70 °C under mechanical stirring at 500 rpm for 30 min. The mixtures were poured in silicon molds and left cooling at room temperature. To evaluate the confinement capability, the prepared specimens were put on an absorbent paper towel and heated in an oven at 80 °C. By visual observation, it was clear that the specimens containing CNTs showed by far the lowest leakage compared to the samples containing other carbonaceous nanofillers at the same concentration.

The optimum weight fraction of CNTs in this application is the minimum amount at which no paraffin leakage is detected, since an excess of CNTs would decrease the

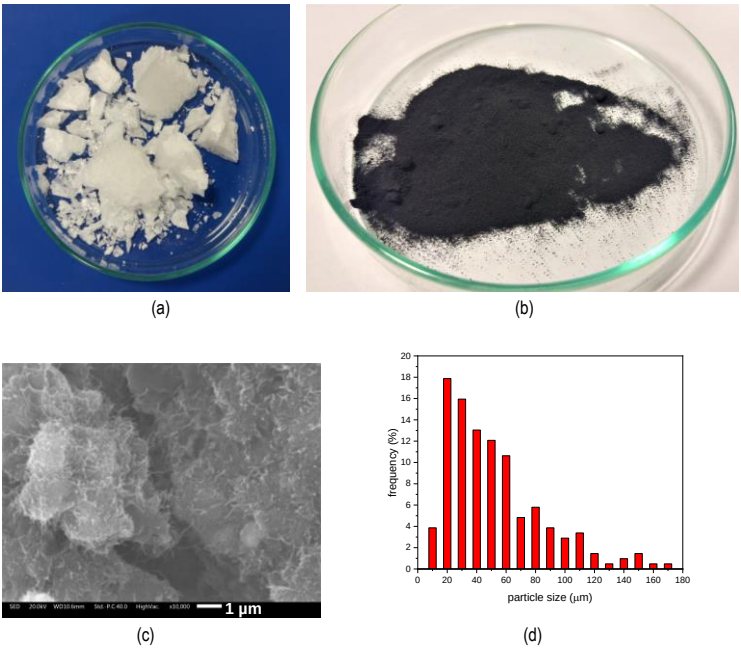

Figure III - 1. (a) paraffin RT44HC (Rubitherm), as received; (b) ParCNT: paraffin shape-stabilized with CNTs and grinded cryogenically; (c) SEM micrograph of ParCNT; (d) particle size distribution of ParCNT.

overall phase change enthalpy of the mixture. Samples with various CNT amounts (5-20 wt%) were prepared and confinement tests were performed. While the samples with a CNT content of less than 10 wt% showed visible leakage of paraffin on the absorbent paper, no leakage was detected above that CNT concentration. Therefore, a CNT concentration of 10-15 wt% was selected as the optimal one for the subsequent process. The exact CNT concentration (either 10 wt% or 15 wt%) was chosen according to the specific application, mainly to tune the final phase change enthalpy, as will be explained in the corresponding sections (Subchapters 4.2 and 5.2).

The CNT-confined paraffin with a CNT fraction of 10 wt% or 15 wt% (from now on called ParCNT) was cryogenically grinded under liquid nitrogen with an IKA Labortekink M20 universal mill (IKA-Werke GmbH, Staufen, Germany), and then sieved with a 300-µm metallic sieve to obtain a micrometric powder that can be easily mixed with a polymer matrix (Figure III - 1b). From the scanning electron microscopy (SEM) micrograph of the ParCNT powder (Figure III - 1c), single CNTs are clearly visible and they appear to be well dispersed in the paraffin wax. Their elevated specific surface area is most likely the reason for their superior shape-stabilizing capability compared to the other carbon nanofillers considered in the preliminary activity, as also

observed elsewhere in the literature (Hasnain, 1998). Optical microscope images of the obtained particles were acquired as described in Section 3.3.1.1 and analyzed with the software ImageJ. The resulting particle size distribution is reported in Figure III - 1d; the average powder size was 53 ± 30 μm. It was observed that a variation of the CNT content from 10 to 15 wt% does not modify the final particle shape nor the size distribution significantly.

3.2.1.2 Paraffin microcapsules

Commercial paraffin microcapsules MPCM43D (Figure III - 2) were purchased by Microtek Laboratories Inc. (Dayton, OH, US). They are composed of a paraffinic core with a nominal melting temperature of 43 °C, encapsulated in a melamine-formaldehyde-based shell that constitutes approximately the 10-15 % of the total capsule mass. The average diameter was 17-20 μm and the melting enthalpy was 200 J/g, as declared by the producer's datasheet. These and other properties of this PCM are summarized in Table III - 1. The thermal resistance is noteworthy, and it is compatible with the processing temperatures of most of the common thermoplastics.

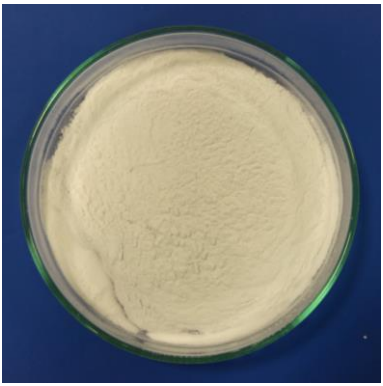

Figure III - 2. Paraffin microcapsules MPCM43D (Microtek Laboratories Inc), as received.

This PCM was employed in combination with several matrix/reinforcement systems in this thesis and was purchased multiple times from the supplier. Since the batch of this material can vary from one Subchapter to another in this thesis work, its main physical and thermal properties (e.g. melting enthalpy and thermal resistance) were characterized every time it was introduced in a new matrix/reinforcement combination.

Table III - 1. Properties of the PCM microcapsules MPCM43D (adapted from the producer's datasheet consulted from the producer's website on July 10, 2018).

Property	Value
Form	Dry powder
Composition	PCM 85-90% wt%; polymer shell 10-15 wt %
Core Material	Paraffin
Particle size (mean)	17-20 µm
Melting Point	43 °C
Heat of Fusion	190 - 200 J/g
Specific Gravity	0.9
Temperature Stability	Extremely stable – less than 1% leakage when heated to 250 °C

3.2.1.3 Docosane

Commercial paraffins are often a mixture of alkanes: the molecular weight (MW) distribution of these paraffin mixtures is designed to obtain the desired melting temperature while maximizing the phase change enthalpy. On the other hand, it can be challenging to investigate a PCM with a broad MW distribution from the microstructural and molecular point of view. Since a part of the thesis work was devoted to understanding how the PCM microstructure and crystallinity is affected by the confinement in small microcapsules, it was important in that case to select a PCM with a known and well-defined chemical formula and molecular weight. The selected alkane was the *n*-docosane (Figure III - 3).

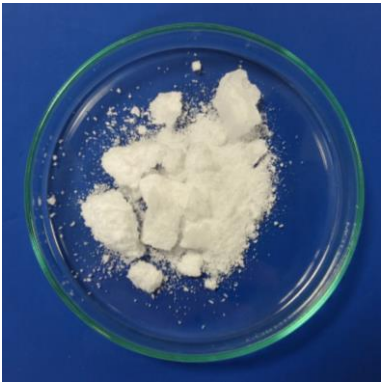

Figure III - 3. *n*-docosane (Sigma-Aldrich), as received.

It has chemical formula $CH_3(CH_2)_{20}CH_3$, (purity ≥ 98.5%) and was purchased from Sigma-Aldrich (Saint Louis, MO, US). This specific *n*-alkane was chosen as it has a nominal melting temperature of 42-45 °C, close to that of the previously mentioned commercial PCMs.

3.2.1.4 Poly(ethylene glycol)

The last PCM employed in this thesis work is a biodegradable organic PCM selected among the poly(ethylene glycol)s family, as they have higher thermal stability then the other class of biodegradable organic PCMs, i.e. fatty acids. The selected PEG grade was PEG2000, purchased by Alfa Aesar (Karlsruhe, Germany). It has a molecular weight of 1,800-2,200 g/mol and a melting temperature of 51–55 °C, according to the producer's datasheet. It was used only in combination with the mentioned biodegradable matrix (see Section 3.2.2.4) and reinforcement (see section 3.2.3.5).

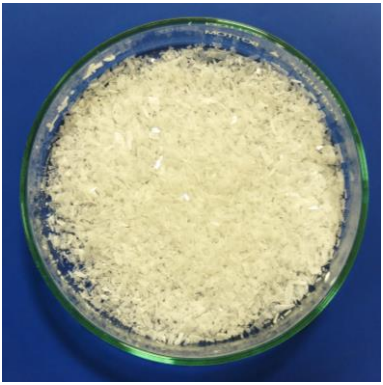

Figure III - 4. PEG2000 (Alfa Aesar), as received.

3.2.2 Matrices

The list of the selected matrices include both traditional thermoplastic and thermosetting polymers, widely used in the composites industry, and innovative and less common products, such as liquid thermoplastic resins and biodegradable plastics.

3.2.2.1 Polyamide 12

Polyamide 12 (PA12) with the commercial name of Rilsan® AECNO TL was supplied by Arkema S. A. (Colombes, France), in the form of polymer granules. Polyamides are largely employed as thermoplastic matrices in combination with

continuous and discontinuous glass and carbon fibers in many industrial fields (Czigany and Karger-Kocsis, 2001; Kim et al., 2012; Biron, 2013). Among the polyamides, PA12 was selected because of the high methylene/amide ratio (11/1), which leads to a lower moisture sensitivity and a lower melting temperature (T_m = 174 °C) than the more common polyamide-6 and polyamide-66. Therefore, PA12 is potentially more easily processable and blendable with organic PCMs, which are prone to thermal degradation being low-molecular-weight compounds.

3.2.2.2 Liquid thermoplastic resin

The selected liquid thermoplastic resin was the acrylic methy-methacrylate-based resin Elium® 150, kindly provided by Arkema S. A. (Colombes, France). This newly developed resin is supplied as a highly fluid precursor that can be processed at room temperature with processing techniques typical of thermosets. The initial viscosity is as low as 100 mPa·s (as reported in the technical datasheet), even lower than that of many precursors for thermosetting polymers. The mechanical properties of this resin are comparable to those of a high-performance epoxy (Chilali et al., 2016), and it can feature even better vibration damping properties (Bhudolia et al., 2017) and a higher fracture toughness (Bhudolia et al., 2018), as well as a good adhesion strength with commercial sized carbon fibers (Pini et al., 2015). The resin was provided with water-free benzoyl peroxide (BPO) with 50% active content, as the polymerization initiator.

3.2.2.3 Polypropylene

Polypropylene (PP) was selected to produce PCM-containing polymer filaments to be embedded commingled hybrid yarns (see Chapter IV, Section 4.4). The chosen PP was supplied by Toray Industries, Inc (Tokyo, Japan). PP is a common choice for the spinning of filaments (Zhang, 2014) and as a matrix for composites (Biron, 2013), and this particular grade was characterized by a high melt fluidity, to minimize the shear stresses on the PCM phase during processing.

3.2.2.4 Thermoplastic starch

Thermoplastic starch (TPS) has recently attracted increasing attention as a bioderived and biodegradable polymer and potential matrix for polymer composites. From the chemical point of view, starch is a polysaccharide with a semicrystalline structure, composed by linear amylose and highly branched amylopectin (Bastioli, 1997). It can be derived from corn and other crops and processed through traditional processing techniques for thermoplastics, such as extrusion and injection molding.

The TPS grade applied in this thesis was the MaterBi® EF51V was supplied by Novamont SpA (Novara, Italy) in the form of foils with a thickness of approx. 100 µm.

This TPS grade is characterized by a density of 1.2 g/cm^3, a melting temperature of 167 °C and a melt flow index (MFI) of 4 g/10 min (190 °C, 2.16 kg).

3.2.2.5 Epoxy resin

The epoxy resin Elan-tech® EC 157 and the hardener Elan-tech® W342 were kindly provided by Elantas Europe Srl. (Collecchio, Italy). According to the manufacturer's datasheet, this epoxy system is ideal to produce high-performance structural composite parts of small and medium size, and it is suitable for a hand layup process. The indicated viscosity of the initial mixture is in the range 300-700 mPa·s. The final, fully cured product exhibits a glass transition temperature of 88-115 °C, according to the curing cycle, and a flexural elastic modulus of 3.1-3.3 GPa.

3.2.3 Reinforcements

Several reinforcement types have been explored, including traditional continuous and discontinuous glass and carbon fibers and less traditional thin wood laminae.

3.2.3.1 Bidirectional glass fiber fabric

The first attempt of producing a laminate containing a PCM was made by employing a thermoplastic matrix and glass fabric as a reinforcement. The glass fiber (GF) fabric was a bidirectional plain-weave E-glass fabric made of Z-twisted yarns, supplied by G. Angeloni Srl (Venice, Italy) (Figure III - 5). The commercial name was VV 380 P, and the nominal areal weight was 385 g/m^2. The diameter of the single fibers was 12 µm.

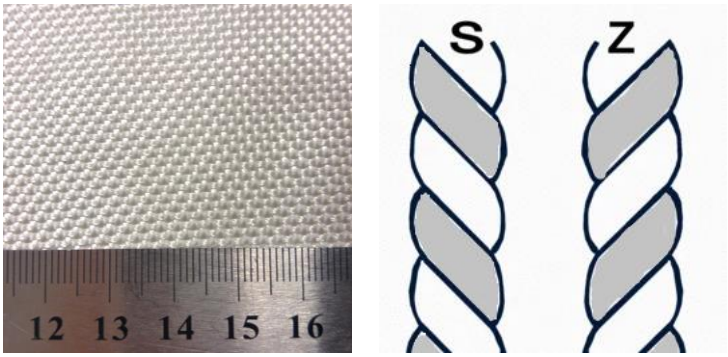

(a) (b)

Figure III - 5. (a) Bidirectional glass fiber fabric VV380P, (G. Angeloni), as received. (b) S- and Z-twisted yarns.

3.2.3.2 Bidirectional carbon fiber fabric

To produce laminates with a higher fiber volume fraction without increasing the fiber weight fraction, glass was substituted with carbon. The carbon fiber (CF) fabric was a bidirectional plain-weave intermediate-modulus carbon fabric made of untwisted tows, supplied by G. Angeloni Srl (Venice, Italy). The commercial name was GG 200 P (Figure III - 6), and the nominal areal weight was 192 g/m^2. The nominal diameter of the single fibers was 7 μm.

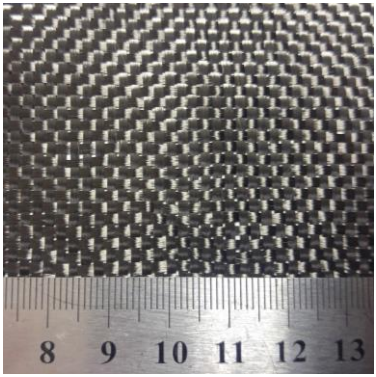

Figure III - 6. Bidirectional carbon fiber fabric GG200P (G. Angeloni), as received.

3.2.3.3 Unidirectional carbon fiber fabric

Unidirectional carbon fiber fabric (Figure III - 7) UCD-15060 was kindly provided by Mike Compositi (Milano, Italy). The nominal areal weight was 150 g/m^2. The fabric supplier declared that the carbon fibers composing the fabric are the Zoltek PX35 (Zoltek Corporation, Bridgeton, MO, US), having a nominal diameter of 7.2 μm, a nominal elastic modulus of 242 GPa and a nominal density of 1.81 g/cm^3.

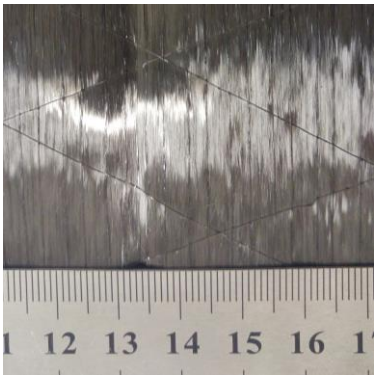

Figure III - 7. Unidirectional carbon fiber fabric UCD-15060 (Mike Compositi), as received.

3.2.3.4 Discontinuous carbon fibers

Two types of discontinuous carbon fibers were employed, both supplied from Zoltek Corporation (Bridgeton, MO, US) and belonging to the category Panex PX35, similarly to the unidirectional carbon fibers described in Section 3.2.3.3. The two selected fiber types are the chopped CFs Panex PX35 type 65 (sizing content 2.75 wt%, average fiber length 6 mm) and the milled CFs Panex PX35 MF150 (unsized, average fiber length 100 μm). Since these two CF types differ mainly in length, they will be denoted as CF "long" (CFL) and CF "short" (CFS), respectively.

(a) (b)

Figure III - 8. Discontinuous carbon fibers (Zoltek), as received. (a) PX35 type 65 ("long", CFL); (b) PX35 MF150 ("short", CFS).

3.2.3.5 Ultra-thin wood laminae

The idea of using wood as a reinforcement for structural TES composites derived from the observation that several organic PCMs are biodegradable. Fatty acids and poly(ethylene glycol)s (PEGs) are often preferred over paraffins in building and biomedical applications due to their biodegradability and biocompatibility.

Therefore, it would be interesting to employ them in combination with fully biodegradable polymer matrices and reinforcements. For the reinforcement, there are several types of wood-derived products and natural fibers available on the market, such as jute, flax, coir, bamboo, and kenaf (Wu, 2009), and in the last years a considerable technological attention was given to Wood Plastic Composites (WPCs), constituted by wood fibers or wood flour compounded with thermoplastic matrices such as PP, PE and PVC (Oksman and Sain, 2008), mainly because of the possibility to transform these materials through traditional technologies of thermoplastics (i.e. extrusion, injection molding).

As the wood-derived products are often porous, a smarter and more effective approach for the production of composites with TES capability is choosing a reinforcement that can also serve as shape-stabilizing agent, by retaining the PCM in its pores. In this perspective, one of the most interesting options for such multifunctional biodegradable reinforcements is represented by thin wood laminae, illustrated in Figure III - 9. From a mechanical point of view, wood behaves like a heterogeneous anisotropic material. Moreover, in the low deformation regime it can be considered as an orthotropic material (Green et al., 1999), and their mechanical performances are strongly influenced by the presence of nodes and defects. Among the different types of wood, beech wood (*Fagus sylvatica*) was selected for its microstructure. It has an ordered microstructure made of large parenchymal cells distended along growth ring boundaries, while the concentration of gum inclusions, salt crystals, nodes and microstructural defects is rather limited. This enhances the mechanical properties in the longitudinal direction and allows the obtainment of thin laminae with uniform thickness, large areal dimensions and no macroscopic defects. Beech wood has an apparent density of 0.73 g/cm^3 (23 °C, relative humidity 50%).

Thin wood laminae, with a thickness of approx. 320 µm, were produced at the CNR Ivalsa Institute (San Michele all'Adige, TN, Italy). The laminae were obtained through a Marunaka Super Meca-s planer (Marunaka Tekkosho Inc., Shizuoka, Japan) from beech boards, conditioned at a temperature of 23 °C and a relative humidity of 50 %. Although this machine allows the production of even thinner laminae (below 100 µm), the choice of the lamina thickness for this thesis work was motivated by the need to reach a compromise between the flexibility of the thinner laminae and the capability of being impregnated with PCM, as a greater thickness offers an increased storage volume.

Figure III - 9. Thin beech laminae obtained at the CNR Ivalsa Institute (San Michele all'Adige, TN, Italy).

3.2.4 Summary and labels of the investigated materials

Table III - 2 lists all the matrices, reinforcements and PCMs used in this thesis, whit the indication of the chapters and sections in which they are employed. From now on, the materials will mostly be referred to with their labels.

Table III - 2. List of the matrices, reinforcements and PCMs employed in this thesis.

Label	Material	Described in Section	Used in Chapters/ Subchapters
Par	Paraffin RT44HC	3.2.1.1	4.2; 5.2.
ParCNT	Paraffin RT44HC with CNTs (10 wt%)	3.2.1.1	4.2; 5.2.
MC	Microcapsules MPCM43D	3.2.1.2	4.2; 4.3; 4.4; 4.5; 5.3; 5.4; 5.5; 7.3.
D	Docosane	3.2.1.3	7.2.
PEG	PEG2000	3.2.1.4	Chapter VI
PA	Polyamide 12	3.2.2.1	4.2; 4.3.
EL	Elium resin	3.2.2.2	4.4.
PP	Polypropylene	3.2.2.3	4.5.
A	Thermoplastic starch	3.2.2.4	Chapter VI
EP	Epoxy resin	3.2.2.5	Chapter V
GF	Bidirectional glass fiber fabric	3.2.3.1	4.2
CF	Bidirectional carbon fiber fabric	3.2.3.2	4.4; 5.2.
CFu	Unidirectional carbon fiber fabric	3.2.3.3	5.4.
CFL	Discontinuous carbon fibers, 6 mm	3.2.3.4	4.3.
CFS	Discontinuous carbon fibers, 100 µm	3.2.3.4	4.3; 5.5.
FA	Wood laminae	3.2.3.5	Chapter VI

3.3 Characterization techniques

The present Subchapter describes the main techniques used for most of the prepared materials. Conversely, the techniques that are proper of a specific system will be described in the corresponding Chapter.

A detailed microstructural, thermal and mechanical characterization was performed both on the polymer/PCM systems and on the reinforced composites, to assess the impact of the PCM addition on the thermo-mechanical properties of the system.

3.3.1 Microstructural properties

3.3.1.1 Optical microscopy (OM)

Optical microscopy was useful to investigate the morphology and the size distribution of the shape-stabilized PCM (ParCNT) and of the prepared composites. In this latter case, it was specifically applied to study the polished cross sections, in order to analyze the arrangement and the integrity of the phases. Specimens were cut and mounted in epoxy cylindrical tabs to ease handling. Then the samples were grinded with a sequence of abrasive papers and finally polished with polishing clothes. Micrographs were obtained with an upright incident-light optical microscope Zeiss Axiophot (Oberkochen, Germany), equipped with Epiplan Neofluar objectives, at various magnifications.

3.3.1.2 Scanning electron microscopy (SEM)

SEM micrographs were acquired to investigate the morphology of some PCMs and the fracture surface of the samples after mechanical tests. SEM investigation was also performed on cryofracture surfaces, obtained by fracturing the specimens after soaking in liquid nitrogen for at least 30 minutes.

This analysis was carried out for most of the samples with a Zeiss Supra 60 field-emission scanning electron microscope (FE-SEM). However, for the samples that resulted unstable under the highly focused FE-SEM electron beam and the ultra-high-vacuum conditions, the SEM investigation was carried out with a Jeol IT300 scanning electron microscope (Jeol Ltd, Tokyo, Japan), under milder vacuum conditions. As all the investigated samples are not good conductors of electricity, it was necessary to make the surface conductive through a Pt-Pd sputtering.

3.3.2 Physical properties

3.3.2.1 Density

Density measurements were useful to determine the pore volume fraction. The density was measured via two methods; the liquid displacement method (Archimedes' balance) and the helium pycnometry.

The liquid displacement method was performed according to the standard ASTM D792 with a Gibertini E42 analytical balance (Gibertini Elettronica Srl, Milano, Italy). The selected liquid was ethanol (purity 99%), purchased by Sigma-Aldrich. At least three specimens were measured for each sample. The density of ethanol was measured with a metallic sphere of known and calibrated volume at the beginning and at the end of each measuring session. The average between the two values was taken as the density of ethanol and used for calculations.

Helium pycnometry was performed with a Micromeritics AccuPyc 1330 helium pycnometer (Micromeritics Instrument Corp., Norcross, GA, US) at 23 °C. Specimens were tested having a mass of 300-500 mg. For each specimen, 99 consecutive measurements were acquired, to reach stationary conditions.

3.3.2.2 Melt flow index (MFI)

Melt flow index (MFI) tests were performed on some PA/PCM combinations as a preliminary investigation. The tests were useful to acquire information on how the PCM addition affects the rheological properties of the PA. The tests were performed with a Dynisco LMI D4000 machine (Dynisco, Franklin, MA, US) at 230°C, with a weight of 2.16 kg.

3.3.2.3 Dynamic rheological properties

Dynamic rheological tests were carried out on the PP/PCM and PA/discontinuous fiber/PCM composites to investigate the impact of PCMs and discontinuous reinforcements on the rheological properties and the processability of the polymer matrices.

PP/PCM composites were investigated at the Leibniz-IPF through a TA ARES G2 rotational rheometer (TA Instruments, New Castle, DE, US) under small amplitude oscillatory frequency sweeps, in a parallel plate configuration (gap 1.5 mm, diameter 8 mm), in isothermal conditions at 190 °C under nitrogen atmosphere. Each test started 4 minutes after the insertion of the specimen, to ensure the thermal equilibrium. The storage and loss moduli were measured as a function of the shear frequency, and parameters as $tan\delta$ and complex viscosity were also calculated.

PA/discontinuous fiber/PCM composites were studied through a Haake Mars III dynamic shear rheometer (Haake Technik GmbH, Vreden, Germany) in parallel plate

configuration, in isothermal conditions at a temperature of 190 °C under nitrogen atmosphere, on square samples of 20x20x1.5 mm^3. Also in this case, the test allowed the measurement of the shear viscosity and the shear dynamic storage modulus, loss modulus and loss factor in the selected frequency range.

3.3.2.4 Brookfield viscosimetry

Brookfield viscosimetry was performed to measure the viscosity of the EP/PCM mixtures before curing, to evaluate the effect of PCM addition on the rheological properties of the epoxy resin. The epoxy base and the PCM were first mixed to ensure a homogeneous dispersion. The hardener was added to the mixture just before the test, to avoid further increases in viscosity due to crosslinking. The tests were performed with a Brookfield Viscometer Model RVT (Brookfield Engineering Laboratories, Inc., MA, US), with spindles chosen among the set RV and the small sample adapter. The viscosity of the mixtures was determined in the speed range between 5 and 100 rounds per minute (rpm).

3.3.3 Thermal and thermo-mechanical properties

3.3.3.1 Differential scanning calorimetry (DSC)

Differential scanning calorimetry (DSC) was performed on the neat PCMs, on the polymer/PCM mixtures and on the reinforced composites to investigate the melting and crystallization enthalpies and temperatures, which are the main parameters determining the TES capability of a sample containing a PCM in a specific temperature range.

By a comparison between the phase change enthalpies measured on the neat PCMs and on the prepared samples, relative phase change enthalpy values (ΔH_m^{rel}, ΔH_c^{rel}) were calculated according to Equation (III - 1), as

$$\Delta H_m^{rel} = \frac{\Delta H_m}{\omega_{PCM} \cdot \Delta H_m^{neat}} ; \Delta H_c^{rel} = \frac{\Delta H_c}{\omega_{PCM} \cdot \Delta H_c^{neat}} \quad \textbf{(III - 1)}$$

where ΔH_m and ΔH_c are the melting and crystallization enthalpy values of the PCM measured on the polymer/PCM mixtures and on the reinforced composites, ω_{PCM} is the nominal weight fraction of PCM in the sample and ΔH_m^{neat} and ΔH_c^{neat} are the melting and crystallization enthalpy values of the neat PCM. A relative phase change enthalpy close to 100 % suggests that the PCM fraction still present in the composite after processing is close to the nominal (initial) fraction, and that the PCM preserves its capability of melting and crystallizing also when embedded in a composite. Conversely, a low relative phase change enthalpy indicates that the PCM degrades or

leaks out of the composite during processing, due to the higher applied temperatures and pressures or to the not efficient shape-stabilization.

DSC analysis also allowed the measurement of the glass transition temperature and, for semicrystalline polymers, the melting temperature and enthalpy of the polymer matrix. These data gave an indication about the degree of curing (for thermosetting matrices) or the crystallization behavior and molecular mobility (for thermoplastic matrices).

DSC tests were performed on a Mettler DSC30 instrument (Mettler Toledo, Columbus, OH), at a heating/cooling rate of 10 °C/min under a nitrogen flow of 100 ml/min. All the specimens, with a mass of approx. 10 mg each, underwent a first heating scan, a cooling scan, and a second heating scan. For each composition, the temperature range was chosen to include all the transitions of interest. PP/PCM samples were tested at the Leibniz-IPF with a TA Instruments Q2000 calorimeter, at the same testing conditions. Some tests were performed at a lower heating rate, to be able to resolve multiple endo/exothermic signals. In these cases, the heating rate is clearly specified while presenting the results.

3.3.3.2 Thermogravimetric analysis (TGA)

Thermogravimetric analysis (TGA) was performed on the as-received materials and on the prepared composites, to assess how the resistance to the thermal degradation varies when adding a PCM. The tests also allowed the measurement of the weight fraction of the reinforcement in the prepared composites. Tests were performed at a heating rate of 10 °C/min up to 700 °C, under a nitrogen flow of 10 ml/min, through a Mettler TG50 instrument on specimens of approximately 20-25 mg or through a TA Instruments Q5000 IR thermobalance on specimens of approx. 10 mg.

PP/PCM samples were tested at the Leibniz-IPF with a TA Instruments Q500 thermobalance. The tests were performed on specimens of 3-4 mg at the same testing conditions. Isothermal tests were also performed on these specimens, to investigate the thermal stability of the PCM to the subsequent processing steps. The details of the experimental conditions will be described in the corresponding Chapter, as they are closely related to the processing parameters of such materials.

3.3.3.3 Thermal camera imaging

Although DSC is the most accurate technique that gives quantitative information on the TES capability of a sample, the small dimensions of the investigated specimen can lead to results that are not fully representative of the prepared composite. Therefore, to check the overall thermal management capacity of the laminates, a simple test was performed with a thermal camera. The composites were heated in an oven at 70 °C for 30 min, then removed and left cooling to room temperature. During

the cooling step, the surface temperature was recorded with an infrared thermal imaging camera FLIR E60 (FLIR® Systems Inc., Wilsonville, OR, US), placed at a fixed position at a distance of 30 cm from the laminate surface. On some selected samples, the test was also performed during the heating stage. The specimens were placed in an oven preheated at 70 °C and the surface temperature was recorded while the specimen uniformed its temperature to that of the surrounding environment.

3.3.3.4 Thermal conductivity

Thermal conductivity is another important parameter for TES systems, as it influences the heat transfer and determines the phase change rate.

Thermal conductivity was measured with a Hot Disk Thermal Constants Analyzer Model TPS 2500S (Hot Disk AB, Göteborg, Sweden), capable of precise measurement of thermal conductivity, thermal diffusivity and specific heat capacity. This machine uses the transient plane source method and theory in accordance with ISO Standard 22007-2:2015. It is equipped with different sensor types and software modules to perform analysis on bulk materials, thin films, powders and liquids. To perform the measurement, the sensor, made of a double spiral nickel wire insulated in a thin layer of Kapton®, is placed between two sheets of material with planar and parallel surfaces. In this work, the specimens were analyzed with Sensor 7577 (radius 2.001 mm) or Sensor 5465 (radius 3.189 mm). The measurement is performed by sending a current through the nickel sensor and measuring the temperature rise of the sensor itself, evaluated through a change in electrical resistance. The temperature rise is influenced by the thermal properties of the sample material that surrounds the sensor, which are evaluated by the instrument software. Important measurement parameters are the power input and the measurement time, which must be chosen to produce a temperature increment of 2-5 K, as recommended by the instrument manual. At least three measurements were performed for each sample, in different zones of the specimen and/or with a different power input. The bulk isotropic module was chosen for all the polymer matrices and polymer/PCM blends investigated with this technique. For these samples, specimens were prepared with an in-plane dimension of 100x50 mm^2 and a thickness of 5 mm.

Another technique used in this work to measure the thermal conductivity was the laser flash analysis (LFA), implemented on a Netzsch LFA 447 instrument (Netzsch GmbH, Selb, Germany). Square samples with a side length of 12.7 mm were cut from the prepared specimens. Each specimen was tested at various temperatures between 20 °C and 60°C, and three pulses were performed for each temperature. Data were analyzed with the software Proteus (Netzsch). Thermal diffusivity (α) was determined using the Cowan method with pulse correction. For the calculation of the specific heat capacity (c_P), the reference material Pyrex 7740, was employed, according to the standard ASTM-E 1461. The thermal conductivity (λ) was calculated according to Equation (III - 2), as

$$\lambda = \alpha \rho c_P, \quad \text{(III - 2)}$$

where ρ is the sample density (g/cm^3).

3.3.3.5 Dynamic-mechanical analysis (DMA)

Dynamic mechanical analysis was performed to assess the dynamic-mechanical behavior of polymer/PCM system and polymer/PCM/reinforcement composites. It was useful in order to understand how the PCM addition affects the viscoelastic parameters and the glass transition of the host matrix or composite, and how such parameters vary before, during and after the PCM phase change. These composites containing a PCM are the ideal systems to study how a dynamic-mechanical investigation is affected by a melting phase transition, which is not usually possible with common polymer composites. All DMA tests were performed with a TA Q800 DMA instrument in single cantilever bending mode, with a distance between the grips of 17.5 mm. Three testing modes were applied; single-frequency scans, multifrequency scans, and heating-cooling cycles.

In single frequency scans, the storage modulus (E'), loss modulus (E''), and loss factor ($tan\delta$) were measured between 0 °C and 180 °C at 3 °C/min, with an applied strain of 0.05 % at a frequency of 1 Hz.

Multifrequency scans were carried out at 0.3 °C/min at the frequency values of 0.3, 1, 3, 10, and 30 Hz. The activation energy of the glass transition (E_a) was determined through the Arrhenius approach, from the slope of the linear regression of the natural logarithm of the applied frequency plotted versus the reverse of the $tan\delta$ peak temperatures, as reported in Equation (III - 3):

$$E_a = R\left(\frac{d(ln\nu)}{d(1/T_P)}\right), \quad \text{(III - 3)}$$

where R is the universal gas constant, equal to 8.314 J/molK, ν is the applied frequency, and T_P is the E'' or $tan\delta$ peak temperature at the glass transition.

As the value of E' was seen to decrease at the PCM melting temperature, cyclic DMA scans were performed to assess the recovery of E' and the behavior of the other viscoelastic parameters upon PCM crystallization. Heating-cooling-heating scans were carried out between −40 and 60 °C, at the scanning speeds of 1 °C/min and 3 °C/min. The test allowed the measurement of all the peak temperatures of E'' and $tan\delta$, the ratio between the values of E' at the beginning of the second and the first heating scan ($E'_{rel,-40°C}$), and the temperature difference at the middle value of E' between the first heating scan (h_1) and the cooling scan (c), defined through Equation (III - 4) as

$$\Delta T_{E',50\%} = T\left(E'_{50\%,h1}\right) - T\left(E'_{50\%,c}\right), \quad \textbf{(III - 4)}$$

where $E'_{50\%}$ is the average between the maximum and the minimum E' values of each sample.

3.3.3.6 Vicat tests

Vicat tests were performed on some polymer/PCM samples, to investigate the dimensional stability below and above the PCM melting temperature. Vicat tests were performed according to the ASTM D 1525 standard, from 30 °C to 300 °C, at a heating rate of 120 °C/h, under an applied load of 10 N, in a silicone oil bath. The samples had a surface of 10x10 mm^2 and a thickness of approx. 5 mm.

3.3.4 Weight and volume fraction of the constituents

In the prepared composite laminates, the weight and volume fractions of the fibers and the matrix (polymer/PCM mixtures) are fundamental parameters that influence the final mechanical and TES performance. The procedure described here is general; the specific procedure for each composite will be specified while commenting each particular result.

As mentioned in Section 3.3.3.2, TGA tests allowed the calculation of an experimental weight fraction of fibers (ω_f) from the residual mass fractions of the virgin fibers, the matrices (polymer/PCM blends) and the composite laminates, through Equation (III - 5) as

$$\omega_f = \frac{m_r - R_m}{R_f - R_m} \quad \textbf{(III - 5)}$$

where m_r is the residual mass of the composite, R_f and R_m are the residual mass fractions of the reinforcement and the matrix, respectively. For the composites investigated in this thesis, R_m was most of the times negligible ($R_m \approx 0\ \%$), while the fibers did not lose mass ($R_f \approx 100\ \%$); therefore, the fiber weight fraction could be almost always approximated with m_r. However, it will be clearly specified when this is not the case.

The measurement of ω_f allowed the calculation of the theoretical density of the laminates (ρ_{th}) through the mixture rule written as a function of the mass fractions of the constituents, represented in Equation (III - 6) as

$$\rho_{th} = \frac{1}{\omega_f/\rho_f + (1-\omega_f)/\rho_m} \quad \textbf{(III - 6)}$$

where ρ_f and ρ_m are the density values of the fibers and the matrix, respectively, measured through the displacement method in ethanol and/or helium pycnometry. The same two measurement techniques were applied to obtain the experimental density of the laminates, ρ_{exp}. The volume fraction of voids (ϑ_v) was subsequently calculated via the Equation (III - 7) as

$$\vartheta_v = \frac{\rho_{th} - \rho_{exp}}{\rho_{th}} \quad \textbf{(III - 7)}$$

Lastly, the knowledge of the weight fraction of the constituents, the void volume fraction and the experimental density of the composites allowed the calculation of the volume fraction of fibers (ϑ_f) and matrix (ϑ_m) through Equation (III - 8) and (III - 9), respectively, as

$$\boldsymbol{\vartheta_f = \omega_f \frac{\rho_{exp}}{\rho_f}} \; ; \quad \textbf{(III - 8)}$$

$$\vartheta_m = (1 - \omega_f)\frac{\rho_{exp}}{\rho_m} . \quad \textbf{(III - 9)}$$

3.3.5 Mechanical properties

3.3.5.1 Tensile tests

Quasi-static tensile tests were performed with a universal testing machine Instron 5969 (Instron, Norwood, MA, US), equipped with a 50 kN load cell.

For polymer/PCM systems and composites reinforced with discontinuous fibers, 1BA specimens (ISO 527 standard) were cut through a Ceast 6051 die-cutter (Ceast, Pianezza, Italy). The measurement of the elastic modulus was performed at a crosshead speed of 0.25 mm/min, the strain was measured with a resistance extensometer Instron 2620 with a gauge length of 12.5 mm and five specimens were tested for each sample. According to the standard ISO 527, the elastic modulus (E) was measured as the secant of the stress-strain curve between the strain values of 0.05 and 0.25%. For each composition, five additional specimens were tested until failure, at a crosshead speed of 10 mm/min for the samples with a PA matrix, and 1 mm/min for the samples with an EP matrix. The test allowed the determination of the stress and strain at yield (σ_y, ε_y) (when applicable), the maximum stress and the corresponding strain (σ_{MAX}, ε_{MAX}), and the stress and strain at break (σ_b, ε_b).

For composites reinforced with continuous fibers, rectangular specimens of 120x10 mm^2 were cut out of the prepared laminates with a diamond saw. Tests were carried out with an initial distance between the grips of 80 mm. The specimens were

tabbed at both ends with glass fiber composite tabs, to avoid damages in the gripping zone. The elastic modulus was measured as described above. The properties at break (σ_b, ε_b) were measured on at least five specimens per sample, at a crosshead speed of 1 mm/min.

3.3.5.2 Flexural tests

Flexural tests were performed with a three-point bending configuration, according to the standard ASTM D790, with a universal testing machine Instron 5969 equipped with a 50 kN load cell.

For polymer/PCM systems and composites reinforced with discontinuous fibers, tests were performed on rectangular specimens with nominal dimensions of 70x10x3 mm^3. The span length was fixed at 50 mm and the crosshead speed at 1.5 mm/min. At least five specimens were tested for each composition. The flexural modulus of elasticity (E_f), the flexural strength (σ_{fM}) and the flexural strain at break (ε_{fb}) were determined for each specimen as described in Equations (III - 10), (III - 11), and (III - 12), respectively:

$$E_f = \frac{mL^3}{4bd^3} \quad \textbf{(III - 10)}$$

$$\sigma_{fM} = \frac{3PL}{2bd^2} \quad \textbf{(III - 11)}$$

$$\varepsilon_{fb} = \frac{6Dd}{L^2} \quad \textbf{(III - 12)}$$

where L is the support span, m is the slope of the tangent to the initial portion of the load-deflection curve, b and d are the specimen width and thickness, P is the maximum load and D is the deflection at the break point.

For continuous-fiber composites, the nominal in-plane dimensions of the tested specimens were 120x10 mm^2. The span length was 85 mm, as the standard recommends increasing the span-to-thickness ratio for samples with in-plane strength considerably higher than the interlaminar shear strength. The crosshead speed was fixed at 9 mm/min, and at least five specimens were tested for each sample. The tangent modulus of elasticity and the flexural strain at break were calculated as described above, while the flexural strength was determined with Equation (III - 13) as

$$\sigma_{fM} = \frac{3PL}{2bd^2}\left[1 + 6\left(\frac{D}{L}\right)^2 - 4\left(\frac{D}{L}\right)\left(\frac{d}{L}\right)\right], \quad \textbf{(III - 13)}$$

to consider the not negligible forces developed at the supports derived by a high span-to-thickness ratio, as the ASTM D790 standard suggests. It should be mentioned that this equation is based on the assumption of a linear stress distribution through the specimen thickness. This is not fully correct for laminates, but the results are still useful for comparison purposes.

3.3.5.3 Charpy impact tests

Charpy impact tests were performed according to ISO 179 with a Ceast 6549 impactor. The hammer had a mass of 1.18 kg and it was placed so that the impact speed resulted of 1 m/s. Rectangular samples of 80x10x4 mm^3 with a notch depth of 2 mm and a notch tip radius of 0.25 mm were utilized. A span length of 62 mm was used, and at least five specimens for each sample were tested. The test allowed the measurement of the maximum load reached during the tests (F_{max}), the specific energy absorbed at the maximum load ($E_{sp,max}$), and the specific energy absorbed at break ($E_{sp,tot}$).

The wood/starch laminate samples were tested with a hammer with a length of 25 cm and a mass of 0.48 kg, positioned at a starting angle of 150 °. In this way, the tests were performed at an impact speed of 2.9 m/s, with a maximum impact energy of 2 J. A thin plasticine layer was used to damp the vibrations to avoid the inertial peak in the force-displacement signal. The tests were performed on rectangular specimens having nominal dimensions of 120x10x2 mm^3, with a span length of 40 mm.

3.3.5.4 Mode I fracture toughness

Mode I fracture toughness tests were performed to evaluate the effect of the introduction of increasing fractions of a PCM on the fracture toughness of the host polymer matrix and laminate. This test was performed on a single polymer/reinforcement/PCM system and the corresponding polymer/PCM matrix; the chosen system was that having a polymer matrix exhibiting a brittle behavior, i.e. the system EP/CFu/MC, composed of an epoxy matrix, unidirectional carbon fibers and various amounts of paraffin microcapsules. These tests were performed with a universal testing machine Instron 5969 equipped with a 50 kN load cell.

For EP/MC systems, tests were performed on single edge notched beam (SENB) specimens with nominal dimensions 80x10x4 mm^3. A sharp notch was machined with a depth of 4.5 mm, and a sharp crack was subsequently initiated by sliding a fresh razor blade in the notch. The measurements were carried out according to the standard ASTM D5045, in a three-point bending configuration, with a span length of 40 mm and crosshead speed of 10 mm/min. A conditional value (K_Q) of the critical stress intensity factor was determined for each specimen through Equation (III - 14) as

$$K_Q = \left(\frac{P_Q}{B\sqrt{W}}\right) f(x), \qquad \textbf{(III - 14)}$$

where P_Q is the load value determined as described in the standard ASTM D5045, B and W are the specimen thickness and depth, respectively.

$f(x)$ is a geometrical function defined in the Equation (III - 15) as

$$f(x) = 6\sqrt{x}\frac{1.99 - x(1-x)(2.15 - 3.93x + 2.7x^2)}{(1+2x)(1-x)^{3/2}} \qquad \textbf{(III - 15)}$$

where x is the ratio between the initial notch length (a) and the specimen depth (W). The calculated K_Q can be considered as the critical stress intensity factor K_{IC} only when the condition of plane-strain defined in Equation (III - 16) are satisfied:

$$B, a, (W - a) > 2.5\left(\frac{K_Q}{\sigma_y}\right)^2, \qquad \textbf{(III - 16)}$$

where σ_y is the yield stress evaluated as the maximum load in the uniaxial tensile tests.

Mode I interlaminar fracture toughness was evaluated on the unidirectional carbon fiber laminates containing paraffin microcapsules, according to the standard ASTM D5528-13. The tests were performed on specimens with in-plane dimensions of 130x20 mm^2, cui out of the prepared laminates with a diamond saw. At least three specimens were tested for each composition. The geometry of the tested specimens is shown in Figure III - 10. The initial crack (a) formed in the middle plane of the laminates was made by inserting a polyethyleneterephthalate (PET) with a thickness of 26 µm in the stacking process of the laminates. The PET film was inserted to create a pre-crack of 55 mm in the final prepared specimens.

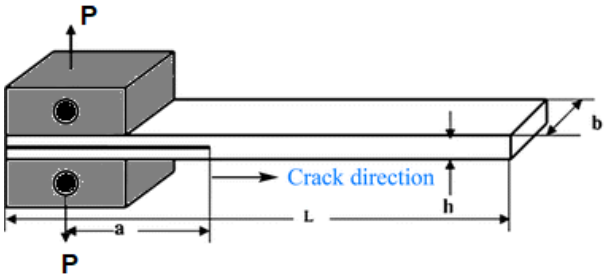

Figure III - 10. Specimen for mode I interlaminar fracture toughness (a = 55 mm, b = 20 mm, L = 130 mm). P indicates the direction of applied load. The crack propagates in the fiber direction.

The specimens were loaded at 0.25 mm/min until an increment of delamination crack growth of 3 to 5 mm and then unloaded at 25 mm/min, and the tip of the precrack was noted. The specimens were then reloaded at 2.5 mm/min until the crack had propagated for at least 50 mm from the tip of the precrack. The test was recorded with a LogiTech C920 USB video camera, to be able to correlate each advancement of the crack tip with the corresponding load value. The specimen was finally unloaded at 25 mm/min.

The value of critical strain energy release rate (G_{IC}) was calculated with the Equation (III - 17) as

$$G_{IC} = \frac{3P\delta}{2b(a + |\Delta|)}, \qquad \textbf{(III - 17)}$$

where P is the applied load, δ is the load point displacement, a is the crack length, b is the specimen width and the term $|\Delta|$ is introduced to take into account the rotations that may occur at the delamination front. Δ was determined experimentally by generating a leasts squares plot of the cube root of compliance ($C^{1/3}$) as a function of delamination length a, where $C = \delta/P$, as specified in the standard.

3.3.5.5 Short-beam shear tests

Short-beam shear (SBS) tests were performed to assess the interlaminar shear strength (ILSS) of the prepared laminates, following the standard ASTM D 2344, with an Instron 5969 universal testing machine equipped with a 50 kN load cell, in a three-point bending configuration. The tested specimens were cut out of the prepared laminates with a diamond saw, and their dimensions were chosen to meet the conditions prescribed by the ASTM standard. The laminate thickness is influenced by several factors, such as the number of layers and the fiber weight fraction, but also the PCM content, as will be explained in the next Chapters. Therefore, the specimen dimensions and the span length were chosen for each sample as a function of the laminate thickness, as represented in Figure III - 11. All the specimens were tested at a crosshead speed of 1 mm/min.

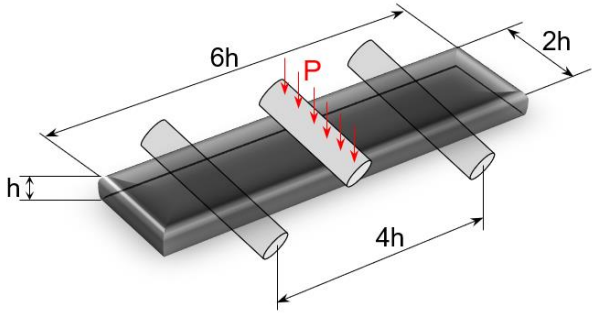

Figure III - 11. Schematic representation of the specimen and test dimensions of the short-beam shear test on the laminates.

The short-beam interlaminar shear strength, $ILSS$, was calculated as reported in Equation (III - 18):

$$ILSS = \frac{3P_m}{4bh}, \qquad \textbf{(III - 18)}$$

where P_m is the maximum load and b and h are the specimen width and thickness, respectively. At least three specimens were tested for each sample. As in case of Equations (III - 12) and (III - 13), also this equation is derived from the classical beam theory, which assumes that the shear stress is parabolically distributed in the specimen cross-section. However, as thoroughly studied in the literature, the shear behavior of composite laminates can deviate markedly from this trend and the maximum shear stress is significantly lower than that predicted by this theory (Cui et al., 1994). Although the real ILSS is expected to be lower than that calculated as described above, the apparent value can be considered suitable for this work, as it is used only for comparison among laminates containing different amounts of PCM (Cui et al., 1994).

Chapter IV

Thermoplastic TES composites

Part of this chapter has been published in:

- G. Fredi, A. Dorigato, A. Pegoretti,
  Multifunctional glass fiber/polyamide composites with thermal energy storage/release capability,
  eXPRESS polymer letters 12, 4 (2018) 349-364

- A. Dorigato, G. Fredi, A. Pegoretti,
  Novel phase change materials using thermoplastic composites,
  AIP Conference Proceedings of the 9th International Conference on "Times of Polymers and Composites". 1981 (2018) 020044/1-020044/4

- G. Fredi, A. Dorigato, S. Unterberger, N. Artuso, A. Pegoretti,
  Discontinuous carbon fiber/polyamide composites with microencapsulated paraffin for thermal energy storage,
  Journal of applied polymer science 136, 16 (2019) 47408/1-47408/14

- G. Fredi, A. Dorigato, A. Pegoretti,
  Novel reactive thermoplastic resin as a matrix for laminates containing phase change microcapsules,
  Polymer Composites 40, 9 (2019) 3711-3724

- G. Fredi, H. Brünig, R. Vogel, C. Scheffler,
  Melt-spun polypropylene filaments containing paraffin microcapsules for multifunctional hybrid yarns and smart thermoregulating thermoplastic composites,
  eXPRESS polymer letters 13, 12 (2019) 1071–1087

4.1 Introduction

The present Chapter describes the methods and results of the polymer/PCM/reinforcement systems with a thermoplastic matrix. Four case studies were investigated, and they will be described in the following four Subchapters.

Subchapter 4.2 describes glass/polyamide laminates containing either a microencapsulated or a shape-stabilized PCM and aims at evidencing the differences in the behavior of the two PCMs when embedded in a traditional thermoplastic laminate. The same polyamide matrix and microencapsulated PCM were employed in combination with discontinuous carbon fibers, as described in the Subchapter 4.3, to produce thermoplastic semi-structural composites with TES capability. A different approach is adopted in Subchapter 4.4, where a carbon fiber laminate containing PCM microcapsules was produced with a reactive thermoplastic matrix, which allows avoiding all the processing steps at high temperature in the molten state. However, since reactive processing is not applicable to the most common thermoplastic matrices, an additional technique is explored that involves the production of multifunctional commingled yarns, where the PCM phase is embedded in the polymer filaments. In this thesis, the experimental work was limited to the production of PP filaments containing PCM microcapsules, and the results of this approach are illustrated in Subchapter 4.5.

4.2 PCM-enhanced glass/polyamide12 laminates

This Subchapter presents the results thermoplastic laminates with a polyamide matrix, reinforced with a glass fiber fabric and containing two types of paraffinic PCMs, namely a commercial microencapsulated paraffin and a CNT-stabilized paraffin.

4.2.1 Materials and methods

This Section describes the materials used to fabricate these samples and the techniques of sample preparation. It subsequently lists all the characterization techniques applied on these samples. Since the materials and the characterization techniques have been already detailed in Chapter III, this Section will specify only the experimental parameters that are specific of this Subchapter.

4.2.1.1 Materials

The materials employed for the preparation of these laminates are listed in Table IV - 1 (please refer to Section 3.2.4 for the details about the materials).

Table IV - 1. Materials employed in Subchapter 4.2.

Phase	Label	Material
Polymer matrix	PA	Polyamide 12
Reinforcement	GF	Bidirectional glass fiber fabric
PCMs	MC	Paraffin microcapsules
	ParCNT	Paraffin shape stabilized with carbon nanotubes (CNTs) in a weight fraction of 15 wt%, and cryogenically pulverized

As observable from the data reported in Table IV - 1, two paraffinic PCMs were employed for the preparation of these samples: the first is a commercial microencapsulated PCM, while the second is a paraffin shape stabilized with CNTs (ParCNT), prepared as described in Chapter III, Section 3.2.3.1. The main aim of this work was to understand which of the two selected PCMs was the best candidate to be embedded in a traditional thermoplastic laminate. Naturally, the comparison would have resulted more effective if the two PCMs had the same initial phase change enthalpy. Therefore, the weight fraction of CNTs in the shape-stabilized PCM was tuned to obtain a phase change enthalpy close to that of the current batch of commercial paraffin microcapsules. From a preliminary study, reported in Section 3.2.3.1, it was found that the optimal CNT concentration was in the interval 10-15 wt%. For this particular work, the CNT-stabilized paraffin powder was prepared with a CNT weight fraction of 15 wt%.

4.2.1.2 Sample preparation

The sample preparation was divided into two steps, namely (a) the preparation of the PA/PCM blends, and (b) the preparation of the composite laminates via the introduction of glass fiber fabric.

The PA/PCM blends were produced by melt compounding and hot pressing. PA granules and the PCMs (either MC or ParCNT) were melt compounded in a Haake Rheomix 600 OS internal mixer equipped with counter-rotating rotors, at PCM concentrations ranging from 15 to 60 wt%. The materials were mixed at 200 °C at 60 rpm for 5 minutes. The resulting compounds were molded through a Carver Laboratory Press Model 2699 (Carver Inc., Wabash, IN, US) at 200 °C for 5 minutes under an applied pressure of 1.75 MPa. Neat PA and PA/PCM samples were obtained in form of square sheets of 120x120 mm^2. The prepared compositions are listed in Table IV - 2. The blends with microcapsules were labelled as PA-MCx and the blends with ParCNT as PA-ParCNTx, where x represents the nominal PCM weight fraction (x = 15, 30, 45, 60).

Table IV - 2. List of the prepared PA/PCM samples with nominal weight compositions.

Sample	PA (wt%)	MC (wt%)	ParCNT (wt%)
PA	100	0	0
PA-MC15	85	15	0
PA-MC30	70	30	0
PA-MC45	65	45	0
PA-MC60	40	60	0
PA-ParCNT15	85	0	15
PA-ParCNT30	70	0	30
PA-ParCNT45	65	0	45
PA-ParCNT60	40	0	60

Some of the prepared PA/PCM blends were used to fabricate composite laminates. Five compositions were chosen, namely PA, PA-MC30, PA-MC60, PA-ParCNT30 and PA-ParCNT60. To produce the laminates, PA/PCM sheets were prepared as described above but with a smaller thickness (approx. 0.3 mm) in order to ease the process of lamination. Such matrix sheets were alternated to GF squares, and the prepared layups (six PA/PCM sheets alternated to five GF squares) were hot-pressed at 200 °C for 5 minutes under an applied pressure of 3.4 MPa. The resulting laminates had surface dimensions of 120x120 mm^2 and a thickness of approx. 2 mm. They were referred to as PA-GF, PA-MC30-GF, PA-MC60-GF, PA-ParCNT30-GF and PA-ParCNT60-GF.

4.2.1.3 Characterization

The PA/PCM samples were investigated through the characterization techniques listed in Table IV - 3 together with the experimental parameters applied specifically on these samples (see Subchapter 3.3 for the full description of the characterization parameters and specimen preparation).

Table IV - 3. Characterization techniques and experimental parameters applied on the samples PA and PA-MCx.

Technique	Specific experimental parameters
Melt flow index (MFI)	Temperature 230 °C; mass 2.16 kg
Helium pycnometer	Temperature 23 °C; 99 measurements
SEM	Instrument Jeol IT300
DSC	Temperature interval 0-230 °C
TGA	TA Q5000 IR thermobalance; specimen mass 10 mg
Vicat test	As described in Section 3.3.3.6
Quasi-static tensile test	As described in Section 3.3.5.1

The PA/PCM/GF laminates were investigated through the characterization techniques listed in Table IV - 4 (see Subchapter 3.3 for the full description of the characterization parameters and specimen preparation).

Table IV - 4. Characterization techniques and experimental parameters applied on the PA/PCM/GF laminates.

Technique	Specific experimental parameters
Optical microscopy	On the polished cross-section
Helium pycnometer	Temperature 23 °C; 99 measurements
DSC	Temperature interval 0-230 °C
TGA	TA Q5000 IR thermobalance; specimen mass 10 mg
Quasi-static tensile test	As described in Section 3.3.5.1
Short-beam shear test	As described in Section 3.3.5.5

4.2.2 Results and discussion

This Section presents the results of the characterization of the PA/PCM samples and the PA/PCM/GF laminates.

4.2.2.1 Characterization of the PA/PCM samples

The results of the MFI tests on the PA/PCM samples are reported in Figure IV - 1. For the samples with microcapsules, the MFI decreases with an increase in the MC content and reaches a minimum of 5.2 g/10 min. A more dramatic MFI decrease is observed for the samples with CNT-stabilized paraffin. Compared to the MFI value of the neat PA, the MFI is halved with a ParCNT content of 15 wt%, and it approaches 0.7 g/10 min when the nominal ParCNT fraction is 30 wt%. Further increases in the ParCNT content reduce the fluidity in such a way that the measurements could not be performed with a mass of 2.16 kg, but a heavier weight had to be used to obtain a reliable MFI result, as indicated in Figure IV - 1. This is probably due to the growing CNT content, since these nanofillers are well known to heavily increase the viscosity of molten polymers (Rueda et al., 2017a). Due to the modification of the applied load, it is not possible to draw a trend of the MFI, but these results suggest that it may be difficult to obtain a composite with low porosity at elevated ParCNT contents. This also implies that, although both PCMs types decrease the fluidity of the PA, the effect of the MC is less intense than that of the ParCNT.

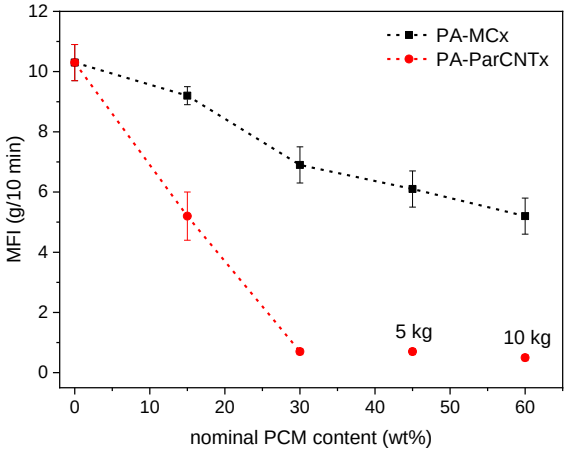

Figure IV - 1. MFI values of the samples PA-MCx and PA-ParCNTx (x = 15,30,45,60).

The results of the DSC tests on the neat PCMs and the PA/PCM samples are reported in Figure IV - 2, which shows the thermograms of the first heating scan. The most important DSC results about the first heating scan and the cooling scan are summarized in Table IV - 5. The data of the second heating scan are not reported for the sake of brevity, as there were no important differences compared to the first heating scan. The peak temperatures of the endo/exothermic signals at around 40 °C were considered as the melting/crystallization temperatures of the PCMs (T_m, T_c), while the areas under those peaks were regarded as the melting/crystallization enthalpies (ΔH_m, ΔH_c). As PA12 is a semicrystalline polymer, DSC tests also gave information about the melting/crystallization transitions of the PA matrix; the phase change temperatures were indicated as T_m^{PA} and T_c^{PA}. Moreover, relative phase change enthalpy values were determined by dividing the values of ΔH_m and ΔH_c by the melting/crystallization enthalpy of the neat PCM and considering the nominal PCM content in the blends, as described in Section 3.3.3.1 (Equation (III-1)).

The DSC characterization of MC and ParCNT was limited to the temperature interval around the phase transition, i.e. from 0 °C to 80 °C. As observable from Figure IV - 2, an intense endothermic peak is observable for both the PCMs at approximately 40–50 °C. The peak temperature, phase change enthalpy and peak shape is similar between the PCMs, which allows a direct comparison of their performance *per se* and embedded in a polymer composite. An analogous exothermic peak is observable on cooling (not reported). The PCM melting peak is visible also on the other PA/PCM samples, where an additional endothermic melting peak can be observed at approximately 180 °C. This peak can be associated to the melting of the PA phase.

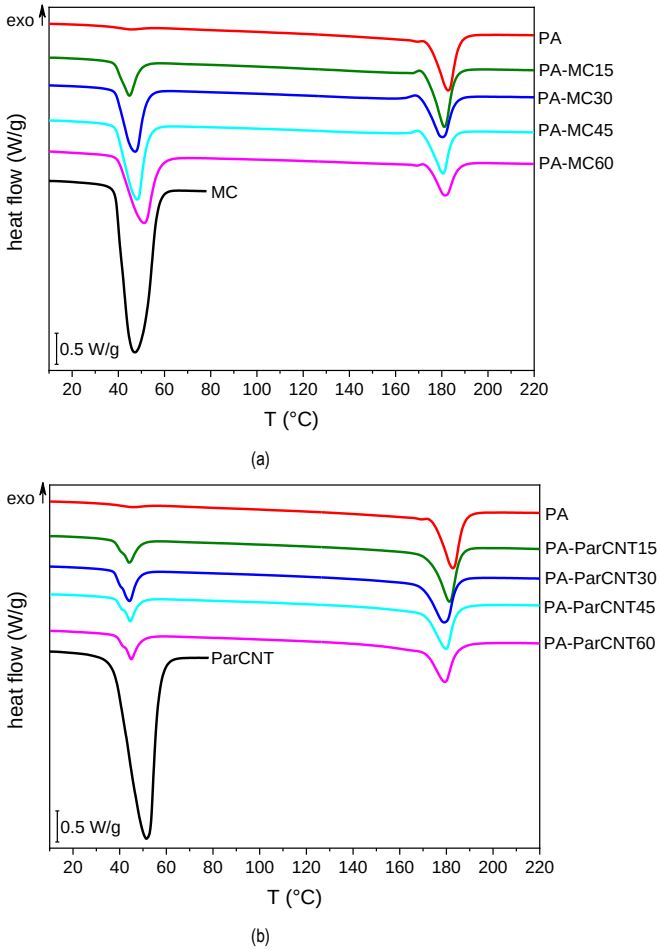

Figure IV - 2. DSC thermograms (first heating scan) of the prepared PA/PCM samples: (a) PA-MCx; (b) PA-ParCNTx (x = 15,30,45,60).

For the samples PA-MCx (Figure IV - 2a), the melting enthalpy of the PCM increases with the MC content. The relative enthalpy is approx. 70 %, which is comparable with literature results about similar blends with paraffin microcapsules embedded in a thermoplastic polymer matrix (Mochane and Luyt, 2012; Krupa et al., 2014). This suggests that a fraction of microcapsules was damaged and the paraffin degraded or leaked out of the blend during processing, which can be due to the combination of high temperature and shear stresses during melt compounding.

Nevertheless, most of the thermal energy storage/release capability is retained. Conversely, for the samples PA-ParCNTx (Figure IV - 2b), the PCM melting enthalpy does not follow a trend with the PCM concentration. The enthalpy values range between 14 J/g and 21 J/g, well below the expected values; this is demonstrated by the remarkably low relative enthalpy values, which implies a considerable PCM degradation during processing. Interestingly, the crystallization temperature of the PA matrix increases of approx. 5 °C in the ParCNT-based blends, which is probably related to the nucleating effect played by CNTs and is observed also on the composite laminates (see Table IV - 8). Similar results were observed elsewhere in the literature, e.g. in a work on PA6/clay nanocomposites (Dorigato et al., 2016).

It is worth noticing that the thermogram of the neat PA shows a further small endothermic signal due to the glass transition at 40.7 °C. However, this transition is not visible in the other compositions containing a PCM, as it is hidden by the more intense PCM melting peak.

Table IV - 5. Results of the DSC tests on the samples PA-MCx and PA-ParCNTx (x = 15,30,45,60).

Sample	T_m (°C)	ΔH_m (J/g)	ΔH_m^{rel} (%)	T_m^{PA} (°C)	T_c (°C)	ΔH_c (J/g)	T_c^{PA} (°C)
PA	--	--	--	181.2	--	--	155.7
PA-MC15	43.9	20.5	68.3	179.8	32.4	18.1	153.2
PA-MC30	45.9	46.8	77.9	179.3	23.0	46.8	152.0
PA-MC45	46.2	61.2	67.9	172.2	24.7	61.2	155.7
PA-MC60	49.1	76.3	63.8	180.2	21.8	71.2	152.6
PA-ParCNT15	43.3	16.1	57.3	172.2	33.2	11.3	160.5
PA-ParCNT30	43.1	21.1	37.6	177.7	32.6	15.6	165.4
PA-ParCNT45	43.5	14.0	16.7	178.4	29.2	8.6	158.7
PA-ParCNT60	44.0	16.4	14.6	178.0	30.4	12.2	160.7
MC	43.5	200.1	100	--	30.0	200.0	--
ParCNT	42.6	205.5	100	--	33.5	206.0	--

T_m = melting temperature of the PCM (°C); ΔH_m = PCM melting enthalpy (J/g); ΔH_m^{rel} = relative PCM melting enthalpy (%); T_m^{PA} = melting temperature of PA (°C); T_c = crystallization temperature of the PCM (°C); ΔH_c = PCM crystallization enthalpy (J/g) T_c^{PA} = crystallization temperature of PA (°C).

The paraffin leakage/degradation effect is observable also through the TGA results. The thermograms of the residual mass and mass loss derivative as a function of temperature are displayed in Figure IV - 3, while Table IV - 6 reports the temperature values corresponding to a mass loss of 1 wt% ($T_{1\%}$) and 5 wt% ($T_{5\%}$), as well as the degradation temperature measured at the peak of the mass loss derivative (T_d).

The thermal degradation of the neat PA happens in two subsequent steps, but the vast majority of the mass loss occurs in the first. The thermal degradation resistance of the microcapsules is lower than that of the neat PA, and the MC addition shifts the curves towards lower temperatures (Figure IV - 3a). For the neat MC, the degradation begins with many small subsequent steps. Four steps can be identified, which correspond to four local maxima in the mass loss derivative signal, as also reported by other studies on with paraffin encapsulated in melamine-formaldehyde microcapsules (Krupa et al., 2014). The weight loss during the first step (up to approx. 180 °C) can be attributed to absorbed water and residual low-molecular-weight species, not fully removed after the capsule synthesis. This step is not so evident in the other samples containing MC, as most of the low-molecular-weight compounds have probably been removed during the processing steps at 200 °C. The following steps are related to the thermal degradation of the paraffinic core and the melamine-formaldehyde shell.

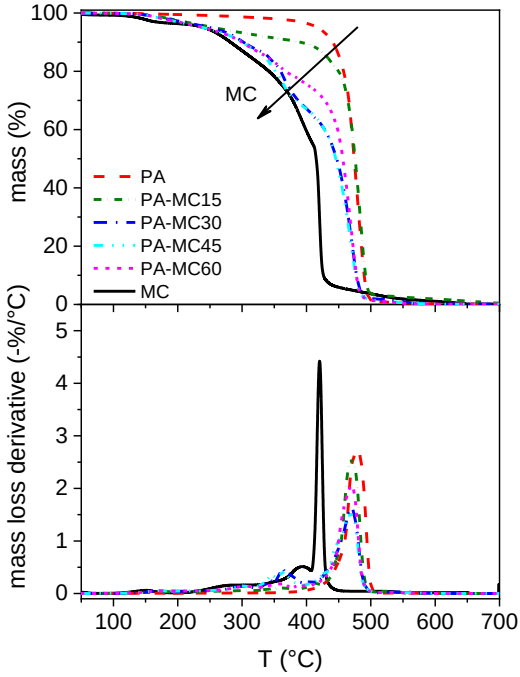

(a)

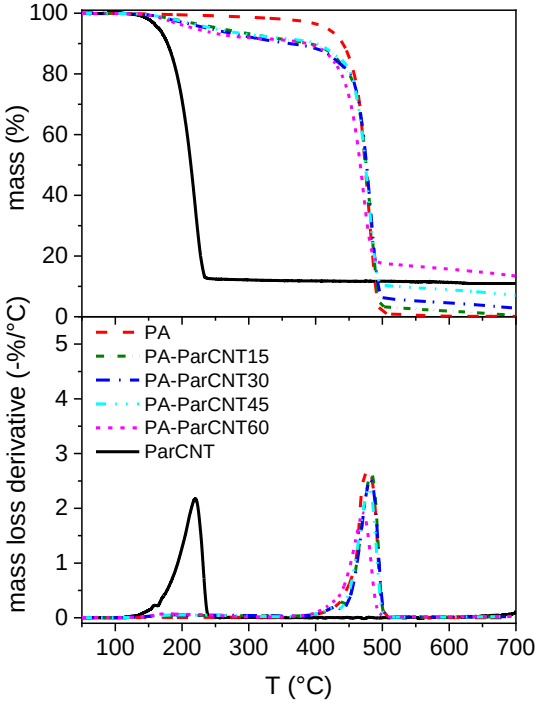

(b)

Figure IV - 3. TGA thermograms of the prepared PA/PCM samples: (a) PA-MCx; (b) PA-ParCNTx (x = 15,30,45,60).

The considerably high and narrow peak in the mass loss derivative signal suggests that most of the mass loss occurs in a relatively small temperature interval. It can be associated to the damage of the MC shells and the sudden release of the core. This spike was always observed on repeated measurements, but it was not detected in any of the MC-containing composites. This can be due to the fact that the surrounding polymer matrix, which is not yet degraded at the end of the MC degradation process, modifies the mass loss rate and the heat transmission in the sample. The other steps observed for the neat microcapsules, between 200 °C and 420 °C are also partially evident for the MC-containing samples.

For the PA-MC systems, the thermograms are observed to shift to lower temperatures and the values of $T_{1\%}$ and $T_{5\%}$ decrease with an increase in the MC content. This was expected, since the degradation temperature of the MC is lower than that of the neat PA. The blends degrade in two distinct steps; the first, at 200-420 °C, is related to the degradation of the capsules and increasing with the MC content, while

the second, at 450-500 °C, is related to the degradation of the PA phase. The mass loss observed in the first temperature range is less than expected if the nominal capsule weight fraction is considered, but this result is in good agreement with the DSC results, where the phase change enthalpy is less than expected due to some leakage of the PCM during the melt compounding and hot-pressing operations.

Similar results were found for the blends with ParCNT (Figure IV - 3b). However, ParCNT presents a degradation peak temperature (T_d) of 220 °C, remarkably lower than that of MC. Since the two investigated PCMs contain approximately the same fraction of active paraffin content (85-90 wt%), it can be concluded that the MC shell delays the thermal degradation of the PCM core, while CNTs do not perform any thermal barrier effect. This suggests that an encapsulated PCM is more suitable to be embedded in a polymer such as PA, having a processing temperature of approx. 200 °C.

Also for the PA-ParCNT samples, the thermograms show two degradation steps, related to the degradation of the PCM and the PA. However, the mass loss associated to the PCM degradation does not increase with the ParCNT fraction, but it is nearly constant and equal to approx. 9 wt%. This agrees with the DSC results and suggests that the majority of the PCM abandons the system during the production process. On the other hand, the residual mass at the end of the test increases with the ParCNT content. The residue is mostly due to the CNTs, as also the degradation of ParCNT demonstrates. This implies that, unlike the paraffin, the CNTs do not degrade nor leave the blends during processing. This is consistent with the MFI results, as the CNTs are considered as the major responsible for the dramatic increase in viscosity observed for the matrices with ParCNT.

Table IV - 6. Results of the TGA tests on the samples PA-MCx and PA-ParCNTx (x = 15,30,45,60).

Sample	$T_{1\%}$ (°C)	$T_{5\%}$ (°C)	T_d (°C)
PA	269.7	418.0	479.1
PA-MC15	164.0	256.2	469.9
PA-MC30	161.8	250.9	470.1
PA-MC45	161.5	244.1	470.0
PA-MC60	159.8	242.9	469.6
PA-ParCNT15	164.6	255.8	483.2
PA-ParCNT30	162.1	239.2	482.1
PA-ParCNT45	165.3	247.1	480.0
PA-ParCNT60	159.2	219.2	479.8
MC	120.5	241.6	420.4
ParCNT	140.6	165.2	220.2

$T_{1\%}$ = temperature corresponding to a mass loss of 1 wt% (°C); $T_{5\%}$ = temperature corresponding to a mass loss of 5 wt% (°C); T_d = degradation temperature, corresponding to the peak of the mass loss derivative (°C).

For the mechanical and thermo-mechanical properties of the PA/PCM samples, Figure IV - 4 shows representative tensile stress-strain curves, while Figure IV - 5 illustrates the trends of the tensile elastic modulus and strength as a function of the PCM weight fraction.

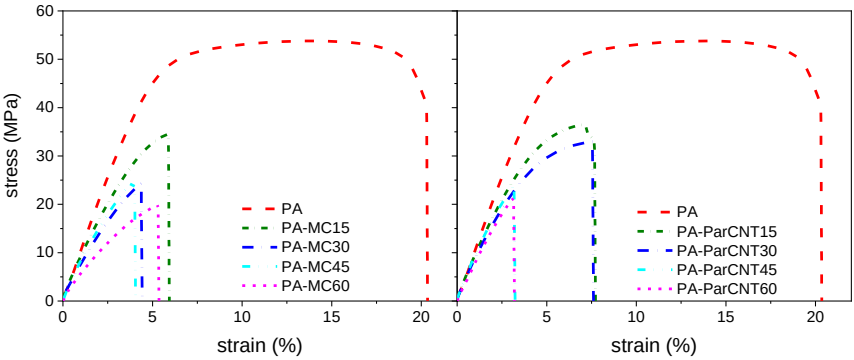

Figure IV - 4. Representative stress-strain curves obtained in quasi-static tensile tests on the samples PA-MCx (left) and PA-ParCNTx (right).

All the considered mechanical properties of the blends are lower than those of the neat PA. For both systems, the mechanical performance is negatively affected by an increase in the PCM content, which can be related to the poor mechanical properties of the PCMs. The only exception is the elastic modulus in the matrices with ParCNT, which increases with the nominal ParCNT amount. This can be related to the fact that the effective amount of paraffin is fairly constant, as suggested by TGA, but the CNT content increases.

This is supported by the results of the Vicat tests. As observable in Figure IV - 5, the Vicat softening temperature (VST) of the blends does not differ remarkably from that of the PA, which indicates that the melting of both PCMs does not lead to a considerable softening of the matrix. For the samples with ParCNT, the VST slightly increases with the PCM fraction, which can be due to the presence of CNTs.

The characterization of the PA/PCM samples evidenced that, by considering both the processability and the thermo-mechanical properties, the microencapsulated PCM may be more appropriate than ParCNT to be mixed with PA12, in order to produce long fiber multifunctional composites. However, laminates were produced with both matrix systems, at two different PCM fractions (30 wt% and 60 wt% of the total matrix weight) and compared with the laminate without PCM.

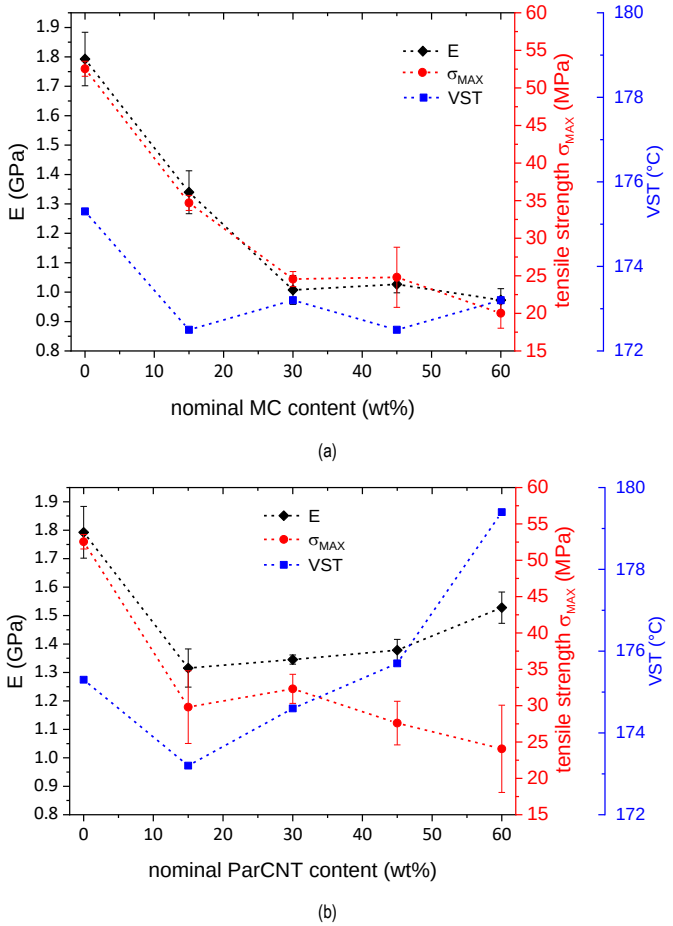

Figure IV - 5. Trends of the tensile modulus, tensile strength and Vicat softening temperature as a function of the nominal PCM fraction: (a) PA-MCx; (b) PA-ParCNTx (x = 15,30,45,60).

4.2.2.2 Characterization of the PA/PCM/GF laminates

The optical microscope images of the polished cross sections of the prepared laminates are reported in Figure IV - 6.

The laminate PA-GF (Figure IV - 6a-b) appears of good quality; there are few matrix-rich zones, the fibers are properly wetted, and the visible porosity is exiguous. Similar considerations can be made for the laminates with capsules (PA-MCx-GF samples, Figure IV - 6c/h). However, the interlaminar matrix-rich region is thicker than

that of PA-GF, as the matrix is more viscous due to the PCM and flows out of the prepared samples with higher difficulty. Moreover, the matrix that flows into the rovings is rich in PA, while the microcapsules tend to remain in the interlaminar zone. This is observable also for the laminates with ParCNT (samples PA-ParCNTx-GF, Figure IV - 6i/n). However, for these laminates the quality appears worse than in the previous cases; especially in the laminate PA-ParCNT60-GF, the fibers are not properly wetted, and the fabric weaving seems distorted.

A further assessment of the quality of the laminates was performed via TGA and density measurements, as described in Section 3.3.4. TGA measurements allowed an evaluation of the fiber weight fraction (ω_f) and the calculation of a theoretical density of the composites (ρ_{th}), while the helium pycnometry allowed a measurement of the density of the constituents (GF and PA/PCM systems) and the experimental density of the laminates (ρ_{exp}); from the comparison between the experimental and theoretical density, the porosity (void volume fraction, ϑ_v) and the volume fraction of the constituents could be calculated. The results of this investigation are summarized in Table IV - 7, which reports the volume composition of the prepared composites.

Table IV - 7. Volume compositions of the PA/PCM/GF laminates.

Sample	ϑ_f (vol%)	ϑ_m (vol%)	ϑ_v (vol%)
PA-GF	53.4	44.5	2.1
PA-MC30-GF	55.5	42.2	2.3
PA-MC60-GF	53.2	44.3	2.5
PA-ParCNT30-GF	50.5	47.7	1.8
PA-ParCNT60-GF	32.4	57.8	9.8

ϑ_f = volume fraction of fibers; ϑ_m = volume fraction of matrix (PA/PCM system); ϑ_v = volume fraction of voids.

It can be observed that the fiber volume fraction and the porosity are nearly the same for all the laminates (besides PA-ParCNT60-GF), being approx. 50-55 vol% and approx. 2 vol%, respectively. On the other hand, in the PA-ParCNT60-GF laminate the void volume fraction is noticeably higher (9.8 vol%) and the fiber content lower (32.4 vol%). This implies that the fluidity of the matrix is impaired by ParCNT in such a way that the fibers cannot be properly wetted, thereby compromising the quality of the laminate.

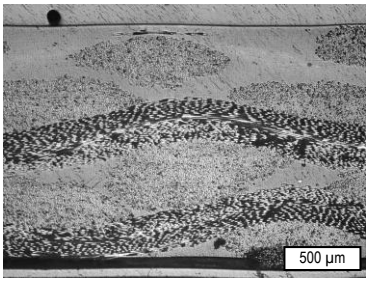

(a)

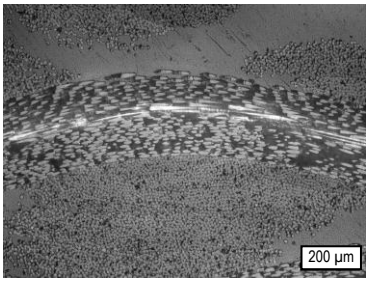

(b)

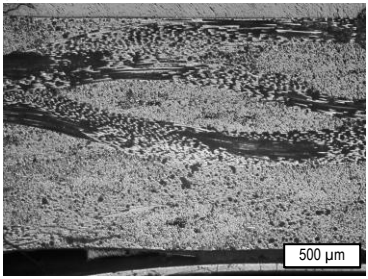

(c)

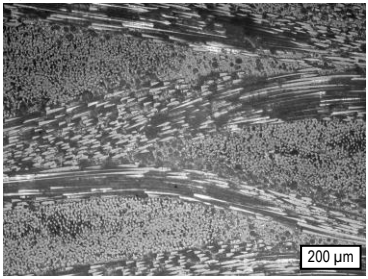

(d)

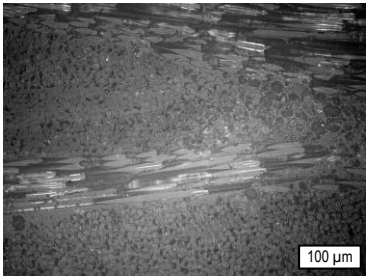

(e)

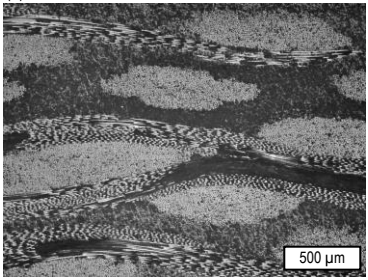

(f)

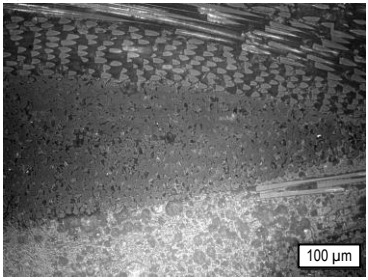

(g)

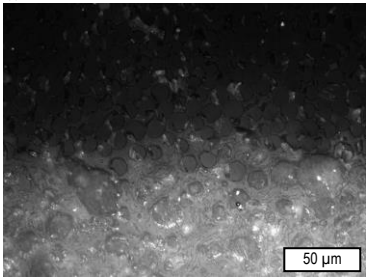

(h)

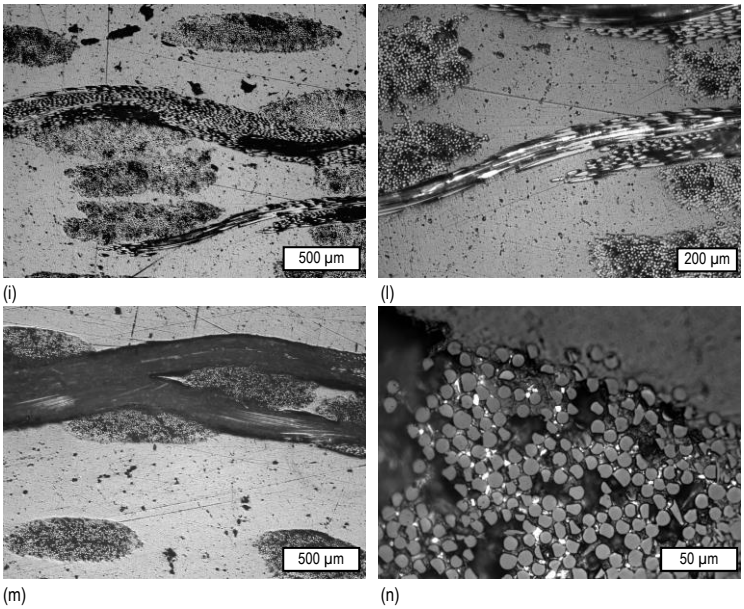

Figure IV - 6. Optical microscope micrographs of the polished cross sections of the PA/PCM/GF laminates. (a,b) PA-GF; (c,d,e) PA-MC30-GF; (f,g,h) PA-MC60-GF; (i,l) PA-ParCNT30-GF; (m,n) PA-ParCNT60-GF.

As for the PA/PCM systems, the most important test to assess the TES capability of the prepared laminates is DSC. The results of this test are reported in Table IV - 8, while the DSC thermograms are not shown for the sake of brevity, as they are qualitatively similar to those obtained for the PA/PCM samples. The laminate with the best thermal performance is PA-MC60-GF, which develops a melting enthalpy of 17.1 J/g.

The aim of this analysis was to evaluate if the additional processing step of hot-pressing required to produce laminates further worsens the PCM energy storage/release capability. Therefore, the values of relative melting enthalpy for the laminates were calculated starting from the experimental weight fraction of matrix (PA/PCM blend) and the theoretical PCM weight fraction within the matrix. Since the values of the relative melting enthalpy calculated in this way are lower than those of the corresponding matrices (Table IV - 5), it can be concluded that the hot-pressing step causes a further decrease in the TES capability of the samples.

The composites with ParCNT present a much greater decrease in ΔH_m^{rel}, which do not even show a trend with the ParCNT fraction. This suggests that the degradation of ParCNT during the process is greater than that of the microencapsulated PCM, which is in good agreement with the TGA results. This supports the observation that,

considering the processing conditions, the microcapsules can be more easily incorporated in a glass fiber/PA12 laminate.

Table IV - 8. Results of the DSC tests on the samples PA-GF, PA-MCx-GF and PA-ParCNTx-GF (x = 30,60).

Sample	T_m (°C)	ΔH_m (J/g)	ΔH_m^{rel} (%)	T_m^{PA} (°C)	T_c (°C)	ΔH_c (J/g)	T_c^{PA} (°C)
PA-GF	--	--	--	179.9	--	--	154.2
PA-MC30-GF	43.9	6.5	44.2	178.8	25.2	3.1	152.4
PA-MC60-GF	46.3	17.1	52.7	178.9	23.2	13.8	152.4
PA-ParCNT30-GF	43.0	5.3	31.9	178.5	39.7	2.0	160.3
PA-ParCNT60-GF	43.5	8.4	15.8	178.7	31.3	5.6	160.1

T_m = melting temperature of the PCM (°C); ΔH_m = PCM melting enthalpy (J/g); ΔH_m^{rel} = relative PCM melting enthalpy (%); T_m^{PA} = melting temperature of PA (°C); T_c = crystallization temperature of the PCM (°C); ΔH_c = PCM crystallization enthalpy (J/g) T_c^{PA} = crystallization temperature of PA (°C).

Finally, the mechanical properties of the laminates were evaluated through quasi-static tensile tests and short beam shear tests. Table IV - 9 summarizes the main results obtained from both mechanical tests.

Table IV - 9. Main results of the mechanical investigation of the PA/PCM/GF laminates (tensile tests and short-beam shear tests).

Sample	E (GPa)	σ_b (MPa)	ε_b (%)	ILSS (MPa)
PA-GF	13.1 ± 0.3	160 ± 29	2.7 ± 0.3	11.2 ± 1.7
PA-MC30-GF	12.7 ± 0.9	124 ± 18	3.0 ± 0.4	9.8 ± 1.7
PA-MC60-GF	13.3 ± 0.7	114 ± 10	3.0 ± 0.7	9.4 ± 2.1
PA-ParCNT30-GF	9.9 ± 0.4	92 ± 9	3.5 ± 0.1	6.7 ± 0.3
PA-ParCNT60-GF	6.5 ± 0.1	56 ± 15	3.5 ± 1.1	5.5 ± 1.8

E = elastic modulus (GPa); σ_b = stress at break, corresponding also to the maximum stress σ_{MAX} (MPa); ε_b = strain at break, corresponding also to the strain at the maximum stress ε_{MAX} (%); ILSS = interlaminar shear stength.

The stress at break decreases upon PCM addition, and this effect is more evident for the laminates with ParCNT, in which also the elastic modulus is lower than that of the neat PA-GF laminate. Conversely, the elastic moduli of the laminates with capsules are not significantly different from that of PA-GF, which suggests that the stiffness is determined by the elastic properties of the reinforcement, and the matrix fulfils properly the role of transferring the load to the fibers. Also the strain at break is not negatively affected by the PCM addition. Therefore, it can be concluded that the addition of PCM microcapsules influences the mechanical properties of the host

laminate only marginally, while a sensible decrease in the mechanical performance can be appreciated with ParCNT addition.

A similar observation can be made for the interlaminar shear strength. The laminates with capsules do not perform significantly differently from the laminate without PCM, while the ILSS values of the of the laminates with ParCNT sharply decrease with an increase in the PCM fraction. This can be attributed to the noticeable porosity and the lower mechanical properties of the matrices with ParCNT.

4.2.3 Conclusions

This Subchapter presented the results of the characterization of glass-fiber-reinforced thermoplastic composite laminates with TES capability, prepared by combining a PA12 matrix with two different paraffinic PCMs (MC and ParCNT).

It was found that both the selected PCMs (MC and ParCNT) increase the viscosity of the molten PA, but the effect of ParCNT is considerably more marked, due to the high CNT content. This is part of the reason for the remarkable differences in the quality of the produced laminates, as the porosity of the laminate PA-ParCNT60-CF is considerably higher than that of the other laminates.

It was also evident that the two steps of the production process, i.e. the melt compounding and hot-pressing, partially degrade the PCMs and decrease the phase change enthalpy measured on the PA/PCM samples and PA/PCM/GF laminates, as demonstrated by values of relative melting enthalpy lower than 100 %. The effect is greater on the laminates, and the impact of the additional hot-pressing stage is clearly observable from the lower relative melting enthalpy values than those of the PA/PCM samples. The effect is smaller for the laminates containing MC, because the shell increases the thermal resistance of the paraffinic core, while the CNTs do not perform any thermal protection functions.

Additionally, the PCM introduction decreases the mechanical properties of PA and the tensile strength of the laminates. However, for the laminates containing microcapsules, the elastic modulus and the strain at break are not negatively affected by the PCM, whose behavior was observed to be dominated by the nearly constant fiber volume fraction. Conversely, the laminates containing ParCNT showed a sensible loss of mechanical performance compared to the neat PA-GF.

The results of this work indicated that the microencapsulated PCM was more suitable to produce laminates in combination with PA and GF, since it exercised a lower influence on the matrix viscosity, a greater thermal stability and a marginal impact on the mechanical properties of the laminates. However, due to the PCM degradation during melt compounding and hot-pressing, the losses in TES capability are massive.

Two strategies were adopted to try to produce thermoplastic composites while reducing the PCM degradation. The first strategy was to employ discontinuous fibers instead of a continuous fiber fabric. In this way, the composites can be produced by

melt compounding followed by a single hot-pressing step, which allows avoiding one processing step necessary for the production of GF laminates. Continuous fibers were instead employed in the second strategy: it went towards even milder processing conditions as it involved a reactive thermoplastic resin, which is provided as a low viscosity precursor and can be processed at room temperature like a thermosetting resin, thereby drastically reduce the possibility of thermo-mechanical degradation. As this second strategy nowadays is not implementable with traditional thermoplastics, an additional approach was considered that involves the production of commingled yarns containing PCM-enhanced thermoplastic filaments and continuous reinforcing fibers. This approach not only allows the production of a component made of traditional thermoplastic laminate in fewer processing steps, but it also shifts the multifunctionality from the composite level to the yarn level.

The methods and results of these three pathways are presented in the following three Subchapters.

4.3 Discontinuous carbon fiber/polyamide composites containing paraffin microcapsules

The present Subchapter describes the results obtained from the characterization of semi-structural thermoplastic composites containing discontinuous carbon fibers as a reinforcing agent and paraffin microcapsules as the PCM. Compared to the case study described in Subchapter 4.2, this approach allows the production of reinforced composites avoiding one of the two processing steps, thereby reducing the damage and degradation to the microcapsules.

Two different discontinuous fiber reinforcements were adopted, with the aim of investigating the effect of different fiber length on the processability, mechanical properties and TES capability of the final composites.

4.3.1 Materials and methods

The present Section lists the materials used to fabricate these samples, and then it describes in detail the techniques for the preparation of the same. It subsequently lists all the characterization techniques applied on these samples. Since the materials and the characterization techniques have been already detailed in Chapter III, this Section will specify only the experimental parameters that are specific of this Subchapter.

4.3.1.1 Materials

Table IV - 10 lists the materials used to prepare these composites (please refer to Section 3.2.4 for the details about the materials).

Table IV - 10. Materials employed in Section 4.3.

Phase	Label	Material
Polymer matrix	PA	Polyamide 12
Reinforcement	CFL	Discontinuous carbon fibers (length 6 mm)
	CFS	Discontinuous carbon fibers (length 100 μm)
PCM	MC	Paraffin microcapsules

4.3.1.2 Sample preparation

The composites were prepared by melt compounding and hot-pressing. PA was mixed with MC and either CFL or CFS in different weight concentrations. The mixtures were melt compounded at 190 °C through a Thermo Haake Rheomix 600 OS internal mixer equipped with counter-rotating rotors, operating at 40 rpm for 6 minutes.

Table IV - 11. List of the prepared PA/MC/CFL and PA/MC/CFS samples with weight compositions.

Sample	PA (wt%)	MC (wt%)	CFL or CFS (wt%)
PA12	100	-	-
PA-MC20	80	20	-
PA-MC40	60	40	-
PA-MC50	50	50	-
PA-MC60	40	60	-
PA-CFL10	90	-	10
PA-CFL20	80	-	20
PA-CFL30	70	-	30
PA-MC20-CFL20	64	16	20
PA-MC40-CFL20	48	32	20
PA-MC50-CFL20	40	40	20
PA-MC60-CFL20	32	48	20
PA-CFS10	90	-	10
PA-CFS20	80	-	20
PA-CFS30	70	-	30
PA-MC20-CFS20	64	16	20
PA-MC40-CFS20	48	32	20
PA-MC50-CFS20	40	40	20
PA-MC60-CFS20	32	48	20

The resulting composites were subsequently hot pressed at 190 °C for 10 minutes in a Carver Laboratory Press Model 2699, under an applied pressure of 1.2 MPa, to obtain square sheets of 200x200x1.5 mm^3.

The processing conditions were milder than those applied to prepare the PA/PCM blends described in Subchapter 4.2, due to the lower compounding temperature and rotation speed and the lower hot-pressing temperature and pressure. This was done to try to minimize the degradation and damage to the MC phase.

The samples were denoted as PA-MCx-CFLy or PA-MCx-CFSy, where "PA" represents the matrix, "MC" the PCM microcapsules, and "CFL" and "CFS" the "long" and "short" carbon fibers, respectively; "x" is the weight fraction of microcapsules in the matrix (with respect to the amount of PA12 and capsules), and "y" is the weight fraction of CFs with respect to the total mass of the composite. The prepared samples are listed in Table IV - 11.

4.3.1.3 Characterization

The prepared samples were investigated through the characterization techniques listed in Table IV - 12 together with the experimental parameters applied specifically on these samples (see Subchapter 3.3 for the full description of the characterization parameters and specimen preparation).

Table IV - 12. Characterization techniques and experimental parameters applied on the samples PA-MCx-CFL and PA-MCx-CFS.

Technique	Specific experimental parameters
SEM	Cryofracture surface; Instrument Zeiss Supra 60 FE-SEM
DSC	Temperature interval -20-240 °C
TGA	TA Q5000 IR thermobalance; specimen mass 10 mg
Vicat test	As described in Section 3.3.3.6
LFA	As described in Section 3.3.3.4
Dynamic rheological test	Haake Mars III dynamic shear rheometer
Thermal camera imaging	As described in Section 3.3.3.3
Quasi-static tensile test	As described in Section 3.3.5.1

4.3.2 Results and discussion

Figure IV - 7 reports the SEM micrographs of the cryofracture surface of some selected compositions, acquired at different magnifications. Both CFL (Figure IV - 7a-b) and CFS (Figure IV - 7c-d) are uniformly dispersed in the matrix, without agglomeration. For the CFL-containing samples, this means that the shear stresses applied during the melt compounding operations are sufficient to disaggregate the fiber bundles (see Section 3.2.2.4). It is also evident that the production process does not

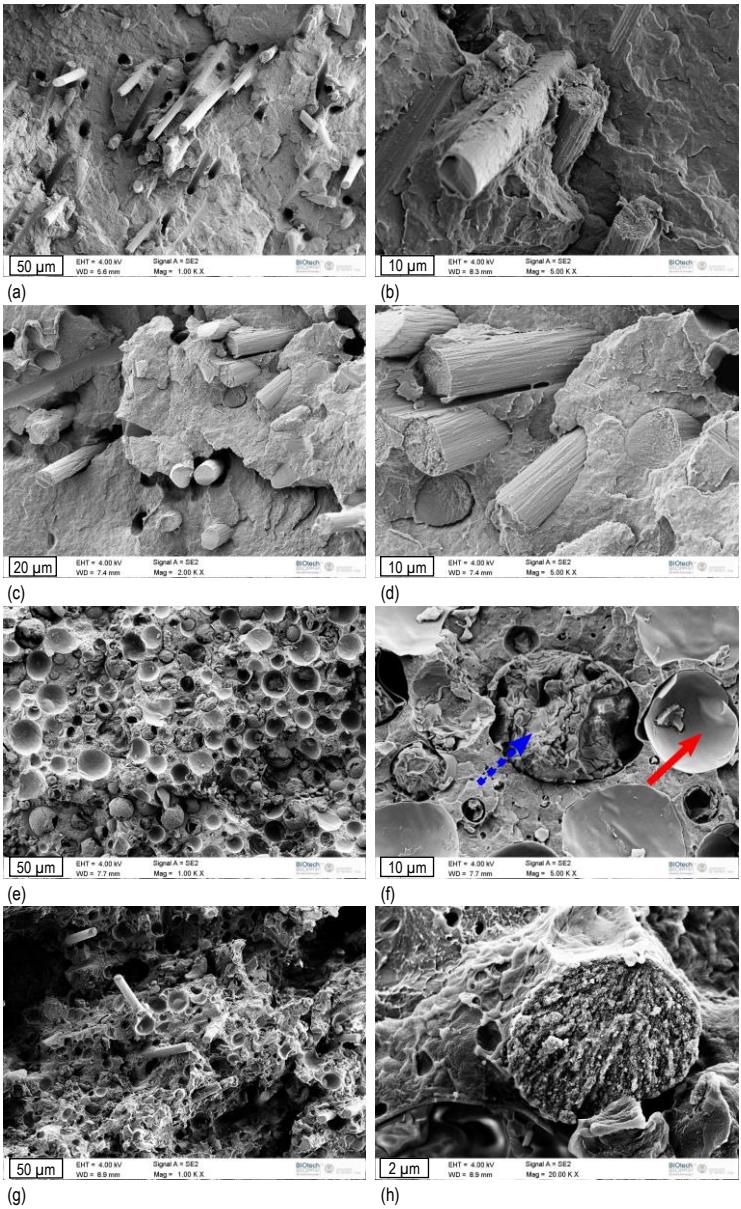

Figure IV - 7. SEM micrographs of the cryofracture surface of the samples PA/MC/CFL and PA/MC/CFS. (a,b) PA-CFL20; (c,d) PA-CFS20; (e,f) PA-MC50; (g,h) PA-MC50-CFL20.

impart a unidirectional orientation of the reinforcement, although the fibers may be preferentially oriented in the plane orthogonal to the pressing direction. The adhesion with the PA matrix is good for both the fiber types, although it seems better for CFL, which was expected since the CFS are unsized. As observed for the samples PA/PCM/GF described in in Subchapter 4.2, the PCM microcapsules (Figure IV - 7e-f) are uniformly distributed in the matrix. The core-shell structure of this PCM is clearly observable from these micrographs, especially in that acquired at higher magnification (Figure IV - 7f). The microcapsule indicated with a dashed blue arrow shows both the thin polymer shell and the paraffinic core. The irregular morphology and the voids of the core indicate a certain aptitude of the capsules to accommodate the volume variation during the phase change and avoid the shell rupture (Jamekhorshid et al., 2014). In other cases (solid red arrow), the shell is still partly observable, but the core has been almost completely removed.

The adhesion between the shell and the PA matrix is fairly good, even though some debonding is observable. However, the micrographs show many residues of the shells of broken capsules, which implies that, in the majority of the cases, the fracture propagates across the capsules and not at the capsule-matrix interface. It is important to notice that the breakage of some capsules could have happened also during processing and not only during the cryofracturing operations. The same considerations can be made for the samples containing both capsules and fibers, as appreciable from the micrograph of the sample PA-MC50-CFL20, reported in Figure IV - 7g-h.

The outcomes of the DSC analysis are shown in Figure IV - 8, which reports representative thermograms of the first heating scan and the cooling scan for some selected compositions, i.e. the samples PA-MCx-CFS20. The main results of the DSC analysis of all the samples are summarized in

Table IV - 13.

As found for the PA-based samples described in Subchapter 4.2, the thermogram of the neat PA shows an endothermic melting peak in the heating scan at approx. 180 °C, and an exothermic crystallization peak in the cooling scan at approx. 155 °C. The glass transition of PA is detectable at approx. 41 °C. The melting/crystallization peaks of PA are clearly visible in all the other samples, while the glass transition is detectable only in the samples without capsules, because, when the PCM is present, the T_g signal is hidden by the intense melting and crystallization peaks of MC at approx. 43 °C and 30 °C, respectively.

The melting/crystallization temperatures of the PCM (T_m, T_c) do not vary significantly with the carbon fiber content. The phase change enthalpy of the PCM (ΔH_m, ΔH_c) increases with the weight fraction of MC. Also for these samples, a relative melting enthalpy ΔH_m^{rel} was calculated by dividing the melting enthalpy of each sample by the melting enthalpy of the neat MC and normalizing the obtained result by the nominal MC weight fraction, as described in Equation (III - 1). From the data in

Table IV - 13 it can be seen that the values of ΔH_m^{rel} are generally below 100 % and decrease as the MC content increases. However, these values are mostly higher than those calculated for the PA/PCM samples presented in Section 4.2, comparing the samples containing only PA and a PCM, which highlights that the milder processing conditions (lower processing temperature and lower compounding rotation speed) are helpful to preserve the PCM integrity and minimize the degradation.

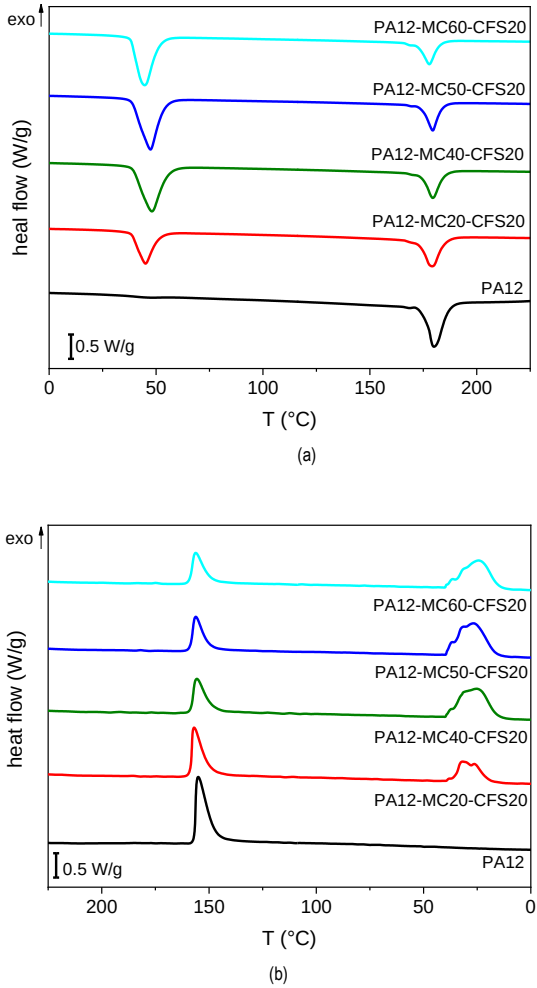

Figure IV - 8. DSC thermograms of the samples PA-MCx-CFS (x=20,40,50,60). (a) first heating scan; (b) cooling scan.

Table IV - 13. Results of the DSC tests on the samples PA-MCx-CFL and PA-MCx-CFS.

Sample	T_m (°C)	ΔH_m (J/g)	ΔH_m^{rel} (%)	T_m^{PA} (°C)	T_c (°C)	ΔH_c (J/g)	T_c^{PA} (°C)
PA12	-	-	-	179.9	-	-	155.0
MC	44.1	220.1	100	-	30.2	208.2	-
PA-MC20	46.2	44.5	101.1	178.7	26.7	38.1	154.2
PA-MC40	47.3	91.8	104.3	178.6	26.4	84.1	153.3
PA-MC50	49.9	100.8	91.6	180.0	25.3	93.8	152.5
PA-MC60	47.8	116.6	88.3	177.6	24.1	108.9	151.8
PA-CFL10	-	-	-	180.2	-	-	154.1
PA-CFL20	-	-	-	181.2	-	-	152.4
PA-CFL30	-	-	-	181.0	-	-	153.4
PA-MC20-CFL20	45.5	33.0	93.8	178.9	31.5	27.9	153.4
PA-MC40-CFL20	45.8	28.9	41.1	179.9	31.4	23.8	152.7
PA-MC50-CFL20	46.6	46.9	53.3	178.2	26.1	40.9	151.6
PA-MC60-CFL20	45.8	44.5	42.1	178.4	30.2	37.6	151.8
PA-CFS10	-	-	-	180.4	-	-	156.7
PA-CFS20	-	-	-	180.0	-	-	159.3
PA-CFS30	-	-	-	180.6	-	-	157.5
PA-MC20-CFS20	45	33.3	94.6	179.2	31.7	28.8	157.0
PA-MC40-CFS20	48.1	58.8	83.5	179.6	25.2	54.3	155.6
PA-MC50-CFS20	47.5	60.4	61.0	179.4	26.6	57.7	156.2
PA-MC60-CFS20	44.8	54.6	51.7	177.8	24.5	51.4	156.2

T_m = melting temperature of the PCM (°C); ΔH_m = PCM melting enthalpy (J/g); ΔH_m^{rel} = relative PCM melting enthalpy (%); T_m^{PA} = melting temperature of PA (°C); T_c = crystallization temperature of the PCM (°C); ΔH_c = PCM crystallization enthalpy (J/g); T_c^{PA} = crystallization temperature of PA (°C).

Nevertheless, some degradation and leakage are still present. The decrease in ΔH_m^{rel} is increasingly evident with an increase in the MC fraction; this is linked to the higher melt viscosity and the consequently higher shear stresses to which the capsules are subjected during compounding, which causes damage to the thin capsule shell and therefore the leakage and degradation of the paraffinic core. Some paraffin was even observed leaking out of the mixing chamber during the compounding process. Additionally, it is interesting to observe that the values of ΔH_m^{rel} are lower for samples containing CFL compared to those containing CFS. This can be related to the higher viscosity and higher shear stresses obtained while compounding mixtures containing CFL, which agrees with the results of the dynamic rheological tests described hereafter. Nevertheless, most of the heat storage/release capability is retained, especially in the samples with a low fiber content.

The leakage and loss of paraffin during processing is also confirmed by the TGA results, displayed in Figure IV - 9 and Table IV - 14. Figure IV - 9 reports representative TGA thermograms of the neat PA, MC, and some selected compositions, namely the samples PA-MCx-CFL20.

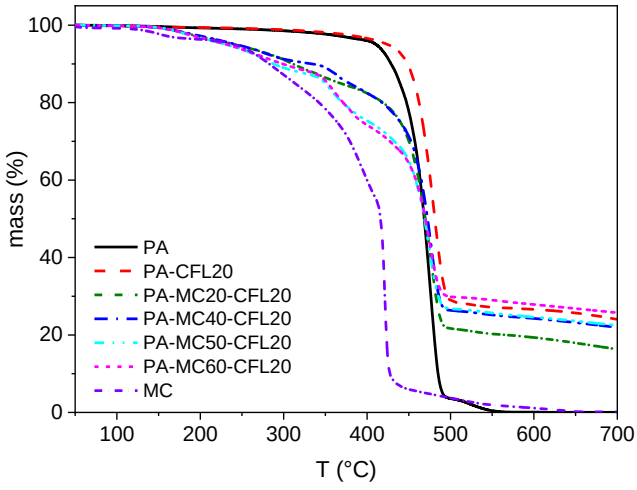

(a)

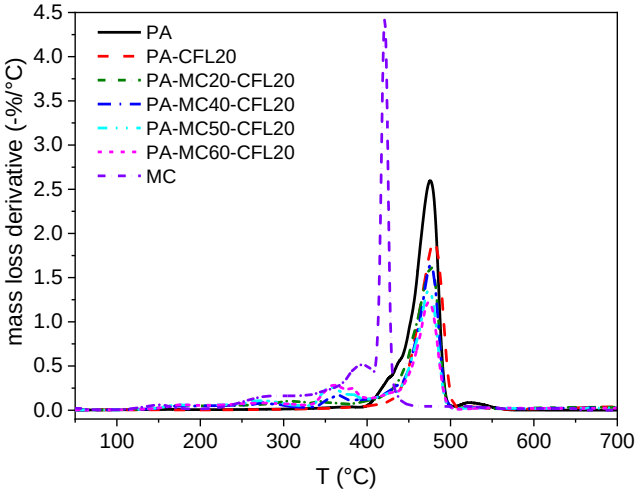

(b)

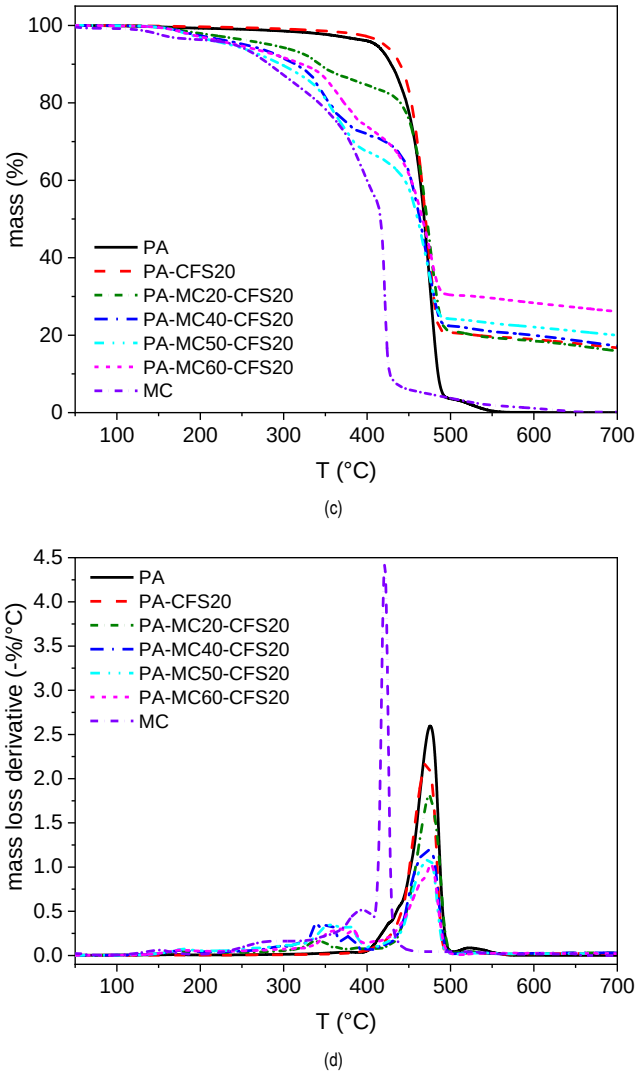

Figure IV - 9. TGA thermograms of the prepared samples; residual mass and mass loss derivative as a function of temperature. (a, b) samples PA-MC-CFL; (c, d) samples PA-MC-CFS.

As observed for the PA-based samples described in Section 4.2, the thermal degradation of the neat PA happens in two subsequent steps, and the vast majority of the mass loss occurs in the first. The addition of carbon fibers delays the beginning of

thermal degradation, as the values of $T_{1\%}$, $T_{3\%}$, and $T_{5\%}$ increase (Table IV - 14) with the carbon fiber content, for both CFL- and CFS-containing samples. This effect is more marked for the CFS-containing samples. On the other hand, the value of $T_{d,}$ is hardly ever significantly different from that of the neat PA and does not follow a trend with the carbon fiber content.

Conversely, the addition of MC shifts the curves towards lower temperatures. Similar considerations can be made for these samples as those made for the MC-containing samples described in Subchapter 4.2. Also in this case, the mass loss corresponding to the MC degradation is less than expected if the nominal MC weight fraction is considered, but this result is in good agreement with the DSC outcomes, where the phase change enthalpy is less than expected due to some leakage of the PCM during the melt compounding and hot-pressing operations. This effect is more evident for the CFL-containing samples than for the samples reinforced with CFS.

Table IV - 14. Results of the TGA tests on the samples PA-MC-CFL and PA-MC-CFS.

Sample	$T_{1\%}$ (°C)	$T_{3\%}$ (°C)	$T_{5\%}$ (°C)	T_d (°C)
PA12	250.9	372.5	410.9	475.7
MC	118.4	164.0	241.0	421.2
PA-MC20	163.6	219.4	267.1	471.5
PA-MC40	165.2	204.5	243.7	471.7
PA-MC50	167.0	201.9	240.0	468.6
PA-MC60	159.6	186.8	217.4	468.9
PA-CFL10	263.8	388.0	414.3	481.8
PA-CFL20	278.8	390.5	424.9	480.3
PA-CFL30	291.2	396.9	422.8	476.6
PA-MC20-CFL20	159.0	201.0	240.1	479.0
PA-MC40-CFL20	161.0	204.6	243.2	476.2
PA-MC50-CFL20	160.0	195.8	230.5	474.1
PA-MC60-CFL20	159.9	196.2	231.5	474.0
PA-CFS10	300.6	398.5	419.2	474.7
PA-CFS20	311.0	403.0	421.1	471.5
PA-CFS30	314.5	406.8	425.6	479.2
PA-MC20-CFS20	171.1	230.2	285.0	474.1
PA-MC40-CFS20	167.1	208.4	254.1	474.0
PA-MC50-CFS20	165.5	197.4	235.8	475.0
PA-MC60-CFS20	164.8	201.4	243.8	477.3

$T_{1\%}$ = temperature corresponding to a mass loss of 1 wt% (°C); $T_{3\%}$ = temperature corresponding to a mass loss of 3 wt% (°C); $T_{5\%}$ = temperature corresponding to a mass loss of 5 wt% (°C); T_d = degradation temperature, corresponding to the peak of the mass loss derivative (°C).

The results of the LFA test are reported in Figure IV - 10.

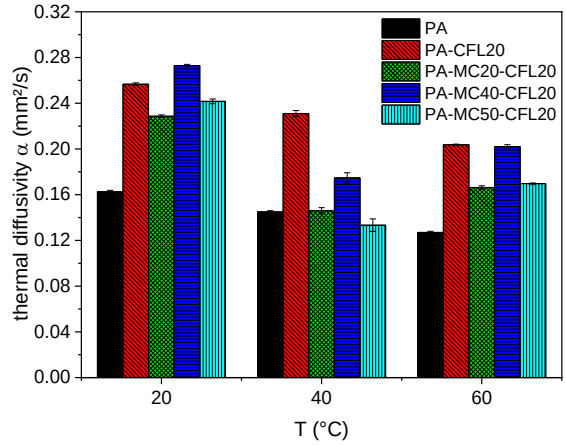

(a)

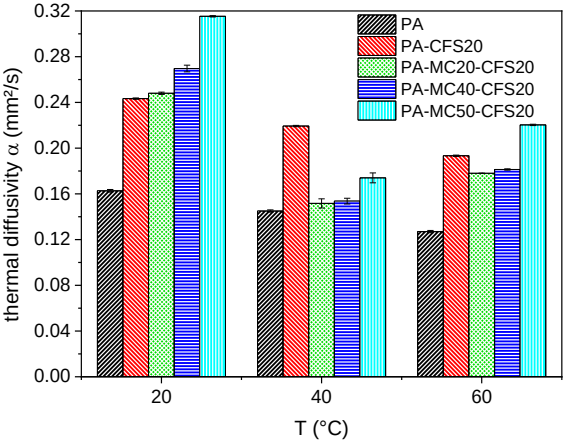

(b)

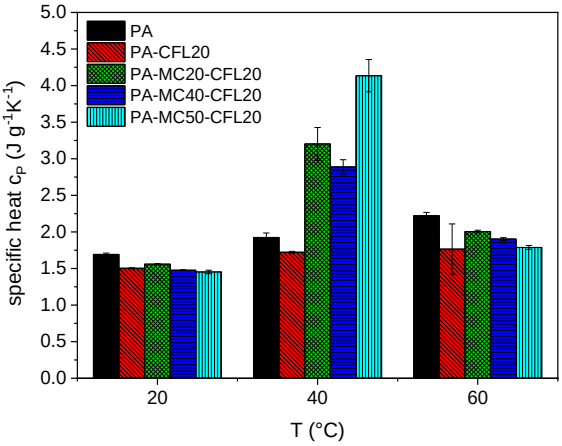
PA
PA-CFL20
PA-MC20-CFL20
PA-MC40-CFL20
PA-MC50-CFL20
specific heat c_P (J g^{-1}K^{-1})
T (°C)
0.0
0.5
1.0
1.5
2.0
2.5
3.0
3.5
4.0
4.5
5.0
20
40
60

(c)

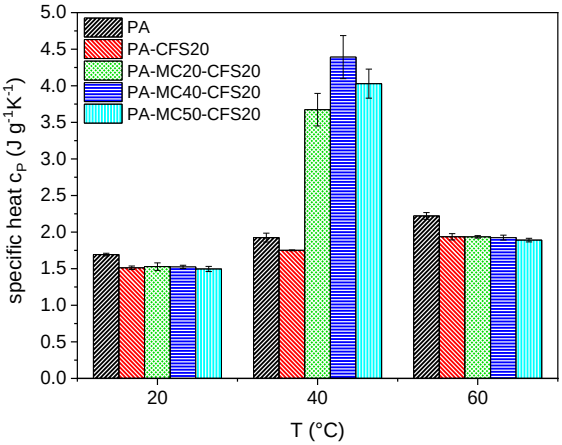
PA
PA-CFS20
PA-MC20-CFS20
PA-MC40-CFS20
PA-MC50-CFS20
specific heat c_P (J g^{-1}K^{-1})
T (°C)
0.0
0.5
1.0
1.5
2.0
2.5
3.0
3.5
4.0
4.5
5.0
20
40
60

(d)

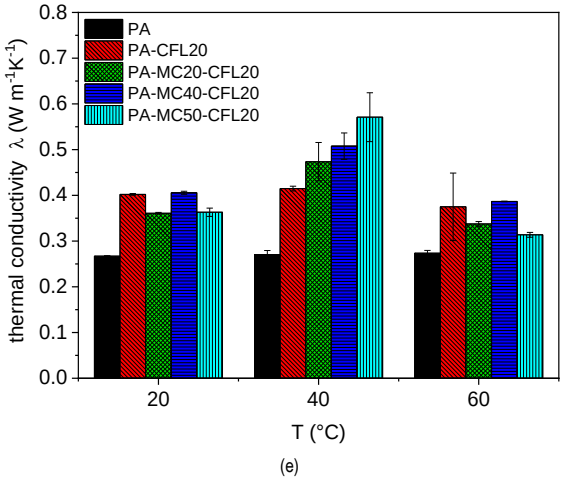

(e)

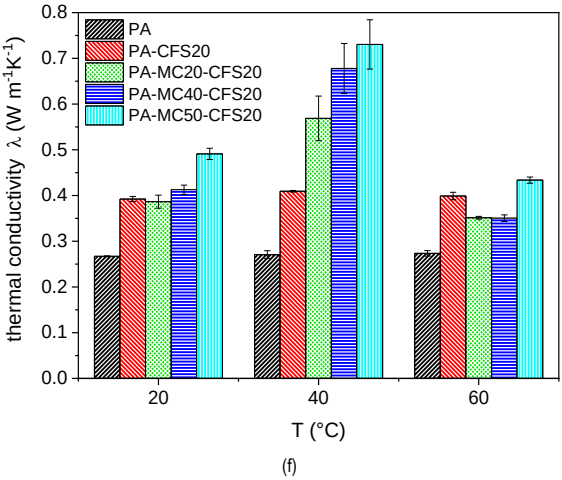

(f)

Figure IV - 10. Results of the laser flash analysis test on the samples PA, PA-CFL20, PA-MCx-CFL20 and PA-MCx-CFS20. (a, b) thermal diffusivity; (c, d) specific heat capacity; (e, f) thermal conductivity.

The thermal diffusivity of the neat PA varies between 0.16 mm^2/s and 0.14 mm^2/s and decreases slightly with an increase in temperature, while the specific heat capacity and the thermal conductivity slightly increase with temperature. The thermal conductivity varies in the range 0.26-0.28 W/(m·K), in agreement with the producer's datasheet. As expected, the introduction of carbon fibers increases the

thermal diffusivity and consequently the thermal conductivity, which is positive for the overall thermal exchange rate. A higher thermal conductivity can be beneficial for some applications, as it reduces the charging/discharging periods of the PCM. For the investigated samples containing only carbon fibers and not MC, namely PA-CFL20 and PA-CFS20, the effect of CFL on the thermal diffusivity is slightly higher than that of CFS, but the thermal conductivity does not differ significantly, being approx. 0.4 W/(m·K) for both samples. For the samples containing carbon fibers and MC, the specific heat capacity and the thermal conductivity show a maximum at 40 °C, while approaching the melting temperature of the PCM. This phenomenon, also observed in other researches from the literature (Fang et al., 2014), is more manifest for the samples containing CFS; this suggests that the effective PCM content is higher for these samples compared to the CFL-reinforced ones, which is consistent with the DSC and TGA results.

Figure IV - 11 shows the results of the thermal imaging test and reports the values of temperature as a function of time during the cooling step for three selected samples, namely PA, PA-MC50-CFL20, and PA-MC50-CFS20. In the MC-containing samples, the temperature decrease is slower than that measured on the neat PA, and it exhibits a plateau-like trend. This is the result of the heat released by the PCM as it crystallizes. The effect is considerably more evident for the sample PA12-MC50-CFS20 compared to the sample containing CFL. Also this result suggests that the real PCM content is higher for the CFS-containing samples, in accordance with the previous results. This test, although simple, gives a clear idea of the potential of these composites in applications of thermal management.

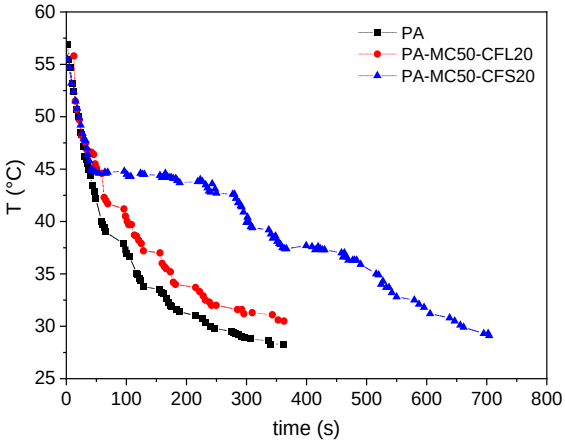

Figure IV - 11. Results of the thermal camera imaging test. Values of surface temperature of the composite panels as a function of time during cooling.

After the thermal characterization, dynamic rheological tests were performed to link the MC breakage and degradation to the viscosity increase and shear stresses developed during processing. Since the purpose of such tests were to investigate this specific aspect, they were run only on some representative compositions. The rheological properties were studied only at low frequency (up to 20 Hz), because this is close to the frequency range the materials are subjected to during processing; moreover, while investigating the shear viscosity of composites with various microfiller fractions, large differences can generally be detected at lower frequencies, whereas small differences are normally measured at high shear rates, at which the viscosity almost approaches that of the neat matrix, as widely explained in the literature (Greene and Wilkes, 1995; Guo et al., 2005; Thomasset et al., 2005; Doumbia et al., 2015; Rueda et al., 2017b).

Figure IV - 12 and Figure IV - 13 report the results of the dynamical rheological test. Figure IV - 12 shows the shear viscosity as a function of the applied frequency for the neat PA and some representative compositions. The general trends of the viscosity reflect the well-known behavior of particulate-filled polymers (Poslinski et al., 1988). The shear viscosity of the neat PA is not markedly affected by frequency and the Newtonian plateau extends over the whole investigated frequency range. The viscosity increases upon MC and carbon fiber addition, and the effect is more evident al lower shear rates. Moreover, the filled compositions show a shear-thinning behavior, and the increase in the filler content anticipates the beginning of the shear thinning region to lower frequencies. For the compositions where the filler concentration is the highest, a yield stress becomes manifest at the lowest limit of the applied frequency interval. By comparing the three panels of Figure IV - 12, it is evident that the MC increase the viscosity significantly only at very high concentrations. On the other hand, the samples containing both MC and carbon fibers show more clearly phenomena such as the viscosity increase, the yield stress rise and the anticipation of the shear thinning region.

It can be also noticed that the viscosity is higher for the samples containing CFL than for those containing the same amount of CFS. This suggests that the CFL produce a higher viscosity rise also in the melt compounding process, thereby intensifying the shear stress, microcapsule damage and paraffin degradation. This is in good agreement with DSC and TGA results, which highlight a higher PCM experimental weight fraction and enthalpy in the samples containing CFS. However, the difference in the measured viscosity seems too small to justify such discrepancies in the DSC results. It should be considered, though, that the samples analyzed by dynamic shear rheometry have been subjected to melt compounding and hot pressing, which can significantly shorten the fiber length. As fibers with a higher aspect ratio are generally more influent on the polymer melt viscosity, it is reasonable to hypothesize that the shear stresses in the melt compounder are higher at the beginning of the compounding stage, which causes an even more extensive MC damage.

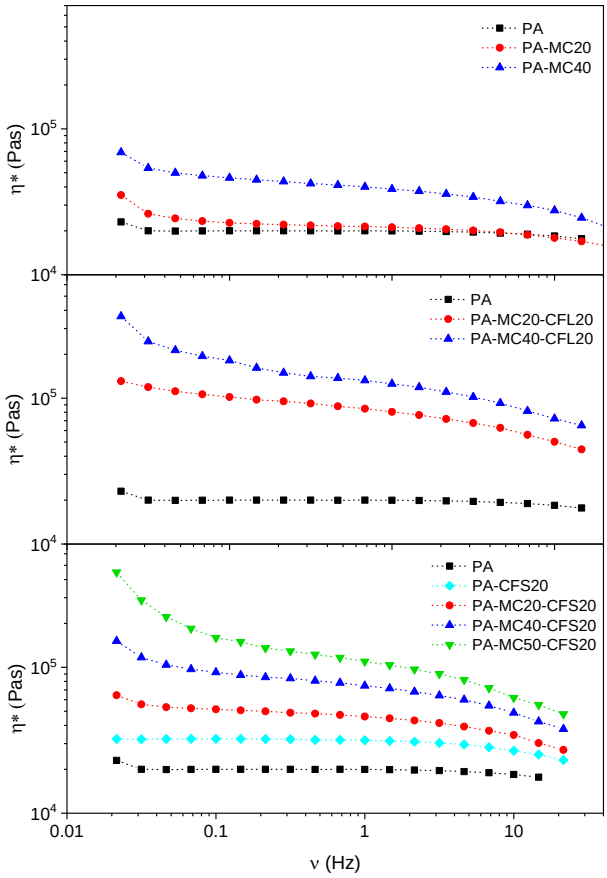

Figure IV - 12. Results of the dynamic rheological test. Values of viscosity as a function of the applied frequency for some representative compositions.

Further information about the dynamic rheological properties of these samples can be obtained from the trends of the shear storage modulus (G'), loss modulus (G'') and loss factor ($tan\delta$) as a function of frequency, displayed in Figure IV - 13. Only the results of the composites with CFS are presented, as they are the most promising from the TES point of view. As expected, the filler addition considerably modifies the rheological viscoelastic properties of the polymer melt; G' and G'' are strongly increased, especially at low frequencies, while the values of $tan\delta$ decreases and the peak shifts to higher frequencies. As the $tan\delta$ peak can be associated to the

breakdown of the filler network, the shift of the peak to higher frequencies can be interpreted as a stronger interparticle interaction (Dorigato et al., 2010).

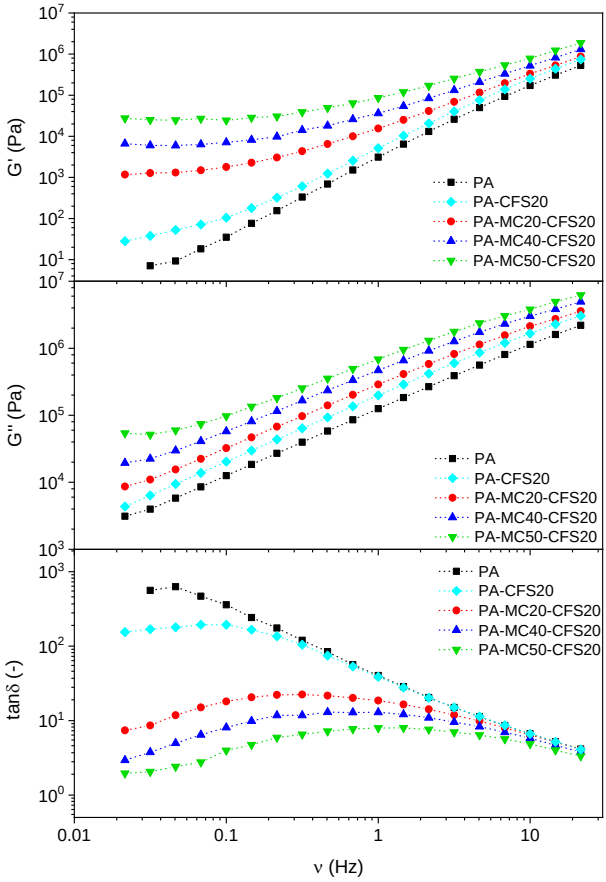

Figure IV - 13. Shear storage modulus (G'), loss modulus (G'') and loss factor ($tan\delta$) as a function of frequency for the samples containing CFS.

The results of the quasi-static tensile tests are shown in Figure IV - 14, which shows representative stress-strain curves, and in Table IV - 15, which reports the values of the elastic modulus (E), the maximum stress (σ_{MAX}) and the strain at break (ε_b).

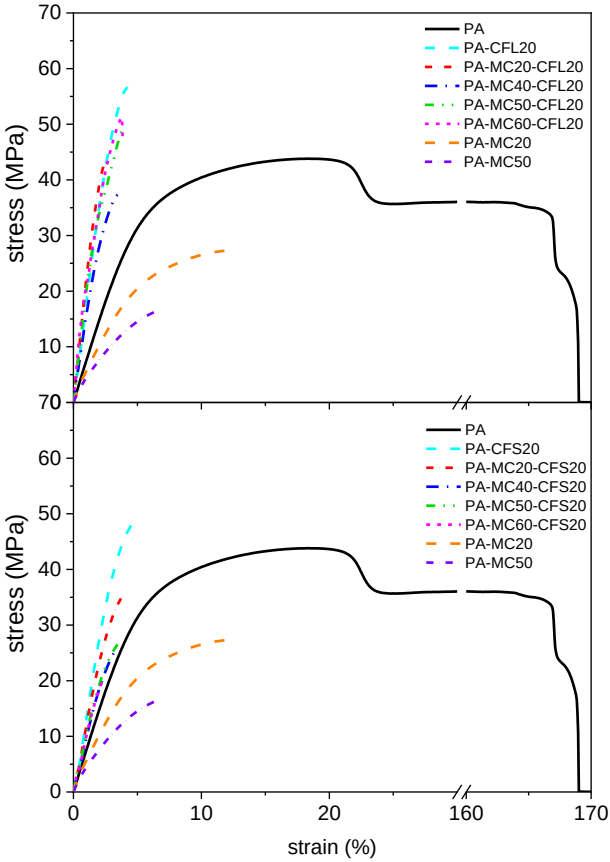

Figure IV - 14. Representative stress-strain curves obtained in the quasi-static tensile tests on the samples PA-MCx-CFL and PA-MCx-CFS.

As observed for the PA-based samples described in Subchapter 4.2, the introduction of MC decreases the elastic modulus, while the addition of a reinforcing agent such as the carbon fibers increases it. This effect is more evident for the CFL than for the CFS, because the greater load transfer length brings to a higher stiffening and reinforcing capability, as thoroughly reported in the literature (Fu and Lauke, 1996; Rezaei et al., 2009). Similar considerations are valid for the values of σ_{MAX}, which decrease with an increase in the MC fraction and increase with the carbon fiber concentration. The addition MC and/or carbon fibers causes a strong decrease in the strain at break and a considerable embrittlement; for the microcapsules, this is evident

already with a MC weight fraction as low as 20 %, but further decrease for higher capsule concentrations is almost negligible. This effect, already observed for the samples described in Subchapter 4.2, could be due to the poor mechanical properties of the MC phase and/or to the not excellent adhesion between the PA matrix and the capsule shell.

Table IV - 15. Results of the quasi-static tensile tests on the samples PA-MC-CFL and PA-MC-CFS.

Sample	E (GPa)	σ_{MAX} (MPa)	ε_b (%)
PA12	1.20 ± 0.07	43.7 ± 0.3	125.2 ± 72.4
PA-MC20	0.82 ± 0.03	27.5 ± 0.8	14.1 ± 4.8
PA-MC40	0.68 ± 0.03	15.0 ± 2.6	4.7 ± 1.1
PA-MC50	0.60 ± 0.04	16.3 ± 0.4	6.6 ± 0.3
PA-MC60	0.59 ± 0.07	14.2 ± 1.5	6.6 ± 1.1
PA-CFL10	3.66 ± 0.80	63.9 ± 8.4	5.9 ± 0.6
PA-CFL20	5.03 ± 0.23	53.9 ± 8.7	3.3 ± 0.6
PA-CFL30	5.92 ± 0.34	55.7 ± 7.6	4.0 ± 0.7
PA-MC20-CFL20	3.50 ± 0.69	39.1 ± 6.9	2.5 ± 0.3
PA-MC40-CFL20	2.61 ± 0.65	31.6 ± 4.3	3.4 ± 0.6
PA-MC50-CFL20	2.32 ± 0.54	44.4 ± 8.0	3.6 ± 0.7
PA-MC60-CFL20	2.11 ± 0.37	54.3 ± 12.2	3.4 ± 0.9
PA-CFS10	1.74 ± 0.13	48.3 ± 1.0	6.0 ± 0.6
PA-CFS20	2.70 ± 0.24	49.8 ± 0.7	5.6 ± 0.7
PA-CFS30	3.48 ± 0.62	54.6 ± 4.0	4.2 ± 0.4
PA-MC20-CFS20	2.51 ± 0.19	31.8 ± 3.8	3.2 ± 0.5
PA-MC40-CFS20	2.00 ± 0.23	25.8 ± 1.6	3.2 ± 0.3
PA-MC50-CFS20	1.69 ± 0.21	25.7 ± 1.1	3.5 ± 0.4
PA-MC60-CFS20	1.57 ± 0.14	20.9 ± 3.7	2.6 ± 0.4

E = elastic modulus (GPa); σ_{MAX} = tensile strength (maximum stress) (MPa); ε_b = strain at break (%).

The experimental data were fitted with the Halpin-Tsai model, a useful tool to predict the stiffness of a composite reinforced with discontinuous fibers (Halpin and Kardos, 1976; Shokrieh and Moshrefzadeh-Sani, 2016). This model allows the calculation of the longitudinal and transversal moduli (E_L, E_T) assuming a fiber alignment in the L direction, and with a modified mixture rule it is possible to determine the modulus of a composite, E_C, for a random 2D or 3D fiber orientation. In the present work, for each composition, E_L and E_T were determined through Equation (IV - 1) and Equation (IV - 2), respectively, as:

$$E_L = E_m \frac{1 + \frac{l}{r}\eta_L \vartheta_f}{1 - \eta_L \vartheta_f} \qquad \textbf{(IV - 1)}$$

$$E_T = E_m \frac{1 + 2\eta_T \vartheta_f}{1 - \eta_T \vartheta_f} \quad \textbf{(IV - 2)}$$

where E_m is the modulus of the matrix, measured on the neat PA and the samples PA-MCx, while ϑ_f is the fiber volume fraction, which was determined for each composition from the nominal weight fraction considering a volume of voids equal to zero. The coefficients η_L and η_T were determined through Equation (IV - 3) and Equation (IV - 4), respectively, as

$$\eta_L = \frac{\frac{E_f}{E_m} - 1}{\frac{E_f}{E_m} + \frac{l}{r}} \quad \textbf{(IV - 3)}$$

$$\eta_T = \frac{\frac{E_f}{E_m} - 1}{\frac{E_f}{E_m} + 2} \quad \textbf{(IV - 4)}$$

where E_f is the nominal fiber modulus (242 GPa), and l and r are the fiber average length and radius, respectively. Finally, E_C could be calculated through Equation (IV - 5) as

$$E_C = aE_L + (1 - a)E_T \quad \textbf{(IV - 5)}$$

where a is equal to 0.375 for a 2D (in-plane) random orientation and 0.185 for a 3D random orientation.

The results of the theoretical modulus calculated with the Halpin-Tsai model are compared with the experimental data in Figure IV - 15. For the CFL-containing compositions (Figure IV - 15a), the experimental data are reported with square red symbols with their standard deviation. It is evident that the use of the nominal fiber length (6 mm) in the model causes an overestimation of the elastic modulus. The results of this calculation are reported in Figure IV - 15a as E_{c_th} (2D) and E_{c_th} (3D), calculated with a equal to 0.375 and 0.184, respectively. The reason of the overestimation is related to the fiber fragmentation during processing, which leads to a reduction of the average length. To confirm this hypothesis, small pieces of some selected CFL-reinforced composites were dissolved in concentrated formic acid, then the fibers were recovered and measured with an optical microscope, and the images were analyzed with the software ImageJ. The measured average length was 0.42 ± 0.10 mm for the sample PA-CFL20 and 0.32 ± 0.09 mm for the sample PA-MC50-CFL20. This not only confirms a reduction in the fiber length, but it also evidences that the intensity of the shear stresses that the fibers undergo during processing increases with MC addition, which agrees with the dynamic rheological measurements. These fiber length values were used in the Halpin-Tsai model, and the

value measured on PA-MC50-CFL20 was applied also for the other MC-containing compositions. The results of this investigation are reported in Figure IV - 15a as E_{c_exp} (2D) and E_{c_exp} (3D). It is clear that the model fits the experimental data more precisely, and the experimental data are comprised between the trends of the theoretical moduli calculated considering a 3D and a 2D orientation. This indicates that the hot-pressing step partially orients the fibers in the plane perpendicular to the compression direction, and a completely random orientation cannot be assumed. The same investigation was performed on the samples containing CFS and, as observable from Figure IV - 15b, the model fits the experimental data also with the nominal fiber length. This can be clarified by noticing that the milled fibers have an initial short fiber length and a generally negligible length reduction during processing (Rueda et al., 2017b). This was verified also in this thesis work, by measuring the residual CFS length as done for CFL.

These results suggest that, during the processing of thermoplastic discontinuous-fiber composites, it is crucial to evaluate how the melt viscosity and the initial fiber length influence the residual fiber length. Also for the CFS-containing samples, the experimental data lay between the trends of the theoretical moduli calculated considering a 3D and a 2D orientation, which implies that also in this case the hot-pressing step imparts a certain degree of orientation to the fibers. This can be appreciated for both the sample classes from Figure IV - 15c. It reports the experimental values of a calculated from the inverse of Equation (IV - 5), using the experimental value of elastic modulus for each composition and the values of E_L and E_T calculated with the experimental fiber length. Again, it can be seen that the values of a for the prepared samples are comprised between the case of 3D random orientation and that of 2D in-plane orientation.

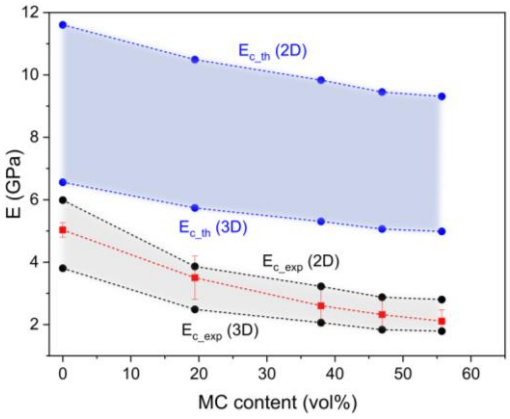

(a)

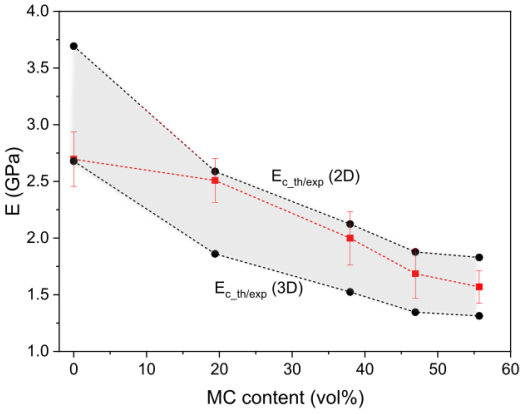

(b)

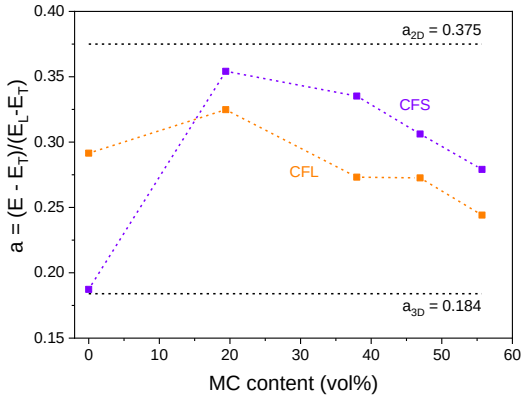

(c)

Figure IV - 15. Experimental values of the elastic modulus compared with the theoretical values obtained with the Halpin-Tsai model with the nominal ("th" subscript) and experimental ("exp" subscript) fiber length, for a 2D and 3D fiber orientation. (a) samples PA-MCx-CFL20; (b) samples PA-MCx-CFS20; (c) values of a calculated from the experimental values of elastic modulus.

4.3.3 Conclusions

This Subchapter illustrated the results of the characterization of thermoplastic discontinuous-fiber composites with TES capability, obtained by combining PA12 with MC and discontinuous carbon fibers of two different lengths.

DSC tests highlighted that the phase change enthalpy measured on these composites is higher than that of the PA-PCM-GF laminates described in Subchapter 4.2, which implies that the applied processing conditions are milder and more suitable to retain most of the TES capability of the PCMs. However, the values of relative phase change enthalpies are still far below 100 %, which highlights that the high melt viscosity and shear stresses developed during the melt compounding and hot pressing steps are still responsible for a not negligible PCM degradation and enthalpy loss. This effect was seen increasing with the MC fraction and the carbon fiber fraction and was more evident on samples containing CFL because this reinforcement type caused a higher increase in viscosity than CFS, as also evidenced by dynamic rheological tests.

Also in this case, quasi-static tensile tests highlighted a decrease in mechanical properties upon PCM addition, while the presence of CF positively contributed to increase the elastic modulus. As expected, the experimental data and the Halpin-Tsai modeling evidenced a higher effect of CFL, due to the higher aspect ratio, even though the residual fiber length was considerably lower than the initial one, while for CFS the initial and final fiber lengths were not significantly different. The Halpin-Tsai approach also evidenced that the orientation of both the reinforcement types is not comparable to a fully 3D random distribution, as there is a certain degree of in-plane orientation, likely due to the hot-pressing operation.

The following Subchapter illustrates a completely different approach for the production of thermoplastic laminates containing a PCM, which involves a reactive thermoplastic resin that allows avoiding the processing steps in the molten state.

4.4 Reactive thermoplastic resin as a matrix for carbon fiber laminates containing paraffin microcapsules

This Subchapter presents a different approach to produce thermoplastic laminates containing a PCM. This approach, aimed at preserving the integrity of paraffin microcapsules by avoiding the high-temperature processing of highly viscous molten polymer, is made possible by adopting the newly developed thermoplastic resin Elium®, provided as low-viscosity liquid and processable as a thermosetting resin.

This technique is nowadays applicable only to some selected polymer formulations and not to the majority of the most common thermoplastic polymer matrices. Nevertheless, it is a powerful and effective method that is worth investigating to produce post-thermoformable PCM-enhanced composites containing continuous reinforcing fibers.

4.4.1 Materials and methods

The present Section lists the materials used to fabricate these samples, and then it describes in detail the techniques for the preparation of the same. It subsequently lists all the characterization techniques applied on these samples. Since the materials and the characterization techniques have been already detailed in Chapter III, this Section will specify only the experimental parameters that are specific of this Subchapter.

4.4.1.1 Materials

Table IV - 16 lists the materials employed to prepare these samples (please refer to Section 3.2.4 for the details about the materials).

Table IV - 16. Materials employed in Section 4.4.

Phase	Label	Material
Polymer matrix	EL	Thermoplastic liquid resin Elium®
Reinforcement	CF	Bidirectional carbon fiber fabric
PCM	MC	Paraffin microcapsules

4.4.1.2 Sample preparation

The Elium® resin was manually mixed with benzoyl peroxide (BPO), provided from the resin producers as the polymerization initiator and added in a fraction of 2 wt%. The components were mixed at room conditions until the BPO was completely dissolved. The MC were then added in various weight concentrations and stirred at 200 rpm for 5 min, to ensure a good dispersion. Four compositions were prepared, containing 0, 20, 30, and 40 wt% of MC, respectively. The mixtures were degassed and poured in silicon molds with dimensions of 70x10x3 mm^3, to produce specimens for the subsequent characterization. The specimens were left 4 h at room temperature and then thermally treated at 80 °C for 8 h, to bring the polymerization process to completion. The labels and the nominal composition of the prepared samples are reported in Table IV - 17; it contains additional information about the experimental composition of the samples, which will be discussed in Section 4.4.2.

The same four compositions were employed as matrices to prepare laminates via hand lay-up. Five plies of carbon fabric (in-plane area 130x200 mm^2) were stacked together. The laminates were vacuum-bagged for 4 h at room temperature and thermally treated at 80 °C for 8 h. The resulting laminates were called EL-CF, EL-MC20-CF, EL-MC30-CF and EL-MC40-CF, evidencing the nominal MC weight fraction in the initial matrix composition.

Table IV - 17. List of the prepared matrices with nominal composition, mass loss after sample preparation, and experimental capsule weight fraction.

Sample	Nom. EL content (wt%)	Nom. MC content (wt%)	Exp. mass loss (wt%)	Exp. MC content (wt%)
EL	100.0	0.0	33.3 ± 3.3	0.0
EL-MC20	80.0	20.0	20.9 ± 1.9	25.3 ± 0.6
EL-MC30	70.0	30.0	18.6 ± 2.8	36.9 ± 1.2
EL-MC40	60.0	40.0	16.6 ± 0.7	48.0 ± 0.4

EL = Elium resin + benzoyl peroxide (2 wt%); Nom. = nominal; Exp. = experimental.

4.4.1.3 Characterization

The prepared EL-MCx samples were investigated through the characterization techniques listed in Table IV - 18 together with the experimental parameters applied specifically on these samples (see Subchapter 3.3 for the full description of the characterization parameters and specimen preparation).

Table IV - 18. Characterization techniques and experimental parameters applied on the samples EL-MCx.

Technique	Specific experimental parameters
SEM	Cryofracture surface; Instrument Jeol IT300 SEM
DSC	Temperature interval 0-130 °C
TGA	Mettler TG50 thermobalance; specimen mass 25 mg
DMA	Single-frequency scans
Three-point bending test	As described in Section 3.3.5.1

The prepared EL-MCx-CF laminates were investigated through the characterization techniques listed in Table IV - 19.

Table IV - 19. Characterization techniques and experimental parameters applied on the samples EL-MCx-CF.

Technique	Specific experimental parameters
SEM	Cryofracture surface; Instrument Zeiss Supra 60 FE-SEM
Optical microscope	Polished cross section
Liquid displacement	Density measurements; ethanol
DSC	Temperature interval 0-130 °C
TGA	Mettler TG50 thermobalance; specimen mass 25 mg
DMA	Single-frequency scans; multifrequency scans; heating/cooling cycles
Thermal camera imaging	Specimen in-plane dimensions: 90x120 mm^2
Three-point bending test	As described in Section 3.3.5.1

4.4.2 Results and discussion

The present section describes illustrates the results of the characterization of the samples EL-MCx (Section 4.4.2.1) and the laminates EL-MCx-CF (Section 4.4.2.2).

4.4.2.1 Characterization of the samples EL-MCx

The aforementioned Table IV - 17 reports the labels and the nominal compositions of the prepared samples; as indicated, the nominal weight fraction of MC was 0, 20, 30, or 40 wt%. Nevertheless, a not negligible mass loss was witnessed during the sample preparation, caused by the evaporation of the most volatile components of the resin, as also suggested by a sensible temperature decrease during mixing. From the initial (just after casting) and final (after the thermal treatment) masses of the samples, the mass loss was measured for each sample and reported in Table IV - 17. It is reasonable to assume that the entire mass loss is imputable to the EL phase and that the MC phase does not lose mass at room temperature. Therefore, from the measured mass loss, it is possible to calculate an experimental MC weight fraction for the three samples containing MC, which is higher than the nominal one. These values are also reported in Table IV - 17.

Figure IV - 16 reports the micrographs of the cryofracture surface of the samples EL-MCx, acquired by SEM. In the sample EL-MC20, the microcapsules appear homogeneously distributed in the polymer matrix, which can be better appreciated on the micrographs acquired at the lowest magnification (Figure IV - 16a). The large presence of broken capsules is likely due to the cryofracturing stage and not to the processing conditions, which were rather mild. As discussed for the samples described in Subchapter 4.3, the core-shell structure of the capsules is clearly observable, especially from the micrographs at higher magnifications. In the sample EL-MC20, it can be observed that the fracture propagates mostly across the capsules and not at the capsule-matrix interface, which suggests a rather good adhesion with the polymer matrix (Brown et al., 2004). However, from a comparison between the samples EL-MC20 (Figure IV - 16a-c-e) and EL-MC40 (Figure IV - 16b-d-f), it is evident that in this latter case the number of broken capsules is remarkably lower, which also confirms the hypothesis that the processing conditions do not bring a considerable damage to the microcapsules. For EL-MC40, the fracture propagates at the polymer/MC interface and probably follows the defects and voids path in the polymer matrix. In this case, the EL volume fraction appears not sufficient to wet all the capsules completely, which leads to a high level of porosity.

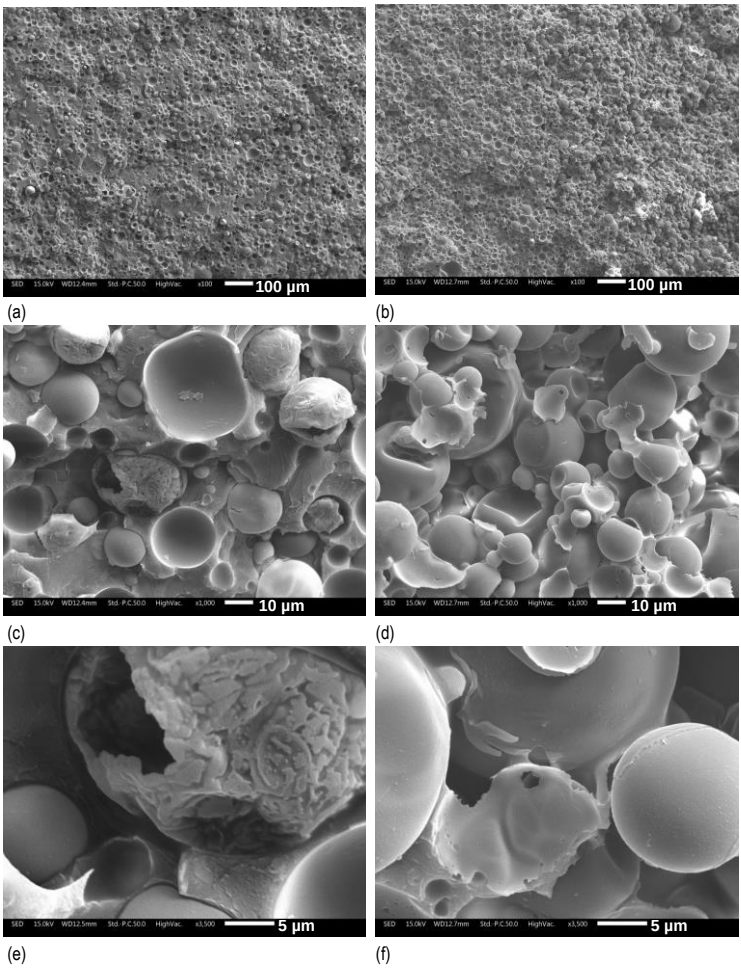

Figure IV - 16. SEM micrographs of the cryofracture surface of the samples EL-MCx at different magnification levels. (a,c,e) EL-MC20; (b,d,f) EL-MC40.

Figure IV - 17 shows the DSC thermograms of the first heating scan and the cooling scan of the samples EL-MCx, while Table IV - 20 summarizes the main DSC results. The thermograms of all the MC-containing samples show the PCM endothermic melting peak at 45-49 °C and the corresponding exothermic peak at 25-30 °C. The melting and crystallization temperatures (listed in Table IV - 20) are respectively higher and lower than those of the neat MC, which is probably linked to inertial phenomena. The amplitude of these signals increases with the MC weight fraction. The measured values of phase change enthalpy (ΔH_m, ΔH_c) are in excellent

agreement with the expected values, as demonstrated by the relative phase change enthalpy values (ΔH_m^{rel}), equal to 100 % for all the compositions. In this case, ΔH_m^{rel} was calculated by considering the experimental weight fractions of MC reported in Table IV - 17 and not the nominal value, otherwise the resulting ΔH_m^{rel} would have largely overcome 100 % and would not have reflected any damage or loss of the PCM during processing and thermal treatment. Nevertheless, the values of ΔH_m^{rel} close to 100 % indicate that the processing conditions are mild enough to preserve the MC integrity and the thermal treatment is performed at sufficiently low temperatures to avoid PCM degradation.

The DSC tests also allowed the measurement of the glass transition temperature (T_g) of the EL phase; the T_g values of the samples EL-MCx are not considerably different from that of the neat Elium sample (EL), which suggests that the MC phase does not significantly inhibit or modify the polymerization process. The T_g measured in the second heating scan (not reported) does not differ from that of the first scan for more than 3 °C, which suggests that the applied thermal treatment led to a higher degree of polymerization.

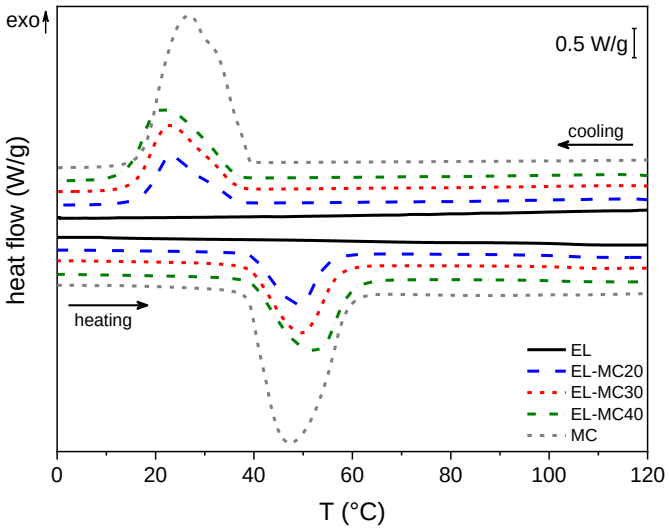

Figure IV - 17. DSC thermograms of the samples EL-MCx (first heating scan and cooling scan).

Table IV - 20. Main DSC results for the samples EL-MCx (first heating scan and cooling scan).

Sample	T_g (°C)	T_m (°C)	ΔH_m (J/g)	ΔH_m^{rel} (J/g)	T_c (°C)	ΔH_c (J/g)
EL	103.6	-	-	-	-	-
EL-MC20	103.8	47.0	53.1	100.8 ± 2.3	25.0	53.5
EL-MC30	104.6	47.7	80.8	105.2 ± 3.4	24.8	81.6
EL-MC40	101.7	49.9	101.4	101.4 ± 0.8	23.7	100.1
MC	-	45.0	208.2	-	29.8	208.2

T_g = glass transition temperature of Elium; T_m, T_c = melting and crystallization temperatures of the PCM; ΔH_m, ΔH_c = experimental melting and crystallization enthalpies of the PCM; ΔH_m^{rel} = relative melting enthalpy of the PCM calculated from the measured capsule weight fraction MC (exp. wt%).

The results of the TGA tests are presented in Figure IV - 18 and Table IV - 21. The neat EL resin manifests degradation in a single step at approx. 415 °C, while the neat MC show a higher peak degradation temperature. It should be pointed out that the TGA thermogram of the neat MC reported here is slightly different from that of the same nominal sample (MC) reported in Figure IV - 3 and Figure IV - 9, which are relative to the glass-fiber-reinforced PA-based laminates (Subchapter 4.2) and the PA-based composites reinforced with discontinuous carbon fibers (Subchapter 4.3). As mentioned in Chapter III, these differences can be related to two main causes, namely the different production batches of the MC, and the different instrument used to run the TGA tests. In this test, the neat MC shows a higher peak degradation temperature (~466 °C). The peak temperatures of the two phases are too close to each other to allow the presence of two distinct degradation steps in the mass loss trend (Figure IV - 18), thereby preventing the possibility of estimating an experimental PCM weight fraction. However, in the mass loss derivative signal of the samples EL-MCx, two peaks can be easily distinguished. The height of the first peak (degradation of the EL phase) decreases with an increase in the MC weight fraction, while the second follows the opposite trend. This is why the absolute maximum in the mass loss derivative signal (T_d) shifts to higher temperatures with an increase in the MC content.

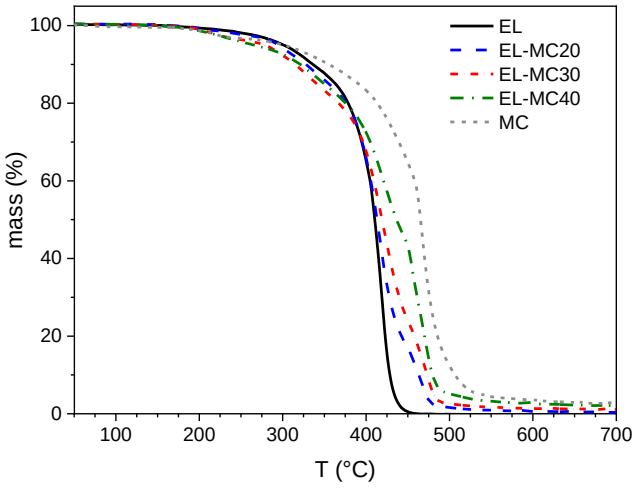

(a)

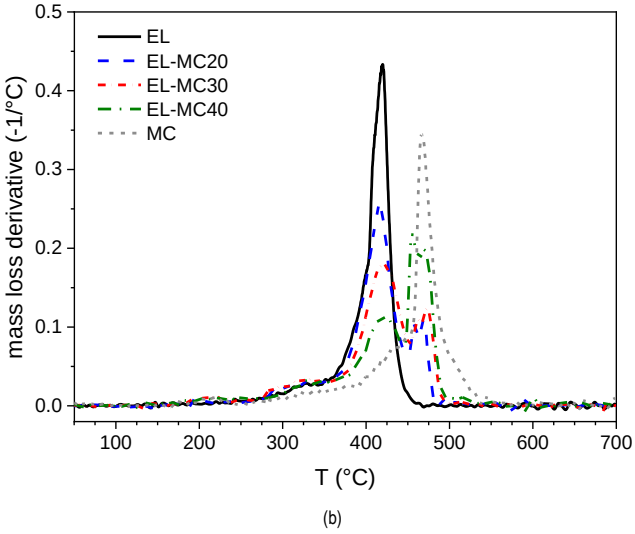

(b)

Figure IV - 18. TGA thermograms of the samples EL, MC and EL-MCx. (a) residual mass; (b) mass loss derivative.

Table IV - 21. Results of the TGA tests on the samples EL, MC and EL-MCx (x=20,30,40).

Sample	$T_{1\%}$ (°C)	$T_{3\%}$ (°C)	$T_{5\%}$ (°C)	T_d (°C)	m_r (%)
EL	221.7	279.1	301.7	415.0	0
EL-MC20	208.3	275.0	295.0	416.2	0.35
EL-MC30	201.7	240.2	281.7	420.3	1.10
EL-MC40	188.3	228.3	268.3	455.2	2.09
MC	186.3	235.0	298.7	466.2	2.67

$T_{1\%}$, $T_{3\%}$, $T_{5\%}$= temperature corresponding to a mass loss of 1 %, 3%, 5%; T_d = temperature of maximum degradation kinetics (peak of the mass loss derivative); m_r = residual mass after the test.

Figure IV - 19 and Table IV - 22 illustrate the results of the DMA tests. Figure IV - 19 shows the trend of the storage modulus (E') normalized to the value of E' at 0 °C. The trend of the storage modulus of the neat EL sample decreases with an increase in temperature, and the decrement is faster at temperatures higher than approx. 60 °C. In the samples containing the PCM, the effect of the paraffin melting inside the microcapsules is observable from a higher decrease in the values of normalized E', and this effect is more evident for the samples with the higher MC concentration, as also observable from the values of normalized E' at 60 °C ($E'_{60°C}/E'_{0°C}$, Table IV - 22). The thermogram of $tan\delta$ (Figure IV - 19b) shows two peaks. The first, at 40-50 °C, is due to the PCM melting; it is noteworthy to observe that not only the height but also the peak temperature increases with the MC concentration. These results suggest the possibilities to apply DMA to study a phase change of melting, specifically that of a PCM embedded in the polymer matrix, which is quite unusual in the field thermo-mechanical analysis of polymers. The second $tan\delta$ peak, observable at 115-125 °C, is due to the glass transition of the EL phase, and also the position of this peak increases the MC loading. This is likely due to the fact that the capsule shells partially obstacle the mobility of the EL polymer chains. The same effect is probably at the basis of an increase in the residual storage modulus at 160 °C (E'_R) for higher MC concentrations. Similar results and considerations can be found somewhere else in the literature for other thermoplastic composites containing various types of fillers (Gamon et al., 2013).

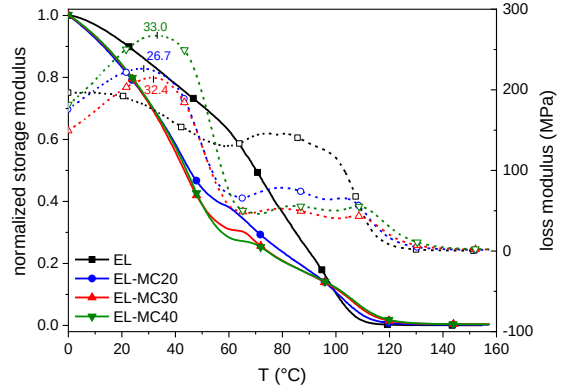

(a)

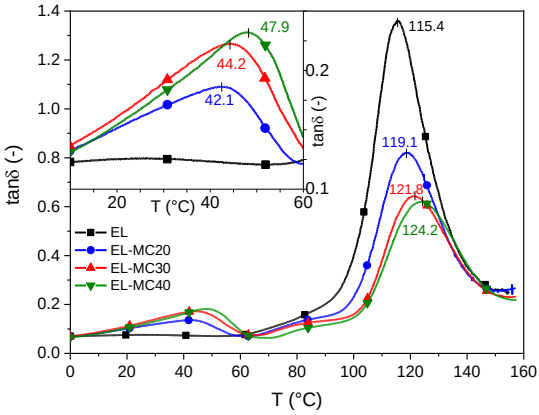

(b)

Figure IV - 19. DMA thermograms of the samples EL and EL-MCx (x =20,30,40): (a) normalized storage modulus (solid lines) and loss modulus (dashed lines); (b) loss tangent $tan\delta$. The reported values represent the peak temperatures.

Table IV - 22. Main results of the DMA tests on the samples EL and EL-MCx (x=20, 30, 40).

Sample	$T_{m,peak}$ (°C)	$T_{g,peak}$ (°C)	$E'_{60°C}/E'_{0°C}$ (-)	E'_R (MPa)
EL	-	115.4	0.627	1.71
EL-MC20	42.1	119.1	0.382	5.49
EL-MC30	44.2	121.8	0.311	8.37
EL-MC40	47.9	124.2	0.284	10.03

$T_{m,peak}$= peak of $tan\delta$ at the PCM melting; $T_{g,peak}$= peak of $tan\delta$ at the glass transition of Elium. E'_R = residual storage modulus at 160 °C.

Finally, three-point bending tests were performed to evaluate how the introduction of MC impacts the mechanical properties of EL. The results of this test are reported in Figure IV - 20a-b. The flexural elastic modulus decreases with an increase in the MC fraction; it spans from 2.08 ± 0.25 GPa for the neat EL to 1.35 ± 0.18 GPa for EL-MC40, with a decrease of 35 %. This trend can be explained by assuming that the MC phase is less stiff than the neat resin. Considerably higher is the decrease in the flexural strength, which drops from 63 MPa of the neat EL to 17 MPa of the sample EL-MC40, with a decrease of 73 %. This is probably due to the low strength of the MC and the non-optimal adhesion to the polymer matrix. Conversely, the flexural strain at break is not heavily affected by the presence of MC.

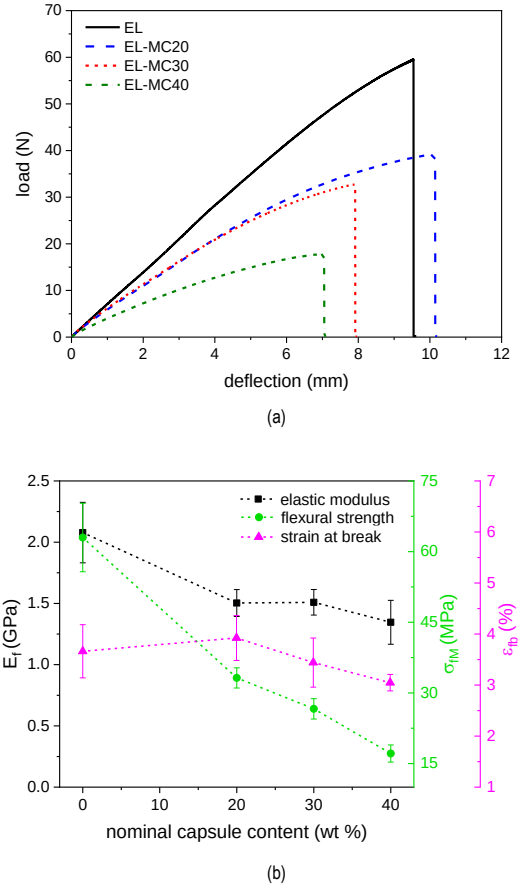

Figure IV - 20. Results of the three-point bending tests on the samples EL-MCx. (a) representative load-displacement curves; (b) trends of the flexural modulus, flexural strength and strain at break as a function of the nominal MC content.

4.4.2.2 Characterization of the samples EL-MCx-CF

The optical microscope (OM) images of the polished cross sections of the laminates are shown in Figure IV - 21. It can be observed that the MC phase is preferentially distributed in the interlaminar region and not among the fibers of the same tow, which is due to the different dimensions of carbon fibers (av. diameter 7 µm) and microcapsules (av. diameter 20 µm). This was observed also in the PA/GF laminates presented in Subchapter 4.2. Moreover, it can be qualitatively appreciated that the MC concentration in the interlaminar zone does not vary considerably with an increase in the MC fraction. What is clearly seen increasing with the MC fraction is the thickness of the interlaminar region, and thus that of the whole laminate. Similar considerations can be drawn from the SEM micrographs of the delamination plane and the cross section of the laminates (Figure IV - 22). The delamination plane is rich in microcapsules, and similar results were obtained by Yoo et al. (Yoo et al., 2016). By comparing the cross-sections of the samples EL-CF (Figure IV - 22c) and EL-MC30-CF (Figure IV - 22d), it is clear that the thickness of the interlaminar zone increases with MC, which are concentrated in this region.

The results of the DSC tests on the laminates are reported in Figure IV - 23 and Table IV - 23. The DSC thermograms are qualitatively similar to those obtained on the samples EL-MCx (see Figure IV - 17). As for those samples, the glass transition of the resin is not significantly affected by MC addition, which suggests that the polymerization process is not influenced by MC and CF. Again, the phase change temperatures of the PCM do not follow a trend with the MC fraction, even though the values of T_m are generally lower than those of the samples EL-MCx and the values of T_c higher, which can be linked to the higher thermal conductivity of the carbon-fiber-containing samples. The phase change enthalpy values increase with the MC loading, up to 66.8 J/g for the sample EL-MC40-CF. This indicates that the processing conditions of the Elium resin are suitable to avoid damage to the microcapsules, thereby retaining the heat storage ability of the paraffinic core, unlike the previous described cases including a traditional thermoplastic matrix.

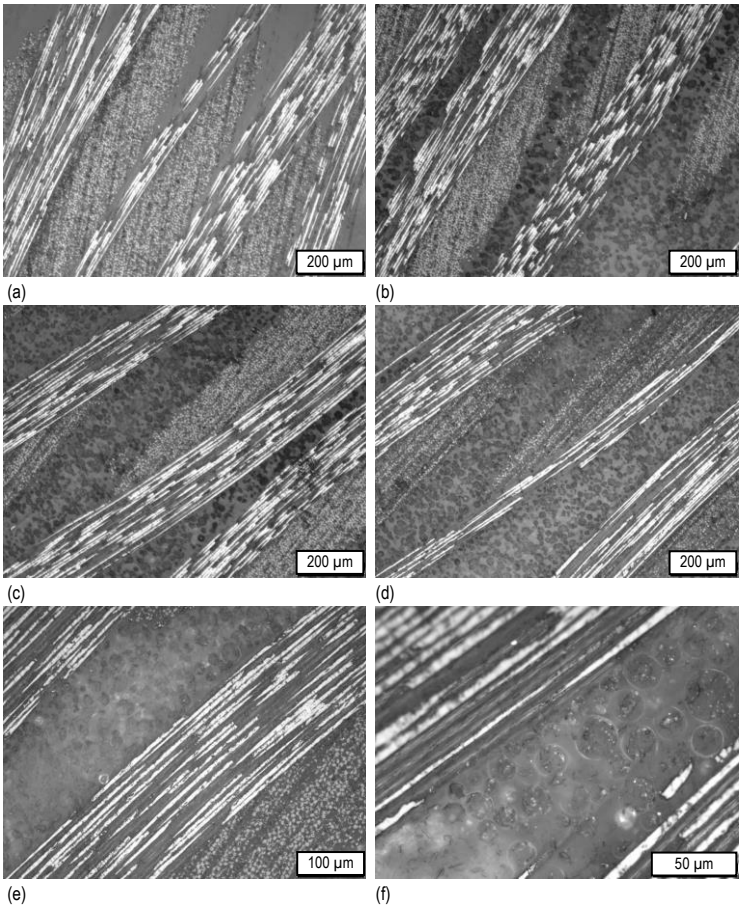

Figure IV - 21. Optical microscope micrographs of the polished cross section of the prepared laminates (a) EL-CF; (b) EL-MC20-CF; (c) EL-MC30-CF; (d) EL-MC40-CF; (e) and (f) EL-MC30-CF, higher magnification.

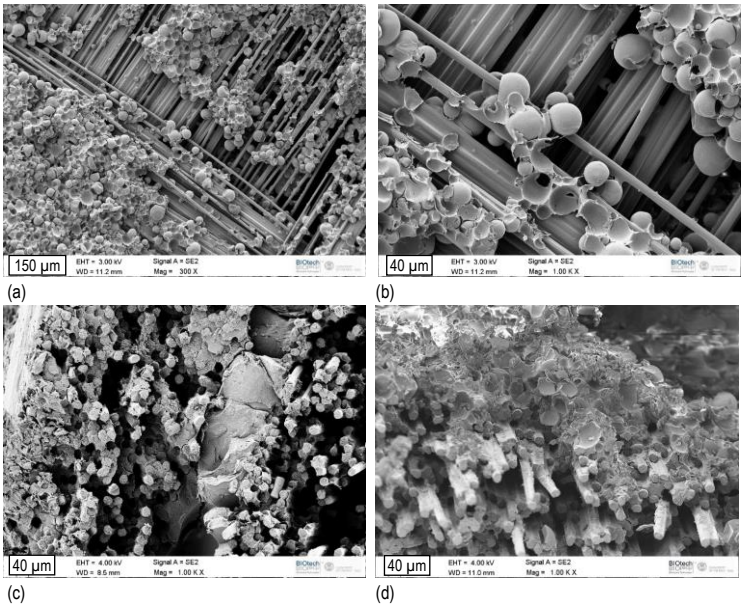

Figure IV - 22. SEM micrographs of the cryofracture surface of the prepared laminates. (a) and (b) EL-MC30-CF, delamination plane; (d) EL-CF, cross section; (c) EL-MC30-CF, cross section.

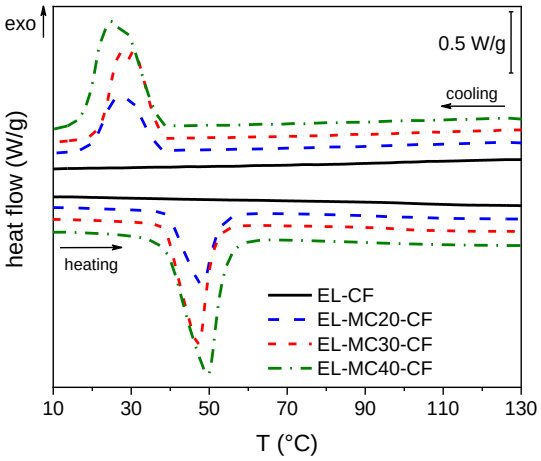

Figure IV - 23. DSC thermograms of the samples EL-MCx-CF (first heating scan and cooling scan).

Table IV - 23. Results of the DSC tests on the EL-MCx-CF laminates.

Sample	T_g (°C)	T_m (°C)	ΔH_m (J/g)	T_c (°C)	ΔH_c (J/g)	ω_{MC} (wt%)
EL	101.0	-	-	-	-	-
EL-MC20-CF	102.5	46.6	30.2	27.5	31.6	14.5
EL-MC30-CF	99.6	45.3	45.9	29.5	45.6	22.1
EL-MC40-CF	98.6	46.4	66.8	27.4	65.6	32.1

T_g = glass transition temperature of Elium; T_m, T_c = melting and crystallization temperatures of the PCM; ΔH_m, ΔH_c = experimental melting and crystallization enthalpies of the PCM; ω_{MC} = experimental capsule weight fraction calculated from the measured melting enthalpy.

While preparing the laminates, the nominal and experimental weight fractions of MC in the initial EL-MC mixtures were known or easily measurable, but the MC weight fraction in the laminates is also influenced by the resultant weight fraction of fibers and matrix, which is affected by the matrix viscosity that in turn depends on the starting MC loading. Since the nominal MC weight fraction in the laminates is not known *a priori*, it is not possible to calculate a relative melting enthalpy (ΔH_m^{rel}), as done for the samples described in the previous Subchapters. However, an experimental MC weight fraction can be still estimated from the values of phase change enthalpy measured with DSC, assuming that the MC maintain their energy storage efficiency also after the lamination process, which is a reasonable hypothesis if the results of the characterization of the EL-MCx samples are considered. These values of experimental MC weight fraction (ω_{MC}) are reported in Table IV - 23 with the DSC results.

The fiber weight fraction of the laminates was then investigated through TGA, which was also useful to assess their thermal stability. The results of this characterization are reported in Figure IV - 24 and Table IV - 24. The trends of the residual mass and mass loss derivative resemble qualitatively those of the EL-MCx samples (Figure IV - 18). As expected, the residual mass (m_r) after the test is considerably higher in this case, as the degradation of carbon fibers is negligible in an N_2 atmosphere. As the value of m_r decreases with an increase in the MC fraction, it can be concluded that the weight fraction of the reinforcement follows the same trend. The weight fractions of carbon fibers calculated from these results ($\omega_{f,TGA}$) are reported in Table IV - 24. These values range from 66 wt% for the neat EL-CF laminate to 37 wt% for the laminate EL-MC40-CF, and the decrease does not follow a linear trend with the MC weight fractions.

The weight compositions of the laminates determined through TGA are in accordance with those determined by weighing the whole laminates and subtracting the weight of the fibers, known through the areal mass of the fabric and the in-plane surface of the laminates. These values are reported in Table IV - 24 as $\omega_{f,mass}$. This accordance is an indication of the homogeneity of the produced samples, as the TGA

tests are performed on specimens of few milligrams. The lower CF content is probably the at the basis of the decreased thermal stability of the laminates with the highest MC loading, as can be appreciated form the lower values of $T_{1\%}$, $T_{3\%}$, and $T_{5\%}$. These temperatures are always higher than those obtained from the samples EL-MCx (Table IV - 21), which evidences the positive contribution of the CF to the thermal stability. The mass loss derivative trends as a function of temperature show two main degradation peaks, which represent the degradation of the EL and of the MC phases, respectively. The peak position is nearly the same as that measured on the EL-MCx samples and it is not heavily influenced by CF addition.

Table IV - 24. Results of the TGA tests on the laminates EL-MCx-CF.

Sample	$T_{1\%}$ (°C)	$T_{3\%}$ (°C)	$T_{5\%}$ (°C)	T_d (°C)	m_r (%)	$\omega_{f,TGA}$ (wt%)	$\omega_{f,mass}$ (wt%)
EL-CF	301.7	335.0	361.7	416.3	65.9	65.9	67.8
EL-MC20-CF	210.5	281.7	315.0	415.0	48.5	48.3	47.8
EL-MC30-CF	195.0	268.3	308.3	420.3	37.7	37.1	40.7
EL-MC40-CF	188.3	235.0	281.7	413.6	38.2	36.9	39.5

$T_{1\%}$, $T_{3\%}$, $T_{5\%}$= temperature corresponding to a mass loss of 1 wt%, 3 wt%, 5 wt%; T_d = temperature of the maximum degradation kinetics (peak of the mass loss derivative); m_r = residual mass; $\omega_{f,TGA}$ = weight fraction of carbon fibers determined from the TGA residual mass; $\omega_{f,mass}$ = weight fraction of carbon fibers calculated from laminate weighing.

The data on the weight composition of the prepared laminates are summarized in Table IV - 25. It specifically shows the CF weight fraction, determined for each composition as the average of $\omega_{f,TGA}$ and $\omega_{f,mass}$, and the MC weight fraction, calculated from the DSC results. With these data, the theoretical density of the samples (ρ_{th}) could be calculated, while the experimental density (ρ_{exp}) was obtained through the displacement method. The comparison between ρ_{th} and ρ_{exp} allowed the calculation of the porosity (ϑ_v), and then of the volume fraction of fibers, microcapsules and EL phase. The fiber volume fraction and the MC volume fraction follow opposite trends. This is mainly due to the viscosity increase of the Elium/MC mixtures, which reduces the matrix flowing out of the carbon fabric during the vacuum bag process. It can be also observed that the porosity is approx. 2 vol% for all compositions except EL-MC40-CF, where it rises up to 5.2 vol%.

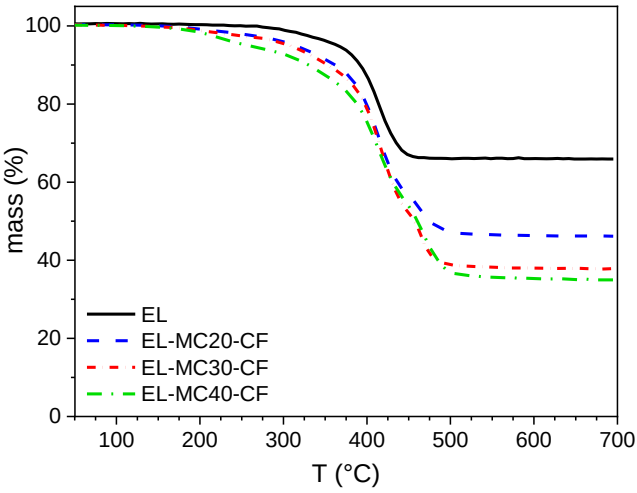

(a)

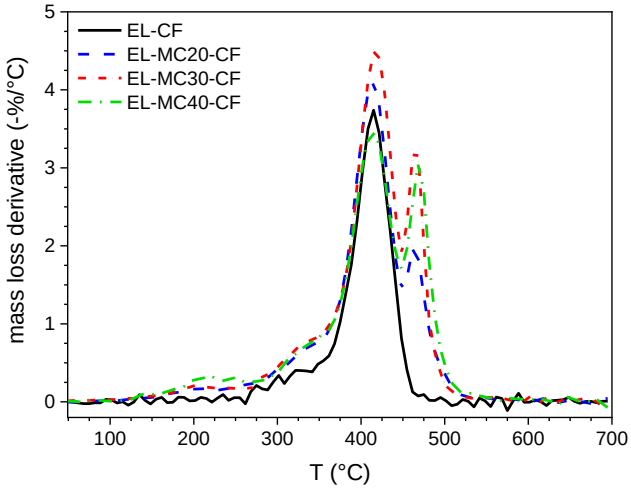

(b)

Figure IV - 24. TGA thermograms of the laminates EL-MCx-CF. (a) residual mass; (b) mass loss derivative.

Table IV - 25. Theoretical and experimental density and weight and volume compositions of the laminates EL-MCx-CF.

Sample	ω_f^* (wt%)	ω_{MC} (wt%)	ρ_{th} (g/cm³)	ρ_{exp} (g/cm³)	ϑ_v (vol%)	ϑ_f (vol%)	ϑ_{MC} (vol%)
EL-CF	66.9 ±1.4	0	1.511 ±0.019	1.487 ±0.013	1.6 ±2.1	56.7 ±1.6	0
EL-MC20-CF	48.1 ±0.3	14.5	1.329 ±0.005	1.300 ±0.012	2.2 ±1.3	35.6 ±0.6	20.95 ±0.19
EL-MC30-CF	38.9 ±2.6	22.1	1.253 ±0.036	1.238 ±0.003	1.2 ±3.2	27.4 ±1.9	30.41 ±0.07
EL-MC40-CF	38.2 ±1.8	32.1	1.211 ±0.026	1.148 ±0.001	5.2 ±2.4	25.0 ±1.2	40.93 ±0.04

*average between $\omega_{f,TGA}$ and $\omega_{f,mass}$, see Table IV - 24

Although the DSC test is the main characterization technique that gives quantitative information on the heat absorption and release in a certain temperature range, it has the disadvantage of being performed on samples of few milligrams. Therefore, to study the thermal management properties of the prepared laminates on a slightly bigger scale, a simple yet effective test was performed with thermal imaging techniques. The laminates were heated in an oven at 70 °C, then taken out and left cooling to room temperature, while their surface temperature was measured with a thermal imaging camera. Figure IV - 25 reports the values of temperature as a function of time during the cooling stage. In the MC-enhanced laminates, the temperature trend shows plateau-like regions, caused by the latent heat release at the crystallization temperature of the PCM. Due to this phenomenon, the time to reach room temperature increases remarkably. For instance, for the EL-CF composite, the time required to reach 30 °C is approx. 3 min 30 s, while for the sample EL-MC40-CF it increases to approx. 20 min. It should be noticed that the rate of cooling is also dependent on the laminate mass, which varies as a consequence of the variation in the matrix content.

However, the observed plateau-like trends are a clear sign of the variation in the thermal behavior of the laminates (and therefore of the thermal management capability) as a function of the MC content.

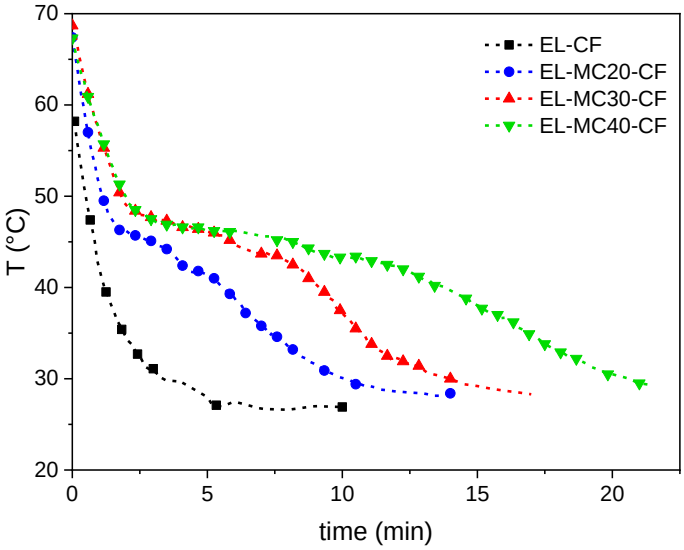

Figure IV - 25. Results of the thermal camera imaging tests on the laminates EL-MCx-CF.

The following paragraph describes the results of the DMA characterization, which comprises single-frequency, multifrequency and heating/cooling cyclic tests, all performed in single cantilever mode. The results of the single-frequency scans are illustrated in Figure IV - 26, which reports the values of E' and E'' as a function of temperature. To facilitate the comparison among the samples, the values of E' have been normalized to the value at 0 °C.

The storage modulus of the laminate EL-CF decreases with increasing temperature throughout all the investigated temperature interval, but the decrease below the glass transition is considerably less evident than for the unreinforced EL sample. Moreover, the trend of the loss modulus does not present intense peaks in the temperature range from 0 °C to 40 °C; the low-temperature transition of the EL resin may be hampered by the constrains exercised by the carbon fibers. Another possible reason could be related to the strong exothermicity of the polymerization of acrylic resins.

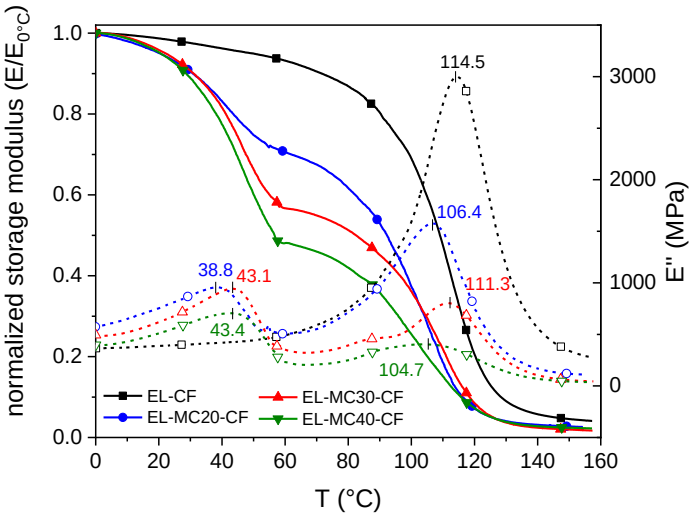
normalized storage modulus (E/E0°C)
E'' (MPa)
T (°C)
114.5
106.4
111.3
38.8
43.1
43.4
104.7
EL-CF
EL-MC20-CF
EL-MC30-CF
EL-MC40-CF

(a)

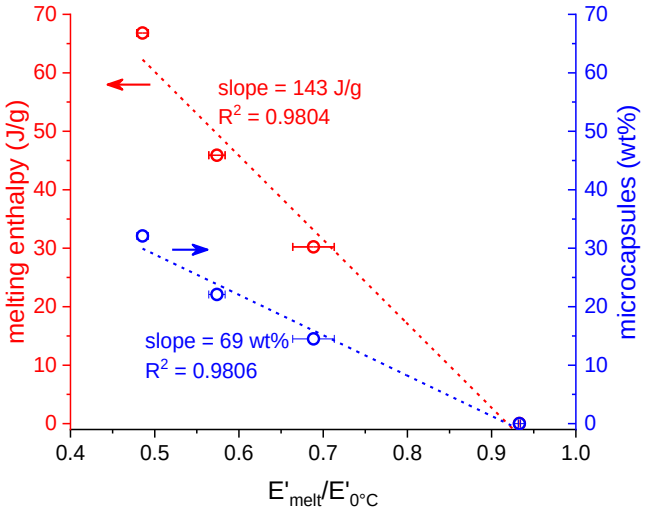
melting enthalpy (J/g)
microcapsules (wt%)
E'melt/E'0°C
slope = 143 J/g
R2 = 0.9804
slope = 69 wt%
R2 = 0.9806

(b)

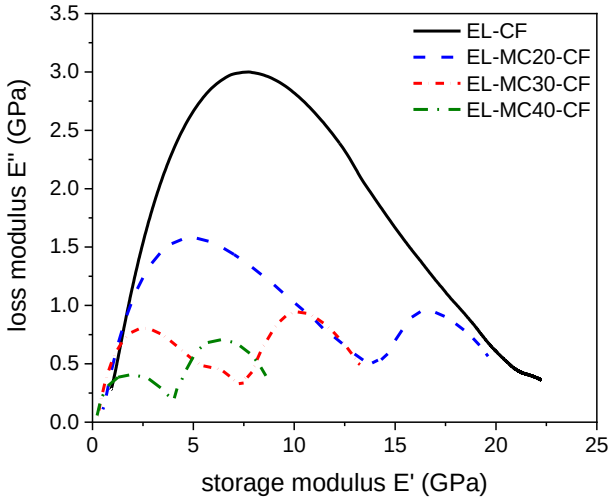

(c)

Figure IV - 26. DMA results (single frequency scans) of the samples EL-CF and EL-MCx-CF (x = 20, 30, 40). The reported values represent the peak temperatures. (a) normalized storage modulus E' (solid lines) and loss modulus E'' (dashed lines); (b) relative decrease in E' after PCM melting (60 °C) as a function of the melting enthalpy and the microcapsules weight fraction, with the results of the linear fitting; (c) Cole-Cole plots.

Due to the presence of a highly thermally conductive phase such as the carbon fibers, the local temperature can be different from that of the unfilled polymer, which may affect the matrix properties and thus the DMA behavior. Nevertheless, further research is required to verify any hypotheses. On the other hand, the peaks of the loss modulus and the loss factor at the T_g are still visible. In the MC-enhanced composites, two main steps are observable in the trend of E'; the first at the paraffin melting, the second at the glass transition of the EL phase. The drop of E' at the first step increases with the MC fraction. Interestingly, the correlation between the drop amplitude and the MC weight fraction or the melting enthalpy is linear, with R^2 values higher than 0.98. This implies that the DSC test allows one to predict, to a certain extent, the trend of the viscoelastic properties of the composite in the temperature range around the PCM phase change. At the PCM melting, the signals of E'' and $tan\delta$ manifest peaks (Figure IV - 26a and Figure IV - 27a); those of E'' are markedly asymmetrical and qualitatively analogous to those of $tan\delta$. This was not observable on the thermograms of the samples EL-MCx (Figure IV - 19), probably due to the contribution of the low-temperature transition of the EL phase, not appreciable for the laminates.

As for the EL-MCx samples, the peaks at the PCM melting shift to higher temperatures and the intensity of the $tan\delta$ signals increase with the PCM content. It is worth noticing that also the area under the $tan\delta$ signal shows a quite good linear correlation with the MC fraction and melting enthalpy. This correlation was observed also on the EL-MCx samples and is shown in Figure IV - 27b for both the classes of samples. The slope of the fitting line is higher for the EL-MCx-CF laminates than for the EL-MCx samples: that is, for a fixed value of enthalpy (or MC fraction), the intensity of the $tan\delta$ peak is lower for the laminates than for the EL-MCx samples.

Another useful representation of E' and E'' is the Cole-Cole plot (Figure IV - 26c), in which E'' is plotted as a function of E'. This representation has been described informative on the system heterogeneity and on the existence of secondary relaxations and structural changes after filler addition (Flores et al., 1996; Devi et al., 2009) as well as on the thermorheological simplicity or complexity of a system (Menard, 2008). Homogeneous polymer systems, which are monophasic or with well dispersed fillers, have semicircular Cole-Cole plots, while heterogeneous multiphasic compounds show imperfect or elliptical curves (Chee et al., 2019). For the laminates described in this section, the sample EL-CF exhibits an imperfect semicircle, similar to those reported for other Elium®/carbon laminates from the literature (Bhudolia et al., 2017) and considered as indicative of a good adhesion between the matrix and the reinforcement (Bagotia and Sharma, 2019; Chee et al., 2019). For the samples containing the PCM, the E' and E'' data are spread on a smaller range, as the values of E' and E'' at the beginning of the test decrease with increasing PCM concentration. The Cole-Cole plots assume the form of two subsequent imperfect semicircles, representative of the PCM melting and the glass transition of EL, respectively. The semicircles related to the T_g, found at low E''-E' data close to the axes origin, shrinks and changes shape with an increasing MC content. It is interesting to notice that also the PCM melting transition appears in these plots as imperfect semicircles, which have a qualitatively similar shape for the different samples and are shifted to lower values of E' and E'' with increasing MC concentration.

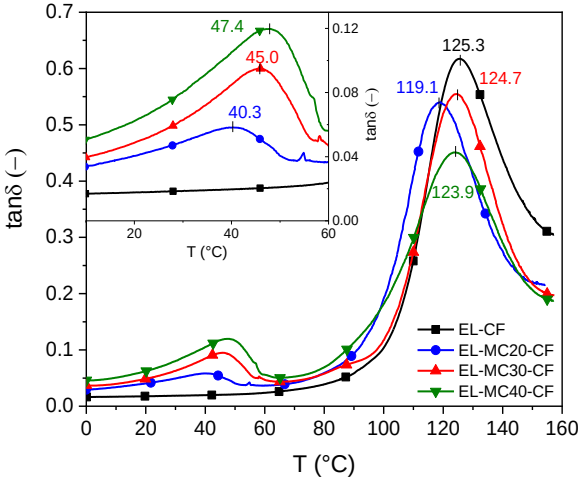

(a)

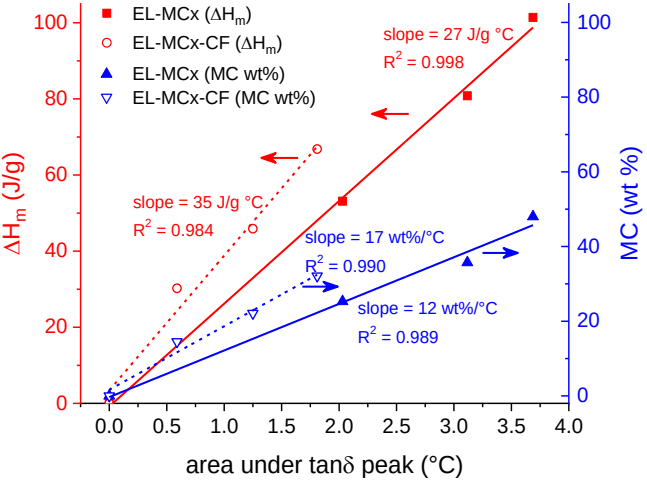

(b)

Figure IV - 27. DMA results (single frequency scans) of the samples EL-CF and EL-MCx-CF (x = 20, 30, 40). The reported values represent the peak temperatures. (a) loss tangent ($tan\delta$); (b) area under the $tan\delta$ melting peak as a function of the melting enthalpy and the microcapsules weight fraction, for the samples EL-MCx and EL-MCx-CF (x = 20, 30, 40).

As the structural TES composites must withstand repeated thermal cycles around the phase change temperature of the PCM, the variation of the dynamic-mechanical behavior was investigated not only on heating, but also on cooling, between -40 °C and 60 °C. This is not a common approach as, to the best of the author's knowledge, the literature does not report any other studies that analyze the trend of viscoelastic parameters PCM-enhanced polymers on cooling. The results of this analysis are reported in Figure IV - 28 and Table IV - 26.

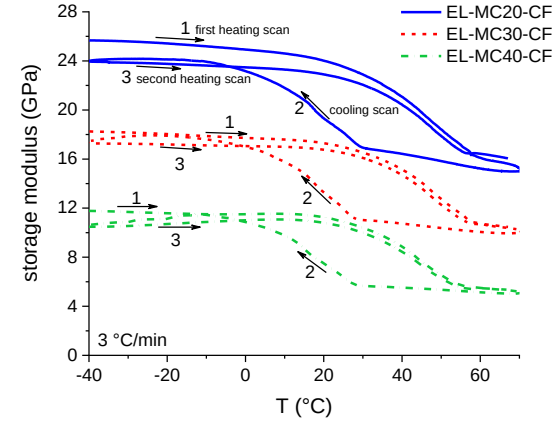

(a)

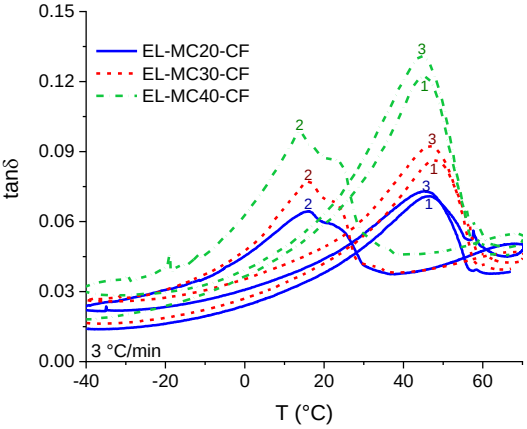

(b)

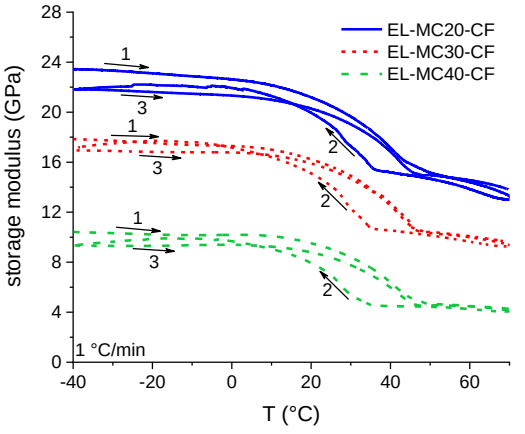

(c)

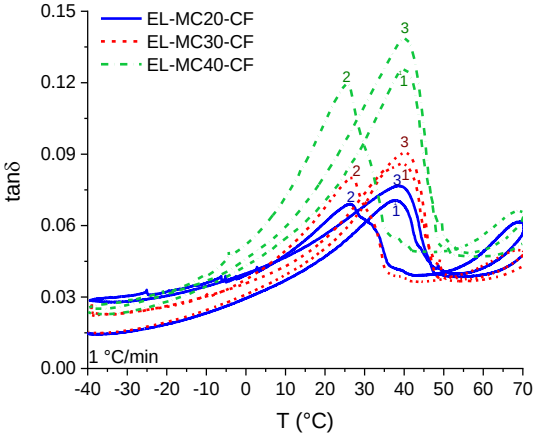

(d)

Figure IV - 28. DMA heating(1)-cooling(2)-heating(3) scans on the samples EL-MCx-CF (x = 20, 30, 40) in the temperature range around the phase change temperature of the PCM, at different heating rates. (a) storage modulus at 3 °C/min; (b) $tan\delta$ at 3 °C/min; (c) storage modulus at 1 °C/min; (d) $tan\delta$ at 1 °C/min.

Figure IV - 28 shows the trend of E' in a heating-cooling-heating scan performed at 3 °C/min on the three prepared MC-containing laminates. E' decreases with increasing MC concentration and manifests a decreasing step at the PCM melting,

which is almost completely recovered on cooling, as it reaches 90-95% of the initial value, as reported in Table IV - 26 as $E'_{rel}(-40°C)$ (see Section 3.3.3.5). The recovery happens with a certain hysteresis, as the crystallization is found at lower temperatures than the melting, as also observed in DSC tests. This is due to reasons related both to thermal inertia and to the thermodynamics of crystallization. The temperature interval describing this delay, calculated for each sample at the middle value of E', it is approx. 26-28 °C for all the compositions and it is reported in Table IV - 26 as $\Delta T_{E'50\%}$. The values of E'' (not reported) and $tan\delta$ also show that the peak on cooling (crystallization) is found approx. 30 °C lower than the melting peak (Table IV - 26). It is interesting to notice that the $tan\delta$ peak on cooling is the superposition of two distinct signals, which are also observed in DSC. This suggests that the liquid-solid and solid-solid thermal transitions of the PCM can be detected also through DMA, as each of them affects the values of E'' and $tan\delta$.

The same considerations can be made on the cyclic DMA tests performed at lower heating/cooling rate (1 °C/min) and reported in Figure IV - 28c-d. It can be noticed that the hysteresis cycles are narrower: $\Delta T_{E'50\%}$ is approx. 10 °C and the difference between the $tan\delta$ peak temperatures is 12-14 °C.

Table IV - 26. Results of the heating/cooling DMA cycles performed on the laminates EL-MCx-CF (x = 20, 30, 40).

3 °C/min	**EL-MC20-CF**	**EL-MC30-CF**	**EL-MC40-CF**
$\Delta T_{E'50\%}$ **(°C)**	26.7	28.0	26.2
$E'_{rel}(-40°C)$ **(%)**	93.3	94.8	89.4
$T_{h1,tan\delta}$ **(°C)**	46.6	47.5	45.1
$T_{c,tan\delta}$ **(°C)**	16.0	16.1	13.7
$T_{h2,tan\delta}$ **(°C)**	45.5	46.6	44.4
$T_{h2,tan\delta}$ **-** $T_{c,tan\delta}$ **(°C)**	29.5	30.5	30.7
1 °C/min	**EL-MC20-CF**	**EL-MC30-CF**	**EL-MC40-CF**
$\Delta T_{E'50\%}$ **(°C)**	9.6	10.7	12.7
$E'_{rel}(-40°C)$ **(%)**	93.1	95.0	89.6
$T_{h1,tan\delta}$ **(°C)**	38.0	39.1	40.2
$T_{c,tan\delta}$ **(°C)**	26.1	26.8	25.7
$T_{h2,tan\delta}$ **(°C)**	38.5	40.3	40.1
$T_{h2,tan\delta}$ **-** $T_{c,tan\delta}$ **(°C)**	12.4	13.5	14.4

$\Delta T_{E'50\%}$ = temperature interval between the middle value of E' in the first heating scan and in the cooling scan; $E'_{rel}(-40°C)$ = ratio between the value of E' at -40 °C in the second heating scan and the first heating scan; $T_{h1/c/h2,tan\delta}$ = $tan\delta$ peak temperature in the first heating (h1), cooling (c) and second heating (h2) scans.

The last DMA characterization mode was the multifrequency analysis; it was performed to assess the effect of frequency on the PCM melting and the glass transition of the matrix in the prepared composites. The results of the laminates EL-CF and EL-MC40-CF are shown in Figure IV - 29. For the composite EL-CF, the frequency increase determines a shift of all the parameters to higher temperatures; this effect, although present in the whole investigated temperature range, is more evident at the glass transition of the EL phase. For the sample EL-MC40-CF, the frequency dependence is observable not only at the glass transition, but also at the PCM melting, and in this temperature range the frequency sensitivity is higher below the peak temperature than above it. This can be appreciated more clearly in Figure IV - 29c, reporting the $tan\delta$ peaks at the PCM melting for the four laminates and the DSC melting peak of the neat MC acquired at the same heating rate (0.3 °C/min). At this heating rate, the DSC peak temperature is higher than the $tan\delta$ maxima. The DMA signals show a high frequency sensitivity before the peak temperature, but when the PCM is almost completely molten the frequency dependence weakens considerably.

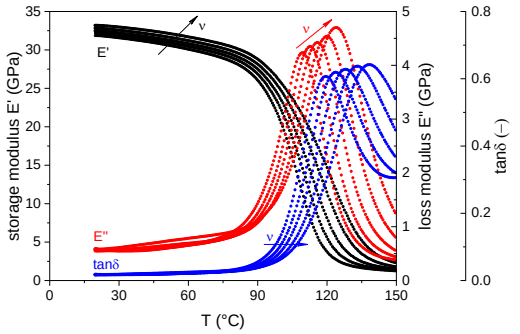

(a)

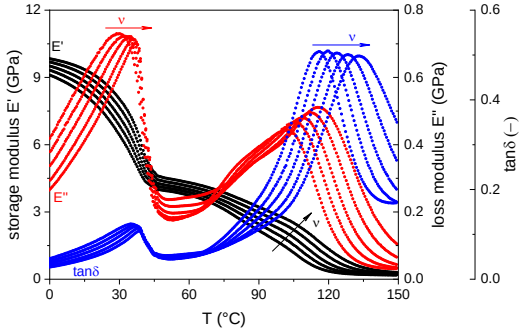

(b)

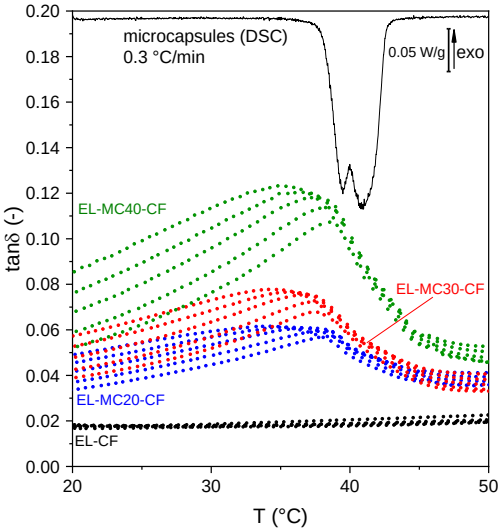

(c)

Figure IV - 29. Results on the DMA multifrequency scans on the samples EL-CF and EL-MCx-CF (x = 20, 30, 40). Investigated frequencies: 0.3-1-3-10-30 Hz. (a) sample EL-CF; (b) sample EL-MC40-CF; (c) trend of $tan\delta$ in the multifrequency scans for the samples EL-CF and EL-MCx-CF (x = 20, 30, 40), showing the peak of the melting process of the PCM, compared with a DSC scan on the PCM performed at the same scanning speed.

Multifrequency DMA tests allowed the calculation of the activation energy of the glass transition (E_a) from the $tan\delta$ peak temperatures through the Arrhenius approach, as described in Section 3.3.3.5. The results of this analysis are presented in Figure IV - 30, while the calculated E_a values are reported in Table IV - 27. It can be observed that E_a is not considerably affected by the MC concentration. Since the peaks of E'' and $tan\delta$ at the PCM melting also appear to depend on frequency, an attempt was made to apply the Arrhenius approach to calculate the activation energy of this transition. The results of this attempt are reported in Figure IV - 30b. A linear correlation could be estimated for the four lower frequency points, but the last point deviates considerably from the linear trend, which makes the application of a precise linear regression unfeasible. Nevertheless, this DMA investigation led to a better understanding of how the viscoelastic parameters of the structural TES composites are influenced by temperature and frequency and provided an interesting insight on the use of DMA to study a melting phase change, as well as the effects of such transition on the dynamic mechanical properties of the host laminate.

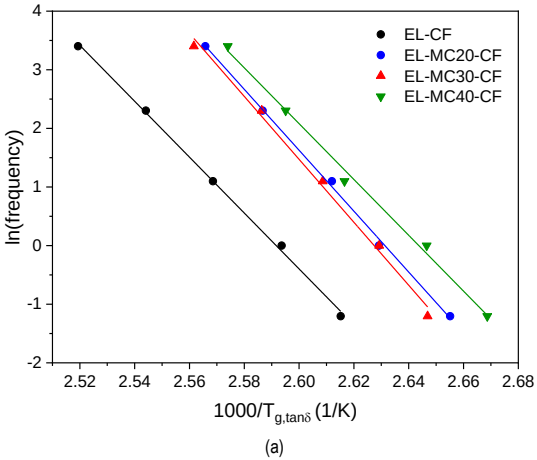

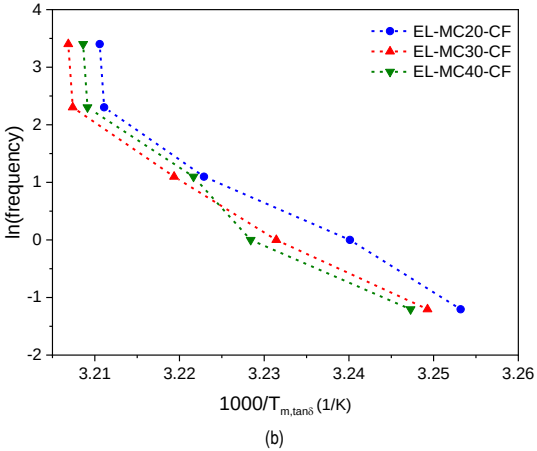

Figure IV - 30. Natural logarithm of frequency as a function of 1000/T (peaks of $tan\delta$ at the glass transition (a) and at the paraffin melting (b)) for the samples EL-CF and EL-MCx-CF (x = 20, 30, 40).

Table IV - 27. Results of the multifrequency DMA scans on the samples EL-CF and EL-MCx-CF (x = 20, 30, 40).

Sample	EL-CF	EL-MC20-CF	EL-MC30-CF	EL-MC40-CF
E_a (kJ/mol)	328 ± 12	320 ± 4	339 ± 8	341 ± 14
R^2	0.995	0.999	0.998	0.995

E_a = activation energy of the glass transition calculated from the $tan\delta$ peaks; R^2 = value of R^2 of the linear regression.

The last characterization technique applied on these laminates aimed to study their mechanical properties. The results of the three-point bending tests are reported in Figure IV - 31a-b.

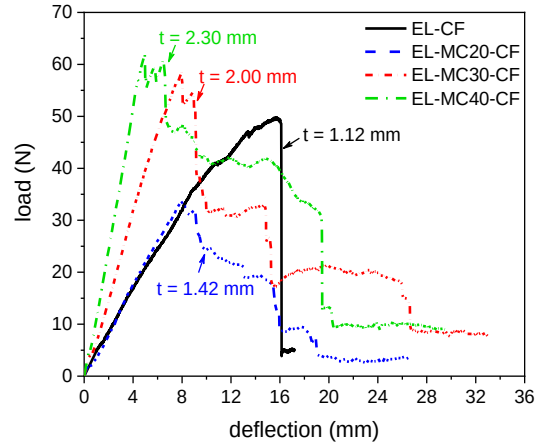

(a)

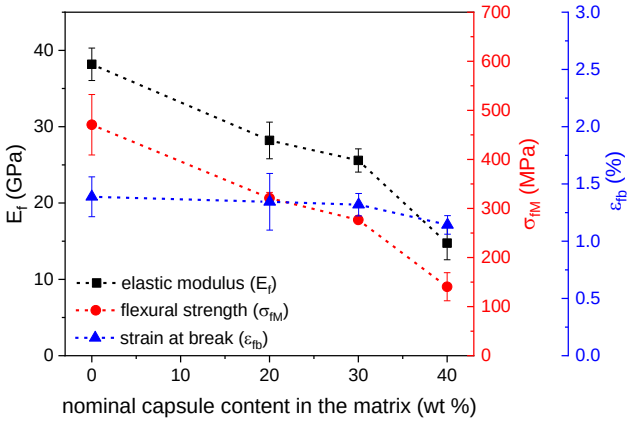

(b)

Figure IV - 31. Results of the three-point bending tests on the EL-MCx-CF laminates. (a) representative load-deflection curves (t = laminate thickness); (b) flexural modulus, strength and strain at break as a function of the nominal capsule content in the matrix.

Figure IV - 31a shows representative load-displacement curves. It can be seen that the curves of all the samples present an initial linear zone followed by a region of decreasing slope until the maximum load is reached. After the maximum load, the neat laminate undergoes a catastrophic failure, starting from the tensile-stressed mid-lower region of the specimen. Such failure mode is often associated to a good interlaminar adhesion (Abdel Ghafaar et al., 2006; Ary Subagia et al., 2014). On the other hand, the PCM-containing laminates are subjected to a progressive failure and present a drop-plateau sequence, which indicates a mechanical energy dissipation also during damage propagation. The damage was observed starting either in the mid-upper zone, subjected to compression, or in the interlaminar zone. This failure mode, commonly reported for woven fabric composites (Abdel Ghafaar et al., 2006), has been described as typical of materials having a tensile in-plane strength considerably higher than the interlaminar shear strength, which is likely the case for the MC-containing laminates reported in this work.

Figure IV - 31b reports the results of the three-point bending test. The elastic modulus decreases with an increase in the MC fraction, but this is partially due to the decreasing fiber volume fraction. The flexural strength follows the same trend, and this is probably due to the presence of additional failure mechanisms such as delamination and failure in the zone subjected to compression. Conversely, the flexural strain at break is not dramatically affected by the presence of MC.

4.4.3 Conclusions

The results presented in this Subchapter clearly demonstrate that the processing conditions of a reactive thermoplastic resin are milder than those of traditional thermoplastic polymer matrices that must be processed in the molten state. This makes it suitable to fabricate PCM-enhanced thermoplastic laminates.

This was evident in the production of EL-MCx-CF laminates, for which the melting/crystallization enthalpy values increased with the capsule content, up to 66.8 J/g for the sample EL-MC40-CF. The considerably high phase change enthalpy was at the basis of the good thermal management performance, measured through thermal camera imaging. Microstructural analysis showed that the PCM phase was preferentially distributed in the interlaminar region, and that the laminate thickness increased with an increase in the capsule content, and so did the matrix (EL+MC) volume fraction, as also evidenced by TGA tests. These two effects were the main causes of the decrease in the mechanical properties of the laminates observed at elevated PCM contents.

Moreover, the thorough DMA characterization gave interesting results. Single frequency scans evidenced the PCM melting as a decreasing step in E' and asymmetric peaks in E'' and $tan\delta$, while the glass transition peaks of the acrylic matrix are visible at 100-120 °C. At the PCM melting, the amplitude of the E' step and

the intensity of the $tan\delta$ peak showed a linear correlation with the MC weight fraction and the melting enthalpy, which suggests a new interesting approach to compare two powerful techniques such as DSC and DMA to study the thermally activated transitions. Multifrequency scans highlighted a strong dependency of E' on the applied frequency throughout the whole temperature range and pointed out that the not only the T_g peaks but also the PCM melting peaks shifted to higher temperatures with increasing frequency. Cyclic DMA tests showed that the decrease in E' at the PCM melting is almost completely recovered (90–95 %) upon crystallization, and the measured difference between the melting and crystallization points (supercooling) increases with the heating/cooling rate. Multifrequency DMA tests allowed the measurement of the activation energy of the glass transition, which appeared not to be affected by the PCM fraction. The peaks related to PCM melting are also affected by the applied frequency, and this is true mostly before than after the peak maximum, when the melting process is only partially complete. As also the position of this peaks changes with frequency, an attempt to apply the Arrhenius approach to these peaks was made, but the strong nonlinearity of the correlation prevented a precise application of the linear regression.

This work contributed to shed light on how the dynamic-mechanical properties of polymers and laminates are affected by the presence of a PCM and by its phase change, which is extremely important for composites designed to combine the structural and TES functions. It also experimented the uncommon use of DMA to study a melting/crystallization phase change and found noteworthy correlations between DMA and DSC parameters.

Although the reactive processing is advantageous as its mildness allows retaining most of the TES capability of the inserted PCM, this approach is implementable only on some specific resin formulations, whereas the vast majority of the thermoplastic polymers must be processed in the molten state. A possible strategy to reduce the impact of processing on the PCM degradation is to change the process from film stacking to commingled yarn compaction. The results of this approach are presented in Subchapter 4.5.

4.5 Melt-spun polypropylene filaments containing a microencapsulated PCM

This Subchapter presents a different approach to produce PCM-containing continuous fiber composites with a traditional thermoplastic polymer as the matrix. This approach involves the production of commingled yarns containing PCM-enhanced thermoplastic filaments and continuous reinforcing fibers. This technique not only allows the production of a component made of a traditional thermoplastic laminate in fewer processing steps than the film stacking method, but it

also shifts the multifunctionality from the level of the composite to the level of the yarn. The approach comprises two steps: the first is the production of polymer filaments containing the PCM, while the second is the combination of these filaments with continuous reinforcing fibers to produce a yarn and the subsequent hot compaction to produce a component. This Subchapter will present the results only of the first step, as the second step will be object of future work. The methods and results presented in this Subchapter were implemented at the research center Leibniz-IPF, in Dresden (Germany).

4.5.1 Materials and methods

The present Section lists the materials used to fabricate these samples, and then it describes in detail the techniques for the preparation of the same. It subsequently lists all the characterization techniques applied on these samples. Since the materials and the characterization techniques have been already detailed in Chapter III, this Section will specify only the experimental parameters that are specific of this Subchapter.

4.5.1.1 Materials

The materials used for the preparation of these laminates are listed in Table IV - 28 (please refer to Section 3.2.4 for the details about the materials).

Table IV - 28. Materials employed in Section 4.5.

Phase	Label	Material
Polymer matrix	PP	Polypropylene
PCM	MC	Paraffin microcapsules

4.5.1.2 Sample preparation

PP-MC monofilaments were produced via melt compounding and melt spinning. The melt compounding step was needed to uniformly disperse the microcapsules and to prevent clogging during spinning. The importance of this step was made evident from a preliminary attempt to avoid the melt mixing phase and manually mix the microcapsules and the PP granules: it resulted in severe inhomogeneity of the spun filament and considerable obstruction of the die capillary. PP granules and microcapsules were melt-mixed in a small-scale micro-compounder Xplore DSM 15 (Xplore Instruments BV, Sittard, The Netherlands), equipped with conical co-rotating screws. The microcapsules were introduced in the compounding chamber gradually, only after the PP was completely molten. The mixing was carried out in batches of 12 g, at 190 °C, for 5 minutes, at a rotor speed of 80 rpm. These mild parameters were

chosen to limit the damage to the thin microcapsule shell, and they were proven sufficient to obtain a homogeneous mixture. The compounded material was then pelletized to ease its loading into the spinning chamber. Three compositions were produced that contained 10, 20 and 30 % by weight of microcapsules.

The filament spinning was performed with a laboratory-scale piston spinning device with a chamber size of 10 g, designed and built at IPF-Dresden. As observable in Figure IV - 32a, the device features two cylindric chambers that make it possible to co-extrude two different materials and to produce core-sheath filaments. In this thesis, the filaments were produced using a single chamber. Monofilaments were spun through a single-hole die with capillary length of 0.6 mm and diameter of 0.3 mm. The spinning temperature was 180 °C up to a MC content of 20 wt%, and 185 °C for the sample containing 30 wt% of MC (Figure IV - 32b). As-spun filaments were collected at a take-up speed of 50, 100 and 200 m/min (Figure IV - 32c). The prepared compositions will be from now on called PP-MCx, where x represents the MC weight fraction in the sample.

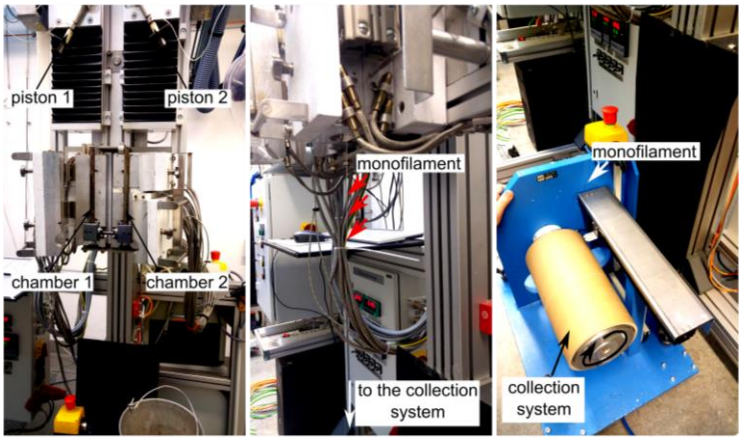

Figure IV - 32. Laboratory-scale piston spinning device designed and built at IPF-Dresden. (a) open chambers with heaters; (b) close chamber with monofilament; (c) collecting step.

4.5.1.3 Characterization

Since the samples are monofilaments, the characterization techniques applied on these samples were quite different from those reported so far for the other polymer composites. Therefore, all the applied techniques are described here in detail, as most of them were not described in Chapter III.

The characterization involved both the compounded PP-MC mixtures and the spun monofilaments, which will be identified from now on as 'as-compounded' (or with a 'c' subscript) and 'as-spun filament' (or with a 'f' subscript), respectively.

The morphology of the filaments and the collocation of the MC were investigated through optical and scanning electron microscopy (OM and SEM). OM micrographs of the lateral surface and the polished cross section of the filaments were acquired with the optical microscope Keyence VHX-2000 (Osaka, Japan), equipped with a VHX-S15 stage control software and a VH-Z500 objective lens. The diameter of the single filaments was measured on the polished cross sections through the software ImageJ. The OM images of the fiber cross section were obtained by embedding the fibers in cylindrical epoxy beads, which were subsequently grinded with a sequence of abrasive papers of decreasing roughness and then polished with polishing clothes. The SEM micrographs of the lateral surface of the filaments were acquired with a SEM Zeiss Ultra Plus (Oberkochen, Germany), after Pt-Pd sputtering.

The density of PP and MC was measured with a helium Ultrapycnometer 1000 (Quantachrome Instruments, Boynton Beach, FL, US). Approx. 5 g of material were loaded in the instrument chamber and several measurements were acquired until a stable output was obtained. The density was calculated as the average of the last 15 measurements. The density of the compounded and as-spun filaments was calculated with the mixture rule considering a pore volume fraction equal to zero. As the density of a composite with no porosity can be calculated by the average density of the constituents weighted by the their volume fraction, the MC volume fraction (ϑ_{MC}) for each sample was first calculated with Equation (IV - 6) as

$$\vartheta_{MC} = \frac{\omega_{MC}}{\omega_{MC} + (1 - \omega_{MC})\frac{\rho_{MC}}{\rho_{PP}}}, \qquad \textbf{(IV - 6)}$$

where ω_{MC} is the MC weight fraction, and ρ_{MC} and ρ_{PP} are the density of MC and PP, respectively. The density of the prepared samples (ρ) was then calculated via the mixture rule through the Equation (IV - 7) as

$$\rho = \rho_{MC} \cdot \vartheta_{MC} + \rho_{PP} \cdot (1 - \vartheta_{MC}). \qquad \textbf{(IV - 7)}$$

The density calculated in this way was compared with that measured on some selected samples, i.e. the three filaments collected at 100 m/min.

Rheological tests were carried out on the as-compounded samples, to assess the effect of MC on the viscosity and the other rheological parameters affecting the spinnability of the polymer melts. These tests were performed on an ARES G2 rotational rheometer (TA Instruments, New Castle, DE, US) under small-amplitude oscillatory frequency sweeps, in a parallel-plate configuration (gap 1.5 mm, diameter 8 mm), at 190 °C under nitrogen flow. Each test started 4 minutes after the specimen

insertion, to ensure the thermal equilibrium. The test allowed the measurement of the storage modulus and loss modulus and the calculation of the loss factor ($tan\delta$) and the complex viscosity. The tests were performed on the neat PP and the three as-compounded PP-MC mixtures. To isolate the effect of the MC addition and exclude that of compounding, the test on the neat PP was not performed on virgin PP granules, but on a PP sample previously subjected to melt compounding with the same parameters used for the PP-MC mixtures. the test was performed also on compounded samples containing 2 wt%, 5 wt% and 15 wt% of MC, to achieve a better understanding of the MC effect on the rheological properties of PP.

DSC was performed with a TA Instruments Q2000 calorimeter (New Castle, DE, US) on specimens of approx. 3 mg. Each sample was subjected to a heating-cooling-heating cycle from -20 °C to 180 °C, at 10 °C/min, under nitrogen atmosphere. As for other polymer/PCM samples presented in this thesis, the tests allowed the measurement of the melting/crystallization temperatures and enthalpy values of the PCM (T_m, T_c, ΔH_m, ΔH_c) related to the effective microcapsule content and integrity. The test was carried out on all the as-compounded and the as-spun samples, but also on the neat MC and the PP granules.

TGA was performed on a TA Instruments Q500 thermobalance, on samples of approx. 3-4 mg, at a heating rate of 10 °C/min up to 700 °C, under nitrogen atmosphere. The tests allowed the calculation of the temperatures corresponding to a mass loss of 1 wt%, 3 wt% and 5 wt% ($T_{1\%}$, $T_{3\%}$ $T_{5\%}$), as well as the peak temperature of the mass loss derivative, measured as the temperature at the maximum degradation rate (T_d). As the residence time of the material in the spinning chamber is of up to 10 minutes, isothermal tests were also performed on the neat MC and the as-compounded samples, to investigate the thermal stability of the MC phase at the selected spinning temperature. The specimens were subjected to a heating ramp of 50 °C/min up to 180 °C, 190 °C or 200 °C, followed by an isothermal step of 20 minutes.

The mechanical properties of the as-spun monofilaments were investigated through single-filament tensile tests, performed with the single-fiber analyzer Textechno Favigraph (Mönchengladbach, Germany). Single filaments were clamped with an initial length of 10 mm and tested at 15 mm/min, with a preload of 1 N. At least 20 specimens were tested per composition. The test allowed the measurement of the strain at break (ε_b) and the filament tenacity (σ_M), calculated as the maximum load divided by the fiber fineness and measured in cN/tex. The elastic modulus (E) was measured as the slope of the secant to the stress-strain curve between the strain values 0.05 % and 0.25 %.

4.5.2 Results and discussion

4.5.2.1 Microstructure

The OM micrographs of the filaments are displayed in Figure IV - 33a-f.

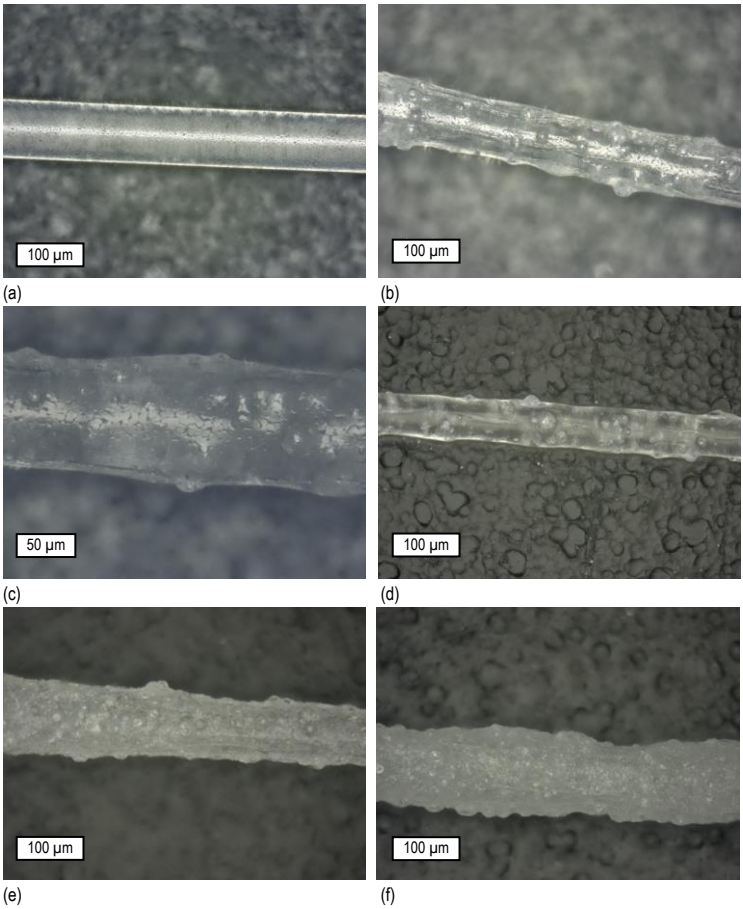

Figure IV - 33. Optical microscope images of the lateral surfaces of the as-spun filaments. (a) PP (100 m/min); (b) PP-MC10 (100 m/min); (c) PP-MC10 (100 m/min), higher magnification; (d) PP-MC10 (200 m/min); (e) PP-MC20 (100 m/min); (f) PP-MC30 (100 m/min).

The surface of the neat PP fibers (Figure IV - 33a) is smooth and regular, and this is observed on the samples collected at all the collection speeds. Conversely, the surface of the MC-containing fibers is irregular; some capsules are visible as projections underneath the fiber surface, and this effect increases with the MC content. This peculiar fiber morphology depends largely on the capsule dimensions, as they are of the same order of magnitude as the fiber diameter. Some possible strategies to avoid this effect include the use of smaller capsules (Leskovšek et al., 2004) or their confinement in the fiber core by producing core-sheath filaments, as exemplified by Zhang et al. (Zhang et al., 2005). However, even though a rough fiber surface may be an issue for fibers intended for the textile industry, it is not a concern for the production of hybrid yarns, as these PP-MC filaments are only a way to distribute the PP matrix and the MC more homogeneously. For this application, an increased fiber roughness may rather improve the mechanical interlocking between the different fiber types in the hybrid yarn and ease the yarn handling (Brody, 1985). Moreover, the capsules are completely covered with PP matrix, as more clearly observable from the SEM micrographs (Figure IV - 34), which prevents capsule damage and removal in the operations after spinning.

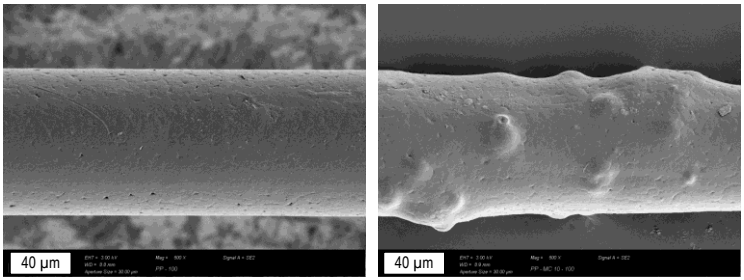

(a) (b)

Figure IV - 34. SEM micrographs of the lateral surface of the as-spun filaments. (a) PP, spun at 100 m/s; (b) PP-MC10, spun at 100 m/s.

Figure IV - 34 also shows that the surface of the fibers collected at 50 and 100 m/min have the typical pattern of polymer crystals; this implies that the drawing imposed by the set collection speed was not sufficient to strongly orient the polymer chains, which is one of the reasons for the scarce mechanical properties of these filaments (see Section 4.5.2.4). This phenomenon is slightly reduced for fibers collected at 200 m/min. Nevertheless, once again, this is not fundamental for the application intended for these fibers.

Considerably more important are the capsule distribution and the filament homogeneity. It can be noticed that, in the samples PP-MC10 and PP-MC20, the capsules are homogeneously distributed along the fiber length and they are not aggregated, but in the sample PP-MC30 the diameter varies remarkably, which was

also appreciable from a visual observation of the as-spun fibers, especially for the filaments collected at the highest speed. This effect prevents a consistent characterization of the mechanical properties, which will be described in Section 4.5.2.4. More information on the fiber diameters and morphology can be acquired from the filament cross-sections, shown in Figure IV - 35a-f.

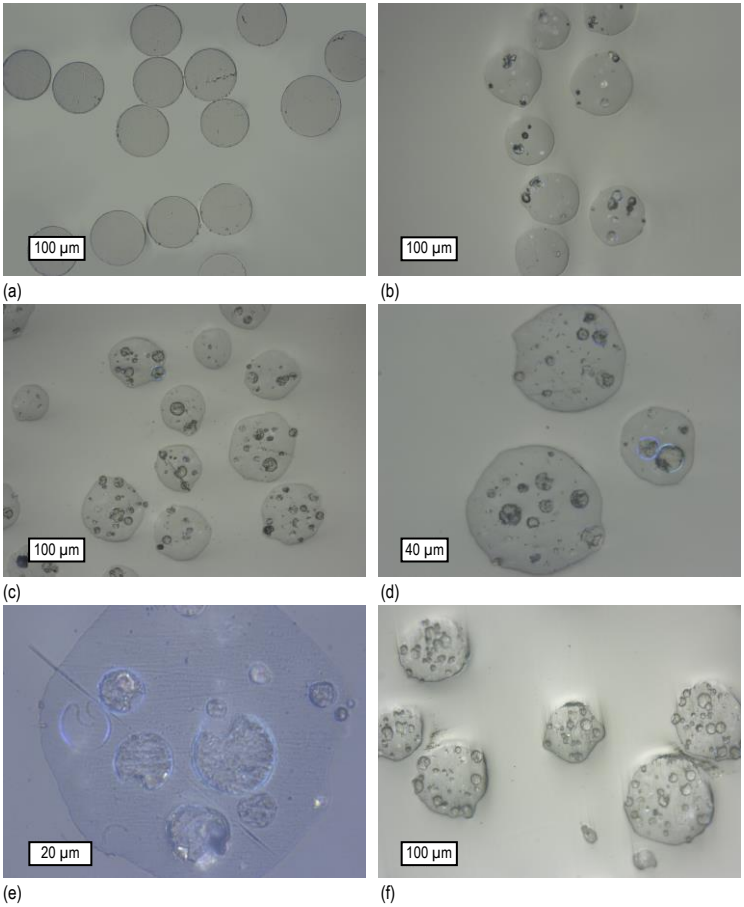

Figure IV - 35. Optical microscope images of the polished cross section of the as-spun filaments, collected at 100 m/min. (a) PP; (b) PP-MC10; (c) PP-MC20; (d,e) PP-MC20 (higher magnification); (f) PP-MC30.

The neat PP fibers have a regular circular cross section, while the profile of the PP-MC fibers is irregular and presents protuberances in correspondence of the capsules. The capsules are homogeneously distributed in the cross section and are

visible as well-defined domains. Their core-shell morphology is clearly observable, especially at high magnifications, which suggests that the integrity of most of them is preserved during spinning. As observable from the data reported in Figure IV - 36, the fiber diameter decreases with increasing collection speed, but, at a fixed collection speed, it is not significantly different for fibers containing different amounts of capsules. What is remarkably affected from the MC concentration is the measurement scatter, as the standard deviation increases with the MC fraction.

These results suggest that smaller capsules could allow the production of more regular filaments. However, smaller capsules generally have a lower core-to-shell mass ratio, and thus a lower total phase change enthalpy, and for the intended application it is probably not appropriate to reduce the TES performance to maximize the fiber homogeneity and mechanical properties.

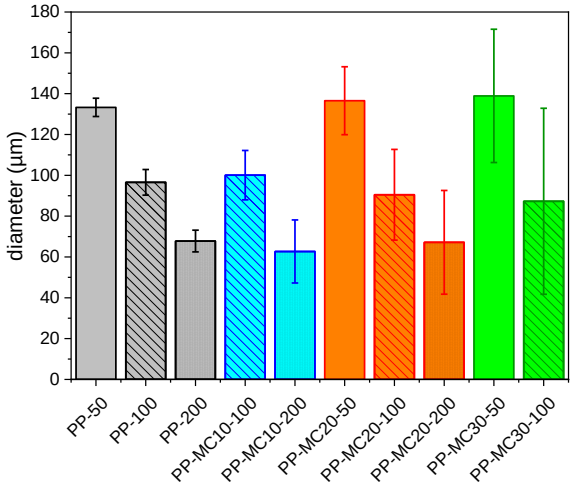

Figure IV - 36. Filament diameters (mean values and standard deviation) obtained from the micrographs of the polished cross-sections.

4.5.2.2 Physical properties

Table IV - 29 reports the results of the density measurements. These values were useful to calculate the elastic modulus from the measured fineness of the filaments and the stress values reported in cN/tex (see par. 4.5.2.4), and to obtain values of the diameters to be compared with those acquired from the OM analysis.

The measured density for the neat PP is 0.8654 g/cm^3, while the bulk density of the microcapsules is 0.9425 g/cm^3, in good accordance with the nominal value reported on the datasheet (0.9 g/cm^3) and slightly higher than that of PP. Such

similarity in density between PP and MC is advantageous for the preparation of the PP-MC mixtures, as it favors a homogeneous dispersion and limits phase separation. Table IV - 29 also reports the calculated density and capsule volume fraction (ϑ_{MC}) for each sample. These values of density, calculated via the Equation (IV - 7), were in good agreement with those measured on some selected compositions, i.e. the filaments PP-MC10-f, PP-MC20-f and PP-MC30-f collected at 100 m/min. Their density resulted as 0.8698±0.0005 g/cm^3, 0.8805±0.0004 g/cm^3, and 0.8938±0.0004 g/cm^3, respectively.

Table IV - 29. Results of the density measurements on PP and MC and calculation of the MC volume fraction and density for the samples PP-MCx (x = 10, 20, 30).

Sample	Density (g/cm^3)	ϑ_{MC} (vol %)
PP	0.8654 ± 0.0001	0
MC	0.9425 ± 0.0014	100
PP-MC10	0.8731 ± 0.0001	0.0925 ± 0.0004
PP-MC20	0.8807 ± 0.0002	0.1867 ± 0.0006
PP-MC30	0.8885 ± 0.0003	0.2824 ± 0.0007

ϑ_{MC} = MC volume fraction.

Dynamic rheological tests were performed on the as-compounded mixtures, in order to assess the effect of the microcapsules on the rheological behavior of the melted PP. The values of complex viscosity are presented in Figure IV - 37a.

All the compositions show a typical non-Newtonian pseudoplastic behavior, as their complex viscosity decreases with increasing shear rate, and this shear-thinning effect is stronger at high shear rates. As expected, the complex viscosity increases with the MC content, and this effect is more evident at lower shear stresses, as also observed for the polyamide-based composites containing paraffin microcapsules described previously in this Chapter (Section 4.3) and widely reported in the literature for polymer systems containing microfillers (Doumbia et al., 2015; Rueda et al., 2017b). The neat PP shows a Newtonian plateau at low frequencies and a noticeable shear-thinning zone above approx. 30 rad/s. This behavior is observed also in the samples containing up to 10–15 wt% of microcapsules. Above this MC loading, the noticeable viscosity increase at the lowest limit of the considered shear rate interval implies the presence of a yield stress. This is commonly reported for highly-filled polymer microcomposites, and it is generally attributed to the increasing particle-particle interaction and the formation of a filler network (Rueda et al., 2017a). As the MC fraction increases, the transition from the Newtonian plateau to the shear-thinning region becomes broader and occurs at lower shear rates, while the slope of the power-law region increases. These trends are consistent with those reported in the literature for micro- and nano-filled polymer composites (Poslinski et al., 1988; Dorigato et al., 2010).

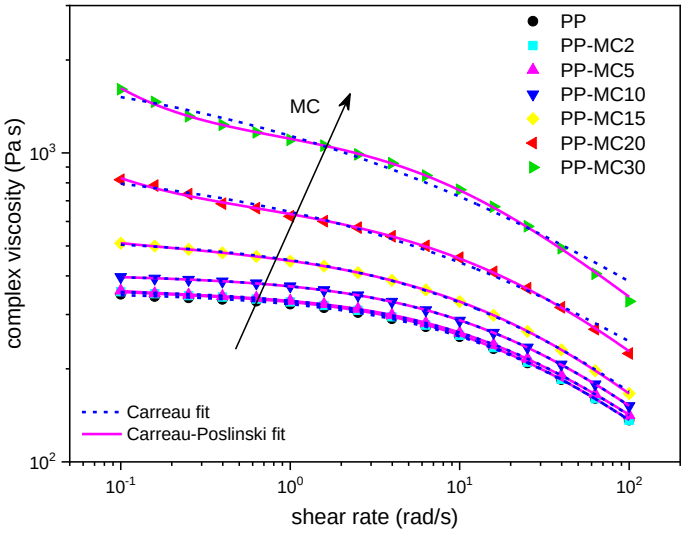

(a)

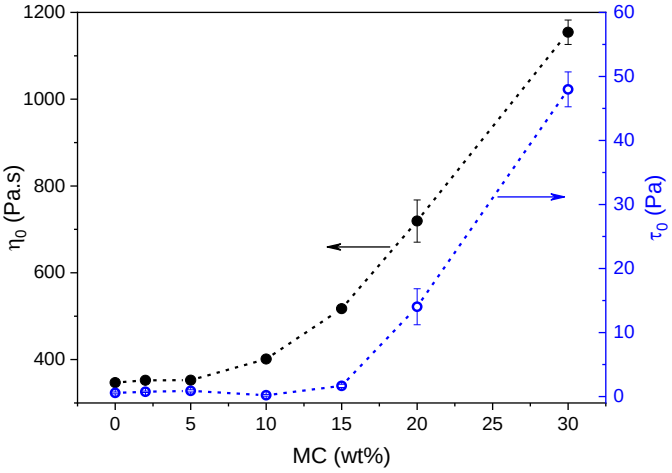

(b)

Figure IV - 37. (a) Complex viscosity as a function of the shear rate for the compounded samples PP and PP-MCx (x = 2, 5, 10, 15, 20, 30), with the results of the fitting with the Carreau and the Carreau-Poslinski model; (b) Parameters derived from the fitting with the Carreau-Poslinski model: zero-shear viscosity (η_0) and yield stress (τ_0) as a function of the MC weight fraction.

An attempt was made to fit the experimental data with the Carreau model (Carreau, 1972; Osswald and Rudolph, 2015), one of the most common models to describe the rheological behavior of polymer melts. The model is reported in Equation (IV - 8):

$$\frac{\eta_{\dot{\gamma}} - \eta_{\infty}}{\eta_0 - \eta_{\infty}} = (1 + |t\dot{\gamma}|^{a})^{\frac{n-1}{a}}, \qquad \textbf{(IV - 8)}$$

where $\eta_{\dot{\gamma}}$ is the value of viscosity at a specific shear rate, η_0 and η_{∞} are the values of viscosity at zero and infinite shear rate, respectively, $\dot{\gamma}$ is the shear rate, t is a time constant, n is the power law or flow index, which accounts for the shear thinning behavior, and a is related to the width of the transition region between the Newtonian plateau and the power law region (Osswald and Rudolph, 2015).

The results of the fit are reported in Figure IV - 37a. This model is able to fit properly the experimental data only up to a MC content of 15 wt%, above which it fails in predicting the experimental trend. This derives from the fact that the Carreau model does not take into account the rise in viscosity at lower shear stresses, which implies the presence of a yield stress that must be overcome to initiate the flow. The Carreau model can be modified by adding a term that includes the yield stress, according to the model presented by Poslinski et al. (Poslinski et al., 1988), reported in Equation (IV - 9:

$$\frac{\eta_{\dot{\gamma}} - \eta_{\infty}}{\eta_0 - \eta_{\infty}} = \frac{\tau_0}{\dot{\gamma}} + (1 + |t\dot{\gamma}|^{a})^{\frac{n-1}{a}}, \qquad \textbf{(IV - 9)}$$

where τ_0 is the yield stress and the other parameters have the same values as for Equation (IV - 8). In the model presented by Poslinski et al. (Poslinski et al., 1988), a was kept equal to 2 as in the former Carreau model, while in the present work, a is a free parameter. Figure IV - 37a also reports the results of the fitting with this model. With the additional term, the fitting for the highly filled samples improves remarkably. Figure IV - 37b reports the trends of η_0 and τ_0 obtained from the fit, presented with their standard error. Both these parameters increase with an increase in the MC content and the value of τ_0 is significantly higher than 0 for an MC concentration higher than 15–20 wt%, which explains the suitability of the unmodified Carreau model (Equation (IV - 8)) to fit the experimental data for the less concentrated compositions.

Figure IV - 38 reports the values of the storage modulus (G'), the loss modulus (G''), and the loss factor ($tan\delta$) as a function of the applied shear rate.

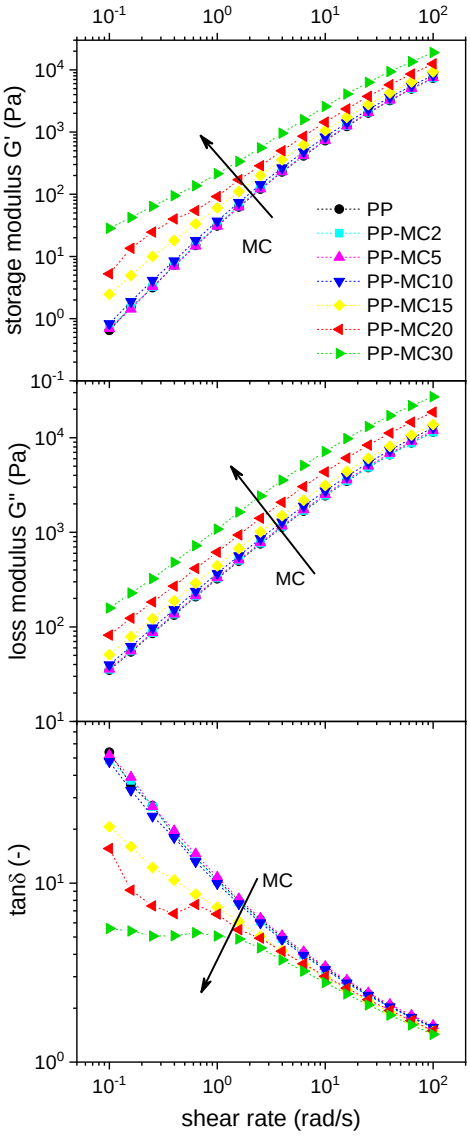

Figure IV - 38. Storage modulus G', loss modulus G'' and $tan\delta$ as a function of the shear rate for the compounded samples PP and PP-MCx (x = 2, 5, 10, 15, 20, 30).

G' and G'' increase with the MC fraction, which is more evident at lower shear rates, and the values of G' especially evidence the occurrence of a yield stress for the highly filled compositions. Conversely, the values of $tan\delta$ follow the opposite trend, as the $tan\delta$ curve is shifted to lower values with an increase in the MC fraction; moreover, the shape of the trend of the MC-loaded samples differs sensibly from that of the neat PP, especially for MC loadings higher than 15 wt%.

4.5.2.3 Thermal properties

One of the most important properties that these PCM-enhanced fibers should exhibit is a high phase change enthalpy, which depends on the effective PCM weight fraction at the end of the filament production. This was assessed through DSC tests, performed to evaluate the TES properties after each processing step, i.e. the melt compounding and the melt spinning. The DSC thermograms obtained on the filaments collected at 100 m/min are reported in Figure IV - 39a, while Figure IV - 39b reports the first heating scan of the filaments and the compounded samples and also shows the enthalpy values and the peak temperatures.

Similarly to the results found for the samples previously reported in this Chapter, for all the thermograms reported in Figure IV - 39a, the heating scan presents two main endothermic signals: the first at 40-50 °C, related to the PCM melting, and the second at 140-160 °C, associated to the PP melting. The cooling scan shows the exothermic signals of the crystallization of the two phases, at 30-40 °C and 110-130 °C, respectively. For the transition of the PCM, the signals show two main peaks, which resemble those visible in the DSC thermogram of the neat MC. As already described previously in this Chapter and elsewhere in the literature (Wang et al., 2003) for various types of paraffinic PCMs, the presence of two or more peaks derive from a sequence of transitions on heating and on cooling. The first smaller peak encountered on heating is associated to the solid-solid transition from the crystalline phase to the so-called "rotator phase", while the second peak could be related to the solid-liquid melting transition. Analogous transitions are observable on cooling. This explanation is in good agreement with the detailed investigation performed by Wang et al. (Wang et al., 2003) on the transitions of *n*-docosane ($C_{22}H_{46}$), which has approximately the same melting temperature as the PCM contained in the MC. This aspect will be described more in detail in Chapter VII. Since all the mentioned transitions contribute to the total enthalpy and occur in a relatively narrow temperature interval, the precise assignment of each peak is out of the scope of this work, and it would be also relatively difficult, as the PCM contained in the microcapsules is probably a mixture of alkanes and the precise molecular weight distribution has not been measured.

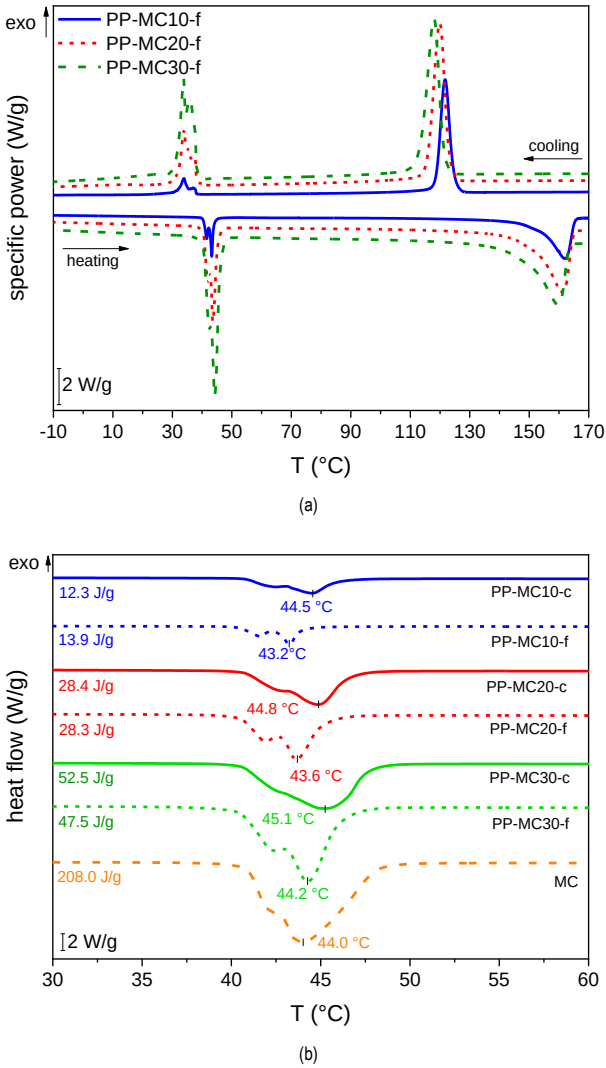

Figure IV - 39. (a) DSC thermograms of the MC-containing filaments collected at 100 m/min (first heating scan and cooling scan); (b) thermograms of the as-compounded mixtures and the MC-containing filaments (100 m/min), with a focus on the melting peak of the PCM. The plot shows the peak temperatures and the melting enthalpies.

As reported in Figure IV - 39b and in Table IV - 30, the melting enthalpy of the PCM increases with the nominal MC content. If considered that the phase change

enthalpy of the neat MC in this specific work is 208.0 J/g, the enthalpy of the filaments is lower than expected, being approx. 70 % of the value calculated considering the nominal PCM content. These results are detailed in Table IV - 30.

Table IV - 30. expected and measured phase change enthalpy and nominal and experimental PCM content in the prepared filaments (samples PP-MCx-f, x = 10, 20, 30).

Sample	Nominal PCM content (wt%)	Expected enthalpy (J/g)	Measured enthalpy (J/g)	Relative enthalpy (%)	Experimental PCM content (wt%)
PP-MC10-f	10	20.8	13.9	66.8	6.7
PP-MC20-f	20	41.6	28.3	68.0	13.6
PP-MC30-f	30	62.4	47.5	76.1	22.8

From the measured enthalpy data, an experimental residual PCM weight fraction can be calculated for each sample, by applying an approach similar to that employed in Subchapter 4.4 for the EL-MC-CF laminates and also reported by Rezaie et Montazer (Rezaie and Montazer, 2018); these data are also presented in Table IV - 30. The PCM mass fraction measured at the end of the process is lower than the initial one. This is a consequence of the thermo-mechanical degradation of the MC during processing and could be alleviated by applying milder processing parameters.

It is important to understand which processing step is the major responsible for the PCM degradation, and this was evaluated through a comparison between the DSC scans of the filaments and the compounded mixtures (Figure IV - 39b). The signals of the filament samples are narrower and their peak temperatures (also reported in Figure IV - 39b) are slightly lower than those of the corresponding compounded mixtures. This could derive from the different specimen geometry, which may have influenced the contact with the crucible and the heat transfer during the test, even though the specimen mass is similar. However, the melting enthalpy of the filaments is approximately the same (never less than 88 %) as that measured on the compounded mixtures, which implies that the majority of the PCM degradation happens during the melt compounding step. Therefore, although the employed PP grade has a remarkably low viscosity, the shear stresses developed during melt compounding are sufficient to damage a certain fraction of MC. This effect was observed also on the PA-MC composites mixtures presented in Subchapter 4.3. The results could be improved by employing microcapsules with a mechanically stronger shell or by changing the compounding parameters to reduce the shear stresses. Conversely, the decrease in enthalpy is considerably lower during melt spinning, which suggests that in this case the processing parameters are mild enough to preserve the residual microcapsule integrity and PCM fraction.

A measured specific enthalpy lower than the nominal one can be not only due to PCM degradation, but also to the fact that a fraction of PCM has leaked out of the capsules and dissolved into the PP phase, which prevents the single PCM chains from

crystallizing properly and contributing to the total developed phase change enthalpy (Zhang et al., 2010b). This aspect could be evaluated through TGA, which allows the estimation of the weight fraction of the different constituents. TGA tests were performed also to assess the thermal stability of the virgin materials, the compounded mixtures and the filaments. The results of this investigation are reported in Figure IV - 40 and Table IV - 31.

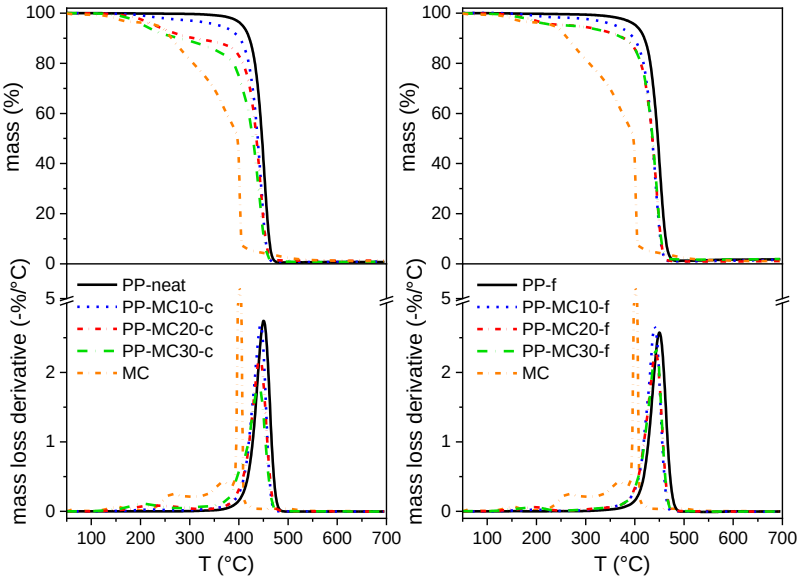

Figure IV - 40. TGA thermograms of the virgin and as-compounded (left) and the as-spun samples (right). Residual mass and mass loss derivative as a function of temperature.

The virgin PP degrades in a single step at approx. 450 °C, and the same behavior is observed also on the PP filament, which suggests that the spinning step does not decrease the thermal stability of PP. Conversely, the thermal degradation of the microcapsules, as already described in the previous Subchapters, begins with several small steps, related to free (non-encapsulated) paraffin and some low molecular weight compounds, while the subsequent steps are related to the thermal degradation of the paraffin and the melamine-formaldehyde shell. The sharp peak in the mass loss derivative signal indicates that most of the mass loss happens in a relatively narrow temperature interval. This mass loss can be associated to the damage of the microcapsule shell and the sudden release of the PCM core. This spike was observed also on repeated measurement, but it is not observed in any of the other PP-MC composites, as the surrounding matrix may modify the thermal conductivity of

the specimen and the mass loss rate. The degradation curves of the as-compounded mixtures and the as-spun filaments consist in an initial mass loss at 200-300 °C, which increases with the MC content, followed by a second step at 400-500 °C that corresponds to the degradation of the PP phase. Generally speaking, the thermal stability of the blends decreases with an increase in the MC content, as the MC phase is less thermally resistant than PP. This is deducible both from the trend of the mass loss (Figure IV - 40) as an anticipation in the degradation onset, and from the data reported in Table IV - 31.

Table IV - 31. Main results of the TGA tests on the virgin, as-compounded and as-spun samples.

Sample	$T_{1\%}$ (°C)	$T_{3\%}$ (°C)	$T_{5\%}$ (°C)	T_d (°C)
PP-neat	359.5	395.8	407.7	450.8
PP-f	335.3	384.8	402.5	450.7
PP-MC10-c	205.0	302.0	361.7	444.3
PP-MC10-f	197.0	324.4	361.6	442.4
PP-MC20-c	169.3	207.6	231.2	442.8
PP-MC20-f	153.7	198.2	276.5	443.4
PP-MC30-c	155.7	189.2	208.3	440.6
PP-MC30-f	148.3	193.3	271.0	443.0
MC	125.3	164.0	235.3	402.6

$T_{1\%}$, $T_{3\%}$ $T_{5\%}$= temperatures corresponding to a mass loss of 1 wt%, 3 wt% and 5 wt%; T_d = peak temperature of the mass loss derivative; PP-neat = virgin granules of PP; -f = as spun; -c = as compounded.

It can be further observed that, especially for the samples PP-MC20 and PP-MC30, the initial mass loss is significantly higher for the compounded samples than for the filaments. This suggests that the filaments contain less PCM than the compounded specimen, but the almost negligible decrease in melting enthalpy after spinning (see DSC results, Figure IV - 39b) seems to disagree with this hypothesis. These results can be explained by considering that the compounding step causes the breakage of a consistent fraction of microcapsules, but a portion of the leaked paraffin does not degrade, but it rather dissolves in the PP matrix. As observed in other studies (Zhang et al., 2010b), the surrounding matrix could prevent this PCM fraction to crystallize properly, and therefore it does not contribute to the total phase change enthalpy. Since it is not protected by the shell, the fraction of free paraffin degrades at low temperatures and could also partially degrade during the spinning step.

These TGA tests, performed by applying a heating ramp, have been useful to investigate the thermal degradation temperatures of the PP-MC mixtures. However, a complete thermal analysis must ensure that the materials do not degrade during processing: the thermal history applied during melt compounding and melt spinning is more complex than a temperature ramp, and it is important to take into account the residence times at certain temperatures during the compounding and spinning steps.

Therefore, isothermal TGA tests were performed at three different temperatures on the neat PP and MC, as well as on the three as-compounded samples. The results of this analysis are reported in Figure IV - 41 and Table IV - 32.

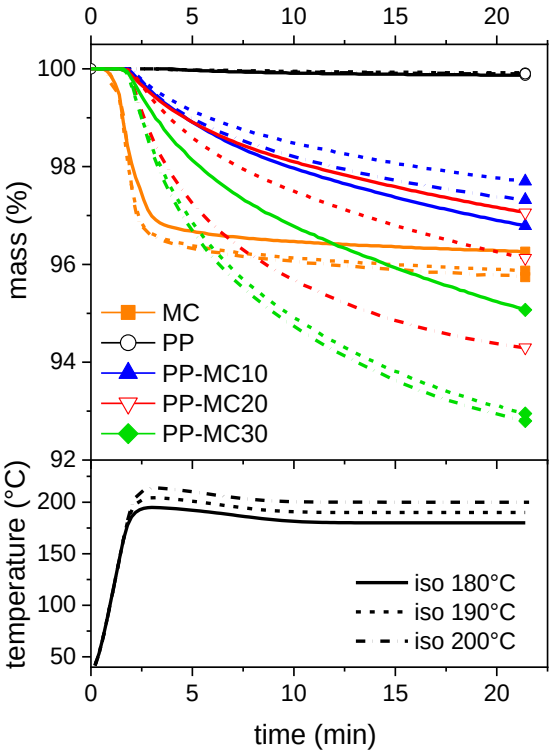

Figure IV - 41. Isothermal TGA tests on the samples PP, MC and as-compounded PP-MCx (x = 10, 20, 30). The residual mass and the applied temperature profiles are reported as a function of time. Solid = test at 180 °C; dashed = test at 190 °C; dash-dot = test at 200 °C.

As expected, the neat PP experiences a negligible mass loss in the investigated time span for all the considered temperatures. The neat microcapsules undergo an initial mass loss of approx. 3-4 wt%, as happens in the TGA ramp tests. The residual mass is then stable over time for all the considered temperatures, which agrees with the results of the ramp TGA tests and the indication of the thermal stability provided in the producer's datasheet. This suggests that the chosen microcapsules can withstand the temperatures needed to process a polymer melt, unlike most of the non-encapsulated organic PCMs mentioned in the literature (Jeong et al., 2014; Huang et al., 2017; Cherif et al., 2018; Yuan et al., 2018). Conversely, the behavior of

the compounded mixtures deviates markedly from this trend, as the mass loss continuously increases with time, temperature and MC concentration. As the PP phase has proven to be thermally stable, the mass loss can be ascribed to the degradation of free paraffin released from the capsules broken during compounding. This implies that the thermo-mechanical stresses during compounding are the main reason for the decreasing thermal stability of the PCM, which suggests that a milder compounding would help in preserving the MC integrity and the overall thermal stability. This degradation must be considered when setting the subsequent processing parameters (i.e. those of the melt spinning). Nevertheless, the mass loss at the chosen spinning temperature (180 °C) and after the maximum residence time during spinning (10 min) never exceeds 3 wt%, which proves the suitability of the chosen parameters and processes.

Table IV - 32. Results of the isothermal TGA tests on the as-compounded samples. Values of mass loss (wt%) after 10 minutes at the three test temperatures.

Sample	180 °C	190 °C	200 °C
PP	0.09	0.05	0.07
MC	3.53	3.87	3.93
PP-MC10	2.03	1.52	1.80
PP-MC20	1.90	2.50	4.32
PP-MC30	3.22	5.09	5.26

4.5.2.4 Mechanical properties

Figure IV - 42 illustrates the main results of the single-fiber tensile tests. Since the tensile testing dynamometer measures directly the fineness of each tested fiber specimen, the values of stress are indicated in cN/tex, a common procedure for fibers and filaments. It was not possible to test the filaments containing an MC fraction of 30 wt%, as they broke always before the beginning of the test or in the preload phase; this was probably due to the strong inhomogeneity of the cross section (see Section 4.5.2.1). The PP filaments collected at 50 m/min (PP-50) could not be brought to breakage, because their elongation at break was higher than the maximum displacement allowed by the testing device. Therefore, the values of tenacity and strain at break reported in Figure IV - 42 concern the last measured point in the stress-strain curve.

It can be observed that the fineness decreases as the collection speed increases, but it does not change significantly for fibers collected at the same speed containing different amounts of MC. On the other hand, the MC addition dramatically affects the stress-strain behavior. The tenacity of the fibers increases with the collection speed, thanks to a higher chain orientation, but it decreases with an increase

in the MC content. For example, the PP filaments collected at 100 m/min feature a tenacity of 7.0 ± 0.4 cN/tex, whereas for the sample PP-MC20-100 the tenacity is 2.3 ± 0.5 cN/tex, being approx. 33% of the original value. The elongation at break decreases with increasing MC fraction and collection speed.

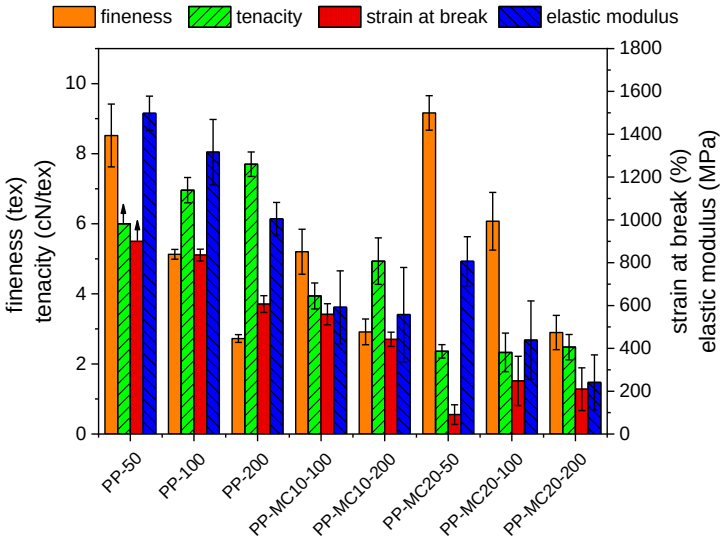

Figure IV - 42. Mechanical properties of the produced filaments: main parameters obtained from the single-fiber tensile tests.

It can be observed that the tenacity of all the produced filaments is rather low and the elongation at break remarkably high compared to other polymeric fibers for textile applications (Morton and S., 2008); this is likely due to the limited draw ratio, not sufficient to significantly align the polymer chains along the fiber axis. The density values reported in Table IV - 29 were used to calculate the filament diameters from the fineness values measured by the tensile testing machine. It was observed that these values were not significantly different from those measured with the optical microscope and reported in Figure IV - 35; therefore, the values of density were employed to calculate the elastic modulus in MPa. The results of this calculation are also reported in Figure IV - 42. The filament stiffness is also negatively affected by the MC introduction. The decreasing mechanical performance of polymer filaments after the addition of a PCM is a common phenomenon, and it is reported elsewhere in the literature (Iqbal and Sun, 2015; Cherif et al., 2018). It could be mitigated by a post-drawing process (Cherif et al., 2018), or by employing microcapsules with a smaller diameter and/or a narrower particle size distribution (Cho et al., 2002).

However, as these filaments are intended for the production of hybrid yarns and not for the textile industry, the mechanical properties are not the most important parameter, and their optimization lies outside the scope of this thesis.

4.5.3 Conclusions

PCM-enhanced polypropylene filaments were successfully produced via small-scale melt compounding and piston-type melt spinning devices, and the subsequent characterization of the physical, thermal and mechanical properties demonstrated their suitability for the production of multifunctional hybrid yarns where they are considered to serve as polymer matrix. Isothermal TGA on the neat PP and MC revealed that their thermal stability is sufficiently high to withstand the applied processing temperatures, but the same test on the as-compounded mixtures showed a not negligible mass loss, which is due to the degradation of the PCM leaked out from those microcapsules that were damaged during compounding. Nevertheless, the mass loss after 10 minutes, which is the maximum residence time in the spinning chamber, is still acceptably low, which indicates that the compounding parameters were mild enough to preserve the integrity of a considerable fraction of MC. For the characterization of the filaments, microscopy techniques highlighted that the inclusion of MC increased the filament surface roughness, but it did not significantly influence the diameter, which varied in the range 70-140 μm according to the collection speed. DSC tests revealed that the melting enthalpy increases with an increasing MC fraction, up to 48 J/g, while single-filament tensile tests evidenced a decrease in the mechanical properties with an increase in the MC content.

These results are promising for the production of PCM-enhanced hybrid yarns. Future work will involve the use of these MC-containing filaments to produce a thermoplastic laminate via hot compaction, as well as the study of the scalability of the process with the use of a twin-screw extruder and the co-winding with reinforcing fibers for the production of hybrid yarns.

4.6 General conclusions of Chapter IV

This Chapter presented the method and the results of four case studies of PCM-enhanced composites having thermoplastic matrices.

In Subchapter 4.2, the characterization of the PA/PCM/GF laminates evidenced that the microcapsules are more suitable than CNT-stabilized paraffin (ParCNT) to be compounded with a traditional thermoplastic matrix, due to their higher thermal resistance. However, the melt-compounding and the two hot-pressing operations damage the microcapsule shells considerably, thereby causing paraffin leakage and degradation and diminishing the total final phase change enthalpy.

A remarkable improvement of the final TES properties was obtained by reinforcing the PA-based composites with discontinuous carbon fibers, as described in the Subchapter 4.3. This was possible because this strategy allows avoiding one of the two hot-pressing steps. However, this approach is only applicable to discontinuous fiber composites.

Further increases in the mechanical and TES properties were achieved by using a reactive thermoplastic matrix, as reported in Subchapter 4.4. Such resin allows avoiding all the processing steps at high temperature in the molten state, thus requiring considerably milder processing conditions that do not cause PCM degradation.

Since reactive processing is not applicable to the most common thermoplastic matrices, an additional approach was explored that involves the production of multifunctional commingled yarns, where the PCM phase is embedded in the polymer filaments. Subchapter 4.5 illustrates the results of this approach, which was limited to the production of PP filaments containing PCM microcapsules. The approach is promising, but the processing parameters still need adjustment to limit the PCM degradation. Future work in this topic will involve experimental trials to produce the multifunctional commingled yarn by coupling the produced PP-MC filaments with continuous glass or carbon fibers, and further experimental work will be then needed to produce a composite part starting from this hybrid yarn.

4.7 Acknowledgements

Dr. Seraphin H. Unterberger (Universität Innsbruck) is acknowledged for performing LFA and rheological tests (Subchapter 4.3). Ms. Claudia Gavazza (DII Unitn) is acknowledged for her support to SEM analysis (Subchapters 4.3 and 4.4). Dr. Harald Brünig (Leibniz-IPF Dresden) is acknowledged for providing access and expertise about the melt spinning device (Subchapter 4.5). Dr. Roland Vogel (Leibniz-IPF Dresden) is acknowledged for his experimental support to the rheological tests (Subchapter 4.5). Ms. Sabine Krause (Leibniz-IPF Dresden) is acknowledged her contribution to the thermal analysis (Subchapter 4.5). Ms. Steffi Preßler (Leibniz-IPF Dresden) is acknowledged for her contribution in the single-fiber tensile tests (Subchapter 4.5). Mr. Holger Scheibner (Leibniz-IPF Dresden) is acknowledged for his contribution to the pycnometer tests (Subchapter 4.5).

Chapter V

Thermosetting TES composites

Part of this chapter has been published in:

- G. Fredi, A. Dorigato, L. Fambri, A. Pegoretti,
  Wax confinement with carbon nanotubes for phase changing epoxy blends,
  Polymers 2017, 9 (9), 405/1-405/16

- A. Dorigato, G. Fredi, L. Fambri, A. Pegoretti,
  Multifunctional epoxy/carbon fiber laminates for thermal energy storage and release,
  Composites Science and Technology 2018, 158, 101-111

- A. Dorigato, G. Fredi, A. Pegoretti
  Application of the thermal energy storage concept to novel epoxy/short carbon fiber composites,
  Journal of applied polymer science 2019, 136 (21), 47434/1-47434/9.

- G. Fredi, A. Dorigato, L. Fambri, A. Pegoretti,
  Thermal Energy Storage with Polymer Composites,
  American Society for Composites 2019 - Thirty-Fourth Technical Conference Atlanta, GA, US, Kalaitzidou, K., Ed. Atlanta, GA, US, 2019.

- G. Fredi, A. Dorigato, A. Pegoretti,
  Detailed experimental and theoretical investigation of the thermo-mechanical properties of epoxy composites containing paraffin microcapsules for thermal management,
  Polymer Engineering and Science, In press

- G. Fredi, A. Dorigato, L. Fambri, A. Pegoretti,
  Effect of phase change microcapsules on the thermo-mechanical, fracture and heat storage properties of unidirectional carbon/epoxy laminates
  Polymer Testing, Submitted

5.1 Introduction

The aim of this Chapter is to illustrate the experimental techniques and the results of the characterization of PCM-containing composites having a thermosetting matrix. Since epoxy resins are the most widely used thermosetting matrices for high-performance composites, one resin of this type was selected as the matrix for this thesis work. It was combined with both microencapsulated and shape-stabilized PCMs and with continuous and discontinuous carbon fibers.

Subchapter 5.2 deals with the incorporation of CNT-stabilized paraffin powder (ParCNT) in an epoxy resin and the study of the thermo-mechanical properties of the resulting samples. The prepared mixtures were then employed to prepare laminates via the introduction of a bidirectional carbon fiber fabric.

The same epoxy resin was then combined with a different PCM, the microencapsulated paraffin MC, and the results of the characterization of these systems are the subject of the Subchapter 5.3.

Such epoxy/MC systems were then employed with continuous carbon fibers and discontinuous milled carbon fibers, and the resulting reinforced composites are analyzed in Subchapters 5.4 and 5.5, respectively.

5.2 Carbon fiber/epoxy laminates containing paraffin shape-stabilized with carbon nanotubes

This Subchapter presents the results of the characterization of carbon/epoxy laminates containing paraffin powder shape-stabilized with carbon nanotubes (CNTs). The preparation of this kind of PCM powder, called ParCNT, was described in Section 3.2.1.1 together with partial preliminary results of its characterization, comprising particle morphology and size distribution. This shape-stabilized PCM was also already applied in the fabrication of the multifunctional glass/polyamide laminates described in Subchapter 4.2. However, the characterization of those laminates indicated that the CNT-stabilized paraffin is a less performant choice than the paraffin microcapsules (MC), mostly because ParCNT exhibited a lower thermal resistance than MC. The CNT content brought a considerable viscosity rise in the processing of the polyamide matrix in the molten state. Since most of the problems of using ParCNT stem from the high temperatures and shear stresses involved during processing of a thermoplastic matrix, an attempt was made to combine it with a thermosetting matrix, namely an epoxy resin, whose production process is milder and especially requires a lower temperature. This Subchapter will first present the results of the characterization of epoxy/ParCNT mixtures and then introduce the methods and results of using such mixtures as matrices for carbon-fiber thermosetting laminates.

5.2.1 Materials and methods

The present Section lists the materials used to fabricate these samples, and then it describes in detail the techniques for the preparation of the same. It subsequently lists all the characterization techniques applied on these samples. Since the materials and the characterization techniques have been already detailed in Chapter III, this section will specify only the experimental parameters that are specific of this Subchapter.

5.2.1.1 Materials

The materials used for the preparation of these laminates are listed in Table V - 1 (please refer to Section 3.2.4 for the details about the materials).

Table V - 1. Materials employed in Subchapter 5.2.

Phase	Label	Material
Polymer matrix	EP	Epoxy resin
Reinforcement	CF	Bidirectional carbon fiber fabric
PCM	ParCNT	Paraffin shape-stabilized with carbon nanotubes (CNTs) in a weight fraction of 10 wt%, and cryogenically pulverized

As observable from the data reported in Table V - 1, the PCM contained in the matrices and laminates described in this Subchapter is a paraffin shape-stabilized with CNTs, prepared as described in Chapter III, Section 3.2.3.1, similar to that employed for the preparation of the polyamide/glass laminates described in Subchapter 4.2.

The aim of this work was to assess if the processing conditions of a thermosetting laminate, which require lower temperature and pressure than those applied for a traditional thermoplastic laminate, are mild enough to prevent the degradation of a shape-stabilized PCM, thus preserving its TES capability. In this case, the shape-stabilized PCM was prepared with the minimum CNT content required to reach a proper shape-stabilization, i.e. 10 wt%, lower than that used in the polyamide/glass laminate (15 wt%), in order to maximize the melting enthalpy per unit mass and avoid superfluous filler content (see Chapter III, Section 3.2.3.1).

5.2.1.2 Sample preparation

The epoxy base and the hardener were mixed at room temperature at a weight ratio of 100:30, as suggested by the producer, and magnetically stirred at 500 rpm for 5 min. The ParCNT powder, containing the paraffin wax (Par) and the carbon nanotubes (CNTs), was then added at different weight concentrations (20 wt%, 30 wt% or 40 wt%), and the resulting mixture was vigorously stirred to obtain a

homogeneous dispersion of the powder in the resin. The mixtures were degassed by means of a vacuum pump, casted in silicon molds, cured at room temperature for 24 hours and post-cured at 80 °C for 10 hours. The same procedure was followed to prepare neat epoxy samples. Table V - 2 lists the prepared samples and their nominal weight composition.

Table V - 2. List of the prepared EP-ParCNTx samples with weight compositions.

Sample	EP (wt%)	Par (wt%)	CNTs (wt%)
ParCNT	0	90	10
EP	100	0	0
EP-ParCNT20	80	18	2
EP-ParCNT30	70	27	3
EP-ParCNT40	60	36	4

The prepared EP/ParCNT mixtures were also used as matrices to prepare laminates. The laminates were produced via a wet lay-up technique and the relative amounts of components were chosen to obtain a nominal fiber weight fraction of 50 %. Five plies were stacked together, and the resulting laminates had an in-plane area of 120x120 mm^2. The laminates were vacuum-bagged, left to cure at room temperature for 24 h under a variable pressure and post-cured at 100 °C for 10 h in a hot-plate press. A carbon fiber/epoxy laminate without ParCNT was prepared with the same procedure. The results described in the previous chapters showed that the fiber weight (and volume) fractions of PCM-containing laminates decreased with an increase in the initial PCM content, due to an increase in viscosity of the matrix that partially hindered its flowing out of the fiber fabric and resulted in a higher matrix fraction in the final composite. To try to compensate this effect, in the preparation of the laminates object of this Chapter the applied pressure during curing was increased with the starting fraction of ParCNT in the epoxy/ParCNT mixture. This was not done for the laminates containing microcapsules to prevent MC breakage due to excessive applied pressure.

Table V - 3 displays the list of prepared laminates with the nominal weight fractions of constituents. The composites were denoted as EP-ParCNTx-CF, where x represents the weight percentage of ParCNT powder on the total mass of the matrix. As mentioned before, x assumes the values of 20, 30 and 40.

Table V - 3. List of the EP-ParCNTx-CF samples with nominal weight compositions.

Sample	CF (wt%)	EP (wt%)	Par (wt%)	CNTs (wt%)
EP-CF	50	50	0	0
EP-ParCNT20-CF	50	40	9	1
EP-ParCNT30-CF	50	35	13.5	1.5
EP-ParCNT40-CF	50	30	18	2

5.2.1.3 Characterization

The prepared EP-ParCNTx samples were investigated through the characterization techniques listed in Table V - 4 together with the experimental parameters applied specifically on these samples (see Section 3.3 for the full description of the characterization parameters and specimen preparation).

Table V - 4. Characterization techniques and experimental parameters applied on the samples EP-ParCNTx.

Technique	Specific experimental parameters
SEM	Cryofracture surface; Instrument Jeol IT300 SEM
DSC	Temperature interval 0-150 °C
TGA	TA Q5000 IR thermobalance; specimen mass 10 mg

The prepared EP-ParCNTx-CF laminates were investigated through the characterization techniques listed in Table V - 5.

Table V - 5. Characterization techniques and experimental parameters applied on the samples EP-ParCNTx-CF.

Technique	Specific experimental parameters
SEM	Cryofracture surface; Instrument Jeol IT300 SEM
Optical microscope	Polished cross section
Liquid displacement	Density measurements; ethanol
DSC	Temperature interval 0-150 °C
TGA	Mettler TG50 thermobalance; specimen mass 25 mg
DMA	Single-frequency scans; multifrequency scans
LFA	As described in Section 3.3.3.4
Thermal camera imaging	Specimen in-plane dimensions: 70x100 mm^2
Three-point bending test	As described in Section 3.3.5.1
Short-beam shear test	As described in Section 3.3.5.5

5.2.2 Results and discussion

The present Section reports the results of the characterization of the samples EP-ParCNTx and the laminates EP-ParCNTx-CF. The results of the first class of samples are only hinted, and only the results important for the comprehension of the properties of the laminates will be described.

5.2.2.1 Results of the EP/ParCNT samples

Figure V - 1 reports the SEM micrographs of the cryofracture surface of the samples EP-ParCNTx. In the micrographs at low magnification, ParCNT particles are observable with an irregular shape and a rough surface topography, while the epoxy matrix shows a smooth profile, due to its brittle fracture behavior. In the sample with the highest PCM content, i.e. EP-ParCNT40, the PCM and the epoxy resin assume a co-continuous structure. Some spherical pores can be noticed in all samples, which are due to the air entrapped during processing.

In the micrographs at high magnification, the interface between the two phases can be better appreciated. Some interfacial debonding phenomena are visible, but the adhesion seems rather good. A parallel research activity (not reported) showed that the adhesion in these samples is better than that between epoxy and neat paraffin particles (without CNTs), which highlights the positive role played by CNTs in the adhesion enhancement.

Figure V - 2 shows the TGA thermograms of the neat paraffin powder (Par), ParCNT powder, neat epoxy (EP) and samples EP-ParCNTx. By a comparison between the samples Par and ParCNT, it can be observed that the degradation of paraffin occurs in a single step in both samples, and the ParCNT sample shows a residual mass of approx. 10 wt%, attributable to the CNT fraction. The derivative peak of the degradation process occurs at a higher temperature for ParCNT (218.0 °C) than for Par (209.4 °C), which is an index that the CNTs slightly improve the thermal stability of the paraffin. However, the effect is much more modest than that observed on the PCM microcapsules, previously reported in this thesis. Since the paraffinic core of the microcapsules has a similar melting point than the paraffin described in this Subchapter, these two PCMs reasonably show a similar chain length and thermal degradation behavior, but the shell is remarkably more effective in protecting the core from thermal degradation than CNTs.

For the samples EP-ParCNTx, the degradation occurs in two distinct steps, located at 220 °C and 360 °C and associated to the degradation of paraffin and epoxy resin, respectively. From the degradation step of the paraffin (regarded as complete at 280 °C) and considering the mass loss of the epoxy resin at that temperature, it is possible to estimate the effective paraffin amount contained in each sample.

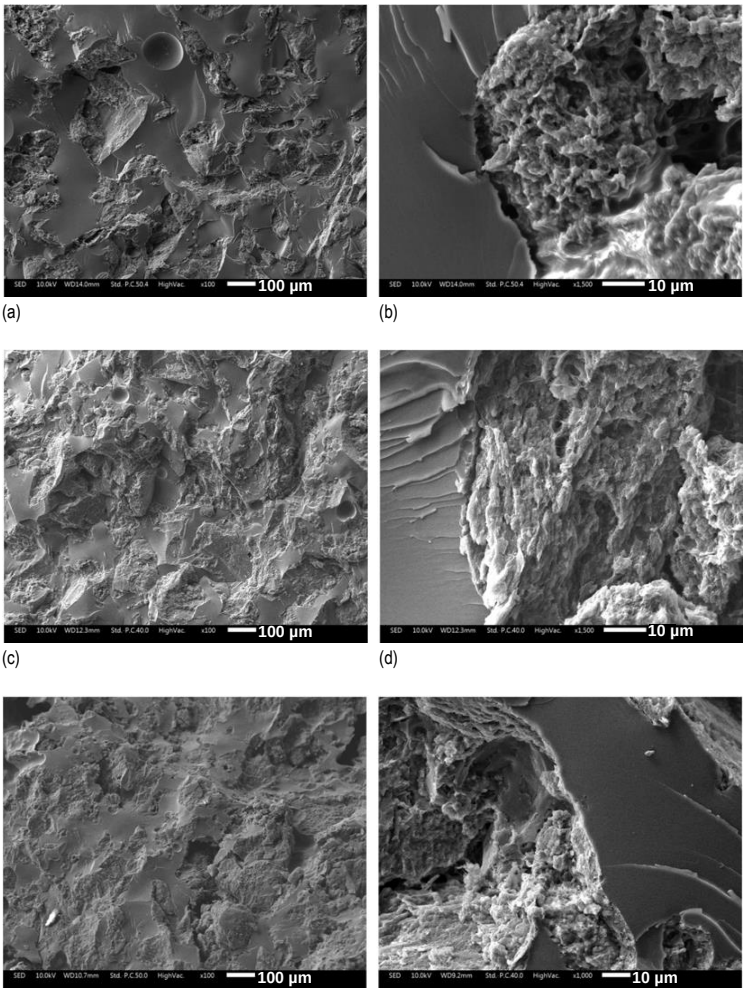

(a) (b)

(c) (d)

(e) (f)

Figure V - 1. SEM micrographs of the cryofracture surface of the samples EP-ParCNTx, at two magnification levels. (a,b) EP-ParCNT20; (c,d) EP-ParCNT30; (e,f) EP-ParCNT40.

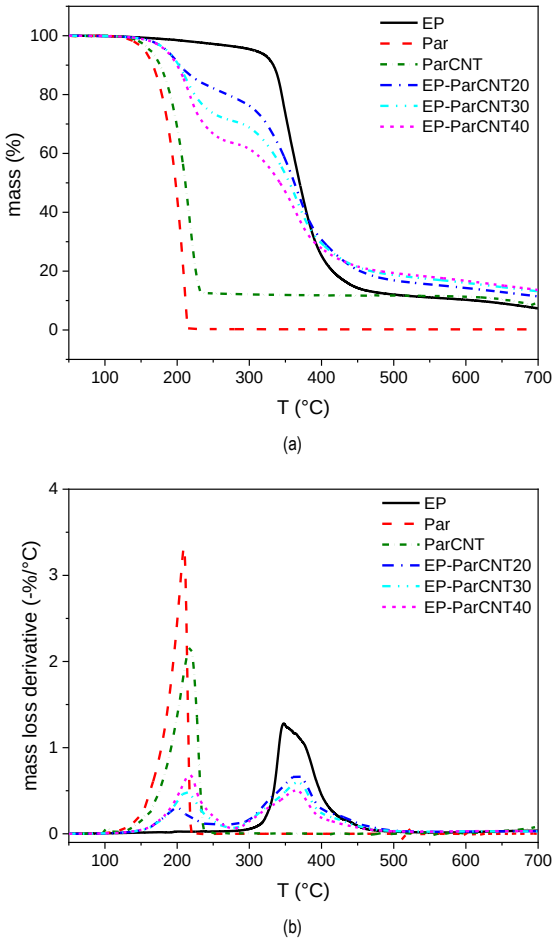

Figure V - 2. TGA thermograms of the samples EP, Par, ParCNT and EP-ParCNTx.

The data reported in Table V - 6 show that the experimental paraffin weight fraction is very close to the nominal one, which indicates that the CNTs perform an effective shape-stabilization and prevent the paraffin from exuding out of the epoxy sample during the curing step performed at 100 °C. A parallel research activity (not reported) showed that, when CNTs are not present, the experimental fraction of paraffin after curing is considerably lower (approx. 60 %) than the nominal one, and the specimens appear oily after curing, due to the paraffin exudate. This evidences the importance of CNTs in preventing loss of PCM during the processing steps.

Table V - 6. Nominal and experimental paraffin weight fraction in the samples EP-ParCNTx.

Sample	Nominal paraffin content (wt%)	Experimental paraffin content (wt%)
ParCNT	90	90.0
EP-ParCNT20	18	17.5
EP-ParCNT30	27	27.2
EP-ParCNT40	36	35.7

The results of the DSC tests are reported in Figure V - 3 and Table V - 7. The T_g of the epoxy resin is not substantially affected by the presence of paraffin, and the melting and crystallization temperature peaks and intervals of the PCM do not change when the PCM is embedded in the epoxy resin, as they are very similar to those of the neat PCM.

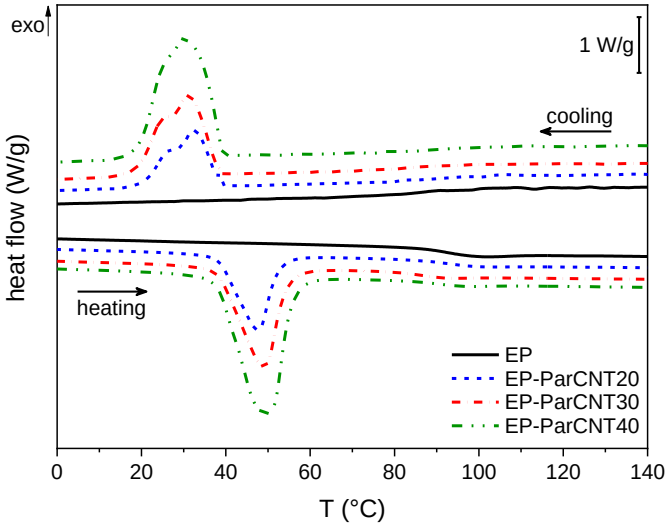

Figure V - 3. DSC thermograms of the samples EP-ParCNTx (first heating scan and cooling scan).

On the other hand, the effect of the blending process on the melting and crystallization enthalpies can be evaluated by considering the relative melting (and crystallization) enthalpies with respect to the nominal paraffin content $\Delta H_m^{rel,n}$ ($\Delta H_c^{rel,n}$), and to the experimental paraffin content calculated from TGA tests $\Delta H_m^{rel,e}$ ($\Delta H_c^{rel,e}$).

$\Delta H_m^{rel,n}$ and $\Delta H_c^{rel,n}$ are around 80-85 %, similar to what is found in the literature for other polymer/organic PCM blends (Zhang et al., 2010b). These results are commonly explained in the literature by considering an exudation of paraffin from the epoxy sample. However, the results from TGA confirm that the experimental fraction of PCM is very close to the nominal one, thereby excluding the hypothesis of conspicuous exudation. In fact, if the enthalpy values are normalized to the effective paraffin content calculated with TGA (Table V - 6), all the samples still show values of $\Delta H_m^{rel,e}$ and $\Delta H_c^{rel,e}$ close to 80-90 %. Another explanation commonly found in the literature is a non-homogeneous dispersion of the PCM in the matrix (Luyt and Krupa, 2009), but it is probably not the case of this work, since TGA and DSC analyses on multiple specimens of the same sample gave consistent results. Other possible reasons involve the confinement of paraffin macromolecules played by the surrounding matrix, or the partial dissolution in the matrix of a fraction of paraffin (Zhang et al., 2010b). However, further tests would be needed to fully understand this aspect.

Table V - 7. List of the prepared EP-ParCNTx samples with weight compositions.

Sample	T_g (°C)	T_m (°C)	ΔH_m (J/g)	$\Delta H_m^{rel,n}$ (%)	$\Delta H_m^{rel,e}$ (%)	T_c (°C)	ΔH_c (J/g)	$\Delta H_c^{rel,n}$ (%)	$\Delta H_c^{rel,e}$ (%)
Par	-	44.5	242.1	100.0	100.0	32.0	241.2	100.0	100.0
ParCNT	-	46.4	219.1	100.6	100.6	32.4	215.5	99.1	99.1
EP	92.2	-	-	-	-	-	-	-	-
EP-ParCNT20	92.7	46.2	37.1	85.1	87.6	33.6	33.8	77.9	80.1
EP-ParCNT30	91.8	47.1	56.2	86.0	85.2	32.5	53.1	81.5	80.8
EP-ParCNT40	89.3	47.6	71.4	81.9	82.7	32.3	70.7	81.4	82.2

T_g = glass transition temperature of the epoxy resin; T_m = melting temperature of the PCM; ΔH_m = melting enthalpy; $\Delta H_m^{rel,n}$ = melting enthalpy relative to the nominal paraffin content; $\Delta H_m^{rel,e}$ = melting enthalpy relative to the experimental paraffin content; T_c = crystallization temperature; ΔH_c = crystallization enthalpy; $\Delta H_c^{rel,n}$ = crystallization enthalpy relative to the nominal paraffin content; $\Delta H_c^{rel,e}$= crystallization enthalpy relative to the experimental paraffin content.

5.2.2.2 Results of the EP/ParCNT/CF laminates

The optical microscope images of the prepared laminates are shown in Figure V - 4. ParCNT particles tend to aggregate, probably because of the compaction pressure and temperature applied during the curing and the post-curing processing steps. The PCM phase is mainly distributed in the interlaminar zones between two subsequent fiber layers, while the portion of matrix infiltrating the tows and wetting each single fiber is almost exclusively composed by epoxy resin. This is mainly due to the size of PCM particles (approx. 50 µm at the beginning of the production process). Thus, the interlaminar zone is enriched in PCM, which is present in a higher amount in these regions. This is even more clearly visible in Figure V - 4(e-f), taken at higher

magnifications. Additionally, since the ParCNT domains are solid in the first part of the curing process at room temperature, they tend to deform the tows.

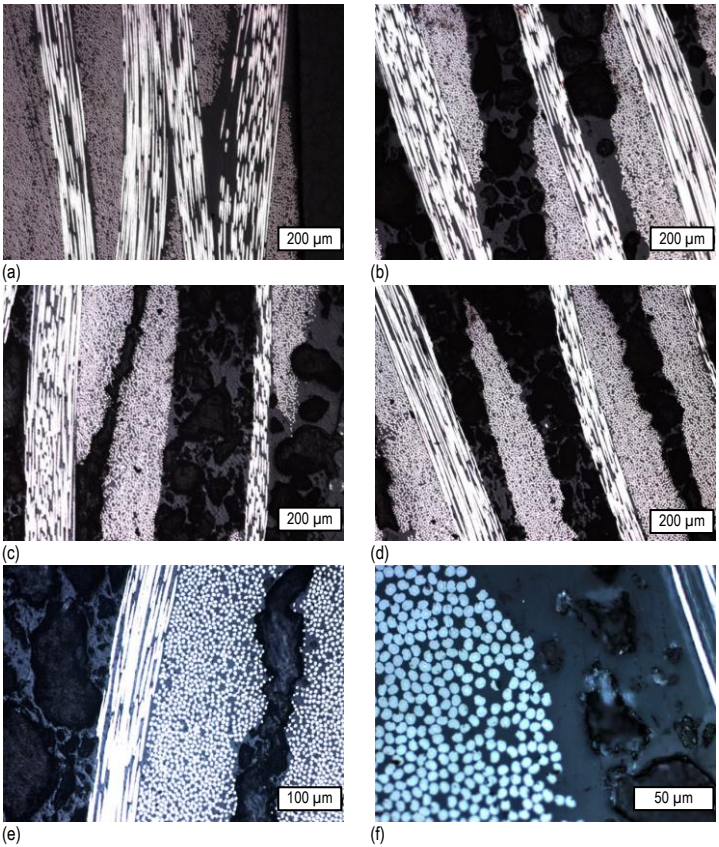

Figure V - 4. optical microscope images of the polished cross sections of the laminates EP-ParCNTx-CF (a) EP-CF; (b) EP-ParCNT20-CF; (c) EP-ParCNT30-CF; (d) EP-ParCNT40-CF; (e) and (f) EP-ParCNT30-CF at higher magnification.

A more detailed analysis of the microstructural behavior of the prepared laminates can be appreciated with the SEM micrographs at different magnifications of the cryofracture surface of the samples EP-CF (Figure V - 5(a-b)) and EP-ParCNT40-CF (Figure V - 5(c-d)). These SEM micrographs confirm that there are no evident traces of ParCNT particles between the fibers, as suggested by the fact that there are no noticeable microstructural differences between Figure V - 5b and Figure V - 5d. The differences are instead clearly visible between the interlaminar zones of the two laminates; in Figure V - 5c the interlaminar zone (indicated by red arrows) is rich in ParCNT, which is not present in the EP-CF sample (Figure V - 5a).

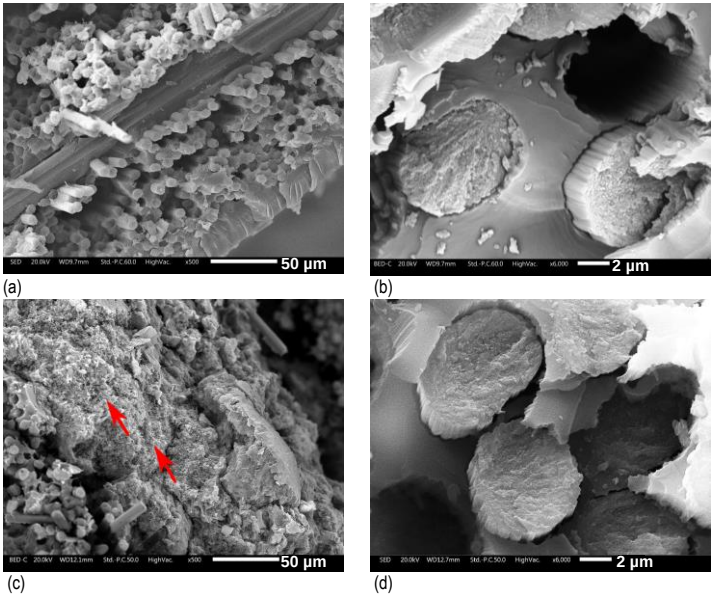

Figure V - 5. SEM micrographs of the cryofracture surface of the laminates. (a,b) EP-CF and (c,d) EP-ParCNT40-CF. The red arrows in Figure (c) indicate the ParCNT-rich zone.

Figure V - 6 reports the TGA thermograms of the laminates, compared with that of the neat epoxy resin, the carbon fibers and the ParCNT particles. As observed for the EP-ParCNTx samples, the degradation of the polymeric fraction of the samples occurs in two distinct steps, associated to the degradation of paraffin and the epoxy resin, respectively. As expected, the addition of paraffin leads to a decrease in the thermal degradation resistance of the laminates, with a decrease in the values of $T_{3\%}$. The residual mass after the test is mainly represented by carbon fibers and CNTs, but it also partly consists of epoxy resin, as evidenced by the thermogram of the neat epoxy.

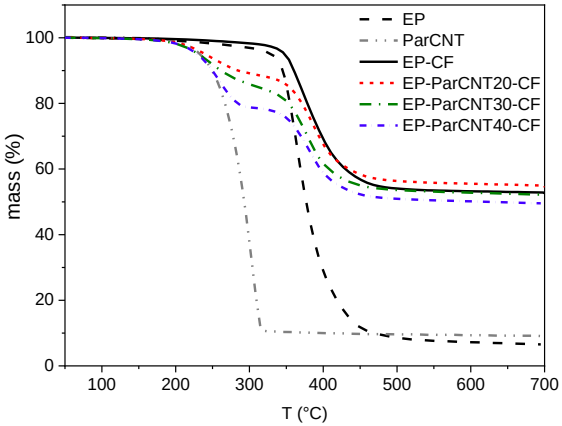

Figure V - 6. TGA thermograms of EP, ParCNT and the laminates EP-ParCNTx-CF.

From the degradation profiles, it is possible to determine an experimental mass fraction of paraffin in the samples, also considering the mass loss of the epoxy resin. The matrix and fiber weight fractions ($\omega_{f,TGA}$) can be determined from the mass residues. These values, reported in Table V - 8, are close to the nominal ones reported in Table V - 3 and to those determined by weighing the whole laminates and subtracting the weight of the fibers, known through the areal mass of the fabric and the in-plane surface of the laminates. These values are reported in Table V - 8 as $\omega_{f,mass}$. This is an indication of the homogeneity of the produced samples, as the TGA tests are performed on specimens of few milligrams.

After the determination of the weight fractions of paraffin and epoxy in the laminates, the paraffin-to-epoxy ratio was calculated. From Table V - 8 it can be seen that also this value is close to the nominal one, which suggests that not only the total paraffin content is preserved, but also the relative amount of components in the matrix.

Table V - 8. Results of the TGA tests on the laminates EP-ParCNTx-CF.

Sample	$T_{3\%}$ (°C)	Paraffin (wt%)	Paraffin-to-Epoxy ratio	Paraffin-to-Epoxy nominal ratio	$\omega_{f,TGA}$ (wt%)	$\omega_{f,mass}$ (wt%)
EP-CF	333.4	0	0	0	50.0	50.7 ± 0.7
EP-ParCNT20-CF	222.8	9.02	0.237	0.225	51.6	49.2 ± 0.6
EP-ParCNT30-CF	215.0	12.78	0.345	0.386	48.2	48.9 ± 0.3
EP-ParCNT40-CF	208.3	19.52	0.598	0.600	49.2	52.2 ± 0.4

$T_{3\%}$= temperature corresponding to a mass loss of 3 wt%.

The data on the weight composition of the prepared laminates are summarized in Table V - 9. It specifically shows the CF weight fraction, determined for each composition as the average of $\omega_{f,TGA}$ and $\omega_{f,mass}$, and the ParCNT weight fraction, calculated from the TGA results of the paraffin content. With these data, the theoretical density of the samples (ρ_{th}) could be calculated, by knowing the density of each constituent: the density of the CF phase, ParCNT phase and EP phase was 1.816 g/cm^3, 1.154 g/cm^3 and 0.985 g/cm^3, respectively, all determined through helium pycnometry techniques. The experimental density of the prepared laminates (ρ_{exp}) was obtained through the displacement method in ethanol. The comparison between ρ_{th} and ρ_{exp} allowed the calculation of the porosity (ϑ_v), and then of the volume fraction of the fibers (ϑ_f), ParCNT (ϑ_{ParCNT}) and EP phase.

The obtained fiber volume fraction is similar for all the produced composites, which allows a direct comparison of the mechanical properties. The obtained fiber volume fraction is rather low with respect to traditional structural composites (Michaud et al., 2006), but it is compatible with the hand lay-up process, compared with previous studies (Deng et al., 1999; Abdel Ghafaar et al., 2006; Sudarisman and Davies, 2008; Poyyathappan et al., 2014). Furthermore, for the production of multifunctional composites, a low fiber volume and weight fraction leads to a high matrix weight fraction, which enhances the thermal energy storage properties of the laminates.

Moreover, the porosity ranges between 2.1 vol% and 4.9 vol% with values increasing with the ParCNT content in the laminates.

Table V - 9. Theoretical and experimental density and weight and volume compositions of the laminates EP-ParCNTx-CF.

Sample	ω_f^* (wt%)	ω_{ParCNT} (wt%)	ρ_{th} (g/cm^3)	ρ_{exp} (g/cm^3)	ϑ_v (vol%)	ϑ_f (vol%)	ϑ_{ParCNT} (vol%)
EP-CF	50.4 ±0.5	0.0	1.413	1.384 ±0.004	2.1 ±0.2	38.4 ±0.5	0.0
EP-ParCNT20-CF	50.4 ±1.7	10.0	1.385	1.323 ±0.011	4.4 ±0.8	36.7 ±1.5	13.5 ±0.1
EP-ParCNT30-CF	48.5 ±0.5	14.2	1.362	1.295 ±0.021	4.9 ±1.5	34.6 ±0.9	18.7 ±0.3
EP-ParCNT40-CF	50.7 ±2.1	21.7	1.354	1.303 ±0.012	3.7 ±0.9	36.4 ±1.8	28.7 ±0.2

*average between CF_{TGA} and CF_{mass}, see Table V - 8; density of ethanol = 0.7995 g/cm^3

The DSC thermograms on the laminates during the first heating scan and the cooling scan are reported in Figure V - 7. The most important parameters obtained from these tests are summarized in Table V - 10. The glass transition temperature of the epoxy resin is not remarkably affected by the presence of the PCM, even though it is significantly lower than that measured on the EP-ParCNTx samples (Table V - 7), which can be due to the higher total filler content. However, also in the case of the laminates, the curing was brought to completion, as demonstrated by the absence of

a residual curing reaction peak in the first DSC thermogram and by the similarity between the T_g measured in the first and in the second (not reported) heating scans. Moreover, as for the EP-ParCNTx samples, the T_m of the paraffin is not influenced by the presence of the surrounding epoxy phase. The effect of the production process of the laminates on the phase change enthalpies of the PCM can be evaluated by considering the values of relative enthalpies (ΔH_m^{rel}, ΔH_c^{rel}), which are in the range 80-90 %. Values in this range were found also for EP-ParCNTx samples. Therefore, also the lamination process does not impair the thermal properties of this PCM, nor does it cause its degradation more than the process of fabrication the EP-ParCNTx samples.

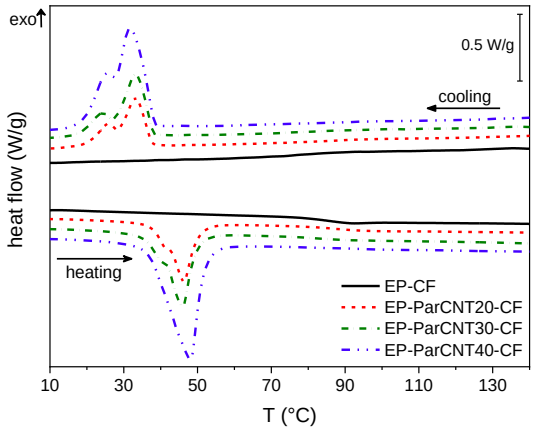

Figure V - 7. DSC thermograms of the laminates EP-ParCNTx-CF (first heating scan and cooling scan).

Table V - 10. Results of the TGA tests on the laminates EP-ParCNTx-CF.

Sample	T_g (°C)	T_m (°C)	ΔH_m (J/g)	ΔH_m^{rel} (%)	ΔH_m (J/cm³)	T_c (°C)	ΔH_c (J/g)	ΔH_c^{rel} (%)
EP-CF	84.0	-	-	-	-	-	-	-
EP-ParCNT20-CF	85.7	45.0	20.3	91.5	26.9	34.3	19.5	88.6
EP-ParCNT30-CF	82.1	43.8	27.3	81.8	35.4	35.0	26.3	79.1
EP-ParCNT40-CF	82.0	45.1	36.4	87.4	47.4	33.9	36.2	87.3

T_g = glass transition temperature of the epoxy resin; T_m = melting temperature of the PCM; ΔH_m = melting enthalpy; ΔH_m^{rel} = melting enthalpy relative to the nominal paraffin content; T_c = crystallization temperature; ΔH_c = crystallization enthalpy; ΔH_c^{rel} = crystallization enthalpy relative to the nominal paraffin content.

The retention of TES properties after several thermal cycles was evaluated through cyclic DSC tests. Tests were run in the temperature interval 10-70 °C for 50 times at 10 °C/min. For all the samples, the thermograms of all the 50 cycles (not

reported) almost overlap each other, and there are no appreciable differences in the phase change temperatures and enthalpies measured at different cycles. This suggests that the thermal properties of the laminates are stable up to fifty cycles in the analyzed temperature range, which is an indication of the thermal reliability of the prepared composites.

The values of thermal diffusivity, specific heat and thermal conductivity of the investigated laminates are reported in Figure V - 8. Each column represents the mean value and the standard deviation of all the measurements performed on each composition (at least two specimens, three pulses each). The values observed for the sample without ParCNT (EP-CF) are compatible with similar measurements found in literature for polymer-matrix composites analyzed in the thickness direction (Kandare et al., 2015; Yu et al., 2015). For the laminate without ParCNT (EP-CF), the diffusivity does not change significantly with temperature, while the specific heat and the thermal conductivity slightly increase. For the laminates containing paraffin, the trends of specific heat and thermal conductivity show a maximum at 35 °C, as the PCM is approaching the solid-liquid phase change, as already observed in the literature (Fang et al., 2014). For these laminates, at a given temperature the values of thermal conductivity and diffusivity increase with the content of ParCNT, as a consequence of the presence of the CNTs. The results of this test are important as they show that the addition of a CNT-stabilized PCM positively increase the thermal conductivity through the thickness of a carbon/epoxy laminate, both below and above the melting temperature of the PCM.

Figure V - 9 reports the results of the thermal imaging test. The starting temperature is lower than the temperature of the oven because the laminates slightly cooled down during the time required to take them out of the oven and begin the measurements, but it is still above the onset crystallization temperature of the PCM. In the laminates containing the PCM the temperature decreases with a plateau-like trend induced by the heat released during PCM crystallization, which is not occurring in the neat EP-CF laminate. As a consequence, the time to reach room temperature increases considerably. For example, the time required to reach 30 °C is approx. 200 s for the laminate EP-CF and increases up to approx. 700 s for the laminate EP-ParCNT40-CF. Although this is a simple test that investigates only the cooling stage, it clearly highlights the remarkable differences in the thermal behavior of the laminates as a function of the PCM content.

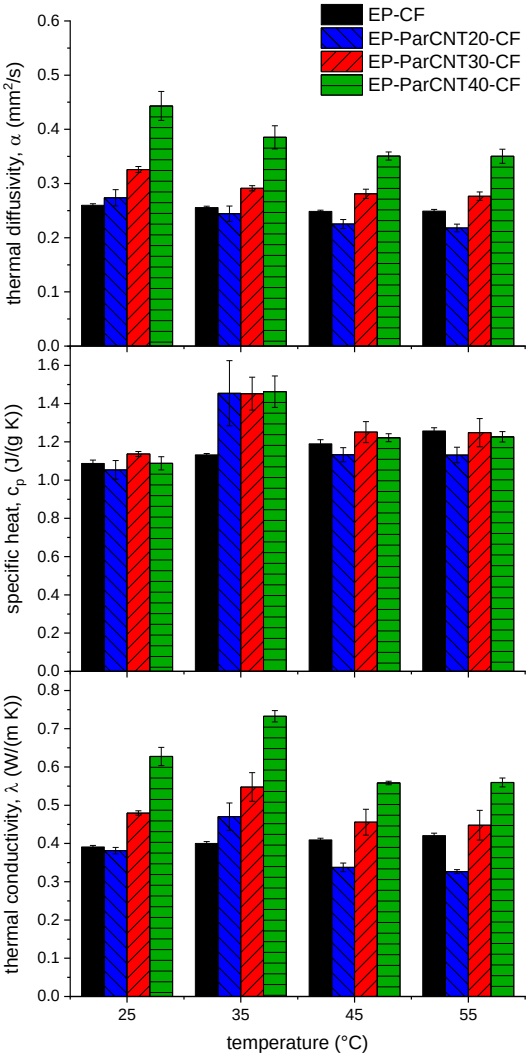

Figure V - 8. Results of the LFA measurements on the laminates EP-ParCNTx-CF

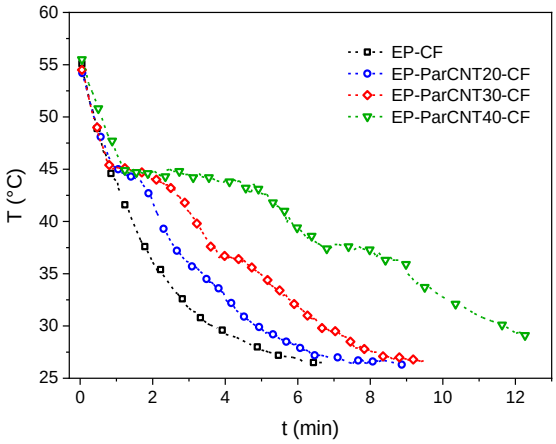

Figure V - 9. Results of the thermal imaging camera tests performed on the laminates EP-ParCNTx-CF. Surface temperature as a function of time during cooling to room temperature.

The following paragraph describes the results of the DMA characterization, which comprises single-frequency and multifrequency scans performed in single-cantilever mode, as described for the laminates containing a microencapsulated PCM described in Subchapter 4.4. The results of the single-frequency scans are reported in Figure V - 10. The values of E' and E'' as a function of temperature are plotted in Figure V - 10a. To facilitate the comparison among the samples, the values of E' have been normalized to the value at 0 °C.

As observed for the EL-MCx-CF laminates described in the Subchapter 4.4, the storage modulus of the laminate EP-CF decreases with increasing temperature throughout all the investigated temperature interval, but with a more marked decrease at the T_g of the epoxy matrix. In the EP-ParCNTx-CF laminates, two main steps are observable in the trend of E'; the first at the PCM melting, the second at the glass transition of the EP phase. Also in this case, the drop of E' at the first step increases with the MC fraction, and again the correlation between the drop amplitude and the PCM weight fraction or the melting enthalpy is linear, with high R^2 values (Figure V - 10b). This confirms that the DSC test allows one to predict, to a certain extent, the trend of the viscoelastic properties of the composite in the temperature range around the PCM phase change. At the PCM melting, the signals of E'' and $tan\delta$ manifest peaks; those of E'' (not reported) are markedly asymmetrical and qualitatively analogous to those of $tan\delta$ (Figure V - 10c). As for the EL-MCx-CF samples, the intensity of the $tan\delta$ signals increase with the PCM content, but unlike those samples,

the peaks at the PCM melting do not shift to higher temperatures with an increase in the PCM content.

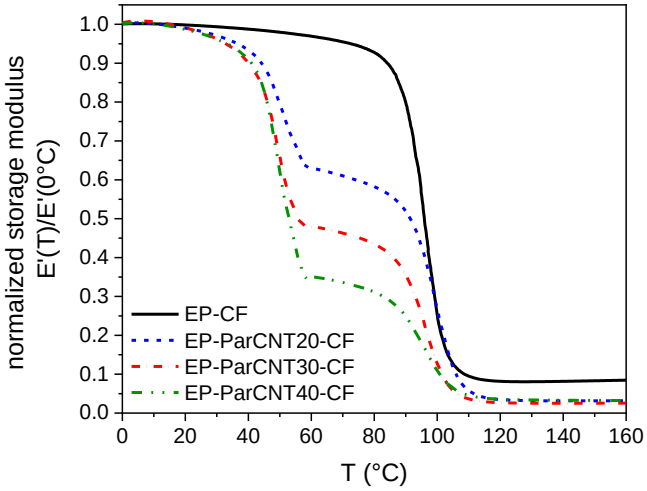

(a)

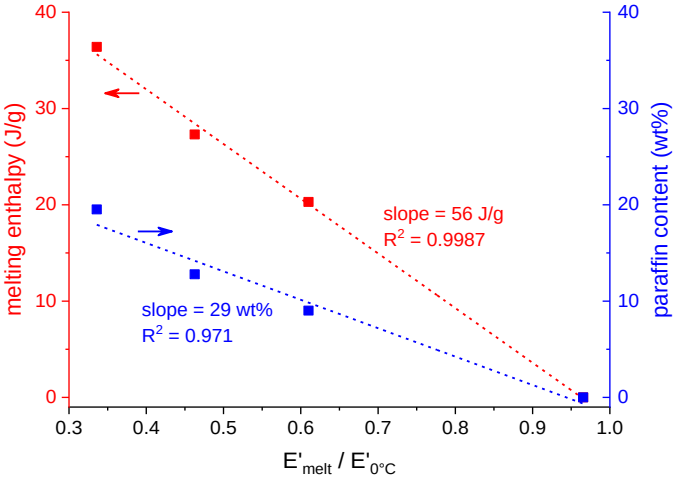

(b)

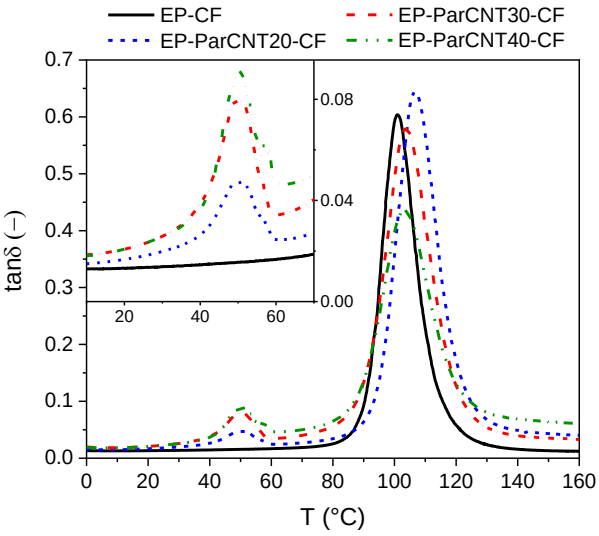

(c)

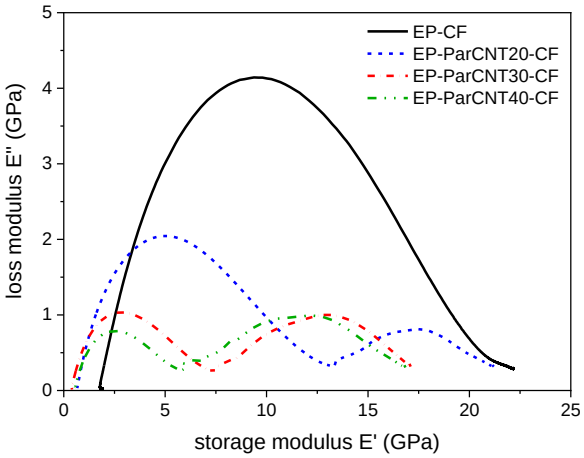

(d)

Figure V - 10. DMA results (single frequency scans) of the samples EP-CF and EP-ParCNTx-CF. (a) normalized storage modulus; (b) relative decrease in E' after PCM melting (60 °C) as a function of the melting enthalpy and the PCM weight fraction, with the results of the linear fitting; (c) loss tangent (tanδ), with an inset showing the region of the peak of the PCM melting; (d) Cole-Cole plots.

The Cole-Cole plot, in which E'' is plotted as a function of E', is reported also for these samples and it is shown in Figure V - 10d. For the samples containing the PCM, the E' and E'' data are spread on a smaller range, as the values of E' and E'' at the beginning of the test decrease with increasing PCM concentration. For these samples, the Cole-Cole plots assume the shape of two subsequent imperfect semicircles, representative of the PCM melting and the glass transition of EP, respectively. The semicircles related to the T_g, found at low E''-E' data close to the axis origin, shrink and change shape with an increasing MC content. Also for these samples, it is interesting to notice that the PCM melting transition appears in these plots as imperfect semicircles, which have a qualitatively similar shape for the different samples and are shifted to lower values of E' and E'' with increasing MC concentration.

DMA multifrequency tests were performed to assess the effect of frequency on the PCM melting and the glass transition of the matrix in the prepared composites. The results of the laminates EP-CF and EP-MC40-CF are shown in Figure V - 11a and Figure V - 11b, respectively. For the composite EP-CF, the frequency increase determines a shift of all the parameters to higher temperatures; this effect, although present in the whole investigated temperature range, is more evident at the glass transition. For the sample EP-MC40-CF, the frequency dependence is observable not only at the glass transition, but also at the PCM melting, although in this temperature range the frequency sensitivity is higher below the peak temperature than above it.

This can be better appreciated in Figure V - 11c, which shows the $tan\delta$ peaks in the PCM melting interval for the four laminates and the DSC melting peak of the neat paraffin acquired at the same heating rate (0.3 °C/min). It is interesting to observe that the two components of the DSC peak, associated to the subsequence of a solid-solid and a solid-liquid phase change, are visible also in the DMA peaks, which implies that it is possible to distinguish the contributions of each transitions to the variations in the viscoelastic parameters. Moreover, the height of the $tan\delta$ peak increases with the weight fraction of the PCM like the single frequency scans, and the $tan\delta$ peak is at a slightly lower temperature than the melting DSC peak with the same scanning speed (0.3 °C/min). The position of this peaks is not influenced by the applied frequency (the same is true for the loss modulus peaks at the melting of the PCM), and this differs from the case of the laminates EL-MCx-CF, for which also the melting peaks were shifted to higher temperature with an increase in the applied frequency.

This interesting difference may stem from the different PCMs applied in the two cases, namely the paraffin microcapsules MC in the laminates EL-MCx-CF (Figure IV - 29), and a mixture of paraffin and CNTs in the laminates EP-ParCNTx-CF. As observable by a comparison between Figure V - 11 and Figure IV - 29, ParCNT shows a sharper solid-liquid phase transition than the microcapsules MC. Moreover, after melting, ParCNT does not flow under its weight, unlike the paraffin contained in the capsules, which shows a negligible dependence on the applied frequency after

melting. The different physical state of the melted paraffin in the two laminates may affect the way in which the melting phenomenon influences the viscoelastic parameters of the host laminate.

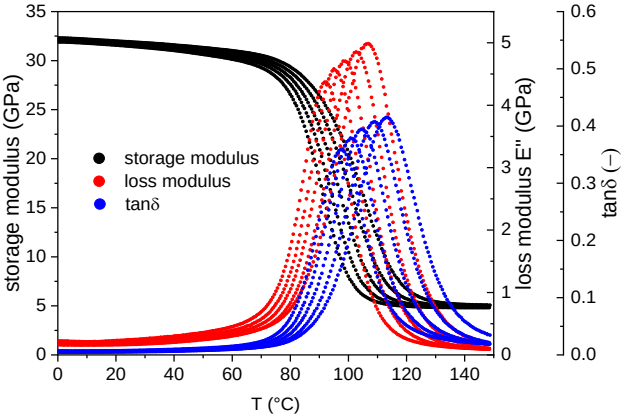

(a)

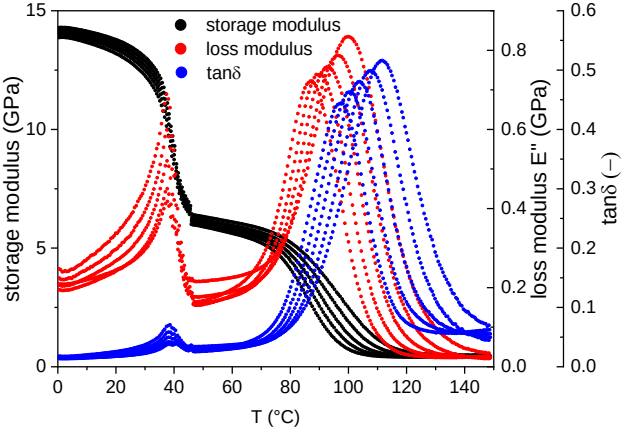

(b)

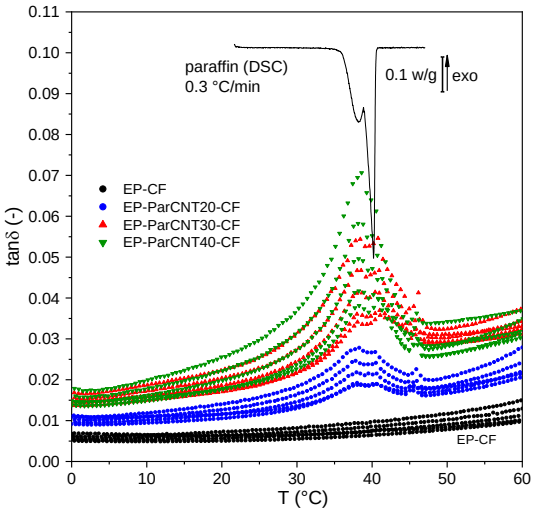

(c)

Figure V - 11. Results on the DMA multifrequency scans on the samples EP-CF and EP-ParCNTx-CF. Investigated frequencies: 0.3-1-3-10-30 Hz. (a) sample EP-CF; (b) sample EP-ParCNT40-CF; (c) trend of $tan\delta$ in the multifrequency scans for the samples EP-CF and EP-ParCNTx-CF (x = 20, 30, 40), showing the peak of the melting process of the PCM, compared with a DSC scan on the PCM performed at the same scanning speed.

The DMA multifrequency tests also allowed the calculation of the activation energy of the glass transition (E_a) from the $tan\delta$ peak temperatures through the Arrhenius approach, as described in Section 3.3.3.5. The results of this analysis are presented in Table V - 11. E_a is not considerably affected by the MC concentration, even tough the average value slightly increases with the ParCNT content.

Table V - 11. Results of the DMA multifrequency scans on the samples EP-CF and EP-ParCNTx-CF.

Sample	EP-CF	EP-ParCNT20-CF	EP-ParCNT30-CF	EP-ParCNT40-CF
E_a (kJ/mol)	348 ± 9	369 ± 4	355 ± 4	385 ± 11
R^2	0.998	0.999	0.999	0.998

E_a = activation energy of the glass transition calculated from the $tan\delta$ peaks; R^2 = value of R^2 of the linear regression.

The results of the mechanical characterization are reported in Figure V - 12 and Figure V - 13. Figure V - 12 shows experimental representative load-deflection curves

obtained from three-point bending tests. For all the compositions, after the initial linear portion of the curve, the slope decreases until the maximum load, but for higher deflections the behavior of the EP-CF laminate is remarkably different from that of the laminates containing ParCNT. For the EP-CF laminate, the load reaches a maximum value and suddenly drops to zero, and the specimens break with a catastrophic failure. This phenomenon, observed for all the tested specimens, is generally indicated as a sign of a quite strong interlaminar adhesion (Abdel Ghafaar et al., 2006; Pegoretti et al., 2008; Ary Subagia et al., 2014). On the other hand, the samples containing ParCNT show a progressive failure, and the load-displacement curves present a sequence of drops and plateaus. Thus, the specimens absorb mechanical energy also during the damage propagation.

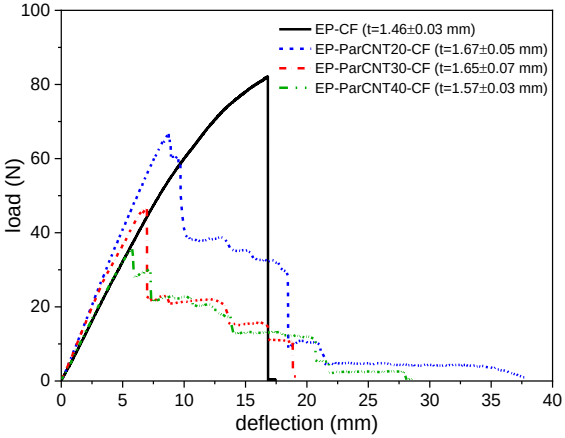

Figure V - 12. Representative load-deflection curves obtained during three-point bending tests on the laminates EP-ParCNTx-CF. The values in brackets in the legend represent the average thickness of the specimens.

Moreover, the maximum load is decreasing as the PCM content in the laminates increases. From a visual observation of the specimens during the test, it was seen that in the EP-CF laminate the failure starts from the mid lower region of the specimen, subjected to tensile stress, and quickly propagates through the specimen thickness, while for the laminates with ParCNT the failure is a combination of delamination and damage in the mid-upper zone, subjected to compression. This failure mode, associated with a multi-stage failure in bending, was previously reported in the literature for woven-fabric-reinforced composites (Abdel Ghafaar et al., 2006). The presence of delamination in the early stages of failure suggests that the tensile strength is remarkably higher than the in-plane shear strength of the laminates with PCM.

The most important mechanical parameters measured in bending tests are summarized in Figure V - 13. The flexural modulus decreases only slightly with the increase of the PCM content. This result was expected, since the flexural modulus is evaluated at low deformations and strongly depends on the volume fraction of the reinforcement phase (Abdel Ghafaar et al., 2006), which is almost the same for the investigated composites. Although early-stage delamination can reduce the elastic modulus (Sudarisman and Davies, 2008), this is likely not the case in the present work, because the delamination mechanisms were observed to start at values of deflection higher than those considered for the measurement of the elastic modulus. This suggests that the chosen span-to-thickness ratio was sufficiently high to correctly evaluate the modulus. The fact that the modulus does not decrease with the PCM content is positive for the development of composites in which both high stiffness and thermal energy storage capabilities are combined. However, the appearance of these new failure mechanisms is most probably the cause of the decrease in both flexural strength and strain at break with the PCM content. It should be noted that, as already mentioned in Chapter III (Section 3.3.5.2), the calculated value of σ_{fM} represents an apparent flexural strength, because the stress is not linear through the thickness and because, since the failure is not due to the pure bending moment, the calculated stress differs from the real stress in the mid-lower portion of the specimen, subjected to the highest tensile stress (Dong and Davies, 2015). Nevertheless, these results clearly highlight the differences in the failure mode and in the behavior during the damage propagation, after the maximum load is reached.

The effects of PCM introduction on the interlaminar shear strength of the laminates were investigated through short-beam shear tests. The obtained values of short-beam interlaminar shear strength ($ILSS$) are reported in Figure V - 13. The results are in good agreement with the three-point bending tests, since the values of $ILSS$ decrease almost linearly with the PCM content in the matrix. This is probably due to the uneven distribution of PCM, preferentially located in the interlaminar region, as evidenced by microscopical observations. This is believed to reduce the interlaminar shear strength, as the PCM phase could create a preferential site for damage propagation, since it is formed by paraffin wax and CNTs and has a low strength and ductility. During short-beam shear tests, many mechanisms of failure can generally be observed, such as delamination in several planes, failure in compression or in tension due to the bending moment, damages due to the stresses applied by the loading nose and the supports on the lower face, crushing of the specimens between the nose and the supports, etc. (Cui et al., 1994; Demirbas, 2006). Some of these phenomena were also observed during the present study, at the final stages of the test. However, the main observed failure mode, corresponding to the first drop in the load, was associated to delamination. Thus, although the reported values of $ILSS$ may not coincide with the real interlaminar shear strength of the composite, they are still

important for a comparison of the shear properties of the different laminates (Deng et al., 1999).

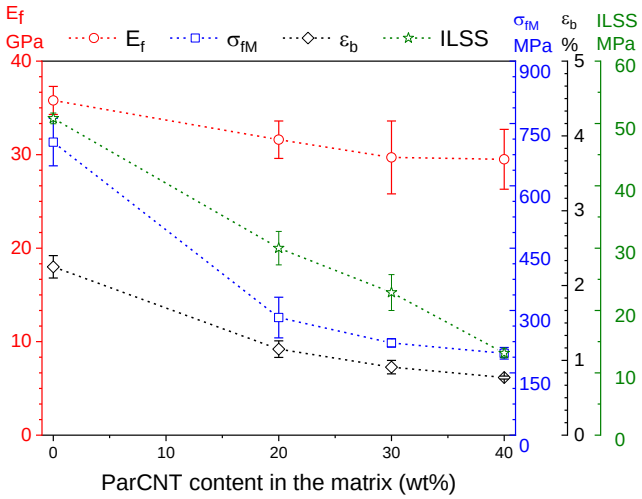

Figure V - 13. Results of the three-point bending test and the short-beam shear test on the laminates EP-ParCNTx-CF. Values of flexural modulus (E_f), flexural strength (σ_{fM}), flexural strain at break (ε_b) and interlaminar shear strength ($ILSS$).

5.2.3 Conclusions

This Subchapter presented the results of the characterization of carbon/epoxy laminates containing ParCNT as the PCM. DSC revealed that the paraffin keeps its thermal properties also in the laminates, and the melting enthalpy was 80-90 % of the expected enthalpy. The thermal properties of the laminates were retained even after fifty thermal cycles. Moreover, the thermal conductivity increased proportionally to the content of stabilized PCM. This effect could be attributed to the presence of CNTs as a stabilizing filler in the PCM domains. The positive contribution of the developed TES laminates to the thermal management was also proven by monitoring their cooling rates through thermal imaging.

Three-point bending test showed that the flexural modulus was only slightly impaired by the presence of PCM, while the flexural strength and strain at break were significantly reduced. For example, for EP-ParCNT40-CF, which was the least performant in the mechanical tests, the flexural strength and strain at break were 30 % and 35 %, respectively, of the values of the laminate without ParCNT. The interlaminar shear strength was also negatively affected by PCM addition. As revealed by optical

microscope images, it could be attributed to the preferential location of the PCM in the interlaminar region rather than between the fibers of the same tow.

The results of the DMA tests were in agreement with those found on the laminates EL-MCx-CF (Subchapter 4.4). Single frequency scans evidenced the PCM melting as a decreasing step in E' and asymmetric peaks in E'' and $tan\delta$, while the glass transition peaks of the epoxy matrix are visible at approx. 100 °C. From a comparison with the EL-MCx-CF laminates, it was found that ParCNT shows a sharper solid-liquid phase transition than the microcapsules MC. Moreover, after melting, ParCNT does not flow under its weight, unlike the paraffin contained in the capsules, which shows a negligible dependence on the applied frequency after melting. The different physical state of the melted paraffin in the two laminates affects the way in which the melting phenomenon influences the viscoelastic parameters of the host laminate.

The results of this Subchapter evidence that ParCNT is a better PCM in thermosetting matrices than in thermoplastic ones, because the milder production process and the lower processing temperatures limit the PCM degradation. However, it was found that the surrounding matrix influences and partially hinders the melting-crystallization process. Therefore, it is worth it to explore, in combination with the epoxy resin, a PCM that is completely insulated from the environment, i.e. a microencapsulated PCM. This is the object of the following parts of this Chapter.

5.3 Effect of paraffin microcapsules on the thermo-mechanical properties of an epoxy resin

This Subchapter presents a detailed theoretical and experimental investigation on epoxy matrices containing paraffin microcapsules, with the aim of using them as matrices in combination with continuous or discontinuous carbon fibers.

More specifically, the processability and flowability of the epoxy/MC mixtures was assessed through measurements of the viscosity before curing. To the best of the author's knowledge, no studies can be found that investigate how the addition of PCM microcapsules affects the viscosity of an epoxy formulation. The thermal properties were evaluated with a broad spectrum of characterization techniques. They comprise not only the state-of-the-art experimental methods normally applied on PCM-containing systems, e.g. the assessment of the phase change enthalpy though differential scanning calorimetry (DSC), but also more sophisticated techniques such as the evaluation of the thermal conductivity. This is an important property influencing the heat transfer inside the composite and thus the overall thermal management performance. The importance of measuring and tuning the thermal conductivity on PCM-filled polymer composites has already been stressed by Su et al. (Su et al., 2011b; Su et al., 2012), who also started identifying the key parameters influencing

the conductivity by considering potential theoretical models. However, they did not apply the identified models to their experimental data. The present Subchapter aims at doing so, by selecting the most appropriate theoretical models that take into account the core-shell particle morphology and the elevated volume fraction of the most highly loaded compositions. Finally, this Subchapter aims at investigating how the introduction of microencapsulated PCM affects the mechanical performance of the host epoxy resin, not only with quasi-static tests but also with fracture mechanics and impact characterization techniques. The experimental data were then fitted with theoretical models, to understand the role of the fillers' stiffness and strength and the interfacial properties on the overall mechanical performance.

This detailed analysis was performed only on epoxy/MC systems because the microcapsules have shown better thermal stability and higher final TES properties also when embedded in a thermosetting matrix. Even though this Subchapter is not strictly about a multifunctional composite containing a reinforcing agent, it is a standalone section because it represents a detailed thermo-mechanical investigation of an important matrix/PCM system and because this system is the matrix for two classes of composites, which will be described in Subchapters 5.4 and 5.5, respectively.

5.3.1 Materials and methods

The present Section lists the materials used to fabricate these samples, and then it describes in detail the techniques for the preparation of the same. It subsequently lists all the characterization techniques applied on these samples. Since the materials and the characterization techniques have been already detailed in Chapter III, this section will describe only the experimental parameters that are specific of this Subchapter.

5.3.1.1 Materials

The materials used for the preparation of these samples are listed in Table V - 12 (please refer to Section 3.2.4 for more details).

Table V - 12. Materials employed in Subchapter 5.3.

Phase	Label	Material
Polymer matrix	EP	Epoxy resin
PCM	MC	Paraffin microcapsules

5.3.1.2 Sample preparation

The epoxy base and the hardener were combined in a weight ratio of 100:30, as indicated by the producer, and vigorously stirred for 5 min to ensure an intimate

mixing. The PCM microcapsules (MC) were subsequently added in different weight fractions (10, 20, 30, 40, and 50 wt%) and the mixtures were stirred to ensure a homogeneous dispersion of the MC phase. The resulting mixtures were degassed under vacuum and casted into rectangular silicon molds of different sizes and shapes, to prepare specimens for the subsequent characterization. The specimens were left cure at room temperature for 24 hours and then post-cured at 100 °C for 10 hours. Neat epoxy specimens (EP) were also prepared for comparison. Table V - 13 lists the prepared compositions with the nominal weight fractions of the components.

Table V - 13. List of the prepared EP-MCx samples with weight compositions.

Sample	EP (wt%)	MC (wt%)
EP	100	0
EP-MC10	90	10
EP-MC20	80	20
EP-MC30	70	30
EP-MC40	60	40
EP-MC50	50	50
MC	0	100

5.3.1.3 Characterization

The prepared samples were investigated through the characterization techniques listed in Table V - 14 together with the experimental parameters applied specifically on these samples (see Section 3.3 for the full description of the characterization parameters and specimen preparation).

Table V - 14. Characterization techniques and experimental parameters applied on the samples EP-MCx.

Technique	Specific experimental parameters
Brookfield viscosimetry	At 23 °C. As described in Section 3.3.2.4.
SEM	Cryofracture surface; Instrument Zeiss Supra 60 FE-SEM
Liquid displacement	Density measurements on the EP-MCx samples; ethanol
Pycnometry	Density measurements on the MC
DSC	Temperature interval 0-120 °C
TGA	Mettler TG50 thermobalance; specimen mass 20-25 mg
Hot Disk test	Sensor 5645; bulk isotropic module
Thermal camera imaging	As described in Section 3.3.3.3
Quasi-static tensile test	As described in Section 3.3.5.1
Flexural test	As described in Section 3.3.5.2
Mode I fracture toughness	SENB specimens; as described in Section 3.3.5.4
Charpy impact test	As described in Section 3.3.5.3

5.3.2 Results and discussion

This Section describes the results of the characterization of the EP-MCx samples.

5.3.2.1 Viscosity

The results of the Brookfield viscosity tests are reported in Figure V - 14. It was not possible to test the mixture containing 50 wt% of MC (EP-MC50), because its viscosity was out of the range investigable with the available equipment (>$4 \cdot 10^4$ cP). Due to the geometry of some of the spindles, a precise and uniform value of shear rate could not be calculated. Therefore, the values of viscosity were reported as a function of the rotation speed. However, since different spindles were used, a direct quantitative comparison could not be made. In any case, the obtained results were sufficient to draw important conclusions on the effect of MC on the sample viscosity and processability. The neat base/hardener mixture (EP) exhibits a slight pseudoplastic behavior, as the viscosity decreases with an increase in the rotation speed; this is especially evident at the lower limit of the investigated rotation speed range. This behavior is observable also in the MC-filled mixtures, which do not exhibit the dilatant (shear-thickening) behavior commonly observed in fluids containing particles (Gürgen et al., 2016). Since this behavior is generally associated to the particle order loss and aggregate formation at high shear stresses, it can be concluded that the aggregation tendency of MC is low, which is also reasonable if considering that the particles are of micrometric size.

For a fixed rotation speed, the viscosity increases remarkably with the MC loading, as commonly reported in the literature for uncured epoxy systems containing micro- or nano-particles (Nguyen et al., 2019). For example, at 20 rpm, the viscosity of the neat EP was measured as 390 cP, while that of the EP-MC30 mixture is 3200 cP and that of the EP-MC40 mixture is as high as 15400 cP. It should be stressed that the comparison between the different compositions cannot be made from a quantitative point of view because the test was performed by using different spindles. However, these results give at least an idea of the increase in viscosity due to the MC addition. Such a large increase was observed also on polypropylene melts containing the same type of paraffin microcapsules, described in Subchapter 4.5. This result suggests that an increase in the MC fraction decreases the processability of the mixtures in terms of degassing and casting, thereby hindering the possibility to obtain defect-free and perfectly dense specimens. This is confirmed by the increase in porosity with the PCM content, described in Section 5.3.2.3.

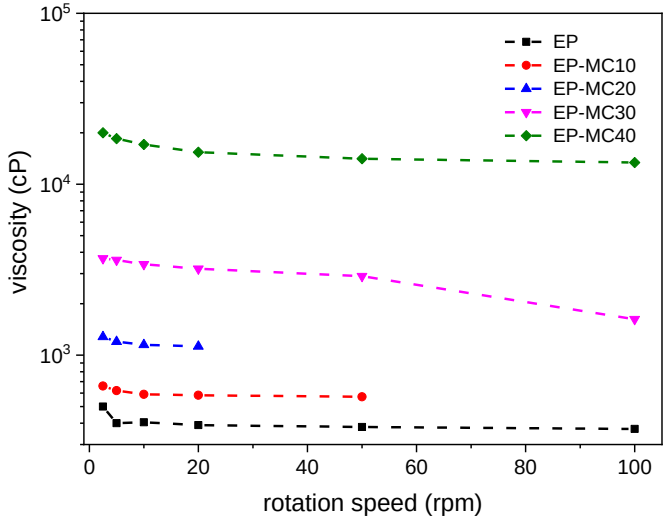

Figure V - 14. Results of the Brookfield viscosity tests on the EP/MC uncured mixtures.

5.3.2.2 Microstructural characterization

Figure V - 15 shows the SEM micrographs of the cryofracture surface of the prepared samples. As already evidenced in the previous Subchapters, the core-shell structure of the microcapsules is well visible, together with their spherical morphology and diameter mainly in the range 10-30 μm, in good agreement with what reported in the producer's datasheet. From micrographs acquired at higher magnification (not reported) and image processing with the ImageJ software, it was possible to estimate the shell thickness as (0.150 ± 0.011) μm. Micrographs at lower magnification (Figure V - 15b-d-f) show that the microcapsules are homogeneously distributed in the matrix, without evident aggregation or agglomeration. The micrograph of the sample EP-MC50 (Figure V - 15e-f) shows that, at such a high MC concentration (50 wt%), the microcapsules hinder one another, and this causes a deformation and partial loss of spherical shape.

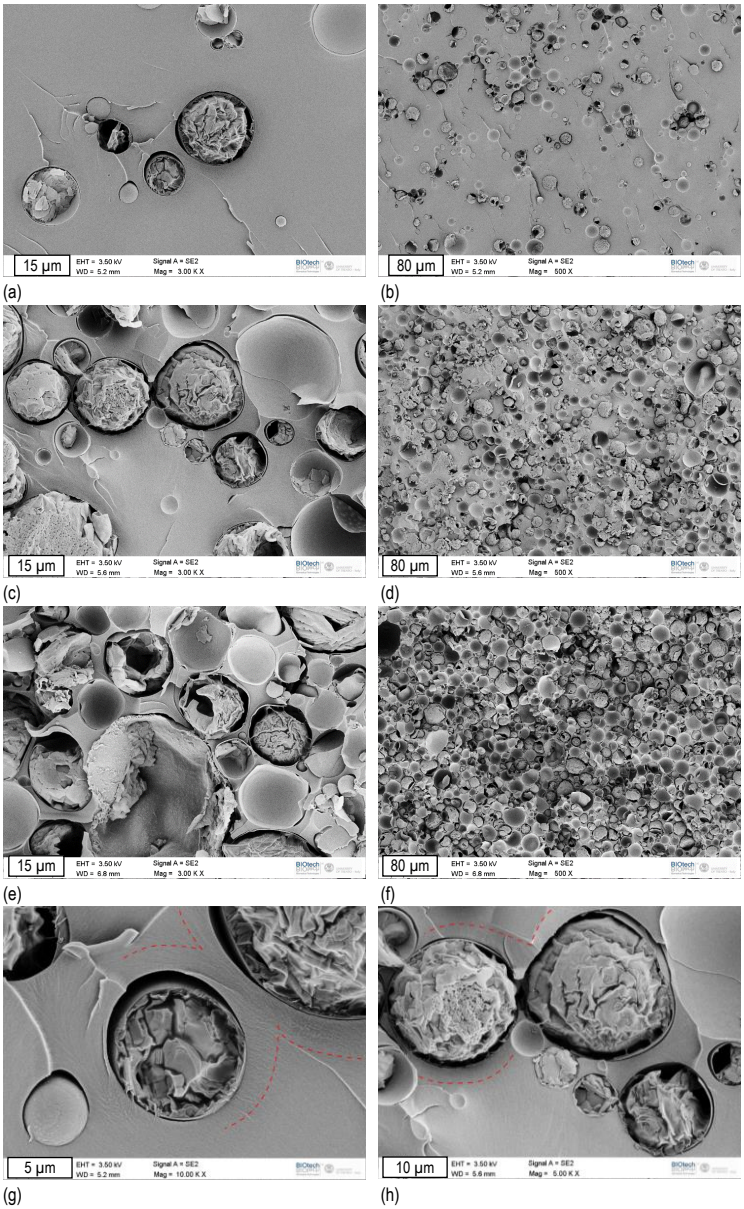

Figure V - 15. SEM micrographs of the cryofracture surface of the EP and EP-MCx (x = 10, 20, 30, 40, 50) samples at different magnification levels. (a,b) EP-MC10; (c,d) EP-MC30; (e,f) EP-MC50; (g) EP-MC10, with the indication of the interphase region; (h) EP-MC30, with the indication of the interphase region.

Micrographs at higher magnification (Figure V - 15a-c-e) indicate that nearly all the microcapsules are broken, which implies that the fracture propagates across the capsules and not at the capsule-matrix interface. Nevertheless, the capsule-matrix interfacial adhesion is poor, as evidenced by gaps and debonding zones. Poor interfacial adhesion was observed previously on polymer composites containing this kind of MC and having an acrylic matrix (see Subchapter 4.4) and is mainly due to the lack of reactivity of the fully cured melamine-formaldehyde shell. The present work, focused on the effects of PCM introduction in an epoxy matrix, allowed a deeper investigation also on the properties of the interface and the interphase. As observable in Figure V - 15g-h, the region surrounding the capsules and evidenced with a red dashed line has a darker color than the matrix far from the capsules; it can be described as an interphase zone and shows the formation of microcracks along the stress propagation lines.

5.3.2.3 Density and porosity

Figure V - 16 reports the results of the evaluation of density and porosity of the prepared samples. The neat cured EP has a measured density of 1.158 ± 0.002 g/cm^3, while that of the MC phase was found to be 0.901 ± 0.005 g/cm^3, in excellent agreement with what reported on the datasheet. These two values allowed the calculation of the theoretical density of the EP-MCx samples via the mixture rule by using the volumetric compositions. These values, reported in Figure V - 16 as ρ_{th}, decrease with an increase in the MC fraction. Figure V - 16 also reports the experimental density (ρ_{exp}) for these samples, which is increasingly lower than ρ_{th} with an increase in the MC content. This leads to an increase in the calculated porosity, which ranges from 1.64 vol% for Ep-MC10 to 7.78 vol% for EP-MC50. This confirms the increasing difficulty to fabricate defect-free specimens for the highly-filled compositions, already predictable by the considerable increase in viscosity (see Section 5.3.2.1). The increase in porosity is modest up to an MC fraction of 30 wt% and increases considerably at higher MC fractions.

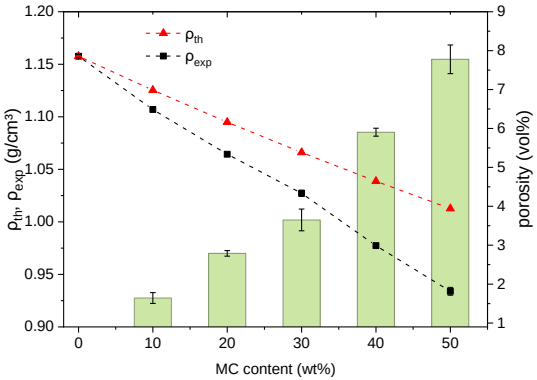

Figure V - 16. Theoretical density (ρ_{th}), experimental density (ρ_{exp}) and porosity of the EP and EP-MCx (x = 10, 20, 30, 40, 50) samples, as a function of the nominal MC weight fraction. $\rho_{etOH} = 0.793 \pm 0.004$ g/cm³ (liquid displacement method).

5.3.2.4 Thermal characterization

The results of the DSC tests are shown in Figure V - 17. Figure V - 17(a-b) shows the DSC thermograms of the first heating scan and the cooling scan on the prepared samples, while the main results of the DSC tests for all the three scans are summarized in Table V - 15. All EP and EP-MCx samples show glass transition of the epoxy at 80-90 °C, and small fluctuation in these values do not seem to show a trend with the MC weight fraction. The thermograms of all the samples containing MC show an endothermic peak at 45-49 °C, which corresponds to the melting of the PCM contained in the microcapsules, and an exothermic peak at 25-30 °C corresponding to the crystallization transition. For all compositions, both thermal transitions interest a temperature range of approx. 20-30 °C; the melting transition is found in the temperature range between 35 °C and 60 °C, while the crystallization transition between 40 °C and 15 °C. Moreover, the breadth of the peak and the involved temperature range slightly increases with the MC fraction, which indicates that the interval in which the material is active as a TES medium increases. Although the indicated temperature intervals are strictly a function of the applied heating/cooling rate (10 °C/min), these results suggest that it is important to evaluate the intervals of thermal transition for a specific sample, as they determine the temperature range in which the sample is actively performing TES.

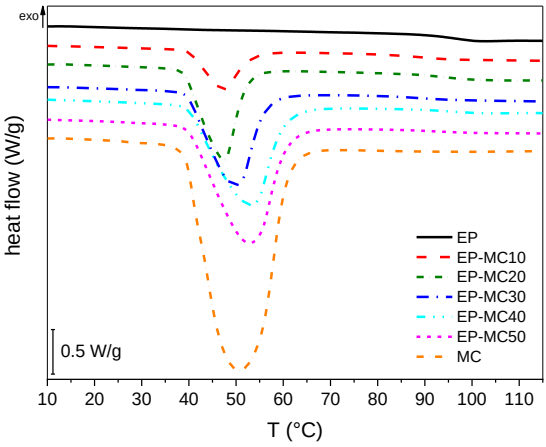
exo
heat flow (W/g)
0.5 W/g
EP
EP-MC10
EP-MC20
EP-MC30
EP-MC40
EP-MC50
MC
10 20 30 40 50 60 70 80 90 100 110
T (°C)

(a)

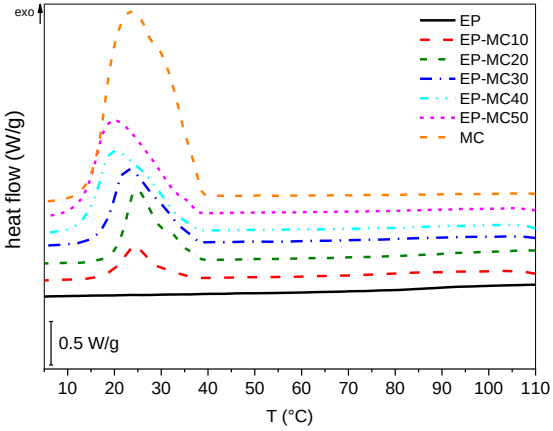
exo
heat flow (W/g)
0.5 W/g
EP
EP-MC10
EP-MC20
EP-MC30
EP-MC40
EP-MC50
MC
10 20 30 40 50 60 70 80 90 100 110
T (°C)

(b)

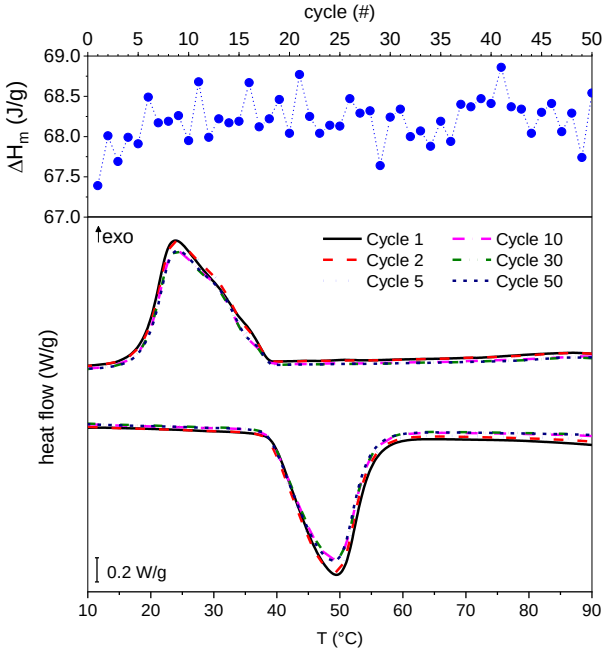

(c)

Figure V - 17. DSC thermograms of the samples EP and EP-MCx (x = 10, 20, 30, 40, 50). (a) first heating scan; (b) cooling scan; (c) representative thermograms of the cyclic DSC test on the sample EP and EP-MC30, with the values of melting enthalpy measured at each cycle.

As observable especially in the cooling scan (Figure V - 17b), these peaks are the superposition of at least two peaks, imputable to the subsequence of a solid-solid and a solid-liquid transition, as already observed and explained in the previous Chapters. The intensity of these peaks increases with the MC weight fraction. From the peak areas, the experimental values of the melting and crystallization enthalpy were calculated and reported in Table V - 15 as ΔH_m and ΔH_c for the first heating and cooling scans, respectively. These values are in good agreement with those expected by considering the nominal MC weight fraction, and this is evident from the values of ΔH_m^{rel} and ΔH_c^{rel}, always close to 100 %. This indicates that the processing parameters are mild enough to preserve the integrity of the microcapsule shells and the melting-crystallization capability of the PCM, and the small deviations from 100 % could be attributed to slight inhomogeneities of the MC distribution inside the samples.

The values of the second heating scan are nearly the same as those of the first, which indicates that the TES capability of the contained PCM are preserved after the first cycle. The aptness of the prepared samples to undergo many subsequent thermal cycles was studied more in detail through a cyclic DSC test. The results of this test for the sample EP-MC30 are reported in Figure V - 17c, which shows DSC thermograms relative to some representative cycles and the measured melting enthalpy for all the cycles. The shape of the thermograms and the phase change temperatures and enthalpies do not vary remarkably over the whole test, which is sign of a good thermal stability. This is even more significant considering that these cyclic DSC tests were run between 0 °C and 100 °C, a temperature interval abundantly broader than that to which the material will be subjected in service; these composites are intended to work in the temperature interval around the phase change temperature of the PCM, but not above the glass transition temperature of the epoxy resin.

Table V - 15. Results of DSC tests on EP and EP-MCx (x = 10, 20, 30, 40, 50) samples.

Sample	T_g (°C)	T_m (°C)	ΔH_m (J/g)	ΔH_m (J/cm^3)	ΔH_m^{rel} (%)	T_c (°C)	ΔH_c (J/g)	ΔH_c^{rel} (%)	$T_{g,2}$ (°C)	$T_{m,2}$ (°C)	$\Delta H_{m,2}$ (J/g)	$\Delta H_{m,2}^{rel}$ (%)
EP	96.2	-	-	-	-	-	-	-	97.6	-	-	-
EP-MC10	88.9	46.2	21.6	23.9	94.9	25.6	22.2	98.1	89.6	46.1	21.8	96.4
EP-MC20	94.9	46.5	43.9	46.7	96.4	25.4	44.0	97.3	96.6	46.5	43.4	95.9
EP-MC30	89.2	48.1	67.7	69.5	99.1	24.7	68.8	101.4	91.1	47.9	67.7	99.8
EP-MC40	95.3	51.1	86.3	84.3	94.8	21.9	88.9	98.3	96.3	50.9	88.2	97.5
EP-MC50	91.7	50.6	107.0	99.9	94.0	22.2	106.4	94.1	98.6	50.8	106.4	94.1
MC	-	44.7	227.7	204.9	100.0	29.0	226.2	100.0	-	44.4	226.2	100.0

T_g = glass transition temperature of the epoxy phase in the first heating scan (°C); T_m = melting temperature of the PCM in the first heating scan (°C); ΔH_m = PCM melting enthalpy in the first heating scan (J/g); ΔH_m^{rel} = relative PCM melting enthalpy in the first heating scan (%); T_c= crystallization temperature of the PCM (°C); ΔH_c = PCM crystallization enthalpy (J/g). $T_{g,2}$ = glass transition temperature of the epoxy phase in the second heating scan (°C); $T_{m,2}$ = melting temperature of the PCM in the second heating scan (°C); $\Delta H_{m,2}$ = PCM melting enthalpy in the second heating scan (J/g); $\Delta H_{m,2}^{rel}$ = relative PCM melting enthalpy in the second heating scan (%).

Figure V - 18(a-b) reports the thermograms relative to the TGA test, while the main TGA results are shown in Table V - 16. As already observed in the previous Chapters, the initial thermal degradation of the MC presents several small subsequent steps. The mass loss at lower temperature can be related to free (non-encapsulated) paraffin and some low molecular weight compounds present as residuals of the capsule synthesis.

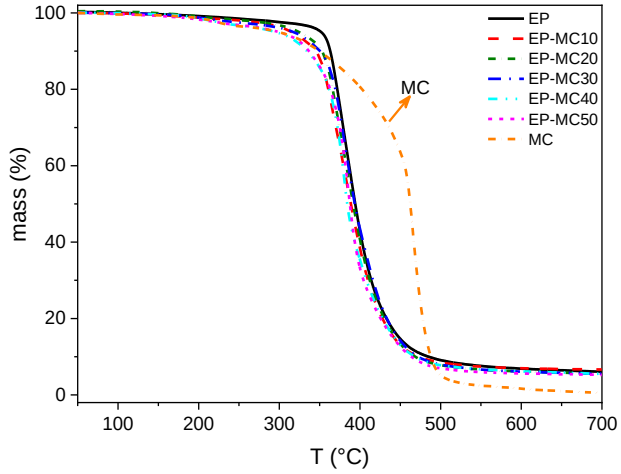

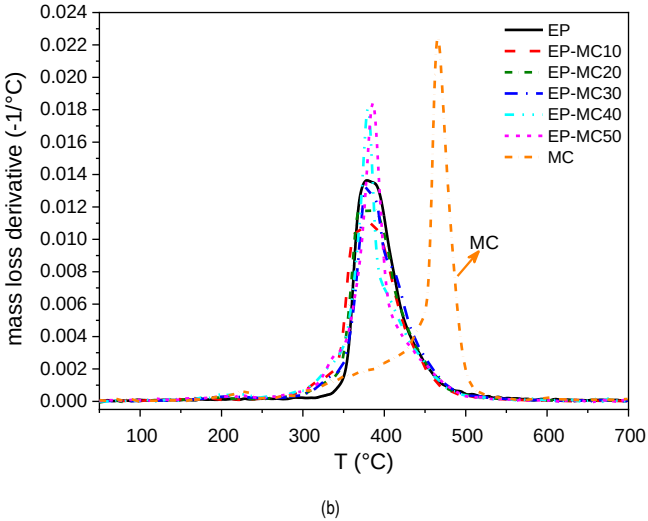

Figure V - 18. TGA thermograms of the EP and EP-MCx (x = 10, 20, 30, 40, 50) samples. (a) residual mass as a function of temperature; (b) mass loss derivative as a function of temperature.

A certain mass loss between 200 °C and 300 °C is observable also on the EP-MCx samples, and it is responsible for the decrease in $T_{1\%}$, $T_{3\%}$ and $T_{5\%}$ with an increase in the MC loading. On the other hand, for MC the main degradation step

is related to the thermal degradation of the paraffin and the melamine-formaldehyde shell. The narrow derivative peak indicates that most of the mass loss occurs in a small temperature interval. This mass loss can be associated to the damage of the microcapsule shell and the sudden release of the PCM core. This spike was observed also on the repeated measurements and in previous works on the same PCM, but it is not observed in any of the EP-MCx sample, as the presence of the surrounding matrix may modify the heat transfer and the mass loss rate. In these samples, the degradation of the EP phase and the MC happen in a relatively narrow temperature interval, which makes it difficult to separate the degradation steps and employ them to evaluate the weight composition of the samples. Finally, the peak derivative temperature T_d is only marginally affected by the MC content, which implies that the MC addition does not impair the thermal degradation resistance of the EP phase.

Table V - 16. Results of TGA tests on the samples EP and EP-MCx (x = 10, 20, 30, 40, 50).

Sample	$T_{1\%}$ (°C)	$T_{3\%}$ (°C)	$T_{5\%}$ (°C)	T_d (°C)	m_r (%)
EP	213.6	325.0	351.8	378.8	5.99
EP-MC10	199.2	293.8	325.2	390.3	6.50
EP-MC20	201.4	294.7	324.4	370.0	5.40
EP-MC30	191.2	272.4	318.0	378.3	5.56
EP-MC40	189.1	239.5	294.9	379.8	5.55
EP-MC50	163.8	241.1	299.3	386.0	5.18
MC	184.8	233.6	299.7	465.8	0.46

$T_{1\%}$ = temperature corresponding to a mass loss of 1 wt% (°C); $T_{3\%}$ = temperature corresponding to a mass loss of 3 wt% (°C); $T_{5\%}$ = temperature corresponding to a mass loss of 5 wt% (°C); T_d = degradation temperature, corresponding to the peak of the mass loss derivative (°C); m_r = residual mass at 700 °C (%).

The thermal imaging test, although simple, was able to give immediate information on the thermal management capability of the prepared EP-MCx samples. The results of this characterization for some compositions are displayed in Figure V - 19(a-b). Figure V - 19a reports some thermographic images acquired during the tests, while Figure V - 19b shows the trends of surface temperature (measured in the center of the specimen) as a function of time after extraction from the oven. For the neat EP sample, the temperature decreases quickly, while in the samples containing MC the temperature exhibits a plateau-like trend, due to the heat released during crystallization of the PCM. This effect delays the cooling to room temperature and is increasingly evident with an increase in the MC weight fraction, as also appreciable from the reported thermographic images (Figure V - 19a). For example, the sample EP takes 11.9 minutes to reach 35 °C, while almost 35.0 minutes are needed for the sample EP-MC20 and 48.5 minutes for the sample EP-MC40, with an increase of 194 % and 307 %, respectively.

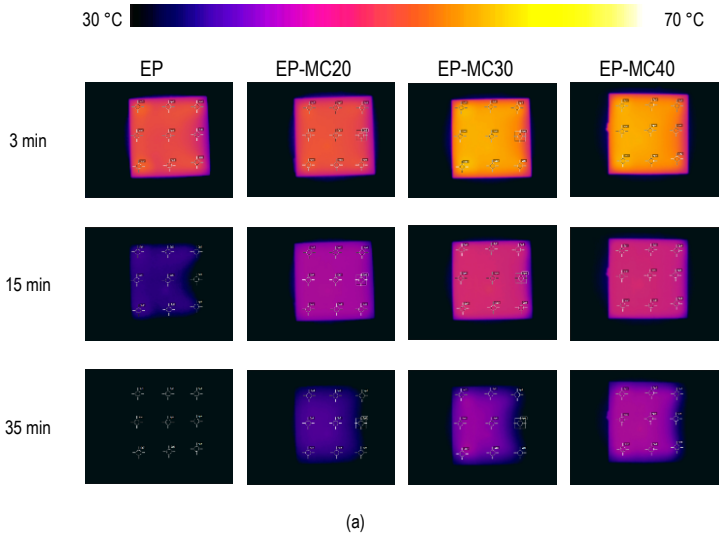

(a)

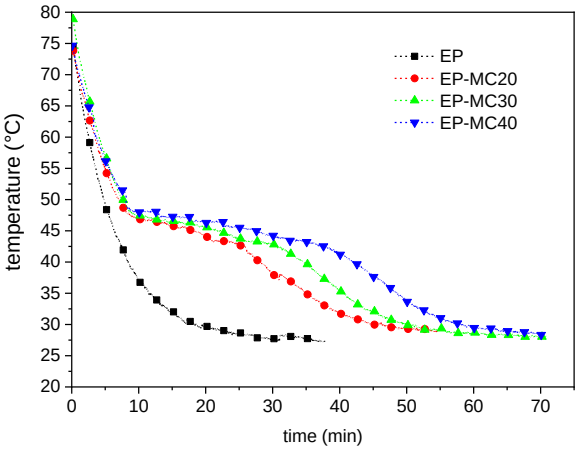

(b)

Figure V - 19. Results of the thermal imaging camera tests on the EP and EP-MCx (x = 20, 30, 40) samples. (a) Selected thermography images acquired during the test. (b) Values of surface temperature as a function of the cooling time.

The results of the Hot Disk test are reported in Table V - 17. The thermal conductivity of the neat epoxy resin is 0.222 W/mK, in good agreement with literature data (Fu et al., 2014), and it increases slightly but significantly with the MC loading.

Table V - 17. Results of the Hot Disk tests on the EP and EP-MCx (x = 20, 30, 40) samples.

Sample	λ (W/mK)	α (mm²/s)	c_P (MJ/m³K)
EP	0.222 ± 0.003	0.156 ± 0.009	1.55 ± 0.07
EP-MC20	0.242 ± 0.002	0.170 ± 0.003	1.52 ± 0.02
EP-MC30	0.257 ± 0.002	0.173 ± 0.006	1.54 ± 0.04
EP-MC40	0.267 ± 0.002	0.156 ± 0.004	1.55 ± 0.03

λ = thermal conductivity (W/mK); $\boldsymbol{\alpha}$ = thermal diffusivity (mm²/s); c_P = specific heat capacity (MJ/m³K).

This was found also for other epoxy-based systems filled with microencapsulated PCM in the solid state and/or approaching the melting transition (Su et al., 2011b), even when the shell was not made of a highly conductive metallic or ceramic material. On the other hand, the values of thermal diffusivity and specific heat capacity do not follow a trend with the MC content. However, it is well known that these values are not as reliable as the thermal conductivity when measured with a Hot Disk Thermal Constant Analyzer.

Although the scientific literature reports many experimental, theoretical and numerical studies on the thermal conductivity of two-phase polymer composites, little has been done to investigate the thermal conductivity of polymers filled with core-shell particles. Felske (Felske, 2004) developed a model to predict the thermal conductivity (λ) of a non-diluted composite (volume fraction of filler does not tend to zero) filled with core-shell particles, as a function of the conductivity of the matrix (λ_m), particle shell (λ_s) and particle core (λ_c), the filler volume fraction (ϑ_{fi}), and the ratio between the outer and the inner particle radius (δ). The model describes the behavior of the relative thermal conductivity of the composite (λ_r), defined as the ratio between the conductivity of the composite and that of the matrix. The model is reported in Equations (V - 1), (V - 2), (V - 3) as

$$\lambda_r = \frac{\lambda}{\lambda_m} = \frac{2\left(1-\vartheta_{fi}\right)+(1+2\vartheta_{fi})(B/A)}{\left(2+\vartheta_{fi}\right)+(1-\vartheta_{fi})(B/A)} \qquad \textbf{(V - 1)}$$

where

$$A = 1 + 2\delta^3 - (1-\delta^3)(\lambda_c/\lambda_s) \qquad \textbf{(V - 2)}$$

$$B = \frac{(2+\delta^3)\lambda_c - 2(1-\delta^3)\lambda_s}{\lambda_m} \qquad \textbf{(V - 3)}$$

More recently, Pal (Pal, 2008) pointed out that the model described in Equation (V - 1) succeeds in predicting the thermal conductivity of a composite only when ϑ_{fi} is less than approx. 0.2, while it is less accurate when ϑ_{fi} approaches ϑ_{max}, where

ϑ_{max} is the maximum packing volume fraction. Therefore, Pal proposed a new model that is illustrated in Equations (V - 4) and (V - 5) as

$$(\lambda_r)^{1/3}\frac{\beta-1}{\beta-\lambda_r}=\left(1-\frac{\vartheta_{fi}}{\vartheta_{max}}\right)^{-\vartheta_{max}} \quad \textbf{(V - 4)}$$

$$\beta=\frac{(2+\delta^3)(\lambda_c/\lambda_m)-2(1-\delta^3)(\lambda_s/\lambda_m)}{(1+2\delta^3)-(1-\delta^3)(\lambda_c/\lambda_s)} \quad \textbf{(V - 5)}$$

If, as in the present work, the particle shell is thin, and the shell material exhibits a thermal conductivity of the same order of magnitude as the core and the surrounding matrix (λ_s does not tend to ∞), then the value of δ can be approximated to 1 and Equation (V - 4) can be rewritten as the Equation (V - 6) as

$$(\lambda_r)^{1/3}\frac{(\lambda_c/\lambda_m)-1}{(\lambda_c/\lambda_m)-\lambda_r}=\left(1-\frac{\vartheta_{fi}}{\vartheta_{max}}\right)^{-\vartheta_{max}} \quad \textbf{(V - 6)}$$

The model described in Equation (V - 6) was used to fit the experimental data of thermal conductivity. The value of ϑ_{max} was fixed at 0.637, which is the maximum packing volume fraction in the case of spherical particles (Pal, 2008). The value of λ_m was put equal to the measured thermal conductivity of the neat epoxy, while λ_c was treated as a free parameter. The results of this analysis are reported in Figure V - 20. The model is suitable to estimate the thermal conductivity of the prepared composites, as the fitting converged with a value of R^2 equal to 0.999. The value of the parameter λ_c, the thermal conductivity of the core material, resulted as (0.308 ± 0.003) W/(m·K), which is in good agreement with literature data on paraffinic PCMs (Rastgarkafshgarkolaei, 2014; Matias et al., 2018). These results prove that the Pal model with the approximation of thin shell is suitable to predict the thermal conductivity of these epoxy composites filled with core-shell paraffinic PCMs.

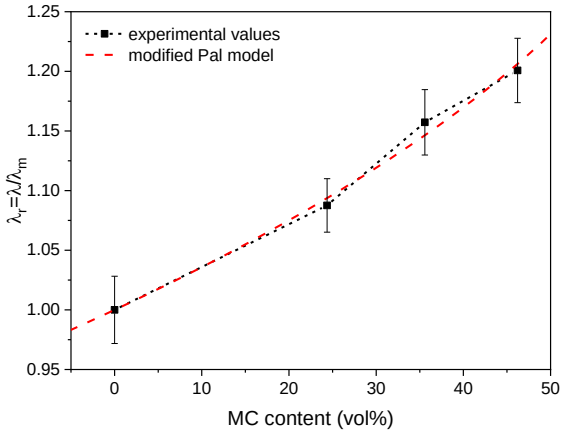

Figure V - 20. Relative thermal conductivity of the prepared samples (λ_r) as a function of the MC volume fraction. Experimental data and fitting with the modified Pal model. The fitting converged with a value of R^2 of 0.999. (λ = thermal conductivity of the EP-MCx samples; λ_m = thermal conductivity of the neat EP)

According to the model introduced by Pal (Pal, 2008) and the results presented by Su et al. (Su et al., 2012), when interfacial debonding happens between the MC and the epoxy matrix, then the model can be rewritten as the ratio λ_c/λ_m tended to zero, as a considerable thermal resistance hinders the heat transfer between the matrix and the particles. Therefore, the model can be rewritten as shown in Equation (V - 7):

$$\lambda_r = \left(1 - \frac{\vartheta_{fi}}{\vartheta_{max}}\right)^{\frac{3\vartheta_{max}}{2}} \qquad \textbf{(V - 7)}$$

Following Equation (V - 7), the overall thermal conductivity of the composite should decrease with an increase in the MC fraction, but this is not the case with the experimental results. The tests were made on as-produced undeformed samples, and the results of the fitting implies that the condition of zero thermal resistance (and no gaps at the interface) is closer to reality than the condition in which gaps are present. This implies that the gaps at the interface observed on the SEM micrographs are not generated during sample preparation (due to the different thermal expansion coefficient of MC and epoxy during cooling after the post curing step, for example), but are generated at higher deformation levels, during the specimen fracture. These results agree with the modelling of the elastic modulus with the Lewis-Nielsen model, presented in Section 5.3.2.5.

5.3.2.5 *Mechanical characterization*

The results of the flexural tests are reported in Figure V - 21(a-b), which show representative load-displacement curves and the trends of the flexural modulus, strength and strain at break as a function of the MC weight fraction.

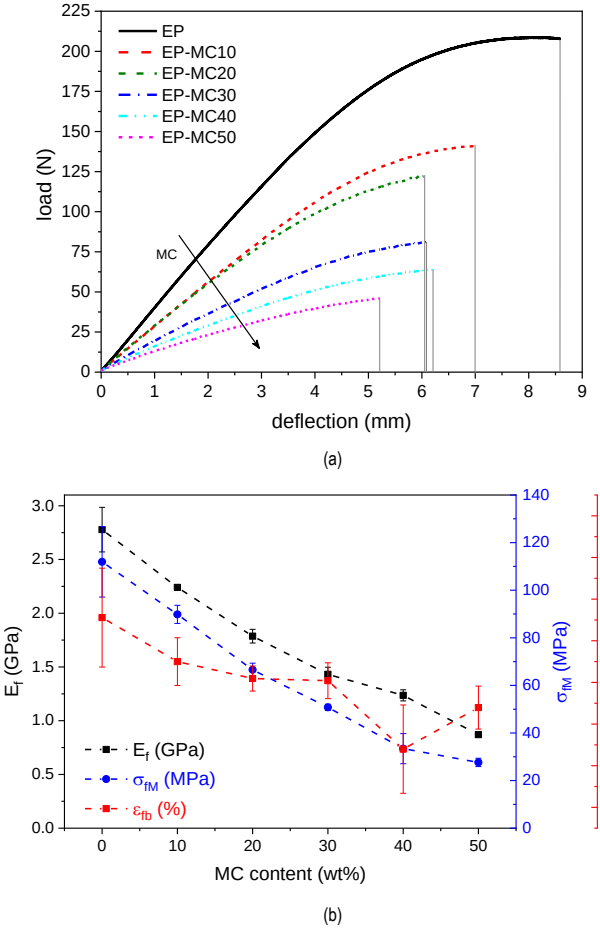

Figure V - 21. Results of the three-point bending tests on the EP and EP-MCx (x = 10, 20, 30, 40, 50) samples. (a) Representative load-displacement curves; (b) values of flexural modulus, strength and strain at break as a function of the nominal MC weight content.

As already observed for MC-filled acrylic resin (see Subchapter 4.4), the elastic modulus decreases with an increase in the MC content. The lowest value is measured on the sample EP-MC50 and is equal to (0.87 ± 0.02) GPa, which implies a decrease

of 68.7 % compared to the neat EP resin, exhibiting a modulus of (2.78 ± 0.21) GPa. The flexural strength is also negatively affected by the MC addition, as it decreases from (112 ± 15) MPa of the neat EP to (28 ± 2) MPa of the sample EP-MC50. This is probably associated to the lower stiffness and strength of the MC phase compared to EP, as well as to a non-optimal adhesion with the matrix. On the other hand, the strain at break is less affected by the MC fraction.

Similar comments can be made for the results of the quasi-static tensile tests, reported in Figure V - 22(a-b). Also in this case, the mechanical properties are negatively affected by an increase in the MC fraction. The experimental data of elastic modulus were fitted with the Halpin-Tsai model, a useful tool to predict the stiffness of a composite containing a particulate filler (Halpin and Kardos, 1976; Shokrieh and Moshrefzadeh-Sani, 2016). According to the Halpin-Tsai model, the modulus of the composites (E) can be computed through the Equation (V - 8) as

$$E = \frac{1 + \zeta\eta\vartheta_{fi}}{1 - \eta\vartheta_{fi}} E_m \,, \qquad \textbf{(V - 8)}$$

where E_m is the elastic modulus of the matrix, ϑ_{fi} is the filler volume fraction, ζ is the shape factor of the filler, equal to 2 in the case of spherical particles, and η can be computed through Equation (V - 9) as

$$\eta = \frac{\frac{E_f}{E_m} - 1}{\frac{E_f}{E_m} + \zeta}, \qquad \textbf{(V - 9)}$$

where $E_f = E_{MC}$ is the elastic modulus of the filler (the MC phase).

Considering an estimation of the value of E_f, it depends on the elastic moduli of the shell and the core. Since the shell is a thin membrane with a thickness of approx. 150 nm, if an average particle diameter of 20 μm is considered, the shell accounts for only 4.5 % of the total MC volume. Since also the shell is polymeric (melamine-formaldehyde resin), it is reasonable to suppose that its elastic modulus is of the same order of magnitude of the epoxy resin and the paraffinic core, and not orders of magnitude grater as if it was made of a ceramic or metallic material.

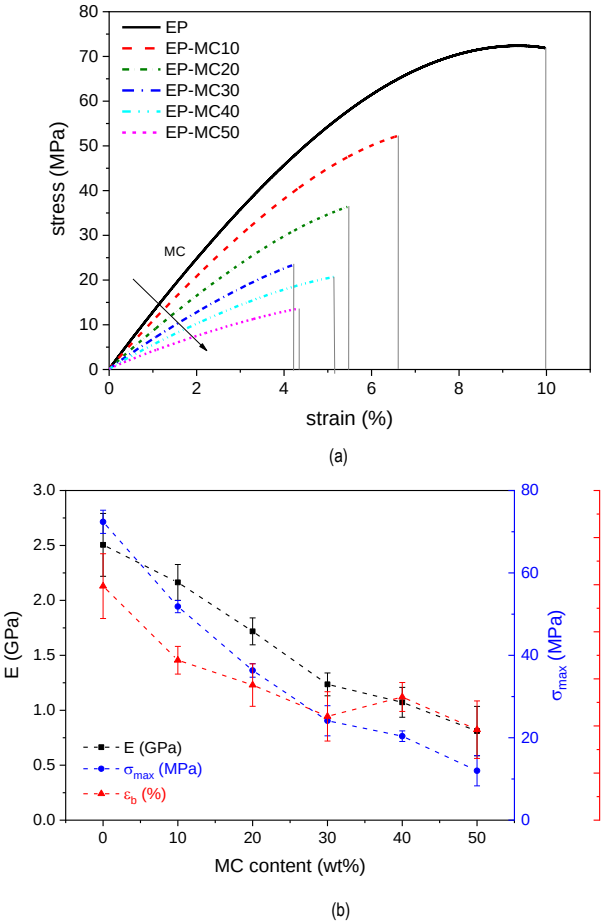

Figure V - 22. Results of the quasi-static tensile tests on the samples EP and EP-MCx (x = 10, 20, 30, 40, 50). (a) Representative stress-strain curves; (b) values of tensile modulus, strength and strain at break as a function of the nominal MC weight content.

Therefore, the shell contribution to the total elastic modulus can be in first approximation neglected. The elastic modulus of a solid paraffin wax with a melting temperature of approx. 50 °C is in the range of 150-250 MPa (DeSain et al., 2009), therefore a tentative value of 200 MPa was put in the model as E_f, and the results of this evaluation are reported in Figure V - 23a. The model succeeds in predicting the elastic modulus for low MC volume fraction, but it tends to overestimate the experimental results above a MC content of 20 vol%. A more accurate fit is found if the value of E_{MC} is put equal to 0.028 GPa. This value was found in a previous work

from our group on PCM-enhanced thermoplastic polyurethane (TPU) blends (Dorigato et al., 2018). In that work, the employed microcapsules had a liquid core, as the melting temperature of the paraffin applied in that work was below room temperature. It is also interesting to observe that the results of the model would not be considerably different if E_{MC} is put equal to 0 GPa, which would result if the filler behaved mechanically like spherical porosity.

The effect of the adhesion between the epoxy matrix and the MC shell can be taken into account by applying the Lewis-Nielsen model (Lewis and Nielsen, 1970; Giannakopoulos et al., 2010), reported in Equation (V - 10) as

$$E = \frac{1 + (k_E - 1)\beta\vartheta_{fi}}{1 - \beta\mu\vartheta_{fi}} E_m \,, \qquad \textbf{(V - 10)}$$

where k_E is the generalized Einstein coefficient, ϑ_{fi} is the filler volume fraction, E_m is the modulus of the matrix, and β and μ are coefficients defined through Equations (V - 11) and (V - 12), respectively, as

$$\beta = \frac{\frac{E_f}{E_m} - 1}{\frac{E_f}{E_m} + (k_E - 1)} \,, \qquad \textbf{(V - 11)}$$

$$\mu = 1 + \frac{1 - \vartheta_{fi}}{\vartheta_{max}} \left[\vartheta_{max}\vartheta_{fi} + (1 - \vartheta_{max})\left(1 - \vartheta_{fi}\right)\right], \qquad \textbf{(V - 12)}$$

where E_f=E_{MC} is the elastic modulus of the filler (the MC phase) and ϑ_{max} is the maximum volume fraction. The value of k_E depends on the filler-matrix adhesion. According to Nielsen and Landel (Nielsen and Landel, 1994), for a matrix with a Poisson's ratio of 0.5 containing dispersed spheres, k_E assumes the value 2.5 if there is no slippage at the interface and 1.0 if there is slippage, but k_E is decreased if the Poisson's ratio of the matrix is lower than 0.5. The literature value for the Poisson's ratio of epoxy resins is 0.30-0.35, so a value of 0.35 was selected here, following also what reported elsewhere in the literature for particulate-filled epoxy composites (Giannakopoulos et al., 2010; Chaudhary et al., 2015), so values of k_E are reduced by a factor of 0.867. Hence, k_E = 2.167 if there is no slippage and k_E = 0.867 if there is slippage (Nielsen and Landel, 1994). Both values were used to fit the data and the results are reported in Figure V - 23b. For the case with k_E = 2.167, the value of E_{MC} was alternatively set to 0.200 GPa or 0.028 GPa.

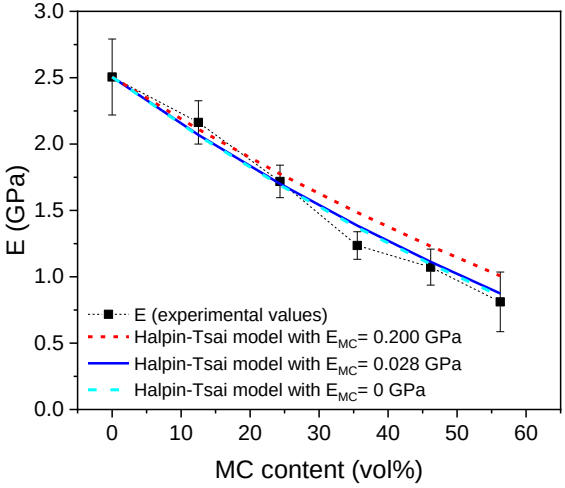

(a)

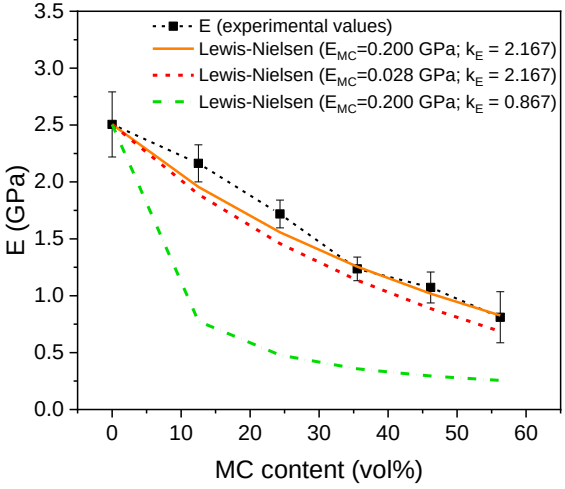

(b)

Figure V - 23. Application of theoretical models to the values of tensile modulus of the EP and EP-MCx (x = 10, 20, 30, 40, 50) samples. (a) Halpin-Tsai model; (b) Lewis-Nielsen model.

The model with k_E = 2.167 results in a good fitting of the experimental data when E_{MC}= 0.200 GPa and slightly underestimates the data when E_{MC}= 0.028 GPa,

although the two trends do not differ remarkably. On the other hand, the model with the hypothesis of slippage (k_E = 0.867) largely underestimates the data and fails in fitting the experimental results. This suggests that the hypothesis of no slippage is closer to the experimental data, thus the adhesion is good, there are no evident gaps at the interface and the interphase is able to transfer load from the matrix to the fillers, at least at zero or low deformation levels where the elastic modulus is calculated. These consideration agree with those made for the thermal conductivity results.

On the other hand, considering the data of tensile strength, they were fitted with two theoretical models that both take into account the adhesion and interfacial properties intended as the capability of the interface to transfer load from the matrix to the fillers. The selected model were that proposed by Nicolais-Narkis and that developed by Pukanszky. The model of Nicolais-Narkis is reported in Equation (V - 13) as

$$\frac{\sigma_{MAX,c}}{\sigma_{MAX,m}} = 1 - K(\vartheta_{fi})^{2/3} \qquad \textbf{(V - 13)}$$

where $\sigma_{MAX,c}$ and $\sigma_{MAX,m}$ are the tensile strength of the composite and the matrix, respectively, $\vartheta_{fi}$is the filler volume fraction and K is a parameter that takes into account the interfacial adhesion between the filler and the matrix and assumes a maximum value of 1.21 for a scarce adhesion. The model of Pukanszky is reported in Equation (V - 14) as

$$\frac{\sigma_{MAX,c}}{\sigma_{MAX,m}} = \frac{1 - \vartheta_{fi}}{1 + 2.5\vartheta_{fi}}\, e^{B\vartheta_{fi}} \qquad \textbf{(V - 14)}$$

where $\sigma_{MAX,c}$, $\sigma_{MAX,m}$, and ϕ_f assume the same meanings as for Equation (V - 13), and B is an empirical parameter that considers the load-transfer capability of the interphase.

The experimental data of tensile strength were fitted with both models with either K or B as free parameters. The results of the fitting are reported in Figure V - 24. The model of Nicolais-Narkis converged (R^2 = 0.992) with a value of K equal to 1.21, which evidenced a scarce capsule-matrix interfacial adhesion. Analogous results emerged from the fitting with the Pukanszky model, which converged with a value of R^2 of 0.993 and a coefficient B equal to 0.272. This value of B indicates an interphase with low mechanical properties that, although able to transfer load between the matrix and the fillers, is a weak point in the composite.

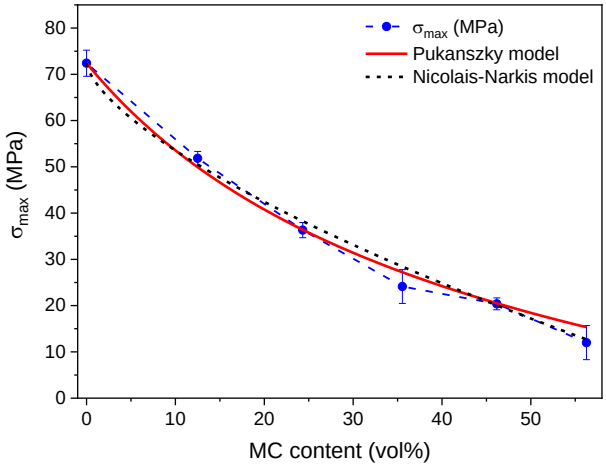

Figure V - 24. Application of Nicolais-Narkis and Pukanszky models to the values of tensile strength of the EP and EP-MCx (x = 10, 20, 30, 40, 50) samples.

The prepared composites were also investigated trough a Charpy impact tests, and the results of this characterization are reported in Figure V - 25(a-b). Also in this case, the MC addition impairs the mechanical properties of the composites, as both the absorbed total specific energy and the maximum load decrease noticeably with an increase in the MC fraction. For example, the total specific energy decreases from 6.37 kJ/m^2 of the neat EP sample to 1.21 kJ/m^2 of the sample EP-MC30 and 0.87 kJ/m^2 of the sample EP-MC50, with a decrease of 81 % and 86 %, respectively. This effect is another consequence of the embrittlement and the defectiveness brought by MC insertion.

Lastly, the results of the fracture toughness test are reported in Figure V - 26 and in Table V - 18. It is important to point out that, for all the specimens considered in the calculation, both the condition expressed in Equation (III – 16) and the condition $P_{max}/P_Q < 1.1$ were always verified, as recommended by the ASTM standard.

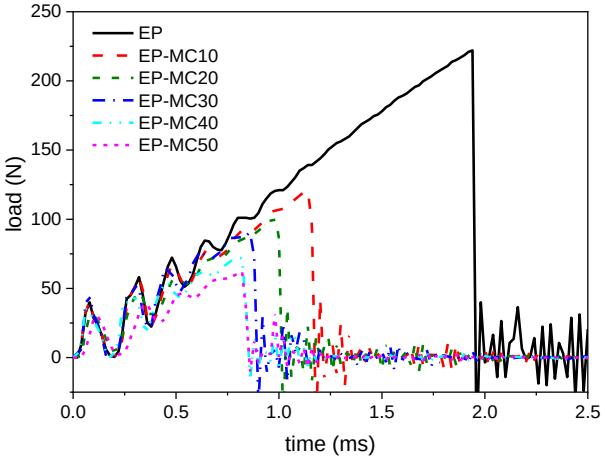

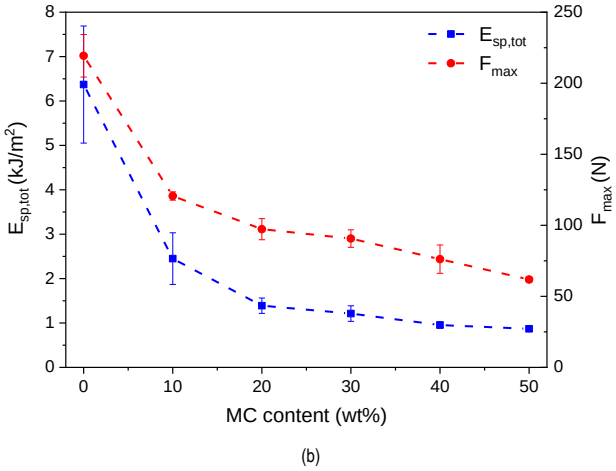

Figure V - 25. Results of the Charpy impact tests on the EP and EP-MCx (x = 10, 20, 30, 40, 50) samples. (a) Representative load-time curves; (b) values of total specific energy (kJ/m²) and maximum force (N) as a function of the nominal MC weight fraction.

The values of fracture toughness K_{IC} are negatively affected by an increase in the MC weight fraction. The decreases are not statistically significant for a capsule weight fraction of up to 20 %, while the decrease becomes significant for MC contents of 30 wt% and above. For example, the value of K_{IC} is 1.28 ± 0.34 MPa·m$^{1/2}$ for EP but decreases to 1.11 ± 0.10 MPa·m$^{1/2}$ for EP-MC20 and 0.57 ± 0.04 MPa·m$^{1/2}$ for EP-MC50. In a similar way, the value of G_{IC} slightly increases up to 20 wt% of MC,

and then decreases with a further increase in the MC content. The value of G_{IC} increases from 400 ± 158 J/m² of the neat EP to 634 ± 42 J/m² of the sample EP-MC20, with an increase for the mean value of 58.5 %.

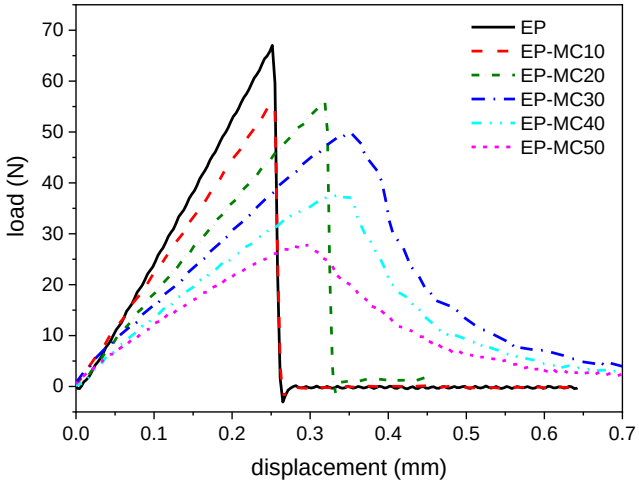

Figure V - 26. Representative load-displacement curves obtained during the fracture toughness tests on the EP and EP-MCx (x = 10, 20, 30, 40, 50) samples.

MC addition modifies also the behavior of the material during the test. The compositions with up to 20 wt% of MC fail suddenly and break in two pieces after reaching the maximum load, whereas the formulations with an MC content above 30 wt% absorb a significant amount of energy also after the maximum load. This can be quantified through the parameter E_p/E_i, which is the ratio between the energy absorbed after the maximum load (E_p, propagation energy) and that absorbed before the maximum load (E_i, initiation energy), reported in Table V - 18. This parameter increases considerably with MC addition, especially for an MC content above 30 wt%, and is probably due to the crushing and deformation of the capsules that collapse onto each other. Although the maximum load and thus the value of K_{IC} decrease with an increase in the MC content, the ability of the material to absorb a non-negligible amount of energy during crack propagation helps slow crack advancement, thus making the material somewhat more reliable.

Table V - 18. Results of the fracture toughness tests on the EP and EP-MCx (x = 10, 20, 30, 40, 50) samples.

Sample	K_{IC} (MPa·m$^{1/2}$)	E_p/E_i (%)	G_{IC} (J/m^2)
EP	1.28 ± 0.34	4.3 ± 1.0	400 ± 158
EP-MC10	0.95 ± 0.12	4.4 ± 1.7	404 ± 72
EP-MC20	1.11 ± 0.10	3.6 ± 0.1	634 ± 42
EP-MC30	0.77 ± 0.10	50.7 ± 11.6	417 ± 102
EP-MC40	0.64 ± 0.07	61.9 ± 6.2	333 ± 23
EP-MC50	0.57 ± 0.04	77.5 ± 3.2	269 ± 25

K_{IC} = mode I fracture toughness (MPa·m$^{1/2}$); E_p/E_i = ratio between the energy absorbed after the maximum load (E_p, propagation energy) and the energy absorbed before the maximum load (E_i, initiation energy).

5.3.3 Conclusions

This Subchapter reported a detailed thermal and mechanical characterization of epoxy samples filled with microencapsulated paraffin. Brookfield viscosity tests evidenced that the MC addition strongly increases the viscosity of the resin/hardener mixtures, thereby decreasing their processability and making the degassing and casting steps more difficult. This caused an increase in porosity with the MC content, as evidenced by density measurements and SEM microscopy.

The microstructural characterization also highlighted that the MC phase is uniformly distributed in the matrix and that the adhesion between the matrix and the MC shell is not optimal. This was at the basis of the considerable decrease in the mechanical strength of the prepared samples, as also demonstrated by the fitting of the experimental data with the models of Nicolais-Narkis and Pukanszky, both of which evidenced scarce adhesion and considerable interphase weakness. The Halpin-Tsai model was used to predict the tensile elastic modulus of the composites. When employing a filler modulus of 0.2 GPa, which is that of a solid paraffin wax, the Halpin-Tsai model resulted in a slight overestimation of the experimental data for a high MC concentration (above 30 wt%), while a much more accurate prediction resulted when employing a filler modulus of 0 GPa (porosity) or 0.028 GPa (found in a previous work for microcapsules containing a liquid PCM). The modelling of the elastic modulus with the Lewis-Nielsen approach evidenced that, at low deformations, the interfacial interaction between fillers and matrix is good, and this also agrees with the data of thermal conductivity, which resulted in excellent agreement with the Pal model calculated considering no gaps at the interface. The fitting of the thermal conductivity data also allowed estimating the thermal conductivity of the MC phase as 0.308 ± 0.003 W/mK, in good accordance with data from the literature. The fracture mechanics experiments also evidenced that an increase in MC content causes a

decrease in fracture toughness, but above an MC fraction of 30 wt% the material absorbs a considerable amount of energy also after the maximum load. In this perspective, the sample EP-MC30 can be considered the most promising composition, as it shows good TES capability, but also reasonably low porosity, acceptable mechanical properties and an interesting behavior in fracture propagation tests.

The thermal characterization evidenced that the phase change enthalpy of the prepared composites was proportional to the MC weight fraction, which indicated that the processing parameters were mild enough to preserve the MC integrity and avoid PCM degradation. Further assessment of the thermal management capability of the prepared samples was made through a test with a thermal camera, which evidenced that the heat released during PCM crystallization slows down the cooling of the material considerably. The presented characterization contributes to shed light on the impact of adding a core-shell PCM to an epoxy matrix and paves the way for using such systems in applications of thermal energy storage and temperature management. The comparison between these results and those reported in Subchapter 5.2 evidences the superiority of a microencapsulated PCM compared to a shape-stabilized one when embedded in an epoxy resin, in terms of thermal resistance and final TES capability.

The two following Subchapters describe the use of the presented epoxy/MC systems in combination with continuous (Subchapter 5.4) or discontinuous milled (Subchapter 5.5) carbon fibers.

5.4 Unidirectional carbon fiber/epoxy laminates containing PCM microcapsules

The previous Chapter illustrated the effect of the addition of a microencapsulated PCM on the microstructural, thermal and mechanical properties of an epoxy resin. In the present Chapter, those PCM/epoxy mixtures are used as matrices to fabricate unidirectional carbon-fiber composites. The aim of this Chapter is to understand the impact of the addition of PCM microcapsules on the thermo-mechanical behavior of these composites and to highlight the differences compared to the bidirectional carbon fiber fabric used so far, in terms of processing, final properties and ability to accommodate the PCM.

5.4.1 Materials and methods

The present Section lists the materials used to fabricate these samples, and then it describes in detail the techniques for the preparation of the same. It subsequently lists all the characterization techniques applied on these samples. Since the materials and the characterization techniques have been already detailed in

Chapter III, this section will specify only the experimental parameters that are specific of this Subchapter.

5.4.1.1 Materials

Table V - 19 lists the materials used for the preparation of these samples (please refer to Section 3.2.4 for more details).

Table V - 19. Materials employed in Subchapter 5.4.

Phase	Label	Material
Polymer matrix	EP	Epoxy resin
Reinforcement	CFu	Unidirectional carbon fiber fabric
PCM	MC	Paraffin microcapsules

5.4.1.2 Sample preparation

The epoxy base and the hardener were mixed at room temperature at a weight ratio of 100:30, as suggested by the producer, and magnetically stirred at 500 rpm for 5 min. The MC phase was then added at different weight concentrations (20 wt%, 30 wt% or 40 wt%), and the resulting mixture was vigorously stirred to obtain a homogeneous dispersion of the microcapsules in the resin. These mixtures were used as matrices to prepare laminates via a wet lay-up technique. Eight plies were stacked together, and the resulting laminates had an in-plane area of 130x200 mm^2. The laminates were vacuum-bagged, left to cure at room temperature for 24 h and post-cured in an oven at 100 °C for 10 h. A carbon fiber/epoxy laminate without MC was prepared with the same procedure for comparison. The same procedure was applied to produce additional laminates made of 16 laminae. In such laminates, a PET film with a thickness of 26 μm and half the in-plane area of the laminates was placed in the mid plane to generate a pre-crack, necessary for the sample preparation of the mode I fracture toughness tests. Table V - 20 displays the list of prepared laminates, with the nominal weight fractions of constituents and the average thickness. The composites were denoted as EP-MCx-CFu, where x represents the initial weight percentage of MC on the total mass of the matrix. As mentioned before, x assumes the values of 20, 30 and 40. From the thicker laminates, labelled “B”, specimens were cut for the sole tests of mode I fracture toughness and short-beam shear strength. All the other mechanical and dynamic-mechanical tests were performed on the thinner laminates, labelled “A”.

Table V - 20. List of the prepared EP-MCx-CFu laminates with nominal compositions. The matrices were labelled as in Subchapter 5.3.

Sample	Matrix	Number of laminae	PET film (y/n)	Thickness (mm)
EP-CFu-A	EP	8	n	1.33 ± 0.03
EP-MC20-CFu-A	EP-MC20	8	n	2.00 ± 0.05
EP-MC30-CFu-A	EP-MC30	8	n	2.13 ± 0.03
EP-MC40-CFu-A	EP-MC40	8	n	2.42 ± 0.07
EP-CFu-B	EP	16	y	3.00 ± 0.17
EP-MC20-CFu-B	EP-MC20	16	y	4.71 ± 0.19
EP-MC30-CFu-B	EP-MC30	16	y	4.84 ± 0.04
EP-MC40-CFu-B	EP-MC40	16	y	5.58 ± 0.13

5.4.1.3 Characterization

The prepared samples were investigated through the characterization techniques listed in Table V - 21 together with the experimental parameters applied specifically on these samples (see Subchapter 3.3 for the full description of the characterization parameters and specimen preparation).

Table V - 21. Characterization techniques and experimental parameters applied on the samples EP-MCx-CFu.

Technique	Specific experimental parameters
SEM	Cryofracture surface; Instrument Zeiss Supra 60 FE-SEM
Optical microscope	Polished cross section
Pycnometry	As described in Section 3.3.2.1
DSC	Temperature interval -20-120 °C
TGA	Mettler TG50 thermobalance; specimen mass 20-25 mg
DMA	Single-frequency scans; multifrequency scans; heating/cooling cycles
LFA	As described in Section 3.3.3.4
Thermal camera imaging	As described in Section 3.3.3.3
Quasi-static tensile test	Elastic modulus; as described in Section 3.3.5.1
Flexural test	As described in Section 3.3.5.2
Mode I fracture toughness	As described in Section 3.3.5.4

5.4.2 Results and discussion

The optical microscope (OM) images of the polished cross sections of the laminates are shown in Figure V - 27. The neat EP-CFu laminate (Figure V - 27a) shows fibers homogeneously distributed in the laminate thickness, without evident matrix-rich zones. The porosity present in this laminate derives from the hand lay-up technique and is evident also in the other compositions. As already reported for bidirectional carbon fiber composites containing MC (See Subchapter 4.4), the PCM phase is preferentially distributed in the interlaminar region and not among the fibers of the same tow. Moreover, the thickness of the interlaminar region increases with the initial MC fraction in the epoxy, which causes an overall increase in the laminate thickness and a decrease in the fiber volume fraction.

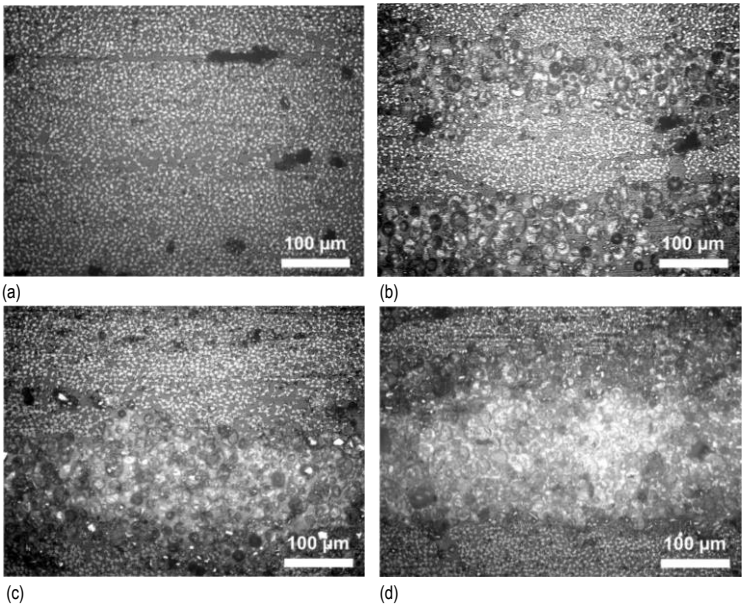

Figure V - 27. Optical microscope micrographs of the polished cross section of the laminates EP-MCx-CFu-A. (a) EP-CFu-A; (b) EP-MC20-CFu-A; (c) EP-MC30-CFu-A; (d) EP-MC40-CFu-A.

Figure V - 28 shows representative DSC thermograms of the laminates EP-MCx-CFu-A, while the main DSC results for all the prepared laminates (types A and B) are summarized in Table V - 22. The thermograms of the type B laminates are not reported for the sake of brevity, as they are qualitatively similar to those reported for the type A laminates. As already shown for the EP-MCx samples described in

Subchapter 5.3, all samples exhibit glass transition at approx. 100 °C, while the samples containing MC also show endo-/exothermic peaks at the PCM phase change. The glass transition slightly increases with the MC loading, while the increase in melting temperature and the decrease in crystallization temperature are probably linked to a decrease in the thermal diffusivity and conductivity of the samples, as confirmed by the results of the LFA analysis presented hereafter. However, the melting and crystallization temperature intervals are not heavily affected by the composition of the laminate, which indicates that the working temperature interval does not change with the MC content.

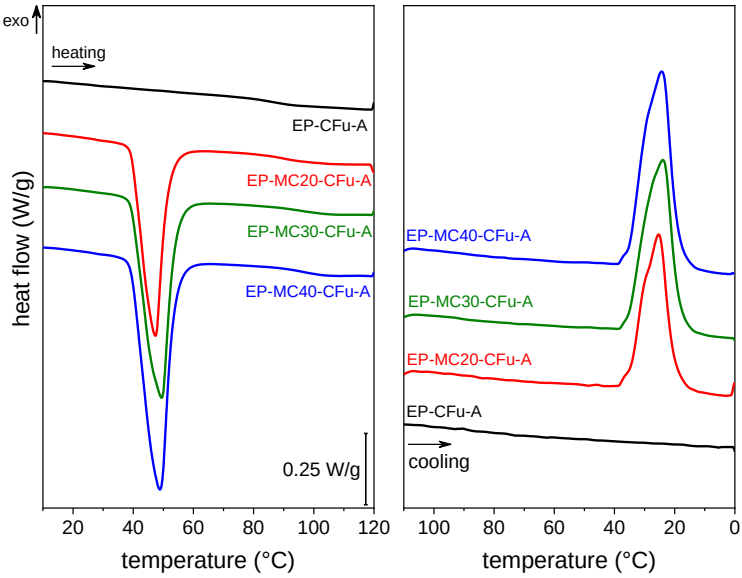

Figure V - 28. Representative DSC thermograms of laminates EP-MCx-CFu-A. First heating scan and cooling scan.

The phase change enthalpy also increases with the MC loading, up to 48.7 J/g for the sample EP-MC40-CFu-A. While preparing the laminates, the nominal and experimental weight fractions of MC in the initial EP/MC mixtures were known, but the MC weight fraction in the laminates is also influenced by the resultant weight fraction of fibers and matrix, which is affected by the matrix viscosity that in turn depends on the starting MC loading, if the processing conditions (applied pressure) are not modified. As in the case of the Elium-based laminates reported in Subchapter 4.4, since the nominal MC weight fraction in the laminates is not known *a priori*, it is not possible to calculate a relative melting enthalpy (ΔH_m^{rel}). However, an experimental

MC weight fraction can be still calculated from the values of phase change enthalpy measured with DSC, by dividing the melting enthalpy measured on the laminates by that measured on the neat MC. This can be done by assuming that the MC maintain their energy storage efficiency also after the lamination process, which is a reasonable hypothesis considering the results of the characterization of the EP-MCx samples (Subchapter 5.3). These values of experimental MC weight fraction (ω_{MC}) are reported in Table V - 22 with the other DSC results. The MC weight fraction increases with the initial MC loading in the epoxy mixture and spans from 13.2 wt% to 22.0 wt%, without remarkable differences between the type A and type B laminates, which indicates that the final MC loading is not significantly influenced by the number of layers in the laminate.

Table V - 22. Results of the DSC tests on the laminates EP-MCx-CFu-A and EP-MCx-CFu-B (first heating scan and cooling scan).

Sample	T_g (°C)	T_m (°C)	ΔH_m (J/g)	T_c (°C)	ΔH_c (J/g)	ω_{MC} (wt%)
MC	-	46.5	221.7	27.6	223.5	100
EP-CFu-A	87.1	-	-	-	-	0
EP-MC20-CFu-A	89.0	45.4	29.3	27.0	29.8	13.2
EP-MC30-CFu-A	95.9	47.8	40.3	25.5	40.2	18.2
EP-MC40-CFu-A	93.4	48.2	48.7	24.9	48.7	22.0
EP-CFu-B	84.7	-	-	-	-	0
EP-MC20-CFu-B	90.5	49.2	30.6	23.8	30.5	13.8
EP-MC30-CFu-B	93.1	51.0	42.0	21.9	41.9	19.0
EP-MC40-CFu-B	94.2	53.7	47.5	19.4	47.1	21.4

T_g = glass transition temperature of the epoxy phase (°C); T_m = melting temperature of the PCM (°C); ΔH_m = PCM melting enthalpy (J/g); T_c = crystallization temperature of the PCM (°C); ΔH_c = PCM crystallization enthalpy (J/g); ω_{MC}= experimental capsule weight fraction calculated from the measured melting enthalpy (wt%).

The effective fiber weight fraction of the laminates was then investigated through TGA, which was also useful to assess their thermal stability. The results of this characterization are reported in Figure V - 29 and Table V - 23. All the tested samples present a single degradation step, which represents the degradation of the epoxy and MC phases and is observable as a single peak also in the signal of the mass loss derivative. The residual mass after the test (m_r) allowed the calculation of the fiber weight fraction, which was computed by considering the residual mass of the EP/MC systems determined in Subchapter 5.3 and that of the employed carbon fibers that resulted as 96.0 wt%.

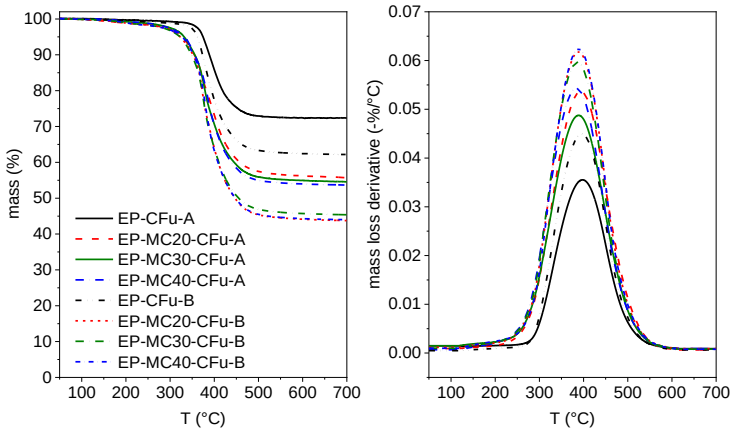

Figure V - 29. TGA thermograms of the laminates EP-MCx-CFu-A and EP-MCx-CFu-B. Residual mass and mass loss derivative as a function of temperature.

The weight fractions of carbon fibers calculated from these results ($\omega_{f,TGA}$) are reported in Table V - 23. It decreases with an increase in the MC loading and it is lower for the type B laminates, which indicates that the flow of the matrix out of the CF fabric is hindered by the increase in the laminate thickness and by the viscosity increase determined by the MC addition. $\omega_{f,TGA}$ ranges from 71.5 wt% of the sample EP-CFu-A to 41.8 wt% for the sample EP-MC40-CFu-B, and the decrease does not follow a linear trend with the MC content. As the TGA is performed on specimens of few milligrams, the test was repeated on at least three specimens and the standard deviation never overcame 1.5 wt%. The lower fiber content and the consequent higher epoxy and MC weight fraction are probably at the basis of the decreased thermal stability of the laminates with the highest MC loading, as can be appreciated from the lower values of $T_{1\%}$, $T_{3\%}$, and $T_{5\%}$. On the other hand, the degradation interval is not remarkably affected by the composition of the laminate, and the lowest degradation peak temperature is 387.6 °C, which is 14 °C lower than that of the laminate EP-CFu-A. In all cases, the thermal degradation is far below the operative temperature interval for which these materials are intended.

A comment shall be made on the degradation behavior in TGA of the carbon fibers used in this Chapter, for which the residual mass is 96.0 wt%, with a mass loss of 4.0 wt%. For the other continuous carbon fibers object of this thesis (the bidirectional carbon fiber fabric labelled CF), the mass loss in TGA performed in inert atmosphere resulted as approx. 99 wt%, with a mass loss of less than 1 wt% attributed to the sizing agent. This implies that the fraction of organic degradable phase over these CFu is not negligible and claimed a deeper investigation of their surface. Such investigation, performed with SEM (not reported for the sake of brevity), revealed a certain amount

of organic residues on the fiber surface, which could explain the degradation behavior; in fact, this residues were not anymore present on the surface of the fibers after TGA. This surface state could not only influence the mechanical properties of the fibers, but also impair the adhesion with the host matrix and thus the mechanical performance of the final composite. However, the aim of this work is to study the effect of the introduction of microcapsules in a host unidirectional composite and make a comparison between the neat epoxy/carbon laminate and those containing MC. Therefore, the fibers were used as received and the properties of the MC-containing laminates were compared to those measured on the neat laminate without MC.

Table V - 23. Results of the TGA tests on the laminates EP-MCx-CFu-A and EP-MCx-CFu-B (first heating scan and cooling scan).

Sample	$T_{1\%}$ (°C)	$T_{3\%}$ (°C)	$T_{5\%}$ (°C)	T_d (°C)	m_r (%)	$\omega_{f,TGA}$ (wt%)
EP-CFu-A	310.5	358.1	368.9	401.2	70.6	71.5
EP-MC20-CFu-A	199.2	307.6	330.2	388.1	53.2	52.6
EP-MC30-CFu-A	207.3	301.1	328.4	387.2	51.9	51.0
EP-MC40-CFu-A	226.4	307.6	333.4	387.6	50.9	50.0
EP-CFu-B	301.3	357.5	365.5	397.2	67.0	67.5
EP-MC20-CFu-B	237.6	310.4	330.5	390.3	50.6	49.6
EP-MC30-CFu-B	215.3	306.6	329.5	388.2	48.4	47.2
EP-MC40-CFu-B	192.5	282.6	323.6	387.6	43.6	41.8

$T_{1\%}$, $T_{3\%}$, $T_{5\%}$= temperature corresponding to a mass loss of 1 %, 3%, 5%; T_d = temperature of the maximum degradation kinetics (peak of the mass loss derivative); m_r = residual mass; $\omega_{f,TGA}$ = weight fraction of carbon fibers determined from the TGA residual mass.

The DSC and TGA data allowed the calculation of the weight fractions of MC and CFu in the laminates, respectively. These data, summarized in Table V - 24, allowed the calculation of the theoretical density (ρ_{th}) of the laminates, by knowing the density of the microcapsules (0.923 ± 0.002 g/cm^3), of the CFu (1.633 ± 0.027 g/cm^3) and of the EP phase (1.158 ± 0.002 g/cm^3), all measured via helium pycnometry. It is worth noticing that the density measured for the fibers is lower than that indicated on the producer's datasheet (1.75-1.80 g/cm^3), which matches the values of density for carbon fibers generally reported in the literature. This could partially be attributed to the organic residues on the fiber surface.

The same technique was employed to measure the experimental density (ρ_{exp}) of the prepared laminates, also reported in Table V - 24. The comparison between ρ_{th} and ρ_{exp} allowed the calculation of the porosity, and then of the volume fraction of the fibers, the microcapsules and the EP phase. As already reported elsewhere in this thesis, the fiber volume fraction and the MC volume fraction follow opposite trends. This is mainly due to the viscosity increase of the EP/MC mixtures, which reduces the

matrix flow out of the carbon fabric during the vacuum bag process. For the same initial MC fraction, the fiber volume fraction decreases with an increase in the laminate thickness, as it is lower for the laminates type B than for the type A. On the other hand, this parameter does not heavily influence the volume fraction of MC. It can be also observed that the experimental MC weight fraction in the matrix $MC/(MC+EP)$ is almost everywhere higher than the initial nominal one, equal to 0, 20, 30 or 40 wt%. This implies that during the vacuum bagging operations the EP phase flows out of the CFu fabric more easily than the microcapsules, thereby increasing the resulting MC concentration with respect to the total matrix faction.

The porosity (ϑ_v) also increases with the MC concentration, which is once again linked to the increased matrix viscosity, but is not remarkably different for the laminates type A and type B.

Table V - 24. Theoretical density, experimental density, and compositions of the laminates EP-MCx-CFu.

Sample	$\omega_{f,TGA}$ (wt%)	ω_{MC} (wt%)	$\frac{MC}{MC+EP}$ (wt%)	ρ_{th} (g/cm^3)	ρ_{exp} (g/cm^3)	ϑ_v (vol%)	ϑ_f (vol%)	ϑ_{MC} (vol%)
EP-CFu-A	71.5	0	0	1.462	1.428	2.31	62.5	0.0
EP-MC20-CFu-A	52.6	13.2	27.8	1.315	1.226	6.78	39.4	17.5
EP-MC30-CFu-A	51.0	18.2	37.1	1.290	1.223	5.14	38.2	24.1
EP-MC40-CFu-A	50.0	22.0	44.0	1.272	1.163	8.53	35.6	27.7
EP-CFu-B	67.5	0	0	1.441	1.423	1.25	58.8	0.0
EP-MC20-CFu-B	49.6	13.8	27.4	1.300	1.236	4.90	37.6	18.5
EP-MC30-CFu-B	47.2	19.0	36.0	1.271	1.225	3.68	35.4	25.1
EP-MC40-CFu-B	41.8	21.4	36.8	1.241	1.140	8.14	29.2	26.5

ρ_{th} = theoretical density; ρ_{exp} = experimental density measured via pycnometry; $\omega_{f,TGA}$ = fiber weight fraction determined through TGA; ω_{MC} = MC weight fraction determined via DSC; ϑ_v = porosity; ϑ_f = fiber volume fraction; ϑ_{MC} = MC volume fraction.

Although the DSC test is the main characterization technique that gives quantitative information on the heat absorption and release in a certain temperature range, it has the limitation of being performed on samples of few milligrams. Therefore, to study the thermal management properties of the prepared laminates on a slightly bigger scale, a simple yet effective test was performed with thermal imaging techniques also on these samples. For the laminates described in this Subchapter, this test was performed both on heating and on cooling stages. For the tests on heating ramp, an oven was heated up to 70 °C, then the laminates were inserted in the oven one by one and their surface temperature was recorded with a thermal camera while the laminates were heating up to equilibrate their temperature to that of the oven. For the tests on cooling ramp, the laminates were first heated in an oven at 70 °C, then

taken out and left cooling to room temperature, while their surface temperature was measured with a thermal camera.

Figure V - 30 reports the values of temperature as a function of time during both the heating and the cooling stages. As observed for other PCM-containing laminates, the temperature trend shows plateau-like regions, caused by the latent heat absorbed during melting and released during crystallization of the PCM, and this phenomenon causes a remarkable increase in the temperature needed to reach that of the surrounding environment.

Also for these samples, It should be noticed that the rate of heating/cooling is dependent on the laminate mass, which varies as a consequence of the variation in the matrix content. However, the observed plateau-like trends are a clear sign of the variation in the thermal behavior of the laminates (and therefore of the thermal management capability) as a function of the MC content.

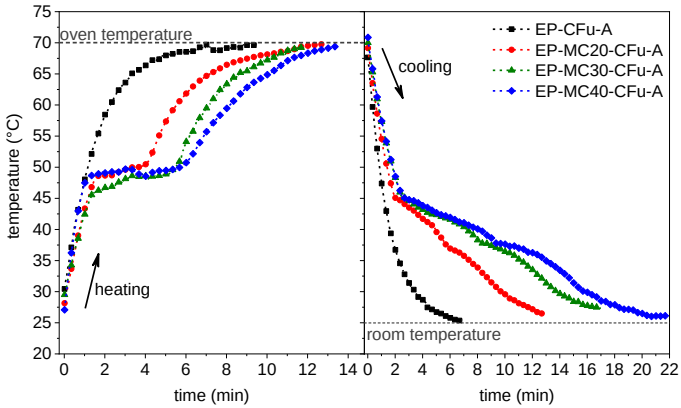

Figure V - 30. Results of the thermal camera imaging tests on the laminates EP-MCx-CFu-A. Surface temperature of the laminates as a function of the testing time.

The results of the LFA test on the laminates EP-MCx-CFu-A are shown in Figure V - 31. The thermal diffusivity of the neat EP-CFu-A decreases slightly with an increase in temperature from 0.42 mm^2/s and 0.40 mm^2/s and, while the specific heat capacity and the thermal conductivity slightly increase with temperature. The thermal conductivity varies in the range 0.61-0.63 W/mK. For the laminates containing MC, the thermal diffusivity and thermal conductivity are lower than for the neat laminate EP-CFu-A, which is in large part due to the lower fraction of carbon fibers and not to the thermal conductivity of the MC phase, since it was observed that the thermal conductivity of the epoxy/MC samples increases with the MC content (see Subchapter 5.3). On the other hand, the specific heat capacity increases with the MC content due to the PCM phase change.

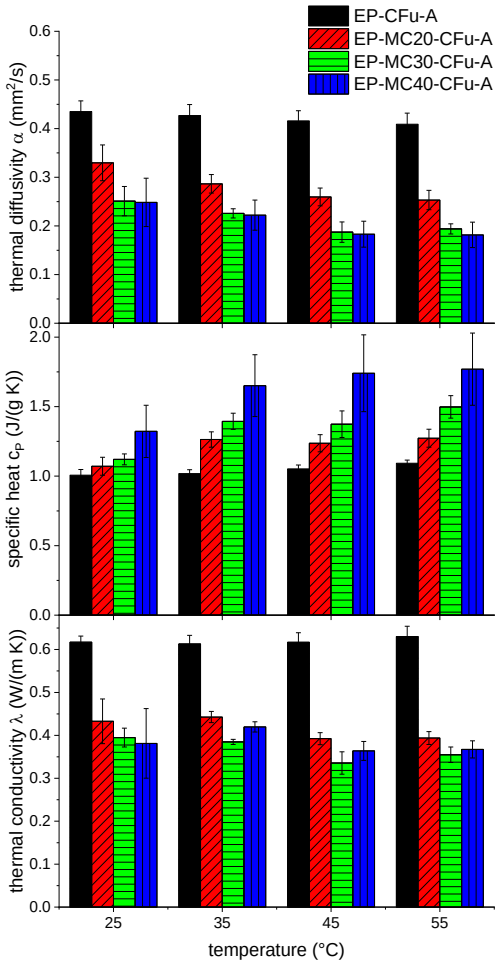

Figure V - 31. Results of the LFA measurements on the laminates EP-MCx-CFu-A.

The following paragraph describes the results of the DMA characterization, which comprises single-frequency, multifrequency and heating/cooling cyclic tests, all performed in single cantilever mode. The results of the single-frequency scans are illustrated in Figure V - 32(a-b) and Figure V - 33.

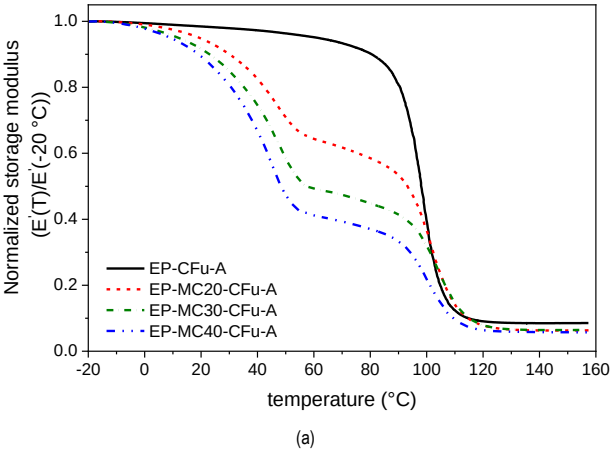

(a)

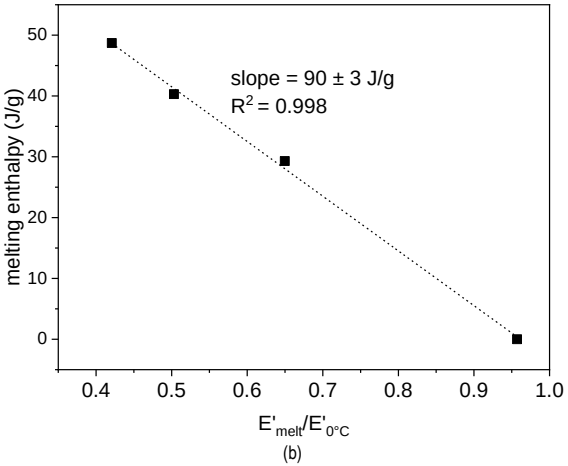

(b)

Figure V - 32. Results of the single-frequency DMA tests on the laminates EP-MCx-CFu-A. (a) storage modulus as a function of temperature, normalized to the value at the beginning of the test (-20 °C); (b) value of E' after PCM melting (60 °C) normalized to the value at 0 °C, as a function of the melting enthalpy, with the results of the linear fitting.

To facilitate the comparison among the samples, the values of E' have been normalized to the value at -20 °C. The storage modulus of the laminate EP-CFu-A (Figure V - 32a) decreases with increasing temperature throughout all the investigated temperature interval, but the decrease is particularly evident at the glass transition of the epoxy phase, where the trends of E'' and $tan\delta$ exhibit peaks (Figure V - 33).

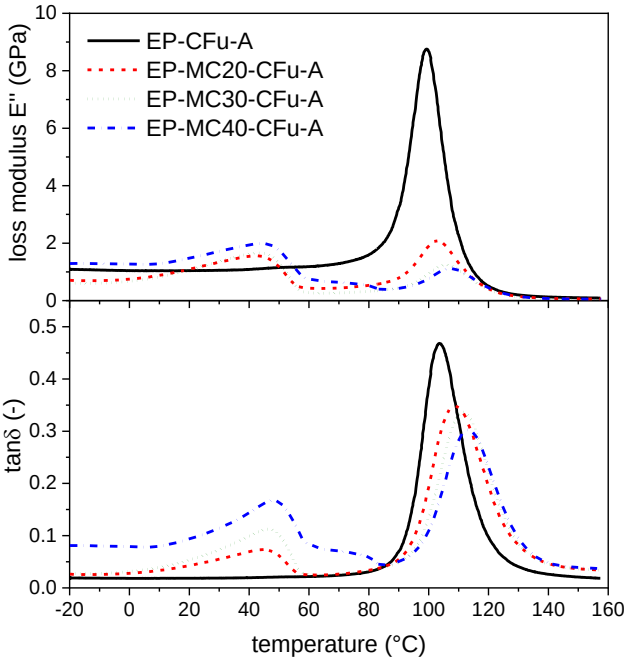

Figure V - 33. Results of the single-frequency DMA tests on the laminates EP-MCx-CFu-A. Loss modulus and $tan\delta$ as a function of temperature.

In the MC-containing composites, two main steps are observable in the trend of E'; the first at the paraffin melting, the second at the glass transition of the EP phase. The drop of E' at the first step increases with the MC fraction. Interestingly, the correlation between the drop amplitude and the MC weight fraction or the melting enthalpy is linear, with R^2 values of 0.998. The trends in Figure V - 33 were obtained with a normalization to the value of E' at 0 °C, to facilitate the comparison with the analysis performed on the laminates EL-MCx-CF described in Subchapter 4.4. However, if a normalization is made to the initial value of E' at -20 °C, the slope of the linear fitting and the value of R^2 would have resulted 89 ± 3 J/g and 0.998, respectively. These values are not significantly different from those reported in Figure V - 32b, which indicates that the variation in E' between -20 °C and 0 °C is negligible. The trends of E'' and $tan\delta$ show peaks in correspondence of the melting step. These peaks shift to higher temperatures and their intensity increases with the PCM content.

As the structural TES composites must withstand repeated thermal cycles around the phase change temperature of the PCM, the variation of the dynamic-mechanical behavior was investigated not only on heating, but also on

cooling, between -40 °C and 60 °C. The results of this analysis are reported in Figure V - 34, which shows the trend of E' in a heating-cooling-heating (h-c-h) scan performed at 3 °C/min on the prepared laminates. To verify the behavior after the first cycle and detect any first-cycle effects, two complete cycles (sequence h-c-h-c-h) were performed on the laminate with the highest PCM content, i.e. EP-MC40-CFu-A.

E' decreases with increasing MC concentration and manifests a decreasing step at the PCM melting, which is almost completely recovered on cooling, as it reaches approx. 95% of the initial value. More specifically, this value is 99.6 % of the initial value for the neat EP-CFu-A laminate, 94.4 % for the laminate EP-MC20-CFu-A, 94.6 % for the laminate EP-MC30-CFu-A, and 95.8 % for the laminate EP-MC40-CFu-A (95.0 % of the initial value after the second cycle), similarly to what reported for the Elium-based laminates described in Subchapter 4.4. Also the trends of E'' and $tan\delta$ (not reported) show similar features and behavior as those of the Elium-based laminates.

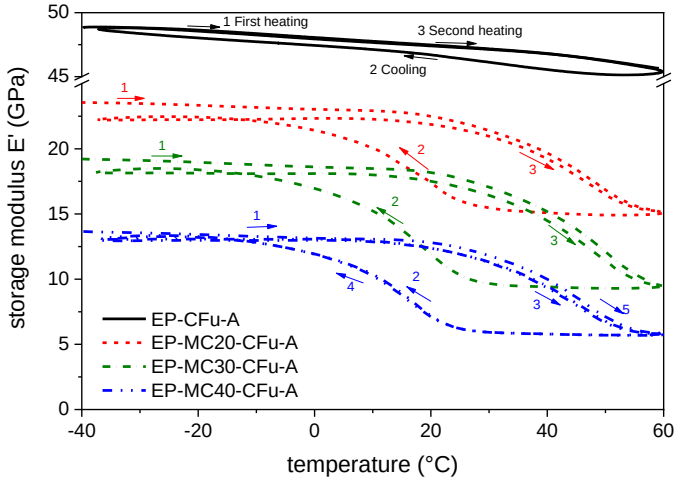

Figure V - 34. Cyclic DMA tests. Storage modulus as a function of temperature during the thermal cycles.

Multifrequency DMA scans were performed to assess the effect of frequency on the PCM melting and the glass transition of the matrix in the prepared composites. The results of the laminates EP-CFu-A and EP-MC40-CFu-A are shown in Figure V - 35(a-b).

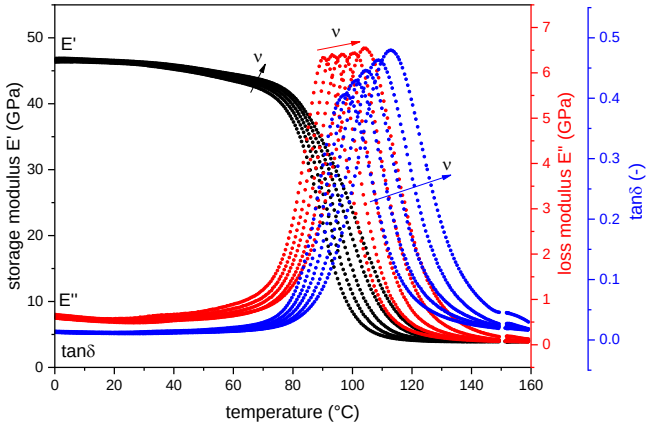

(a)

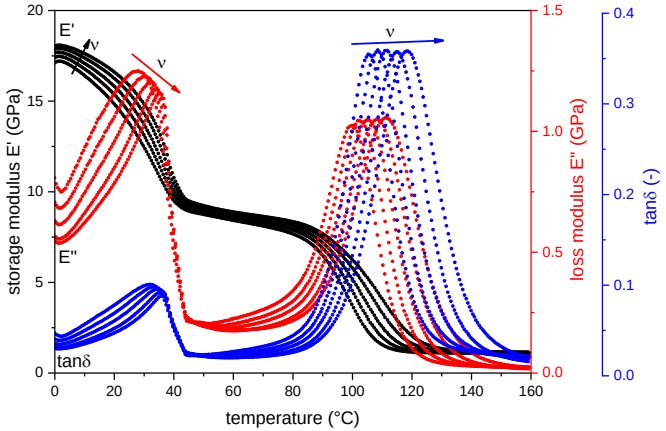

(b)

Figure V - 35. Results on the DMA multifrequency scans on the samples EP-MCx-CFu-A. Investigated frequencies: 0.3-1-3-10-30 Hz. (a) sample EP-CFu-A; (b) sample EP-MC30-CFu-A. Investigated frequencies: 0.3-1-3-10-30 Hz.

For the composite EP-CFu-A, the frequency increase determines a shift of all the parameters to higher temperatures; this effect, although present in the whole investigated temperature range, is more evident at the glass transition of the EP phase. For the composite EP-MC40-CFu-A (and for the other MC-containing laminates) the frequency dependence is observable not only at the glass transition,

but also at the PCM melting, and in this temperature range the frequency sensitivity is higher below the peak temperature than above it, so when the PCM is almost completely melted the frequency dependence weakens considerably, as observed for the Elium-based laminates described in Subchapter 4.4.

These tests allowed the calculation of the activation energy of the glass transition (E_a) from the $tan\delta$ peak temperatures through the Arrhenius approach, as described in Section 3.3.3.5. The results of this analysis are presented in Figure V - 36 and Table V - 25. E_a generally increases with the MC concentration, which implies that the glass transition is hindered by the presence of an increasing amount of fillers (Palumbo et al., 1996; Park et al., 2005). Since the peaks of E'' and $tan\delta$ at the PCM melting also appear to depend on frequency, an attempt was made to apply the Arrhenius approach to calculate the activation energy of this transition. The results of this attempt are reported in Figure V - 36b. A linear correlation could be estimated for the four lower frequency points, but the last point deviates considerably from the linear trend, which makes the application of a precise linear regression difficult. Nevertheless, this DMA investigation contributed to provide an interesting insight on the use of DMA to study a melting phase change, as well as the effects of such transition on the dynamic mechanical properties of the host laminate.

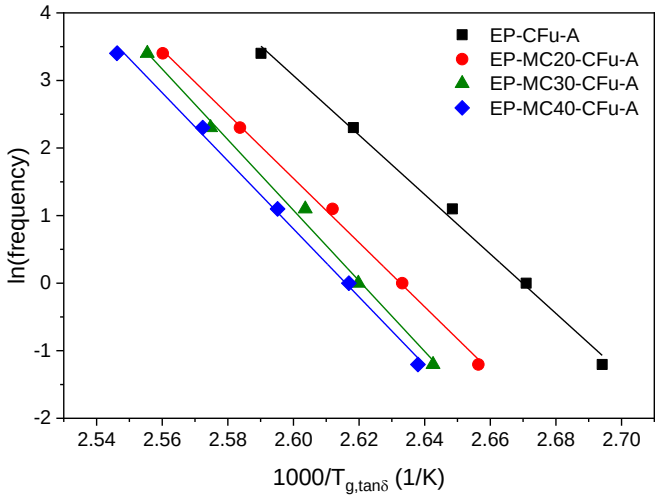

(a)

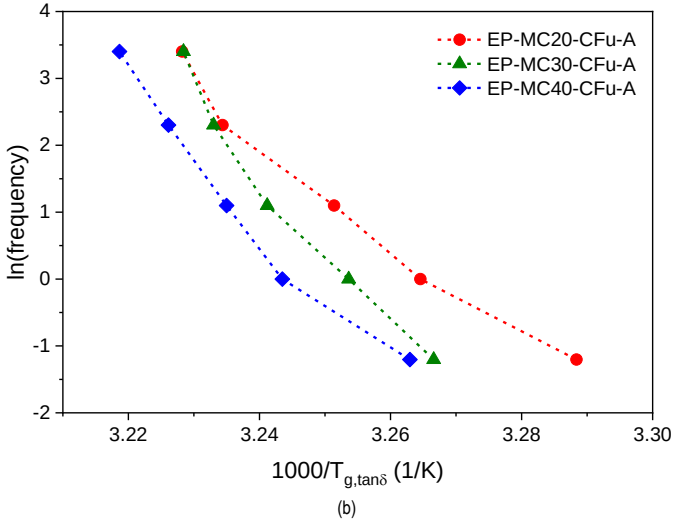

(b)

Figure V - 36. Natural logarithm of frequency as a function of 1000/T (peaks of $tan\delta$ at the glass transition (a) and at the paraffin melting (b)) for the samples EP-MCx-CFu-A.

Table V - 25. Results of the multifrequency DMA scans on the samples EP-MCx-CFu-A

Sample	EP-CFu-A	EP-MC20-CFu-A	EP-MC30-CFu-A	EP-MC40-CFu-A
E_a (kJ/mol)	365 ± 14	395 ± 9	434 ± 17	419 ± 13
R^2	0.996	0.998	0.995	0.997

E_a = activation energy of the glass transition calculated from the $tan\delta$ peaks; R^2 = values of R^2 of the linear regression.

The following paragraphs describe the results of the mechanical characterization on the prepared laminates. Three techniques were applied, i.e. quasi-static tensile tests, three-point bending tests and mode I interlaminar fracture toughness tests. The results of the tensile tests are reported in Table V - 26, which shows the values of tensile moduli in the fiber direction (longitudinal, E_L) and in the transversal direction (E_T). E_L decreases with an increase in the MC fraction, which is mostly due to the decrease in the fiber volume fraction. To separate the contribution of the decrease in the fiber content to that of the change in the properties of the matrix due to MC addition, a theoretical elastic modulus was calculated via the mixture rule reported in Equation (V - 15):

$$E_c = E_f \cdot \vartheta_f + E_m \cdot (1 - \vartheta_f) \quad \textbf{(V - 15)}$$

where E_c is the longitudinal modulus of the composite, E_f and E_m are the moduli of the fibers and the matrix, respectively, and ϑ_f is the fiber volume fraction.

Table V - 26. Experimental longitudinal and transversal tensile moduli measured on the laminates EP-MCx-CFu-A.

Sample	E_L (GPa)	E_T (GPa)
EP-CFu-A	112 ± 7	5.7 ± 0.6
EP-MC20-CFu-A	86 ± 5	4.4 ± 0.6
EP-MC30-CFu-A	72 ± 7	3.1 ± 0.3
EP-MC40-CFu-A	66 ± 2	3.4 ± 0.3

E_L = longitudinal tensile modulus; E_T = transversal elastic modulus;

The calculation of the theoretical elastic modulus was performed as follows. First, the experimental value of elastic modulus of the neat laminate EP-CFu-A was used to calculate an experimental value of E_f via the mixture rule, by knowing ϑ_f (from previous measurements) and E_m (from the data of the Subchapter 5.3). This value of E_f was applied to calculate theoretical values of E_c, with values of ϑ_f equal to those calculated on the MC-containing laminates. For the value of E_m, two approaches were adopted; the first was to put E_m equal to that of the neat epoxy resin for all compositions, and the second was to vary E_m according to the MC content, by considering the elastic moduli of the samples EP-MCx described in Subchapter 5.3. The results of the calculations with these two approaches are reported in the upper part of Figure V - 37, as "E_L theoretical (matrix is EP)" and "E_L theoretical (matrix varies)", respectively.

The two theoretical approaches give approximately the same results, which was expected as the elastic modulus of the matrix has little relevance when calculating the modulus of a unidirectional carbon-reinforced composite in the fiber direction. Additionally, the theoretical values are equal to (or in some cases even lower than) the experimental values, which means that the decrease in the elastic modulus with an increase in MC concentration is entirely due to a decrease in the fiber volume fraction, and the MC phase does not actively contribute to decrease it, for instance by decreasing the fiber alignment. In some cases, as for the laminate EP-MC20-CFu-A, the MC phase seems even to contribute positively to the elastic modulus, as the experimental value deviates positively from the theoretical trend, but further analysis is needed to verify this hypothesis. This approach is conservative, as it does not take into account the pore volume fraction in the calculation of the theoretical moduli, which would have resulted in even lower values.

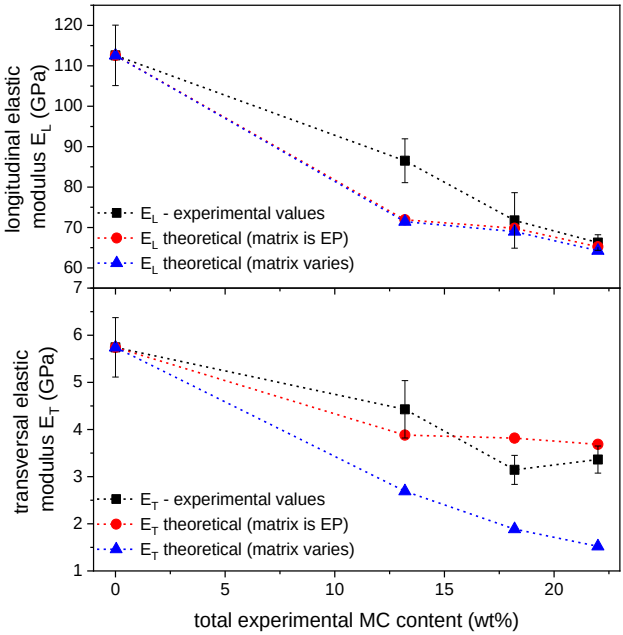

Figure V - 37. Experimental and theoretical tensile moduli of the laminates EP-MCx-CFu-A. The theoretical moduli E_L and E_T were calculated via the direct and inverse mixture rule, respectively, starting from the properties measured on the neat laminate EP-CFu-A.

A similar analysis was performed on the values of the transversal modulus, but in this case the inverse mixture rule was applied, as reported in Equation (V - 16):

$$\frac{1}{E_c} = \frac{\vartheta_f}{E_f} + \frac{1-\vartheta_f}{E_m}. \qquad \textbf{(V - 16)}$$

The results of this calculation are reported in Figure V - 37. In this case, the two approaches for the calculation of the theoretical moduli gave different results, because a variation in E_m determines important variations in the transversal modulus, and since the elastic modulus of the epoxy/MC samples decreases with an increase in the MC content, also the theoretical transversal modulus of the composites is lower when in is calculated with the approach "matrix varies". The experimental values of E_T are higher than the theoretical values calculated with this approach, so a much lower decrease in E_T was expected if considering the elastic moduli of the epoxy/MC samples. On the other hand, the experimental values of E_T are closer to those calculated only by considering a decrease in the fiber volume fraction.

Therefore, it can be concluded that the longitudinal and transversal moduli of these composites are affected by the MC phase only because it determines an increase in the matrix viscosity and thus a decrease in the final fiber volume fraction. This conclusion is similar to that obtained from the evaluation of the elastic modulus of the epoxy/carbon laminates containing ParCNT (Subchapter 5.2). In those laminates, the fiber volume fraction was almost independent from the PCM content, and the flexural elastic modulus was not significantly affected by the laminate composition.

The results of the three-point bending tests are shown in Figure V - 38 and Figure V - 39. Figure V - 38 reports representative load-displacement curves, which show a behavior similar to that observed on other PCM-containing laminates described in the previous chapters of this thesis. The curves of all the samples present an initial linear zone, but the behavior after the maximum load of the neat EP-CFu laminate is different from that observed on the MC-containing laminates.

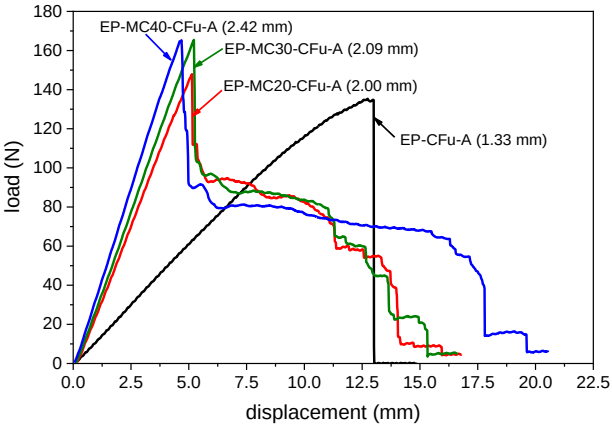

Figure V - 38. Representative load-displacement curves obtained in three-point bending tests on the laminates EP-MCx-CFu-A. The value in brackets represents the laminate thickness.

The neat laminate is subjected to a catastrophic failure, which always started from the tensile-stressed mid-lower region of the specimen. Such failure mode is often associated to a good interlaminar adhesion (Abdel Ghafaar et al., 2006; Ary Subagia et al., 2014). On the other hand, as already observed elsewhere in this thesis, the PCM-containing laminates are subjected to a progressive failure and present a drop-plateau sequence, which indicates a dissipation of mechanical energy also during damage propagation. The damage was observed starting either in the

mid-upper zone, subjected to compression, or in the interlaminar zone. This is observable also from the optical microscope micrographs of the specimens after the test shown in Figure V - 40. This failure mode has been described as typical of materials having a tensile in-plane strength considerably higher than the interlaminar shear strength, which is the case for the MC-containing laminates reported in this work.

Figure V - 39 summarizes the main results of the three-point bending tests, as it shows the trends of the flexural elastic modulus, stress and strain at break as a function of the MC weight fraction. Figure V - 39 also shows the values of interlaminar shear strength ($ILSS$) obtained during short-beam shear tests on the type B laminates. The elastic modulus is seen decreasing with an increase in the MC content, which is due to the reduction in the fiber volume fraction. However, also the flexural strength decreases, and this is probably related to the introduction of new damaging mechanisms such as the delamination and interlaminar fracturing. The same phenomena are also at the basis of the reduction of the $ILSS$.

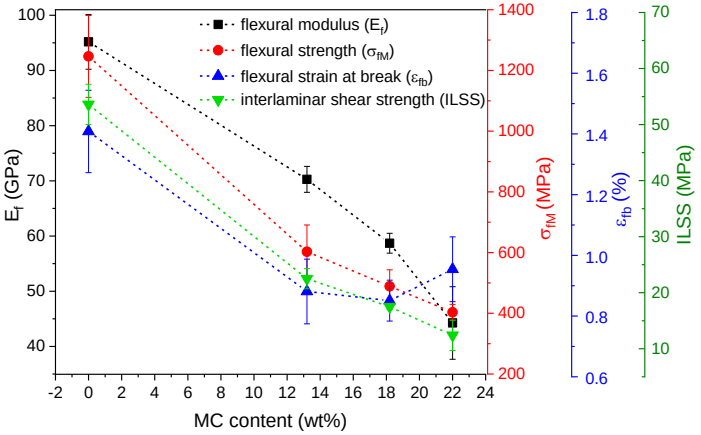

Figure V - 39. Main results of the three-point bending tests on the laminates EP-MCx-CFu-A. Flexural modulus (E_f), strength (σ_{fM}), and strain at break (ε_{fb}) as a function of the MC weight fraction. Results of the short-beam shear tests on the laminates EP-MCx-CFu-B. Interlaminar shear strength (ILSS) as a function of the MC weight fraction.

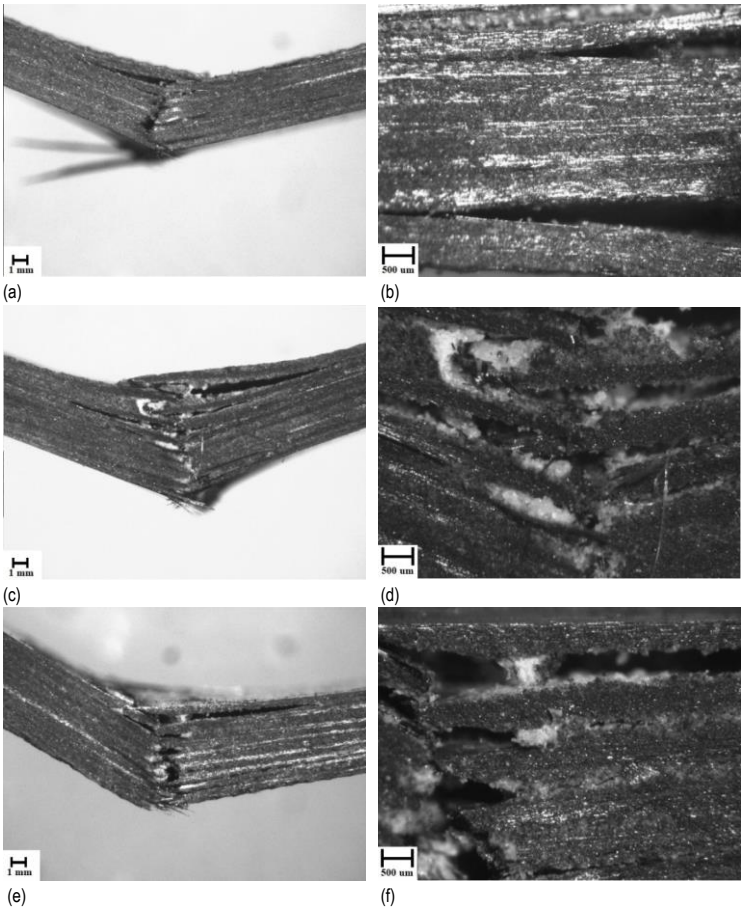

Figure V - 40. Optical microscope micrographs of the specimens after three-point bending tests at room temperature. (a-b) EP-MC20-CFu-A; (c-d) EP-MC30-CFu-A; (e-f) EP-MC40-CFu-A.

The same three-point bending tests were performed at 65 °C, above the PCM melting temperature. The results of this characterization are reported in Table V - 27. The elastic modulus is only marginally affected by temperature, as the values are approx. the same as those measured at room temperature for the laminate EP-MC20-CFu-A and slightly lower for greater MC concentrations. On the other hand, the decrease in the properties at failure (flexural strength and strain at break) is more dramatic, and the decrease is higher for higher MC content. This is probably due to a decrease in the mechanical properties of the microcapsules when the core is melted, thus causing a further decrease in the mechanical properties of the interlaminar region.

Moreover, the behavior of the load-deflection curve in the region of the defect propagation was different from that observed at room temperature (Figure V - 41); all the tested specimens containing MC presented a long plateau, and for some of them the load did not drop to zero.

Table V - 27. Results of the three-point bending tests on the laminates EP-MCx-CFu-A performed at 65 °C. Values of flexural modulus (E_f), strength (σ_{fM}), and strain at break (ε_{fb}) and relative values compared to the results at room temperature.

Sample	$E_f^{65\,°C}$ (GPa)	$\frac{E_f^{65\,°C}}{E_f^{RT}}$ (%)	$\sigma_{fM}^{65\,°C}$ (MPa)	$\frac{\sigma_{fM}^{65\,°C}}{\sigma_{fM}^{RT}}$ (%)	$\varepsilon_{fb}^{65\,°C}$ (%)	$\frac{\varepsilon_{fb}^{65\,°C}}{\varepsilon_{fb}^{RT}}$ (%)
EP-MC20-CFu-A	69.8 ± 0.9	99.2	447 ± 26	74.1	0.69 ± 0.05	78.6
EP-MC30-CFu-A	50.1 ± 2.2	85.3	290 ± 1	59.2	0.60 ± 0.06	70.2
EP-MC40-CFu-A	40.9 ± 2.1	92.6	238 ± 1	58.9	0.67 ± 0.10	70.0

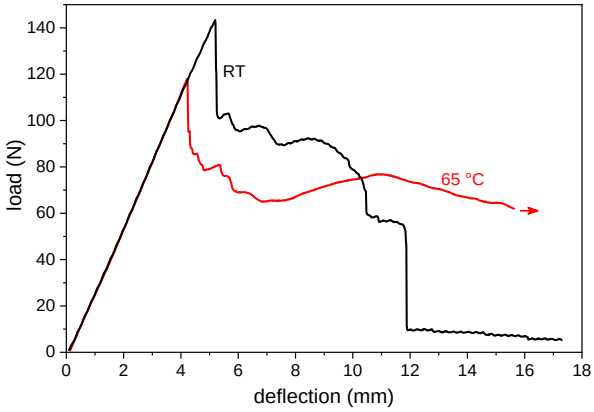

Figure V - 41. Representative load-deflection curves obtained during three-point bending tests on the laminate EP-MC20-CFu-A at room temperature (RT) and at 65 °C.

Figure V - 42 shows representative load-displacement curves obtained in the mode I interlaminar fracture toughness tests, while Figure V - 43 shows the obtained R-curves, i.e. the delamination resistance as a function of the crack length, for the four prepared compositions. All the load-displacement curves are a subsequence of load drops and plateaus, especially that of the neat laminate EP-CFu-B, which may impair the reliability of the results.

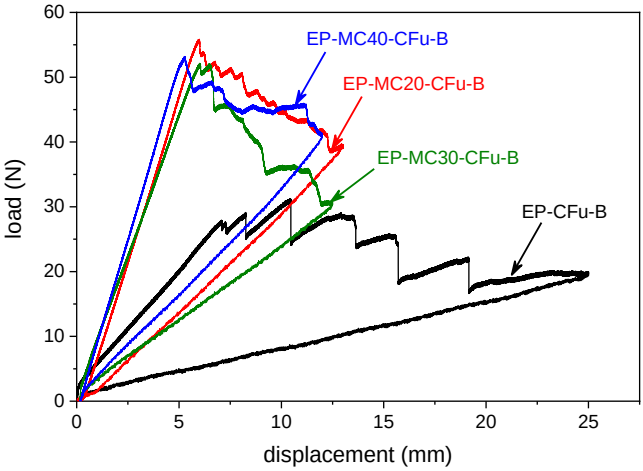

Figure V - 42. Load-displacement curves obtained in mode I interlaminar fracture toughness tests on the laminates EP-MCx-CFu-B.

Table V - 28 collects the mode I critical strain energy release rates for crack initiation (G_{Ii}) and steady-state propagation (G_{Ic}). The G_{Ii} is determined at the initial delamination of the specimen, when the pre-crack start to grow. The first point of G_{Ii} could be evaluated in different ways; the way adopted in this work is the deviation from the linearity of the load-displacement curve. The G_{Ic} is obtained as the average value in the steady state region, after approx. 5-10 mm of crack propagation (a > 60 mm). Generally, G_{Ii} is independent from the fiber volume fraction, while G_{Ic} can vary as a function of this parameter (Compston and Jar, 1999; Thakre et al., 2011). For the laminate EP-MC20-CFu-B, both G_{Ii} and G_{Ic} are higher than those of the neat EP-CFu-B, which implies that the introduction of a modest amount of MC activates different toughening mechanisms; such mechanisms could be the particle debonding, crack pinning, crack deflection and micro-cracking. On the other hand, above a certain MC concentration, both G_{Ii} and G_{Ic} decrease with increasing MC content, which can be due to an excessive thickening and decrease in the mechanical properties of the interlaminar region, in turn caused by a poor capsule/matrix adhesion and by their intrinsic low mechanical properties. From a visual observation of the specimens during the test, the samples EP-CFu-B and EP-MC20-CFu-B showed fiber bridging, while this phenomenon was not observed for the laminates with a higher MC concentration, for which the crack propagated mostly through the matrix (

Figure V - 44).

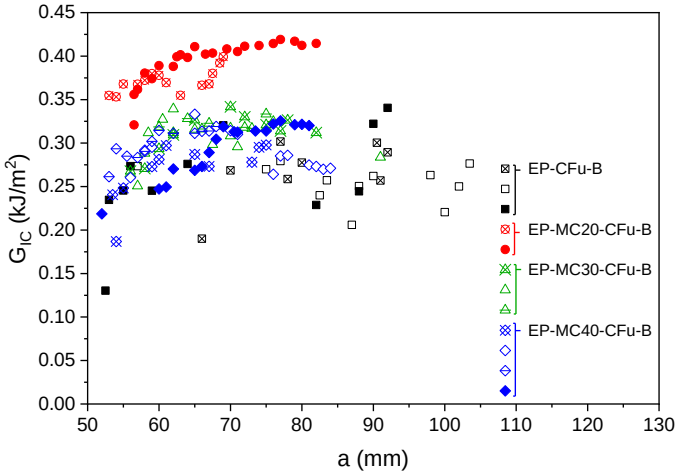

Figure V - 43. R-curves of the laminates EP-MCx-CFu-B. The results of two to four specimens are shown for each sample.

Table V - 28. Mode I critical strain energy release rates for crack initiation (G_{Ii}) and steady-state propagation (G_{Ic}) for the laminates EP-MCx-CFu-B

Sample	G_{Ii} (MPa·m$^{1/2}$)	G_{Ic} (MPa·m$^{1/2}$)
EP-CFu-B	0.15 ± 0.03	0.27 ± 0.01
EP-MC20-CFu-B	0.34 ± 0.02	0.40 ± 0.01
EP-MC30-CFu-B	0.27 ± 0.02	0.32 ± 0.01
EP-MC40-CFu-B	0.24 ± 0.02	0.30 ± 0.02

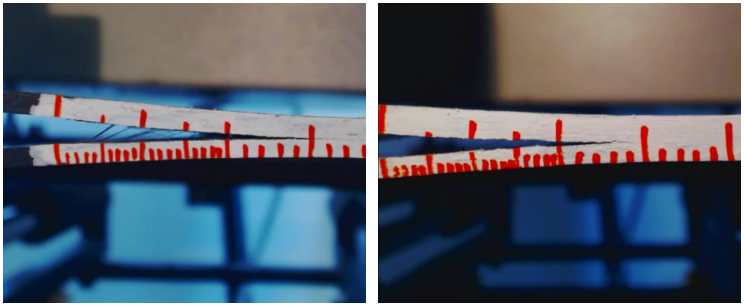

(a) (b)

Figure V - 44. Specimens of the mode I interlaminar fracture toughness tests. (a) EP-MC20-CFu-B, with evidence of fiber bridging; (b) EP-MC40-CFu-B, without evidence of fiber bridging.

5.4.3 Conclusions

The present Subchapter described the thermo-mechanical evaluation of unidirectional carbon/epoxy composites containing paraffin microcapsules. As already reported elsewhere in this thesis, the MC phase increased the viscosity of the epoxy matrix, which limited the flow of the epoxy/MC mixtures out of the fiber fabric, thereby increasing the matrix weight and volume fraction and reducing that of the fibers. This was at the basis of a decrease in the mechanical properties of the prepared laminates with high MC concentration, but the application of theoretical models showed that this decrease was only due to the decrease in volume fraction of the reinforcement and not due to a change in the properties of the constituents and the fiber-matrix interaction.

The MC phase was preferentially distributed in the interlaminar region, which lead to a thickening of this region and a decrease in properties such as the interlaminar shear strength. On the other hand, a modest MC fraction lead to an increase in the mode I interlaminar fracture toughness, probably due to the introduction of new toughening mechanisms such as the debonding, crack deflection, and microcracking. However, an excessive MC content reduced the values of G_{Ic}, because the crack propagated through the matrix and not at the fiber/matrix interface, thereby reducing the toughening mechanism of the fiber bridging.

For the thermal properties, the melting enthalpy increased with the initial MC fraction and reached a value of 48.7 J/g. Therefore, the TES and thermal management capability of the prepared laminates increased with the MC fraction, as also demonstrated by thermal imaging tests. The DMA characterization confirmed that this techniques is an useful complement to DSC to study the melting and crystallization of a PCM when embedded in a polymer composite, in terms of the effects of the phase change on the viscoelastic properties of the host composite.

The following Subchapter will illustrate the application of the same epoxy/MC systems in combination with discontinuous reinforcements.

5.5 Epoxy/milled carbon fibers composites containing paraffin microcapsules

Short carbon fibers are one of the most widely used reinforcements to improve the mechanical and tribological performance of polymers. Compared to continuous fiber reinforced composites, short fiber reinforced composites (SFRCs) combine easier processability with a low manufacturing cost and fill the mechanical property gap between the continuous-fiber laminates used as primary structures and the unreinforced polymers used for non-structural applications (Rezaei et al., 2009). This

is the main reason why in the last few years the use of SFRCs has grown rapidly in various engineering applications, especially in the automotive and mechanical engineering sectors, in combination with thermoplastic and thermosetting resins. These fields could benefit from the introduction of novel semi-structural composites combining good mechanical properties and thermal management capability.

Therefore, the aim of this Subchapter is to explore the thermomechanical properties of epoxy resins reinforced with discontinuous carbon fibers and containing paraffin microcapsules.

5.5.1 Materials and methods

The present Section lists the materials used to fabricate these samples, and then it describes in detail the techniques for the preparation of the same. It subsequently lists all the characterization techniques applied on these samples. Since the materials and the characterization techniques have been already detailed in Chapter III, this section will illustrate only the experimental parameters that are specific of this Subchapter.

5.5.1.1 Materials

Table V - 29 lists the materials used for the preparation of these composites (please refer to Section 3.2.4 for the details about the materials).

Table V - 29. Materials employed in Subchapter 5.5.

Phase	Label	Material
Polymer matrix	EP	Epoxy resin
Reinforcement	CFS	Discontinuous carbon fibers (length 100 μm)
PCM	MC	Paraffin microcapsules

5.5.1.2 Sample preparation

The epoxy base and the hardener were mixed at a constant weight ratio of 100:30 together with the CFS and MC at different relative concentrations. The resulting mixtures were degassed under vacuum and poured in silicone molds. The samples were cured at r.t. for 24 hours and post-cured for 10 hours at 100 °C. The prepared neat epoxy and composite samples with various fiber and MC concentrations are listed in Table V - 30. A first sample series was prepared by keeping a constant fiber amount of 10 wt% and varying the MC content from 5 wt% up to 30 wt% of the total matrix (epoxy + MC). In a second group, the MC amount was kept constant at 20 wt% of the total matrix, and the reinforcement varied between 5 wt% and 20 wt%.

Table V - 30. List of the prepared EP-MC-CFS samples with nominal weight compositions.

Sample	EP (wt%)	MC (wt%)	CFS (wt%)
EP	100.0	0.0	0.0
MC	0.0	100.0	0.0
EP-CF10	90.0	0.0	10.0
EP-MC5-CFS10	85.5	4.5	10.0
EP-MC15-CFS10	76.5	13.5	10.0
EP-MC30-CFS10	63.0	27.0	10.0
EP-MC20	80.0	20.0	0.0
EP-MC20-CFS5	76.0	19.0	5.0
EP-MC20-CFS10	72.0	18.0	10.0
EP-MC20-CFS15	68.0	17.0	15.0

EP = epoxy resin; MC = paraffin microcapsules; CFS = short discontinuous carbon fibers.

5.5.1.3 Characterization

The prepared samples were investigated through the characterization techniques listed in Table V - 31 with the experimental parameters applied specifically on these samples (see Section 3.3 for the full description of the characterization parameters and specimen preparation).

Table V - 31. Characterization techniques and experimental parameters applied on the samples EP-MC-CFS.

Technique	Specific experimental parameters
SEM	Cryofracture surface; Instrument Zeiss Supra 60 FE-SEM
Liquid displacement	As described in Section 3.3.2.1
DSC	Temperature interval 0-130 °C
TGA	TA Q5000 IR thermobalance; specimen mass 10 mg
Flexural test	As described in Section 3.3.5.2
Charpy impact test	As described in Section 3.3.5.3

5.5.2 Results and discussion

Figure V - 45(a-d) shows the SEM micrographs of the composites with a MC content of 20 wt%, at two different CF amounts (5 and 15 wt %).

As for the unreinforced EP-MCx samples described in Subchapter 5.3, the capsules have a dimension of approx. 20 μm and are homogeneously distributed within the polymer matrix. The same considerations can be done also for the adhesion between the MC shell and the epoxy matrix, which is not optimal, but it is still enough to allow the fracture propagate across the microcapsules and not at the interface. The adhesion between the matrix and the fibers is also not optimal and the failure of the

interphase is adhesive, which can partially depend on the fact that these fibers are not sized. No substantial morphological differences can be detected by varying the CF content. The fracture morphology resembles that of the polyamide/short carbon fiber composites containing paraffin microcapsules described in Subchapter 4.3.

Table V - 32 reports the values of the theoretical density (ρ_{th}), experimental density (ρ_{exp}) and pore volume fraction (ϑ_v). As done for EP-MCx samples, for the neat epoxy sample only an experimental value can be determined (the theoretical values may depend on the base/hardener ratio and the curing conditions), and therefore the theoretical density was set equal to the experimental density, thereby determining a pore volume fraction equal to zero. The density of the neat microcapsules was put equal to 0.901 ± 0.005 g/cm^3, as found for the EP-MCx samples.

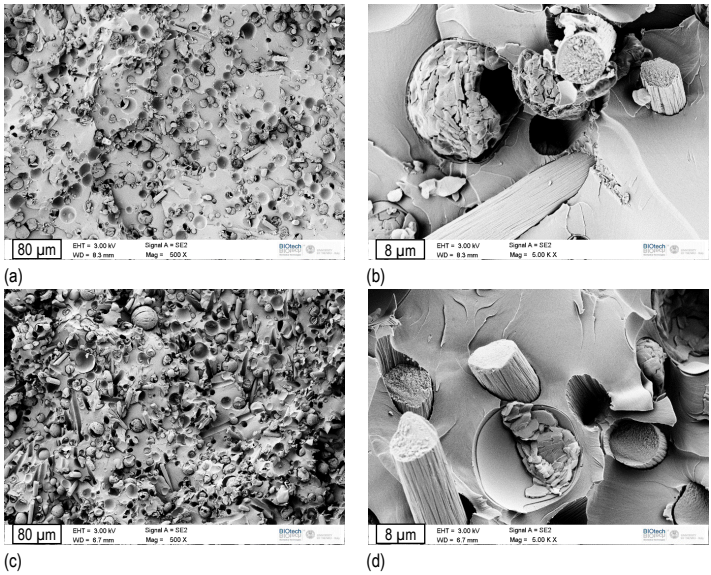

Figure V - 45. SEM micrographs of the cryofracture surfaces of the composites EP-MC-CFS. (a) EP-MC20-CF5, 500x; (b) EP-MC20-CF5, 5000x; (c) EP-MC20-CF15, 500x; (d) EP-MC20-CF15, 5000x.

Table V - 32. Theoretical density (ρ_{th}), experimental density (ρ_{exp}), and pore volume fraction (ϑ_v) of the EP-MC-CFS samples.

Sample	ρ_{th} (g/cm³)	ρ_{exp} (g/cm³)	ϑ_v (vol %)
EP	1.1470*	1.1470 ± 0.0014	-
EP-CFS10	1.2093	1.2005 ± 0.0002	0.73 ± 0.02
EP-MC5-CFS10	1.1982	1.1774 ± 0.0018	1.73 ± 0.15
EP-MC15-CFS10	1.1760	1.1310 ± 0.0028	3.82 ± 0.24
EP-MC30-CFS10	1.1426	1.0686 ± 0.0009	6.48 ± 0.08
EP-MC20	1.0976	1.0573 ± 0.0014	3.67 ± 0.13
EP-MC20-CFS5	1.1312	1.0736 ± 0.0013	5.09 ± 0.11
EP-MC20-CFS10	1.1648	1.0998 ± 0.0012	5.58 ± 0.10
EP-MC20-CFS15	1.1985	1.1184 ± 0.0006	6.68 ± 0.05

ρ_{etOH} = 0.7848 g/cm³.

Also in this case, the introduction of an increasing amount of MC leads to a decrease in the density values. This is not surprising, since the density of MC is lower than that of the neat epoxy. On the other hand, MC addition produces a progressive increase in the pore volume fraction. For instance, a ϑ_v value of 6.5 % was determined for the EP-MC30-CF10 sample, which is imputable to the increase in viscosity and decrease in processability with an increase in the MC fraction. The same trend in pore concentration can be seen in samples with an increasing amount of CF at a constant MC loading. Also in this case, this result can be ascribed to the rise in the viscosity of the mixtures.

Thermogravimetric analysis (TGA) was performed to investigate trends in the thermal degradation resistance. Figure V - 46 reports TGA thermograms of EP-MCx-CFS10 (x = 5, 15, 30) samples (left) and EP-MC20-CFSx (x = 5, 10, 15) samples (right). The most important results of TGA tests are summarized in Table V - 33.

The tests allowed the measurements of the temperature corresponding to a mass loss of 1 wt% ($T_{1\%}$), the temperature at the peak of mass loss derivative, which is the temperature at the maximum degradation kinetics (T_d), and the mass residue after the test (m_r). Then, an experimental mass fraction of CFS (ω_f) could be calculated with Equation (V - 17), as

$$\omega_f = m_r - m_r^{EP} \cdot \omega_{EP} \qquad \textbf{(V - 17)}$$

where m_r is the residual mass of the composite at the end of the test, m_r^{EP} is the residual mass of the neat epoxy and ω_{EP} is the weight fraction of epoxy in the composites.

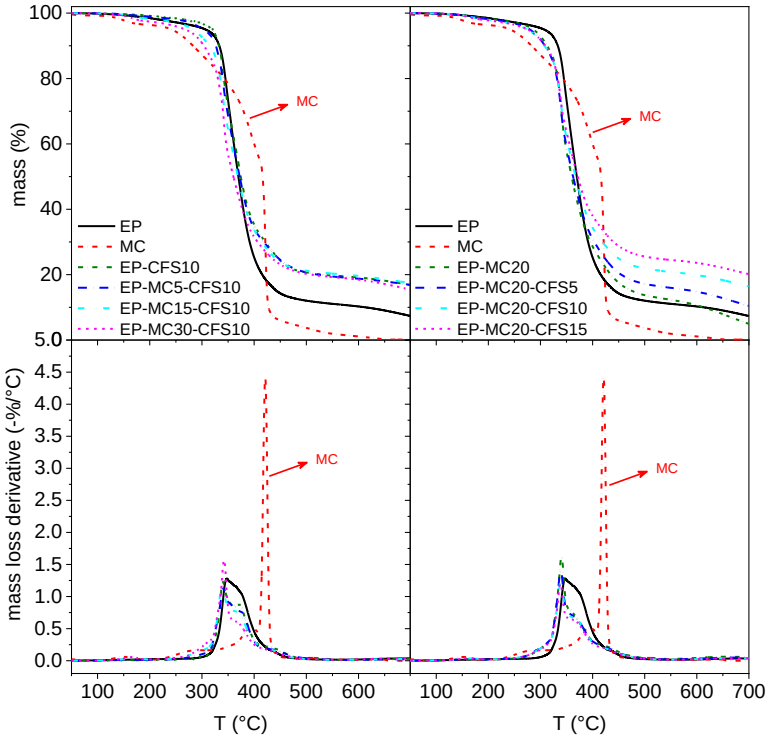

Figure V - 46. TGA thermograms of the samples EP-MC-CFS. Mass and mass loss derivative as a function of temperature.

As expected from the EP-MCx results described in Subchapter 5.3, the introduction of MC leads to a decrease in the thermal stability, as $T_{1\%}$ decreases with an increase in the MC fraction. On the other hand, the CFS phase has a positive impact on the thermal resistance of the composites. However, in all the considered compositions, T_d is not remarkably affected by the CFS and MC content, and the degradation temperature is everywhere far above the processing and service temperatures of the composites. The experimental weight fraction of CFS is close to the nominal value in all compositions, which is index of the compositional homogeneity of the prepared composites.

Table V - 33. Results of the TGA tests on the samples EP-MC-CFS.

Sample	$T_{1\%}$ (°C)	T_d (°C)	m_r (wt %)	ω_f (wt %)
EP	171.7	346.7	7.35	-
EP-CFS10	208.2	340.4	16.79	10.20
EP-MC5-CFS10	196.6	341.4	16.86	10.60
EP-MC15-CFS10	162.6	338.2	17.40	11.50
EP-MC30-CFS10	156.6	342.4	15.42	10.80
EP-MC20	165.0	339.9	4.96	-
EP-MC20-CFS5	163.5	329.1	10.43	4.84
EP-MC20-CFS10	163.8	330.8	16.42	11.13
EP-MC20-CFS15	158.3	327.9	20.17	15.17

$T_{1\%}$ = temperature corresponding to a mass loss of 1 wt%; T_d = degradation temperature, corresponding to the peak of mass loss derivative; m_r = residual mass faction after the test; m_{CFS} = mass fraction of CFS, calculated from m_r.

Figure V - 47 reports the DSC thermograms of the first heating scan and the cooling scan of the samples EP-MCx-CFS10 (x = 5, 15, 30), while the most important DSC results are listed in Table V - 34. The values of the second heating scan are not reported as they are not remarkably different from those of the first. As for the samples EP-MCx described in Subchapter 5.3, the thermograms show both the endo/exothermic signals of the PCM phase change and the inflection point of the glass transition of the epoxy phase.

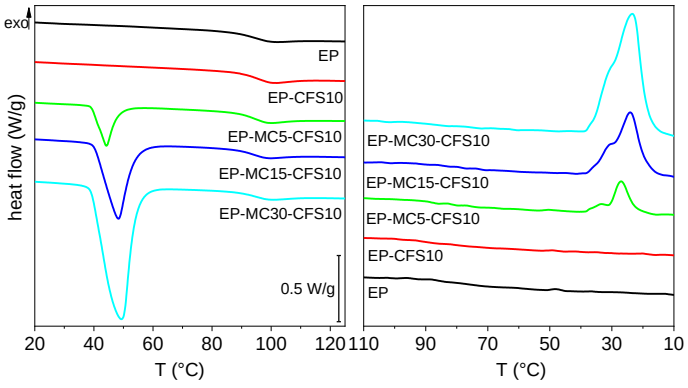

Figure V - 47. DSC thermograms of the samples EP, EP-CF10 and EP-MCx-CF10 (x = 5, 15, 30). First heating scan (left) and cooling scan (right).

The T_g is not significantly affected by the introduction of MC and CFS, while, if the CFS fraction increases, the T_m of the PCM phase slightly decreases and the T_c increases, which is probably due to the increase in the thermal conductivity caused by

the addition of a very conductive filler. However, in all the cases, the variation is quite small.

Table V - 34. Results of DSC tests on the samples EP-MC-CFS (data from the first heating scan and cooling scan).

Sample	T_g (°C)	T_m (°C)	ΔH_m (J/g)	ΔH_m^{rel} (%)	T_c (°C)	ΔH_c (J/g)	ΔH_c^{rel} (%)
EP	94.3	-	-	-	-	-	-
MC	-	44.1	227.7	100.0	29.6	224.2	100.0
EP-CFS10	94.7	-	-	-	-	-	-
EP-MC5-CFS10	93.3	42.8	10.6	103.4	28.2	10.5	104.1
EP-MC15-CFS10	92.8	46.5	29.5	96.0	25.8	29.1	96.1
EP-MC30-CFS10	93.6	46.4	60.8	98.9	26.2	60.8	100.4
EP-MC20	95.8	47.8	47.3	103.9	24.2	46.9	104.6
EP-MC20-CFS5	92.7	45.7	43.0	99.4	26.7	42.5	99.8
EP-MC20-CFS10	90.0	45.9	40.2	98.1	26.3	39.6	98.1
EP-MC20-CFS15	90.1	45.0	39.8	102.8	27.8	39.3	103.1

T_g = glass transition temperature of the epoxy phase (°C); T_m = melting temperature of the PCM (°C); ΔH_m = PCM melting enthalpy (J/g); ΔH_m^{rel} = relative PCM melting enthalpy (%); T_c = crystallization temperature of the PCM (°C); ΔH_c = PCM crystallization enthalpy (J/g); ΔH_c^{rel} = relative PCM crystallization enthalpy (%).

The values of phase change enthalpy are proportional to the MC weight fraction, as indicated by the values of ΔH_m^{rel} and ΔH_c^{rel} always close to 100 %. This indicates that the production process is mild enough to preserve the shell integrity and avoid loss of PCM. As already indicated elsewhere in this thesis work, values of relative enthalpy slightly above 100 % can be due to slight compositional inhomogeneities.

The mechanical behaviour of the prepared composites was investigated through three-point bending tests. Figure V - 48(a-b) shows representative load-displacement curves, while Table V - 35 summarizes the most important flexural properties. The addition of CFS determines a considerable increase in the flexural modulus (E_f) and a strong reduction of the strain at break (ε_{fb}), as expected. For instance, for the EP-CFS10 sample an enhancement of the elastic modulus of 65 % compared to the neat epoxy can be determined, while ε_{fb} is reduced of 50 %. The flexural strength (σ_{fM}) is also slightly reduced. The observed reduction of the failure properties is not surprising, since the utilized fibers are unsized. The application of a surface treatment with silane- or other types of coupling agents could probably help to improve the fiber-matrix adhesion, thereby increasing the failure properties. The introduction of an increasing amount of MC determines a systematic reduction of the stiffness, which is probably due to the fact that the intrinsic stiffness of the MC is much lower than that of a thermosetting matrix, in good accordance with what described in Subchapter 5.3.

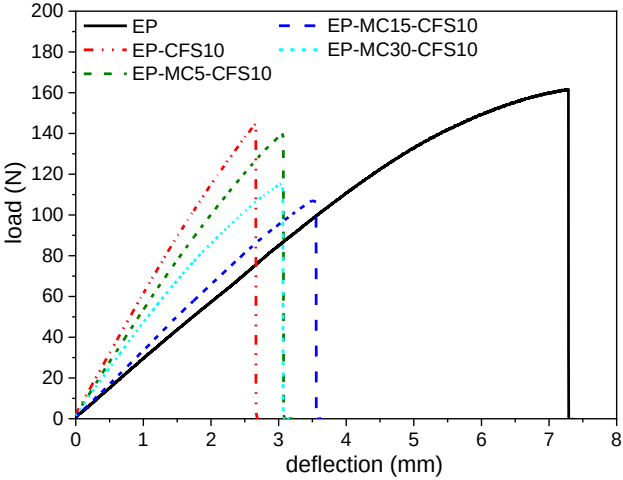

(a)

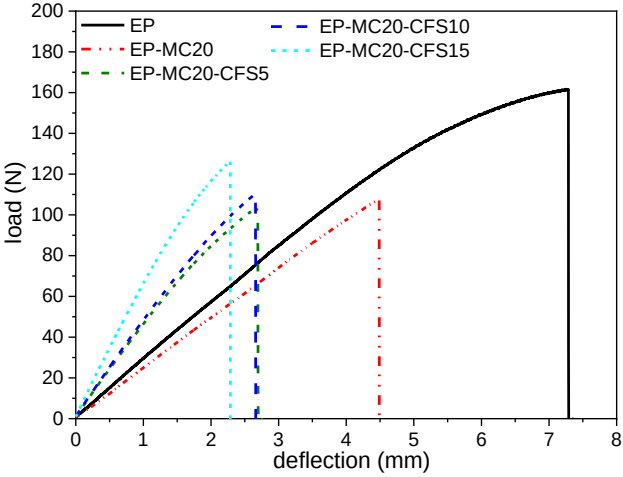

(b)

Figure V - 48. Representative load-displacement curves obtained in the three-point bending tests. (a) Samples EP-MCx-CF10 (x = 5, 15, 30); (b) samples EP-MC20-CFx (x = 5, 10, 15).

However, the E_f of the sample EP-MC20-CFS10 is still higher than that shown by the neat epoxy, which evidences the positive contribution of CFS in retaining the

original mechanical properties of the host epoxy matrix, even with a high MC fraction. This effect is increasingly evident with an increase in the CFS fraction. The decrease in the failure properties elevated MC concentrations is probably intensified by the non-optimal adhesion between MC and the polymer matrices. In these conditions, MC represent micrometric defects within the materials, which lead to the premature failure of the samples. It is also important to underline that the presence of CFS could also increase the thermal conductivity, thereby leading to a more efficient heat diffusion and a higher heat exchange efficiency.

Table V - 35. Results of the three-point bending tests on the samples EP-MC-CFS.

Sample	E_f (GPa)	σ_{fM} (MPa)	ε_{fb} (%)
EP	2.8 ± 0.5	117 ± 19	5.1 ± 0.4
EP-CFS10	4.6 ± 0.2	100 ± 7	2.4 ± 0.2
EP-MC5-CFS10	4.1 ± 0.3	93 ± 2	2.5 ± 0.3
EP-MC15-CFS10	3.9 ± 0.2	77 ± 2	2.4 ± 0.1
EP-MC30-CFS10	3.6 ± 0.1	60 ± 1	2.0 ± 0.1
EP-MC20	2.0 ± 0.4	52 ± 3	3.1 ± 0.2
EP-MC20-CFS5	2.5 ± 0.2	53 ± 2	2.6 ± 0.3
EP-MC20-CFS10	3.5 ± 0.2	60 ± 7	2.0 ± 0.2
EP-MC20-CFS15	4.5 ± 0.3	72 ± 2	2.0 ± 0.1

E_f = flexural modulus; σ_{fM} = flexural strength; ε_{fb} = strain at break.

Charpy tests were carried out to evaluate the effect of MC and CFS on the impact properties of the host matrix. The results of this characterization are summarized in Figure V - 49, which shows load-time curves, and Table V - 36, which reports the values of maximum force reached during the test (F_{max}), and total absorbed energy normalized by the load-bearing section ($E_{sp,tot}$). The sample EP-CFS10 shows both F_{max} and $E_{sp,tot}$ slightly lower than those of EP, which can be due to a non-optimal fiber-matrix interfacial adhesion. It is interesting to note that, with the introduction of MC, F_{max} and $E_{sp,tot}$ are higher than those of EP-CFS10, but both parameters do not follow a trend with the MC fraction. These results can be explained by considering a synergistic plasticizing effect played by paraffin microcapsules within the material under impact conditions. However, the data dispersion is not negligible and the results of this class of samples are not significantly different from one another. On the other hand, the impact properties displayed by the EP-MC20 sample are lower than those of the neat matrix, in good agreement with what reported for the EP-MCx samples described in Subchapter 5.3, but the addition of an increasing CFS loading determines an increase in the F_{max} values up to a level comparable to that of the neat epoxy, and also $E_{sp,tot}$ slightly increases. As reported for flexural tests, it can be generally concluded that the reduction in the impact

properties of the prepared composites is not dramatic, and the presence of CFS brings a positive contribution also in this case.

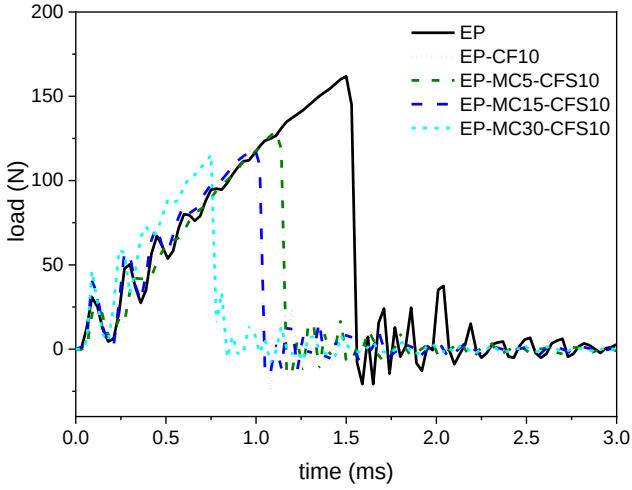

(a)

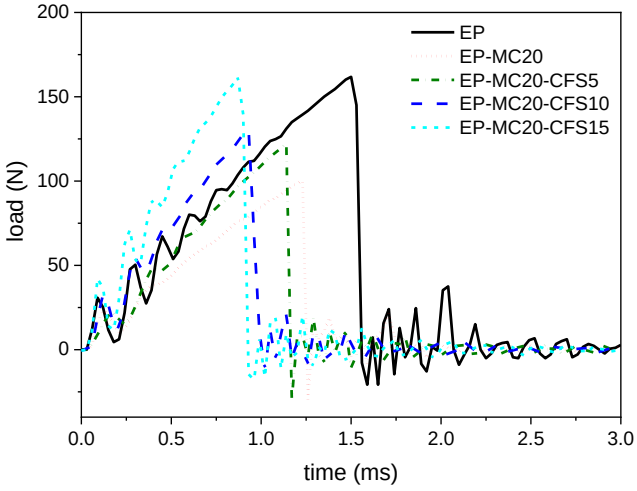

(b)

Figure V - 49. Representative load-time curves obtained in the Charpy impact tests. (a) samples EP-MCx-CF10 (x=5, 15, 30); (b) samples EP-MC20-CFx (x = 5, 10, 15).

Table V - 36. Results of the Charpy impact tests on the samples EP-MC-CFS.

Sample	F_{max} (N)	$E_{sp,tot}$ (kJ/m²)
EP	138 ± 52	3.6 ± 2.3
EP-CFS10	110 ± 22	1.7 ± 0.6
EP-MC5-CFS10	131 ± 3	3.0 ± 0.5
EP-MC15-CFS10	123 ± 5	2.5 ± 0.2
EP-MC30-CFS10	116 ± 13	1.8 ± 0.1
EP-MC20	97 ± 10	1.7 ± 0.5
EP-MC20-CFS5	126 ± 19	2.2 ± 0.4
EP-MC20-CFS10	132 ± 6	1.9 ± 0.1
EP-MC20-CFS15	163 ± 9	2.2 ± 0.1

F_{max} = maximum value of load reached during the test; $E_{sp,tot}$ = total absorbed specific energy.

5.5.3 Conclusions

This Subchapter illustrated the results of the characterization of thermosetting discontinuous-fiber composites with TES capability, obtained by combining EP with MC and discontinuous milled carbon fibers. Even though the fiber-matrix adhesion is not optimal due to the surface conditions of the fibers, CFS increase the mechanical and impact properties of EP-MC samples and help in retaining the original mechanical properties of the host epoxy matrix. Moreover, CFS could contribute to increase the thermal conductivity of the composites.

Therefore, even though the mechanical properties are not comparable with those of the continuous-fiber laminates, the addition of (milled) discontinuous fibers to polymer/PCM systems is a fast, effective and relatively cheap way to increase their mechanical properties.

5.6 General conclusions of Chapter V

This Chapter illustrated the results of the thermo-mechanical characterization of three PCM-enhanced composites having an epoxy matrix.

In Subchapter 5.2, the shape-stabilized PCM powder ParCNT was mixed with an epoxy resin and used to prepare bidirectional carbon fiber laminates. The use of a shape-stabilized PCM in this case gave better results than when it was used in combination with a thermoplastic matrix, as the milder processing conditions allowed avoiding the PCM degradation and loss of melting enthalpy. However, it was found that the surrounding matrix influences and partially hinders the melting-crystallization process. Therefore, the epoxy resin was used in combination with a PCM that is completely insulated from the environment, i.e. a microencapsulated PCM, and

specifically the microcapsules MC. This has been the objective of the Subchapters 5.3, 5.4 and 5.5.

The results of Subchapter 5.3 provided an interesting insight on the effect of the MC and their phase change on the physical-mechanical properties of an epoxy resin, from the experimental and the theoretical point of view. It was found that the capsule/matrix interface plays a fundamental role not only for the mechanical performance, but also for the thermal conductivity.

The results of this Chapter were preliminary to those presented in Subchapters 5.4 and 5.5, in which the epoxy/MC systems were combined with continuous and discontinuous carbon fibers, respectively. These results confirmed that the processing conditions of an epoxy composite are mild enough to preserve the integrity of the microcapsules and their TES capability. For the continuous fiber composites, it was also confirmed that an increase in the MC fraction impairs the mechanical properties mostly because of the decrease in the final fiber volume fraction and because the MC phase tends to concentrate in the interlaminar region, thereby lowering the interlaminar shear strength. On the other hand, it was found that a small amount of microcapsules can enhance the mode I interlaminar fracture toughness, as the MC introduced other energy dissipation mechanisms such as the debonding, the crack deflection, crack pinning and micro-cracking, which add up to the fiber bridging.

5.7 Acknowledgements

Dr. Seraphin H. Unterberger (Universität Innsbruck) is acknowledged for performing LFA tests (Subchapters 5.2 and 5.4). Ms. Claudia Gavazza (DII Unitn) is acknowledged for her support to SEM analysis (Subchapters 5.2, 5.3 and 5.5).

Chapter VI

Biodegradable TES laminates: thermoplastic starch/wood laminate containing poly(ethylene glycol)

Part of this chapter has been published in:

A. Dorigato, G. Fredi, M. Negri, A. Pegoretti,
Thermo-mechanical behaviour of novel wood laminae-thermoplastic starch biodegradable composites with thermal energy storage/release capability,
Frontiers in Materials, 6 (2019) 1-12

6.1 Introduction

This Chapter illustrates the methods and the results of the characterization of a thermoplastic starch/wood laminate containing poly(ethylene glycol) (PEG) as a PCM. There are three main differences between this laminate and the other TES composites presented in this thesis. The first novelty is its full biodegradability, as all the three constituents are biodegradable. This is positive especially if considering that the life cycle assessment of traditional composite materials generally evidences their limits in terms of recyclability and final disposal operations.

The second peculiarity of this laminate is the non-fibrous nature of the employed reinforcement. All the other composites described in this thesis feature a traditional fibrous reinforcement, while this biodegradable laminate is reinforced with thin wood laminae, prepared as described in Section 3.2.3.5.

The third novelty is that the reinforcement is also the shape-stabilizing agent for the PCM. In fact, due to its porous microstructure, wood is also an interesting candidate for the shape-stabilization of organic PCMs in the molten state. In this way, the wood laminae represent multifunctional elements themselves, thereby shifting the level of multifunctionality from the composite level to the phase level.

6.2 Materials and methods

The present Subchapter lists the materials used to fabricate these wood laminates, and then the techniques for their preparation and characterization are described. Since the materials and the characterization techniques have been already detailed in Chapter III, this section will specify only the experimental parameters that are peculiar of this Subchapter.

6.2.1 Materials

The materials used for the preparation of these laminates are listed in Table VI - 1 (please refer to Section 3.2.4 for the details about the materials).

Table VI - 1. Materials employed in Chapter VI.

Phase	Label	Material
Polymer matrix	A	Thermoplastic starch
Reinforcement	FA	Wood laminae
PCM	PEG	Poly(ethylene glycol) 2000 g/mol

6.2.2 Sample preparation

Wood laminae (Figure VI - 1a) were cut in square sheets of 120x120 mm^2, with the wood fibers oriented either parallel or at 45 ° with respect to the square edge. The sheets were immersed in PEG melted at 70 °C for 5 min, then removed and immediately gently blotted with absorbent paper to remove excess PEG from the surface (Figure VI - 1b). The weight fraction of absorbed PEG was evaluated by weighing each wood lamina before and after the immersion in liquid PEG. Preliminary experiments showed that a soaking time of 5 min is enough to reach the maximum weight increment due to PEG absorption, as a longer soaking time (up to 24 h) did not result in a further weight increase.

The wood/PEG laminae were interleaved with starch foils of 120x120 mm^2 and compacted in a hot-plate press at 170 °C for 7 min, with an applied pressure of 1 MPa. Each laminate (Figure VI - 1c) consisted of 5 wood/PEG laminae interleaved with 6 starch sheets. The samples were produced by following two stacking sequences, i.e. $[0_5]$ (unidirectional) and [+45/−45/+45/−45/+45] (angle ply). Laminates with virgin wood laminae (without PEG impregnation) were prepared for comparison. The mass of each constituent of each laminate was measured before the hot-pressing stage and compared to the final mass of the prepared laminates, to assess the PEG leakage during the preparation of the laminate.

Specimens with different orientations were cut out of the prepared laminates for the subsequent characterization. The characterization was performed also on the constituents, i.e., the starch foils, the virgin wood laminae, and the PEG-impregnated laminae. The list of the prepared samples is reported in Table VI - 2. From now on, the constituents will be labelled as following: thermoplastic starch (A), single wood lamina (F), single PEG-impregnated wood lamina (FP), laminate without PEG (FA), laminate with PEG (LAM). When applicable, a reference to the wood fiber orientation will be added to the label: longitudinal (L), transversal (T), angle ply (O).

All composite laminates and their constituents were stored at 23 °C and at a relative humidity of 50%. This production process, which consists of embedding the PCM directly in the reinforcing phase and employing matrix foils, allows the preparation of thermoplastic laminates by avoiding mixing the PCM in the thermoplastic matrix via melt compounding, which was shown to partially degrade the PCM (see Chapter IV).

(a)

(b)

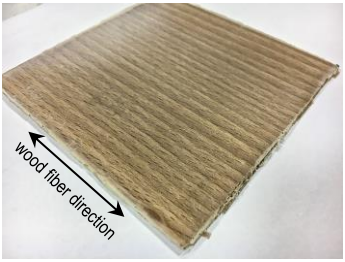

(c)

Figure VI - 1. Representative images of (a) neat wood lamina; (b) wood laminae after PEG impregnation; (c) wood/PEG/starch laminate.

Table VI - 2. List of the prepared samples of Chapter VI.

Acronym	Description of the constituents	Wood fiber orientation
F-L	Single wood lamina	Longitudinal
F-T	Single wood lamina	Transversal
PEG	Poly(ethylene glycol)	-
A	Single starch foil	-
FP-L	Single wood lamina impregnated with PEG	Longitudinal
FP-T	Single wood lamina impregnated with PEG	Transversal
FA-L	5 wood laminae and 6 starch foils	Unidirectional (longit.)
FA-T	5 wood laminae and 6 starch foils	Unidirectional (transv.)
FA-O	5 wood laminae and 6 starch foils	Angle ply
LAM-L	5 wood laminae impregnated with PEG and 6 starch foils	Unidirectional (longit.)
LAM-T	5 wood laminae impregnated with PEG and 6 starch foils	Unidirectional (transv.)
LAM-O	5 wood laminae impregnated with PEG and 6 starch foils	Angle ply

6.2.3 Characterization

The samples were investigated through the characterization techniques listed in Table VI - 3 together with the experimental parameters applied specifically on these samples (see Section 3.3 for the full description of the characterization parameters and specimen preparation).

Table VI - 3. Characterization techniques and experimental parameters applied on the wood/starch/PEG laminates.

Technique	Specific experimental parameters
SEM	Instrument Jeol IT300; cryofracture surface
DSC	Temperature interval -20-100 °C
TGA	TA Q5000 IR thermobalance; specimen mass 10 mg
DMA	Single-frequency tests
Quasi-static tensile test	As described in Section 3.3.5.1
Charpy impact test	As described in Section 3.3.5.3

6.3 Results and discussion

Table VI - 4 reports the weight composition of a single wood lamina impregnated with PEG (FP), the nominal mass of each component before the hot-pressing step, and the nominal weight composition for each of the two prepared laminate types, namely that with PEG (LAM) and that without PEG (FA). It can be observed that the quantity of PEG absorbed by a single lamina is approx. 86 wt% of its initial mass. On the other hand, if five of these laminae are alternated to 6 starch foils, the experimental mass of the laminate obtained through hot-pressing (LAM) is approx. 25 wt% lower than the sum of its components. This mass loss can be almost entirely attributed to the leakage of PEG out of the wood laminae, as the mass loss of the laminate without PEG (FA) is almost negligible, which means that the mass loss of the thermoplastic starch (A) and wood (F) phases is almost negligible. Therefore, the effective PEG weight fraction in the laminate is approx. 11 wt%. This loss of PEG is probably entirely due to leakage and not to degradation, as the hot-compaction temperature (170 °C) is below the degradation temperature of PEG (see results of the TGA characterization reported hereafter). The leakage of PEG suggests that a considerable fraction of the absorbed PEG has just solidified on the surface of the laminae and is not properly confined in the wood porosity, and the gentle blotting is not sufficient to remove excess PEG. However, a conspicuous fraction of PEG was successfully stabilized into the wood laminae and remained in the laminate after the hot-compaction stage.

Table VI - 4. Mass and mass composition of the single PEG-impregnated wood lamina (FP) and the two laminates, without (FA) and with PEG (LAM).

Sample	Constituent	Mass (g)	Nominal weight fraction (%)	Experimental total weight (g)
FP	F (wood)	2.9 ± 0.1	53 ± 6	5.4 ± 0.5
	PEG	2.5 ± 0.4	46 ± 11	
FA	A (starch)	10.1 ± 0.3	41 ± 2	24.3 ± 0.9
	F (wood)	14.6 ± 0.6	59 ± 3	
LAM	A (starch)	10.1 ± 0.3	27 ± 2	28.2 ± 0.8
	F (wood)	14.6 ± 0.6	39 ± 3	

Figure VI - 2(a-f) shows the SEM micrographs of the cryofracture surface of the prepared samples. Since this technique allowed the investigation of the cross section, in the samples with longitudinal wood fibers (L) the wood fibers are perpendicular to the fracture plane, while they are parallel in the samples with transversal fibers (T). Figure VI - 2(a-b) shows micrographs of the wood laminae cut in the transversal and in the longitudinal direction, respectively. As reported in a previous paper on ultra-thin wood laminae impregnated with poly(vinyl alcohol) in the longitudinal direction (Dorigato et al., 2018a), the laminae show the peculiar structure of beechwood, with tracheids, wood fibers and vessels, while the parenchymal cells are less clearly visible (Giordano, 1981). Tracheids and wood fibers are characterized by a mean diameter of approx. 10 μm, while wood vessels present an average size of 40 μm. The presence of some tracheids in radial direction can be appreciated in the transversal section. From the micrographs of the laminae impregnated with PEG (Figure VI - 2(c-d)), it can be observed that PEG fills the wood porosity only partially. This could be explained by assuming that the volume fraction of the closed porosity is not negligible, and that the viscosity of the molten PEG is too high to allow the smallest pores to be filled in the time window of the impregnation process (up to 24 h). The surface of the lamina hosts a considerable amount of PEG, as suggested by the smoothness of the surfaces of the laminae containing PEG (indicated by arrows), compared to the remarkably rough surfaces of the neat wood laminae. This may complicate the adhesion between the wood laminae and the starch matrix, as partially visible from the fracture surface of the two laminates (Figure VI - 2(e-f)). In the laminate containing PEG (Figure VI - 2f) the interlaminar adhesion between starch and wood seems worse than that of the neat laminate, as the cryofracturing operations caused delamination (indicated by the arrows), which is not observed in the neat laminate. However, this apparent worsening in the interlaminar adhesion due to the PCM does not negatively affect the mechanical and impact properties, as reported hereafter.

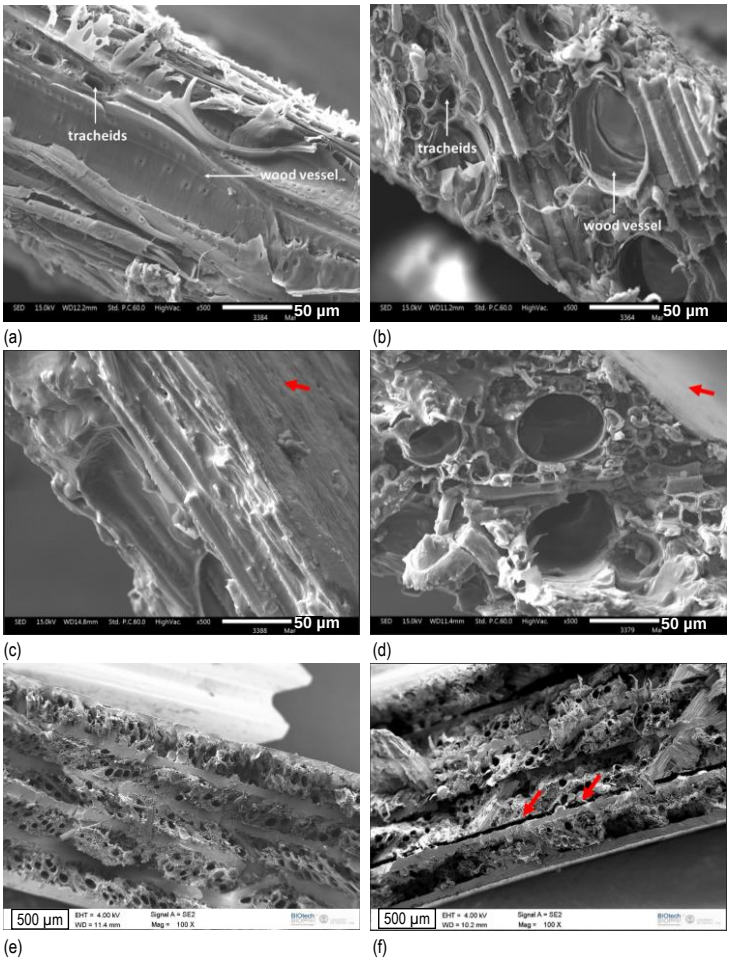

Figure VI - 2. SEM micrographs of the cryofracture surface (cross-section) of the prepared samples. (a) F-T; (b) F-L; (c) FP-T (red arrow indicates PEG deposited onto the surface); (d) FP-L (red arrow indicates PEG deposited onto the surface); (e) FA-T; (f) LAM-T (red arrows indicate delamination).

TGA analysis was performed to evaluate the resistance to the thermal degradation of the laminates and of each constituent. Figure VI - 3 shows the TGA thermograms (with the residual mass and the derivative of the mass loss) of the sample LAM and of its three constituents, i.e., PEG, F, and A, while Table VI - 5 also reports the results on the sample FP. Table VI - 5 shows the values of the temperatures corresponding to a mass loss of 1 wt% and 5 wt% ($T_{1\%}$ and $T_{5\%}$), the

degradation temperature, corresponding to the peak of the mass loss derivative and to the maximum degradation kinetics (T_d), the temperature corresponding to the initial stages of degradation, after water evaporation (T_{onset}), the initial mass loss before T_{onset} (m_i), and the residual mass at 700 °C (m_r).

For the sample F, the initial mass loss (m_i) of approx. 5.8 wt% is imputable to water evaporation. This behavior is also observed in the samples FP and LAM, but to a lesser extent, as for these samples the wood laminae are only a fraction of the total mass. After water evaporation, the thermal degradation of the wood phase becomes appreciable above 250 °C and occurs in two main steps. Conversely, no water was detected on the starch (A) and PEG, which indicates that the total water fraction of the composites is entirely absorbed by the wooden phase. The thermal degradation of these two polymer phases starts to be evident at 320-350 °C (T_{onset}) and reaches the maximum rate at approx. 400 °C. From these results, it can be concluded that the thermal stability of all the constituents is sufficient to withstand the processing temperature of 170 °C. Moreover, as expected, the degradation thermogram of the PEG-impregnated lamina (FP) lies between those of its constituents, i.e., F and PEG. The thermal degradation of the sample LAM shows all the degradation steps of its three constituents, as can be better appreciated from the mass loss derivative signal.

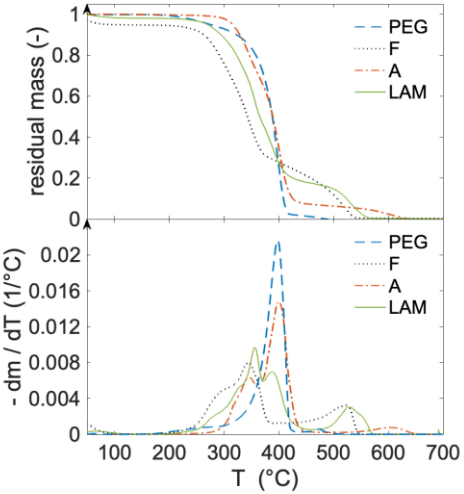

Figure VI - 3. Results of the TGA tests on the samples F, A, PEG and LAM: residual mass and mass loss derivative as a function of temperature.

Table VI - 5. Results of the TGA tests on the prepared wood laminates and the constituents.

Sample	$T_{1\%}$ (°C)	$T_{5\%}$ (°C)	T_d (°C)	T_{onset} (°C)	m_i (%)	m_r (%)
F	53.0	241.3	345.0	263.0	5.76	0.38
PEG	208.4	274.5	396.9	352.4	0.00	0.00
A	281.3	316.0	400.0	316.8	0.00	0.00
FP	89.3	265.4	405.1	317.8	2.01	0.04
LAM	29.4	260.7	365.5	293.5	2.04	0.27

$T_{1\%}$, $T_{5\%}$ = temperature corresponding to a mass loss of 1 wt% and 5 wt% (°C); T_d = degradation temperature, corresponding to the peak of the mass loss derivative (°C); T_{onset} = temperature corresponding to the initial stages of degradation, after water evaporation (°C); m_i = initial mass loss before T_{onset} (%); m_r = residual mass at 700 °C (%).

DSC tests were performed to investigate the thermal transitions of the constituents and to assess the thermal energy storage capability of the PEG within the laminates. In the present paper, this test allowed the determination of the melting and crystallization temperatures and enthalpy values of the PEG phase within the laminates (T_m^{PEG}, T_c^{PEG}, ΔH_m^{PEG}, ΔH_c^{PEG}), but also of the starch phase (T_m^A, T_c^A, ΔH_m^A, ΔH_c^A). The DSC thermograms of the prepared samples are reported in Figure VI - 4, while the most important results are collected in Table VI - 6.

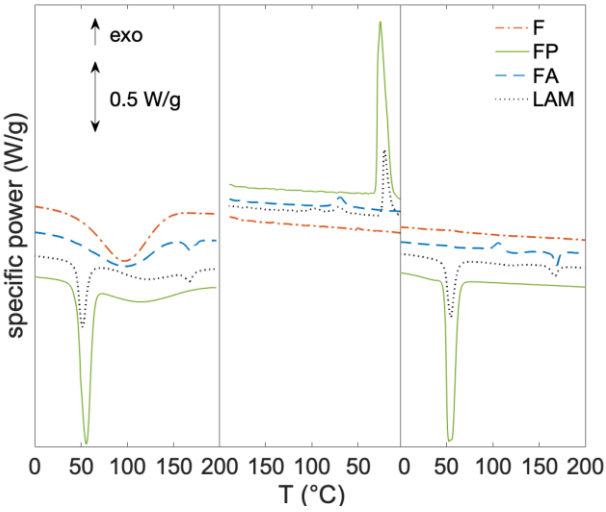

Figure VI - 4. DSC thermograms of the prepared wood laminates, showing the three scans (first heating, cooling, second heating). Samples F, FP, FA, and LAM.

The DSC thermogram of the neat starch (A) was not reported here for the sake of brevity, but this test was performed as a preliminary experiment to find a suitable hot-pressing temperature of the laminates, and some results of the DSC on the starch sample are reported in Table VI - 6. The thermogram of the neat beech (F) shows a broad endothermic peak on the heating scan that is not present in the cooling and second heating scan. This peak, associated with water evaporation, has an enthalpy of 161.5 J/g. Considering that the latent evaporation heat of water is 2,272 J/g, the water fraction in the neat beech can be estimated at approx. 7.1 wt%, which is in good agreement with the mass losses observed by TGA in the low temperature region (below T_{onset}). The other DSC signals of the F sample, such as those associated with the glass transitions of the amorphous wood components, are not clearly visible in this plot, but they have been thoroughly described in a recent work on wood/starch composite laminates (Dorigato et al., 2018b). The signal of water evaporation is partially visible also in the first heating scan on the sample FP, which also presents the signals of the melting and crystallization transitions of PEG, through the presence of narrow peaks at 55 °C and 25 °C, respectively. The phase change enthalpy measured in the first heating scan is 88.5 J/g. Assuming that the phase change performance and the crystallization behavior of the PEG embedded in the wood are not different from those of the virgin PEG, the total PEG weight fraction in the sample FP can be calculated from the phase change enthalpy of the neat PEG (169 J/g), with the result being 52.4 wt%, in good agreement with the nominal PEG content (Table VI - 4).

Table VI - 6. Results of the DSC tests on the prepared wood laminates and the constituents.

Sample	T_m^{PEG} (°C)	ΔH_m^{PEG} (J/g)	T_c^{PEG} (°C)	ΔH_c^{PEG} (J/g)	T_m^A (°C)	ΔH_m^A (J/g)	T_c^A (°C)	ΔH_c^A (J/g)
PEG	52.6	168.9	30.9	155.3	-	-	-	-
A	-	-	-	-	168.1	9.8	71.1	10.09
FP	56.1	88.5	25.8	86.7	-	-	-	-
FA	-	-	-	-	168.7	4.6	70.9	5.1
LAM	54.7	27.4	21.5	24.1	166.8	4.4	71.8	4.8

T_m^{PEG}, T_c^{PEG} = melting and crystallization temperatures of PEG (°C); ΔH_m^{PEG}, ΔH_c^{PEG} = melting and crystallization enthalpy values of PEG (J/g); T_m^A, T_c^A = melting and crystallization temperatures of thermoplastic starch (°C); ΔH_m^A, ΔH_c^A = melting and crystallization enthalpy values of thermoplastic starch (J/g).

The peak of water evaporation is also present in the thermograms of the two prepared laminates (FA and LAM). The sample FA also clearly shows all the thermal transitions of the starch phase, which are visible in the second heating scan, i.e., a glass transition at approx. 60 °C, post-crystallization at 110 °C and a melting peak at 168 °C. The thermal transitions of the starch phase are also visible in the thermogram of the sample LAM (except for the post-crystallization in the second heating scan),

although the most intense signal is represented by the phase change transitions of PEG, whose enthalpy is 27.4 J/g (first heating scan). From this signal, the effective PEG weight fraction in the LAM can be calculated as 16.2 wt%, slightly higher than that calculated from the masses of the laminates, but in the same order of magnitude. This DSC signal clearly demonstrates that the prepared composites could be potentially applied for TES applications.

Figure VI - 5(a-d) shows the thermograms obtained from DMA on the tested materials, performed to investigate their viscoelastic response below and above the melting temperature of PEG. Figure VI - 5(a-b) shows the thermograms of the samples A, F and FP. The latter two samples have been tested with the wood fibers oriented parallel (L) and perpendicular (T) to the applied load. The thermogram of the neat starch (A) has been reported together with the samples in the T directions for a better comprehension of the plots. The starch phase (A) exhibits a storage modulus at 0 °C of approx. 250 MPa, and it shows a considerable drop at approx. 60 °C in correspondence of the glass transition, in good agreement with the DSC results. The same phenomenon is visible through peaks in the signals of E'' and $tan\delta$. For the neat wood lamina (F), the value of E' in the L direction is one order of magnitude higher than that in the T direction, and in both cases it shows a slight decrease at approx. 50 °C, because of the transitions of wood amorphous fraction (i.e. lignin) (Kelley et al., 1987). From a comparison between the signals of the neat wood (F) and the PEG-impregnated wood (FP) laminae, is it immediately evident that the presence of PEG significantly contributes to increase the storage modulus of the wood laminae in both directions, probably due to a partial filling of the wood porosity. The major signals in the FP thermograms are those related to the PEG phase transition, evidenced by a drop in E' and peaks in E'' and $tan\delta$ signals and appreciable especially in the L direction (Figure VI - 5a).

The positive contribution of PEG in increasing E' is also transferred to the laminates (Figure VI - 5(c-d)), even though to a less extent. Also in this case, the thermograms present all the signals related to the thermal transitions of the PEG and starch phases. For example, the PEG melting is clearly detectable through the DMA thermograms. This effect, which evidences the interesting and unusual possibility to study a melting event through DMA, was also observed in the other PCM-containing composites presented in the other Chapters of thesis work.

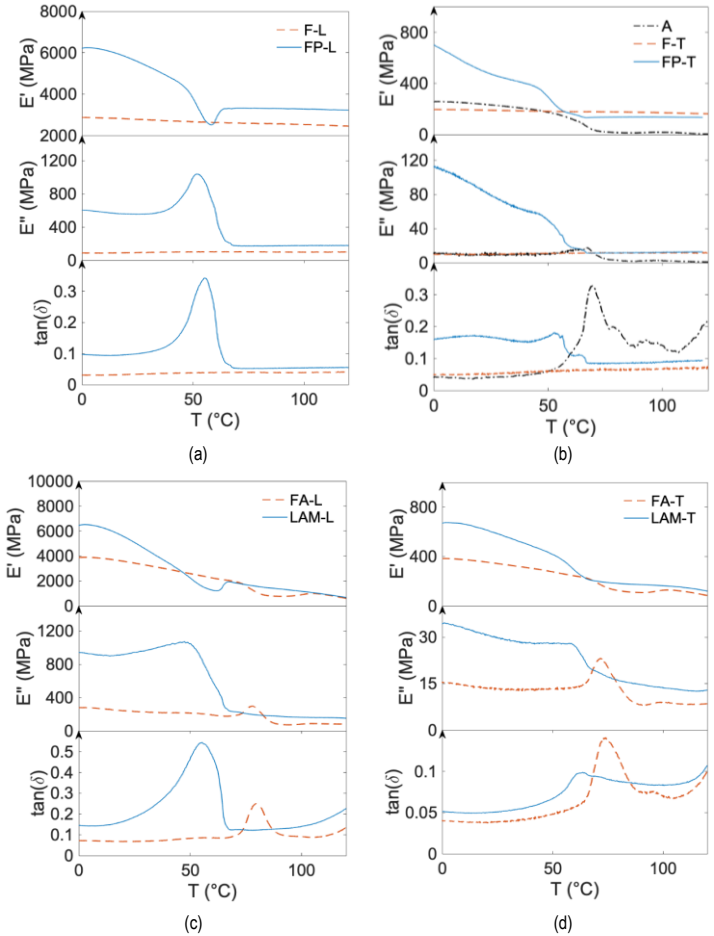

Figure VI - 5. DMA thermograms of the wood laminates and the constituents, showing the storage modulus E', the loss modulus E'', and the loss factor $tan\delta$. (a) samples F and FP (longitudinal direction); (b) samples F, FP (transversal direction) and A; (c) samples FA and LAM (longitudinal direction); (d) samples FA and LAM (transversal direction).

Finally, two tests were performed to investigate the effect of PEG on the mechanical properties of the wood laminae and the prepared laminates, i.e. quasi-static tensile tests and Charpy impact tests. For the tensile tests, representative curves of the sample FA and LAM in all the three considered directions are reported in Figure VI - 6(a-b), while Figure VI - 6(c-d) shows the trends of the elastic modulus and the tensile strength. The neat wood lamina (F) has a linear stress-strain curve until failure in both the L and T directions, with a rather low strain at break (approx. 1 %).

PEG-impregnated laminae (FP) show an initial linear behavior, followed by a region in which the slope decreases until failure. By a comparison of the tensile properties of the samples F and FP in Figure VI - 6(c-d), it is clear that PEG positively influences the mechanical properties of the wood laminae, especially in the T direction, as the average elastic modulus increases from 120 MPa to 310 MPa and the tensile strength from 60 MPa to 170 MPa, while the properties in the L direction of the two samples are not significantly different from each other.

The mechanical properties measured on these thin laminae are remarkably lower than those reported for bulk beech, which exhibits a flexural elastic modulus of 14.5 GPa and a flexural strength of 120 MPa (Giordano, 1981). This effect, already observed in previous works of our group (Dorigato et al., 2018a), is attributable to the destroying of the pristine cellular morphology to which the ultrathin laminae are subjected during cutting.

The stress-strain curve of the starch film (A) is typical of a thermoplastic, highly ductile polymer. The initial linear region terminates with a relative maximum, conventionally regarded as the yield point, followed by a strain-hardening region until failure, which happens at high strain values (approx. 450 %). The properties measured on this starch film are consistent with those reported in the literature for similar materials (Bastioli, 1997; Mark, 1999). From Figure VI - 6(a-b) it is immediate to observe that, as expected, for both the prepared laminates, the mechanical properties of the angle ply (O) laminates are intermediate in respect to those of the samples L and T. From the results reported in Figure VI - 6(c-d), it is also evident that the properties measured on the laminates are considerably higher than those expected from the traditional rule of mixture, largely used to predict the performance of composites. This effect, already observed in previous works (Dorigato et al., 2018b) stems from the partial filling of the wood porosity by the interpenetrated matrix, which reduces the total pore volume fraction. As reported before for the single lamina, this porosity filling effect is also the reason of the enhanced tensile stiffness and strength of the sample LAM (containing PEG) compared to FA (not containing PEG), in all the investigated directions.

Considering the elastic modulus results reported in Figure VI - 6c, it should be pointed out that the laminates (i.e. FA and LAM) and the constituents (i.e. FP, F, and A) were not tested at the same speed, and therefore the results can be directly compared only from a qualitative point of view. However, the most important comparison in the mechanical properties should be performed between the laminates FA and LAM in different orientations, which were tested at the same speed.

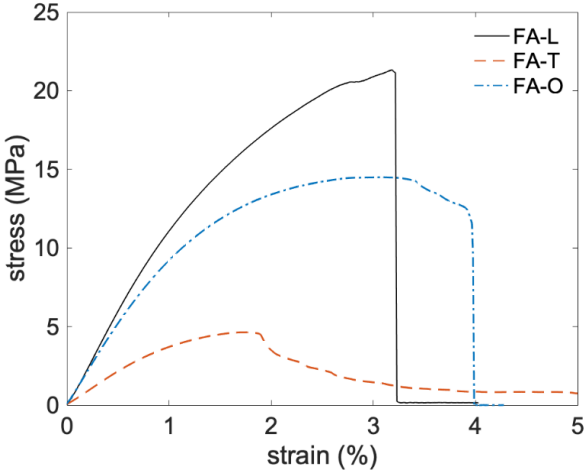
FA-L
FA-T
FA-O
stress (MPa)
strain (%)
0
5
10
15
20
25
0
1
2
3
4
5

(a)

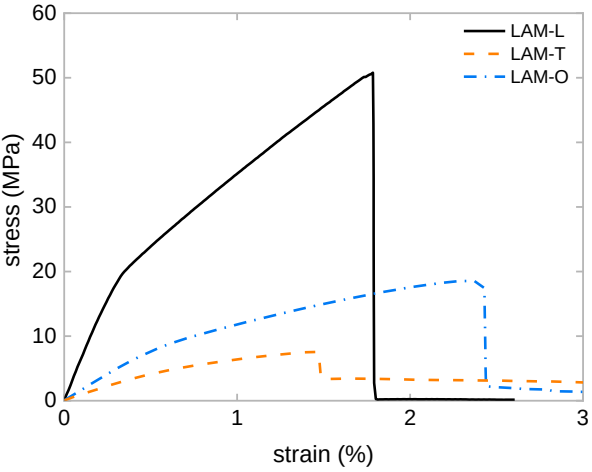
LAM-L
LAM-T
LAM-O
stress (MPa)
strain (%)
0
10
20
30
40
50
60
0
1
2
3

(b)

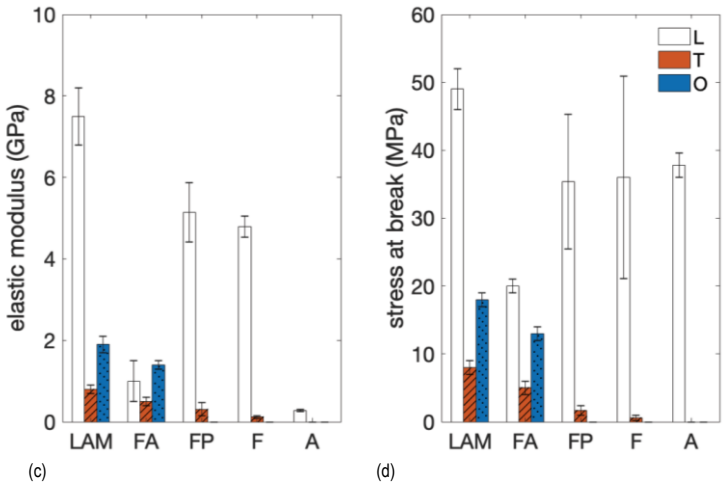

Figure VI - 6. Results of the quasi-static tensile tests (a) Representative stress-strain curves of the sample FA (all the three considered directions); (b) Representative stress-strain curves of the sample LAM (all the three considered directions); (c) tensile modulus of the prepared wood laminates and the constituents; (d) tensile strength (stress at break) of the prepared wood laminates and the constituents.

Similar conclusions can be drawn by analyzing the results of the Charpy impact tests, summarized in Table VI - 7. The maximum load (F_{max}) measured during the test is considerably higher for the LAM samples, and so is the absorbed specific energy ($E_{sp,tot}$), for all the considered fiber orientations. This suggests that, contrarily to what has been reported up to now for PCM-containing polymer composites, the PCM contributes positively to the mechanical properties of the host composite.

Table VI - 7. Results of Charpy impact tests on the prepared wood laminates, performed in different orientations.

Sample	F_{max} (N)	$E_{sp,tot}$ (J/m²)
FA-L	24	1.2 ± 0.2
FA-T	11	0.6 ± 0.3
FA-O	18	1.0 ± 0.2
LAM-L	138	23.7 ± 3.6
LAM-T	52	7.5 ± 1.6
LAM-O	95	14.8 ± 4.9

F_{max} = maximum value of load reached during the test; $E_{sp,tot}$ = total absorbed specific energy.

6.4 General conclusions of Chapter VI

This Chapter presented the preparation and thermo-mechanical properties of multifunctional fully biodegradable laminates with thermal energy storage/release capability, based on thermoplastic starch and thin wood laminae impregnated with PEG. It was found that not all the PEG introduced in the samples is effectively confined within the wood pores, due to the not negligible fraction of porosity that is closed or interconnected with too small channels; nevertheless, a PEG fraction of approx. 11 wt% of the whole laminate remained effectively entrapped within wood laminae. This was confirmed through DSC tests, which evidenced that the stabilization of PEG within the wood pores was responsible for the endothermic signal at 55 °C, with a total specific melting enthalpy of 27.4 J/g. DMA analysis revealed that the presence of PEG significantly contributed to increasing the dynamic moduli of the laminates, likely because of the partial filling of the wood porosity. For the same reason, the quasi-static properties (stiffness and strength) measured on the laminates were considerably higher than those expected from the traditional rule of mixture on the constituents, and Charpy tests also showed that the impact resistance of the composites was considerably higher than that of their constituents and of the neat wood/starch laminate.

For the first time, contrarily to what has been reported up to now for PCM-containing polymer composites, the presence of PCM resulted in a positive contribution to the mechanical properties of the host composite. Therefore, the mechanical and TES properties can be considered as synergistic and not parasitic. This is remarkably important in the perspective of developing multifunctional materials combining structural and thermal management functions. This also evidences that the wood laminae, which perform both the roles of reinforcement and shape-stabilizing agent for the PCM, are not the only multifunctional component, but also PEG can be regarded as multifunctional, since, besides absorbing and releasing heat, it also enhances the tensile and impact properties.

6.5 Acknowledgements

Dr. Martino Negri (CNR Ivalsa) is acknowledged for preparing and providing the thin wood laminae. Ms. Claudia Gavazza (DII Unitn) is acknowledged for her support to SEM analysis. Prof. Andrea Dorigato (DII Unitn) is acknowledged for his contribution to writing the manuscript for publication.

Chapter VII

Tailoring the properties of PCM microcapsules

Part of this chapter has been published in:

- G. Fredi, S. Dirè, E. Callone, R. Ceccato, F. Mondadori, A. Pegoretti,
  Docosane-organosilica microcapsules for structural composites with thermal energy storage/release capability,
  Materials 12 (2019) 1286/1-1286/26

- G. Fredi, F. Simon, D. Sychev, I. Melnyk, A. Janke, C. Scheffler, C. Zimmerer
  Bioinspired polydopamine coating as adhesion enhancer between paraffin microcapsules and an epoxy matrix,
  ACS Omega, Submitted

7.1 Introduction

The thermal and mechanical properties of a polymer composite containing PCM microcapsules are affected by the intrinsic properties of the capsules and the filler-matrix adhesion. This Chapter focuses on tailoring the thermo-mechanical or interfacial properties of paraffin microcapsules and is divided into two Subchapters. Subchapter 7.2 deals with the exploration of sol-gel techniques to synthesize paraffin microcapsules with an organosilica shell. Subchapter 7.3 concerns the deposition of polydopamine (PDA) on the surface of commercial paraffin microcapsules to enhance the interfacial adhesion with an epoxy resin.

7.2 Encapsulation of docosane in organosilica microcapsules via a sol-gel approach

As already introduced in Chapter II, the shell of PCM microcapsules can be made of polymeric or inorganic material. Polymeric shells are often the preferred choice, as they can be prepared with well consolidated and industrially available chemical techniques and feature a low density, which allows a high core-to-shell weight ratio and therefore an enhanced total TES performance. On the other hand, organic shells are often highly flammable, can release toxic gases, and exhibit lower thermal and mechanical stability and lower thermal conductivity than their inorganic counterparts (Yu et al., 2014).

The most common inorganic shell material is silica prepared via sol-gel techniques, for which the most widely used precursor is tetraethyl orthosilicate (TEOS) (Wang et al., 2006; Fang et al., 2010; Chen et al., 2013b). However, the resulting shell is often too brittle and easily subjected to damages and cracks (Chen et al., 2013a). A valid alternative is methyltriethoxysilane (MTES), which leads to the formation of an organosilica network.

This Subchapter deals with the identification of an effective sol-gel route to encapsulate paraffin within organosilica shells of various dimensions, and to deeply investigate how the confinement influences the microstructural and phase change properties of the PCM with a broad range of characterization techniques. Commercial paraffins are often a mixture of alkanes, and therefore it can be challenging to investigate a PCM with a broad MW distribution from the microstructural and molecular point of view. Hence, it was important to select a PCM with a known and well-defined chemical formula and molecular weight. The selected alkane was the *n*-docosane, having chemical formula $CH_3(CH_2)_{20}CH_3$, (purity ≥ 98.5%). This specific *n*-alkane was chosen as it has a nominal melting temperature of 42-45 °C, close to that of the previously used commercial PCMs.

To the best of the author's knowledge, only one study has been reported on the production of organosilica microcapsules with docosane as the PCM (Sun et al., 2019b), which specifically refers to the encapsulation of *n*-docosane in ZnO/SiO_2 shells prepared from TEOS. Moreover, although the reported research investigates the microstructural properties of the microcapsules to some extent, no studies have been found that use powerful techniques such as the nuclear magnetic resonance (NMR) to deeply examine the phase change behavior in a confined volume and relate the results to the outcome of microstructural and thermal analyses such as X-ray diffraction (XRD) and differential scanning calorimetry (DSC).

7.2.1 Materials and methods

The present Section lists the materials used to produce these microcapsules and describes in detail the sample preparation and the characterization methods.

7.2.1.1 Materials

To prepare PCM microcapsules, *n*-docosane $CH_3(CH_2)_{20}CH_3$ (purity ≥ 98.5 %) and absolute ethanol (purity ≥ 99.8 %) were purchased from Sigma-Aldrich (Saint Louis, MO, US), methyltriethoxysilane (MTES) (purity ≥ 98 %) was provided by ABCR GmbH (Karlsruhe, Germany), and cetyltrimethylammonium bromide (CTAB) was purchased from Sigma-Aldrich (Saint Louis, MO, US). Distilled water was used throughout the whole process. All materials were used as received, without further purification.

7.2.1.2 Sample preparation

Docosane-organosilica microcapsules were prepared with a protocol based on the indications reported in (Tang et al., 2017), which was modified in some key synthesis parameters in order to improve the emulsion stability and to obtain capsules with two remarkably different sizes. The masses of the reagents for the three different preparations are reported in Table VII - 1, while Figure VII - 1 reports a schematic overview of the experimental protocol.

Table VII - 1. Composition of the docosane o/w emulsion and the MTES solution for all the prepared microcapsules.

Sample	Docosane o/w emulsion			MTES solution		
	docosane (g)	CTAB (g)	water (ml)	MTES (ml)	HCl 10^{-2} M (ml)	ethanol (ml)
MC1	5	0.05	50	4.2	6.7	5.1
MC2						25.5
Si	-	-				5.1

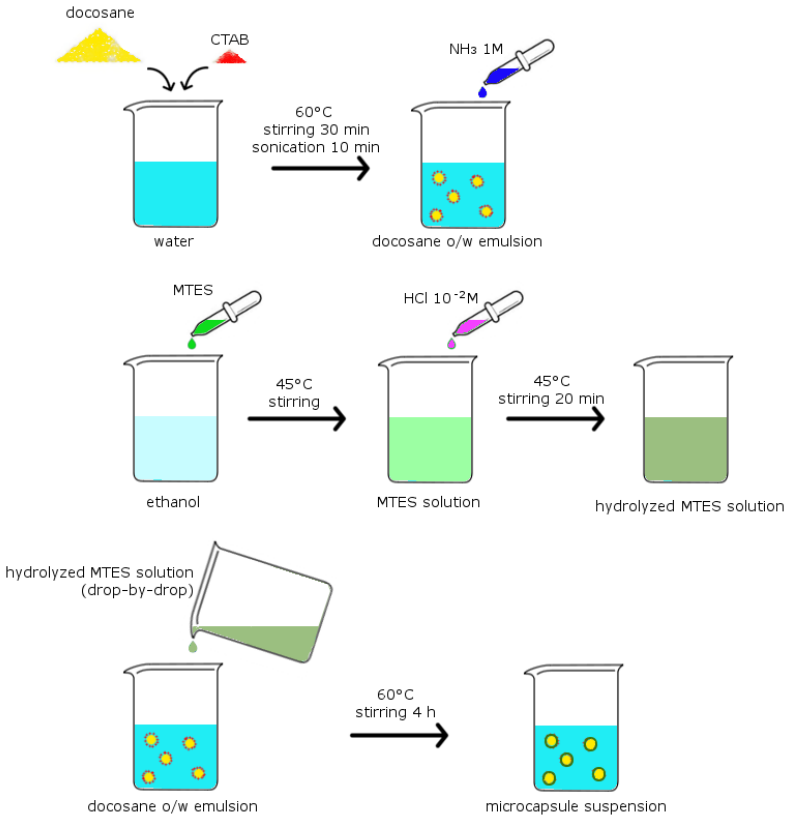

Figure VII - 1. Experimental steps followed for the synthesis of docosane microcapsules.

The docosane o/w emulsion was prepared by adding 4 g of docosane and 0.05 g of CTAB to 50 ml water. The mixture was stirred for 30 min at 2500 rpm via a Dispermat F1 laboratory dissolver (VMA-Getzmann GmbH, Reichshof, Germany), and then sonicated for 10 min with a UP400S ultrasonic processor (Hielscher GmbH, Teltow, Germany). During stirring and sonication, the temperature was kept at 60 °C, above the melting point of the docosane. After sonication, the pH was adjusted to 8-9 by adding $NH_{3(aq)}$ 1M solution. The MTES solution was prepared in a different beaker, by adding 4.2 ml of MTES to ethanol at 45 °C under stirring. Then, 6.7 ml of $HCl_{(aq)}$ 10^{-2} M were added drop by drop to promote the acid-catalyzed hydrolysis of MTES, and the solution was magnetically stirred at 45 °C for 20 minutes at 350 rpm. The MTES solution was then dropped into the docosane emulsion, and the total mixture was magnetically stirred at 60 °C for 4 h at 350 rpm. Finally, the suspension was

filtered, and the filtrate was washed with hot water and ethanol (to remove free docosane and unreacted species) and dried overnight in a vacuum oven at 80 °C. The MTES solution was prepared with two different volumes of ethanol, i.e. 5.1 ml and 25.5 ml, respectively, to modify the concentration, the polarity of the synthesis medium and the micelle size in the final suspension (MC1 and MC2). Each synthesis yielded approximately 2.5 g of microcapsules. Neat organosilica microparticles (Si) were also prepared without docosane and CTAB, under the same hydrolysis-condensation conditions (Dirè et al., 2011; Tang et al., 2017).

7.2.1.3 Characterization

The morphology of the microcapsules was investigated through a field-emission scanning electron microscope (FE-SEM) Zeiss Supra 60 operating in high vacuum mode, after Pt-Pd sputtering at 30k and 70k magnifications.

Fourier-transformed infrared spectroscopy (FTIR) was performed in attenuated total reflectance (ATR) mode with a Perkin Elmer Spectrum One instrument. Data were collected in the wavenumber interval between 650 and 4000 cm^{-1}, and four scans were superimposed for each spectrum (resolution 4 cm^{-1}).

X-ray diffraction (XRD) measurements were collected by means of a Rigaku D-Max III powder diffractometer using Cu-Kα radiation (λ = 0.154056 nm) and a graphite monochromator in the diffracted beam. A θ–2θ Bragg-Brentano configuration was adopted with the following scan conditions: scan range: 5–50° (in 2θ); sampling interval and counting time: 0.025° and 2 s, respectively.

Nuclear magnetic resonance (NMR) has been used to further investigate the structure and molecular dynamics of the microcapsules. Solid state NMR analyses were carried out with a Bruker 400WB spectrometer operating at a proton frequency of 400.13 MHz. ^{13}C and ^{29}Si cross-polarization (CP) magic angle spinning (MAS) spectra and proton-decoupled MAS spectra were collected. Spectra with CP pulse sequences were acquired under the following conditions: ^{13}C frequency: 100.48 MHz, π/2 pulse: 3.5 μs, decoupling length: 5.9 μs, recycle delay: 4 s, 512 scans; contact time: 2 ms. ^{29}Si frequency: 79.48 MHz, contact time: 5 ms, decoupling length: 6.3 μs, recycle delay: 20 s, 2k scans. ^{13}C proton-decoupled MAS spectra were acquired under the following conditions: ^{13}C frequency: 100.48 MHz, π/4 pulse: 2.5 μs, decoupling length: 5.9 μs, recycle delay: 10 s, 300 scans. Samples were packed in 4 mm zirconia rotor and spun at 8 kHz under air flow. ^{13}C spin-lattice relaxation times ($T1_C$) were measured at room temperature with a CP Inversion Recovery Experiment (Alamo et al., 2002) with τ from 1 ms to 30 s and using the already reported CP MAS parameters. The decay curves were fitted with the nonlinear least-square method. The $T1_C$ constant represents the rate needed by the z-component of net magnetization vector (represented by the NMR signal intensity) to go back exponentially to the equilibrium state aligned to the external magnetic field. The process depends on the interaction between the spin system and the close environment. Crystallinity and molecular

mobility, together with the closeness to paramagnetic centers or unpaired electrons, strongly affect the relaxation mechanism generally described by the Bloch equation (Bloch, 1946).

Samples were packed in 4 mm zirconia rotor and spun at 8 kHz under air flow. Adamantane and Q_8M_8 were used as external secondary references. Si units were labeled according to the usual NMR notation, T^n representing trifunctional Si units with n bridging O atoms.

Differential scanning calorimetry (DSC) was performed to study the variation in the phase transition temperature and enthalpy values of docosane in its bulk and encapsulated state. Specimens of approx. 8 mg were sealed in aluminum crucibles and tested in a Mettler DSC 30 calorimeter, at 10 °C/min, between 0 and 70 °C, under a nitrogen flow of 100 ml/min. The employed cooling medium was liquid nitrogen. A heating scan, a cooling scan and a second heating scan were performed for each specimen. The test allowed the measurement of the melting and crystallization temperatures (T_m, T_c) and enthalpy values (ΔH_m, ΔH_c,) of the PCM phase. The encapsulation efficiency η was evaluated for each sample as the ratio between its phase change enthalpy and that of the neat docosane, through Equation (VII - 1), as

$$\eta = \frac{\Delta H_m^{MC} + \Delta H_c^{MC}}{\Delta H_m^{D} + \Delta H_c^{D}}, \qquad \textbf{(VII - 1)}$$

where ΔH_m^{MC} and ΔH_c^{MC} are the melting and crystallization enthalpy values of the microcapsules and ΔH_m^{D} and ΔH_c^{D} are those of the neat docosane.

Moreover, a kinetic analysis was performed on neat docosane and MC1 to investigate the effect of encapsulation on the activation energy of the phase change. Tests were performed a 10 °C/min, 1 °C/min and 0.2 °C/min. The activation energy E_a was determined as the slope of the linear regression, through a standard Arrhenius approach, as reported in Equation (VII - 2):

$$\frac{d \ln(\varphi)}{d\left(1/T_{pc}\right)} = -\frac{E_a}{R}, \qquad \textbf{(VII - 2)}$$

where φ is the heating or cooling rate, T_{pc} is the peak phase change temperature (in K) and R is the universal gas constant, equal to 8.314 J/mol·K.

Lastly, thermogravimetric analysis (TGA) was performed to study the thermal stability of the docosane and the microcapsules. The tests were performed on a Mettler TG50 instrument. Specimens of approx. 15 mg were tested at 10 °C/min up to 700 °C, under a nitrogen flow of 10 ml/min. The test allowed the measurement of the temperatures corresponding to a mass loss of 1 wt% ($T_{1\%}$), 3 wt% ($T_{3\%}$), and 5 wt% ($T_{5\%}$), as well as the peak temperatures of the mass loss derivative signal,

corresponding to the maximum degradation rate of the docosane (T_p^D) and organosilica (T_p^{Si}) phases. Moreover, the weight fraction of docosane (ω_D^{TGA}) could be estimated for each sample from the mass loss after the degradation of this phase, and the residual mass after the test (m_r) was also measured.

7.2.2 Results and discussion

7.2.2.1 Sample preparation and quality of the docosane o/w emulsion

The first part of the activity was focused on optimizing the emulsion parameters, to maximize the amount of encapsulated docosane. Since an important factor is the type of surfactant, a first attempt was made with sodium dodecyl sulphate (SDS), employed in many research works to obtain o/w emulsions with different types of paraffins (Fang et al., 2010; Chen et al., 2013a; Chen et al., 2013b; Cao et al., 2014b; Jamekhorshid et al., 2014; Tang et al., 2017; Lin et al., 2019).

However, in the present work, it was found that SDS is not highly effective with docosane and leads to low fractions of emulsified paraffin. This behavior could be related to the higher molecular weight of docosane with respect to the paraffins employed in other studies (e.g. octadecane, eicosane). Nevertheless, most of the considered works do not report information on the quality of the emulsion nor on the synthesis yield, related to the ratio of encapsulated paraffin with respect to the initial amount, and therefore it is difficult to make a direct comparison. It should be pointed out that the study of PCM emulsion stability is important not only to maximize the final encapsulation yield, but also for other applications of PCMs, for example the development of highly performing heat transfer fluids (Shao et al., 2015; Wang et al., 2017; Wang et al., 2019), which often contain emulsified PCM.

In the present study, a considerably more effective emulsification of docosane was obtained with CTAB, probably due to its higher hydrophobic character denoted by its lower hydrophile-lipophile balance (HLB) number (Park et al., 2003; Proverbio et al., 2003; Ciriminna et al., 2011; Cardoso et al., 2017).

7.2.2.2 SEM microscopy

Figure VII - 2(a-f) reports SEM micrographs of the prepared microcapsules.

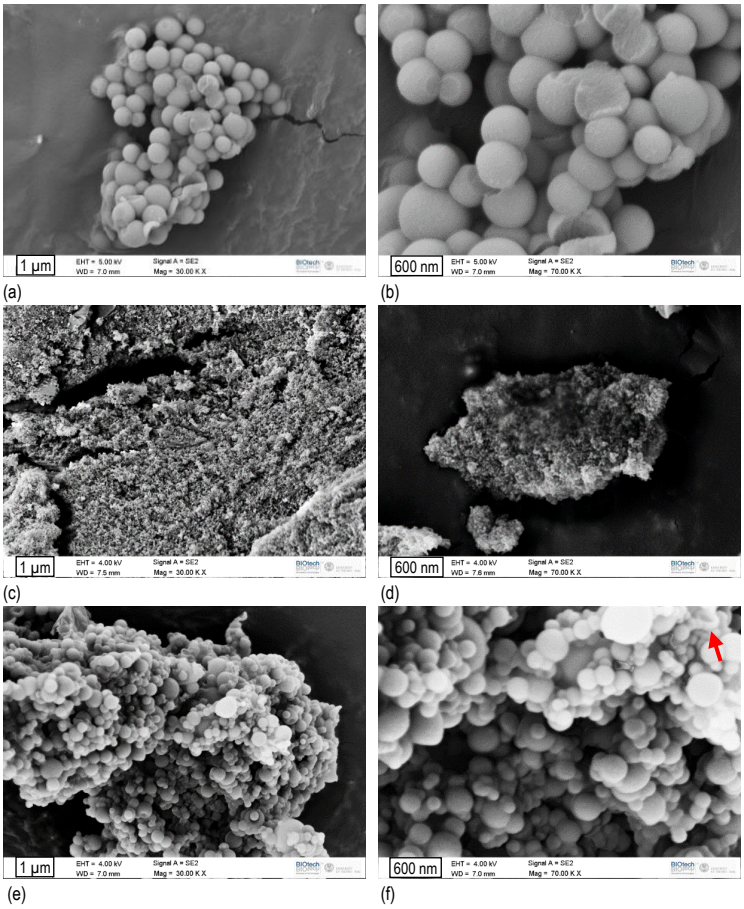

Figure VII - 2. SEM micrographs of the prepared microcapsules. (a, b) Si; (c, d) MC1; (e, f) MC2; the red arrow indicate a microcapsule showing core-shell structure.

The neat organosilica particles (Si, Figure VII - 2(a-b)) present a spherical shape, a smooth surface, and dimensions of 606 ± 110 nm. They are monodispersed with a relatively narrow size distribution in agreement with previous results (Alkan et al., 2009; Felix De Castro and Shchukin, 2015). However, microparticles appear strongly aggregated, as clearly observable at higher magnification in Figure VII - 2b. For the samples containing microencapsulated docosane, the first manifest difference between MC1 (Figure VII - 2(c-d)) and MC2 (Figure VII - 2(e-f)) is the particle size. The sample MC1 is composed of strongly aggregated and extremely small particles, with a diameter of approximately 50 nm. It was not possible to acquire images at higher magnifications, due to the instability of the sample under the electron beam during

focusing, and thus the analysis of the particle size was performed manually (with the software ImageJ) on a zoomed micrograph. Due to the blurriness of the resulting image, it was difficult to perform an accurate analysis, but the measured diameters fell in the range 35-60 nm. The particles of the sample MC2 are bigger, spherical, and with shape, surface roughness and state of aggregation resembling those of neat organosilica spheres. MC2 particles are smaller than those of the sample Si (244 ± 98 nm) and have a higher coefficient of variation. The majority of the capsules are intact, but a core-shell morphology can be observed from the sporadic broken capsules, as indicated with a red arrow in Figure VII - 2f.

7.2.2.3 FTIR spectroscopy

Figure VII - 3 reports the FTIR spectra obtained on the bulk docosane (D), MC1 and MC2 microcapsules and the neat organosilica microparticles (Si).

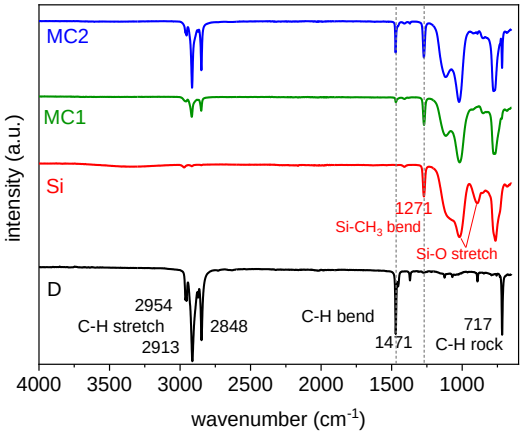

Figure VII - 3. FTIR spectra of the bulk docosane (D), docosane-organosilica core-shell microparticles (MC1 and MC2) and neat organosilica microparticles (Si).

The spectrum of the neat docosane is characterized by the typical vibrations of methylene groups; the peaks at 2954, 2913, 2872 and 2848 cm^{-1} can be assigned to the C-H bond stretching vibration in $-CH_2$ and $-CH_3$ groups, while the peaks at 1471, 1454 and 1370 cm^{-1} can be attributed to the asymmetric and symmetric bending of $-CH_2$ and $-CH_3$ groups, respectively, and the peak around 717 cm^{-1} is due to the rocking vibration of the $-CH_2$ group (Alkan et al., 2009; Felix De Castro and Shchukin, 2015).

On the other hand, the sample Si shows the peaks of the organosilica network originated from MTES. The small peaks in the interval 3000-2800 cm^{-1} are related to

the stretching vibration of the C-H bond in the methyl group, and the peak at 1271 cm^{-1} is due to the bending vibration of the Si-CH_3 bonds (Socrates, 2001). The two broad bands around 1117 and 1021 cm^{-1} and the weak signal at 924 cm^{-1} are due to the asymmetric stretching vibrations of siloxane bonds and silanols, respectively (Dirè et al., 2018). The peak at 853 cm^{-1} is due to Si-O symmetric stretching and the signal at 777 cm^{-1} can be attributed to the Si-C bond vibration (Dirè et al., 2018). Both docosane and organosilica signals are present with different relative intensity in the spectra of the two prepared microencapsulated samples, thus proving the presence of the paraffin core in MC1 and MC2. The peaks associated to docosane are more intense in MC2 than in MC1, indicating a higher docosane content in the larger microcapsules. The siloxane band appears narrower in comparison with Si sample, particularly in the case of MC2.

From the FTIR analysis it is possible to make some semi-quantitative considerations based on sharp peaks belonging to the same spectral region. By measuring the intensity ratio of the two peaks indicated with dotted lines in Figure VII - 3, i.e. the signal at 1471 cm^{-1} related to methylene docosane, and the one at 1271 cm^{-1} attributed to Si-CH_3 in organosilica, the docosane-to-organosilica molar ratios result of 0.15 and 0.55 for MC1 and MC2, respectively, in agreement with the results of NMR and TGA analyses reported below.

7.2.2.4 XRD analysis

Figure VII - 4 reports the XRD spectra of the samples D, MC1, MC2 and Si.

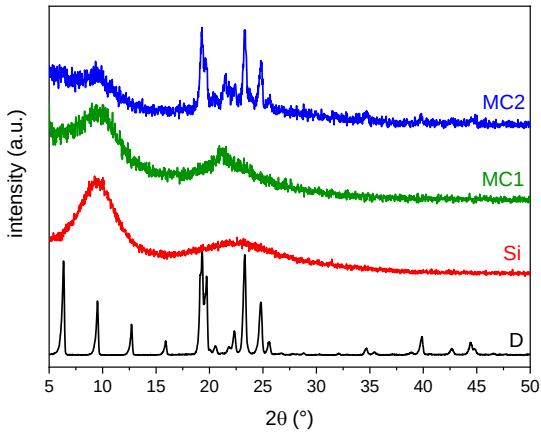

Figure VII - 4. XRD spectra of the bulk docosane (D), MC1 and MC2 microcapsules and the neat organosilica microparticles (Si).

For the spectrum of the neat docosane, the signals can be attributed to the triclinic phase of solid docosane, stable up to approx. 40 °C (Lüth et al., 1974; Nouar et al., 1998). This phase is characterized by the spatial group $P\bar{1}$, generally indicated as γ_0(C22), with cell parameters a=4.2805 Å, b=4.8212 Å, c=28.2877 Å, α=91.14°, β=94.63°, γ=106.39°. On the other hand, the Si spectrum displays the typical diffraction pattern of the amorphous MTES-derived organosilica, with two broad halos located at around 10° and 23° (Chen et al., 2013a; Tang et al., 2017; Lin et al., 2019).

The XRD spectrum of the microcapsules MC1 resembles that of the neat organosilica, and the diffraction pattern of the docosane phase is not detectable, unless a broad and less intense peak centered at 21°. On the contrary, in the spectrum of MC2 both the broad halos of the organosilica phase and the sharp peaks of the docosane phase, especially between 18° and 28°, are clearly detectable, whereas the peaks at lower angles are not visible. In this spectrum, the docosane reflection at 21.4° is relatively more intense with respect to the spectrum of D. This may indicate the presence of a different solid crystallographic phase, the so-called rhombohedral rotator phase R-II, which in normal conditions is stable near the melting temperature. This rotator phase is a crystalline mesostate with rotational degree of freedom along the chain axis (Peng et al., 2018). This finding therefore suggests that the confinement of the paraffin chains inside the organosilica shells induces a structural disorder; in fact, the absence of (00l) peaks in MC2 spectrum, located at angles lower than 18°, can be attributed to the disappearance of the lamellar ordering of the $\gamma_0(C_{22})$ structure, whereas the lateral arrangements of the chains remain unchanged (peaks located at angles greater than 18°) (Wang et al., 2019a). On the other hand, the reduction of the particle size in MC1 sample, as revealed by SEM analysis, leads to a more pronounced distorted situation, and only the finding of the rotator state appears with a shift towards lower angle than for MC2 sample. These evidences suggest that the degree of confinement of docosane in organosilica microcapsules can be related to the particle size (Wang et al., 2019a).

7.2.2.5 Solid state NMR analysis

Solid state NMR analysis was performed to deeply investigate the microstructure, morphology and confinement effect of the different microcapsules. Figure VII - 5(a-b) shows the ^{13}C and ^{29}Si CP MAS spectra of the neat docosane, the two microencapsulated PCMs and the organosilica particles.

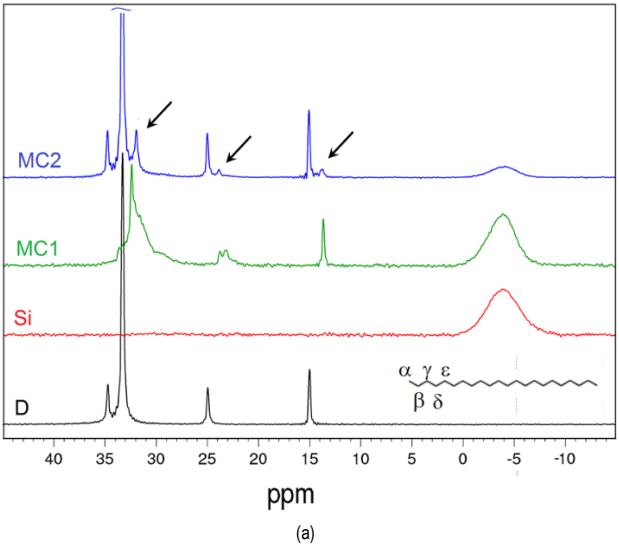

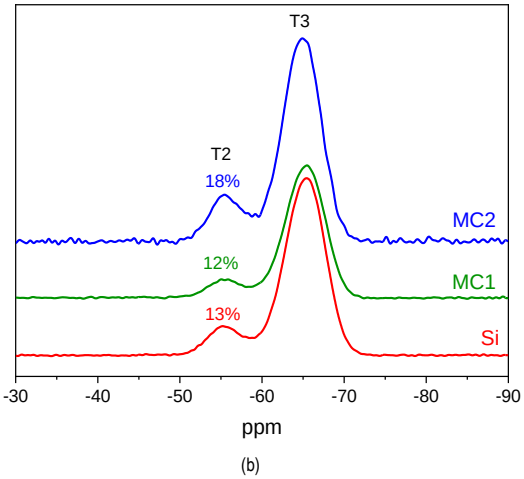

Figure VII - 5. NMR spectra of docosane (D), MC1 and MC2 microcapsules and the neat organosilica microparticles (Si): (a) ^{13}C CP MAS spectra with docosane carbon labeling and arrows to highlight rotator phase signals; (b) ^{29}Si CP MAS spectra.

The spectrum of bulk docosane in Figure VII - 5a shows the typical signals of the *n*-alkanes, associated to the first four carbon atoms in the chain (indicated as α, β, γ, δ in the structural scheme, Figure VII - 5a), while the chemical shifts are not anymore resolvable from the fifth (ε) carbon atom (Speight et al., 2011).

For the neat organosilica microcapsules (Si), the only signal is found at approx. -4 ppm and it is due to the methyl carbon atoms linked to silicon, while the absence of signals associable to the ethoxy groups indicates the completion of MTES hydrolysis (Dirè et al., 2018). Together with all the paraffin and MTES signals, the docosane phase in the sample MC2 shows also some minor upfield shifted peaks (approx. 2 ppm) close to the α, β and ε signals, indicated with arrows in Figure VII - 5a, which can be associated to α, β and ε methylene groups in a different environment. Interestingly, in the spectrum of MC1, the chemical shift of docosane signals fits with the weak upfield resonances of MC2 spectrum, and there are no signals in the original positions. The upfield shifted resonances can be due to the presence of the rotator phase or also to the γ-gauche effect near the chain ends, which causes a non-uniform distribution of the conformational disorder, thereby broadening the peaks (Okazaki and Toriyama, 1989). This behavior could be attributed to the confinement effect of the docosane inside the capsules, and the fact that it is more evident for the smaller (MC1) capsules supports this hypothesis (Möller et al., 1987) in agreement with XRD conclusions.

In this sense, it could be useful to evaluate the signals of the ^{13}C proton-decoupled MAS spectrum, reported in Figure VII - 6.

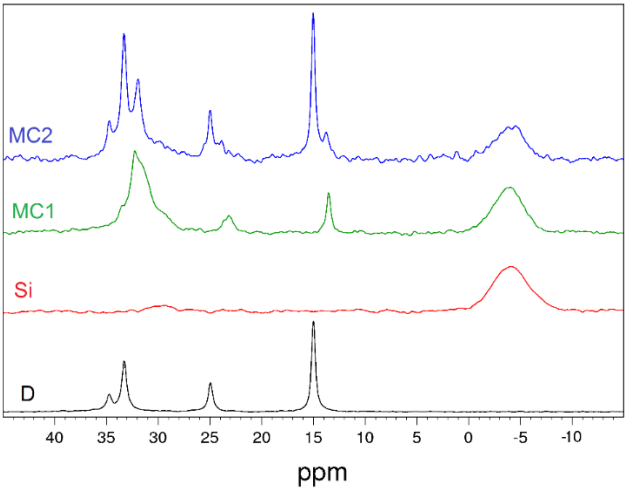

Figure VII - 6. ^{13}C proton-decoupled MAS NMR spectra of docosane (D), MC1 and MC2 microcapsules and the neat organosilica microparticles (Si).

As the spin-lattice relaxation times of the various carbon atoms are remarkably different from each other (e.g. for α-C it is 1.2 s, for β-C 16 s, for γ-C and ε-C >700 s), with the selected experimental parameters it is possible to make a quantitative

comparison among the methyl groups. From the ratio between the areas of H_3C-Si (-4 ppm) and H_3C-CH_2 (14 ppm) signals, the molar ratio organosilica/docosane can be deduced, considering that the signal at -4 ppm counts for one carbon atom and that at 14 ppm for two. The results of this calculation give docosane-to-organosilica molar ratios of 0.09 and 0.53 for MC1 and MC2, respectively. What is immediately evident is that for the sample MC1 the silica fraction is approx. 6 times higher than for MC2, which is in good agreement with both the ratios calculated from FTIR peaks and the DSC results. Moreover, by integrating the area of α and α' signals it is possible to estimate that the rotator phase (represented by α') is the 20 % of all the encapsulated alkane for sample MC2, while for the MC1 it represents the 100 %.

Furthermore, through molecular dynamics NMR experiments (Figure VII - 7), and especially from the evaluation of ^{13}C spin-lattice relaxation times ($T1_C$), it is possible to prove that the two detected phases represent respectively a free bulk paraffin fraction and a docosane fraction interacting with the inner silica shell, since the interaction causes a remarkable reduction of $T1_C$. A similar effect was already observed by Inoue et al. (Inoue et al., 1995), who studied the behavior of polyethylene on silica surfaces and imputed the constraints of the molecular motions of the polymer chains to the interaction with the silica surface. As evidenced by the XRD measurements, the inclusion can cause an alteration of the crystalline structure. This effect was already mentioned by Okazaky and Toriyama (Okazaki and Toriyama, 1989), who studied through T1 analysis the different behavior of even and odd alkanes. As a matter of facts, despite the very long $T1_C$ of main chain carbons of neat docosane measured by Okazaky and Toriyama, the present samples show a reduced and capsule size-dependent T1 value for main chain methylenes, whereas it is practically unchanged for methyls (Table VII - 2). No effects due to interaction can be detected for silica methyls, as showed also by Okazaky and Toriyama's samples. The overall size-dependent $T1_C$ reduction is a proof of the effective paraffin inclusion and the lower values shown by α' and β' with respect to α and β further indicate the interaction of a docosane fraction with the silica shell, which leads to the alteration of the crystal structure, in agreement with XRD conclusions.

Table VII - 2. $T1_C$ relaxation times of MC1 and MC2 expressed in seconds.

C type	MC1	MC2
γ	61.6	117.0
ε	61.5	109.6
δ	36.5	44.3
β	-	33.7
β'	2.1	4.1
α	-	1.6
α'	1.3	1.2
Si-CH_3	5.0	4.6

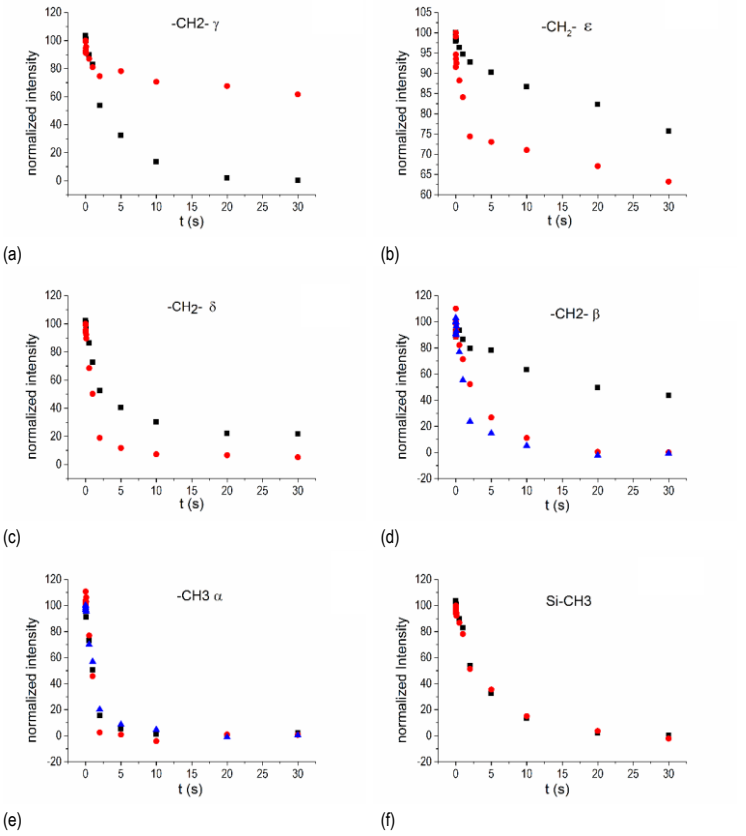

Figure VII - 7. $T1_C$ curves of the carbons detected in the ^{13}C CP MAS spectra for MC2 (black squares for original signals, blue triangles for interfacial peaks) and MC1 samples (red circles): (a)+ (b)+ (c) chain methylenes from C-3, (d) C-2 methylenes, (e) methyls, (f) MTES methyls.

Finally, Figure VII - 5b shows the ^{29}Si CP MAS of the samples MC1, MC2 and Si, to investigate the degree of condensation of the organosilica phase. All the samples show the signals of the T^2 ($R\text{-}Si(OSi)_2(OH)$) and T^3 ($R\text{-}Si(OSi)_3$) units, at -55.7 ppm and -65.6 ppm, respectively (Dirè et al., 2018), and the intensity ratios are comparable in the three cases, which implies that the presence of docosane and CTAB surfactant does not influence MTES hydrolysis-condensation process. The quantitative analysis was performed on the ^{29}Si proton-decoupled MAS spectra (not reported), and confirms the trends observed in the CP MAS spectra, being the condensation levels approx. 96% for the sample Si and 94% for the sample MC2.

7.2.2.6 DSC analysis

Figure VII - 8a shows the DSC thermograms of the samples Si, D, MC1 and MC2. The neat organosilica does not manifest any thermal transition in the considered temperature interval. On the other hand, in the heating scan, all the samples containing docosane experience the melting phase change, visible as a single broad peak at the adopted heating scan (10 °C/min).

The data reported in Table VII - 3 show that the peak melting temperature (T_m) measured on the microcapsules is lower than that of the neat docosane, and this is more evident for the smaller (MC1) than for the bigger (MC2) capsules. This effect, also reported by other literature studies (Wang et al., 2006; Chen et al., 2013a; Li et al., 2013; Liu and Lou, 2015; Felix De Castro et al., 2016; Sun and Xiao, 2017; Tang et al., 2017), can be ascribed to the fact that the confinement in a small volume hinders the crystallization, but in this specific case also to the interaction of docosane with the inner shell surface, which limits the chain mobility as evidenced by NMR studies. This hypothesis is supported by the reduction in melting enthalpy, which is more evident for the smaller capsules presenting a higher surface-to-volume ratio. The same effect is at the basis of the decrease in the peak crystallization temperature for the sample MC1; as the paraffin domains are confined in smaller volumes, a higher supercooling degree is needed to initiate the crystallization. This phenomenon must be taken into account when designing a microencapsulated PCM, as it could change its application temperature interval. The cooling scans are characterized by the presence of several peaks. The neat docosane shows two peaks, the first (33.5 °C) related to the liquid-solid phase change, and the second (28.5 °C) associated to a solid-solid transition (Wang et al., 2003), while the microcapsules show several peaks, visible especially in the sample MC2, which can be due to confinement effect and the presence of different crystalline phases. The measured phase change enthalpies are reported in Table VII - 3. The neat docosane develops 234.2 J/g, and the melting enthalpies measured on MC1 and MC2 provide information about the docosane fraction in each sample, described by the efficiency (η) reported in Table 3. The sample MC2 contains approx. 60 % of docosane, while the PCM fraction decreases to 14 % for MC1. These data are in good agreement with the results of NMR and TGA.

Figure VII - 8(b-c) reports the DSC thermograms of D and MC2 acquired at 0.2 °C/min. As the lower heating rate allows a better resolution of the signals, the neat docosane (Figure VII - 8b) shows two endothermic peaks in the heating scan, one (at lower temperature) associated to the solid-solid transition from the crystalline phase to the rotator phase, and the other due to the solid-liquid phase transition, in good agreement with the detailed investigation performed by Wang et al. (Wang et al., 2003). The cooling scan shows two sharp peaks with a broad halo in between, which is better visible from the inset plot. Following Wang's analysis, the peak at higher temperature can be attributed to the transition from the liquid state to the rotator phase,

Table VII - 3. Main results of the DSC tests on the bulk (D) and microencapsulated (MC1 and MC2) docosane. The table reports data of the phase change temperatures and enthalpies, as well as the encapsulation efficiency.

Sample	T_m (°C)	T_c (°C)	ΔH_m (J/g)	ΔH_c (J/g)	η (%)
D	46.2	33.5	234.6	234.2	100
MC1	41.2	25.1	33.0	32.9	14.1
MC2	43.8	34.5	142.7	141.4	60.6

T_m, T_c = melting and crystallization temperatures of the PCM; ΔH_m, ΔH_c = melting and crystallization enthalpies of the PCM; η = encapsulation efficiency.

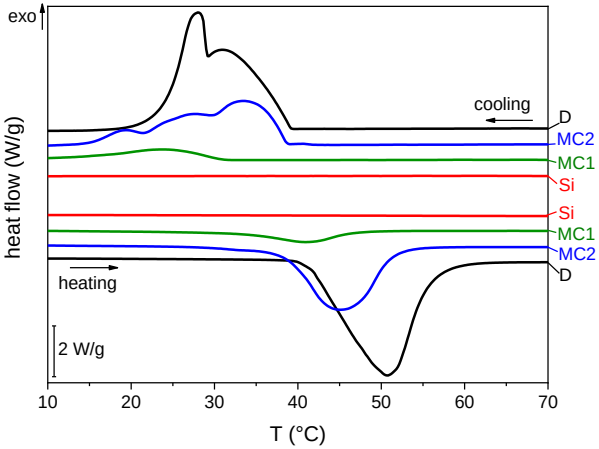

(a)

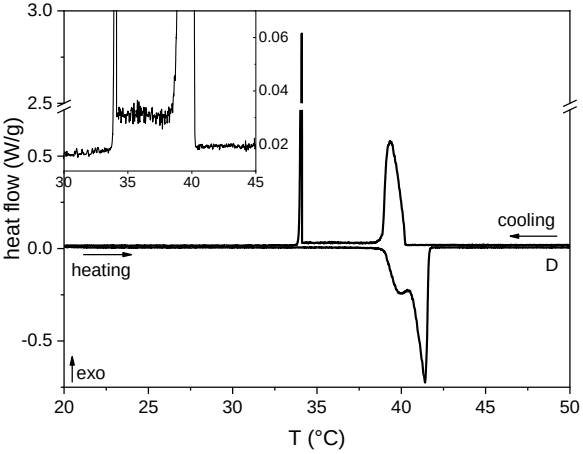

(b)

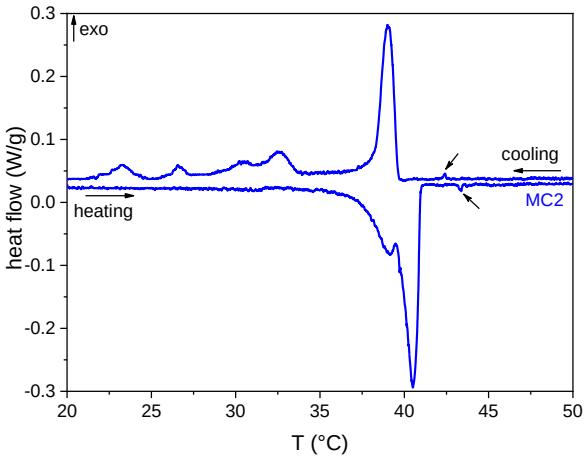

(c)

Figure VII - 8. (a) DSC thermograms of the bulk (D) and microencapsulated (MC1 and MC2) docosane and the neat organosilica microparticles (Si). The first heating scans and the cooling scans are reported. (b) DSC thermogram of the neat docosane acquired at 0.2 °C/min (heating and cooling scan). (c) DSC thermogram of the microcapsules MC2, acquired at 0.2 °C/min (heating and cooling scan).

the broad halo is related to the rotational action of CH_2 bonds, and the last sharp peak due to the last solid-solid transition, which ends with the formation of an ordered crystalline phase. The encapsulated docosane MC2 shows the same two peaks as the sample D in the heating scan, but at a slightly lower temperature, and at least five intense peaks in the cooling scan. This implies a different crystallization behavior due to confinement and interaction with the organosilica shell. A very small peak (indicated with arrows on Figure VII - 8c) can be also observed both on heating and on cooling. This is probably due to the surface freezing phenomenon, i.e. to the fusion/crystallization of a monolayer formed on the surface of liquid docosane, observable here due to the high surface-to-volume ratio of the microencapsulated docosane and not normally observable on bulk samples (Wang et al., 2003).

The DSC tests at different heating scans were also performed to determine the apparent activation energy (E_a) of the phase transition of the bulk and microencapsulated docosane. The results are reported in Figure VII - 9.

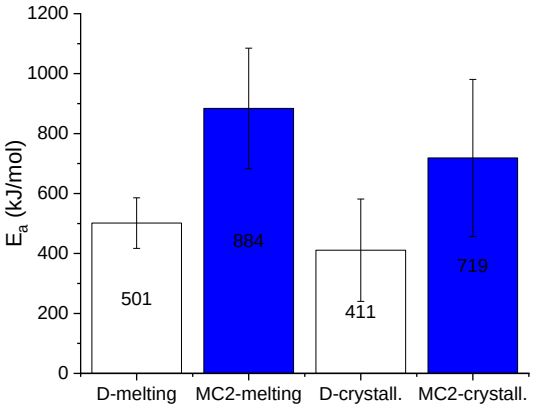

Figure VII - 9. Activation energy for the melting and crystallization processes calculated through the Arrhenius equation (slope of the linear regression).

The value of E_a for docosane melting is 501 kJ/mol, in good agreement with similar systems (Anghel et al., 2014). Despite the not negligible error bands, related to the values of R^2 well lower than 1 in the linear regressions of the phase change temperatures, it can be appreciated that the values of E_a increase upon encapsulation, probably due to steric effects and interaction with the capsule shell.

7.2.2.7 TGA tests

Figure VII - 10(a-b) shows the TGA thermograms on the prepared microcapsules, while the most important results are displayed in Table VII - 4. The bulk docosane undergoes a single-step thermal degradation with T_p^D at 291 °C, while the neat organosilica is thermally stable until approx. 500 °C. Both the degradation steps are present in the samples MC1 and MC2, but the derivative peak temperatures are of some degrees lower than those of the neat samples, which was already reported in the literature, especially for the PCM phase (Tang et al., 2017).

From the amplitude of the degradation step of docosane, it is possible to estimate the docosane weight fraction for the samples MC1 and MC2, which are reported in Table VII - 4. The fraction of docosane calculated for MC2 is 65 wt%, and this is in good agreement with the DSC results, while that determined for MC1, 26 wt%, is slightly higher than that calculated via DSC, and this can be due to sample inhomogeneity, but also to the fact that the crystallinity degree of the docosane encapsulated in small microcapsules such as the sample MC1 is lower than that of the free docosane, and thus the developed enthalpy is lower than expected, which is in agreement with the XRD results. It is worth of noting that the docosane weight content

calculated by TGA is in good agreement with the molar amount estimated by both FTIR and NMR analyses.

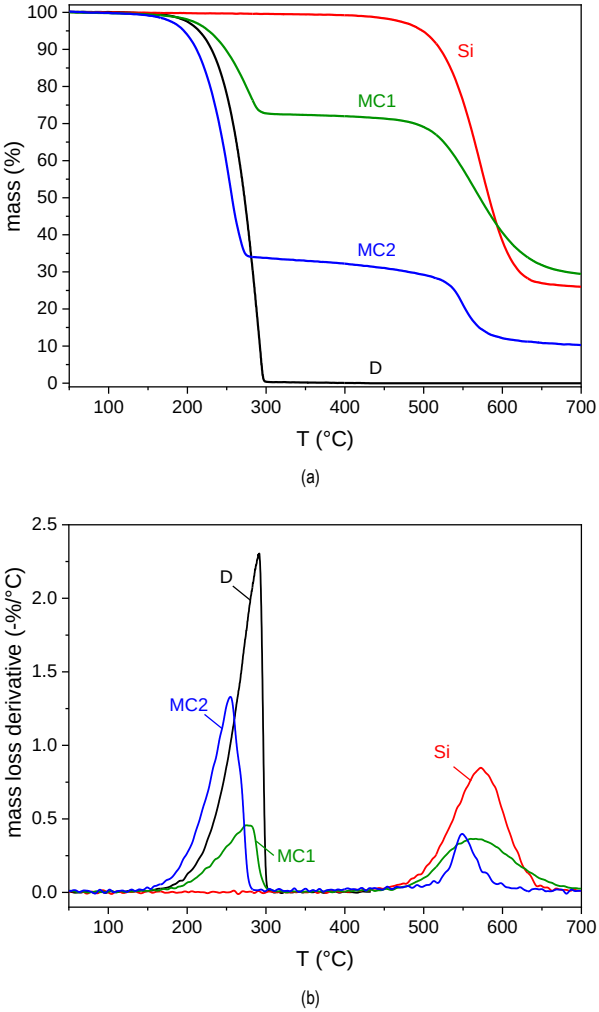

Figure VII - 10. TGA thermograms of the bulk (D) and microencapsulated (MC1 and MC2) docosane and the neat organosilica microparticles (Si). (a) mass; (b) mass loss derivative.

Table VII - 4. Main results of the TGA tests on the bulk (D) and microencapsulated (MC1 and MC2) docosane and the neat organosilica microparticles (Si).

Sample	$T_{1\%}$ (°C)	$T_{3\%}$ (°C)	$T_{5\%}$ (°C)	T_p^D (°C)	T_p^{Si} (°C)	ω_D^{TGA} (%)	m_r (%)
D	179.8	203.5	214.8	291	-	100	-
MC1	175.3	212.8	227.0	278	572	26	30
MC2	156.2	184.0	195.5	255	547	65	10
Si	421.8	479.3	498.7	-	563	-	26

$T_{1\%}$, $T_{3\%}$, $T_{5\%}$ = temperatures corresponding to a mass loss of 1 wt%, 3 wt% and 5 wt%; T_p^D= peak temperature of the mass loss derivative, at the degradation of the docosane phase; T_p^{Si} = peak temperature of the mass loss derivative, at the degradation of the organosilica phase; ω_D^{TGA} = weight fraction of docosane; m_r = residual mass after the test.

7.2.3 Conclusions

In this work, docosane was encapsulated via a sol-gel process in organosilica shells of two different sizes. The microcapsules (MC1 and MC2) were extensively characterized and compared to bulk docosane (D) and neat organosilica microspheres (Si).

The FTIR spectra of MC1 and MC2 showed all the signals of D and Si, and the analysis suggested that the docosane fraction was considerably higher in MC2 than in MC1, as confirmed by other techniques. The XRD spectrum of MC1 resembled that of the neat organosilica, due to the low docosane fraction, while the spectrum of MC2 contained the patterns of both organosilica and docosane phases, with probable indication of the presence of the solid rotator phase R-II. Solid state NMR has proved to be a powerful technique to investigate microencapsulated PCMs, providing an in-depth insight into the different microstructures and phases of the samples. In the ^{13}C CP MAS spectra, the sample MC2 showed some minor peaks with an upfield shift of approx. 2 ppm next to the α, β and ε signals, appreciable also in the proton-decoupled spectrum, while the spectrum of MC1 contains only the upfield shifted signals. This shift is related to the presence of rotator phase or to the reduced docosane chain mobility and interaction with the shell wall (γ-gauche effect). From the areas of α and α' signals it was possible to estimate that the rotator phase is the 20 % of all the encapsulated alkane for sample MC2, while for the MC1 it represents the 100 %. DSC analysis revealed that the melting and crystallization temperatures decreased upon encapsulation, which is due to the difficulty to form perfect crystals in a confined volume and the need for a higher supercooling to start the crystallization. The melting enthalpy measured on MC2, the top-performing microcapsules, was 143 J/g, which implies an encapsulation efficiency of approx. 60 %.

This work contributed to highlight the potentialities of the sol-gel route as a PCM encapsulation technique and to shed light on the change in structural, microstructural and thermal properties due to confinement effect and interaction with the shell wall.

7.3 Bioinspired polydopamine coating as an adhesion enhancer between paraffin microcapsules and an epoxy matrix

In a polymer composite, the interface between the matrix and the discontinuous phase(s) plays a fundamental role in determining the final thermo-mechanical properties and aging resistance. In a composite containing PCM microcapsules, an additional issue is represented by repeated thermal cycles, which cause cyclic volume variations of the PCM. This could further damage the interphase zone, thereby causing microcracks and debonding phenomena that deteriorate the mechanical properties and thermal conductivity and shorten the service life of the component. The damage at the interface could also undermine the mechanical integrity of the capsule shell, thus favoring PCM leakage and reducing the energy storage capability of the composite (Keblinski et al., 2002; Su et al., 2011a; Su et al., 2012; Burger et al., 2016).

Despite being such a critical aspect, the adhesion between PCM microcapsules and polymer matrices has not been object of intensive investigation so far. The scientific literature reports numerous studies on the modification of polymer microcapsules for other applications, via the addition of silane compounds during (*in situ*) (Wang et al., 2009; Wang et al., 2010) or after (*a posteriori*) (Tong et al., 2013; Cai et al., 2014; Cai et al., 2015; Mirabedini et al., 2019) the microcapsule synthesis. However, these works focus almost exclusively on the modification of urea-formaldehyde resin, while there is a considerable lack of investigation on melamine-urea-formaldehyde (MUF) or melamine-formaldehyde (MF) microcapsules, which are by far the most common and commercially available shells containing a PCM, due to cheapness, thermal stability, and the easily controlled production process (Su et al., 2011a). Due to the lack of reactive functional groups of a fully cured MF surface, the *a posteriori* modification of the microcapsule surface presents considerable challenges, especially when addressed with traditional surface modification techniques like the silane chemistry.

Among the possible alternative treatments, a method that has attracted increasing attention in the last decade is the deposition of polydopamine (PDA) (Ryu et al., 2018). PDA is a bioinspired synthetic polymer that has emerged as one of the most powerful tools for broad applications, as it allows the production of continuous layers with relative simplicity and noteworthy versatility and exhibits great adhesion onto a great variety of metallic, polymeric and ceramic surfaces (Lynge et al., 2011; Jeong et al., 2018). It is particularly appealing to functionalize chemically inert surfaces; it has been employed to improve the fiber/matrix interfacial adhesion of highly inert reinforcing fibers, such as ultra-high molecular weight polyethylene (UHMWPE) and poly(*p*-phenylene-2,6-benzobisoxazole) (PBO) fibers (Tang et al., 2018; Shanmugam et al., 2019).

Produced by the self-polymerization of dopamine, PDA contains catechol and amine groups and presents a chemical composition analogous to that of the mussel adhesive proteins (Liu et al., 2016b; Kwon and Bettinger, 2018). Due to its unique chemistry and the interesting assortment of reactive functional groups, this bioinspired coating can act as compatibilizer in multiple filler/matrix systems and can be further functionalized with additional surface chemistry techniques (Tang et al., 2018).

This Subchapter presents the results of the surface modification through PDA of the commercial PCM microcapsules used also in other Chapters of this thesis, which have a shell of fully cured formaldehyde-based resin. The PDA layer, instantly formed by the oxidative polymerization of the applied dopamine, improved the interfacial adhesion with an epoxy matrix. This work specifically focuses on employing microscopy techniques to study how the interphase between the microcapsules and the epoxy matrix varies between uncoated and coated capsules, on relating the PDA deposition parameter to the layer thickness and morphology, and on investigating how the PDA layer influences the heat storage properties of the microcapsules.

The sample preparation and most of the characterization were carried out at the Leibniz Institute of Polymer Research (Dresden, Germany).

7.3.1 Materials and methods

7.3.1.1 Materials

The microencapsulated PCM Microtek MPCM43D and the bi-component epoxy system Elan-tech® EC157 / W342 were already introduced in Chapter III. Dopamine hydrochloride and tris(hydroxymethyl)aminomethane (TRIS buffer, Trizma®) were purchased from Sigma-Aldrich (Steinheim, Germany). Acetone was supplied by Fisher Scientific (Nidderau, Germany). Deionized water was prepared employing a PURELAB Chorus 2+® water purification system (Elga LabWater, High Wycombe, UK). Bisphenol A diglycidyl ether (DGEBA) was supplied by Sigma-Aldrich (Steinheim, Germany).

7.3.1.2 Sample preparation

2.0 g dopamine hydrochloride (as supplied) were added to 600 ml of TRIS solution (0.1 mol/L) in an uncovered beaker and dissolved in an ultrasonic bath (VWR International, Leuven, Belgium) at room temperature. Then, the microcapsules were slowly added to the dopamine solution under vigorous magnetic stirring (1000 rpm). In the uncovered beaker the suspension was stirred for 24 hours at room temperature. The PDA-coated microcapsules were filtered off under vacuum by a Büchner funnel lined with a Sartorius 389 filter (Sartorius AG, Göttingen, Germany). The coated microcapsules were rinsed twice with 50 ml deionized water before each cycle of drying under vacuum at room temperature for 4 hours. Washing and drying cycles

were repeated to constant weight of the surface-modified microcapsules. After their modification the formerly white microcapsules were dark brown, which indicated the presence of insoluble and irreversibly bonded PDA layers on their surfaces. The same procedure was repeated with a more diluted dopamine hydrochloride solution (1.2 g in 600 ml).

PDA reference material was synthesized by adding 2.0 g dopamine hydrochloride (as supplied) to 600 ml of TRIS solution (0.1 mol/l) in an uncovered beaker. Dopamine polymerization was performed at room temperature for 24 hours. The black-brownish polymer was filtered, washed twice with deionized water and dried under vacuum to constant weight.

7.3.1.3 Reaction of neat and PDA-coated microcapsules with oxirane-carrying molecules

The surface reactivity of the PDA-coated microcapsules was assessed by investigating the crosslinking reaction with two oxirane-carrying molecules, namely the DGEBA and the commercial epoxy base Elan-tech® EC 157. 1 g of coated microcapsules was introduced into a 20 ml glass vial. Then, 5 ml of either DGEBA or Elan-tech® EC 157 were added. The suspension was stirred for 4 h with a magnetic stirrer. The microcapsules were separated by vacuum filtration with a Sartorius 389 filter. To remove unbound resin, the microcapsules were rinsed twice with 20 ml acetone. The epoxy-crosslinked PDA-coated microcapsules were dried under vacuum at room temperature for approx. 1 h. The surface investigation was performed through X-ray photoelectron spectroscopy (XPS). It should be noted that the epoxy base EC157 is a commercial name for DGEBA. This experiment was designed and performed entirely by Dr. Frank Simon at Leibniz-IPF and was added to this thesis for completeness.

7.3.1.4 Preparation of the MC-filled epoxy composites

MC-filled epoxy composites were produced by mixing the epoxy base and the hardener in a weight ratio of 100:30, as suggested by the producer. Neat or PDA-coated microcapsules were added to the epoxy preparation in a weight fraction of 10 wt% and stirred with a SpeedMixer DAC 400 FVZ (Landrum, SC, USA) at 1000 rpm for 1 min, to ensure a homogeneous dispersion. The mixtures were degassed for 5 min, casted in stainless steel molds and cured at 100 °C for 10 h. The curing was followed by a slow cooling to room temperature.

7.3.1.5 Characterization

The morphology and roughness of the neat and PDA-coated microcapsules were studied by a Zeiss Gemini Neon 40ESB scanning electron microscope

(Oberkochen, Germany). The powder samples were prepared on SEM stubs equipped with conductive tape. No further conductive coating was applied, not to alter the surface morphology of the samples.

AFM tests were carried out to study the morphology and the surface roughness before and after PDA coating. Neat and PDA-coated microcapsules were glued with a double-sided tape on glass slides. The measurements were done in the peak force tapping mode by a Dimension FastScan atomic force microscope (Bruker-Nano, Santa Barbara, USA), equipped with silicon nitride sensors ScanAsyst Fluid+ (Bruker, USA) with a nominal spring constant of 0.7 N/m and tip radius of 2 nm. The setpoint was 0.04 V. The mean roughness Sa was calculated through the program NanoScope Analysis 1.9 (Bruker-Nano, Santa Barbara, USA) after removing the curvature of the spheres by a 6^{th} order flatten command.

XPS was carried out to study the surface chemistry and functional groups of the neat and PDA-coated microcapsules, and to study the different surface reactivity, molecular interactions and chemical bond formation when the microcapsules were reacted with two oxirane-carrying compounds, namely the epoxy base Elan-tech 157 and the DGEBA molecule. Four samples were analyzed with this technique, namely (i) neat microcapsules; (ii) PDA-coated microcapsules; (iii) PDA-coated microcapsules reacted with DGEBA; (iv) PDA-coated microcapsules reacted with the epoxy base Elan-tech® EC 157. All the XPS studies were carried out by means of an Axis Ultra photoelectron spectrometer (Kratos Analytical, Manchester, UK). The spectrometer was equipped with a monochromatic Al Kα ($h \cdot \nu$ = 1486.6 eV) X-ray source of 300 W at 15 kV. The kinetic energy of photoelectrons was determined with hemispheric analyzer set to pass energy of 160 eV for wide-scan spectra and 20 eV for high-resolution spectra. Employing double-sided adhesive tape (3M Company, Maplewood, MN, USA), the powder samples were prepared as thick films on a sample holder that allowed their introduction in the recipient of the XPS spectrometer. During all the measurements, electrostatic charging of the sample was avoided by means of a low-energy electron source working in combination with a magnetic immersion lens. All the recorded peaks were shifted by the same value that was necessary to set the C 1s peak to 285.00 eV. Quantitative elemental compositions were determined from peak areas using experimentally determined sensitivity factors and the transmission function of the spectrometer. Spectrum background was subtracted according to Shirley (Shirley, 1972). The high-resolution spectra were deconvoluted by means of the Kratos spectra deconvolution software (Kratos Analytical, Ltd., Manchester, UK). Free parameters of component peaks were their binding energy (BE), height, full width at half maximum (FWHM) and the Gaussian-Lorentzian ratio. This experiment was designed entirely by Dr. Frank Simon at Leibniz-IPF. It was added to this thesis for completeness.

The FTIR spectra of the neat microcapsules, PDA-coated microcapsules, and PDA as reference coating material were recorded in the attenuated-total reflection

(ATR) mode (Golden Gate accessory with diamond crystal, Specac Limited, Orpington, England) using a FTIR spectrometer Tensor 27 (Bruker Optics GmbH, Ettlingen, Germany). All samples were placed on the horizontal ATR diamond crystal. A reference spectrum was recorded from the pure ATR crystal. 100 interferograms were co-added at a spectral resolution of 2 cm^{-1}. The interferograms were Fourier transformed applying Blackman-Harris-3 apodization and zero filling factor of 2. Calculated absorbance spectra were subjected to atmospheric compensation, limited to the fingerprint region (1900 cm^{-1} to 600 cm^{-1}), the baseline function of OPUS software was used (2 pt. baseline- 2 iterations concave rubber band method), and normalized to the height of band appearing at 716 cm^{-1}.

DSC was performed to measure the most important thermal properties of a PCM, such as the phase transition enthalpies and temperatures, and to evaluate their changes after the coating process. Powder samples of approx. 5 mg were placed in standard aluminum DSC pans and analyzed with a TA Instruments Q2000 calorimeter (New Castle, DE, USA). Each sample was subjected to a heating/cooling/heating cycle at 10 °C/min from -20 °C to 80 °C, under nitrogen atmosphere. The test allowed the measurement of the peak temperature and enthalpy of each phase transition and an evaluation of the variation in the core-to-shell mass ratio after the coating.

TGA was performed to assess the evolution of the thermal resistance of the coated capsules. A TA Instruments Q5000 IR thermobalance (New Castle, DE, USA) was employed to record thermograms from approx. 5 mg of the powder samples. The samples were heated up to 700 °C with a heating rate of 10 °C/min, under nitrogen atmosphere. The tests allowed the determination of the temperatures corresponding to a mass loss of 1 wt%, 3 wt% and 5 wt% ($T_{1\%}, T_{3\%}, T_{5\%}$), the temperature at the maximum degradation rate, corresponding to the peak of the mass loss derivative (T_d), and the residual mass after the test (m_r).

The melting of the core of the microcapsules in dependence on temperature has been investigated by an optical microscope equipped with a hot stage. Microcapsules were placed on light microscopy glass-slide on a temperature controlled stage LTS-420 (Linkam, Surrey, United Kingdom) and heated from r.t. to 50 °C and re-cooled to r.t. Visual images have been recorded with an Axio Imager (Zeiss, Jena, Germany). Temperature controlled microscopy was performed on the neat microcapsules and the PDA-coated microcapsules.

SEM micrographs of the fracture surface of the prepared epoxy/MC samples (prepared as described in Section. 7.3.1.2) were recorded to visually observe the modification of the adhesion and the interfacial region after PDA coating, to study the fracture morphology and propagation, and to measure the thickness of the coating as a function of the deposition parameters. Then, the composites were cryofractured in liquid nitrogen and the fracture surface was investigate through SEM. The specimens were glued on SEM stubs with a conductive tape and investigated with a Zeiss Supra 60 field emission scanning electron microscope, after Pt-Pd sputtering.

7.3.2 Results and discussion

The whole results discussion refers to the comparison between neat MC and MC modified in the solution with the highest concentration of dopamine hydrochloride, called MC-PDAc, where “c” stands for “concentrated”. The MC modified with the least concentrated solution (MC-PDAd, “diluted”) will be introduced only in final part of the results discussion, dealing with the thermal and adhesion properties.

7.3.2.1 Surface morphology of neat and PDA-coated microcapsules

Figure VII - 11(a-f) shows the SEM micrographs of neat and PDA-coated samples. The neat microcapsules appear smooth and spherical, while the roughness increases considerably for the PDA-coated microcapsules. The PDA layer presents a globular appearance, which could contribute to the filler-matrix interfacial strength by mechanical interlocking. The PDA is deposited uniformly on the whole MC surface, as observable from Figure VII - 11d. The coating caused a change in the microcapsule color from white to brown, but this is not an issue for the proposed application.

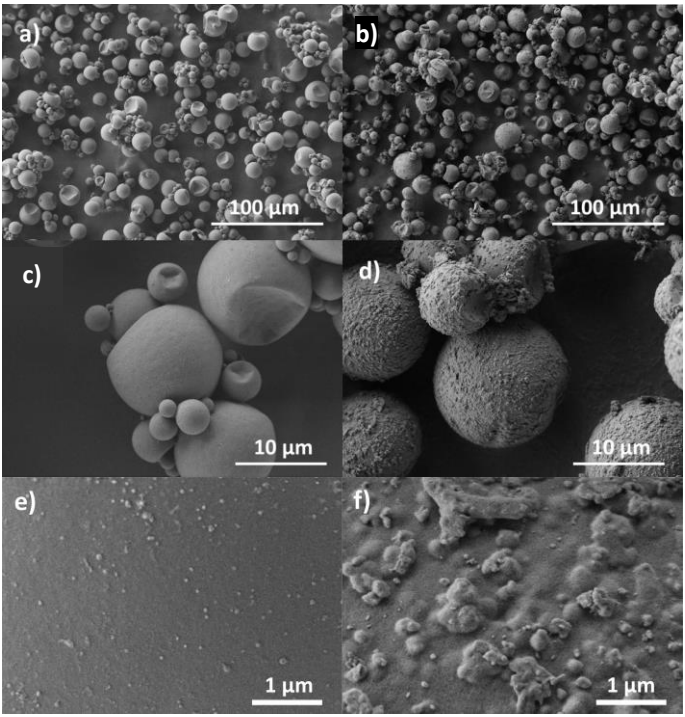

Figure VII - 11. SEM micrographs of neat microcapsules (a, c, e) and PDA-coated microcapsules MC-PDAc (b, d, f) at different magnification levels.

The surface morphology and roughness of the PDA coating was studied quantitatively with AFM. Figure VII - 12 shows the output of the AFM analysis. The neat microcapsule has a relatively smooth surface, while the PDA-coated microcapsule shows a nodular surface structure with varying nodule size. The mean surface roughness (S_a) increases from 9 nm for the neat MC, to 86 nm for the PDA-coated MC.

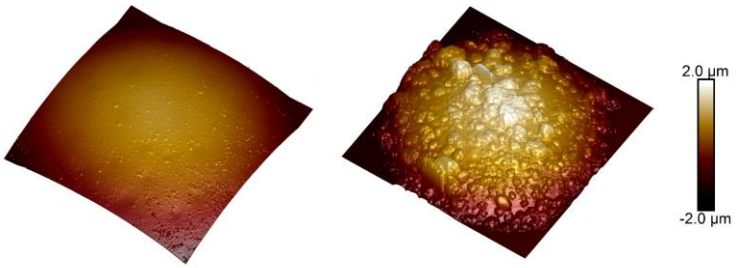

Figure VII - 12. 3D AFM images of neat microcapsules (left) and PDA-coated microcapsules (MC-PDAc) (right). Lateral image dimension 10 µm, color coded height range 4 µm.

7.3.2.2 FTIR spectroscopy

Although FTIR is a widely used non-destructive method for many compounds, complex samples, and coatings, an accurate investigation of the structure of PDA through FTIR is still a challenge. The PDA polymer consists of a number of different monomer units with various oxidation states and chemical and physical linking, organized in different hierarchical aggregates (Roldán et al., 2014). Thus, absorption spectra of PDA do not contain well-resolved bands, unlike single functional groups in defined compounds. On the contrary, wide and featureless spectra are often detected, which show the overlapping contributions of different functional units with absorption energies close to each other.

This is clearly observable from the ATR-FTIR spectrum acquired on PDA, shown in Figure VII - 13 with a dashed line. This spectrum was vertically translated, to facilitate the interpretation of the results. A complex PDA spectrum with broad bands was obtained as a result of different oxidation states, a variety of cyclic hetero- or aromatic structures and different bridging bonds and positions. Figure VII - 13 also shows the ATR-FTIR spectra of the neat and PDA-modified microcapsules, with a dotted and solid line, respectively. Both spectra show narrow hydrocarbon bands of the paraffin core, which is crystalline, and broader bands of the melamine-formaldehyde shell, as elucidated in Table VII - 5.

The PDA-modification of the microcapsules can be evaluated by the intensity increase between 1650 cm^{-1} and 1050 cm^{-1}. The subtraction of the spectrum of neat

microcapsules from that of the PDA-modified microcapsules results in a good approximation of the PDA spectrum. Most characteristic band positions and intensities are recovered for both the PDA spectrum and the subtracted one, shown as red line. The spectral band positions of PDA, reported in Table VII - 6, are consistent with other reports (Roldán et al., 2014; Perna et al., 2016; Al Aani et al., 2018; Sun et al., 2019a; Furtado et al., 2020) and assignments are based on literature data and on the comparison with pyrrolic, indolic and catecholic structures (Socrates, 2004). These results prove that ATR-FTIR technique is a fast and cost-effective characterization method to detect and investigate polymer shells and thin PDA coatings, even though they represent a small fraction of the total sample mass and their spectroscopic signals are not identified by sharp peaks.

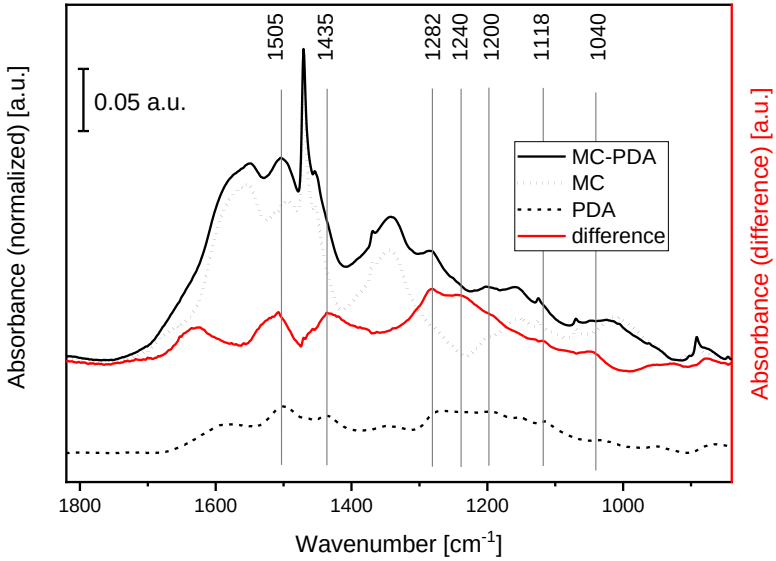

Figure VII - 13. ATR-FTIR spectra of neat microcapsules (MC, dotted line), polydopamine-coated microcapsules (MC-PDAc, solid line), and a polydopamine layer (PDA, dashed line). Difference spectrum (red line) was calculated by subtraction of MC from MC-PDAc.

Table VII - 5. FTIR band assignments for the microcapsules

wn (cm^{-1})	Band assignment	Intensity	Molecular structure	Material	Reference
1653	deformation	vw, shoulder	N-H	melamine-formaldehyde	(Salaün et al., 2009)

1548	stretching	s, broad	triazine ring	melamine-formaldehyde	(Weiss et al., 2019)
1500	deformation	s, broad	C-H, in CH_2, CH_2-OH, CH_2-O-	melamine-formaldehyde	(Socrates, 2004),(Günzler and Gremlich, 2003)
1470	asymmetric bending	vs	CH_2	paraffin	(Salaün et al., 2009)
1455	deformation	s, broad	C-H, in CH_2, CH_2-OH, CH_2-O-	melamine-formaldehyde	(Socrates, 2004),(Weiss et al., 2019), (Günzler and Gremlich, 2003)
1367	deformation, symmetric bending	w	C-H, in CH_2, CH_2-OH, CH_2-O- CH2, bridge	melamine-formaldehyde	(Salaün et al., 2009)
1341	stretching	s, broad	$C_{aromatic}$-N	melamine-formaldehyde	(Weiss et al., 2019)
1156	stretching	s, broad	C-N / -CH_2-O-	melamine-formaldehyde	(Weiss et al., 2019)
1070	symmetric stretching	vw	-CH_2-O-CH_2-, ether	melamine-formaldehyde	(Weiss et al., 2019)
891	twisting	m	C-H in CH_2	paraffin	(Salaün et al., 2009)
813	deformation	s	triazine ring	melamine-formaldehyde	(Weiss et al., 2019)
755	deformation	w	N-H, in amines, triazine ring	melamine-formaldehyde	(Weiss et al., 2019)
716	in-plane rocking	vs	C-H in CH_2	paraffin	(Salaün et al., 2009)

Abbreviations for band assignments. ν: stretching vibration; δ: deformation vibration; ω: wagging vibration
Abbreviations for band intensities. vw: very weak; w: weak; m: medium; s: strong; vs: very strong

Table VII - 6. FTIR band assignments for the PDA phase

wn (cm^{-1})	Band assignment	Intensity	Molecular structure	Structure unit	Reference

3612-3140	w-m, broad	ν(OH) ν (NH)	O-H, N-H	phenolic 36	(Roldán et al., 2014)
3033	m, broad	ν (CH)	aromatic C-H	aromatic ring, pyrrol, indole	(Roldán et al., 2014)
2963	w	ν_{as} (CH)	CH_3		(Roldán et al., 2014)
2954	w	ν_{as} (CH)	CH_2		(Roldán et al., 2014)
2916	m	ν_s (CH)	CH_3		(Roldán et al., 2014)
2850	m	ν_s (CH)	CH_2		(Roldán et al., 2014)
1725	w-m	ν (C=O)	carbonyl group		(Roldán et al., 2014), (Perna et al., 2016)
1574	s	ν (C-C), δ (C-H)	ring	aromatic ring, pyrrol, indole, catechol	(Roldán et al., 2014),(Al Aani et al., 2018)
1502	vs	ν (C-C), ν (C=N)	aromatic C-C, C=N	aromatic ring, pyrrol, indole	(Roldán et al., 2014),(Perna et al., 2016)
1472	w	ν (C=C)	C-H	pyrrol, indole ring	(Perna et al., 2016), (Wang et al., 2018)
1436	s	ν_{ring} (C-C) + ν (C-N) + δ (O-H), δ (C-H) + δ (N-H) + ν (C-N)	C-H, C-N, O-H	aliphatic CH_x indole ring	(Roldán et al., 2014),(Sun et al., 2019a), (Furtado et al., 2020)
1347	m	ν_{ring} (C-C) + ν (C-N) + δ (O-H)	C-N, O-H, aromatic ring, C-N-C	aliphatic CH_x, indole ring	(Roldán et al., 2014),(Sun et al., 2019a) (Wang et al., 2018)
1266	w	ν (C-O) + δ (N-H) + δ (C-H), ν (C-O) + δ (C-H) + δ_{ring},	C-O	catechol	(Roldán et al., 2014),(Perna et al., 2016) (Furtado et al., 2020),(Al Aani et al., 2018)

1198	s	δ (OH) + δ (CH), ν (C-O)	C-O-C, C-O		(Roldán et al., 2014)
1153	w	δ (OH) + δ (CH), ν (C-O)	C-O		(Roldán et al., 2014)
1115	w	δ (OH) + δ (CH) +ν (C-O)	C-O		(Roldán et al., 2014)
1035	w	δ (CH) + δ (NH) + ν (C-O)	aromatic ring	indole ring	(Roldán et al., 2014)
954	m	δ_{ring} + δ (C-H)		indole ring	(Roldán et al., 2014)
864	m	γ(C-H)		indole ring	(Roldán et al., 2014),(Sun et al., 2019a)
807	s	γ(C-H) + γ_{ring}		indole ring	(Roldán et al., 2014),(Sun et al., 2019a)
632	w				
589	w				
455	m				

Abbreviations for band assignments. ν: stretching vibration; δ: deformation vibration; ω: wagging vibration
Abbreviations for band intensities. vw: very weak; w: weak; m: medium; s: strong; vs: very strong

7.3.2.3 XPS characterization

The XPS tests were carried out and analyzed entirely by Dr. Frank Simon at Leibniz-IPF. They were added to this thesis for completeness.

The results of the XPS investigation are reported in Figure VII - 14. The C 1s spectrum of a cured melamine-formaldehyde sample should present peaks relative to the carbon atoms of the 1,3,5-triazine ring networks (expected at approx. 287.15 eV), the carbon atoms carrying amino groups (expected at approx. 286 eV), and – as usually found on all surfaces – saturated hydrocarbons (at 285.00 eV) (Beamson and Briggs, 1992). However, the recorded C 1s spectrum of the neat microcapsules (Figure VII - 14a) did not show the presence of amino groups; neither primary amino groups (C–NH_2) nor secondary amino groups (C–NH–C) could be detected. Amino groups are able to open the oxirane rings of the epoxy molecules and initiate the formation of epoxy networks. Their absence on the surfaces of the microcapsules explains the poor adhesion in epoxy polymer matrices, as it frustrates the formation of covalent bonds at the microcapsule-matrix interface.

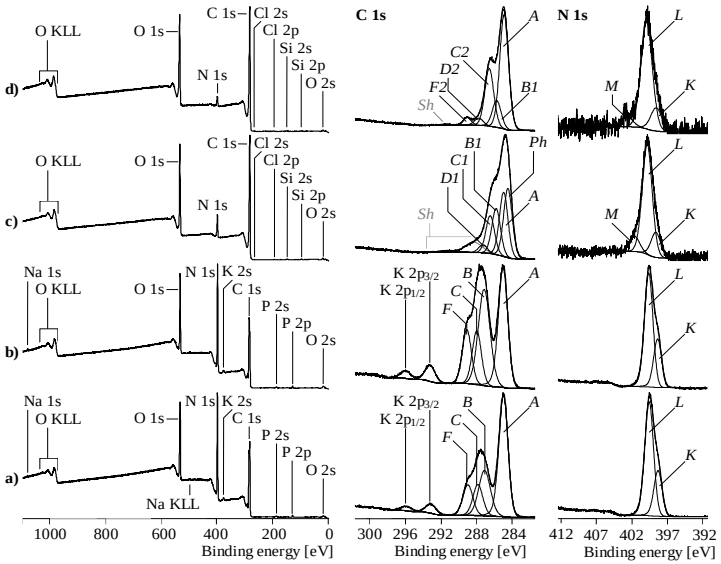

Figure VII - 14. Wide-scan (left column), C 1s (middle column), and N 1s (right column) high-resolution XPS spectra recorded from: (a) neat microcapsules; (b) neat microcapsules reacted with DGEBA; (c) PDA-coated microcapsules (MC-PDAc); (d) PDA-coated microcapsules (MC-PDAc) reacted with Elan-tech® EC 157.

According to the shape of the recorded C 1s spectrum, it can be assumed that the melamine-formaldehyde was cured in presence of urea. During the hardening reaction, the urea molecules were condensed on the -OH groups of the intermediately formed hexamethylolmelamine. The chemical structure of the reaction product reported in Figure VII - 15 confirms the C 1s spectrum recorded from the neat microcapsules depicted in Figure VII - 14a.

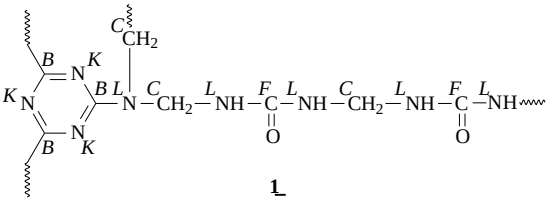

1

Figure VII - 15. Presumed chemical structure (cut out from the polymeric network) of the surface of the neat microcapsules derived from the C 1s high-resolution XPS spectrum (Figure VII - 14a). The italic letters indicate the assignment of the carbon or nitrogen atoms to the component peaks of the C 1s (*B*, *C* and *F*) and N 1s (*K* and *L*) spectra.

Photoelectrons escaped from the carbon atoms of the 1,3,5-triazine rings contributed to component peak *B* at 287.16 eV. The binding energy value found for that component peak was slightly lower than the value of the tertiary amino groups ([^{C}C–]$_3$N, component peak *C* at 287.91 eV), which were not involved in the conjugated electron-rich π-electron systems of the triazine rings. According to the stoichiometry of structure **1** (Figure VII - 15), the intensity of component peak *C* was equal to that of component peak *F* at 289.03 eV that represents the carbonyl carbon atoms of the condensed urea molecules ([NH–]$_2$^{F}C=O). Moreover, a further component peak *A* was observed at 285.00 eV. This component peak was caused by photoelectrons from carbon atoms bonded as saturated hydrocarbons (^{A}C$_x$H$_y$). As mentioned above, saturated hydrocarbons are always observed when the samples were prepared under ambient conditions or came in contact with the atmosphere (Beamson and Briggs, 1992). However, this peak component could also be due to some paraffin diffused out of the capsules and partly covering the outer shell surfaces. The chemical inertness of the paraffin film also contributes to limit the chemical interaction between the epoxy matrix and the microcapsule surfaces. The corresponding N 1s spectrum (Figure VII - 14a, right column) was clearly composed of the two component peaks *K* and *L*. The binding energy value of the nitrogen atoms involved in the conjugated π-electron systems of the triazine rings (component peak *K*) were found at 398.63 eV, at a slightly lower energy than the value for the tertiary amines ([C–]$_3$^{L}N) and the urea units ([^{L}NH–]$_2$C=O), which were observed as component peak *L* at 399.84 eV.

To investigate more in detail the poor chemical reactivity of the neat microcapsule surface, an attempt was made to directly graft DGEBA on the untreated MC shell, via the sample preparation route described in par. 2.3. Figure VII - 14b shows the C 1s and N 1s spectra of these samples. As can be seen, neither the C 1s nor the N 1s spectrum showed significant differences the spectra recorded from the neat microcapsules. In the case of a successful grafting of DGEBA the corresponding C 1s spectrum should be characterized by an intensive component peak at approx. 286.4 eV, resulted from alcohol (C–OH) and ether (C–O–C) groups formed after the ring opening reaction of the oxirane groups. From the absence of this characteristic component peak, it can be concluded that DGEBA were not bonded to the surface of the microcapsule sample, which implies the impossibility of direct grafting of oxirane groups-carrying substances on the microcapsule surface.

After the deposition of dopamine and its polymerization to PDA, the C 1s spectrum of the PDA-coated microcapsules (Figure VII - 14c) showed the characteristic shape found for PDA (Silva et al., 2019). Electron transitions between π- and π*-orbitals cause not only the dark color observed after the polymerization of dopamine, but also intense *shake-up* peaks (*Sh*) in the high-resolution C 1s spectrum (Figure VII - 14c, middle column). The C 1s area remaining after subtraction the *shake-up* peaks was deconvoluted into five component peaks, which confirmed the number of different structural units in the PDA molecules. At low energy, the

component peak *Ph* (284.53 eV) evidences the presence of sp^2-hybridized carbon atoms of the PDA phenyl rings, whereas the ^{B1}C–N bonds in the amino groups led to component peak *B1* at 285.83 eV. Since its intensity was two-thirds of component peak *Ph,* it can be concluded that preferably secondary amino (^{B1}C–NH–^{B1}C) groups and cyclic imide (^{B1}C=N–^{B1}C) were formed during the polymerization of dopamine (Figure VII - 16). Component peak *C1* at 286.49 eV was assigned to the carbon atoms carrying the phenolic OH groups of the catechol units (^{C1}C–OH). Its intensity was smaller than that of the component peak *C1*, even though, according to the chemical structures **2** and **3** suggested in Figure VII - 16, the intensities should be equal, [*C1*] = [*B1*]. This may be due to the fact that some of the catechol groups were present in their oxidized form. During the polymerization of dopamine, oxidation reactions are in equilibrium with reduction reactions. Photoelectrons escaping from the carbon atoms of remaining quinone-like structures **4** (^{D1}C=O) were collected as component peak *D1* at 287.29 eV. The sum of the intensities of the component peaks *D1* and *C1* exactly equaled the intensity of component peak *B* ([*D1*] + [*C1*] = [*B1*]), which corresponds to the stoichiometric ratio in the binding states of the carbon atoms suggested in Figure VII - 16. The findings also supported the assumption that cyclic amine and imine structures were preferably formed during the oxidative polymerization of dopamine.

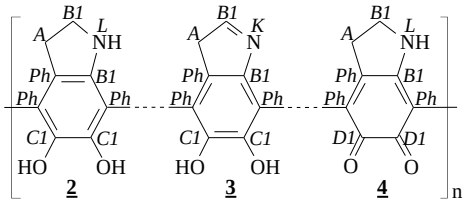

Figure VII - 16. Characteristic cut-outs from the chemical structure of PDA. Italic letters denote the assignment of the carbon and nitrogen atoms to the component peaks in the C 1s and N 1s high-resolution spectra.

Also the N 1s spectrum of the PDA-coated microcapsules is different from that recorded on the neat microcapsules. Besides the component peaks *K* and *L,* it was necessary to introduce a third component peak *M* (401.65 eV), showing protonated amino groups (C–^{M}N^{+}H$_2$–C). Unlike the reacted urea groups in the structure **1** (Figure VII - 15), the secondary amines of the PDA (**2**) contain a basic nitrogen atom that can be easily protonated in aqueous environment. The non-protonated nitrogen atoms of the amino groups were identified as the component peak *L* at 399.93 eV.

The ratio of the intensities of the two component peaks [*M*]:[*N*] illustrates the protonation/deprotonation equilibrium of the amino groups. For the subsequent reaction with epoxides it is substantial that the intensity of component peak *M* is small compared to that of component peak *L,* because the protonated species can neither initiate the opening of the oxirane rings, nor be involved in the epoxy crosslinking

reactions. Due to the high electron density at the nitrogen atom of the imide group (**3**) (Figure VII - 16), which is involved in the delocalized π-electron system component peak *K* was shifted to a lower binding energy value (398.74 eV). From the high-resolution element spectra (Figure VII - 14c), it can be concluded that the surfaces of the microcapsules were fully coated by thick layers of PDA. These findings are supported by the complete absence of potassium in the wide-scan spectrum of the PDA-modified sample and the brownish color of the microcapsules after the deposition of dopamine and its polymerization.

The model reaction of the PDA-modified microcapsules with Elan-tech® EC 157 (Figure VII - 14d) strongly reduced the relative amount of nitrogen ($[N]:[C]|_{PDA} = 0.094 \rightarrow [N]:[C]|_{PDA+EC157} = 0.044$) while the [O]:[C] ratio was not significantly affected ($[O]:[C]|_{PDA} = 0.226 \rightarrow [O]:[C]|_{PDA+EC157} = 0.238$). Obviously, the epoxy resin, which is formed on the surface of the microcapsule shells, inelastically scatters the photoelectrons emitted from the nitrogen atoms bonded to the microcapsule surface. The inelastically scattered photoelectrons did not contribute to the spectral information but were counted in the spectrum background. The high-resolution C 1s and N 1s spectra provided more information about the success of the grafting of the Elan-tech® EC 157 molecules on the PDA-modified microcapsule surfaces. The shape of the C 1s spectrum was changed by the epoxy resin formed during the ring opening reactions of the oxirane units and their subsequent self-crosslinking. The recorded C 1s spectrum is very characteristic of weakly cured epoxy resins. Beside the main component peak *A* (285.00 eV), which showed saturated hydrocarbons, an intense component peak *C2* arose at 286.67 eV. This component peak resulted from ^{C2}C–O bonds of alcohol (^{C2}C–OH) and ether (^{C2}C–O–^{C2}C) groups, the typical reaction products of the opened oxirane rings. Between the component peaks *A* and *C2*, the component peak *B1* (285.84 eV) shows the C–N bonds of amine groups. The intensity of this component peak ([*B1*] = 0.123) is significantly larger than twice of the $[N]:[C]|_{PDA+EC157}$ ratio ($[N]:[C]|_{PDA+EC157} = 0.044$), determined from the wide-scan spectrum. This indicates that the secondary amino groups of the PDA molecules were involved as tertiary amines in the depth of epoxy resin network. In principle, the -OH groups of the catechol units are also able to open oxirane rings and form covalent bonds with the epoxy resin. Non-reacted oxirane groups were detected from the component peak *D2* at 287.79 eV. Such groups, frequently observed in weakly cured epoxy resins, can be reacted by a thermal curing process (Frenzel et al., 2015). Even though its origin is unclear, the presence of component peak *F2* at 289.16 eV shows the presence of carboxylate ester groups in the epoxy resin network. While component peak *F* resulted from photoelectrons escaped from the carbonyl carbon atoms (O=^{F2}C–O–^{C2}C), the photoelectrons of the corresponding alcohol-sided carbon atoms (O=^{F2}C–O–^{C2}C) contributed to component peak *C2*. The peak area above 290 eV can be assigned to *shake-up* peaks (*Sh*), indicating small contribution of the PDA interphase to the C 1s spectrum. The shape of the N 1s spectrum recorded from the

epoxy-reacted, PDA-coated microcapsules was not very different to that acquired from the PDA-coated microcapsules. The origin of the three component peaks *K*, *L* and *M* is the same as that discussed for the spectrum in Figure VII - 14c. However, it is interesting to observe that the relative intensities of the component peaks *K* were equal in the two N 1s spectra ([*K*] = 0.166), which indicates that the imide-bonded nitrogen atoms (C=^{K}N–C) were not reacted with the oxirane species and therefore not bonded to the resin.

This detailed investigation further establishes XPS technique as a powerful tool to study the chemical structure, morphology and reactivity of surfaces and contributed to elucidate how the potentialities of this technique can be applied to study PDA coatings.

7.3.2.4 Hot-stage optical microscopy

The results of the melting/crystallization test performed on an optical microscope with a hot-stage equipment are shown in Figure VII - 17, which shows selected micrographs of the neat and PDA-coated microcapsules during heating and cooling ramps.

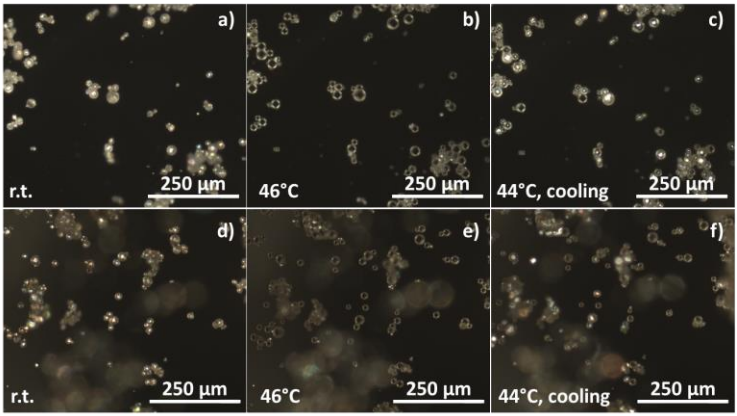

Figure VII - 17. Hot-stage optical microscopy images of microcapsules at different temperatures: (a,b,c) neat MC; (d,e,f) PDA-coated MC (MC-PDAc).

This test was performed in order to follow the melting/crystallization process of both samples and to visually detect any differences in the behavior due to the PDA coating. At the beginning of the test, both the samples are solid and crystalline, as observable from the bright cores in Figure VII - 17a and Figure VII - 17d. As the temperature rises, the core starts melting, and above the melting point all the capsule cores are melted, and so almost transparent at the optical microscope, as observable

from Figure VII - 17b and Figure VII - 17e acquired at 46 °C. During cooling, the recrystallization starts when the temperature falls below the crystallization temperature of the paraffinic core, as observable from Figure VII - 17c and Figure VII - 17f, in which some of the capsules have already crystallized. Such crystallization temperature is different from that found via DSC, due to the different heating/cooling rate. The analysis did not show any appreciable differences on the behavior of the neat and PDA-coated microcapsules, which suggests that the PDA coating does not hinder the melting/crystallization process of the core.

7.3.2.5 Thermal analysis

Figure VII - 18 shows the DSC thermograms of the first heating scan and cooling scan on the neat and PDA-coated microcapsules, while the most important DSC results are reported in Table VII - 7. The neat microcapsules show an endothermic peak at approx. 45 °C, indicating the melting of the PCM contained in the microcapsules, while the cooling scan shows the corresponding crystallization peak at approx. 29 °C, as already commented elsewhere in this thesis. The DSC thermograms of both the PDA-coated microcapsules samples show the same features of the neat sample, since the shape of the thermograms and the transition temperatures are not significantly different, as also appreciable from Table VII - 7.

Since the PDA coating does not contribute to the phase change enthalpy, as it does not show any phase transitions in the investigated temperature range, is it reasonable to expect that the crystallization enthalpy per unit mass measured on the PDA-coated microcapsules is lower than that of the uncoated sample. Since the coating process was performed in mild conditions of temperature, pressure and stirring speed, it can be assumed that the capsules were not damaged during the process and the paraffin did not leak out of the capsule shell, as also confirmed by the SEM micrographs that showed integer capsules.

Therefore, the whole enthalpy decrease can be imputed to the mass gaining due to PDA coating. If this is the case, the total PDA weight fraction can be calculated through the Equation (VII - 3) as

$$PDA\ (wt\%) = 100 - \frac{\Delta H_c^{PDA}}{\Delta H_c^{neat}} \cdot 100\,, \qquad \textbf{(VII - 3)}$$

where ΔH_c^{neat} and ΔH_c^{PDA} are the crystallization enthalpy of the neat and PDA-coated microcapsules, respectively. The PDA mass fraction calculated in this way resulted as 14.3 wt% for the sample obtained from the concentrated dopamine hydrochloride solution (MC-PDAc).

This decrease in phase change enthalpy negatively affects the TES capability of the PCM. Therefore, it is interesting to observe that the modified MC sample obtained from the diluted solution (MC-PDAd) exhibited a much lower decrease in

melting enthalpy, as the deposited PDA was the 4.1 wt% of the total sample mass, which is related to a thinner PDA layer, as better evidenced in Section 7.3.2.1.

This indicates, as expected, that the concentration of the solution affects the total mass of deposited PDA and so the phase change enthalpy, but it does not significantly affect the melting/crystallization temperatures. Therefore, a thinner PDA layer could be beneficial in containing the decrease in TES properties of the coated sample.

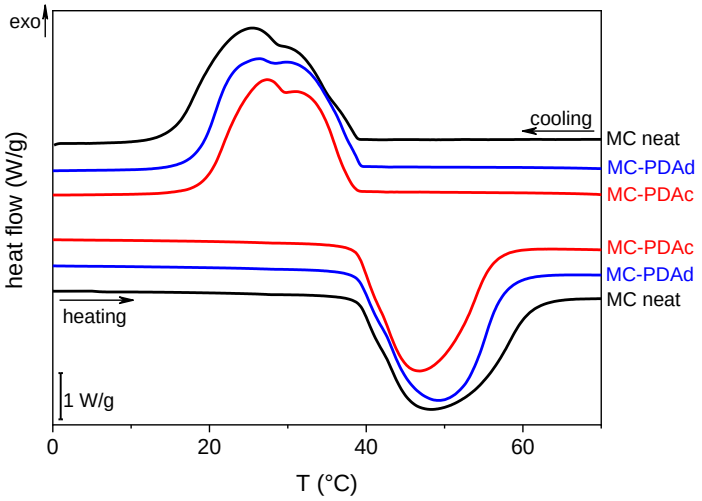

Figure VII - 18. DSC thermograms of neat and PDA-coated microcapsules (first heating scan and cooling scan).

Table VII - 7. Main results of the DSC tests on neat and PDA-coated microcapsules.

Sample	T_m (°C)	ΔH_m (J/g)	T_c (°C)	ΔH_c (J/g)	ω_{MC} (wt%)	ω_{PDA} (wt%)	$T_{m,2}$ (°C)	$\Delta H_{m,2}$ (J/g)
MC	44.7	227.2	29.0	224.1	100	0	44.4	224.0
MC-PDAc	44.3	189.2	29.7	192.1	85.7	14.3	43.8	190.9
MC-PDAd	45.2	218.4	29.2	218.0	95.9	4.1	45.5	218.0

T_m, ΔH_m = melting temperature and enthalpy (first heating scan); ω_{MC}, ω_{PDA}= weight fractions of MC and PDA, calculated from the measured melting enthalpy; T_c, ΔH_c = crystallization temperature and enthalpy (cooling scan); $T_{m,2}$, $\Delta H_{m,2}$= melting temperature and enthalpy (second heating scan).

Figure VII - 19 shows the TGA thermograms on the neat and PDA-coated microcapsules, while the most important TGA results are reported in Table VII - 8. As already observed elsewhere in this thesis, the thermal degradation of the neat microcapsules starts with several small steps between 100 °C and 250 °C, related to

the degradation ow low-molecular-weight compounds, while the degradation phenomena at high temperature, related to the degradation of the capsule core and shell, occur in a considerably narrow temperature interval.

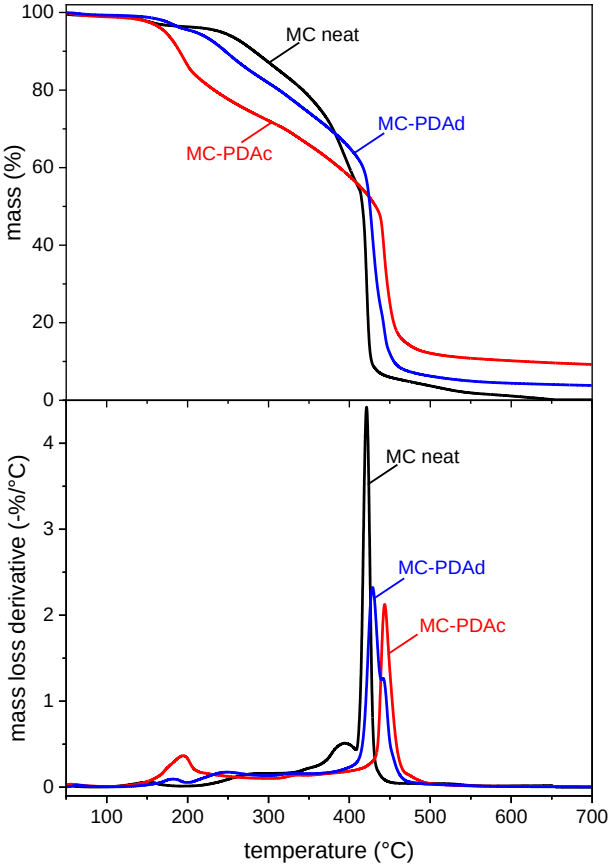

Figure VII - 19. TGA thermograms of the neat and PDA-coated microcapsules. Residual mass and mass loss derivative as a function of temperature.

This spike, also observed in repeated measurements, is lower and broader in the thermograms of both the PDA-coated microcapsule samples. Moreover, the peak temperature was 7 °C (for MC-PDAd) or 22 °C (for MC-PDAc) higher than that of the neat sample, which indicates an improvement in the thermal resistance. However, the onset of the degradation shifts to lower temperatures, which is probably related to the thermal degradation of the PDA coating, but further studies are needed to fully explain

this decrease. Nevertheless, the temperature at the beginning of thermal degradation is well above the processing temperature of the epoxy/MC composites (100 °C) and far above the intended service temperatures, which are around the PCM phase change interval (40-50 °C). It is interesting to observe that this phenomenon is more evident for the MC-PDAc than for the MC-PDAd, i.e. with an increase in the PDA mass fraction. Therefore, a thinner PDA layer could also be beneficial in limiting the decrease in thermal degradation resistance.

Table VII - 8. Main results of the TGA tests on the neat and PDA-coated microcapsules.

Sample	$T_{1\%}$ (°C)	$T_{3\%}$ (°C)	$T_{5\%}$ (°C)	T_d (°C)	m_r (%)
MC	118.4	164.1	241.2	421.2	0.34
MC-PDAc	112.5	158.2	172.5	443.2	9.24
MC-PDAd	140.4	180.1	209.0	428.7	3.81

$T_{1\%}$, $T_{3\%}$, $T_{5\%}$ = temperature corresponding to a mass loss of 1 wt%, 3 wt% or 5 wt%; T_d = temperature at the maximum of the mass loss derivative; m_r = residual mass.

7.3.2.6 Interfacial adhesion and characterization of the epoxy/MC composites

Figure VII - 20 and Figure VII - 21 show SEM micrographs of the cryofracture surface of epoxy matrices containing neat and PDA-modified microcapsules. Most of the capsules are broken due to the cryofracturing process, and this clearly confirms their core-shell structure. From the low-magnification micrographs (Figure VII - 20(a-c)) it is evident that the microcapsules are uniformly dispersed in the epoxy matrix, which is essential for producing a component with homogeneous thermo-mechanical properties. This suggests that the PDA coating does not induce agglomeration of the microcapsules. What is remarkably different between the neat and PDA-coated capsules is the interfacial adhesion between the capsule shell and the surrounding epoxy matrix, as appreciable from the medium- and high-magnification micrographs (Figure VII - 20(d-i). The PDA coating reduces the gap caused by filler-matrix debonding and promotes the chemical and mechanical interaction between the capsule and the surrounding matrix. This is observed for both the PDA-coated samples and seems to be independent from the amount of deposited PDA.

The morphology of the thicker coating can be better appreciated in Figure VII - 21; the PDA coating has an irregular surface morphology and the thickness varies significantly from point to point. The thickness was measured on several zones of different microcapsules with the software ImageJ and resulted as 265 ± 85 nm for the sample MC-PDAc and 75±10 nm for the sample MC-PDAd. The layer thickness is in both cases comparable with the thickness of the shell (158±7 nm). If considered that PDA has a density of 1.52 g/cm^3 (Nishizawa et al., 2016) and that the microcapsules have an average diameter of 20 μm and a density of 0.9 g/cm^3 (data from the

producer's datasheet), the mass fraction of PDA in the PDA-coated capsules can be calculated as 12.1 wt% for the sample MC-PDAc and 3.7 wt% for the sample MC-PDAd, in both cases in good agreement with the results from DSC.

The XPS analysis suggests that the main mechanism of adhesion enhancement is the creation of covalent bonds with the epoxy matrix during curing. Therefore, the same improvement of adhesion could probably be obtained with an even thinner PDA layer; this would also reduce the total deposited PDA mass, which would decrease the PDA weight fraction, thereby increasing the total phase change enthalpy. The optimization of the PDA deposition parameters to tune the PDA layer thickness will be the object of upcoming studies.

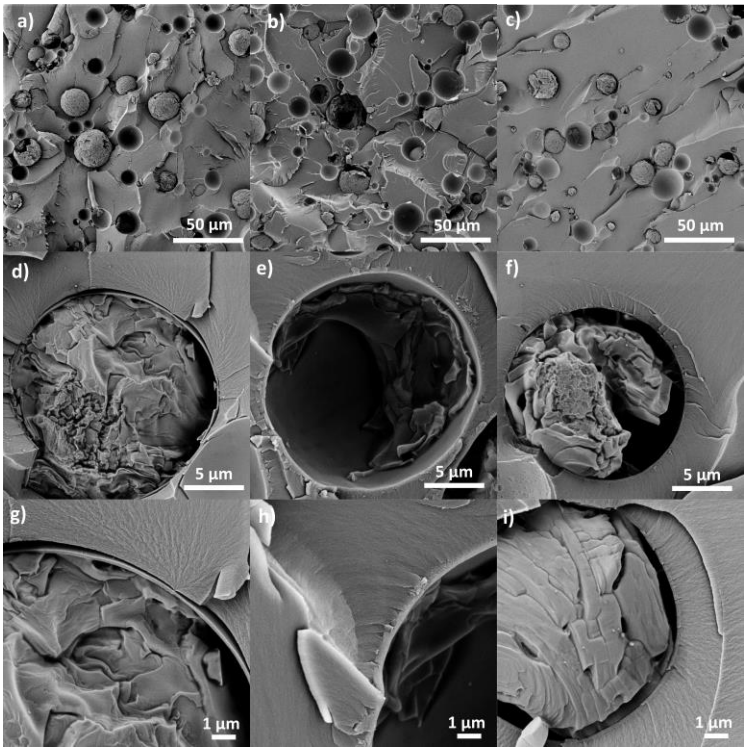

Figure VII - 20. SEM micrographs of the cryofracture surface of epoxy matrices containing 10 wt% of neat or PDA-modified microcapsules. (a,d,g) neat MC; (b,e,h) MC-PDAc; (c,f,i) MC-PDAd.

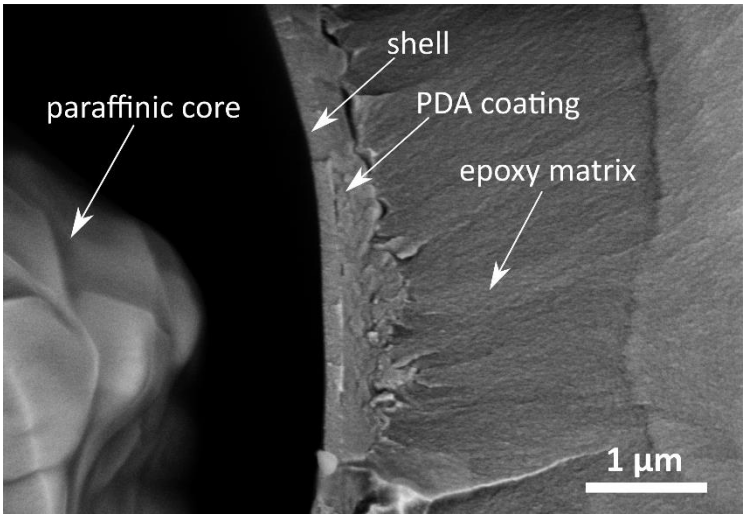

Figure VII - 21. SEM micrograph the cryofracture surface of epoxy matrix containing PDA-modified microcapsules (MC-PDAc). Detail at high magnification level.

7.3.3 Conclusions

PDA layers of varying thickness were successfully deposited onto the outer shell surface of paraffin microcapsules, and the resulting coating considerably enhanced the adhesion with an epoxy matrix. The morphology and roughness of the PDA layer was studied through microscopy techniques such as SEM and AFM, which evidenced that after PDA coating the surface roughness increased from 9 nm to 86 nm, which is positive as it allows a further increase in the interfacial interaction by mechanical interlocking. FTIR and XPS techniques have been fundamental to study the surface chemistry and the assortment of reactive functional groups of the PDA layer, in order to elucidate its complex chemical structure and configuration. XPS also highlighted that, unlike the uncoated microcapsule shells, the PDA layer is able to react with oxirane groups, thereby evidencing the possibility of forming covalent bond with the epoxy matrix during the curing step.

Hot-stage optical microscopy and DSC tests highlighted that the PDA modification does not hinder the melting/crystallization process of the paraffinic core. DSC results were also useful to estimate the deposited PDA mass fraction, which resulted as 14.3 wt% for the PDA-coated microcapsules modified in the more concentrated dopamine hydrochloride solution (MC-PDAc) and 4.1 wt% for those treated in the diluted solution. Finally, the SEM micrographs of the cryofracture surface of epoxy composites containing neat or PDA-modified microcapsules clearly

evidenced an improved adhesion between the capsule shell and the epoxy matrix and allowed an estimation of the PDA layer thickness as 265 ± 85 nm for MC-PDAc and 70 ± 10 nm for MC-PDAd. These results establish the PDA deposition as a promising method to increase the interfacial adhesion in epoxy-matrix composites containing polymer microcapsules, which is remarkably important not only for this specific application, but also in the field of self-healing composites or toughened polymers.

Future work should focus on investigating how the parameters of PDA deposition influence the morphology, roughness and thickness of the PDA layer, and how these features in turn affect the enhancement of the interfacial adhesion. Moreover, attention should be put on evaluating how the PDA layer and the interface resist to multiple thermal cycles, and how this affects the mechanical and thermal properties of the host epoxy matrix.

7.4 General conclusions of Chapter VII

This Chapter presented the results of the synthesis or surface modification of paraffin microcapsules, in order to tailor their microstructural, thermal or interfacial properties.

Subchapter 7.2 dealt with the encapsulation of docosane via a sol-gel process in organosilica shells of two different sizes. This work contributed to highlight the potentialities of the sol-gel route as an encapsulation technique for paraffins and to shed light on the change in structural, microstructural and thermal properties due to confinement effect and interaction with the shell wall. More specifically, solid state NMR has proved to be a powerful technique to investigate microencapsulated PCMs, providing an in-depth insight into the different microstructures and phases of the samples and helping in the interpretation of XRD and DSC results, as the upfield shift of some peaks was related to the presence of rotator phase or to the reduced docosane chain mobility and interaction with the shell wall (γ-gauche effect).

Subchapter 7.3 concerned the deposition of polydopamine (PDA) layers of varying thickness onto the outer shell surface of paraffin microcapsules, and the resulting coatings were proven effective to enhance the interfacial adhesion with an epoxy matrix, as evidenced by SEM micrographs. XPS highlighted that, unlike the uncoated microcapsule shells, the PDA layer is able to react with oxirane groups, thereby evidencing the possibility of forming covalent bond with the epoxy matrix during the curing step. Future work should focus on investigating how the parameters of PDA deposition influence the morphology, roughness and thickness of the PDA layer, and how these features in turn affect the enhancement of the interfacial adhesion. Moreover, attention should be put on evaluating how the PDA layer and the interface resist to multiple thermal cycles, and how this affects the mechanical and thermal properties of the host epoxy matrix.

7.5 Acknowledgements

For the results presented in Subchapter 7.2, Prof. Sandra Dirè (DII Unitn) is acknowledged for the fruitful discussions about PCM encapsulation and for her expertise in sol-gel techniques, Prof. Riccardo Ceccato (DII Unitn) is acknowledged for performing XRD analysis, Dr. Emanuela Callone (DII Unitn) is acknowledged for performing NMR experiments, and Mr. Lorenzo Moschini (DII Unitn) is acknowledged for performing SEM analysis.

For the results presented in Subchapter 7.3, I thank Dr. Frank Simon (Leibniz-IPF Dresden) for performing XPS analysis, Mr. Dmitrii Sychev and Ms. Inga Melnyk (Leibniz-IPF Dresden) for their contribution to FTIR analysis, Ms. Maria Auf der Landwehr (Leibniz-IPF Dresden) for performing hot-stage optical microscopy measurements, Mr. André Krauss (Leibniz-IPF Dresden) for his contribution to PDA modification, and Dr. Cordelia Zimmerer (Leibniz-IPF Dresden) for her contribution to research conceptualization.

Chapter VIII

Conclusions

8.1 Summary and comparison of the investigated systems

The aim of this work was to develop novel polymer-matrix composites containing both an organic PCM and a reinforcing phase (fibers), and to characterize their properties as a function of their composition and PCM content. The intent was to design materials that can combine both the elevated mechanical properties required for structural/semi-structural applications, and heat storage/management capabilities. Since the literature on this topic is scarce, the experimental work considered and compared several polymer/PCM/reinforcement systems, to highlight the respective advantages and drawbacks. The analyzed case studies were divided into three groups according to the type of polymer matrix: (i) a thermoplastic polymer such as polyamide, polypropylene, reactive thermoplastic acrylic resin (Chapter IV); (ii) a thermosetting polymer such as epoxy resin (Chapter V) or (iii) a biopolymer such as thermoplastic starch (Chapter VI).

Chapter IV started with the results discussion of the characterization of the PCM-containing polyamide/glass fiber laminates. It emerged that a microencapsulated PCM (MC) is more suitable than CNT-stabilized paraffin (ParCNT) to be compounded with a traditional thermoplastic matrix, due to its higher thermal resistance. However, also the microcapsules were damaged by the melt-compounding and hot-pressing

steps, thereby causing paraffin leakage and degradation and diminishing the total final phase change enthalpy measured on the laminate. A remarkable improvement of the final TES properties was obtained by reinforcing the polyamide-based composites with discontinuous carbon fibers, which allowed reducing the severity of processing parameters such as the applied temperature, pressure, and number of thermal cycles. However, a considerable step ahead in terms of mechanical and TES properties has been obtained by using a reactive thermoplastic matrix. In fact, it allowed avoiding completely all the processing steps at high temperature in the molten state, thus requiring considerably milder processing conditions that did not cause PCM degradation. However, since reactive processing is not applicable to the most common thermoplastic matrices, an additional approach was explored that involved the production of multifunctional commingled yarns, where the PCM phase is embedded in the polymer filaments. In this thesis, this approach was limited to the production of PP filaments containing PCM microcapsules. The approach was proven to be feasible, but the processing parameters still need adjustment to limit the PCM degradation.

Chapter V illustrated the results of the thermo-mechanical characterization of three PCM-enhanced composites having an epoxy matrix. First, the shape-stabilized PCM powder ParCNT was mixed with an epoxy resin and used to prepare bi-directional carbon fiber laminates. The use of a shape-stabilized PCM in this case gave better results than when it was used in combination with a thermoplastic matrix, as the milder processing conditions allowed avoiding the PCM degradation and loss of melting enthalpy in the final composites. However, the surrounding matrix influenced and partially hindered the melting-crystallization processes of the PCM phase. Therefore, in a second approach, the epoxy resin was combined with a microencapsulated PCM. The characterization of epoxy/MC samples provided an interesting insight on the effect of the MC and their phase change on the physical-mechanical properties of an epoxy resin, from the experimental and the theoretical point of view. It was found that the capsule/matrix interface plays a fundamental role not only for the mechanical performance, but also for the thermal conductivity. This experimental campaign was preliminary to the characterization of epoxy/MC systems combined with continuous and discontinuous carbon fibers. These results confirmed that the processing conditions of an epoxy composite are mild enough to preserve the integrity of the microcapsules and their TES capability. For the continuous fiber composites, it was assessed that the mechanical properties decrease as the MC content increases mostly because of the reduction of the final fiber volume fraction and because the MC phase tends to concentrate in the interlaminar region, thereby lowering the interlaminar shear strength. On the other hand, a small amount of microcapsules can enhance the mode I interlaminar fracture toughness, as they introduce other energy dissipation mechanisms such as debonding, crack deflection, crack pinning and micro-cracking, which add up to the fiber bridging.

However, the only case in this thesis in which the PCM enhances all the mechanical properties is the starch/wood/PEG laminate, described in Chapter VI. The addition of PEG significantly increased the tensile, impact and dynamic-mechanical properties. Therefore, the wood laminae, which perform both the roles of reinforcement and shape-stabilizing agent for the PCM, are not the only multifunctional component, but also PEG can be regarded as multifunctional, since, besides absorbing and releasing heat, it also contributes to the mechanical performance.

These results contribute to elucidate how mechanical and TES properties can be combined in a polymer composite. The values of elastic modulus and mechanical strength as a function of the melting enthalpy for all the considered laminates are shown in Figure VIII - 1 and Figure VIII - 2, respectively. Table VIII - 1 helps recalling all the prepared composites and their constituents, for a better interpretation of Figure VIII - 1.

Table VIII - 1. List of the prepared composites and their constituents and the testing mode for the elastic modulus reported in Figure VIII – 1.

Sample	Matrix	Reinforcement	PCM
PA-ParCNT-GF	Polyamide	Bidirectional glass fibers	CNT-stabilized paraffin
PA-MC-GF	Polyamide	Bidirectional glass fibers	Paraffin microcapsules
EL-MC-CF	Elium	Bidirectional carbon fibers	Paraffin microcapsules
Starch/PEG/wood	Starch	Thin beechwood laminae	PEG
EP-ParCNT-CF	Epoxy	Bidirectional carbon fibers	CNT-stabilized paraffin
EP-MC-CFu-A	Epoxy	Unidirectional carbon fibers	Paraffin microcapsules
EP	Epoxy	-	-
EP-MCx	Epoxy	-	Paraffin microcapsules
EP-MCx-CFSy	Epoxy	Discontinuous carbon fibers (“short”)	Paraffin microcapsules
PA	Polyamide	-	-
PA-MCx	Polyamide	-	Paraffin microcapsules
PA-CFLx	Polyamide	Discontinuous carbon fibers (“long”)	-
PA-CFSx	Polyamide	Discontinuous carbon fibers (“short”)	-
PA-MCx-CFLy	Polyamide	Discontinuous carbon fibers (“long”)	Paraffin microcapsules
PA-MCx-CFSy	Polyamide	Discontinuous carbon fibers (“short”)	Paraffin microcapsules

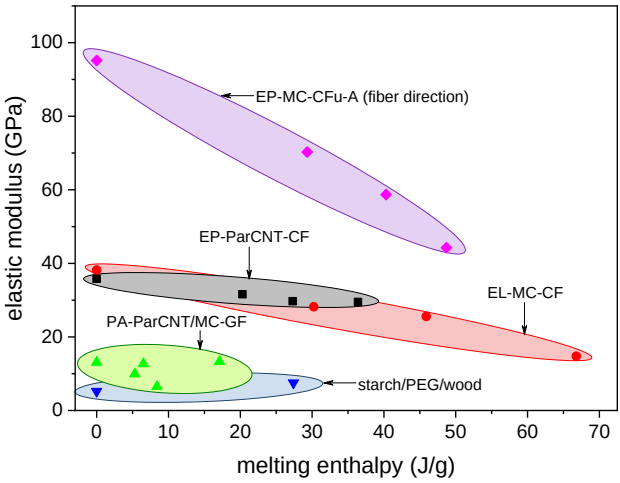

(a)

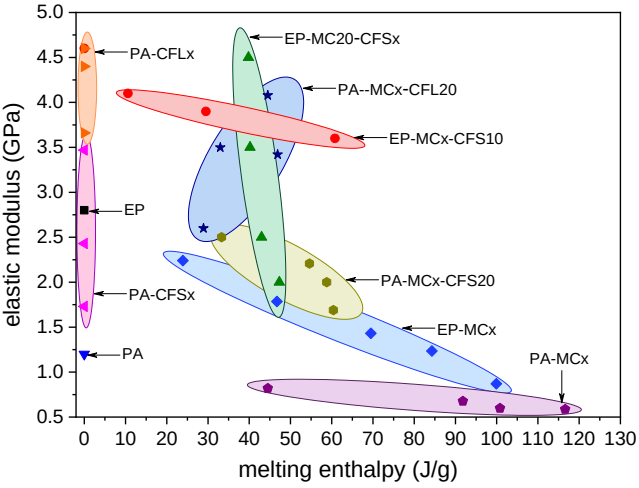

(b)

Figure VIII - 1. Relationship between elastic modulus and melting enthalpy of all the composites characterized in this thesis (flexural modulus, except for the systems with a PA matrix and the starch/PEG/wood composites, for which the tensile modulus is reported). (a) Continuous-fiber composites; (b) Discontinuous-fiber composites.

For almost all the considered systems, the elastic modulus decreases with an increase in melting enthalpy. For continuous-fiber composites (Figure VIII - 1a), especially those with a thermosetting or a reactive thermoplastic matrix, the decrease is mainly due to the fact that the PCM addition determined an increase in viscosity of the matrix system, which prevents it from flowing out of the fiber fabric, thereby decreasing the final fiber weight and volume fraction. Therefore, the decrease in the elastic modulus is mainly due to a decrease in the final volume fraction, which was proven by the calculations on the laminates EP-MCx-CFu (Subchapter 5.4) and it is also clear considering that the decrease in the elastic modulus is almost negligible for those systems where the fiber volume fraction is almost constant, such as in the laminates EP-ParCNT-CF.

The ideal case would be a combination of high stiffness and high melting enthalpy, which would be represented in the top right corner in Figure VIII - 1a. On the other hand, it is difficult to obtain a higher fiber volume fraction and a higher melting enthalpy, because the enthalpy increases with the PCM content, but fiber and PCM fractions follow opposite trends. Since the elastic modulus increases with the fiber volume fraction and the phase change enthalpy with the PCM mass fraction, the best materials for such composites would be a reinforcement with high specific (normalized to density) mechanical properties and a PCM with a large specific (normalized to mass) phase change enthalpy, so that the product between fiber volume fraction and PCM mass fraction is maximized. In any case, the property that must be maximized depends on the specific application, as well as the combination of properties to be considered optimal.

Similar conclusions can be obtained from the results for discontinuous fiber composites (Figure VIII - 1b). In this case, when the PCM fraction is kept constant, the melting enthalpy is nearly constant and the modulus increases with the fiber content; when the fiber fraction is kept constant, the melting enthalpy increases and the elastic modulus slightly decreases with the PCM content. The same can be said for the trend of mechanical strength as a function of the melting enthalpy (Figure VIII - 2), which generally follow an opposite trend.

This is again because, for most of the studied systems, the reinforcement does not contribute to the thermal energy storage and the PCM does not contribute to the stiffness and strength. In order to make these properties truly synergistic and not parasitic, the multifunctionality should be shifted at the level of the single component, as done for the biodegradable laminate containing PEG and reinforced with wood laminae, which acted also as shape-stabilizing agents for PEG.

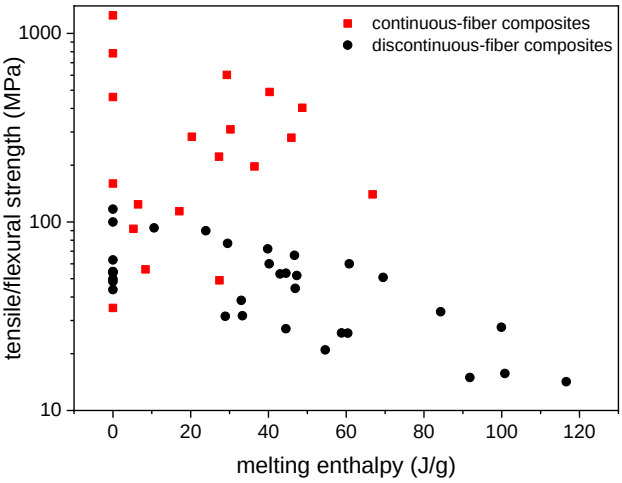

Figure VIII - 2. Relationship between mechanical strength (Log scale) and melting enthalpy of all the composites characterized in this thesis (flexural strength, except for the systems with a PA matrix and the wood/starch/PEG composites, for which the tensile strength is reported).

To reconcile the competing design requirements of the presented multifunctional structural TES composites, it is important to define objective parameters that seize all the important functions of the investigated material. The following analysis is made with an approach similar to that developed by O'Brien et al. (O'Brien et al., 2011) for multifunctional structural composite capacitors and used by other authors for analogous systems (Snyder et al., 2015; Ferreira et al., 2016; Gonzáles et al., 2017). The objective here is to minimize the system mass for a unit presenting both structural and TES requirements.

A conventional system made of two monofunctional units, which perform the structural and the TES function and have masses m_s and m_{TES}, respectively, has a total mass given in Equation (VIII - 1):

$$M = m_s + m_{TES} \quad \textbf{(VIII - 1)}$$

The TES unit has a phase change enthalpy per unit mass of ΔH, measured in J/g, and the structural unit has a specific (normalized by density) elastic modulus of $\bar{E}$. Hence, ΔH and $\bar{E}$ are the parameters describing the performance of the full system. It is supposed that the TES unit does not perform any load-bearing function and does not contribute to the mechanical stiffness, and the structural unit does not participate to the thermal storage and management function. If this system is replaced with

another made of a structural TES material of mass m^*_{mf} performing both functions, the mass of the system is now described by Equation (VIII - 2):

$$M^* = m^*_{mf} \quad \textbf{(VIII - 2)}$$

This new system, having a specific enthalpy of ΔH^*_{mf} and specific elastic modulus of $\bar{E}^*_{mf}$, should maintain the same structural and TES performance as that made of two monofunctional units, in terms of total absorbed and released energy (in J) and total elastic modulus (in GPa). The two conditions are satisfied if Equations (VIII - 3) and (VIII - 4) are met:

$$\Delta H \cdot m_{TES} = \Delta H^*_{mf} \cdot m^*_{mf} \quad \textbf{(VIII - 3)}$$

$$\bar{E} \cdot m_s = \bar{E}^*_{mf} \cdot m^*_{mf} \quad \textbf{(VIII - 4)}$$

if a unit volume is considered. Hence, an effective mass saving is verified if Equation (VIII - 5) is met:

$$M - M^* = \frac{\bar{E}^*_{mf}}{\bar{E}} \cdot m^*_{mf} + \frac{\Delta H^*_{mf}}{\Delta H} \cdot m^*_{mf} - m^*_{mf} = \\ = \left(\frac{\bar{E}^*_{mf}}{\bar{E}} + \frac{\Delta H^*_{mf}}{\Delta H} - 1 \right) \cdot m^*_{mf} > 0 \quad \textbf{(VIII - 5)}$$

Or, as expressed in Equation (VIII - 6),

$$\frac{\bar{E}^*_{mf}}{\bar{E}} + \frac{\Delta H^*_{mf}}{\Delta H} > 1 \quad \textbf{(VIII - 6)}$$

It is now possible to define a structural efficiency η_s and a TES efficiency η_{TES} as described in Equations (VIII - 7) and (VIII - 8),

$$\eta_s = \frac{\bar{E}^*_{mf}}{\bar{E}} \quad \textbf{(VIII - 7)}$$

$$\eta_{TES} = \frac{\Delta H^*_{mf}}{\Delta H} \quad \textbf{(VIII - 8)}$$

and a multifunctional efficiency η_{mf} as described in Equation (VIII - 9):

$$\eta_{mf} = \eta_s + \eta_{TES} \quad \textbf{(VIII - 9)}$$

Therefore, the multifunctional material allows an effective mass saving if $\eta_{mf} > 1$.

This requirement can be met even if η_s and η_{TES} are individually lower than 1, i.e. if the multifunctional material has specific elastic modulus and specific phase

change enthalpy lower than those of the monofunctional structural unit and the monofunctional TES unit, respectively.

The presented analysis can be directly applied to the composites investigated in this thesis, to assess if some of the prepared systems would allow an effective mass saving. The parameters η_s, η_{TES} and η_{mf} were calculated for the prepared composites by considering as monofunctional structural units the respective composite without PCM, i.e., the neat EP-CF composite, the neat EL-CF composite, etc., which present an η_s equal to 1 and an η_{TES} equal to zero. Moreover, the respective microencapsulated or shape-stabilized PCM was considered as the monofunctional TES unit. In a true monofunctional TES unit, the PCM would be probably somehow macro-encapsulated, but the enthalpy loss due to the macro-encapsulation would be comparable to (or maybe slightly greater than) that of the micro-encapsulation or the shape-stabilization performed in this thesis. Therefore, the calculation of the TES efficiency reported here is realistic, or even conservative.

The data of η_s, η_{TES} and η_{mf} calculated with average data of elastic modulus, density and phase change enthalpy, are presented in Figure VIII - 3(a-b). For the composites containing continuous fibers (Figure VIII - 3a), a considerable mass saving is obtained for the system starch/wood/PEG, in which not only η_{mf} is greater than 1, but also η_s is. This result is probably the consequence of the fact that in this system the multifunctionality is at the phase level, as the wood laminae are both the reinforcement and the shape-stabilizing agent and PEG contributes to the mechanical properties of the laminae.

However, η_{mf} is greater than 1 also for some other systems. This means that, even though the multifunctionality for these systems is not at the level of the single constituent but at the level of the whole composite material, they allow a certain (although lower) mass saving. For the composites EP-ParCNTx-CF and PA-MCx-GF, the multifunctional efficiency increases with the PCM content. This depends on two factors: (i) the fiber volume fraction was maintained constant, and (ii) the processing parameters were mild enough to avoid the degradation of most of the PCM. For the other systems, the maximum multifunctional efficiency is generally found at medium PCM concentrations, as not only does the PCM decrease the elastic modulus *per se*, but it also contributes to a decrease in the fiber content due to an increase in the matrix viscosity. For the composites containing discontinuous fibers (Figure VIII - 3b), for each system the pure monofunctional structural component was considered as that having the same matrix type and fiber fraction, but without PCM. In these systems the fiber content is generally lower than that of continuous fibers, and the introduction of PCMs does not determine a decrease in the fiber weight fraction, even though it could sometimes determine a slight decrease in the total fiber volume fraction because the density of the used PCMs is generally slightly lower than that of the employed polymer matrices. For the systems EP-MCx-CFS10 and PA-MCx-CFS20, the multifunctional efficiency is generally higher than 1 and increases with the PCM content, again

because the fiber content is fairly constant, and the processing conditions preserve most of the PCM from degradation.

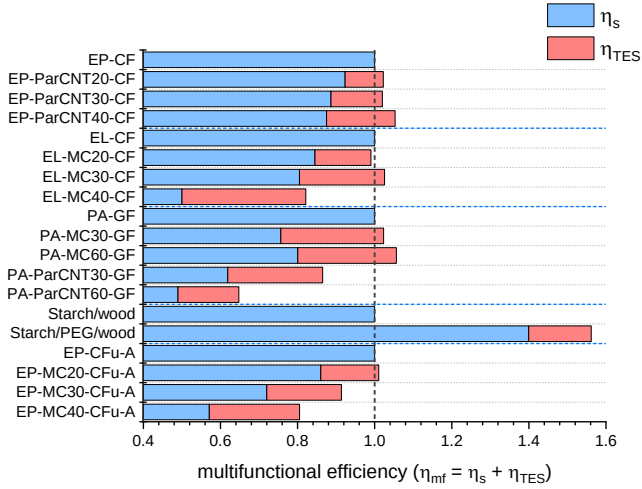

(a)

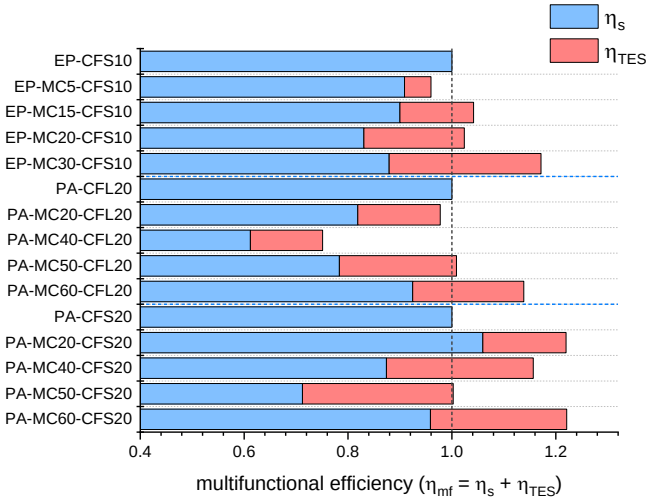

(b)

Figure VIII - 3. Multifunctional efficiency presented as the sum of structural and TES efficiencies of some of the characterized composites. An effective mass saving is obtained when η_{mf} is greater than 1.

With this approach it is possible to identify the optimum composition that maximizes the material's multifunctionality. However, this analysis is valid only if it considers the most important parameters for a specific application, as for other cases it may be more important to perform a volume-saving analysis, or to maximize properties such as the thermal conductivity, mechanical strength, or fracture toughness.

8.2 Recommendations and future perspectives

At the end of this thesis work, some recommendations should be given for future research works in this area, which can be divided into (i) studies about material properties, (ii) characterization techniques run more in detail or on a larger scale, and (iii) suggestions about the design of composites.

(i) Further investigation on material properties should consider the following aspects:

- The characterization presented in this thesis allowed a comparison between microencapsulated and shape-stabilized PCMs and assessed their suitability to be embedded in thermoplastic and thermosetting matrices. It can be concluded that microencapsulated PCMs perform better than shape-stabilized PCMs because the shell enhances the thermal stability and protect the PCM and its melting/crystallization process from the external environment, thereby leading to a higher PCM content in the composite after processing and a higher phase change enthalpy. However, the CNTs used to produce the shape-stabilized paraffin (ParCNT) used in this thesis were proven to enhance the through-thickness thermal conductivity of the host composite, which increases the thermal exchange rate. Finding effective shape-stabilizing agents for organic PCMs is an open research question in the field, and it should be considered also when embedding a PCM in a polymer or a polymer composite. The right shape-stabilizing agent could be a powerful, low-cost alternative to using microencapsulated PCMs.

- In some applications, the use of microencapsulated PCMs can be the only alternative. In these cases, it is important to tailor the properties of the microcapsules to maximize the phase change enthalpy. However, the results presented in this thesis showed that, when embedding PCM microcapsules in a polymer matrix, other factors play a key role, such as the capsule size, mechanical strength of the shell, and surface reactivity. Using smaller capsules than the commercial microcapsules used in this thesis may facilitate the dispersion and the obtainment of a homogeneous composition, but smaller capsules are likely to have a lower core-to-shell mass ratio and therefore a lower specific enthalpy. Moreover, the capsule size influences the PCM phase change in terms of

temperature and enthalpy, due to the confinement effect and interaction with the shell inner wall, as evidenced by the results on the synthesized sol-gel microcapsules described in Subchapter 7.2. These results also evidenced that the sol-gel route is an effective approach to obtain PCMs encapsulated in ceramic or organoceramic shells, which can have higher stiffness and strength than the traditional polymeric shell and may work as a reinforcement when embedded in a polymer matrix, thereby enhancing the multifunctionality of the system. In this sense, such microcapsules would act similarly to the hollow glass microspheres generally used as a microfiller to produce polymer composites with low density. In this thesis work, the matrix/capsule adhesion was also considered and enhanced with a polydopamine (PDA) coating, as investigated in Subchapter 7.3. PDA was successfully deposited onto the commercial microcapsules MC and the coating was proven effective to increase the interfacial adhesion with an epoxy resin. However, the mechanical properties were not tested, due to the scarcity of the material prepared in this way. Further works should consider the effect of the deposition parameters on the morphology, thickness, and stability of the PDA layer and if an increased interfacial interaction effectively translates in an enhancement of the mechanical and thermal properties.

(ii) A stronger emphasis on the characterization techniques should focus on the following points:

- The detailed DMA characterization, comprising single-frequency, multifrequency and heating-cooling tests, led to a better understanding of how the viscoelastic parameters of the structural TES composites are influenced by temperature and frequency. It also provided an interesting insight on the use of DMA to study a melting phase change, on the effects of such transition on the dynamic mechanical properties of the host laminate, and on the correlation between DMA and DSC parameters about a melting/crystallization transition. It could be interesting to analyze these results more in depth and to apply these characterization techniques to other systems containing a PCM.

- The TES properties of the prepared composites were studied through DSC, but tests on a slightly bigger scale were performed with a thermal camera. These tests highlighted the thermal management properties of the samples containing a PCM, since the latent heat stored or released during the phase change slowed down the temperature variation and homogenization to the surrounding environment. However, further studies should be performed on a larger scale and/or simulating real working conditions, to assess the thermal management capacity with real data of temperature and power.

- Since these composites are intended to work in a temperature interval around the phase change temperature of the PCM, it is important to assess the mechanical properties also above the melting temperature, when the PCM is in the molten state. This was done through DMA techniques for some systems and with quasi-static mechanical tests for the samples EP-MCx-CFu (Subchapter 5.4). However, it would be significant to assess how the properties vary also for the other developed systems.

- Mode I fracture toughness tests highlighted that a small fraction of PCM in the interlaminar region is beneficial to enhance the values of interlaminar fracture toughness, because other toughening mechanisms like crack pinning and crack deflection add up to fiber bridging. These results are important not only for structural TES composites, but for the reinforced composites in general, and therefore it may be worth it to explore this toughening effect, to find the optimum PCM fraction in the interlaminar region, try with different PCMs and evaluate the effect of capsule/matrix adhesion.

(iii) The important aspects of processing and material design can be listed as follows:

- As observable from Figure VIII - 1 and Figure VIII - 2, the composites reinforced with short fibers generally allow a higher enthalpy, due to the generally lower required fiber volume fraction and, for traditional thermoplastic composites, also to the milder processing conditions. Therefore, when the requirements of a higher enthalpy are more stringent than those on the mechanical properties, a semi-structural composite reinforced with short fibers should be considered as a better option.

- For the structural TES composites reinforced with continuous fibers, it was found that the PCM is preferentially distributed in the interlaminar region rather than among the fibers of the same tow. Since a high PCM fraction was seen to increase the thickness of the interlaminar region and decrease its mechanical properties, and since the outer layers of a laminate are generally those where the stress and strain are higher (if considering bending moments), an improved design of the stacking sequence could concentrate most of the PCM in the core layers and leave the outer layers richer in the reinforcing phase. A further extension of this concept may consider the production of sandwich structures where all the PCM is concentrated in the core and the mechanical resistance is demanded to the outer skins, thereby shifting the multifunctionality from the material level to the structure level. In this sense, it may be interesting to evaluate the production of syntactic foams as sandwich cores that contain a combination of PCM and reinforcing hollow glass microspheres.

- To produce continuous-fiber thermoplastic composites containing a PCM, an interesting approach could be the production of commingled hybrid yarns where the PCM phase is dispersed in the polymer filaments. The characterization presented in this thesis proved the production of polypropylene/PCM filaments feasible, but the processing parameters should be optimized to avoid excessive rupture of the microcapsules and PCM degradation. Moreover, future work in this topic should involve experimental trials to produce multifunctional commingled yarn by coupling the produced PP-MC filaments with continuous glass or carbon fibers, and further experimental work will be then needed to produce a composite part starting from these hybrid yarns.

References

Abdel Ghafaar, M., Mazen, A.A., and El-Mahallawy, N.A. (2006). Behavior of woven fabric reinforced epoxy composites under bending and compressive loads. Journal of Engineering Sciences 34(2), 453-469.

Agarwal, B.D., Broutman, L.J., and Chandrashekhara, K. (2018). Analysis and Performance of Fiber Composites. John Wiley and Sons, Inc.

Akeiber, H., Nejat, P., Majid, M.Z.A., Wahid, M.A., Jomehzadeh, F., Zeynali Famileh, I., et al. (2016). A review on phase change material (PCM) for sustainable passive cooling in building envelopes. Renewable and Sustainable Energy Reviews 60, 1470-1497. doi: 10.1016/j.rser.2016.03.036.

Al Aani, S., Haroutounian, A., Wright, C.J., and Hilal, N. (2018). Thin Film Nanocomposite (TFN) membranes modified with polydopamine coated metals/carbon-nanostructures for desalination applications. Desalination 427, 60-74.

Al Hallaj, S., and Selman, J.R. (2000). A Novel Thermal Management System for Electric Vehicle Batteries Using Phase-Change Material. Journal of The Electrochemical Society 147 (9), 3231-3236.

Alamo, R.G., Blanco, J.A., Carrilero, I., and Fu, R. (2002). Measurement of the ^{13}C spin–lattice relaxation time of the non-crystalline regions of semicrystalline polymers by a CP MAS-based method. Polymer 43(6), 1857-1865.

Alehosseini, E., and Jafari, S.M. (2019). Micro/nano-encapsulated phase change materials (PCMs) as emerging materials for the food industry. Trends in Food Science & Technology 91, 116-128. doi: 10.1016/j.tifs.2019.07.003.

Alkan, C., Sarı, A., Karaipekli, A., and Uzun, O. (2009). Preparation, characterization, and thermal properties of microencapsulated phase change material for thermal energy storage. Solar Energy Materials and Solar Cells 93(1), 143-147. doi: 10.1016/j.solmat.2008.09.009.

Anghel, E.M., Georgiev, A., Petrescu, S., Popov, R., and Constantinescu, M. (2014). Thermo-physical characterization of some paraffins used as phase change materials for thermal energy storage. Journal of Thermal Analysis and Calorimetry 117(2), 557-566. doi: 10.1007/s10973-014-3775-6.

Ary Subagia, I.D.G., Kim, Y., Tijing, L.D., Sang Kim, C., and Kyong Shon, H. (2014). Effect of stacking sequence on the flexural properties of hybrid composites reinforced with carbon and basalt fiber. Composites: Part B 58, 251-258. doi: 10.1016/j.compositesb.2013.10.027.

Asp, L.E., and Greenhalgh, E.S. (2014). Structural power composites. Composites Science and Technology 101, 41-61. doi: 10.1016/j.compscitech.2014.06.020.

Aydin, D., Casey, S.P., and Riffat, S. (2015). The latest advancements on thermochemical heat storage systems. Renewable and Sustainable Energy Reviews 41, 356-367. doi: 10.1016/j.rser.2014.08.054.

Bagotia, N., and Sharma, D.K. (2019). Systematic study of dynamic mechanical and thermal properties of multiwalled carbon nanotube reinforced polycarbonate/ethylene methyl acrylate nanocomposites. Polymer Testing 73, 425-432. doi: 10.1016/j.polymertesting.2018.12.006.

Bao, X., Tian, Y., Yuan, L., Cui, H., Tang, W., Fung, W.H., et al. (2019). Development of high performance PCM cement composites for passive solar buildings. Energy and Buildings 194, 33-45. doi: 10.1016/j.enbuild.2019.04.011.

Bastioli, C. (1997). Properties and applications of Mater-Bi starch-based materials. Polymer Degradation and Stability 59, 263-272.

Beamson, G., and Briggs, D. (1992). High resolution XPS of Organic Polymers - The Scienta ESCA300 Database. Chichester, UK: John Wiley & Sons.

Bhudolia, S.K., Perrotey, P., and Joshi, S.C. (2017). Enhanced vibration damping and dynamic mechanical characteristics of composites with novel pseudo-thermoset matrix system. Composite Structures 179, 502-513. doi: 10.1016/j.compstruct.2017.07.093.
Bhudolia, S.K., Perrotey, P., and Joshi, S.C. (2018). Mode I fracture toughness and fractographic investigation of carbon fibre composites with liquid Methylmethacrylate thermoplastic matrix. Composites Part B: Engineering 134, 246-253. doi: 10.1016/j.compositesb.2017.09.057.
Biron, M. (2013). Thermoplastics And Thermoplastic Composites. Oxford, UK: Elsevier, Ltd.
Biswas, K., Lu, J., Soroushian, P., and Shrestha, S. (2014). Combined experimental and numerical evaluation of a prototype nano-PCM enhanced wallboard. Applied Energy 131, 517-529. doi: 10.1016/j.apenergy.2014.02.047.
Bloch, F. (1946). Nuclear Induction. Physical Review 70, 4604–4673.
Brody, H. (1985). Process of melt spinning poly propylene and novel rough surfaced fibres produced thereby.
Brown, E.N., White, S.R., and Sottos, N.R. (2004). Microcapsule induced toughening in a self-healing polymer composite. Journal of Materials Science 39, 1703-1710.
Burger, N., Laachachi, A., Ferriol, M., Lutz, M., Toniazzo, V., and Ruch, D. (2016). Review of thermal conductivity in composites: Mechanisms, parameters and theory. Progress in Polymer Science 61, 1-28. doi: 10.1016/j.progpolymsci.2016.05.001.
Cabeza, L.F. (2014). Advances in Thermal Energy Storage Systems: Methods and Applications. 80 High Street, Sawston, Cambridge, CB22 3HJ, UK: Woodhead Publishing.
Cai, Y., Hu, Y., Song, L., Kong, Q., Yang, R., Zhang, Y., et al. (2007). Preparation and flammability of high density polyethylene/paraffin/organophilic montmorillonite hybrids as a form stable phase change material. Energy Conversion and Management 48(2), 462-469. doi: 10.1016/j.enconman.2006.06.021.
Cai, X.L., Fu, D.T., and Qu, A.L. (2014). Effects of surface modification on properties of nanocapsules for self-healing materials. Plastics, Rubber and Composites 43(5), 161-165. doi: 10.1179/1743289814y.0000000081.
Cai, X., Fu, D., and Qu, A. (2015). Effects of surface modification on the properties of microcapsules for self-healing. Journal of Wuhan University of Technology-Mater. Sci. Ed. 30(6), 1234-1239. doi: 10.1007/s11595-015-1301-8.
Campbell, F.C. (2010). Structural Composite Materials. Materials Park, Ohio, US: ASM International.
Cao, L., Tang, F., and Fang, G. (2014a). Preparation and characteristics of microencapsulated palmitic acid with TiO_2 shell as shape-stabilized thermal energy storage materials. Solar Energy Materials and Solar Cells 123, 183-188. doi: 10.1016/j.solmat.2014.01.023.
Cao, L., Tang, F., and Fang, G. (2014b). Synthesis and characterization of microencapsulated paraffin with titanium dioxide shell as shape-stabilized thermal energy storage materials in buildings. Energy and Buildings 72, 31-37. doi: 10.1016/j.enbuild.2013.12.028.
Cao, X., Dai, X., and Liu, J. (2016). Building energy-consumption status worldwide and the state-of-the-art technologies for zero-energy buildings during the past decade. Energy and Buildings 128, 198-213. doi: 10.1016/j.enbuild.2016.06.089.
Cao, V.D., Pilehvar, S., Salas-Bringas, C., Szczotok, A.M., Valentini, L., Carmona, M., et al. (2018). Influence of microcapsule size and shell polarity on thermal and mechanical properties of thermoregulating geopolymer concrete for passive building applications. Energy Conversion and Management 164, 198-209. doi: 10.1016/j.enconman.2018.02.076.
Cardoso, K.P., Ferrão, L.F.A., and Kawachi, E.Y. (2017). Preparation of Paraffin-Based Solid Combustible for Hybrid Propulsion Rocket Motor. Journal of Propulsion and Power 33(2), 448-455. doi: 10.2514/1.B36197.

Carreau, P.J. (1972). Rheological Equations from Molecular Network Theories. Transactions of the Society of Rheology 16(1), 99-127. doi: 10.1122/1.549276.
Casado, J.A., Gutiérrez-Solana, F., Carrascal, I., Diego, S., Polanco, J.A., and Hernández, D. (2016). Fatigue behavior enhancement of short fiber glass reinforced polyamide by adding phase change materials. Composites Part B: Engineering 93, 115-122. doi: 10.1016/j.compositesb.2016.02.059.
Chaudhary, S., Surekha, P., Kumar, D., Rajagopal, C., and Roy, P.K. (2015). Amine-functionalized poly(styrene) microspheres as thermoplastic toughener for epoxy resin. Polymer Composites 36(1), 174-183. doi: 10.1002/pc.22927.
Chee, S.S., Jawaid, M., Sultan, M.T.H., Alothman, O.Y., and Abdullah, L.C. (2019). Thermomechanical and dynamic mechanical properties of bamboo/woven kenaf mat reinforced epoxy hybrid composites. Composites Part B: Engineering 163, 165-174. doi: 10.1016/j.compositesb.2018.11.039.
Chen, F., and Wolcott, M.P. (2014). Miscibility studies of paraffin/polyethylene blends as form-stable phase change materials. European Polymer Journal 52, 44-52. doi: 10.1016/j.eurpolymj.2013.09.027.
Chen, F., and Wolcott, M. (2015). Polyethylene/paraffin binary composites for phase change material energy storage in building: A morphology, thermal properties, and paraffin leakage study. Solar Energy Materials and Solar Cells 137, 79-85. doi: 10.1016/j.solmat.2015.01.010.
Chen, Z., Cao, L., Fang, G., and Shan, F. (2013). Synthesis and Characterization of Microencapsulated Paraffin Microcapsules as Shape-Stabilized Thermal Energy Storage Materials. Nanoscale and Microscale Thermophysical Engineering 17(2), 112-123. doi: 10.1080/15567265.2012.761305.
Chen, Z., Cao, L., Fang, G., and Shan, F. (2013a). Synthesis and Characterization of Microencapsulated Paraffin Microcapsules as Shape-Stabilized Thermal Energy Storage Materials. Nanoscale and Microscale Thermophysical Engineering 17(2), 112-123. doi: 10.1080/15567265.2012.761305.
Chen, Z., Cao, L., Shan, F., and Fang, G. (2013b). Preparation and characteristics of microencapsulated stearic acid as composite thermal energy storage material in buildings. Energy and Buildings 62, 469-474. doi: 10.1016/j.enbuild.2013.03.025.
Cherif, C., Tran, N.H.A., Kirsten, M., Bruenig, H., and Vogel, R. (2018). Environmentally friendly and highly productive bi-component melt spinning of thermoregulated smart polymer fibres with high latent heat capacity. Express Polymer Letters 12(3), 203-214. doi: 10.3144/expresspolymlett.2018.19.
Chilali, A., Zouari, W., Assarar, M., Kebir, H., and Ayad, R. (2016). Analysis of the mechanical behaviour of flax and glass fabrics-reinforced thermoplastic and thermoset resins. Journal of Reinforced Plastics and Composites 35(16), 1217-1232. doi: 10.1177/0731684416645203.
Cho, J.-S., Kwon, A., and Cho, C.-G. (2002). Microencapsulation of octadecane as a phase-change material by interfacial polymerization in an emulsion system. Colloid and Polymer Science 280(3), 260-266. doi: 10.1007/s00396-001-0603-x.
Ciriminna, R., Sciortino, M., Alonzo, G., de Schrijver, A., and Pagliaro, M. (2011). From Molecules to Systems: Sol-Gel Microencapsulation in Silica-Based Materials. Chemical Reviews 111(2), 765–789. doi: 10.1021/cr100161x.
Compston, P., and Jar, P.-Y.B. (1999). The Influence of Fibre Volume Fraction on the Mode I Interlaminar Fracture Toughness of a Glass-Fibre/Vinyl Ester Composite. Applied Composite Materials 6, 353–368.
Cui, W., Wisnom, M.R., and Jones, M. (1994). Effect of specimen size on interlaminar shear strength of unidirectional carbon fibre-epoxy. Composites Engineering 4(3), 299-307.
Czigany, T., and Karger-Kocsis, J. (2001). A comparison of the mechanical behaviour of weft-knitted glass and carbon fiber fabric-reinforced polyamide-12 composites produced with commingled staple yarns. Polymers & Polymer Composites 9(8), 491-497.

Demirbas, M.F. (2006). thermal energy storage and phase change materials: an overview. Energy Sources, Part B: Economics, Planning, and Policy 1(1), 85-95. doi: https://doi.org/10.1080/009083190881481.
Deng, S., Ye, L., and Mai, Y.-W. (1999). Influence of fiber cross-sectional aspect ratio on mechanical properties of glass-fiber/epoxy composites. II. Interlaminar fracture and impact behaviour. Composites Science and Technology 59, 1725-1734.
DeSain, J., Brady, B., Metzler, K., Curtiss, T., and Albright, T. (2009). "Tensile Tests of Paraffin Wax for Hybrid Rocket Fuel Grains. Aerospace report no. ATR-2009(8268)-1". (El Segundo, California: The Aerospace Corporation).
Devi, L.U., Bhagawan, S.S., and Thomas, S. (2009). Dynamic mechanical analysis of pineapple leaf/glass hybrid fiber reinforced polyester composites. Polymer Composites, NA-NA. doi: 10.1002/pc.20880.
Dincer, I., and Rosen, M.A. (2011). Thermal Energy Storage. Systems and Applications. Chichester, West Sussex, PO19 8SQ, United Kingdom: John Wiley and Sons, Ltd.
Dincer, I., Hamut, H.S., and Javani, N. (2017). Thermal Management of Electric Vehicle Battery Systems. John Wiley & Sons.
Dincer, I., and Ezan, M.A. (2018). Heat Storage: A Unique Solution For Energy Systems Springer International.
Dirè, S., Tagliazucca, V., Callone, E., and Quaranta, A. (2011). Effect of functional groups on condensation and properties of sol-gel silica nanoparticles prepared by direct synthesis from organoalkoxysilanes. Materials Chemistry and Physics 126, 909-917.
Dirè, S., Borovin, E., and Ribot, F. (2018). "Architecture of Silsesquioxanes," in Handbook of Sol-Gel Science and Technology: Processing, Characterization and Applications, eds. L. Klein, M. Aparicio & A. Jitanu. Springer International Publishing.
Dong, C., and Davies, I.J. (2015). Flexural strength of bidirectional hybrid epoxy composites reinforced by E glass and T700S carbon fibers. Composites B 72, 65-71. doi: 10.1016/j.compositesb.2014.11.031.
Dorigato, A., Brugnara, M., Giacomelli, G., Fambri, L., and Pegoretti, A. (2016). Thermal and mechanical behaviour of innovative melt-blown fabrics based on polyamide nanocomposites. Journal of Industrial Textiles 45 (6), 1504–1515. doi: 10.1177/1528083714564633.
Dorigato, A., Pegoretti, A., and Penati, A. (2010). Linear low-density polyethylene/silica micro- and nanocomposites: dynamic rheological measurements and modelling. Express Polymer Letters 4(2), 115-129. doi: 10.3144/expresspolymlett.2010.16.
Dorigato, A., Rigotti, D., and Pegoretti, A. (2018). Thermoplastic Polyurethane Blends With Thermal Energy Storage/Release Capability. Frontiers in Materials 5. doi: 10.3389/fmats.2018.00058.
Dorigato, A., Negri, M., and Pegoretti, A. (2018a). Ultrathin Wood Laminae-Polyvinyl Alcohol Biodegradable Composites. Polymer Composites, 1116-1124. doi: 10.1002/pc.24040.
Dorigato, A., Negri, M., and Pegoretti, A. (2018b). Ultrathin Wood Laminae-Thermoplastic Starch Biodegradable Composites. Journal of Renewable Materials 6(5), 493-503. doi: 10.7569/JRM.2017.634177.
Doumbia, A.S., Castro, M., Jouannet, D., Kervoëlen, A., Falher, T., Cauret, L., et al. (2015). Flax/polypropylene composites for lightened structures: multiscale analysis of process and fibre parameters. Materials & Design 87, 331-341. doi: 10.1016/j.matdes.2015.07.139.
Fan, L., and Khodadadi, J.M. (2011). Thermal conductivity enhancement of phase change materials for thermal energy storage: A review. Renewable and Sustainable Energy Reviews 15(1), 24-46. doi: 10.1016/j.rser.2010.08.007.
Fang, G., Chen, Z., and Li, H. (2010). Synthesis and properties of microencapsulated paraffin composites with SiO_2 shell as thermal energy storage materials. Chemical Engineering Journal 163(1-2), 154-159. doi: 10.1016/j.cej.2010.07.054.
Fang, X., Fan, L.W., Ding, Q., Yao, X.L., Wu, Y.Y., Hou, J.F., et al. (2014). Thermal energy storage performance of paraffin-based composite phase change materials filled with

hexagonal boron nitride nanosheets. Energy Conversion and Management 80, 103-109. doi: 10.1016/j.enconman.2014.01.016.
Feldman, D., and Banu, D. (1996). DSC analysis for the evaluation of an energy storing wallboard. Thermochimica Acta 272, 243-251.
Felix De Castro, P., and Shchukin, D.G. (2015). New polyurethane/docosane microcapsules as phase-change materials for thermal energy storage. Chemistry 21(31), 11174-11179. doi: 10.1002/chem.201500666.
Felix De Castro, P., Ahmed, A., and Shchukin, D.G. (2016). Confined-Volume Effect on the Thermal Properties of Encapsulated Phase Change Materials for Thermal Energy Storage. Chemistry 22(13), 4389-4394. doi: 10.1002/chem.201505035.
Felske, J.D. (2004). Effective thermal conductivity of composite spheres in a continuous medium with contact resistance. International Journal of Heat and Mass Transfer 47(14-16), 3453-3461. doi: 10.1016/j.ijheatmasstransfer.2004.01.013.
Ferreira, A.D.B.L., Nóvoa, P.R.O., and Marques, A.T. (2016). Multifunctional Material Systems: A state-of-the-art review. Composite Structures 151, 3-35. doi: 10.1016/j.compstruct.2016.01.028.
Fleischer, A.S. (2015). Thermal energy storage using phase change materials - fundamentals and applications. Minneapolis, MN, USA: Springer Briefs in Applied Science and Technology. Thermal Engineering and Applied Science.
Flores, R., Perez, J., Cassagnau, P., Michel, A., and Cavaille, J.Y. (1996). Dynamic mechanical behavior of poly(vinyl chloride)/poly(methyl methacrylate) polymer blend. Journal of Applied Polymer Science 60, 1439-1453.
Fok, S.C., Shen, W., and Tan, F.L. (2010). Cooling of portable hand-held electronic devices using phase change materials in finned heat sinks. International Journal of Thermal Sciences 49(1), 109-117. doi: 10.1016/j.ijthermalsci.2009.06.011.
Fredi, G., Jeschke, S., Boulaoued, A., Wallenstein, J., Rashidi, M., Liu, F., et al. (2018). Graphitic microstructure and performance of carbon fibre Li-ion battery electrodes. Multifunctional Materials 1(1). doi: 10.1088/2399-7532/aab707.
Freitas, S., Merkle, H.P., and Gander, B. (2005). Microencapsulation by solvent extraction/evaporation: reviewing the state of the art of microsphere preparation process technology. J Control Release 102(2), 313-332. doi: 10.1016/j.jconrel.2004.10.015.
Frenzel, R., Schiefer, T., Jansen, I., Simon, F., Calvimontes, A., Grundke, K., et al. (2015). Polyelectrolytes to promote adhesive bonds of laser-structured aluminium. International Journal of Adhesion and Adhesives 61, 35-45. doi: 10.1016/j.ijadhadh.2015.05.001.
Friedrich, K. (2015). "Routes for achieving multifunctionality in reinforced polymers and composite structures," in Multifunctionality of Polymer Composites: Challenges and New Solutions, eds. K. Friedrich & U. Breuer. (Waltham, MA, US: Elsevier), 3-41.
Fu, S.-Y., and Lauke, B. (1996). Effects of fiber length and fiber orientation distributions on the tensile strength of short-fiber-reinforced polymers. Composites Science and Technology 56, 1179-1190. doi: 10.1016/S0266-3538(96)00072-3.
Fu, Y.-X., He, Z.-X., Mo, D.-C., and Lu, S.-S. (2014). Thermal conductivity enhancement with different fillers for epoxy resin adhesives. Applied Thermal Engineering 66(1-2), 493-498. doi: 10.1016/j.applthermaleng.2014.02.044.
Furtado, L.M., Ando, R.A., and Petri, D.F.S. (2020). Polydopamine-coated cellulose acetate butyrate microbeads for caffeine removal. Journal of Materials Science 55(8), 3243–3258. doi: 10.1007/s10853-019-04169-1.
Gamon, G., Evon, P., and Rigal, L. (2013). Twin-screw extrusion impact on natural fibre morphology and material properties in poly(lactic acid) based biocomposites. Industrial Crops and Products 46, 173-185. doi: 10.1016/j.indcrop.2013.01.026.
Giannakopoulos, G., Masania, K., and Taylor, A.C. (2010). Toughening of epoxy using core–shell particles. Journal of Materials Science 46(2), 327-338. doi: 10.1007/s10853-010-4816-6.

Gibson, R.F. (2010). A review of recent research on mechanics of multifunctional composite materials and structures. Composite Structures 92(12), 2793-2810. doi: 10.1016/j.compstruct.2010.05.003.
Giordano, G. (1981). Tecnologia del legno. La materia prima. Vol. 1. Torino, Italy: UTET.
Goitandia, A.M., Miguel, M.B., Babiano, A.M., and Miguel, O.G. (2018). Use of phase change materials to delay icing or to cause de-icing in wind-driven power generators. US 2018 / 0230972 A1.
Goli, P., Legedza, S., Dhar, A., Salgado, R., Renteria, J., and Balandin, A.A. (2014). Graphene-enhanced hybrid phase change materials for thermal management of Li-ion batteries. Journal of Power Sources 248, 37-43. doi: 10.1016/j.jpowsour.2013.08.135.
González, C., Vilatela, J.J., Molina-Aldareguía, J.M., Lopes, C.S., and Llorca, J. (2017). Structural composites for multifunctional applications: Current challenges and future trends. Progress in Materials Science 89, 194-251. doi: 10.1016/j.pmatsci.2017.04.005.
Green, D.W., Winandy, J.E., and Kretschmann, D.E. (1999). "Mechanical Properties of Wood," in Wood handbook—Wood as an engineering material, ed. F.P. Laboratory. (Madison, WI: U.S. Department of Agriculture, Forest Service, Forest Products Laboratory).
Greene, J.P., and Wilkes, J.O. (1995). Steady-State and dynamic properties of concentrated fiber-filled thermoplastics. Polymer Engineering & Science 35(21), 1670-1681. doi: 10.1002/pen.760352103.
Günzler, H., and Gremlich, H.-U. (2003). IR-Spektroskopie: Eine Einführung. Verlag, Weinheim, Germany Wiley-VCH
Guo, R., Azaiez, J., and Bellehumeur, C. (2005). Rheology of fiber filled polymer melts: Role of fiber-fiber interactions and polymer-fiber coupling. Polymer Engineering & Science 45(3), 385-399. doi: 10.1002/pen.20285.
Gürgen, S., Li, W., and Kuşhan, M.C. (2016). The rheology of shear thickening fluids with various ceramic particle additives. Materials & Design 104, 312-319. doi: 10.1016/j.matdes.2016.05.055.
Halpin, J.C., and Kardos, J.L. (1976). The Halpin-Tsai Equations: A Review. Polymer engineering and science 16(5), 344-352. doi: 10.1002/pen.760160512
Hartmann, M.H., Worley, J.B., and North, M. (2007). Temperature regulating cellulosic fibers and applications thereof USA patent application.
Hasnain, S.M. (1998). Review on sustainable thermal energy storage technologies, Part I: heat storage materials and techniques. Energy Conversion and Management 39(11), 1127-1138. doi: 10.1016/S0196-8904(98)00025-9.
Hsiao, P.-C., Lin, C.-M., Lu, C.-T., Yin, W., Huang, Y.-T., and Lin, J.-H. (2019). Manufacture and evaluations of stainless steel/rayon/bamboo charcoal functional composite knits. Textile Research Journal In Press. doi: 10.1177/0040517518821904.
Huang, X., Lin, Y.X., Alva, G., and Fang, G.Y. (2017). Thermal properties and thermal conductivity enhancement of composite phase change materials using myristyl alcohol/metal foam for solar thermal storage. Solar Energy Materials and Solar Cells 170, 68-76. doi: 10.1016/j.solmat.2017.05.059.
Ianniciello, L., Biwolé, P.H., and Achard, P. (2018). Electric vehicles batteries thermal management systems employing phase change materials. Journal of Power Sources 378, 383-403. doi: 10.1016/j.jpowsour.2017.12.071.
Inoue, D., Kurosu, H., Chen, Q., and Ando, I. (1995). Structural and dynamical studies of 13C-labeled polyethylene adsorbed on the surface of silica gel by high-resolution solid-state ^{13}C NMR spectroscopy. Acta Polymerica 46, 420-423. doi: 10.1002/actp.1995.010460603.
Iqbal, K., and Sun, D. (2015). Development of thermal stable multifilament yarn containing micro-encapsulated phase change materials. Fibers and Polymers 16(5), 1156-1162. doi: 10.1007/s12221-015-1156-9.

Iqbal, K., Khan, A., Sun, D., Ashraf, M., Rehman, A., Safdar, F., et al. (2019). Phase change materials, their synthesis and application in textiles—a review. The Journal of The Textile Institute 110(4), 625-638. doi: 10.1080/00405000.2018.1548088.
Jamekhorshid, A., Sadrameli, S.M., and Farid, M. (2014). A review of microencapsulation methods of phase change materials (PCMs) as a thermal energy storage (TES) medium. Renewable and Sustainable Energy Reviews 31, 531-542. doi: 10.1016/j.rser.2013.12.033.
Jana, P., Fierro, V., Pizzi, A., and Celzard, A. (2015). Thermal conductivity improvement of composite carbon foams based on tannin-based disordered carbon matrix and graphite fillers. Materials & Design 83, 635-643. doi: 10.1016/j.matdes.2015.06.057.
Jarimi, H., Aydin, D., Yanan, Z., Ozankaya, G., Chen, X., and Riffat, S. (2019). Review on the recent progress of thermochemical materials and processes for solar thermal energy storage and industrial waste heat recovery. International Journal of Low-Carbon Technologies 14(1), 44-69. doi: 10.1093/ijlct/cty052.
Jeong, S.-G., Kim, S., and Huh, W. (2014). Preparation of epoxy resin using n-hexadecane based shape stabilized PCM for applying wood-based flooring. Journal of Adhesion Science and Technology 28(7), 711-721. doi: 10.1080/01694243.2013.865331.
Jeong, Y.K., Park, S.H., and Choi, J.W. (2018). Mussel-Inspired Coating and Adhesion for Rechargeable Batteries: A Review. ACS Appl Mater Interfaces 10(9), 7562-7573. doi: 10.1021/acsami.7b08495.
Johnston, J.H., Grindrod, J.E., Dodds, M., and Schimitschek, K. (2008). Composite nano-structured calcium silicate phase change materials for thermal buffering in food packaging. Current Applied Physics 8(3-4), 508-511. doi: 10.1016/j.cap.2007.10.059.
Kahwaji, S., Johnson, M.B., Kheirabadi, A.C., Groulx, D., and White, M.A. (2018). A comprehensive study of properties of paraffin phase change materials for solar thermal energy storage and thermal management applications. Energy 162, 1169-1182. doi: 10.1016/j.energy.2018.08.068.
Kalaiselvam, S., and Parameshwaran, R. (2014). Thermal energy storage technologies for sustainability: systems design, assessment, and applications.
Kandare, E., Khatibi, A.A., Yoo, S., Wang, R., Ma, J., Olivier, P., et al. (2015). Improving the through-thickness thermal and electrical conductivity of carbon fibre/epoxy laminates by exploiting synergy between graphene and silver nano-inclusions. Composites Part A: Applied Science and Manufacturing 69, 72-82. doi: 10.1016/j.compositesa.2014.10.024.
Kandasamy, R., Wang, X.-Q., and Mujumdar, A.S. (2007). Application of phase change materials in thermal management of electronics. Applied Thermal Engineering 27(17-18), 2822-2832. doi: 10.1016/j.applthermaleng.2006.12.013.
Kapsalis, V., and Karamanis, D. (2016). Solar thermal energy storage and heat pumps with phase change materials. Applied Thermal Engineering 99, 1212-1224. doi: 10.1016/j.applthermaleng.2016.01.071.
Keblinski, P., Phillpot, S.R., Choi, S.U.S., and Eastman, J.A. (2002). Mechanisms of heat flow in suspensions of nano-sized particles (nanofluids). International Journal of Heat and Mass Transfer 45, 855-863.
Kelley, S.S., Rials, T.G., and Glasser, W.G. (1987). Relaxation behaviour of the amorphous components of wood. JOURNAL OF MATERIALS SCIENCE 22, 617-624.
Kenisarin, M., and Mahkamov, K. (2016). Passive thermal control in residential buildings using phase change materials. Renewable and Sustainable Energy Reviews 55, 371-398. doi: 10.1016/j.rser.2015.10.128.
Kim, S.S., Shin, M.W., and Jang, H. (2012). Tribological properties of short glass fiber reinforced polyamide 12 sliding on medium carbon steel. Wear 274, 34-42. doi: 10.1016/j.wear.2011.08.009.
Konuklu, Y., Ostry, M., Paksoy, H.O., and Charvat, P. (2015). Review on using microencapsulated phase change materials (PCM) in building applications. Energy and Buildings 106, 134-155. doi: 10.1016/j.enbuild.2015.07.019.

Kreder, M.J., Alvarenga, J., Kim, P., and Aizenberg, J. (2016). Design of anti-icing surfaces: smooth, textured or slippery? Nature Reviews Materials 1(1). doi: 10.1038/natrevmats.2015.3.
Król, K., Macherzyńska, B., and Pielichowska, K. (2016). Acrylic bone cements modified with poly(ethylene glycol)-based biocompatible phase-change materials. Journal of Applied Polymer Science 133(36). doi: 10.1002/app.43898.
Krupa, I., Nógellová, Z., Špitalský, Z., Janigová, I., Boh, B., Sumiga, B., et al. (2014). Phase change materials based on high-density polyethylene filled with microencapsulated paraffin wax. Energy Conversion and Management 87, 400-409. doi: 10.1016/j.enconman.2014.06.061.
Kulshreshtha, A.K., and Vasile, C. (2002). Handbook of Polymer Blends and Composites. Shawbury, Shrewsbury, Shropshire, SY4 4NR, UK: Smithers Rapra Technology.
Kwon, I.S., and Bettinger, C.J. (2018). Polydopamine Nanostructures as Biomaterials for Medical Applications. J Mater Chem B 6(43), 6895-6903. doi: 10.1039/C8TB02310G.
Kylili, A., and Fokaides, P.A. (2016). Life Cycle Assessment (LCA) of Phase Change Materials (PCMs) for building applications: A review. Journal of Building Engineering 6, 133-143. doi: 10.1016/j.jobe.2016.02.008.
Lane, G.A. (1983). Solar Heat Storage Latent Heat Materials, Volume 1: Background and Scientific Principles. CRC Press.
Leskovšek, M., Jedrinović, G., and Elesini, U.S. (2004). Properties of polypropylene fibres with incorporated microcapsules. Acta Chim. Slov. 51, 699−715.
Lewis, T.B., and Nielsen, L.E. (1970). Dynamic mechanical properties of particulate-filled composites. Journal of Applied Polymer Science 14(6), 1449-1471. doi: 10.1002/app.1970.070140604.
Li, B., Liu, T., Hu, L., Wang, Y., and Gao, L. (2013). Fabrication and Properties of Microencapsulated Paraffin/SiO_2 Phase Change Composite for Thermal Energy Storage. ACS Sustainable Chemistry & Engineering 1(3), 374-380. doi: 10.1021/sc300082m.
Li, L., Wang, G., and Guo, C. (2016). Influence of intumescent flame retardant on thermal and flame retardancy of eutectic mixed paraffin/polypropylene form-stable phase change materials. Applied Energy 162, 428-434. doi: 10.1016/j.apenergy.2015.10.103.
Lin, K., Zhang, Y., Xu, X., Di, H., Yang, R., and Qin, P. (2005). Experimental study of under-floor electric heating system with shape-stabilized PCM plates. Energy and Buildings 37(3), 215-220. doi: 10.1016/j.enbuild.2004.06.017.
Lin, Y., Jia, Y., Alva, G., and Fang, G. (2018). Review on thermal conductivity enhancement, thermal properties and applications of phase change materials in thermal energy storage. Renewable and Sustainable Energy Reviews 82, 2730-2742. doi: 10.1016/j.rser.2017.10.002.
Lin, Y., Zhu, C., and Fang, G. (2019). Synthesis and properties of microencapsulated stearic acid/silica composites with graphene oxide for improving thermal conductivity as novel solar thermal storage materials. Solar Energy Materials and Solar Cells 189, 197-205. doi: 10.1016/j.solmat.2018.10.005.
Liu, X., and Lou, Y. (2015). Preparation of Microencapsulated Phase Change Materials by the Sol-gel Process and Its Application on Textiles. Fibres & Textiles in Eastern Europe 23(2), 63-67.
Liu, L., Su, D., Tang, Y., and Fang, G. (2016a). Thermal conductivity enhancement of phase change materials for thermal energy storage: A review. Renewable and Sustainable Energy Reviews 62, 305-317. doi: 10.1016/j.rser.2016.04.057.
Liu, M., Zeng, G., Wang, K., Wan, Q., Tao, L., Zhang, X., et al. (2016b). Recent developments in polydopamine: an emerging soft matter for surface modification and biomedical applications. Nanoscale 8(38), 16819-16840. doi: 10.1039/c5nr09078d.
Long, A.C. (2006). Design and Manufacture of Textile Composites. Boca Raton, FL, US: Woodhead Publishing Limited and CRC Press LLC.

Lüth, H., Nyburg, S.C., Robinson, P.M., and Scott, H.G. (1974). Crystallographic and calorimetric phase studies of the *n*-eicosane, $C_{20}H_{42}$: *n*-docosane, $C_{22}H_{46}$ system. Molecular Crystals and Liquid Crystals 27(3-4), 337-357. doi: 10.1080/15421407408083141.

Luyt, A.S., and Krupa, I. (2009). Phase change materials formed by UV curable epoxy matrix and Fischer-Tropsch paraffin wax. Energy Conversion and Management 50(1), 57-61. doi: 10.1016/j.enconman.2008.08.026.

Lv, Y., Zou, Y., and Yang, L. (2011). Feasibility study for thermal protection by microencapsulated phase change micro/nanoparticles during cryosurgery. Chemical Engineering Science 66(17), 3941-3953. doi: 10.1016/j.ces.2011.05.031.

Mallick, P.K. (2007). Fiber reinforced composites. Materials, manufacturing, and design. Boca Raton, FL, US: Taylor & Francis Group, LLC.

Mark, J.E. (1999). Polymer Data Handbook. Oxford: Oxford University Press.

Martin E. Lynge, Rebecca van der Westen, Postmab, A., and Stadler, B. (2011). Polydopamine—a nature-inspired polymer coating for biomedical science. Nanoscale 3, 4916-4928.

Matias, T., Soares, N., Campos-Gonçalves, I., Costa, J.J., Simões, P.N., and Durães, L. (Year). "Thermophysical characterization of commercial paraffin-based PCMs for low temperature thermal energy storage applications", in: Seminar PCMs4Buildings. PCMs: Thermophysical characterization and buildings' applications. University of Coimbra. Coimbra, 14-16 June), 10-12.

Menard, K.P. (2008). "Chapter 5. Dynamic Testing and Instrumentation.," in Dynamic mechanical analysis. A practical introduction., ed. K.P. Menard. (Boca Raton, FL, US: CRC Press).

Mesalhy, O., Lafdi, K., and Elgafy, A. (2006). Carbon foam matrices saturated with PCM for thermal protection purposes. Carbon 44(10), 2080-2088. doi: 10.1016/j.carbon.2005.12.019.

Michaud, D., Sequeira Tavares, S., Sigg, A., Lavanchy, S., and Månson, J.-A.E. (2006). "Low pressure processing of high fiber content composites ", in: The 8th International Conference on Flow Processes in Composite Materials (FPCM8) (Douai, FRANCE).

Mirabedini, S.M., Esfandeh, M., Farnood, R.R., and Rajabi, P. (2019). Amino-silane surface modification of urea-formaldehyde microcapsules containing linseed oil for improved epoxy matrix compatibility. Part I: Optimizing silane treatment conditions. Progress in Organic Coatings, 105242. doi: 10.1016/j.porgcoat.2019.105242.

Mochane, M.J., and Luyt, A.S. (2012). Preparation and properties of polystyrene encapsulated paraffin wax as possible phase change material in a polypropylene matrix. Thermochimica Acta 544(Supplement C), 63-70. doi: 10.1016/j.tca.2012.06.017.

Möller, M., Cantow, H.-J., Drotloff, H., Emeis, D., Lee, K.-S., and Wegner, G. (1987). Phase transitions and defect structures in the lamellar surface of polyethylene and n-alkane crystallites. Magic angle spinning 13C NMR studies. Die Makromolekulare Chemie 187, 1237- 1252. doi: 10.1002/macp.1986.021870520.

Mondal, S. (2008). Phase change materials for smart textiles – An overview. Applied Thermal Engineering 28(11-12), 1536-1550. doi: 10.1016/j.applthermaleng.2007.08.009.

Morton, W.E., and S., H.J.W. (2008). "Tensile properties," in Physical properties of textile fibres, eds. J.W.S. Hearle & W.E. Morton. 4 ed (Cambridge, UK: Woodhead Publishing), 274–321.

Nguyen, L.T., Vu, C.M., Phuc, B.T., and Tung, N.H. (2019). Simultaneous effects of silanized coal fly ash and nano/micro glass fiber on fracture toughness and mechanical properties of carbon fiber-reinforced vinyl ester resin composites. Polymer Engineering & Science 59(3), 584-591. doi: 10.1002/pen.24973.

Nielsen, L.E., and Landel, R.F. (1994). Mechanical properties of polymers and composites, Second edition. New York: Marcel Dekker, Inc.

Nishizawa, N., Kawamura, A., Kohri, M., Nakamura, Y., and Fujii, S. (2016). Polydopamine Particle as a Particulate Emulsifier. Polymers (Basel) 8(3). doi: 10.3390/polym8030062.
Nouar, H., Petitjean, D., Bouroukba, M., and Dirand, M. (1998). Binary phase diagram of the system: *n*-docosane-*n*-tricosane. Journal of Molecular Structure 443, 197-204.
O'Brien, D.J., Baechle, D.M., and Wetzel, E.D. (2011). Design and performance of multifunctional structural composite capacitors. Journal of Composite Materials 45(26), 2797-2809. doi: 10.1177/0021998311412207.
Okazaki, M., and Toriyama, K. (1989). Alternation of spin-lattice relaxation-times for even and odd linear alkane crystals - a high-resolution solid-state NMR study. Journal of Physical Chemistry 93(8), 2883-2885. doi: 10.1021/j100345a007.
Oksman, K., and Sain, M. (2008). Wood-polymer composites. Cambridge (England): Woodhead Publishing Materials.
Osswald, T.A., and Rudolph, N. (2015). Polymer Rheology: Fundamentals and Applications. Munich, Germany: Carl Hanser Verlag.
Ostry, M., and Charvat, P. (Year). "Materials for advanced heat storage in buildings", in: 11th International Conference on Modern Building Materials, Structures and Techniques (MBMST 2013): Procedia Engineering), 837-843.
Outlast® (2018). Applying Outlast® technology to your line [Online]. Available: http://www.outlast.com/en/applications/ [Accessed 20 Sept 2019].
Pal, R. (2008). Thermal conductivity of three-component composites of core-shell particles. Materials Science and Engineering: A 498(1-2), 135-141. doi: 10.1016/j.msea.2007.10.123.
Palumbo, M., Donzella, G., Tempesti, E., Ferruti, P. (1996) On the Compressive Elasticity of Epoxy Resins Filled with Hollow Glass Microspheres. Journal of Applied Polymer Science 60 47-53. doi: 10.1002/(SICI)1097-4628(19960404)60:1<47::AID-APP6>3.0.CO;2-V
Papanikolaou, I., Arena, N., and Al-Tabbaa, A. (2019). Graphene nanoplatelet reinforced concrete for self-sensing structures – A lifecycle assessment perspective. Journal of Cleaner Production 240, 118202. doi: 10.1016/j.jclepro.2019.118202.
Park, J.-H., Oh, C., Shin, S.-I., Moon, S.-K., and Oh, S.-G. (2003). Preparation of hollow silica microspheres in W/O emulsions with polymers. Journal of Colloid and Interface Science 266(1), 107-114. doi: 10.1016/s0021-9797(03)00645-3.
Park, S.-J., Jin, F.-L., Lee, C. (2005), Preparation and physical properties of hollow glass microspheres-reinforced epoxy matrix resins. Materials Science and Engineering: A 402(1-2), 335-340. doi: 10.1016/j.msea.2005.05.015
Pegoretti, A., Cristelli, I., and Migliaresi, C. (2008). Experimental optimization of the impact energy absorption of epoxy-carbon laminates through controlled delamination. Composites Science and Technology 68(13), 2653–2662. doi: 10.1016/j.compscitech.2008.04.036.
Peng, H., Zhang, D., Ling, X., Li, Y., Wang, Y., Yu, Q., et al. (2018). n-Alkanes Phase Change Materials and Their Microencapsulation for Thermal Energy Storage: A Critical Review. Energy & Fuels 32(7), 7262-7293. doi: 10.1021/acs.energyfuels.8b01347.
Perna, G., Lasalvia, M., and Capozzi, V. (2016). Vibrational spectroscopy of synthetic and natural eumelanin. Polym. Int. 65, 1323-1330.
Petrucci, R., and Torre, L. (2017). "Filled Polymer Composites," in Modification of Polymer Properties, eds. C.F. Jasso-Gastinel & J.M. Kenny. (Chadds Ford, PA, USA: Elsevier), 23-46.
Pielichowska, K., and Pielichowski, K. (2014). Phase change materials for thermal energy storage. Progress in materials science 65, 67-123. doi: 10.1016/j.pmatsci.2014.03.005.
Pini, T., Briatico-Vangosa, F., Frassine, R., and Rink, M. (2015). "Effects of matrix viscoelasticity on interlaminar fracture toughness of acrylic/carbon fibre composites", in: 20th International Conference on Composite Materials. (Copenhagen).

Poslinski, A.J., Ryan, M.E., Gupta, R.K., Seshadri, S.G., and Frechette, F.J. (1988). Rheological behavior of filled polymeric systems. I. Yield stress and shear-thinning effects. Journal of Rheology 32(7), 703-735. doi: 10.1122/1.549987.

Poyyathappan, K., Bhaskar, G.B., Pazhanivel, K., and Venkatesan, N. (2014). Tensile and flexural studies on glass-carbon hybrid composites subjected to low frequency cyclic loading. International Journal of Engineering and Technology (IJET) 6(1), 83-90.

Proverbio, Z.E., Bardavid, S.M., Arancibi, E.L., and Schulz, P.C. (2003). Hydrophile-lipophile balance and solubility parameter of cationic surfactants. Colloids and Surfaces A: Physicochemical and Engineering Aspects 214, 167-171. doi: 10.1016/S0927-7757(02)00404-1.

Qin, P., Liao, M., Zhang, D., Liu, Y., Sun, J., and Wang, Q. (2019). Experimental and numerical study on a novel hybrid battery thermal management system integrated forced-air convection and phase change material. Energy Conversion and Management 195, 1371-1381. doi: 10.1016/j.enconman.2019.05.084.

Qureshi, Z.A., Ali, H.M., and Khushnood, S. (2018). Recent advances on thermal conductivity enhancement of phase change materials for energy storage system: A review. International Journal of Heat and Mass Transfer 127, 838-856. doi: 10.1016/j.ijheatmasstransfer.2018.08.049.

Rastgarkafshgarkolaei, R. (2014). Effect of the chain on thermal conductivity and thermal boundary conductance of long-chain n-alkanes using molecular dynamics and transient plane source techniques. Degree of Master of science. Graduate Faculty of Auburn University.

Resch-Fauster, K., and Feuchter, M. (2018). Thermo-physical characteristics, mechanical performance and long-term stability of high temperature latent heat storages based on paraffin-polymer compounds. Thermochimica Acta 663, 34-45. doi: 10.1016/j.tca.2018.03.004.

Resch-Fauster, K., Hengstberger, F., Zauner, C., and Holper, S. (2018). Overheating protection of solar thermal façades with latent heat storages based on paraffin-polymer compounds. Energy and Buildings 169, 254-259. doi: 10.1016/j.enbuild.2018.03.068.

Rezaei, F., Yunus, R., and Ibrahim, N.A. (2009). Effect of fiber length on thermomechanical properties of short carbon fiber reinforced polypropylene composites. Materials & Design 30(2), 260-263. doi: 10.1016/j.matdes.2008.05.005.

Rezaie, A.B., and Montazer, M. (2018). One-step fabrication of fatty acids/nano copper/polyester shape-stable composite phase change material for thermal energy management and storage. Applied Energy 228, 1911-1920. doi: 10.1016/j.apenergy.2018.07.041.

Risicato, J.-V., Kelly, F., Soulat, D., Legrand, X., Trümper, W., Cochrane, C., et al. (2014). A complex shaped reinforced thermoplastic composite part made of commingled yarns with integrated sensor. Applied Composite Materials 22(1), 81-98. doi: 10.1007/s10443-014-9400-9.

Roldán, M.L., Centeno, S.A., and Rizzo, A. (2014). An improved methodology for the characterization and identification of sepia in works of art by normal Raman and SERS, complemented by FTIR, Py-GC/MS, and XRF. J. Raman Spectrosc. 45, 1160-1171.

Rothon, R.N. (2003). Particulate-Filled Polymer Composites. Shawbury, Shrewsbury, Shropshire, SY4 4NR, UK: Rapra Technology Limited.

Rueda, M.M., Auscher, M.-C., Fulchiron, R., Périé, T., Martin, G., Sonntag, P., et al. (2017a). Rheology and applications of highly filled polymers: a review of current understanding. Progress in Polymer Science 66, 22-53. doi: 10.1016/j.progpolymsci.2016.12.007.

Rueda, M.M., Fulchiron, R., Martin, G., and Cassagnau, P. (2017b). Rheology of polypropylene filled with short-glass fibers: From low to concentrated filled composites. European Polymer Journal 93, 167-181. doi: 10.1016/j.eurpolymj.2017.05.025.

Ryu, J.H., Messersmith, P.B., and Lee, H. (2018). Polydopamine Surface Chemistry: A Decade of Discovery. ACS Appl Mater Interfaces 10(9), 7523-7540. doi: 10.1021/acsami.7b19865.
Safari, A., Saidur, R., Sulaiman, F.A., Xu, Y., and Dong, J. (2017). A review on supercooling of Phase Change Materials in thermal energy storage systems. Renewable and Sustainable Energy Reviews 70, 905-919. doi: 10.1016/j.rser.2016.11.272.
Sahoo, S.K., Das, M.K., and Rath, P. (2016). Application of TCE-PCM based heat sinks for cooling of electronic components: A review. Renewable and Sustainable Energy Reviews 59, 550-582. doi: 10.1016/j.rser.2015.12.238.
Salaün, F., Devaux, E., Bourbigot, S., and Rumeau, P. (2009). Influence of process parameters on microcapsules loaded with n-hexadecane prepared by in situ polymerization. Chemical Engineering Journal 55(1-2), 457-465.
Salonitis, K., Pandremenos, J., Paralikas, J., and Chryssolouris, G. (2010). Multifunctional materials: Engineering applications and processing challenges. International Journal of Advanced Manufacturing Technology 49(5-8), 803-826. doi: 10.1007/s00170-009-2428-6.
Sarı, A., and Karaipekli, A. (2007). Thermal conductivity and latent heat thermal energy storage characteristics of paraffin/expanded graphite composite as phase change material. Applied Thermal Engineering 27(8-9), 1271-1277. doi: 10.1016/j.applthermaleng.2006.11.004.
Sarier, N., and Onder, E. (2012). Organic phase change materials and their textile applications: An overview. Thermochimica Acta 540, 7-60. doi: 10.1016/j.tca.2012.04.013.
Scalat, S., Banu, D., Hawes, D., Paris, J., Haghighata, F., and Feldman, D. (1996). Full scale thermal testing of latent heat storage in wallboard. Solar Energy Materials and Solar Cells 44, 49-61.
Shanmugam, L., Feng, X., and Yang, J. (2019). Enhanced interphase between thermoplastic matrix and UHMWPE fiber sized with CNT-modified polydopamine coating. Composites Science and Technology 174, 212-220. doi: 10.1016/j.compscitech.2019.03.001.
Shao, J., Darkwa, J., and Kokogiannakis, G. (2015). Review of phase change emulsions (PCMEs) and their applications in HVAC systems. Energy and Buildings 94, 200–217. doi: 10.1016/j.enbuild.2015.03.003.
Sharma, R.K., Ganesan, P., Tyagi, V.V., Metselaar, H.S.C., and Sandaran, S.C. (2015). Developments in organic solid-liquid phase change materials and their applications in thermal energy storage. Energy Conversion and Management 95, 193-228. doi: 10.1016/j.enconman.2015.01.084.
Shen, R.Q., Hatanaka, L.C., Ahmed, L., Agnew, R.J., Mannan, M.S., and Wang, Q.S. (2017). Cone calorimeter analysis of flame retardant poly (methyl methacrylate)-silica nanocomposites. Journal of Thermal Analysis and Calorimetry 128(3), 1443-1451.
Sheng, N., Zhu, C., Sakai, H., Akiyama, T., and Nomura, T. (2019). Synthesis of Al-25 wt% Si@Al_2O_3@Cu microcapsules as phase change materials for high temperature thermal energy storage. Solar Energy Materials & Solar Cells 191, 141–147. doi: 10.1016/j.solmat.2018.11.013.
Shenoy, A.V. (1999). Rheology Of Filled Polymer Systems. P.O. Box 17, 3300 AA Dordrecht, The Netherlands.: Kluwer Academic Publishers.
Shirley, D.A. (1972). High-resolution X-ray photoemission spectrum of the valence bands of gold. Phys. Rev. B 5, 4709-4714.
Shokrieh, M.M., and Moshrefzadeh-Sani, H. (2016). On the constant parameters of Halpin-Tsai equation. Polymer 106, 14-20. doi: 10.1016/j.polymer.2016.10.049.
Silva, C., Simon, F., Friedel, P., Pötschke, P., and Zimmerer, C. (2019). Elucidating the chemistry behind the reduction of graphene oxide using a green approach with polydopamine. Nanomaterials 9(6), 902. doi: 10.3390/nano9060902.

Singh, S., Gaikwad, K.K., and Lee, Y.S. (2018). Phase change materials for advanced cooling packaging. Environmental Chemistry Letters 16(3), 845-859. doi: 10.1007/s10311-018-0726-7.
Snyder, J.F., Gienger, E.B., and Wetzel, E.D. (2015). Performance metrics for structural composites with electrochemical multifunctionality. Journal of Composite Materials 49(15), 1835-1848. doi: 10.1177/0021998314568167.
Sobolciak, P., Mrlík, M., Al-Maadeed, M.A., and Krupa, I. (2015). Calorimetric and dynamic mechanical behavior of phase change materials based on paraffin wax supported by expanded graphite. Thermochimica Acta 617, 111-119. doi: 10.1016/j.tca.2015.08.026.
Sobolciak, P., Karkri, M., Al-Maaded, M.A., and Krupa, I. (2016). Thermal characterization of phase change materials based on linear low-density polyethylene, paraffin wax and expanded graphite. Renewable Energy 88, 372-382. doi: 10.1016/j.renene.2015.11.056.
Socrates, G. (2001). Infrared and Raman Characteristic Group Frequencies: Tables and Charts. UK: Wiley.
Socrates, G. (2004). Infrared and Raman Characteristic Group Frequencies. Verlag, Weinheim, Germany: Wiley-VCH
Song, G., Ma, S., Tang, G., Yin, Z., and Wang, X. (2010). Preparation and characterization of flame retardant form-stable phase change materials composed by EPDM, paraffin and nano magnesium hydroxide. Energy 35(5), 2179-2183. doi: 10.1016/j.energy.2010.02.002.
Speight, R.J., Rourke, J.P., Wong, A., Barrow, N.S., Ellis, P.R., Bishop, P.T., et al. (2011). ^{1}H and ^{13}C solution- and solid-state NMR investigation into wax products from the Fischer-Tropsch process. Solid State Nuclear Magnetic Resonance 39(3-4), 58-64. doi: 10.1016/j.ssnmr.2011.03.008.
Sperling, L.H. (2006). Introduction to physical polymer science. Hoboken, New Jersey, US: Wiley.
Su, J.-F., Wang, X.-Y., Wang, S.-B., Zhao, Y.-H., Zhu, K.-Y., and Yuan, X.-Y. (2011a). Interface stability behaviors of methanol-melamine-formaldehyde shell microPCMs/epoxy matrix composites. Polymer Composites 32(5), 810-820. doi: 10.1002/pc.21102.
Su, J.-F., Wang, X.-Y., Huang, Z., Zhao, Y.-H., and Yuan, X.-Y. (2011b). Thermal conductivity of microPCMs-filled epoxy matrix composites. Colloid and Polymer Science 289(14), 1535-1542. doi: 10.1007/s00396-011-2478-9.
Su, J.-F., Zhao, Y.-H., Wang, X.-Y., Dong, H., and Wang, S.B. (2012). Effect of interface debonding on the thermal conductivity of microencapsulated-paraffin filled epoxy matrix composites. Composites Part a-Applied Science and Manufacturing 43(3), 325-332. doi: 10.1016/j.compositesa.2011.12.003.
Sudarisman, and Davies, I.J. (2008). Flexural failure of unidirectional hybrid fibre-reinforced polymer (FRP) composites Containing Different Grades of Glass Fibre. Advanced Materials Research 41-42, 357-362. doi: 10.4028/www.scientific.net/AMR.41-42.357.
Sun, N., and Xiao, Z. (2017). Synthesis and Performances of Phase Change Materials Microcapsules with a Polymer/BN/TiO_2 Hybrid Shell for Thermal Energy Storage. Energy Fuels 31(9), 10186–10195. doi: 10.1021/acs.energyfuels.7b01271.
Sun, G., Zu, F., Koch, N., Rappich, J., and Hinrichs, K. (2019a). In Situ Infrared Spectroscopic Monitoring and Characterization of the Growth of Polydopamine (PDA) Films. Phys. Status Solidi B 256, 1800308.
Sun, K., Liu, H., Wang, X., and Wu, D. (2019b). Innovative design of superhydrophobic thermal energy-storage materials by microencapsulation of n-docosane with nanostructured ZnO/SiO2 shell. Applied Energy 237, 549-565.
Sundararajan, S., Samui, A.B., and Kulkarni, P.S. (2017). Versatility of polyethylene glycol (PEG) in designing solid–solid phase change materials (PCMs) for thermal management and their application to innovative technologies. Journal of Materials Chemistry A 5(35), 18379-18396. doi: 10.1039/c7ta04968d.

Talreja, R., and Varna, J. (2015). Modeling Damage, Fatigue and Failure of Composite Materials. Sawston, Cambridge, UK: Woodhead Publishing Series in Composites Science and Engineering.
Tan, F.L., and Tso, C.P. (2004). Cooling of mobile electronic devices using phase change materials. Applied Thermal Engineering 24(2-3), 159-169. doi: 10.1016/j.applthermaleng.2003.09.005.
Tang, F., Liu, L., Alva, G., Jia, Y., and Fang, G. (2017). Synthesis and properties of microencapsulated octadecane with silica shell as shape–stabilized thermal energy storage materials. Solar Energy Materials and Solar Cells 160, 1-6. doi: 10.1016/j.solmat.2016.10.014.
Tang, Y., Dong, W., Tang, L., Zhang, Y., Kong, J., and Gu, J. (2018). Fabrication and investigations on the polydopamine/KH-560 functionalized PBO fibers/cyanate ester wave-transparent composites. Composites Communications 8, 36-41. doi: 10.1016/j.coco.2018.03.006.
Thakre, P.R., Lagoudas, D.C., Riddick, J.C., Gates, T.S., Frankland, S.-J.V., Ratcliffe, J.G., et al. (2011). Investigation of the effect of single wall carbon nanotubes on interlaminar fracture toughness of woven carbon fiber—epoxy composites. Journal of Composite Materials 45(10), 1091-1107. doi: 10.1177/0021998310389088.
Thomasset, J., Carreau, P.J., Sanschagrin, B., and Ausias, G. (2005). Rheological properties of long glass fiber filled polypropylene. Journal of Non-Newtonian Fluid Mechanics 125(1), 25-34. doi: 10.1016/j.jnnfm.2004.09.004.
Tian, Z., Li, Y., Zheng, J., and Wang, S. (2019). A state-of-the-art on self-sensing concrete: Materials, fabrication and properties. Composites Part B: Engineering 177, 107437. doi: 10.1016/j.compositesb.2019.107437.
Tomizawa, Y., Sasaki, K., Kuroda, A., Takeda, R., and Kaito, Y. (2016). Experimental and numerical study on phase change material (PCM) for thermal management of mobile devices. Applied Thermal Engineering 98, 320-329. doi: 10.1016/j.applthermaleng.2015.12.056.
Tong, X.-M., Zhang, M., Wang, M.-S., and Fu, Y. (2013). Effects of surface modification of self-healing poly(melamine-urea-formaldehyde) microcapsules on the properties of unsaturated polyester composites. Journal of Applied Polymer Science 127(5), 3954-3961. doi: 10.1002/app.37711.
Tyagi, V.V., Kaushik, S.C., Tyagi, S.K., and Akiyama, T. (2011). Development of phase change materials based microencapsulated technology for buildings: A review. Renewable and Sustainable Energy Reviews 15(2), 1373-1391. doi: 10.1016/j.rser.2010.10.006.
Umair, M.M., Zhang, Y., Iqbal, K., Zhang, S., and Tang, B. (2019). Novel strategies and supporting materials applied to shape-stabilize organic phase change materials for thermal energy storage–A review. Applied Energy 235, 846-873. doi: 10.1016/j.apenergy.2018.11.017.
Ünal, M., Konuklu, Y., and Paksoy, H. (2019). Thermal buffering effect of a packaging design with microencapsulated phase change material. International Journal of Energy Research 43(9), 4495-4505. doi: 10.1002/er.4578.
Vasta, S., Brancato, V., La Rosa, D., Palomba, V., Restuccia, G., Sapienza, A., et al. (2018). Adsorption Heat Storage: State-of-the-Art and Future Perspectives. Nanomaterials (Basel) 8(7). doi: 10.3390/nano8070522.
Wang, S., Tozaki, K., Hayashi, H., Hosaka, S., and Inaba, H. (2003). Observation of multiple phase transitions in *n*-$C_{22}H_{46}$ using a high resolution and super-sensitive DSC. Thermochimica Acta 408(1-2), 31-38. doi: 10.1016/s0040-6031(03)00312-5.
Wang, L.Y., Tsai, P.S., and Yang, Y.M. (2006). Preparation of silica microspheres encapsulating phase-change material by sol-gel method in O/W emulsion. J Microencapsul 23(1), 3-14. doi: 10.1080/02652040500286045.
Wang, R., Li, H., Hu, H., He, X., and Liu, W. (2009). Preparation and characterization of self-healing microcapsules with poly(urea-formaldehyde) grafted epoxy functional group

shell. Journal of Applied Polymer Science 113(3), 1501-1506. doi: 10.1002/app.30001.
Wang, R., Li, H., Liu, W., and He, X. (2010). Surface Modification of Poly(urea-formaldehyde) Microcapsules and the Effect on the Epoxy Composites Performance. Journal of Macromolecular Science, Part A 47(10), 991-995. doi: 10.1080/10601325.2010.507982.
Wang, R., Zheng, S., and Zheng, Y. (2011a). Polymer Matrix Composites and Technology. Beijing, China: Woodhead Publishing - Science Press Limited.
Wang, X.-Y., Su, J.-F., Wang, S.-B., and Zhao, Y.-H. (2011b). The effect of interface debonding behaviors on the mechanical properties of microPCMs/epoxy composites. Polymer Composites 32(9), 1439-1450. doi: 10.1002/pc.21174.
Wang, Q., and Zhao, C.Y. (2015). Parametric investigations of using a PCM curtain for energy efficient buildings. Energy and Buildings 94, 33-42. doi: 10.1016/j.enbuild.2015.02.024.
Wang, F., Zhang, C., Liu, J., Fang, X., and Zhang, Z. (2017). Highly stable graphite nanoparticle-dispersed phase change emulsions with little supercooling and high thermal conductivity for cold energy storage. Applied Energy 188, 97–106. doi: 10.1016/j.apenergy.2016.11.122.
Wang, L., Yan, L., and Gao, X. (2018). Effect of electron beam irradiation on polydopamine and its application in polymer solar cells. Int J Energy Res. 42, 3496-3505.
Wang, F., Lin, W., Ling, Z., and Fang, X. (2019). A comprehensive review on phase change material emulsions: Fabrication, characteristics, and heat transfer performance. Solar Energy Materials & Solar Cells 191(218–234). doi: 10.1016/j.solmat.2018.11.016.
Wang, D., Sui, J., Qi, D., Wei, Y., Wang, X., and Lan, X.Z. (2019a). Phase transition of docosane in nanopores. Journal of Thermal Analysis and Calorimetry 135(5), 2869-2877. doi: 10.1007/s10973-018-7267-y.
Weiss, S., Urdl, K., Mayer, H.A., Zikulnig-Rusch, E.M., and Kandelbauer, A. (2019). IR spectroscopy: Suitable method for determination of curing degree and crosslinking type in melamine–formaldehyde resin. J. Appl. Polymer Sci. 136(25), 47691/47691-47691/47610. doi: 10.1002/APP.47691.
Wirtz, R., Fuchs, A., Narla, V., Shen, Y., Zhao, T., and Jiang, Y. (Year). "A Multi-functional graphite/epoxy-based thermal energy storage composite for temperature control of sensors and electronics"), 1-9.
Wu, C.-S. (2009). Renewable resource-based composites of recycled natural fibers and maleated polylactide bioplastic: Characterization and biodegradability. Polymer Degradation and Stability 94(7), 1076-1084. doi: 10.1016/j.polymdegradstab.2009.04.002.
Wu, W., Wu, W., and Wang, S. (2019). Form-stable and thermally induced flexible composite phase change material for thermal energy storage and thermal management applications. Applied Energy 236, 10-21. doi: 10.1016/j.apenergy.2018.11.071.
Xia, Y., Zhang, H., Huang, P., Huang, C., Xu, F., Zou, Y., et al. (2019). Graphene-oxide-induced lamellar structures used to fabricate novel composite solid-solid phase change materials for thermal energy storage. Chemical Engineering Journal 362, 909-920. doi: 10.1016/j.cej.2019.01.097.
Xie, N., Luo, J., Li, Z., Huang, Z., Gao, X., Fang, Y., et al. (2019). Salt hydrate/expanded vermiculite composite as a form-stable phase change material for building energy storage. Solar Energy Materials and Solar Cells 189, 33-42. doi: 10.1016/j.solmat.2018.09.016.
Yoo, S., Kandare, E., Shanks, R., Al-Maadeed, M.A., and Afaghi Khatibi, A. (2016). Thermophysical Properties of Multifunctional Glass Fibre Reinforced Polymer Composites Incorporating Phase Change Materials. Thermochimica Acta 642, 25-31. doi: 10.1016/j.tca.2016.09.003.
Yoo, S., Kandare, E., Mahendrarajah, G., Al-Maadeed, M.A., and Khatibi, A.A. (2017a). Mechanical and thermal characterisation of multifunctional composites incorporating

phase change materials. Journal of Composite Materials 51(18), 2631-2642. doi: 10.1177/0021998316673894.
Yoo, S., Kandare, E., Shanks, R., and Khatibi, A.A. (2017b). "Viscoelastic characterization of multifunctional composites incorporated with microencapsulated phase change materials ", in: International Conference of Materials Processing and Characterization (ICPMC), ed. Elsevier).
Yu, S., Wang, X., and Wu, D. (2014). Microencapsulation of n-octadecane phase change material with calcium carbonate shell for enhancement of thermal conductivity and serving durability: Synthesis, microstructure, and performance evaluation. Applied Energy 114, 632-643. doi: 10.1016/j.apenergy.2013.10.029.
Yu, G.-C., Wu, L.-Z., and Feng, L.-J. (2015). Enhancing the thermal conductivity of carbon fiber reinforced polymer composite laminates by coating highly oriented graphite films. Materials & Design 88, 1063-1070. doi: 10.1016/j.matdes.2015.09.096.
Yuan, W., Yang, X., Zhang, G., and Li, X. (2018). A thermal conductive composite phase change material with enhanced volume resistivity by introducing silicon carbide for battery thermal management. Applied Thermal Engineering 144, 551-557. doi: 10.1016/j.applthermaleng.2018.07.095.
Zalba, B., Marin, J.M., Cabeza, L.F., and Mehling, H. (2003). Review on thermal energy storage with phase change: materials, heat transfer analysis and applications. Applied Thermal Engineering 23, 251-283. doi: 10.1016/S1359-4311(02)00192-8.
Zhang, X.X., Wang, X.C., Tao, X.M., and Yick, K.L. (2005). Energy storage polymer/MicroPCMs blended chips and thermo-regulated fiber. Journal of Materials Science 40, 3729– 3734. doi: 10.1007/s10853-005-3314-8.
Zhang, H., Wang, X., and Wu, D. (2010a). Silica encapsulation of n-octadecane via sol-gel process: a novel microencapsulated phase-change material with enhanced thermal conductivity and performance. J Colloid Interface Sci 343(1), 246-255. doi: 10.1016/j.jcis.2009.11.036.
Zhang, P., Hu, Y., Song, L., Ni, J., Xing, W., and Wang, J. (2010b). Effect of expanded graphite on properties of high-density polyethylene/paraffin composite with intumescent flame retardant as a shape-stabilized phase change material. Solar Energy Materials and Solar Cells 94(2), 360-365. doi: 10.1016/j.solmat.2009.10.014.
Zhang, P., Song, L., Lu, H., Wang, J., and Hu, Y. (2010c). The influence of expanded graphite on thermal properties for paraffin/high density polyethylene/chlorinated paraffin/antimony trioxide as a flame retardant phase change material. Energy Conversion and Management 51(12), 2733-2737. doi: 10.1016/j.enconman.2010.06.009.
Zhang, D. (2014). Advances in filament yarn spinning of textiles and polymers. Cambridge, UK: Woodhead Publishing.
Zhang, J., Zhang, H.-H., He, Y.-L., and Tao, W.-Q. (2016). A comprehensive review on advances and applications of industrial heat pumps based on the practices in China. Applied Energy 178, 800-825. doi: 10.1016/j.apenergy.2016.06.049.
Zhang, Q., and Liu, J. (2019). Anisotropic thermal conductivity and photodriven phase change composite based on RT100 infiltrated carbon nanotube array. Solar Energy Materials and Solar Cells 190, 1-5. doi: 10.1016/j.solmat.2018.10.010.
Zhao, C.Y., and Zhang, G.H. (2011). Review on microencapsulated phase change materials (MEPCMs): Fabrication, characterization and applications. Renewable and Sustainable Energy Reviews 15(8), 3813-3832. doi: 10.1016/j.rser.2011.07.019.
Zhong, Y., Guo, Q., Li, S., Shi, J., and Liu, L. (2010). Heat transfer enhancement of paraffin wax using graphite foam for thermal energy storage. Solar Energy Materials and Solar Cells 94(6), 1011-1014. doi: 10.1016/j.solmat.2010.02.004.
Zhu, K., Li, X., Su, J., Li, H., Zhao, Y., and Yuan, X. (2018). Improvement of anti-icing properties of low surface energy coatings by introducing phase-change microcapsules. Polymer Engineering & Science 58(6), 973-979. doi: 10.1002/pen.24654.

Zou, D., Liu, X., He, R., Zhu, S., Bao, J., Guo, J., et al. (2019). Preparation of a novel composite phase change material (PCM) and its locally enhanced heat transfer for power battery module. Energy Conversion and Management 180, 1196-1202. doi: 10.1016/j.enconman.2018.11.064.

Scientific production

Publications on peer-reviewed journals

[1] Fredi G., Dorigato A., Fambri L., Pegoretti A.: Wax confinement with carbon nanotubes for phase changing epoxy blends. Polymers, **9**, 405/1-405/16 (2017). https://doi.org/10.3390/polym9090405

[2] Fredi G., Dorigato A., Fambri L., Pegoretti A.: Multifunctional epoxy/carbon fiber laminates for thermal energy storage and release. Composites Science and Technology, **158**, 101-111 (2018). https://doi.org/10.1016/j.compscitech.2018.02.005

[3] Fredi G., Dorigato A., Pegoretti A.: Multifunctional glass fiber/polyamide composites with thermal energy storage/release capability. eXPRESS polymer letters, **12**, 349-364 (2018). https://doi.org/10.3144/expresspolymlett.2018.30

[4] Dorigato A., Fredi G., Negri M., Pegoretti A.: Thermo-mechanical behaviour of novel wood laminae-thermoplastic starch biodegradable composites with thermal energy storage/release capability. Frontiers in Materials, **6**, 1-12 (2019). https://doi.org/10.3389/fmats.2019.00076

[5] Dorigato A., Fredi G., Pegoretti A.: Application of the thermal energy storage concept to novel epoxy/short carbon fiber composites. Journal of applied polymer science, **136**, 47434/1-47434/9 (2019). https://doi.org/10.1002/app.47434

[6] Fredi G., Brünig H., Vogel R., Scheffler C.: Melt-spun polypropylene filaments containing paraffin microcapsules for multifunctional hybrid yarns and smart thermoregulating thermoplastic composites. EXPRESS polymer letters, **13**, 1071–1087 (2019). https://doi.org/10.3144/expresspolymlett.2019.93

[7] Fredi G., Dirè S., Callone E., Ceccato R., Mondadori F., Pegoretti A.: Docosane-organosilica microcapsules for structural composites with thermal energy storage/release capability. Materials, **12**, 1286/1-1286/26 (2019). https://doi.org/10.3390/ma12081286

[8] Fredi G., Dorigato A., Pegoretti A.: Novel reactive thermoplastic resin as a matrix for laminates containing phase change microcapsules. Polymer Composites, **40**, 3711-3724 (2019). https://doi.org/10.1002/pc.25233

[9] Fredi G., Dorigato A., Unterberger S., Artuso N., Pegoretti A.: Discontinuous carbon fiber/polyamide composites with microencapsulated paraffin for thermal energy storage. Journal of applied polymer science, **136**, 47408/1-47408/14 (2019). https://doi.org/10.1002/app.47408

[10] Pegoretti A., Fredi G.: Editorial corner - A personal view. Thermal management with polymer composites. Express Polymer Letters, **13**, 844-844 (2019). https://doi.org/10.3144/expresspolymlett.2019.73

[11] Fredi G., Dorigato A., Pegoretti A.: Dynamic-mechanical response of carbon fiber laminates with a reactive thermoplastic resin containing phase change microcapsules. Mechanics of Time-Dependent Materials, (In Press). https://doi.org/10.1007/s11043-019-09427-y

[12] Fredi G., Dorigato A., Fambri L., Pegoretti A.: Detailed experimental and theoretical investigation of the thermo-mechanical properties of epoxy composites containing paraffin microcapsules for thermal management Polymer Engineering and Science (In Press). https://doi.org/10.1002/PEN.25374
[13] Fredi G., Simon F., Sychev D., Melnyk I., Scheffler C., Zimmerer C.: Bioinspired polydopamine coating as adhesion enhancer between paraffin microcapsules and an epoxy matrix. ACS Omega (Submitted).
[14] Fredi G., Dorigato A., Fambri L., Pegoretti A.: Effect of phase change microcapsules on the thermo-mechanical, fracture and heat storage properties of unidirectional carbon/epoxy laminates. Polymer Testing (Submitted).

Publications on conference proceedings

[1] Dorigato A., Fredi G., Meneghini T., Pegoretti A. *Thermo-mechanical behaviour of thermoplastic composite laminates with thermal energy storage/release capability* in *ECCM 2018 - 18th European Conference on Composite Materials*. 2018.
[2] Dorigato A., Fredi G., Pegoretti A. *Novel phase change materials using thermoplastic composites*. in *AIP Conference Proceedings of the 9th International Conference "Times of Polymers and Composites" (TOP)*. 2018. https://doi.org/10.1063/1.5045906
[3] Fredi G., Dirè S., Dorigato A., Fambri L., Pegoretti A. *Multifunctional carbon fiber/epoxy laminates for thermal energy storage and release* in *ECCM 2018 - 18th European Conference on Composite Materials*. 2018. Athens, Greece.
[4] Fredi G., Dorigato A., Fambri L., Pegoretti A. *Multifunctional polymer composites reinforced with discontinuous carbon fibers for thermal energy storage*. in *ECCM 2018 - 18th European Conference on Composite Materials*. 2018.
[5] Fredi G., Dorigato A., Fambri L., Pegoretti A. *Thermal Energy Storage with Polymer Composites*. in *American Society for Composites 2019 - Thirty-Fourth Technical Conference* 2019. Atlanta, GA, US. https://doi.org/10.12783/asc34/31370

Participation to Congresses, Schools and Workshops

Oral presentations at national or international conferences

[1] G. Fredi, A. Dorigato, and A. Pegoretti, "Reactive thermoplastic resin as a matrix for laminates containing microencapsulated phase change materials", 22nd International Conference on Composite Materials (ICCM22), Melbourne, Australia, 11-16 August 2019.

[2] G. Fredi, S. Dirè, E. Callone, R. Ceccato R., F. Mondadori, A. Pegoretti, "Microencapsulation of docosane in organosilica shells for structural composites with thermal energy storage capability", XII INSTM Conference-XV AIMAT Conference, Ischia (NA), Italy, July 21-24, 2019.

[3] G. Fredi, A. Dorigato, A. Pegoretti, "Thermoplastic acrylic laminates containing microencapsulated paraffin for thermal energy storage (TES)", Conference of Associazione Italiana Macromolecole (AIM2018), Catania, Italy, 9-12 September 2018.

[4] G. Fredi, A. Dorigato, L. Fambri and A. Pegoretti, "Flexural quasi-static and dynamic-mechanical behavior of multifunctional epoxy/carbon composites incorporating CNT-confined phase change materials", Mechanics of Time Dependent Materials (MTDM2018), Milan, Italy, 4-7 September 2018.

[5] G. Fredi, A. Dorigato, L. Fambri, and A. Pegoretti, "Multifunctional polymer composites reinforced with discontinuous carbon fibers for thermal energy storage", European Conference on Composite Materials (ECCM2018), Athens, Greece, 24-28 June 2018.

[6] G. Fredi, A. De Col, A. Dorigato, J.-M. Lopez-Cuesta, L. Fambri and A. Pegoretti, "Combined Effect of Fumed Silica and Metal Hydroxides as Fire Retardants in PE Single-Polymer Composites", TOP Conference, Ischia, Italy, 17-21 June 2018.

[7] G. Fredi, A. De Col, A. Dorigato, J.-M. Lopez-Cuesta, L. Fambri and A. Pegoretti, "Study of the synergistic effect of metal hydroxides and fumed silica as flame retardants in polyethylene-based single-polymer composites", Macrogiovani 2018, Salerno, Italy, 14-15 June 2018. Oral presentation.

[8] G. Fredi, A. Dorigato, L. Fambri, A. Pegoretti, "Multifunctional Polymer Composites With Structural Function And Thermal Energy Storage (TES) Capability", 12th International Renewable Energy Storage (IRES 2018), Düsseldorf, Germany, 13-15 March 2018.

[9] G. Fredi, A. Dorigato, A. Pegoretti, "Thermoplastic structural composites with thermal energy storage/release capability", Associazione Italiana Ingegneria dei Materiali (AIMAT2017) Congress, Ischia (NA), Italy, 12-15 July 2017.

[10] G. Fredi, A. Dorigato, L. Fambri, A. Pegoretti, "Development of structural composites with thermal energy storage capability", Macrogiovani 2017, Trento, Italy 22-23 July 2017. Award for the best oral and poster presentation.

Poster presentations at national or international conferences

[1] G. Fredi, A. Dorigato, A. Pegoretti, "Reactive thermoplastic resin as a matrix for multifunctional laminates for thermal energy storage", European Polymer Federation congress (EPF2019), Athens, Greece, 9-15 June 2019.
[2] G. Fredi, A. Dorigato, L. Fambri, A. Pegoretti, "Multifunctional structural composites for thermal energy storage", Milan Polymer Days (MIPOL2018), Milano, Italy, 14-16 February 2018.
[3] G. Fredi, A. Dorigato, L. Fambri, A. Pegoretti, "Development of structural composites with thermal energy storage capability", European Polymer Federation congress (EPF2017), Lyon, France, 2-7 July 2017.

Summer schools

International Summer School "Materials for Industry"
University of Brescia, Department of Mechanical and Industrial Engineering
Brescia, Italy, 18-22 September 2017

Workshops

BeWISE Women in Science and Engineering
Technical University Dresden
Dresden, Germany, 4-8 November 2018

Side research activities

- Study of the synergistic effects of metal hydroxides and fumed nanosilica as fire retardants for polyethylene and preparation and characterization of flame-resistant polyethylene-based single polymer laminates.

- Thermomechanical characterization of epoxy composites containing vulcanized and partially devulcanized ground rubber derived from tire recycling.

- Surface modification of natural fibers (basalt, jute, flax) via thermal- and silane treatment to improve the adhesion with polymer matrices and the mechanical and aging properties of the resulting composites.

- Properties of carboxymethylcellulose films containing nanoclays for active wound dressing: characterization of the microstructural, thermal and mechanical properties.

Scientific production from the side research activities

[1] Dorigato A., Fredi G., Fambri L., Lopez-Cuesta J.-M., Pegoretti A.: Polyethylene-based single polymer laminates: synergistic effects of nanosilica and metal hydroxides. Journal of reinforced plastics and composites, **38**, 62-73 (2019). https://doi.org/10.1177/0731684418802974

[2] Fredi G., Dorigato A., Fambri L., Lopez-Cuesta J.-M., Pegoretti A.: Synergistic effects of metal hydroxides and fumed nanosilica as fire retardants for polyethylene. Flame Retardancy and Thermal Stability of Materials, **2**, 30-48 (2019). https://doi.org/10.1515/flret-2019-0002

[3] Fredi G., De Col A., Dorigato A., Lopez-Cuesta J.-M., Fambri L., Pegoretti A. *Combined effect of fumed silica and metal hydroxides as fire retardants in PE single-polymer composites*. in *9th International Conference on "Times of Polymers and Composites". AIP Conference Proceedings.* 2018. https://doi.org/10.1063/1.5045883

Acknowledgements

The completion of this PhD thesis would not have been possible without the help and support I received from many people.

I would like to express my gratitude my supervisors, Prof. Alessandro Pegoretti and Prof. Luca Fambri, for the possibility to carry out research in their group, and for their technical knowledge, patience and guidance in these years. I would like to thank them also for the chance to work independently and for their availability when I needed the most. I would like to acknowledge the reviewers of this thesis, Prof. Leif E. Asp and Prof. Miroslav Šlouf, for their valuable comments that led to a significant improvement of the initial manuscript.

I wish to express my sincere gratitude to Prof. Andrea Dorigato, for his constant advice, motivation and availability to discuss with me about every result, but also for showing me the passion and effort he puts in his work every day: this is not “only a job” for him, and this is crystal clear for everyone has the luck to share a good amount of work with him. My sincere thanks also goes to Alfredo Casagranda and Claudia Gavazza, the technicians of the laboratory of Polymers and Composites: thank you for your expertise, your patience, and your help during my research. I kindly thank the other professors and technicians of the Department of Industrial Engineering who collaborated with me, shared their knowledge, and gave me their support on some experimental activities. I would like to thank especially Prof. Sandra Dirè, Prof. Riccardo Ceccato, Dr. Emanuela Callone, Prof. Devid Maniglio, Mr. Lorenzo Moschini and Mr. Luca Benedetti.

Special acknowledgements are also due to the professors and technicians of other departments and institutions, who helped me with some research activities. I would like to thank Dr. Lia Vanzetti (FBK, Trento), Prof. José-Marie Lopez-Cuesta (Ecole des Mines d'Alès), Prof. Maurizio Grigiante (DICAM, University of Trento), and Dr. Seraphin Unterberger (Universität Innsbruck).

I wish to express my gratitude to all my colleagues and friends of the Laboratory of Polymers and Composites: thank you Haroon, Prumnea, Daniele, Francesco, and Francesco, for the stimulating scientific discussions and for the fun-time we spent together. I thank all the other PhD students of DII Unitn who I had the chance to meet in the office, in the laboratories or in the lunchroom: thank you for sharing part of your PhD path with me and for making coffee- and lunch-breaks special. I wish to thank also all the Bachelor and Master students that carried out their thesis research in the Laboratory of Polymers and Composites. I especially thank those who worked with me and honored me by putting my name on their thesis as the co-supervisor: thank you Tiziano, Nicolò, Andrea, Federico, Roberto, Francesco, Lorenzo, Giada, and Nicola.

I gratefully acknowledge the German Academic Exchange Service (Deutscher Akademischer Austauschdienst, DAAD) for giving me a grant to spend six months of my PhD research at the Leibniz Institute for Polymer Research (Dresden, Germany), which was a truly enriching experience from the professional and personal point of view and gave me the opportunity to establish many fruitful collaborations. I wish to express my gratitude to Dr. Christina Scheffler, who gave me the chance to join her research group during these months and made me feel part of the group from day one. I also kindly thank the other researchers of the group (Ms. Alma Rothe, Mr. Matthias Krüger, Ms. Janett Hiller, Mr. Enrico Wölfel, Mr. Robert Backes, Ms. Steffi Preßler, Ms. Sabine Krause) for their personal and professional support and their patience with my poor German skills (aber mein Deutsch verbessert sich!). Additionally, I would like to thank Dr. Harald Brünig, Dr. Roland Vogel, Ms. Nicole Schneider, and Mr. Holger Scheibner for their support to some experimental activity. I am also grateful to Dr. Cordelia Zimmerer for her enthusiasm and valuable advice during the research on polydopamine deposition.

My special gratitude is due to my family: I thank heartfully my parents Anna and Tiziano, my brother Francesco, and my grandparents Gino and Teresa for their endless support, trust, and encouragement for every goal I decide to chase.

Devo un ringraziamento particolare alla mia famiglia: ringrazio di cuore i miei genitori Anna e Tiziano, mio fratello Francesco e i miei nonni Gino e Teresa per il loro infinito supporto, la loro fiducia e il loro incoraggiamento per ogni obiettivo che decido di perseguire.

Lastly, I wish to express my gratitude to Michele for his love, support, patience and understanding he demonstrates me every day. Thank you for making me happy, for being with me each day and for being sincerely invested in my life and interests.